The variability of the Strombolian activity

Viviane Souty

▶ **To cite this version:**

Viviane Souty. The variability of the Strombolian activity. Earth Sciences. Université Sorbonne - Paris Cité, 2018. English. NNT : . tel-02458676

HAL Id: tel-02458676
https://hal.science/tel-02458676

Submitted on 28 Jan 2020

HAL is a multi-disciplinary open access archive for the deposit and dissemination of scientific research documents, whether they are published or not. The documents may come from teaching and research institutions in France or abroad, or from public or private research centers.

L'archive ouverte pluridisciplinaire **HAL**, est destinée au dépôt et à la diffusion de documents scientifiques de niveau recherche, publiés ou non, émanant des établissements d'enseignement et de recherche français ou étrangers, des laboratoires publics ou privés.

UNIVERSITÉ SORBONNE PARIS CITÉ

Université Sorbonne Paris Cité

Thèse préparée
à l'INSTITUT DE PHYSIQUE DU GLOBE DE PARIS
École doctorale STEP'UP - ED N°560
IPGP - Équipe de Dynamique des Fluides Géologiques

The variability of the Strombolian activity

par
Viviane Souty

présentée et soutenue publiquement le
29 Novembre 2018

Thèse de doctorat des Sciences de la Terre et de l'Environnement
dirigée par Sylvie Vergniolle

devant un jury composé de :

Wayne Crawford	Membre
Directeur de recherche (IPGP)	
Philippe Lesage	Membre
Maître de conférences (CNRS, ISTerre)	
Andrew Harris	Rapporteur
Professeurs des universités (OPGC, UCA)	
Alexis Le Pichon	Rapporteur
Directeur de recherche (CEA)	
Nicole Métrich	Membre
Directeur de recherche (CNRS, IPGP)	
Sylvie Vergniolle	Directrice de thèse
Directeur de recherche (CNRS, IPGP)	

Yasur, 12/09/2016, 17:47 (local) ©V. Souty

Résumé

L'activité strombolienne, caractérisée par des séries de petites explosions, existe dans le monde entier et dans divers contextes tectoniques. La variabilité de l'activité Strombolienne est observée à l'échelle mondiale et à l'échelle d'un édifice volcanique. Deux études multi-disciplinaires, traitant de nombreuses données avec des programmes MatLab semi-automatiques, nous ont permis de caractériser cette variabilité de l'activité strombolienne.

Une étude thermo-infrasonique à l'Erta'Ale (Éthiopie ; 5 jours en mars 2003), au Piton de la Fournaise (Ile de la Réunion, France ; 4 jours en déc. 2006) et au Yasur (Ile de Tanna, Vanuatu ; 13 jours en juin 2009 et 52 jours en sept.-nov. 2016) a permis de quantifier les limites de l'activité Strombolienne à partir de nombreux paramètres tels que l'amplitude infrasonique (1–2300 Pa à 100 m), les énergies thermiques (2–3.6×10^6 J) et infrasoniques (1.8×10^1–3.8×10^8 J), les vitesses des gaz (<240 $m.s^{-1}$) et des éjecta (<85 $m.s^{-1}$) ou encore le volume de gaz (1.3×10^2–2.3×10^4 m^3) par explosion. Le bilan énergétique thermo-infrasonique valide l'existence d'un mécanisme unique de fragmentation pour l'activité strombolienne de faible à forte intensité. Nous montrons aussi que l'activité strombolienne, souvent persistante émet des gros flux de gaz ($\sim 2.8 \times 10^2$–2.8×10^3 $m^3.s^{-1}$) qui peuvent interagir avec l'atmosphère. Cette étude a été élargie en intégrant 16 autres volcans à partir de données trouvées dans la littérature. Cela nous a permis de caractériser l'activité faible et forte à partir des paramètres infrasoniques, notamment l'amplitude infrasonique (faible : <20 Pa ; forte : >400 Pa à 100 m) et l'énergie infrasonique (faible : $<2 \times 10^4$ J ; forte : $>6 \times 10^6$ J).

Des données infrasoniques, sismiques et thermiques acquises pendant deux missions de terrain au Yasur (∼70 jours en cumulé) montrent la variabilité temporelle de l'activité Strombolienne. L'analyse de 34 phases d'activité, délimitées par le taux d'explosions et l'amplitude infrasonique, la relation sismo-infrasonique de ses phases et la distribution, par phases, des temps de repos et des volumes de gaz par explosions révèlent la coexistence de deux mécanismes de formation des bulles : i) la coalescence progressive, mécanisme persistant dans le conduit génère de petites explosions (<340 Pa à 100 m) et ii) la coalescence massive, mécanisme intermittent au toit du réservoir génère de plus grosses explosions (>340 Pa à 100 m). La coalescence massive au toit du réservoir existe pour un flux de gaz critique de 420 $m^3.s^{-1}$ au delà duquel la mousse de gaz au toit du réservoir devient instable. Cette valeur critique permet d'estimer un diamètre des bulles dans le réservoir (13–14 µm) qui est plus faible que les valeurs données pour d'autres systèmes basaltiques (Etna, Italie ; Kilauea, USA ; Erta'Ale, Éthiopie) mais qui reste supérieur à la taille des bulles à la nucléation.

Abstract

Strombolian activity, characterised by series of small explosions at open-vent volcanoes, exists worldwide in various tectonic contexts. The variability of the Strombolian activity can be observed on a global scale and on the scale of a volcanic system. We performed two multidisciplinary studies, processing numerous data with semi-automatic programs on MatLab, to characterise the variability of the Strombolian activity.

A thermo-infrasonic study at Erta'Ale (Ethiopia; 5 days in March 2003), Piton de la Fournaise (Réunion Island, France; 4 days in Dec. 2006) and Yasur (Tanna Island, Vanuatu; 13 days in June 2009 and 52 days in Sept.-Nov. 2016) provide the boundaries of the Strombolian activity from numerous parameters such as infrasonique amplitudes (1–2300 Pa at 100 m), thermal (2–3.6×10^6 J) and infrasonic (1.8×10^1–3.8×10^8 J) energies, gas (<240 m.s^{-1}) and ejecta (<85 m.s^{-1}) velocities or gas volume (1.3×10^2–2.3×10^4 m^3) per explosion. The thermo-infrasonic energy budget suggests that a sole mechanism of fragmentation exists for all Strombolian explosions regardless of their strength. The Strombolian activity, often persistent, produces large gas flux ($\sim 2.8 \times 10^2$–2.8×10^3 m^3.s^{-1}) that can interact with the atmosphere. This study was extrapolated to 16 other volcanoes from data found in the litterature. We therefore can characterised the weak and strong Strombolian activity from infrasonic parameters, especially infrasonic amplitude (weak: <20 Pa; strong: >400 Pa at 100 m) and infrasonic energy (weak: $<2 \times 10^4$ J; strong: $>6 \times 10^6$ J).

Infrasonic, seismic and thermal measurements during two field campaigns at Yasur ($\sim$70 days) show the temporal variability of the Strombolian activity. The analysis of 34 phases of activity, delimited by the rate of explosions and the infrasonic amplitude per explosion, the sismo-infrasonic relationship of these phases and the distribution per phase of the return time and gas volume of explosions highlighted the coexistence of two mechanims for the bubble formation: i) the progressive coalescence, persistent in the conduit triggers small explosions (<340 Pa à 100 m) and ii) the massive coalescence, intermittent at the top of the reservoir triggers strong explosions (>340 Pa à 100 m). The massive coalescence exists, when the critical gas flux (420 m^3.s^{-1}), above which the foam layer at the top of the reservoir becomes unstable, is exceeded. This critical value of the gas flux can be used to estimate the bubble diameter in the reservoir (13–14 µm) and gave smaller values than values obtained at other basaltic systems (Etna, Italy; Kilauea, USA; Erta'Ale, Ethiopia) but are larger than the size of the bubbles at nucleation.

Remerciements

Je souhaite avant tout remercier Sylvie Vergniolle qui m'a proposé cette thèse de doctorat qui me correspond parfaitement. Je remercie également toute l'équipe qui m'a accueillie dès mon premier stage avec Guillaume Carrazo en 2013. Je remercie Alexandre Nercessian, Angela Limare et Thierry Rivet pour leur aide sur l'utilisation des instruments et leur calibration. Merci à Jean-Philippe Métaxian pour son expertise sismique et le temps qu'il m'a consacré pour m'aider à mieux comprendre mes signaux sismiques. Je remercie également Pascale Besson pour son aide sur la bibliographie des gaz et Yves Gaudemer pour son aide sur les mathématiques.

Je remercie bien évidement chacun des membres de mon jury, Alexis Le Pichon, Andrew Harris, Nicole Métrich, Philippe Lesage et Wayne Crawford qui ont pris le temps d'étudier mes travaux. Je les remercie pour leurs remarques constructives qui m'ont permis d'améliorer mon travail.

Je remercie également toute l'équipe d'Esline Garaebiti, du Vanuatu Meteorology and Geohazard Department, qui m'ont accueillie chaleureusement à Port Vila; Henry, mon guide sur Tanna ainsi que Kelson du Jungle Oasis. Un grand merci à Michel Lardy qui m'a aidé à organiser ma mission au Vanuatu. Je remercie aussi Benjamin Simons et Geoffrey Lerner, de l'université de Auckland qui m'ont aidé sur le terrain.

Je remercie bien sûr tous mes amis qui m'ont soutenue pendant cette thèse mais également pendant mes 7 ans d'études supérieures. Et surtout, je remercie ma famille pour leur soutien dans mon projet, avec une pensée toute particulière et émue pour mon arrière-grand mère, 100 ans cette année, qui nous a encourragées, ma soeur et moi, à travailler dur pour obtenir ce que l'on veut.

Viviane

Contents

List of Figures xiv

List of Tables xix

List of Symbols xxiii

1 Introduction 1
- 1.1 L'activité volcanique . . . 5
- 1.2 L'activité Strombolienne . . . 8
- 1.3 Problématique . . . 16
- 1.4 Cas d'étude . . . 17

2 Data acquisition and calibrations 21
- 2.1 Data acquisition . . . 25
- 2.2 Distance from the vent to the sensor . . . 26
- 2.3 Calibration: response time of the radiometers . . . 27
- 2.4 Calibration: sensitivity of the thermal system . . . 28
- 2.5 Calibration: scale of the video . . . 31

3 Pre-processing of the data 35
- 3.1 Requirement in statistical and signal analysis . . . 39
- 3.2 Chain of acquisition . . . 46
- 3.3 Data conversion to *mat-files* . . . 49
- 3.4 Time correction . . . 50
- 3.5 Filtering the data . . . 50
- 3.6 Detection of events . . . 52
- 3.7 Classification of events . . . 58
- 3.8 Gestion of the gaps of data for the estimations per sliding window . . . 60

4 Processing of the data 63
- 4.1 Infrasonic processing . . . 68
- 4.2 Thermal processing . . . 81
- 4.3 Image processing . . . 91
- 4.4 Seismic processing . . . 95
- 4.5 Combination of different type of data . . . 109

5 Global inventory of Strombolian activity 119
- 5.1 Introduction . . . 125
- 5.2 Strombolian activity . . . 127
- 5.3 Targeted volcanoes . . . 127
- 5.4 Measurements . . . 128
- 5.5 Methodology . . . 130

5.6 Results . . . 137
5.7 Extrapolation to other volcanoes . . . 150
5.8 Conclusion . . . 154

6 Temporal variations at Yasur **157**
6.1 Introduction . . . 163
6.2 Context . . . 164
6.3 Data acquisition . . . 166
6.4 Processing of the data . . . 168
6.5 Results . . . 172
6.6 Discussion . . . 188
6.7 Conclusion . . . 197

7 Conclusions and perspectives **209**
7.1 Conclusions . . . 211
7.2 Perspectives . . . 212

Bibliography **215**

Appendices **235**

A Methodology **237**
A.1 Transfer functions . . . 237
A.2 Measurements for the calibration of the thermal system . . . 240
A.3 List of Earthquakes (USGS) . . . 241

B Global inventory of Strombolian activity **243**
B.1 Example of the calculation of total gas flux from SO_2 and gas ratio measurements 243
B.2 Histograms of the key parameters . . . 244
B.3 Histograms of the energy, velocity and volumes . . . 245
B.4 Depth estimates from the Monte Carlo analysis . . . 246

C Temporal activity at Yasur **253**
C.1 Histograms of the Strombolian explosions per phase . . . 254
C.2 Histograms of the strong Strombolian explosions per phase . . . 258
C.3 Stack of all strong infrasonic events . . . 271
C.4 Classes of infrasonic waveforms . . . 272
C.5 Tables of comparison of the distributions . . . 273
C.6 Bubble diameter in the reservoir . . . 276

D Vanuatu **279**
D.1 Correspondance with Benjamin Simons (Auckland university) and Esline Garaebiti (VMGD) . . . 279
D.2 Alert bulletins . . . 280

List of Figures

Introduction **1**
1.1 Classification of the volcanic eruptions : Walker, 1973 7
1.2 Two-phase flow at basaltic eruptions. 8
1.3 Skech of the Strombolian activity and geophysical measurements. 13
1.4 Sketches of the formation of large gas pockets. 14
1.5 Location of the three targeted volcanoes. 17
1.6 Magma composition of the three targeted volcanoes. 18

Data acquisition and calibrations **21**
2.1 Photos of inrasonic and thermal sensors. 26
2.2 Location of the vents and infrasonic sensors at Yasur volcano. 29
2.3 Efficient response time of the radiometers. 30
2.4 Laboratory experiment: delay between both radiometers 31
2.5 Calibration of the delay between both radiometers. 31
2.6 Laboratory experiment: efficient sensitivity of the radiometers. 32
2.7 Calibration: efficient sensitivity of the thermal systems. 33
2.8 Calibration: video. 33
2.9 Measurement of the diameter of the conduit at Yasur (2009). 34

Pre-processing of the data **35**
3.1 Kurtosis curve with a sliding window of 0.25 s. 40
3.2 Calculation of the FFT of the signal s 41
3.3 Sinusoidal signals to illustrate the Parseval theorem. 42
3.4 Daubechies wavelet with 5 null-moments. 43
3.5 Sketch of the wavelet decomposition 44
3.6 Principle of the Monte Carlo analysis 46
3.7 Monte Carlo analysis: example 1 46
3.8 Monte Carlo analysis: example 2 47
3.9 Chain of data acquisition. 47
3.10 Transfer function of the LE-3Dlite MkII seismometer 48
3.11 Time lag of the RefTek clock. 50
3.12 Fourth order and pass-band Butterworth filter: 0.5 Hz to 5 Hz 51
3.13 Summary of the peaking method of detection. 53
3.14 STA/LTA sliding windows. 53
3.15 Typical infrasonic waveforms at Erta'Ale and Piton de la Fournaise. 57
3.16 Sketch for the links of the explosions recorded on several records. 59
3.17 Eigen values as a function of the rank N. 60

Processing of the data **63**
4.1 Example of infrasonic, thermal and seismic records at Yasur in June 2009. . 67
Infrasonic processing 68
4.2 Sketch of a typical infrasonic waveform at Yasur. 69
4.3 Correction of the maximum amplitude ($p^+ < |p^-|$). 70
4.4 Limits of the infrasonic waveform of the explosions. 71
4.5 Sound speed into the atmosphere as a function of the temperature. 73
4.6 From infrasonic power per sliding window to gas volume. 75
4.7 Generation of infrasonic waveforms considering the mass flux. 76
4.8 Gas volume from two successive integrations of the acoustic pressure. 77
4.9 Parameters for the bubble volume model. 77
4.10 Parts for the weighted correlation coefficient. 80
4.11 Example for the bubble volume mode: fit. 81
Thermal processing 81
4.12 Example for the bubble volume mode: parameters 82
4.12 Example for the bubble volume mode: parameters (continued) 83
4.13 Example for the bubble volume model: synthetic waveform 84
4.14 Atmospheric pressure and density as a function of the elevation. 84
4.15 Sketches for a simple and complexe waveforms from IR-radiometers. 85
4.16 Definition of the thermal characteristic points. 85
4.17 Limits of the thermal waveform of the explosions. 86
4.18 Calculation of the field of view of the radiometer. 86
4.19 Field of view of the radiometers. 87
4.20 Sketch of the estimation of the ejecta velocity. 89
4.21 Error on the ejecta velocity. 91
Image processing 91
4.22 Calculation of ejecta velocity using PIV method - 1. 93
4.23 Calculation of ejecta velocity using PIV method - 2. 93
4.24 Field of view of the radiometers in June 2009. 94
4.25 Sketch of the RGB decomposition of the colours. 94
4.26 Volume of the ejecta and volcanic cloud from videos. 95
Seismic processing 95
4.27 Analysis of a video frame to count the number of pixel with hot liquids or solids. 96
4.28 Count of the number of pixel with hot liquids or solids. 97
4.29 Gas volume fraction from video analysis - 1 98
4.30 Gas volume fraction from video analysis - 2 99
4.31 Combined transfer functions of the Q330 and LE-3Dlite MkII. 100
4.32 Instrumental response of the Guralp CMG-40T seismometer. 101
4.33 Vertical component of seismic records from Y32 and Melkem stations 102
4.34 Fourier transform of the signal from Y32 and Melkem stations 103
4.35 Smoothed Fourier transform of the signal from Y32 and Melkem stations . . 104
4.36 Stacked Fourier transform of the signal cut by 100 s from Y32 and Melkem stations 105
4.37 Transfer function of the Melkem station configured in short period 106
4.38 Instrumental response of the Trillium 40 seismometer. 108
4.39 Typical seismic waveform at Yasur. 108
4.40 Signal envelopes of an explosion on seismic records. 109
Combination of different type of data 109
4.41 Sketch for the polarisation analysis. 110
4.42 Transformation of a VLP (N,E,Z) components to (R,T,Z) components . . . 111

4.43 Diagrams of polarisation of a VLP . . . 112
4.44 Topographic profils at Yasur volcano. . . . 113
4.45 Trace of the profils from previous figure. . . . 114
4.46 RSAM and SSAM at Yasur, Sept-Nov 2016 (EHZ). . . . 115
4.47 Sketch of the depth estimation of the top of the magma column. . . . 115
4.48 Speed of sound in the conduit. . . . 116
4.49 Monte Carlo analysis: gas volume fraction . . . 117

Global inventory of Strombolian activity **119**
5.1 Location of the sensors. . . . 128
5.2 Stack of the waveforms of the detected events . . . 130
5.3 Sketch of the topography of the South lava lake at Erta'Ale. . . . 131
5.4 Typical infrasonic waveforms at Erta'Ale and Piton de la Fournaise. . . . 133
5.5 Sketches of the estimations of ejecta velocity and depth of explosion. . . . 135
5.6 How to read a boxplot? . . . 137
5.7 Distribution of the key parameters at the 3 targeted volcanoes. . . . 138
5.8 Distribution of energy, velocity and volume at the three volcanoes. . . . 140
5.9 Comparison of the two methods (PIV, RDs) to estimate the ejecta velocity. 141
5.10 Partial analysis of video-7, Yasur 2009 . . . 142
5.11 Comparison of the gas volume from two different methods at Erta'Ale and Piton de la Fournaise. . . . 142
5.12 Direct estimation of the depth of the magma column. . . . 144
5.13 Monte Carlo analysis: depth of the magma column (YAS09, gas-rich). . . . 145
5.14 Depth of the magma columns: comparison of the results. . . . 146
5.15 Budget of energy of the three targeted volcanoes. . . . 147
5.16 Distributions of the velocity ratio and the particle size. . . . 148
5.17 Bombs at Yasur, in Sept-Nov 2016. . . . 149
5.18 Input into the atmosphere. . . . 149
5.19 Location of the selected volcanoes . . . 151
5.20 Characterisation of the Strombolian activity at several volcanoes. . . . 152
5.20 Characterisation of the Strombolian activity at several volcanoes (continued). 153

Temporal variations at Yasur **157**
6.1 Topography of the New Hebrides subduction zone. . . . 165
6.2 Strombolian explosions at Yasur during the 2016 field campaign. . . . 166
6.3 Location of the site of measurements at Yasur. . . . 167
6.4 Estimation of the active, passive and total gas flux . . . 170
6.5 Long time series: Gas volume flux by frequency bands . . . 173
6.6 Long time series: Summary of the detection. . . . 173
6.7 Frequency contents of infrasonic records. . . . 174
6.8 Infrasonic energy and gas volume flux per hour by frequency bands. . . . 175
6.9 Infrasonic key parameters. . . . 176
6.10 Infrasonic energy, gas velocity and gas volume. . . . 177
6.11 Gas volume as a function of the maximum acoustic pressure and the proportion of low frequencies. . . . 178
6.12 Proportion of active and passive degasing. . . . 179
6.13 Gas volume flux per hour by frequency bands [1.8–4Hz . . . 180
6.14 Thermal key parameters. . . . 181
6.15 Estimation of thermal energy and ejecta velocity. . . . 182
6.16 Seismic key parameters. . . . 183

6.17 Seismic energy and main seismic frequency per event. 184
6.18 Budget of energy from thermo-infrasonic records. 185
6.19 Depth of the top of the magma column. 186
6.20 Budget of energy from seismo-infrasonic records. 186
6.21 Infrasonic, thermal and seismic RMS per 30 minutes. 187
6.22 Ratio of RMS per 30 minutes. 188
6.23 Distribution of infrasonic, thermal and seismic key parameters. 189
6.24 Distribution of infrasonic, thermal and seismic key parameters for all linked explosions. 190
6.25 Determination on the phases of activity based on the infrasonic data. 191
6.26 Determination of the critical value of the maximum acoustic pressure. . . . 192
6.27 Distribution of the return time per phase for all infrasonic events. 193
6.28 Distribution of the infrasonic energy per phase for all infrasonic events. . . . 194
6.29 Distribution of the gas volume per phase for all infrasonic events. 195
6.30 Category of the phases of activity based on the distribution of key parameters. 196
6.31 Infrasonic RMS per 30 min as a function of the seismic RMS per 30 minutes. 198
6.32 Proportion of small and strong explosions per phase. 199
6.33 Distribution of the return time per phase for all seismo-infrasonic events. . . 200
6.34 Distribution of the infrasonic energy per phase for all seismo-infrasonic events. 201
6.35 Distribution of the gas volume per phase for all seismo-infrasonic events. . . 202
6.36 Distribution of the ground velocity per phase for all seismo-infrasonic events. 203
6.37 Distribution of the seismic duration per phase for all seismo-infrasonic events. 204
6.38 Distribution of the seismic energy per phase for all seismo-infrasonic events. 205
6.39 VATR per event as a function of the VASR per event. 205
6.40 Persistent and intermittent mechanisms of degassing at Yasur. 206
6.42 Photos of Mount Yasur from satellite. 207

Appendices **235**

B.1 Distribution of the key parameters at the three volcanoes (histograms). . . . 244
B.2 Distribution of energy, velocity and volume at the three volcanoes (histograms). 245
B.3 Monte Carlo analysis: depth of the magma column (PdF06) 246
B.4 Monte Carlo analysis: depth of the magma column (YAS09) 247
B.5 Monte Carlo analysis: depth of the magma column (YAS09, ash-rich) 248
B.6 Monte Carlo analysis: depth of the magma column (YAS16) 249
B.7 Monte Carlo analysis: depth of the magma column (YAS16, gas-rich) 250
B.8 Monte Carlo analysis: depth of the magma column (YAS16, ash-rich) 251

C.1 Distribution of the infrasonic duration per phase for all infrasonic events. . . 254
C.2 Distribution of the infrasonic duration per phase for all seismo-infrasonic events. 255
C.3 Distribution of the gas velocity per phase for all infrasonic events. 256
C.4 Distribution of the gas velocity per phase for all seismo-infrasonic events. . . 257
C.5 Distribution of the return time per phase for all strong infrasonic events. . . 258
C.6 Distribution of the return time per phase for all strong seismo-infrasonic events. 259
C.7 Distribution of the infrasonic energy per phase for all strong infrasonic events. 260
C.8 Distribution of the infrasonic energy per phase for all strong seismo-infrasonic events. 261
C.9 Distribution of the gas volume per phase for all strong infrasonic events. . . 262

C.10 Distribution of the gas volume per phase for all strong seismo-infrasonic events. . . . 263
C.11 Distribution of the infrasonic duration per phase for all strong infrasonic events. . . . 264
C.12 Distribution of the infrasonic duration per phase for all strong seismo-infrasonic events. . . . 265
C.13 Distribution of the gas velocity per phase for all strong infrasonic events. . . . 266
C.14 Distribution of the gas velocity per phase for all strong seismo-infrasonic events. . . . 267
C.15 Distribution of the ground velocity per phase for all strong seismo-infrasonic events. . . . 268
C.16 Distribution of the seismic duration per phase for all strong seismo-infrasonic events. . . . 269
C.17 Distribution of the seismic energy per phase for all strong seismo-infrasonic events. . . . 270
C.18 Stack of all strong infrasonic events (YAS16) 271
C.19 Classes, per phase, of infrasonic waveforms of the strong Strombolian explosions. 272
C.20 Bubble diameter in the reservoir as a function of the magma viscosity and surface tension 277

D.1 Yasur safety zones. . . . 281

List of Tables

Data acquisition and calibrations **21**
2.1 Data acquisition: infrasonic and thermal 27
2.2 Data acquisition: seismic 28
2.3 Measurements in pixel for the scaling of the video 32

Pre-processing of the data **35**
3.1 Poles and zeros of the transfer function of the LE-3Dlite MkII seismometer . 48
3.2 Characteristic of each method of detection. 55
3.3 Parameters for the detection of Strombolian events at Yasur volcano. 57

Processing of the data **63**
4.1 Atmospheric pressure and density at the elevation of the three targeted volcanoes. 81
4.3 Calculation of the thermal radiant flux depending on the background temperature. 89
4.4 Height between both radiometers. 90
4.5 Estimates of the gas volume fraction from the count of pixels on video frames. 97
4.6 Poles and zeros of the transfer function of the LE-3Dlite MkII seismometer . 107
4.7 Time delay between the P and S-waves at Yasur. 107
4.8 Duration and cone volume of eruptions at Piton de la Fournaise. 116

Global inventory of Strombolian activity **119**
5.1 Parameters of automatic detections. 132
5.2 Parameters: speed of sound. 143
5.3 Depth of the magma column. 143
5.4 Nomenclature of the size of ejecta. 148
5.5 Volcanoes known to have Strombolian activity 150

Temporal variations at Yasur **157**
6.1 Phases of activity during the field campaigns at Yasur. 197
6.2 Bubble diameter in the reservoir at several basaltic volcanoes. 199

Appendices **235**

A.1 Frequency bands of the Daubechies wavelet db5. 238
A.2 Transfer function of the microbarometers and the seismometers. 239
A.3 Calibration of the efficient sensitivty of the thermal systems. 240
A.4 Lists of the earthquakes. 241

B.1 Estimate of the total gas volume flux from geochemistry measurements . . . 243

C.1 Comparison of the distributions of the infrasonic duration per phase for infrasonic events. . . . 273
C.2 Comparison of the distributions of the infrasonic duration per phase for seismo-infrasonic events. . . . 273
C.3 Comparison of the distributions of the gas velocity per phase for all infrasonic events. . . . 274
C.4 Comparison of the distributions of the gas velocity per phase for seismo-infrasonic events. . . . 274
C.5 Comparison of the distributions of the gas volume per phase for seismo-infrasonic events. . . . 274
C.6 Comparison of the distributions of the ground velocity per phase for seismo-infrasonic events. Be aware that P01 and P02–34 were recorded from two different sites, with different sensors and that the records of P01 are not correct from the instrumental response, yet. . . . 275
C.7 Comparison of the distributions of the seismic duration per phase for seismo-infrasonic events. Be aware that P01 and P02–34 were recorded from two different sites, with different sensors and that the records of P01 are not correct from the instrumental response, yet. . . . 275
C.8 Comparison of the distributions of the seismic energy per phase for seismo-infrasonic events. Be aware that P01 and P02–34 were recorded from two different sites, with different sensors and that the records of P01 are not correct from the instrumental response, yet. . . . 275
C.9 Calculation of the bubble diameter in the reservoir - 1. . . . 276
C.10 Calculation of the bubble diameter in the reservoir - 2. . . . 277

D.1 Vanuatu volcano alert bulletin: Tanna activity. . . . 280
D.2 Vanuatu Volcanic Alert Level System. . . . 281

List of Symbols

The following list describes the symbols that will be later used within the body of the document. The page number of the first use of each variable is written.

c	Wave speed	$\mathrm{m.s^{-1}}$
c_{atm}	Sound speed in the atmosphere, *p. 64*	$\mathrm{m.s^{-1}}$
c_{conduit}	Sound speed into the conduit, *p. 103*	$\mathrm{m.s^{-1}}$
c_{ejecta}	Sound speed in pure magma, *p. 104*	$\mathrm{m.s^{-1}}$
c_{gas}	Sound speed in pure magmatic gas, *p. 104*	$\mathrm{m.s^{-1}}$
c_{layer}	Seismic velocity of surface waves in the rock, *p. 96*	$\mathrm{m.s^{-1}}$
c_{rock}	Seismic velocity of body waves in the rock, *p. 95*	$\mathrm{m.s^{-1}}$
d	Ground displacement, *p. 94*	m
dtt	Length of the sliding window, *p. 33*	s
dz	Difference of elevation between the sensor and the vent, *p. 81*	m
$\mathrm{den_{TF}}$	Denominator of the transfer function TF (polynome), *p. 41*	
d_i	Coefficients of the denominator $\mathrm{den_{TF}}$, *p. 41*	
$\mathrm{d}Y$	absolute error of the estimated value Y, *p. 39*	
f	Frequency, *p. 34*	Hz
f_s	Sampling frequency, *p. 35*	Hz
g	Constant of gravity, *p. 72*	$\mathrm{m.s^{-2}}$
$h_{b,\mathsf{eq}}$	Magma thickness of above the gas bubble at equilibrium, *p. 69*	m
h_{layer}	Thickness of the layer of rock within which the seismic waves propagate, *p. 96*	m
i	Imaginary number	
inc	Angle of incidence, clockwise from the horizontal plan, *p. 98*	rad
k	Constant factor, *p. 65*	
kurt_X	Kurtosis of the random value X (fourth momentum), *p. 33*	
$\mathbf{lg}_{\mathrm{LTA}}$	Length of the window of the LTA, *p. 47*	s
$\mathbf{lg}_{\mathrm{STA}}$	Length of the window of the STA, *p. 47*	s
n_P	Number of poles of the transfer function TF, *p. 41*	
n_Z	Number of zeros of the transfer function TF, *p. 41*	
nfft	Number of points of the Fourier transform, *p. 35*	
n_i	Coefficients of the numerator $\mathrm{num_{TF}}$, *p. 41*	
$\mathrm{num_{TF}}$	Numerator of the transfer function TF (polynome), *p. 41*	
p^+, p^-	maximum acoustic pressure and minimum acoustic pressure of an event, *p. 61*	Pa
$(p_{\mathsf{ac}}(t) - p_{\mathsf{air}}(t))$	Excess of pressure , *p. 64*	Pa
q	Mass flux, *p. 66*	$\mathrm{kg.s^{-1}}$
$d_{b,\mathsf{res}}$	Bubble diameter in the reservoir , *p. 180*	m
respTime	Effective response time of the radiometers, *p. 21*	s
r_{vent}	Distance from the source to the sensor, *p. 64*	m
s	Signal, *p. 34*	
s_a	Analytic signal, *p. 36*	
$s_{\mathsf{digitizer}}$	Sensitivity of the digitizer, *p. 40*	$\mathrm{V.bit^{-1}}$
s_{sensor}	Sensitivity of the sensor, *p. 40*	
t	Time	s
timeLag	Time lag, *p. 47*	s

u	Ground velocity, *p. 93*	$\mathrm{m.s^{-1}}$
$\mathrm{Vol_{cone}}$	Volume of the cone of ejecta, *p. 106*	$\mathrm{m^3}$
z_p	Elevation , *p. 72*	m
z	Elevation , *p. 72*	m
$z_{p,\mathsf{std}}$	Elevation at the sea level, *p. 72*	m
z_{std}	Elevation at the sea level, *p. 72*	m
A_b	normalised amplitude of the bubble radius, linearity parameter, *p. 70*	
$\mathcal{A}_{\mathsf{FOV}}$	area of the field of view of the radiometer, *p. 79*	$\mathrm{m^2}$
$\mathsf{A}_{\mathsf{seismic}}$	Seismic attenuation, *p. 96*	
C_{geom}	Geometrical factor, *p. 181*	
C_D	Drag coefficient: $C_D = 0.5$, *p. 102*	
$C_{\mathcal{P}}$, $C_{\mathcal{V}}$	Heat capacity at constant pressure and volume, *p. 65*	$\mathrm{J.K^{-1}}$
D_P	Size of the ejecta (equivalent diameter), *p. 102*	m
E	Energy	J
$\mathrm{E_{infrasonic}}$	Infrasonic energy, *p. 65*	J
$\mathrm{E_{seismic}}$	Seismic energy, *p. 95*	J
$\mathrm{E_{thermal}}$	Thermal energy, *p. 80*	J
$\mathbb{E}[X]$	Esperance: mean value of the random value X, *p. 33*	
Env	Signal envelope, *p. 36*	
E_s	Signal energy, *p. 35*	
E_{sd}	Energy spectral density, *p. 35*	
$\mathcal{H}$	Hilbert transform, *p. 36*	
I_{thermal}	Thermal radiant flux, *p. 80*	$\mathrm{W.m^{-2}}$
Kurt	Kurtosis per sliding window of length dtt nomeqref 3.1 , *p. 33*	
$L_{\mathsf{atm,std}}$	Standard lapse rate of the atmospheric temperature, *p. 72*	$\mathrm{K.m^{-1}}$
L_b	Length of the bubble, *p. 68*	m
LTA	Long time average, *p. 47*	
M	Mass, *p. 66*	kg
M_{mol}	Molar mass, *p. 72*	$\mathrm{kg.mol^{-1}}$
$\mathcal{N}_f$	Nyquist frequency $\mathcal{N}_f = f_\mathrm{s}/2$, *p. 35*	Hz
P	Poles of the transfer function TF, *p. 41*	
P_{atm}	Atmospheric pressure, *p. 66*	Pa
$P_{\mathsf{atm,std}}$	Standard atmospheric pressure at the sea level, *p. 72*	Pa
$\mathcal{P}_{\mathsf{infrasonic}}$	Infrasonic radiant flux, *p. 64*	W
Pw	Power	W
$\mathrm{Pw_{infrasonic}}$	Infrasonic power, *p. 65*	W
Q	Total mass flux, *p. 66*	$\mathrm{kg.s^{-1}}$
$Q_{\mathsf{gas,res}}$	Gas flux in the reservoir , *p. 180*	$\mathrm{kg.s^{-1}}$
$\mathsf{Q}_{\mathsf{seismic}}$	Quality factor (seismic), *p. 96*	
R_b	Bubble radius, *p. 65*	m
$R_{b,0}$	Initial radius of the bubble, *p. 68*	m
$R_{b,\mathsf{eq}}$	Bubble radius at equilibrium, *p. 68*	m
R_{conduit}	Conduit radius, *p. 65*	m
R_{earth}	Radius of the Earth, *p. 72*	m
$R_{\mathfrak{ig}}$	Universal gas constant $R_{\mathfrak{ig}} = 287\,\mathrm{J.kg^{-1}.K^{-1}}$, *p. 65*	
$R_{\mathfrak{ig},\mathsf{mol}}$	Universal molar gas constant, *p. 72*	$\mathrm{J.mol^{-1}.K^{-1}}$
$\mathcal{S}$	Surface, *p. 86*	$\mathrm{m^2}$
S	Fourier transform of the signal s, *p. 34*	
S_{res}	Surface of the reservoir , *p. 181*	$\mathrm{m^2}$
S_{vent}	Surface of the vent , *p. 181*	$\mathrm{m^2}$
$\mathsf{S}_{\mathsf{seismic}}$	Site effects, *p. 95*	
STA	Short time average, *p. 47*	

STA/LTA	STA/LTAdetector, *p. 47*	
T_{magma}	Magma temperature, *p. 126*	K, °C
T	Temperature, *p. 75*	K
T_{atm}	Atmospheric temperature, *p. 65*	K
$T_{\mathsf{atm,std}}$	Standard atmospheric temprature at the sea level, *p. 72*	K
T_{Back}	Background temperature, *p. 75*	K
TF	Transfer function, *p. 41*	
U	Velocity	$\mathrm{m.s^{-1}}$
$\mathrm{U}_{\mathsf{ejecta}}$	Ejecta velocity, *p. 82*	$\mathrm{m.s^{-1}}$
$\mathrm{U}_{\mathsf{gas}}$	Gas velocity, *p. 65*	$\mathrm{m.s^{-1}}$
Vol	Volume	$\mathrm{m^3}$
u	Volume of ejecta, *p. 86*	$\mathrm{m^3}$
$\mathrm{Vol}_{\mathsf{gas}}$	Gas volume, *p. 66*	$\mathrm{m^3}$
X	Random value, *p. 33*	
Y	Estimated value, *p. 39*	
Z	Zeros of the transfer function TF, *p. 41*	
$\mathrm{Z}_{\mathsf{inc}}$	depth of the seismic source, *p. 99*	m
α	Azimuth, *p. 98*	°
α_{ejecta}	Ejecta volume fraction in the conduit or the reservoir	
α_{FOV}	angle of the field of view of the radiometer, *p. 79*	rad
$\alpha_{\mathsf{gas,res}}$	Gas volume fraction in the foam layer at the top of the reservoir, *p. 180*	
α_{gas}	Gas volume fraction in the conduit or the reservoir, *p. 104*	
β	Back azimuth, *p. 98*	°
$\beta_{S,}$	Isentropic compressibility, *p. 103*	$\mathrm{m.s^2.kg^{-1}}$
γ	Adiabatic constant: $\gamma = C_{\mathcal{P}}/C_{\mathcal{V}}$, *p. 65*	
δh	Height between both radiometers, *p. 82*	m
δt	Flying time between both radiometers, *p. 82*	s
ϵ_b	Variation of the bubble radius, *p. 68*	
$\epsilon_{\mathsf{thermal}}$	Emissivity, *p. 80*	
θ	Clockwise angle with the horizontal, *p. 81*	rad
$\bar{h}_{\mathsf{foam}}$	Dimensionless height of the foam at the top of the reservoir, *p. 180*	
λ	Wavelength, *p. 64*	m
μ_X	Mean of the random value X, *p. 33*	
μ_{magma}	Magma viscosity, *p. 69*	Pa.s
μ_{foam}	Foam viscosity , *p. 180*	Pa.s
ρ_{atm}	Atmospheric density , *p. 64*	$\mathrm{kg.m^{-3}}$
$\rho_{\mathsf{atm,std}}$	Standard atmospheric pressure at the sea level, *p. 72*	$\mathrm{kg.m^{-3}}$
ρ_{ejecta}	Density of the ejecta, *p. 102*	$\mathrm{kg.m^{-3}}$
ρ_{gas}	Density of the gas (dusty gas) , *p. 102*	$\mathrm{kg.m^{-3}}$
ρ_{layer}	Rock density of the layer where the surface waves propagate, *p. 96*	$\mathrm{kg.m^{-3}}$
ρ_{magma}	Magma density, *p. 69*	$\mathrm{kg.m^{-3}}$
ρ_{rock}	Rock density, *p. 95*	$\mathrm{kg.m^{-3}}$
σ_X	Standard deviation of the random value X, *p. 33*	
σ_Y	Standard deviation error of the estimated value Y, *p. 39*	
τ_{eruption}	Eruption duration, *p. 106*	d
$\sigma_{b,\mathsf{tension}}$	Surface tension of the bubble of gas , *p. 180*	$\mathrm{kg.s^{-2}}$
$\sigma_{\mathsf{thermal}}$	Stefan-Boltzmann constant ($5.6703 \times 10^{-8}\,\mathrm{W.m^{-2}.K^{-4}}$), *p. 80*	$\mathrm{W.m^{-2}.K^{-4}}$
τ	Event duration	s
$\tau_{\mathsf{infrasonic}}$	Infrasonic duration, *p. 65*	s
$\psi_{\mathfrak{t},\mathfrak{s}}$	Wavelet function of translation $\mathfrak{t}$ and dilatation $\mathfrak{s}$, *p. 37*	
$\varphi_{\mathsf{ejecta}}$	Volume flux of ejecta, *p. 106*	$\mathrm{m^3.s^{-1}}$
φ_{gas}	Volume flux of gas, *p. 106*	$\mathrm{m^3.s^{-1}}$
ω	Angular frequency, *p. 41*	$\mathrm{rad.s^{-1}}$

ΔH	Depth of the magma column, *p. 103*	m
ΔP_b	Overpressure of the bubble, *p. 68*	Pa
Δt	Thermo-infrasonic delay, *p. 103*	s
Θ	Vertical angle between both radiometers (4°), *p. 82*	rad
Ψ	Wavelet transform, *p. 37*	

Chapter 1

Introduction

À Hélène et Bertrand, parce qu'ils m'ont permis de faire Mon Choix et m'ont conseillée et encouragée quand il le fallait.

Mount St-Helens (16/08/2017) ©V. Souty

Contents

1.1 L'activité volcanique **5**
1.1.1 Quelques notions indispensables 5
1.1.2 Les éruptions basaltiques 6
1.2 L'activité Strombolienne **8**
1.2.1 Mesurer l'activité Strombolienne 8
1.2.1a Mesures des gaz 8
1.2.1b Dynamique du nuage volcanique 10
1.2.1c Études sismiques 11
1.2.1d Le Stromboli et l'Erebus, deux volcans stromboliens très étudiés 12
1.2.2 Mécanismes associés à l'activité Strombolienne 13
1.3 Problématique **16**
1.4 Cas d'étude **17**
1.4.1 Erta'Ale 17
1.4.2 Piton de la Fournaise 18
1.4.3 Yasur 19

Dans ce chapitre je commence par une description minimaliste mais indispensable de l'activité volcanique générale. Je présente ensuite l'activité volcanique basaltique et les différents régimes di-phasiques qui lui sont associés. Je fais ensuite un bilan des études de terrain réalisées sur l'activité Strombolienne avant de présenter l'activité Strombolienne typique du Stromboli. Je me focalise ensuite sur l'activité Strombolienne et les mécanismes de formations des bulles pour introduire la problématique de cette thèse. Je fini avec une présentation des volcans que j'étudie, l'Erta'Ale, le Piton de la Fournaise et le Yasur.

1.1 L'activité volcanique

1.1.1 Quelques notions indispensables

L'activité volcanique est un moyen efficace pour la Terre d'évacuer une importante quantité d'énergie avec de nombreux volcans situés sur ce qu'on appelle la Ceinture de Feu (Introduction *in* Sigurdsson et al., 2015). La Ceinture de Feu est à la frontière de plaques tectoniques, en context de compression, là où les subductions se font. Une grande partie du volcanisme a également lieu, à la frontière de plaques mais dans un context d'extension cette fois-ci (rift continentaux, médiane océaniques, Introduction *in* Sigurdsson et al., 2015). Enfin certains volcans se trouvent être intra-plaques et sont alimentés par ce qu'on appelle des points chauds et qui sont des zones de fusion partielle à grande profondeur (Kilauea, Piton de la Fournaise, etc.).

Le magma, issu de la fusion partielle du manteau (Schmincke, 2004, p.24), peut varier en composition du fait de son context tectonique (mécanisme de fusion), du degrée de fusion partielle et de son temps de séjour, i.e. le temps qu'il lui faut pour remonter à la surface par flottabilité (Schmincke, 2004, p.26). Une fois proche de la surface le magma peut être stocké dans un ou plusieurs réservoirs, appelés chambres magmatiques (i.e. le magma rencontre une couche de roche qui ne lui permet plus de remonter à la surface par flottabilité). Ces réservoirs sont situés à quelques centaines de mètres pour les plus superficiels (Chouet et al., 2003, Stromboli, e.g.), à quelques kilomètres pour des réservoirs, dit aussi superficiels (Etna, e.g. Allard et al., 2005; Spilliaert et al., 2006; Patanè et al., 2002) ou dans des reservoirs dits profonds, atteignant presque 10 km (Shishaldin, e.g. Stelling et al., 2002; Lu et al., 2002). Dans certains cas, le magma peut refroidir par conduction parce que la roche qui l'entoure est plus froide. Différents cristaux peuvent alors se former en fonction de leur solidus et de la température du magma. C'est la cristalisation fragmentée ou différentiation du magma (Schmincke, 2004, p.27).Le magma contient également des gaz qui s'exsolvent, à cause de la décompression du magma lors de sa remontée vers la surface. Ce dégazage dépend des espèces présentes qui sont solubles à différentes conditions de pression et de température (CO_2, H_2O, SO_2, HCl pour les plus gros volumes Schmincke, 2004, p.42).

La composition chimique du magma, sa teneur en cristaux et en eau et sa température sont des paramètres clés qui contrôlent la viscosité du magma (Schmincke, 2004, p.27). Plus un magma est différentié, plus il est riche en silice et cristaux et donc visqueux (dacite : >63 % de silice ; rhyolite : >70 % de silice BAS et al., 1986). Un magma peu différencié est plus pauvre en silice et cristaux et est donc moins visqueux (45 % de silice et une viscosité de 10 Pa.s–100 Pa.s pour les basalts du Kilauea, BAS et al. (1986); Schmincke (2004)). Plus un magma est visqueux, plus sont écoulement est lent (ex : le miel est plus visqueux que l'huile et s'écoule beaucoup plus lentement). Un magma moins visqueux permettra au gaz exsolvé sous forme de petites bulles de circuler plus facilement qu'un magma visqueux.

Cela implique qu'un magma moins visqueux piège moins de gaz (ex : ébullition de l'eau comparée à l'ébullition d'une purée).

La vitesse d'ascension du magma et sa décompression peuvent également plus ou moins faciliter le dégazage. Une ascension rapide et donc une décompression rapide du magma peut générer des éruptions hautement explosives parce que la mixture de gaz et de liquide magmatique se développe en système fermé (Cashman et al., 2004), c'est-à-dire que les gaz ne peuvent pas ou ont du mal à s'échapper (ex : bouteille de champagne que l'on aurait trop secoué). Une ascension plus lente du magma est favorable à la séparation de la phase gazeuse du liquide magmatique et les gaz peuvent alors facilement s'échapper sous forme de grosses bulles (Wilson and Head III, 1981; Jaupart and Vergniolle, 1988, 1989; Parfitt et al., 1995) ; le système est alors partiellement ou totalement ouvert et peut générer de petites explosions. Chaque éruption volcanique produit des ejecta et des gaz qui sont rejetés dans l'atmosphère et peuvent avoir une impact local sur la population (pluie acide, contamination de l'eau et des cultures) et/ou un impact global sur le climat (Krakataua, 1883 Gleckler et al. (2006) ; Pinatubo, 1991 McCormick (1992) ; Ambrym, Allard et al. (2016a)).

Différents types d'éruptions peuvent être observés, de la coulée de lave (Hawaii) à l'éruption Plinienne (éruption du Vésuve, 79A.D. décrit par Pline le Jeune) en passant par les éruptions Stromboliennes du Stromboli et ont été décrits bien avant une quelquonque classification. Les éruptions volcaniques sont aujourd'hui souvent classées par rapport à leur explosivité, et donc leur dangerosité. J'ai retenu deux classifications :

(i) la classification de Walker (1973), ancienne et peu utilisée de nos jours, est basée sur la dispersion des éjecta, c'est-à-dire la distance à la bouche éruptive à laquelle ils tombent, et leur degré de fragmentation. On peut définir le degré de fragmentation comme l'efficacité à produire de fine particules Figure 1.1.
(ii) la classification de Newhall and Self (1982) est basée sur l'index volcanique explosif (VEI : Volcanic Explosity Index). Le VEI est défini par le volume d'éjecta par éruption et la hauteur de la colonne éruptive.

La première classification dépend essentiellement de l'organisation spatiale des bulles de gaz, de leur taille et de leur sur-pression initiale, ainsi que la viscosité du magma. La deuxième classification met en revanche l'accent sur des paramètres plus globaux, tels que le volume d'éjecta, relié au volume de gaz, la densité du mélange des deux phases (gas et ejecta) et la surpression initiale du réservoir, comme par example dans la phase initiale de la fontaine de lave de faible hauteur au Piton de la Fournaise (Hibert et al., 2015). Un volcan peut produire différents types d'éruptions au cours de sa vie qui sont induits par des changements du système volcanique en profondeur (variation du flux de magma et/ou de gaz, changement de composition du magma) ou en surface (destabilisation de flanc). L'étude de Marzocchi and Zaccarelli (2006); Newhall and Self (1982) montre que les éruptions à fort VEI sont moins nombreuses que les éruptions à faible VEI. Cela s'explique par le fait qu'il faut plus de temps pour accumuler les produits (gaz et magma) nécessaires aux éruptions les plus explosives.

Je m'intéresse aux éruptions basaltiques moins explosives mais plus régulières parce qu'elles ont un impact environnemental local important de part les volumes de gaz certes faibles qu'elles émettent mais qui sont très fréquents voir continu et parce que l'instrumentation sur ces volcans en activité quasi-permanente permet de mieux comprendre leur dynamisme éruptif.

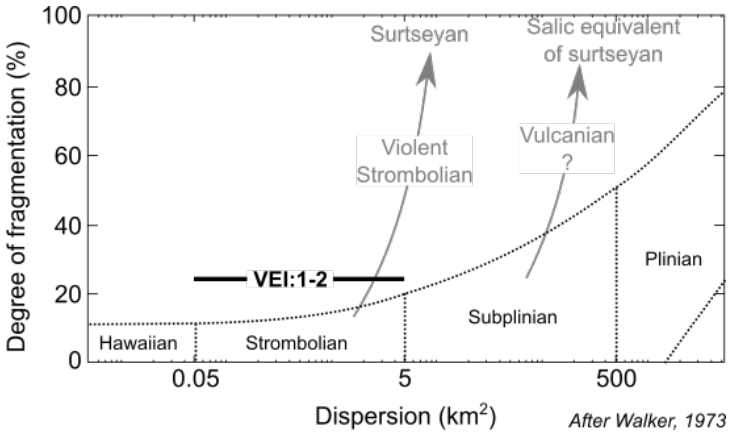

FIGURE 1.1 – Classification des éruptions volcanique d'après la dispersion des éjecta et de leur degré de fragmentation. D'après Walker (1973).

1.1.2 Les éruptions basaltiques

Les éruptions basaltiques existent dans tous les contexts tectoniques et sont fréquentes. Les points chauds génèrent essentiellement des éruptions basaltiques (Kilauea, Hawaii ; Piton de la Fournaise, Île de la Réunion ; Erebus, Antarctique). Les rifts continentaux produisent également des éruptions basaltiques comme à l'Erta'Ale (Éthiopie) ou au Nyiragongo (République Démocratique du Congo). Enfin, on peut également trouver des volcans produisant des éruptions basaltiques au niveau des zones de subductions (Shilshaldin, Alaska ; Yasur et Ambrym, Vanuatu). Certains volcans de magma basique comme le Stromboli ou le Yasur sont en activité Strombolienne persistente.

Comme expliqué précédemment, le magma exsolve ses gaz par décompression lors de son ascension jusqu'à la surface. Ce sont donc deux phases qui remontent jusqu'à la surface, une phase gazeuse légère et une phase liquide plus dense (on suppose que les cristaux font partie intégrante de la phase liquide). Les gaz sont le moteur de ces éruptions basaltiques. Il existe plusieurs régimes di-phasiques, qui dépendent de la proportion volumique de gaz et de liquide magmatique, lors de la remontée de la mixture de gaz et magma dans le conduit volcanique ((Figure 1.2 Vergniolle and Jaupart, 1986; Vergniolle and Mangan, 2000) :

a) un système très pauvre en gaz (fraction volumique de 1 % à ∼10 %, mal connue) a un régime bulleux et génère une activité effusive ;
b) un sytème riche en gaz (∼70 %) a un régime intermittent où de petites bulles de gaz s'accumulent pour en former des grosses. Ce régime est responsable de l'activité Strombolienne ;
c) si on continue d'augmenter la proportion en gaz, le régime devient annulaire, c'est-à-dire qu'on a un jet de gaz central dans un anneau de magma qui génère des fontaines de lave ;
d) enfin dans le cas extrême, à très forte fraction volumique de gaz dans le conduit, le régime est dispersé, c'est-à-dire que qu'il n'y a plus d'anneau de magma autour du jet de gaz, mais que de petites particules de magma sont prise au piège dans le jet de gaz ce qui génère des colonnes éruptives basaltiques.

Il est possible pour un volcan de passer d'un régime di-phasique à un autre en fonction de son alimentation en magma et en gaz. Il est donc important d'étudier l'activiter volcanique de ces différents régimes pour identifier les changements d'alimentation profonde du système.

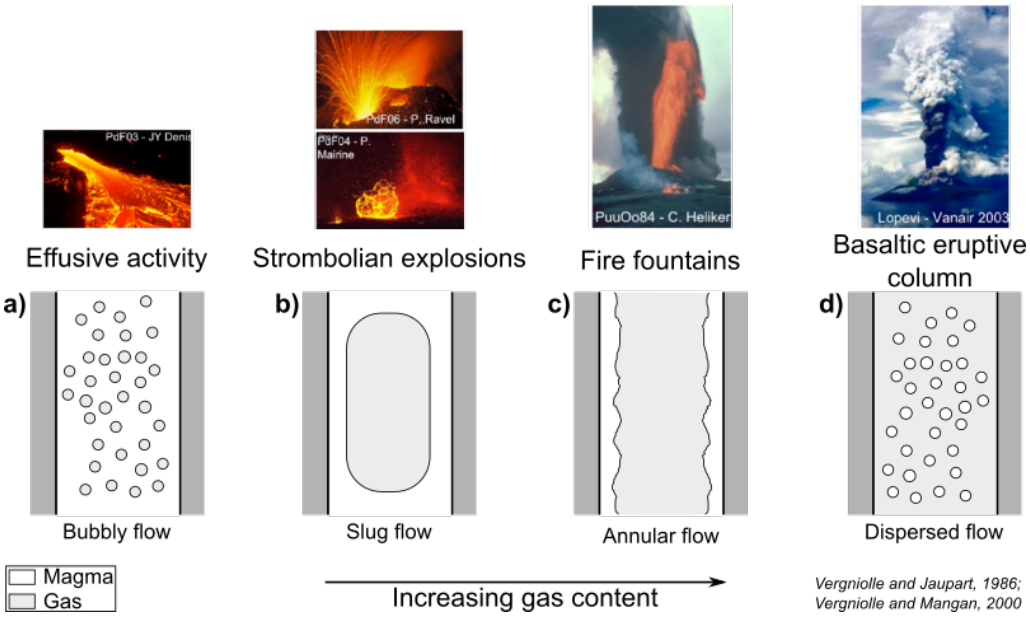

FIGURE 1.2 – Régimes di-phasiques des éruptions basaltiques. a) Le régime bulleux génère une activité effusive, b) le régime de slug des explosions stromboliennes, c) Le régime annulaire des fontaines de lave et d) le régime dispersé des colonnes éruptives basaltiques. Adaptée d'après la figure 1a dans Vergniolle and Jaupart (1986) et la figure 6 dans Vergniolle and Mangan (2000).

Je m'intéresse plus particulièrement à l'activité Strombolienne car, même si elle est modérement explosive, elle est souvent persistante (Stromboli Rosi et al. (2000) ; Erebus Kyle (1994) ; Yasur Firth et al. (2014) ; Erta'Ale Harris et al. (2005a) ; etc.) et elle génère donc de grandes quantités de produits (gaz et ejecta) au cours du temps. La variabilité spatiale de l'activité Strombolienne, en terme de i) contextes tectoniques (i.e. Stromboli : subduction ; Erebus : point chaud ; Erta'Ale : rift continental), ii) composition magmatique (i.e. basaltique au Stromboli, phonolitique à l'Erebus, trachy-andesitique au Yasur), iii) de récurrence de l'activité Strombolienne (i.e. permanant au Stromboli ou intermittant à l'Etna) et iv) taille de l'édifice ainsi la variabilité temporelle à un édifice posent la question des limites de l'activité Strombolienne (définition quantitative) et la question de similitudes et différences de l'activité Strombolienne d'un édifice volcanique à l'autre.

1.2 L'activité Strombolienne

1.2.1 Mesurer l'activité Strombolienne

1.2.1a Mesures des gaz

Les volcans émettent des gaz qui peuvent intéragir avec l'atmosphère et modifier les propriétées et la dynamique de l'atmosphère. Cela peut avoir un impact sur le climat et sur les cycles bio-chimiques (Jourdain et al., 2016; Lefèvre et al., 2016; Sellitto et al., 2017, e.g.). Les différentes espèces de gaz sont produites à différentes profondeur sous la surface, en fonction de leur solubilité (CO_2, H_2O, SO_2, HCl, halogènes, etc.).

Le SO_2 n'est pas le gaz le plus produit en grande quantité par les volcans, pourtant il est aujourd'hui le gaz le plus mesuré lors de missions de terrain (Bani and Lardy, 2007;

Galle et al., 2003; Barrancos et al., 2008, e.g.). Certains observatoires le mesurent en continu comme au Kilauea (United States of America), à Stromboli, Vulcano, l'Etna (Italy) (Burton et al., 2014; Vita et al., 2012) ou au Piton de la Fournaise (Île de la Réunion, France).

Le SO_2 est souvent mesuré par COSPEC (Correlation spectrometry), DOAS (Differentiation Optical Absorption Spectrometry) ou caméra ultra-violet (e.g. Elias et al., 2006; Barrancos et al., 2008). Toutes ces méthodes font une mesure de l'absorption des ultra-violet et ont donc besoin d'une source lumineuse en arrière plan de la source de gaz. Les DOAS sont les plus utilisés, car peu cher, facilement transportables et peu énergivores (Elias et al., 2006). De plus, contrairement aux COSPEC, les DOAS les plus récents, ont moins de problèmes quand la lumière est faible (Elias et al., 2006). Ces mesures de SO_2 peuvent être faites du sol (véhicule, trépied), par avion.

Des méthodes de spectrométries infra-rouges existent également mais sont beaucoup moins utilisées par rapport aux méthodes de spectrométries ultra-violets. Notamment, l'émission de SO_2 des fontaines de lave du Kilauea (USA) a été mesuré par absorption des infrarouges (nau). Des images infrarouges aquises par avion ont permis de déterminer la concentration de et le flux SO_2 à l'Etna (TIMS : Thermal Infrared Multispectral Scanner of the NASA Realmuto et al., 1994). La concentration en SO_2 des fumerolles du volcan Asama (Japon) a aussi été mesuré par radiomètre spectral infrarouge (Notsu et al., 1993). Le SO_2 peut également être mesuré, par absorption différentielle dans les infra-rouge, depuis les satellites pour une couverture globale, mais uniquement pour les grands volumes de SO_2 (SEVIRI, MODIS, IASI, AIRS instruments, e.g. Dubuisson et al., 2014; Carn, 2016; Prata and Bernardo).

Ces mesures par satellites sont très dépendantes de l'état de l'atmosphère et du chemin de propagation des ondes entre les sol et le satellite, qui mesure une quantité de SO_2 intégrée sur toute la colonne atmosphérique. La mesure du SO_2 est des plus utiles parce que le SO_2 n'existe pas dans l'atmosphère en dehors de l'industrie humaine et de l'activité volcanique, contrairement au CO_2 et au H_2O, qui sont des gaz majeurs, en terme de volume produit par les volcans.

Witter et al. (2012) ont associé des caméras infra-rouge et les équations de conservation de la masse et de l'énergie pour déterminer les flux de H_2O. Leur modèle est basé sur l'hypothèse que le H_2O est le gaz le plus abondant dans le panache, en terme de masse. Ils obtiennent des flux de H_2O à Villarrica ($38\,kg.s^{-1}$–$250\,kg.s^{-1}$, Chili), au Stromboli ($4.5\,kg.s^{-1}$–$14\,kg.s^{-1}$, Italie) et à Santa Ana ($168\,kg.s^{-1}$–$219\,kg.s^{-1}$, El Salvador) qui sont cohérents avec les flux H_2O obtenus par d'autres méthodes (méthodologie multi-capteur + miniDOAS à Villarrica et Santa Ana Shinohara (2005) ; méthode développée par Harris and Ripepe (2007b) à Stromboli et qui se base également sur des mesures thermiques).

Les autres espèces de gaz sont mesurées indirectement par multi-gas ou par FTIR (Fourier Transform Infra-Red spectrometer). Ces deux méthodes mesurent les rapports de gaz diatomique comme par exemple, les rapports H_2O/SO_2 ou CO_2/SO_2 (e.g. Oppenheimer et al., 2006; Métrich et al., 2011; La Spina et al., 2015). L'inconvenient du multi-gas, est que l'instrument, placé à distance de la bouche mesure en fait les rapports de gaz après leur mélange avec l'atmosphère et donc après leur dilution. Le FTIR permet d'avoir une mesure directe des gaz qui sortent à la bouche éruptive, mais nécessite une vue claire de la bouche (un panache de cendre ou la pluie biaisent les résultats). En tout état de cause, les mesures par FTIR ne mesurent que l'anneau extérieur de l'explosion si celle-ci est dense en fragments solides et liquides. Nous pouvons obtenir les flux de chacune des espèces de gaz jouant un rôle dans la dynamique de l'atmosphère en combinant les mesures du flux

de SO_2 avec les mesures de rapport des gaz di-atomiques. Nous pouvons alors estimer le flux total de gaz émis dans l'atmosphère.

Alternativement, les volumes de gaz du dégasage actif, lié à l'explosion de poches de gaz surpressurisées, et du dégasage passif, produits par les volcans peuvent être estimées à partir d'enregistrements infrasoniques. Trois méthodes sont couramment utilisées pour estimer le volume de gaz à partir d'enregistrements infrasoniques. Les deux premières considèrent la décharge de gaz dans l'atmosphère lorque la bulle de gaz explose à la surface du magma (Woulff and McGetchin, 1976; Vergniolle et al., 2004; Johnson, 2003). La troisième méthode considère l'oscillation en volume de la bulle de gaz avant son explosion (Vergniolle and Brandeis, 1996). Il convient de choisir la méthode appropriée pour le calcul de volume (Section 4.1.3), un magma trop visqueux empêchant la vibration de la bulle comme dans le cas de l'Erebus (Antarctique, Gerst et al., 2013). Les volumes de gaz par explosion et les flux de gaz ont ainsi pu être estimés au Stromboli (e.g. Vergniolle and Brandeis, 1996; Vergniolle et al., 1996), à Shishaldin (Vergniolle et al., 2004), à l'Etna (Vergniolle, 2008), à l'Erta'Ale (Bouche et al., 2010), à l'Erebus (Johnson, 2003; Johnson et al., 2008b, e.g.), etc.

1.2.1b Dynamique du nuage volcanique

J'appelle ici nuage volcanique la mixture de gaz et d'éjecta émis par une éruption Strombolienne. La dynamique de ce nuage est complexe, puisqu'une éruption injecte dans l'atmosphère une mixture très chaude composée d'au moins deux phases (ejecta + gas). À la base de la bouche éruptive, nous pouvons observer un mélange turbulent qui devient un panache dominé par des mouvements de convections à cause du mélange avec l'atmosphère (Figure 1.3).

La plus ancienne méthode permettant d'étudier la dynamique du nuage volcanique est probablement l'analyse de photographie, notamment les photos avec de long temps d'expositions qui permettent de i) mesurer les angles d'émission moyen des éruptions afin de déterminer si le conduit est incliné proche de la surface et/ou ii) suivre la trajectoire des ejecta, qui combinée à une étude balistique, permet de déduire la vitesse initiale des ejecta (e.g. Chouet et al., 1974; Vanderkluysen et al., 2012).

Les vidéos dans le domaine visible, à haute vitesse ou non, permettent de mesurer les angles d'émission. Ces vidéos permettent également de mesurer la vitesse et la taille des ejectas en traquant manuellement ou automatiquement les ejectas (PIV, PyTV, e.g. Taddeucci et al., 2012; Gaudin et al., 2014a; Shindler et al., 2010).

Les radiomètres thermiques font une mesure spectrales des objets présents dans leur champ de vision pour en déduire leur température à partir d'une inversion de la fonction de Plank (Harris, 2013). Ces radiomètres permettent par example de montrer que l'énergie thermique des explosions Stromboliennes est plus faible d'au moins un ordre de grandeur que les l'énergy thermique des explosions vulcaniennes (Marchetti et al., 2009). La mise en parallèle de deux radiomètres permet également d'estimer une vitesse d'ascension moyennée du nuage volcanique, à partir du délai du signal thermique entre les deux capteurs, comme cela a été proposé au Santiaguito (Guattemala, Sahetapy-Engel and Harris, 2009). L'utilisation d'un seul capteur devrait également permettre une estimation de la vitesse d'ascension du nuage volcanique, en revanche l'étude de Chevalier and Donnadieu (2015) montre que les résultats des techniques proposées (même avec deux capteurs) sont très entâchés d'erreurs du fait des nombreuses incertitudes liées aux méthodes et aux instruments.

Aujourd'hui, les caméras thermiques sont donc plus souvent utilisées que les radiomètres pour étudier la dynamiques des nuages volcaniques et permettent de mesurer la vitesses des ejecta et leur taille de façon similaire aux mesures effectuées sur des vidéos dans le visible (e.g. Vanderkluysen et al., 2012) ou en considérant le profil de température du nuage (e.g. Harris et al., 2012). En outre, il est facile de choisir une partie de l'image thermique pour en déduire la variation temporelle de la température tel qu'elle aurait été mesurée par un radiomètre (e.g. Chevalier and Donnadieu, 2015) ou encore l'énergie thermique du nuage.

Plusieurs types de radars Doppler existent parmis lesquels deux permettent de pointer un *objet* précis : i) le radar Doppler pulsé émet régulièrement un pulse de longueur choisie et enregistre l'écho de ce pulse qui est renvoyé par l'objet étudié(see Donnadieu, 2012, for review) et ii) le radar Doppler à fréquence modulé émet une onde électromagnétique en continu et enregistrement également l'écho renvoyé par l'objet étudié (Voge and Hort, 2009). L'amplitude du signal enregistré permet de quantifier la taille de l'objet (i.e. la quantité de matériaux) tandis que le décalage Doppler permet d'estimer la vitesse de cet objet. Dans le cadre de l'activité Strombolienne, les radars Doppler permettent de mesurer les vitesses des ejectas, même lorsque la couverture nuageuse est importante. Les plus petites particules ont probablement une vitesse très proche de la vitesse des gaz qui les entraînent ce qui permet de déterminer aussi la vitesse du gaz (Donnadieu et al., 2005). Au Yasur les vitesses ascendantes dans le nuage volcanique peuvent atteindre $\sim$300 m.s^{-1} et augmentent lorsque l'activité s'intensifie au contraire de la quantité de cendres, indirectement mesurée par l'amplitude du signal, qui diminue lors des fortes activité (Meier et al., 2016). Cette technique de velocimétrie par radar Doppler à également permis de mettre en évidence le changement temporel de l'activité strombolienne au Stromboli suite à un épisode pluvieux qui a permi une interaction entre l'eau et le magma (Hort et al., 2003).

Toutes ces méthodes permettent une mesure de la vitesse des ejecta ou du front du nuage volcanique. Ces vitesses sont importantes car sont directement liées à la dynamique éruptive de l'activité strombolienne. Associées à la taille des ejecta, ces informations sont donc cruciales pour la modélisation numérique de la dynamique de ces nuages volcaniques (e.g. Girault et al., 2016, 2014; Michaud-Dubuy et al., 2018). L'angle d'ouverture de la colonne éruptive est également un paramètre important puisqu'il donne accès au coefficient d'entraînement qui caractérise le mélange du nuage volcanique avec l'atmosphère (e.g. Kaminski et al., 2005; Carazzo et al., 2006). Un jet turbulent a un coefficient d'entraînement de 0.07 en régime stationnaire, ce qui correspond à un angle d'ouverture d'environ 16°. (Linden et al., 2000). Un panache flottant (buyoant) a en revanche un coefficient d'entraînemet plus élevé (0.16 Linden et al., 2000) qui se traduit par un angle d'ouverture plus important.

1.2.1c Études sismiques

Contrairement aux infrasons qui sont générés essentiellement par l'explosion Strombolienne elle-même, les ondes sismiques peuvent être générées par d'autres mécanismes que l'explosions comme par exemple la formation de la bulle de Taylor, son ascension (e.g. Johnson and Aster, 2005; Nabyl et al., 1997). Ces différents mécanismes génèrent des ondes avec des gammes de fréquences différentes. Les très longues périodes (VLP, <1 Hz) et les longues périodes (LP, <2 Hz) sont associées à des processus *profond*. Les ondes liées aux explosions stromboliennes elles-mêmes (EQ) ont des fréquences entre 1 Hz and 6 Hz. L'onde acoustique est également enregistrée par les sismomètres dans des gammes de fréquences supérieures à 6 Hz. Enfin, les trémors volcaniques, qui consistent en de petits pulses réguliers en temps,

sont associés à des petits jets de gaz à la surface du magma, appelé le puffing (Ripepe et al., 1996).

Ces trémors volcaniques permettent d'identifier les changements de milieu suite à un tremblement de terre par exemple (Battaglia et al., 2012). Le couplage sismo-acoustique est aussi souvent utilisé pour l'étude de l'activité Strombolienne parce qu'il permet de détecter des changement de sources liés à différents paramètres tels que la densité du nuage volcanique, la profondeur de la source, le diamètre du conduit, la taille de la source ou encore le contrast d'inpédance entre le volume de magma et le milieu l'entourant qui est lié à la rhéologie du magma (e.g. Johnson and Aster, 2005; Vergniolle et al., 2015).

Les mesures sismiques permettent aussi la surveillance en temps réel avec des méthodes telles que le RSAM (Real-time Seismic Amplitude Measurements, Endo and Murray, 1991) et le SSAM (real-time Seismic Spectral Amplitude Measurement, Rogers and Stephens, 1995) qui sont souvent utilisées dans les observatoires.

1.2.1d Le Stromboli et l'Erebus, deux volcans stromboliens très étudiés

Stromboli

Le Stromboli est un cône pyroclastique résultant d'une subduction dans les îles Éoliennes (Italie) et dont la base repose sur le fond océanique à environ 2000 m sous le niveau de la mer. Le Stromboli a trois cratères actifs, qui peuvent avoir entre 5 et 15 bouches éruptives, et est en activité Strombolienne permanente depuis au moins 1400 ans (Rosi et al., 2000). Le Stromboli produit une explosion Strombolienne toutes les 270 s environ (Delle Donne et al., 2006). Les ejecta produits par le Stromboli ont un diamètre équivalent pouvant varier de 3 mm à 1 m et sont propulsés dans l'atmosphère avec des vitesses pouvant atteindre 150 $m.s^{-1}$ (Gaudin et al., 2014b; Hort et al., 2003).

Deux types d'explosions Stromboliennes sont observés. Les explosions longues (10 s to 20 s, riches en cendres d'une part et les explosions courtes (5 s to 10 s), riches en scoria et en bombes d'autre part (Patrick et al., 2007). De plus une activité de puffing, consistant en de plus petit volumes de gaz et générant des infrasons de faible amplitude, y est observée avec des temps de retour très courts (e.g. Colò et al., 2010; Ripepe et al., 2008). Le système d'alimentation semble être identique malgré les différents types d'explosions du Stromboli et ses trois cratères, et est situé à ∼500 m au dessus du niveau de la mer (Chouet et al., 2008; Ripepe et al., 2008). Au dessus de ce système d'alimentations différents dykes alimentent les différents cratères qui produisent différents types d'explosions du point de vue sismique (Chouet et al., 2008).

Le Stromboli peut également produire des éruptions dites paroxysmales, qui sont en fait de petites explosions produisant des colonnes éruptives pouvant monter dans la stratosphère et durer plusieurs dizaines de minutes (e.g. Harris and Ripepe, 2007a; Vergniolle and Gaudemer, 2015; Métrich et al., 2005; Andronico and Pistolesi, 2010; Calvari et al., 2006, 2012; La Felice and Landi, 2011; Aiuppa et al., 2009; Andronico et al., 2013). Ces explosions sont uniques lors d'un épisode paroxysmal (une par cratère et par éruption) et sont parfois interprétées comme des éruptions Vulcaniennes. Des coulées de laves ont également été observées au Stromboli, comme en 2003 (Ripepe et al., 2004; Harris et al., 2005b) ou en février 2007 (e.g. Ripepe et al., 2009; Aiuppa et al., 2009).

Erebus

L'Erebus est un stratovolcan de point chaud situé sur l'Île de Ross, en Antarctique. Il est composé de différentes couches de lave de compositions différentes, tephriphonolitiques et phobolitiques pour les plus récentes (i.e. les couches moins profondes) et basanite pour les plus anciennes (i.e. les couches les plus profondes, Kyle et al., 1992) et héberge deux lacs de lave qui sont actifs depuis 1972, au moins (Giggenbach et al., 1973). Les conditions météorologiques idéales et le contexte scientifique de l'Antarctique, fait de l'Erebus un objet d'étude idéal. De plus la composition différenciée du magma de ce volcan fait de lui un cas unique puisque les autres lac de laves connus pour être persistants (Erta'Ale, Kilauea, Nyiragongo, Ambrym) ont des magmas de composition plus pauvre en silice (voir le tableau 5.5 et Smithsonian Institution, 2013).

La viscosité du magma phonolitique de l'Erebus varie probablement de 10^5 Pa.s à 10^7 Pa.s (Le Losq et al., 2015) et deux types d'activité y sont observées, i) la convection et dégazage des lacs (e.g. Peters et al., 2014a,b) et ii) l'explosions de larges bulles de gaz (e.g. Aster, 2003; Johnson et al., 2008b; Gerst et al., 2013). Ces larges bulles de gaz peuvent émettre des volumes de gaz entre $1 \times 10^3\,\mathrm{m}^3$ et $24 \times 10^3\,\mathrm{m}^3$ (e.g. Johnson et al., 2008b).

Le gaz émis, en surface, par l'Erebus provient en majorité d'une source profonde de magma basanite (gaz riche en CO2) et en minorité d'une source plus superficielle de magma phonolite (gaz riche en H2O, Iacovino, 2015; Ilanko et al., 2015). La coexistence de ces deux sources de dégazage génère en surface des cycles (Molina et al., 2015) que l'on peut observer par le niveau du lac de lave, les changement de proportions des gaz émis, les variations de flux de chaleur, de température du lac et de la vitesse de la surface du lac (Oppenheimer et al., 2009; Alletti et al., 2014; Peters et al., 2014a,b; Jones et al., 2015).

Les formes d'ondes sismiques des VLPs sont très reproductibles depuis plusieurs années, indiquant que le système est stable malgré des variations dans le nombre d'explosions par jour (Aster et al., 2008). Les quelques changements dans les VLP semblent liés à la direction caractéristique des éjecta (et des gaz) et la réponse imédiate du conduit à l'explosion (Aster et al., 2008). En outre, le peu de signaux sismiques liés à des événements volcano-tectoniques (Rowe et al., 2000) indique que peu de contraintes ou sur-pression s'accumulent à l'Erebus et est en accord avec l'existence d'un system ouvert (Aster et al., 2008).

1.2.2 Mécanismes associés à l'activité Strombolienne

L'activité Strombolienne consiste en surface à des séries de courtes et petites explosions (VEI<2) en système volcanique ouvert et dont les ejecta, peu fragmentés, retombent à moins de ∼1 km (Figure 1.1, Newhall and Self, 1982; Walker, 1973). Ces explosions sont générées par de larges bulles de gaz qui explosent à la surface du magma parce que la différence de pression entre la pression dans l'air et la pression interne dans la bulle est trop importante. La difference de pression est liée au fait que la bulle de gaz, qui monte par flotabilité vers la surface, va trop vite dans le conduit, par rapport à la viscosité du magma qui l'entoure, pour avoir le temps de décompresser. La compréhension de l'activité Strombolienne commence donc par la compréhension de la formation des grosses bulles de gaz qui remontent dans le conduit volcanique jusqu'à la surface du magma où elles explosent (Figure 1.3).

Plusieurs mécanismes sont proposés dans la littérature pour expliquer la formation de ces

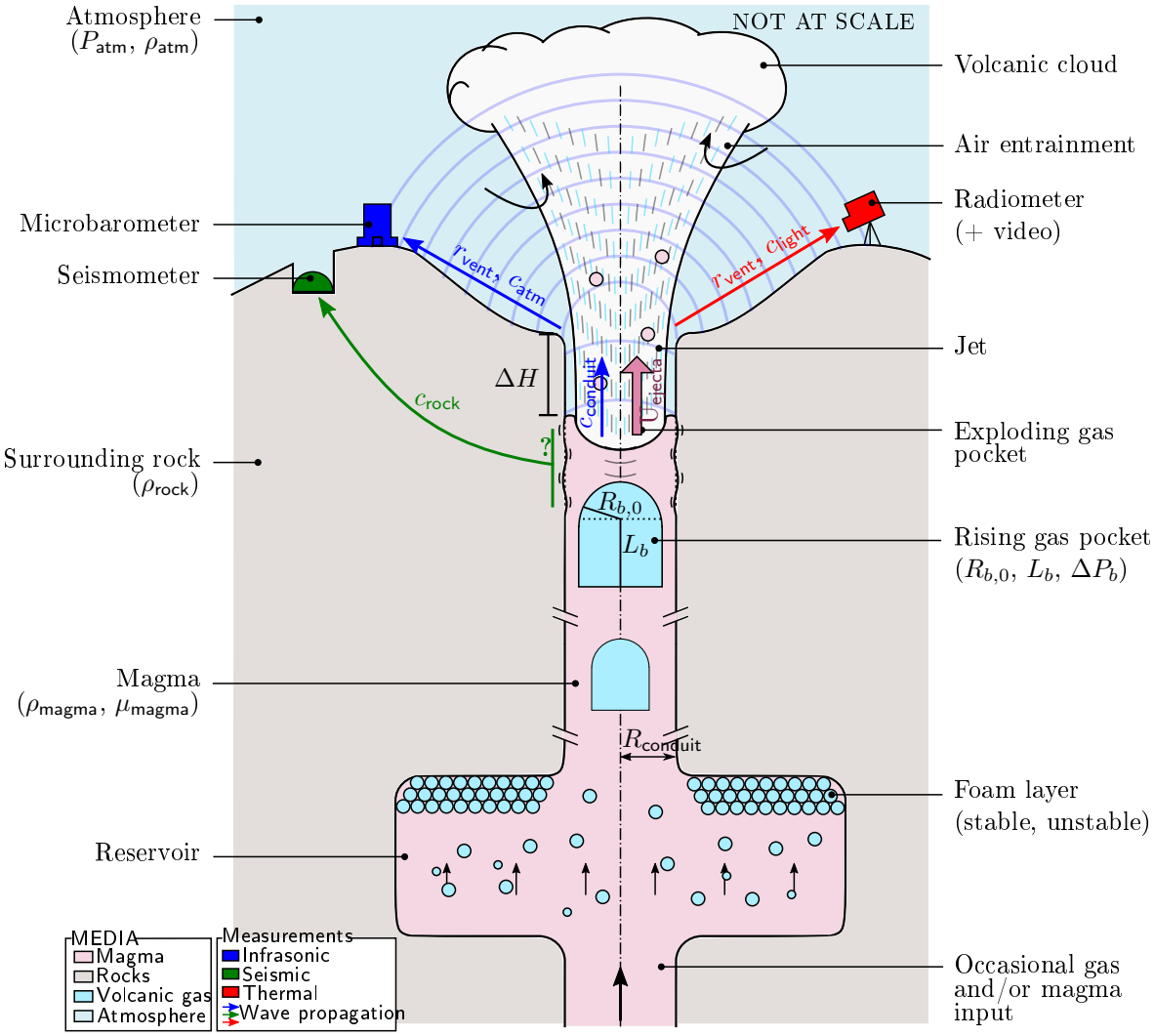

FIGURE 1.3 – Croquis de l'activité strombolienne et des mesures géo-physiques.

grosses bulles de gaz, appelées bulles de Taylor dans le domaine de la dynamique des fluides et *slugs* en volcanologie. Le premier mécanisme est proposé par Jaupart and Vergniolle (1988, 1989) et suppose que la formation des bulles de Taylor se fait en profondeur dans le réservoir magmatique (collapsing foam model). Une couche de gaz mousseuse s'accumule au toit du réservoir à cause d'un apport de gaz plus profond (Figure 1.4b). Cette couche de mousse s'épaissit alors jusqu'à son point de déséquilibre (instabilité) pour coalescer, partiellement ou complètement, sous la forme d'une grosse poche de gaz qui remonte ensuite dans le conduit. La quantité de mousse qui coalesce détermine le volume de gaz initial relâché dans le conduit. Ce modèle considère que la poche de gaz ainsi crée remonte dans le conduit plus rapidement que le magma (separated two-phase flow), approximation valide au vu de la taille des bulles à l'origine des explosions Stromboliennes.

Le deuxième modèle est proposé par Parfitt et al. (1995) et suggère que la formation des grosses poches de gaz se fait par coalescence progressive dans le conduit (rise speed dependant model). De petites bulles de gaz s'aggrègent progressivement dans le conduit pour former des bulles de plus en plus grosses au fur et à mesure de leur accrétion et de leur décompression (Figure 1.4a). Ce modèle considère que le gaz et le magma remontent à la même vitesse dans le conduit (homogeneous two-phase flow). Ce modèle propose que l'activité Strombolienne des volcans basaltiques résulte d'une vitesse du magma dans le

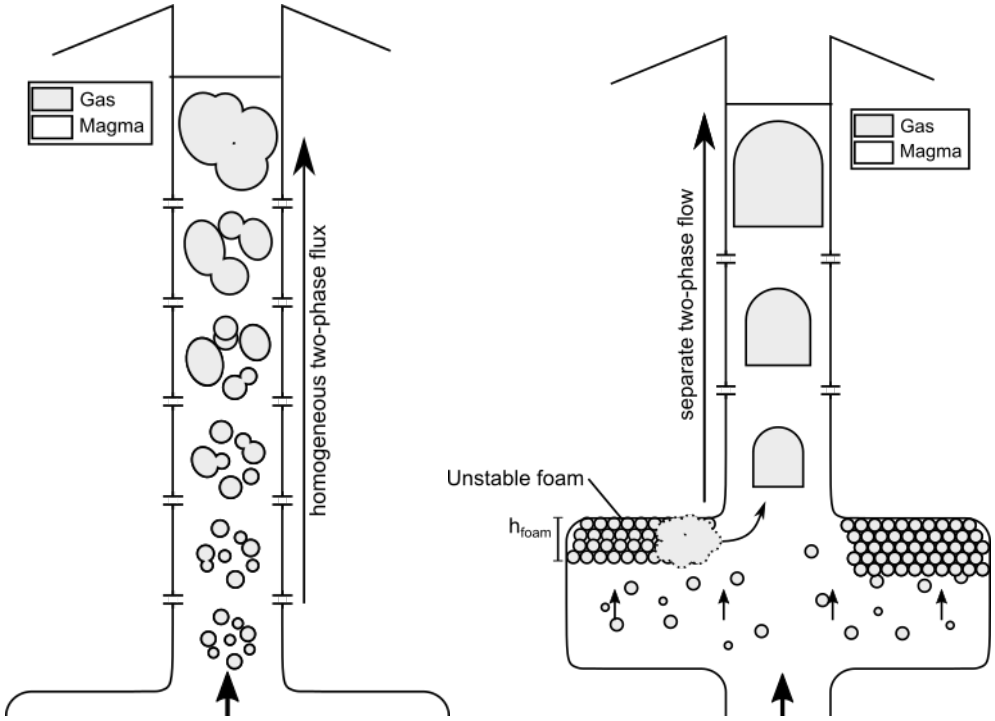

(a) Rise speed dependent model (b) Collapsing foam model

FIGURE 1.4 – Formation des larges bulles de gaz à l'origine des explosions stromboliennes. a) Coalescence progressive du gaz dans le conduit Parfitt et al. (1995). b) Coalescence massive de la couche de mousse au toit du réservoir Jaupart and Vergniolle (1988, 1989).

conduit plus faible dans le cas des explosions Stromboliennes que dans le cas des fontaines de laves.

Un autre modèle suggère que les larges bulles de gaz responsables des explosions Stromboliennes peuvent être formées par des ondes de concentration dans un magma en régime bulleux (Manga, 1997). L'hypothèse de ce modèle est qu'une bulle qui monte plus vite que les bulles dans son voisinage est ralentie par une fraction volumique de gaz localement plus importante. La vitesse d'ascension est d'autant plus réduite que la concentration de bulles augmente. Ce modèle a été proposé pour expliquer les puffs au Stromboli (Ripepe et al., 2002).

Des expériences menées par James et al. (2004) ont également montrées que de grosses poches de gaz peuvent se former dans un conduit incliné, à partir d'un régime bulleux. En effet, l'inclinaison du conduit favorise l'accumulation des petites bulles de gaz sur la partie haute du conduit et améliore donc le mécanisme de coalescence. Ces poches de gaz sont plus volumineuses et plus fréquentes dans un conduit incliné que dans un conduit vertical, pour un même flux de gaz donné. Leur vitesse est également plus importante puisque l'inclinaison du conduit permet de réduire les pertes d'énergie liée à la viscosité du liquide. Par example, la vitesse du slug est augmentée de $\sim$40 % dans un conduit incliné à 30° par rapport à la verticale. Les résultats de ces expériences menées par James et al. (2004) sont cruciales puisque que l'étude de VLPs générés par un mécanisme source fortement reproductible au Stromboli suggère que les conduits au Stromboli sont inclinés d'environ 30° par rapport à la verticale.

Ces grosses poches de gaz, beaucoup moins denses que le magma, remontent rapidement dans le conduit sans avoir le temps de s'équilibrer avec la pression de la colonne de magma

au dessus d'elles ($\rho_{\text{magma}} g h_b$). Ces bulles acquièrent une surpression ΔP_b qui dépend de la vitesse d'ascension de la bulle et de la viscosité du magma. D'autres sources de sur-pression ont été proposées. Le plus vieux modèle propose que les grosses poches de gaz, formées par la coalescence massive de la mousse accumulée au sommet du réservoir, ont une source de sur-pression initiale dans le gaz lié à leur coalescence rapide (e.g. Vergniolle and Caplan-Auerbach, 2004).

Ces larges poches de gaz peuvent, au cours de leur ascension, devenir instables, casser puis se reformer (Suckale et al., 2010; Vergniolle and Gaudemer, 2015). Cela dépend essentiellement de la viscosité du magma et de la taille de la bulle que l'on peut traduire en terme de nombre de Reynolds (rapport des forces inertielles et visqueuses, caracterisant le régime d'écoulement : laminaire – turbulent) et de Bond (rapport des forces gravitationelles et de la tension de surface à l'interface entre deux fluides). Pour un nombre de Bond supérieur à 1, la bulle devient déformable ce qui favorise la coalescence (petit Reynolds) ou la rupture (large Reynolds) de la bulle. La rupture est le résultats de trois processus :

1. la naissance d'une instabilité de Rayleigh-Taylor à la surface de la bulle
2. l'insuffisence de la tension de surface pour restorer la surface de la bulle lorsque le rayon est supérieur à un rayon critique
3. la stabilisation de la bulle par amortissement et transport latéral de la perturbation lié aux forces visqueuses.

Selon l'importance relative de ces trois processus, deux régimes de rupture sont possibles :

- la rupture graduelle, apparaît pour des nombres de Reynolds similaires pour un slug et une bulle
- la rupture catastrophique, apparaît pour des nombres de Reynolds plus faibles pour les slugs que pour les bulles parce que le slug est plus lent que la bulle et qu'il y a plus de contraintes, liées à la paroie du conduit, sur les côtés du slugs que sur les bulles.

Une autre source d'instabilité peut être générée lors de la remontée d'un slug dans un conduit qui s'élargie ou qui se rétrécie (James et al., 2006). La variation du diamètre du conduit génère des changements de pression complexes qui dépendent beaucoup de la taille du slug et de la configuration du conduit. Un élargissement du conduit peut entrainer la rupture du slug parce que la vitesse dans la partie large augmente (fraction volume de gaz moins importante). Cela génère un changement de pression qui peut être à l'origine de VLP mesurés dans le cadre de l'activité strombolienne. Un rétrecissement du conduit, en revanche réduit la vitesse du slug et les effets d'inertie. Les effets visqueux sont quant à eux renforcés et les changements de pression liés au passage du slug d'un conduit large à un conduit étroit génère des oscillations de pression plus complexes (James et al., 2006, table 1).

Une fois proche de la surface, la différence de pression entre le gaz dans la bulle et l'atmosphère est tel que les bulles ne peuvent pas ne pas se casser. Elles explosent donc avec une intensité d'autant plus forte que leur surpression est importante. Chaque explosion propulse dans l'atmosphère des produits à haute température : le gaz de la bulle et des fragments de magma plus ou moins gros (ejecta). L'explosion génère également des ondes acoustiques : l'onde acoustique audible mais également des infrasons qui sont de plus basses fréquences ($<$20 Hz). Les infrasons se propagent sur de plus longues distances avec une moindre atténuations que les ondes sonores de plus hautes fréquences. L'explosion génère aussi des vibrations qui se propagent sous forme d'ondes sismiques dans le sol.

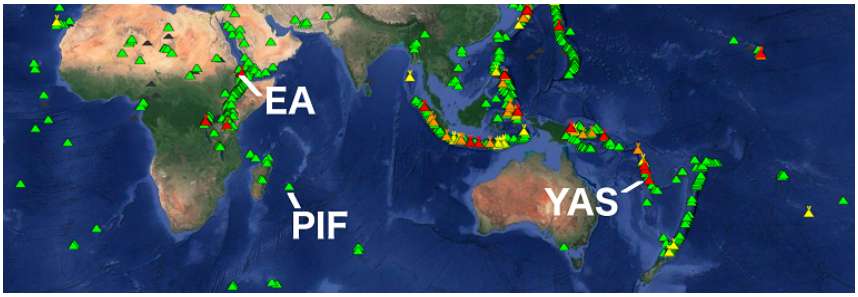

FIGURE 1.5 – Localisation des trois volcans étudiés : Erta'Ale (Est africain), Piton de la Fournaise (Océan Indien) et Yasur (Océan Pacifique). Les volcans en éruption sont symbolisés par des triangles rouges, ceux en éruption mineure en orange, ceux qui présentent une activité en jaune et les autres en vert. (https://earthquakes.volcanodiscovery.com/)

Pour maintenir l'activité Strombolienne pendant de longues periodes, il est nécessaire d'avoir un flux de gaz suffisant pour que le conduit ne se bouche pas par refroidissement du magma. En outre le régime de slug est plus efficace que le régime bulleux pour limiter le refroidessement du magma et la formation d'une croute à la surface puisqu'un slug perturbe plus efficacement la surface que les petites bulles du régime bulleux (James et al., 2004).

1.3 Problématique

Les nombreux volcans, dans des contextes tectoniques différents, pouvant avoir une activité Strombolienne intermittente ou persistante et les changements d'activité du Stromboli posent la question de la variabilité de l'activité Strombolienne et de son impact local sur l'environnement. Cette thèse est orientée selon deux grands axes.

1. La variabilité de l'activité Strombolienne mondiale et de son impact sur l'environnement local est étudiée au travers de l'étude quantitative de l'activité de trois volcans faisant des éruptions Stromboliennes et qui ont été choisis pour leur contexts tectoniques et leur magma différents et leur vigueur d'activité différente ; de faible à Piton de la Fournaise et à l'Erta'Ale à moyenne/forte au Yasur. L'objectif de cette étude quantitative et de pouvoir dire d'un volcan s'il a une activité faible ou forte à partir de paramètres thermiques ou infrasoniques et d'en déduire son impact sur l'environnement local en terme de flux de gaz dans l'atmosphère.
2. La variabilité temporelle de l'activité Strombolienne est étudiée au Yasur, pour lequel nous disposons de plus de dix ans de données infrasoniques quasiment en continu (4.5 ans de données mises bout à bout). Nous nous focalisons cependant sur les données de deux missions de terrains (∼70 jours) pendant lequelles des données infrasoniques, thermiques et sismiques sont disponibles et nous permettent de mieux contraindre et comprendre l'activité Strombolienne.

1.4 Cas d'étude

L'Erta'Ale, le Piton de la Fournaise et le Yasur ont été choisis parce qu'ils présentent des contextes tectoniques variés. Les compositions magmatiques y sont variées (Figures 1.5 and 1.6), ainsi que la viscosité du magma qui est d'environ 10 Pa.s à l'Erta'Ale (Schmincke, 2004), 40 Pa.s au Piton de la Fournaise et de 10^4 Pa.s au Yasur (Gaudin et al., 2014b). Plus

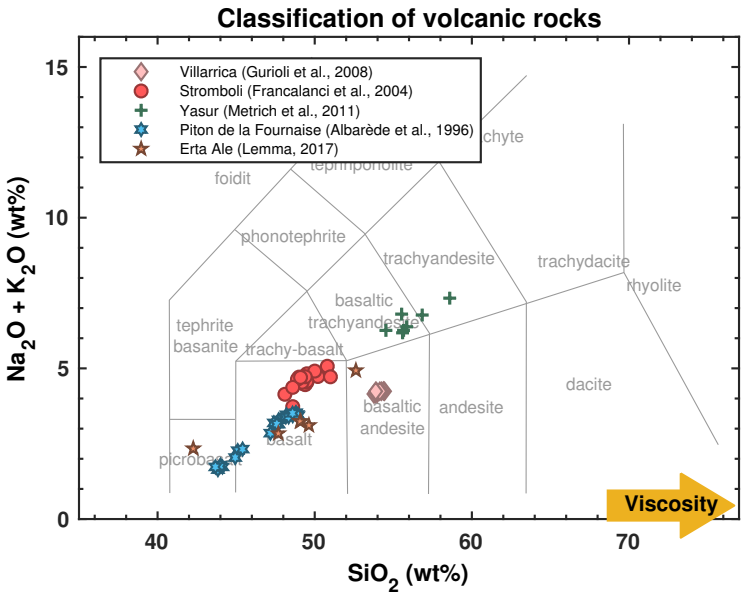

FIGURE 1.6 – Composition des magma des volcans étudiés (Erta'Ale, Piton de la Fournaise et Yasur) et des deux volcans discutés dans Marchetti et al. (2009) (Villarrica, Chili et Stromboli, Italie).

un magma est visqueux, plus le dégazage y est difficile. La pression du gaz pré-explosions est donc d'autant plus importante dans le magma visqueux et les explosions Stromboliennes plus fortes.

Le traitement de données infrasoniques, thermiques et sismiques nous permettent d'étudier la dynamique éruptive dans son intégralité :

- les infrasons sont sensibles aux mouvements de gaz et ils permettent une mesure de la vitesse du gaz et des volumes émis ;
- les données thermiques sont sensibles à la présence des solides et liquides chauds présents dans le champ de vision des radiomètres et permettent une étude des phases solide et liquide (ejecta) ; l'utilisation de deux radiomètres nous permet en plus d'étudier la dynamique des éjecta (i.e. mesure de la vitesse)
- les données sismiques sont sensibles aux mouvements du magma sur toute la hauteur du conduit et peuvent donc contenir des informations sur la formation de la bulle de gaz en profondeur, sa remonté et sur son explosion en surface car tous ces phénomènes induisent des mouvements du magma autour de la bulle.

1.4.1 Erta'Ale

L'Erta'Ale est un volcan situé à l'est de l'Éthiopie, dans la depression Danakil, au nord de l'Afar (Tazieff, 1994). Il est constitué de 2 lacs de lave, le cratère nord inactif depuis des décades et le cratère sur en activité permanente qui peut génerer des explosions Stromboliennes. Le magma y est basaltique peu différencié et peu visqueux (basalt transitionnel, 10 Pa.s Lemma, 2017; Schmincke, 2004).

Le cratère sud était actif en mars 2003, et on pouvait y observer que le niveau de magma était bas dans le lac. Chaque jour, on pouvait également observer que la croute de magma solide et froide s'enfonçer, de par sa densité plus élévée, dans le magma plus chaud (Bouche

et al., 2010). À cette période, le cratère nord ne produit pas d'explosion Strombolienne mais émet un flux de SO_2 comparable à celui du cratère sud (sud : $0.7\,kg.s^{-1}$; nord :$0.6\,kg.s^{-1}$, Oppenheimer et al., 2004)

De larges bulles ont pu être observées partout sur les bords du lac mais surtout toujours au même endroit au milieu du lac. On s'intéresse uniquement à ces bulles qui explosent au centre du lac, car contrairement aux autres, elles viennent probablement directement du conduit, et donc du réservoir.

Les mesures thermiques et acoustiques ont été faites à 110 m du centre du lac, pendant 5 jours du 22 au 27 mars 2003 (Bouche et al., 2010).

1.4.2 Piton de la Fournaise

Le Piton de la Fournaise est un volcan bouclier sur l'Île de la Réunion, qui se situe dans l'Océan Indien (France). Ce volcan est dû au point chaud qui serait responsable des trapps du Decan (e.g. Duncan, 1978, 1981; Duncan et al., 1990). Comme l'Erta'Ale, il produit également un magma peu différencié et peu visqueux (basalt, 40 Pa.s Albarède et al., 1997; Di Muro et al., 2014; Hibert et al., 2015).

La plupart des éruptions du Piton de la Fournaise ont lieu dans l'enclos Fouqué depuis sa formation il y a 4745 ans (Gillot and Nativel, 1989). Une éruption peut présenter plusieurs phases avec un style éruptif différent : coulées de lave, fontaines de lave de faibles hauteurs (<30 m) ou bien séries répétées explosions Stromboliennes de faible intensité.

L'éruption du 30 août 2006 au 1 janvier 2007, a été enregistrée par des capteurs thermiques et infrasoniques à partir du 18 novembre 2006 (Dupont, 2010). On s'intéresse ici à une phase Strombolienne, celle du 10 au 14 décembre. Une seule bouche éruptive était alors active, et les capteurs se situaient à 115 m de cette bouche.

1.4.3 Yasur

Le Yasur est un cône de scories sur l'Île de Tanna, dans l'Océan Pacifique (Vanuatu). L'activité Strombolienne persistente du Yasur est dûe à la subduction des Nouvelles Hebrides où la plaque Australienne plonge sous la plaque Pacifique (Firth et al., 2014). L'activité plus forte du Yasur est probablement dûe à son magma plus différencié et plus visqueux (trachy-andesite basaltique, 10^4 Pa.s Métrich et al., 2011; Gaudin et al., 2014b).

Une première série de mesures thermo-infrasoniques a été faite du 18 juin au 1er juillet 2009 à environ 280 m du centre du cratère. Une activité relativement typique, mais marquée par un niveau assez haut de la colonne de magma, y a été observée par comparaison avec la description d'autres périodes au Yasur. Les mesures thermiques sont optimales à partir du 28 juin. De plus une station sismo-infrasonique, en place sur le mont Melkem (500 m), nous a permis d'acquérir une quantité importante de données du Yasur, en quasi-continu de 2003 à 2014, les trous de données étant de longueurs variables en l'absence d'une présence locale.

La deuxième série de mesures thermo-infrasoniques a été enregistrée pendant 2 mois, du 15 septembre au 6 novembre 2016 à environ 340 m du centre du cratère. Additionnellement,

le centre de surveillance du Vanuatu (VMGD pour Vanuatu Meteorology and Geohazards Department), nous a aimablement prêté les données sismiques de leur station YASH à 1500 m du sommet du volcan. L'activité Strombolienne y était beaucoup plus vigoureuse qu'en 2009 avec une alternance de phases faibles et de phases fortes. L'activité était telle que le niveau d'alerte et passé de 2 (*major unrest*) à 3 (*minor eruption*) du 15 au 18 octobre (Tables D.1 and D.2). Le niveau d'alerte est défini par le VMGD à partir du RSAM (Real-Time Seismic Amplitude Measurements) et du SSAM (Seismic Spectral Amplitude Measurements). Ces méthodes sont expliquées plus tard en section 4.4.5. Les mesures thermiques s'arrêtent définitivement le 10 octobre à cause de problèmes d'alimentation électriques.

Chapter 2

Data acquisition and calibrations

Contents

2.1 Data acquisition **25**
2.2 Distance from the vent to the sensor **26**
2.3 Calibration: response time of the radiometers **27**
2.3.1 Field measurements 27
2.3.2 Laboratory measurements 27
2.4 Calibration: sensitivity of the thermal system **28**
2.5 Calibration: scale of the video **31**

2.1 Measurements of the eruptive dynamics at Erta'Ale, Piton de la Fournaise and Yasur

Infrasonic, seismic and thermal measurements were recorded by several sensors that are described below.

A MB2000 microbarometer, developed by the CEA-DASE (Commisserriat à l'Énergie Atomique, Département Analyse et Surveillance Environnement), was used to measure the acoustic pressure at Erta'Ale, with a sensitivity of $5\,\mathrm{mV.Pa^{-1}}$ in the frequency band 10^{-3} Hz to 80 Hz.

MB2005 microbarometers, also developed by the CEA-DASE, were used to measure the acoustic pressure at Piton de la Fournaise and Yasur (the MB2005 at Yasur is lend by the CEA-DASE), with a sensitivity of $1\,\mathrm{mV.Pa^{-1}}$ in the frequency band 10^{-3} Hz to 40 Hz.

The microbarometers measure the acoustic pressure from all directions, we have a record of the activity from each active vent of a the volcano. The propagation of the infrasonic waves from the vent to the sensor can be disrupted by wind or topographic effects. The microbarometers measure, when occurs a Strombolian explosion, the disturbance wave that is generated by the sudden input of a large volume of gas into the atmosphere. The microbarometers can also measure noise, such as the wind, the oceanic waves (0.08 Hz–0.5 Hz, peak at 0.2 Hz, Landès et al. (2012)), anthropic noise or the ground vibrations.

The brightness temperature of the ejecta was measured by Cyclops 300AF thermopile radiometers (Minolta-Land) and give us estimates of the surface temperature of the ejecta. The thermopiles radiometers are well adapted for volcano studies because they can be used for a wide range of temperatures. The Cyclops 300AF radiometers measure the infra-red radiations (8 µm to 13 µm) in a 1° field of view, with a sensitivity of $1\,\mathrm{°C.mV^{-1}}$ and an effective response time, respTime of 0.19 s (5.27 Hz). The Cyclops send a chopped signal to the digitizer with a sampling rate equal to the response time. This reduces the temporal resolution of the thermal signal (section 2.3). Two radiometers were simultaneously used during the field campaign at Piton de la Fournaise and Yasur. They were settled such a way that their line-of-sight was aligned in the vertical with an angle $\Theta = 4°$ between both line-of-sights. The lower radiometers were targeting the surface of 1 vent because of the narrow field of view (1°). The narrow field of view has the advantage of measuring the direct out-put of the vent.

Radiometers are sensitive to the existence of hot liquids and solids and to their temperature. The radiometers are also sensitive to gases depending on the temperature and pressure (Hottel, 1954; Holman, 1992). The emissivity of a $CO_2{}^{+}H_2O$ mixture can reach 0.70 just above the vent (<1 m) and fastly decreases above 1 m (Hottel, 1954; Holman, 1992). The H_2O, can opacify the field of view of the radiometers (i.e. it hides objects behind the H_2O) when it condensate into liquid water (emissivity of 0.98).

The ground velocity is measured at Yasur, in June 2009, from Mount Melkem using a Trillium 40 (Nanometrics) at ∼500 m from the source. This sensor is lend by the CEA. YASH permanent station, of the Vanuatu Meteorology and Geohazards Departement, measures the ground velocity using a LE-3Dlite MkII[1] (Lenartz electronic) at ∼1500 m from Yasur summit. These 3 components seismometers measure the ground velocity in 3 plans with sensitivities of 1553 V/(m/s) and 400 V/(m/s) for the Trillium 40 and LE-

[1] Not to be confused with the LE-3Dlite MkIII seismometer

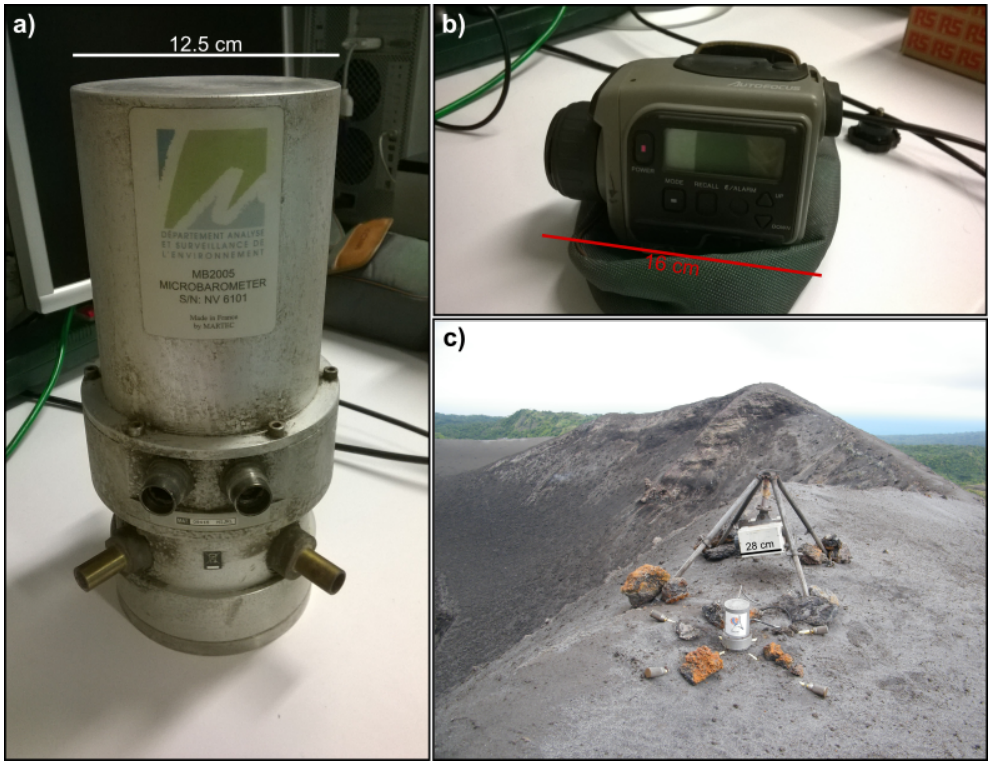

Figure 2.1 – Some sensors. a) Microbarometre MB2005. b) Radiometer Cyclops 300AF. c) Station at Yasur in 2016.

3Dlite-MkII seismometers, respectively.

Infrasonic and thermal measurements were recorded using a Geostar digitizer at Erta'Ale and a RefTek 130 digitizer at Piton de la Fournaise and Yasur. Seismic measurements at Yasur were recorded using Quanterra Q330 digitizers. The details of the sensitivities and sampling frequencies are given in tables 2.1 and 2.2. Note that the digitizers can not record at several sampling frequency. The sampling frequency was configurate in order to record accurate acoustic pressure (>75 Hz). The sampling frequency is then over-sampled for thermal records.

The videos taken during the 2009 field campaign at Yasur were recorded by a Sony camera (DSR-PD170P) with a resolution of 640 px × 480 px and 25 frames per second (fps). The videos were synchronised with the GPS by filming the time on the GPS display (time of Paris).

2.2 Distance from the vent to the sensor

The distance from the sensor was estimated at 110 m and 115 m for the field campaigns at Erta'Ale and Piton de la Fournaise, respectively (Bouche et al., 2010; Dupont, 2010).

The vent-sensor distance during the 2009-field campaign is estimated from the location of the sensors, measured with a GPS and assuming that the active vents observed were approximately at the same location that the active vent observed in 2008 (Marchetti et al., 2013). The vent which was targeted by the radiometers was vent B from Marchetti et al. (2013).

Table 2.1 – Characteristics of the thermo-infrasonic acquisition during the four field campaigns at Erta Ale, Piton de la Fournaise and Yasur Volcanoes.

		EA03	***PdF06***	***YAS09***	***YAS16***
Acquisition					
Date		22/03/2003 27/03/2003	18/11/2006 01/01/2007	18/06/2009 01/07/2009	15/09/2016 05/11/2016
Digitizer		Geostar	RefTek 130	RefTek 130	RefTek 130
*Sensitivity**	$mV.bit^{-1}$	0.153	1.589×10^{-3}	1.589×10^{-3}	1.589×10^{-3}
Sampling rate	Hz	75	1000	1000	100
Acoustic					
Microbarometer		MB2000	MB2005	MB2005	MB2005
Pass-band	Hz	10^{-3} to 80	10^{-3} to 40	10^{-3} to 40	10^{-3} to 40
Sensitivity	$mV.Pa^{-1}$	5	20	20	20
Distance	m	110	115	280	340
Thermal					
Radiometer		Cyclops 300AF	Cyclops 300AF	Cyclops 300AF	Cyclops 300AF
Pass-band	µm	8 to 13	8 to 13	8 to 13	8 to 13
Sensitivity†	$mV.°C^{-1}$	1	1	1	1
Response Time	s	0.19	0.19	0.19	0.19
Field of view	°	1	1	1	1
Distance	m	110	115	270	340
Else					
Period of interest		whole period	10/12/2006 14/12/2006 *Strombolian phase*	28/06/2009 01/07/2009 *Radiometers on*	15/09/2016 10/10/2016 *Radiometers on*
References		Bouche et al. (2010)	Dupont (2010)	This study	This study

*at a gain of 1
†within the range 200 °C to 1000 °C

In the fall 2016, the sensor location at Yasur, were also measured by a GPS, three times for each sensor. The mean value of the measurements is taken as the location for each sensor. The vent location was measured approximately by triangulation from several points of view of known location (figure 2.2b).

2.3 Calibration: response time of the radiometers

2.3.1 Field measurements

The thermal signal is chopped because at 0.19 s, the efficient response time (respTime) of the Cyclops 300AF radiometer (Minolta-Land). It is perfectly clear as steps on figure figure 2.3. Each step corresponds to a measurement sent from the output of the radiometer to the digitizer. The sample rate of 0.19 s is also very clear on the spectrogram at Piton de la Fournaise where the signal to noise ratio is low (Figure 2.3.1). However, it is harder to see it on the spectrogram at Yasur as the signal to noise ratio is higher.

Table 2.2 – Characteristics of the seismic acquisitions during the two field campaigns at Yasur.

		YAS09: Melkem	***YAS16: YASH***
Acquisition			
Digitizer		Quanterra Q330 (Kinemetrics)[†]	
Sensitivity[*]	$mV.bit^{-1}$	2.3842×10^{-3}	
Sampling rate	Hz	100	
Seismic			
Seismometer		Trillium 40[‡]	LE-3Dlite MkII[§]
		Nanometrics	*Lennartz electronic*
Sensitivity	V/(m/s)	1553	400
Bans pass	Hz	0.024 875 to 85.5	1 to 100
Working component		All	Vertical

[*] at a gain of 1
[†] https://www.iris.edu/hq/files/programs/passcal/docs/Q330-BrochureRevK.pdf
[‡] https://www.passcal.nmt.edu/webfm_send/948
[§] https://www.osop.com.pa/wp-content/uploads/2013/11/Manual_LENNARTZ_SISMOMETROS.pdf

2.3.2 Laboratory measurements

I conduct experiments in laboratory to measure the delay in recording between both radiometers. I have targeted at a soldering-iron with both radiometers at distances around 30 cm (Figure 2.4). Measurements were recording by the RefTek 130 digitizer at 1000 Hz. I have set the soldering-iron to its highest temperature (450 °C) and turn it on and off 10 times letting it cooling down between each experiment.

The soldering iron warms up quickly (<1.5 min) but cools down more slowly (>6 min, figure 2.5a–b). Small oscillations are present as the soldering-iron try to maintain its temperature still (start and stop of the resistance, figure 2.5d). The delay between the radiometers can be found when the soldering iron is turned on and when it is the warmest.

We observe on all experiments that both records start and reach their maximum at the same time (Figure 2.5d and f). The calculation, for each experiment, of the cross-correlation between the signal from both radiometers (Figure 2.5) prove their is no delay between both records. The zoom of the figure 2.5a–b, presents a short and variable delay between the extrema of the oscillations (Figure 2.5d). This can be explained by the effects of the air conditioning in the laboratory and the fact the radiometers target the same point but from different directions. No delay exists in records of the radiometers. The difference of amplitude and slope we observe is due to the different sensitivity of each radiometers (Figure 2.5a).

You can also note on figure 2.5e spikes on the steps of the signals. This is due to electronic noise induced by the cabling from the sensor to the digitizer.

2.4 Calibration: sensitivity of the thermal system

The radiometers are set in closed boxes during field measurements for protection against ashes and dust (Figure 2.6). We use Ze–Sn windows to let infra-reds pass through and hit the sensor because the radiometers are sensible to infra-red only (8 µm to 13 µm). The Ze–Sn window and the radiometer form the thermal system.

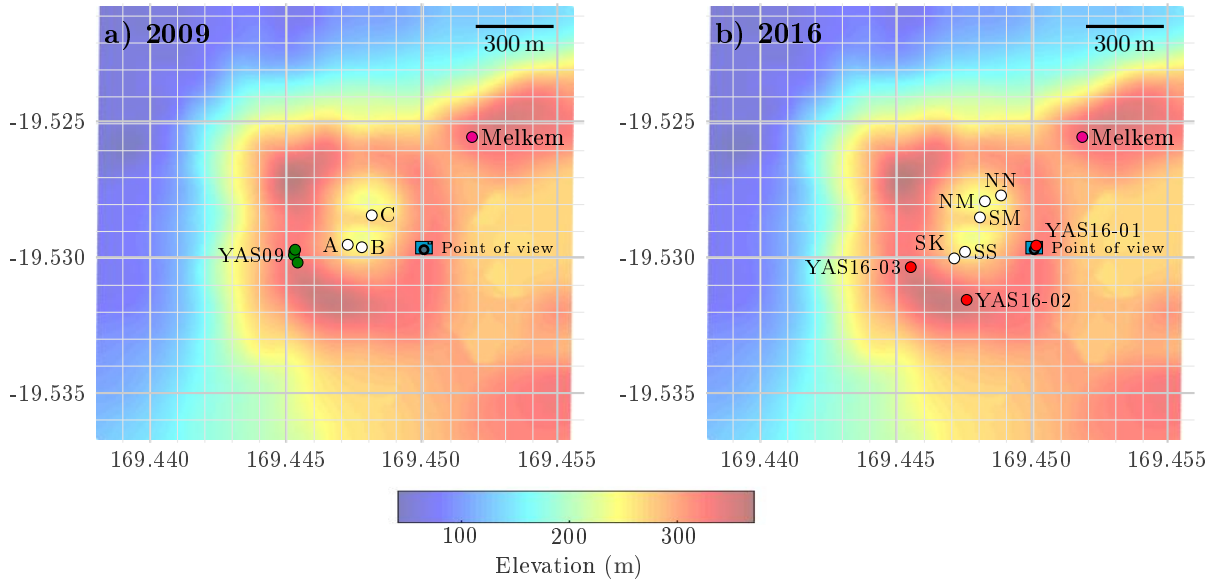

Figure 2.2 – Location of the vents and infrasonic sensors at Yasur volcano during the field campaigns in a) 2009 and b) 2016. The 2008-topography has a grid-resolution of 7 m (Chaput and Finizola, 2009). The permanent station of the Mount Melkem and the point of view of the tourists are also located in magenta and blue, respectively. NN, NM, SM, SS and SK are the notation I have used in my field note-book and stand for North-North, North-Middle, South-Middle, South-South and Skylight, respectively.

The Ze – Sn windows are polished on the outside face and handled anti-reflection on the inside face. In theroy, these windows let pass 85 % of the infra-red radiations (70 % if both faces were handled anti-reflection). Unfortunately, these Ze-Sn windows are not the most adapted windows close to active volcanoes because they get rapidly oxidised due to acid gas reducing the efficient sensitivity of the radiometers. The oxidation of the polished face can reduce amount of infra-red radiations that can pass through the window to 50 %. More adapted windows that can be used in the future is the Se – As – Se window whose calibration is given in Harris et al. (2005a).

Two calibrations were done in the laboratory before and after the field campaign at Yasur volcano in September–November, 2016 (Figure 2.7 and table A.3). First calibration was conducted in August 2016, using a cooking plate as a thermal source. The temperature was controlled by a handhold IR-thermometer at 200 °C (Thermo-hunter, Optex). Second calibration was conduct in November 2017, using boiling water and then a cooking plate as thermal sources. The temperature was controlled by an infra-red camera (FLIR B365) at 100 °C and 460 °C for the boiling water and the cooking plate, respectively. The temperatures were reading directly on the radiometers.

The handhold IR-thermometer, the infra-red camera and the radiometers measure the same radiated temperature T_{rad} which is proportional to the real temperature T_{real} of the warm source depending on its emissivity ϵ

$$T_{\mathsf{rad}} = \epsilon T_{\mathsf{real}}; \tag{2.1}$$

the transmittance of the ambiant air is neglected because all sensors are at the same distance from the warm source. The factor of correction f_{rd} of the sensitivity of the thermal system (radiometer+window) is then estimated from

$$T_{\mathsf{mes,rd}} = f_{\mathsf{rd}} T_{\mathsf{mes,control}}. \tag{2.2}$$

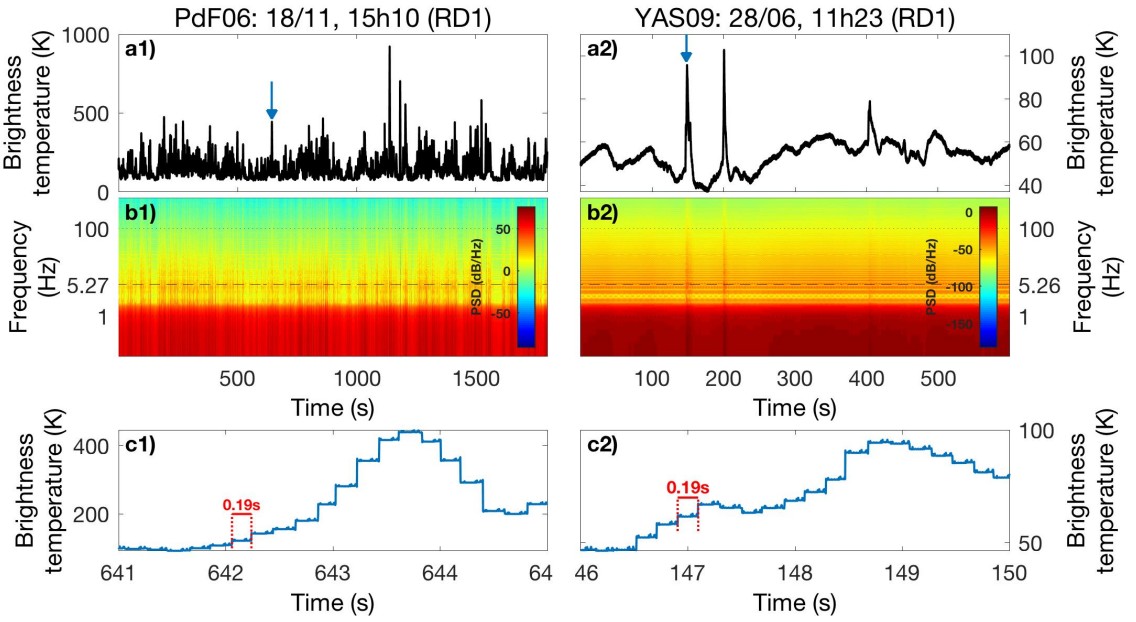

Figure 2.3 – Steps caused by the efficient response time of the radiometers on thermal signal at 1000 Hz at 1) Piton de la Fournaise (2006) and 2) Yasur volcano (2009). a) Raw data and b) the corresponding spectrogram with a sliding window of 1 s, 25 % of overlaps and 2^{13} points for the `fft`. The dashed line at 5.27 Hz hilight the sampling rate the radiometers. c) Zoom around blue arrow in a) to look at the effect of the response time of the radiometers. Note that the signal is much more lower at Yasur than at Piton de la Fournaise.

Both radiometers present a different sensitivity (i.e. different factor of correction), but their sensitivity remains stable before and after the field campaign in the fall 2016 ($R^2 \sim 1$, figure 2.7a). If there were not any oxidation the sensitivity of the thermal system should have been the same before and after the field campaign (Figure 2.7b-c). However, we see greater errors on the temperature after the field campaign than before the field campaign (i.e. the points of measurements are farther from the line 1:1) due to the increasing oxidation of the Ze−Sn windows.

The relative errors on the temperature, in degree celsius, ranges between 24 % and 76.5 % for the field campaign in 2016 when using the windows and having the emissivity $\epsilon_{\text{thermal}}$ of the radiometers set at 0.85. We need to multiply the measured temperature by factors ranging between 1.32 and 4.25 to get the real temperature (the median and the mean being 2.18 and 2.44, respectively).

More experiments could have been done to perform a good calibration of the thermal system. However, we do not know which window was associated to which radiometer during field experiments. We can rely on the calibration to have an order of magnitude of the correcting factor.

In practice, I multiply the recorded brightness temperature in degree Celsius by a factor 2 for all Yasur measurements in 2016 (The radiometers were configurated such a way they automaticaly corrected the 0.15 % of lost signal due to a new Zn−Se window.). The thermal data which are available for the 2009 field campaign were recorded during the 4 last days of the field campaign and the activity was typical. The calibration which was done before the 2016-field campaign is then representative for the 4 days of 2009 thermal data.

Note that, despite the calibration, a temperature variation less than ±50 °C is error prone

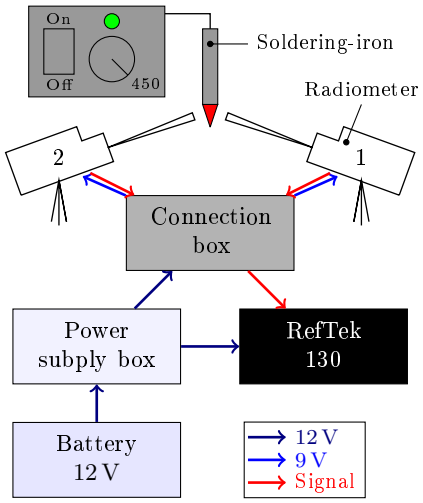

Figure 2.4 – Skech of the experiment to measure the typical delay between both Cyclops 300AF radiometers. RD1 (20002764) is at 30 cm and RD2 (20003181) at 30 cm.

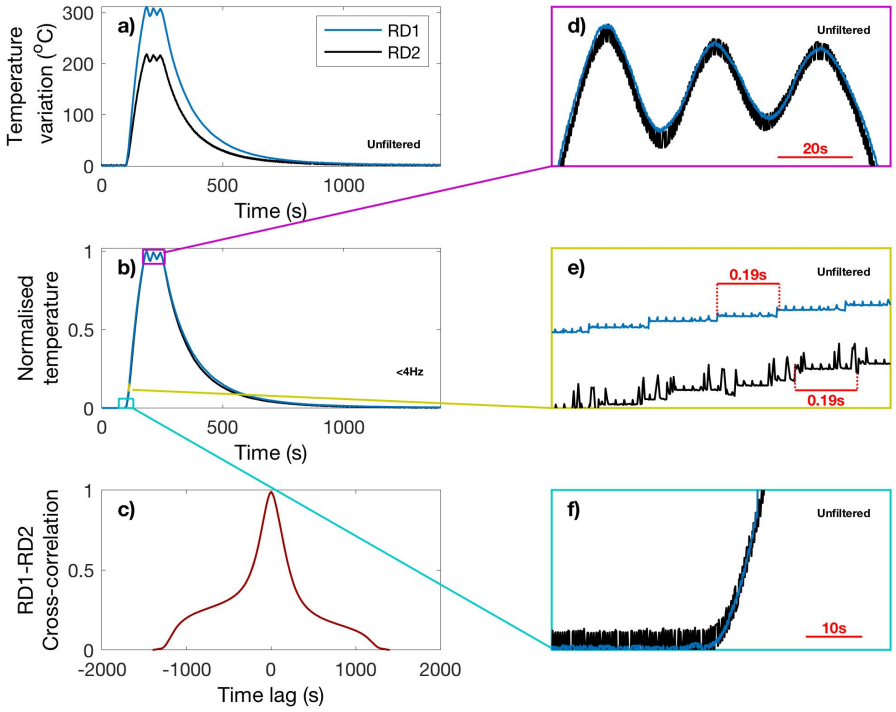

Figure 2.5 – Calibration of the delay between both radiometers: Example of experience 6. a) Raw temperatures of RD1 and RD2; RD1 and RD2 reach different temperatures because of their self-sensitivity. b) Normalized temperature filtered below 4 Hz. c) Cross-correlation between RD1 and RD2.d)–f) Zoom on the selected parts of the signal in b). Oscillation of the temperature due to the warm-up cycles of the soldering iron. e) Response time steps of the radiometers. The spikes on the steps are due to electronic noise. f) Both signals start at the same time.

due to the oxydation of the Ze–Sn windows. Note also that most of the thermal processing done here (Section 4.2) need relative temperatures rather than absolute temperature.

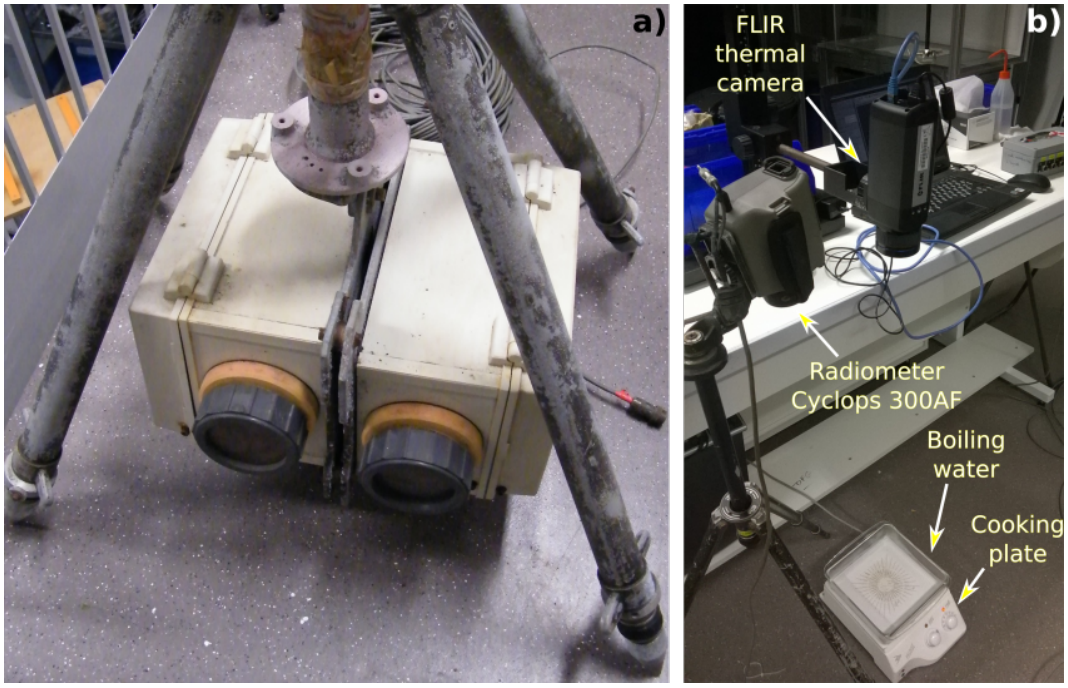

Figure 2.6 – Laboratoy calibration of the efficient sensitivity of the radiometers. a) Home-made box of protection for the radiometers. b) Laboratory calibration of the sensitivity of the thermal systems.

Table 2.3 – Measurements in pixel for the scaling of the video

Distance (cm)	w_1	w_2	w_3	h_1	h_2
140	146	25	53	-	46
180	73	12	27	113	24
410	50	9	18	77	17
460	45	8	16	68	15
Real size (cm)	23.8	3.9	8.8	33.8	7.2

2.5 Calibration: scale of the video

I have recorded the same object, a box of known dimensions, at several distances between 140 cm and 462 cm to find the relationship between the size of the box on the image of the video. Then I use *ImageJ* to measure the number of pixels of the height and width of the box. Alternatively, I measure specific features of the box.

The scaling is different horizontally and vertically (table 2.3 and figure 2.8).

Then we can deduce the size of a pixel, in metre, at any distance d and for any zoom z

$$W_{\text{px}} = 1.13 \times 10^{-3} d \qquad\qquad H_{\text{px}} = 1.04 \times 10^{-3} d,$$

For example, the distance to the volcanic cloud was around 270 m in 2009, giving the size of a pixel of 30.5 cm × 28.1 cm .

This calibration gives a very good estimate of the radius of the conduit at Yasur volcano

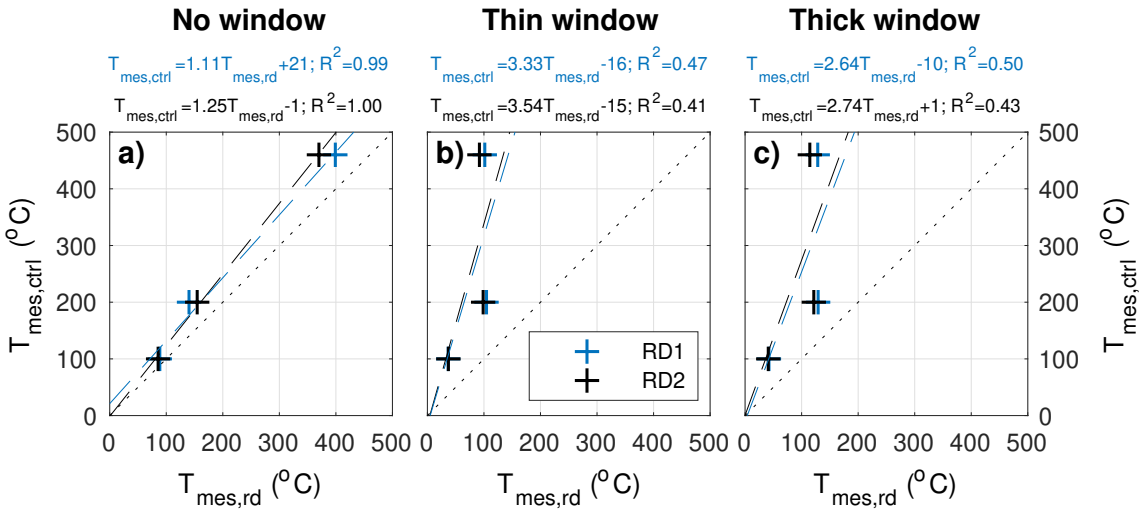

Figure 2.7 – Results of the calibration of the thermal systems in laboratory. The temperatures were taken by direct reading on the radiometers with their emissivity set at $\epsilon_{\text{thermal}} = 1$. The calibration at 200 °C was done in August 2016, while the calibrations at 100 °C and 460 °C were done in November 2017. a) RD1 (20002764) and RD2 (20003181) present a different sensitivity, but their sensitivity remains stable before and after the field campaign in the fall 2016. You can see the effect of the oxidation of the Zn−Se windows on b) and c).

in June 2009 when one vent was appearent. I measure a diameter of 17 px, i.e. 5.1 m by looking a gas pocket, surrounding by magma, just before it explodes (Figure 2.9). Then we round the radius of the conduit, R_{conduit} to 2.5 m for Yasur volcano.

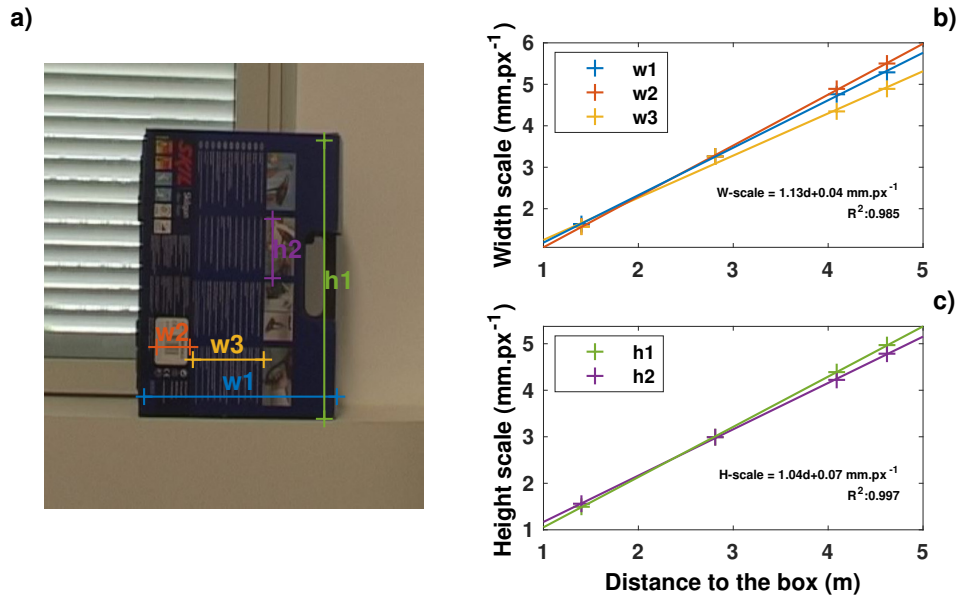

Figure 2.8 – Calibration of the video to find the size of an object filmed by the video. a) Measurements done on the box of known dimension. Scaling b) the width and c) the height.

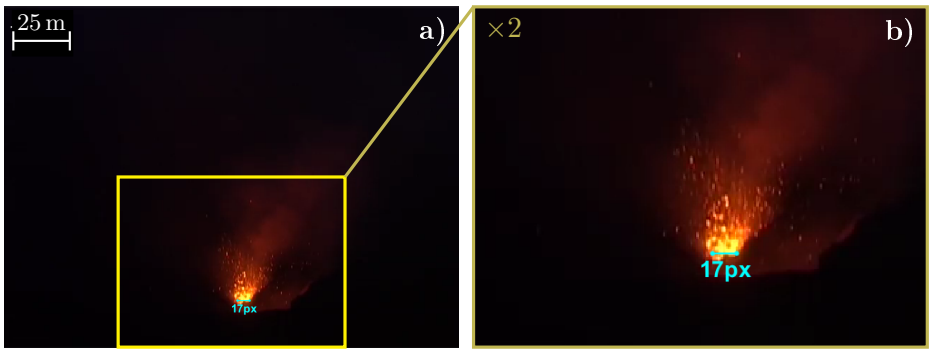

Figure 2.9 – Measurement of the diameter of the conduit at Yasur (June, 2009). The gas pocket, surrounding by magma is 17 px width just before it explodes. The diameter of the conduit is 5.1 m for a scale of 30.5 cm.px^{-1}.

Chapter 3

Pre-processing of the data

Contents

3.1 Requirement in statistical and signal analysis . . . **39**
3.1.1 Kurtosis . . . 39
3.1.2 Fourier transform . . . 39
3.1.3 Hilbert transform and the envelope of the signal . . . 42
3.1.4 Short presentation of the wavelet decomposition . . . 42
3.1.5 Calculation of errors . . . 45
3.2 Chain of acquisition . . . **46**
3.3 Data conversion to *mat-files* . . . **49**
3.4 Time correction . . . **50**
3.5 Filtering the data . . . **50**
3.6 Detection of events . . . **52**
3.6.1 Peaking method . . . 52
3.6.2 STA/LTA detector . . . 52
3.6.3 Cross-correlation . . . 54
3.6.4 Summary of the methods . . . 54
3.6.5 Selection of detections . . . 55
3.6.6 Detection of the Strombolian events during the field-campaigns 56
3.6.7 Link between detections seen by different sensors . . . 58
3.7 Classification of events . . . **58**
3.8 Gestion of the gaps of data for the estimations per sliding window . . . **60**
3.8.1 Energy . . . 61
3.8.2 Power . . . 62
3.8.3 Root-Mean-Square: . . . 62

The signals we record are composed from noise and discrete events due to Strombolian explosions.

Variable sources of noise can exist. Oceanic waves, weather changes, wind and topography effects, such as echos can be responsible for noise on infrasonic signal. Moreover, infrasonic sensors can also measure the ground vibrations.

The noise on thermal records are mostly due to the background temperature (temperature of the wall behind the vent we target). The wind can also blow the volcanic cloud outside from the field of view of the radiometer.

Seismic sensors might record earthquakes and human activity such as cars on a road, an industry or people walking close to the seismic sensor. They also can record the acoustic waves and noise due oceanic waves.

An electric noise can also exists due to the cables or connector (the longer the cables are, the more electric noise there is).

Then it is often necessary to filter data in order to enhance the signals of interest. However the measuremens by itself acts as a filter.

3.1 Requirement in statistical and signal analysis

3.1.1 Kurtosis

The kurtosis is the measure of the flatness distribution of a real-valued random variable. The wider the distribution is, the higher is the kurtosis. The kurtosis of the random variable X, of expected value μ_X and standard deviation σ_X, is the fourth standardized moment of this variable:

$$\mathrm{kurt}(X) = \mathbb{E}\left[\left(\frac{X - \mu_X}{\sigma_X}\right)^4\right] \tag{3.1}$$

where $\mathbb{E}[X]$ is the esperance of the variable X.

In this study, the kurtosis is calculated on sliding windows of length `dtt`, using MatLab function `kurtosis`, to create the kurtosis curve $\mathrm{Kurt}(T)$:

$$\mathrm{Kurt}(T) = \mathrm{kurt}\left(X\left(T \leq t < T + \mathrm{dtt}\right)\right). \tag{3.2}$$

This allows us to detect *anomalies* such as an explosion in the ambient noise. The flatness distribution remains stable and low when only noise is present. But the flatness distribution will increase significantly if a signal is added to the noise (Figure 3.1).

3.1.2 Fourier transform

The Fourier transform is of great interest to analyse the frequency contents of a signal in the spectral domain (Figure 3.2). It is also used for many technics in data processing, such

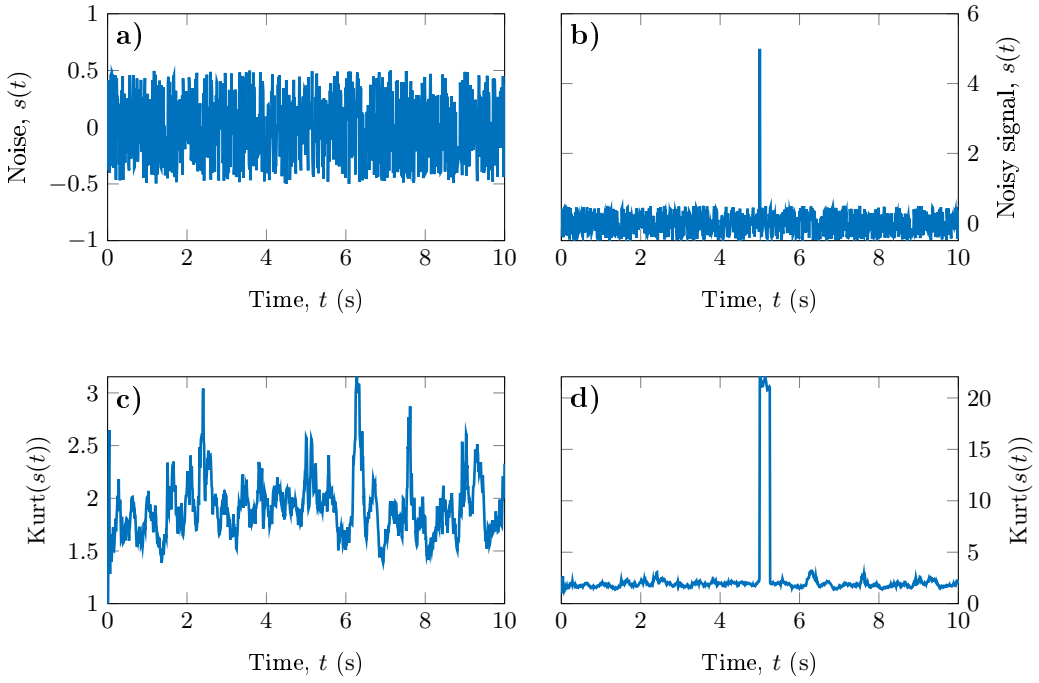

Figure 3.1 – Kurtosis curve with a sliding window of 0.25 s. a) Noisy signal. b) Same noisy signal than a) with an additional spike at 5 s. c) and d) kurtosis curves of the signals in a) and b), respectively. The spike of the signal b) is clearly visible on the kurtosis curve d) by an increase of the kurtosis values for each window that contains the spike.

as data filtering. The convolution of two signals in the time domain is simply the products of their Fourier transform in the spectral domain.

The complex Fourier transform $S(f)$ of a real signal, $s(t)$ defined in the time domain, is defined in the spectral domain by the decomposition of the signal into complex functions of different frequencies:

$$S(f) = \int_{-\infty}^{+\infty} s(t) e^{-2\pi i t f} \mathrm{d}t, \tag{3.3}$$

where i is the complex number. We can also calculate the signal $s(t)$ from its frequency contents $S(f)$ as

$$s(t) = \int_{-\infty}^{+\infty} S(f) e^{+2\pi i t f} \mathrm{d}f. \tag{3.4}$$

We use the discret Fourier transform a signal recorded at the sampling frequency f_s:

$$S_k = \sum_{n=0}^{N-1} s_n e^{-2\pi i k n/N}, \quad k = \{0, 1, \cdots, N\}. \tag{3.5}$$

The `fft` function we use in MatLab (`fft` for Fast Fourier Transform) processes a discrete Fourier transform. This function uses an algorithm to speed up the calculation. The user needs to build the frequency scale himself depending on the sampling frequency and the number of points of the discrete Fourier transform.

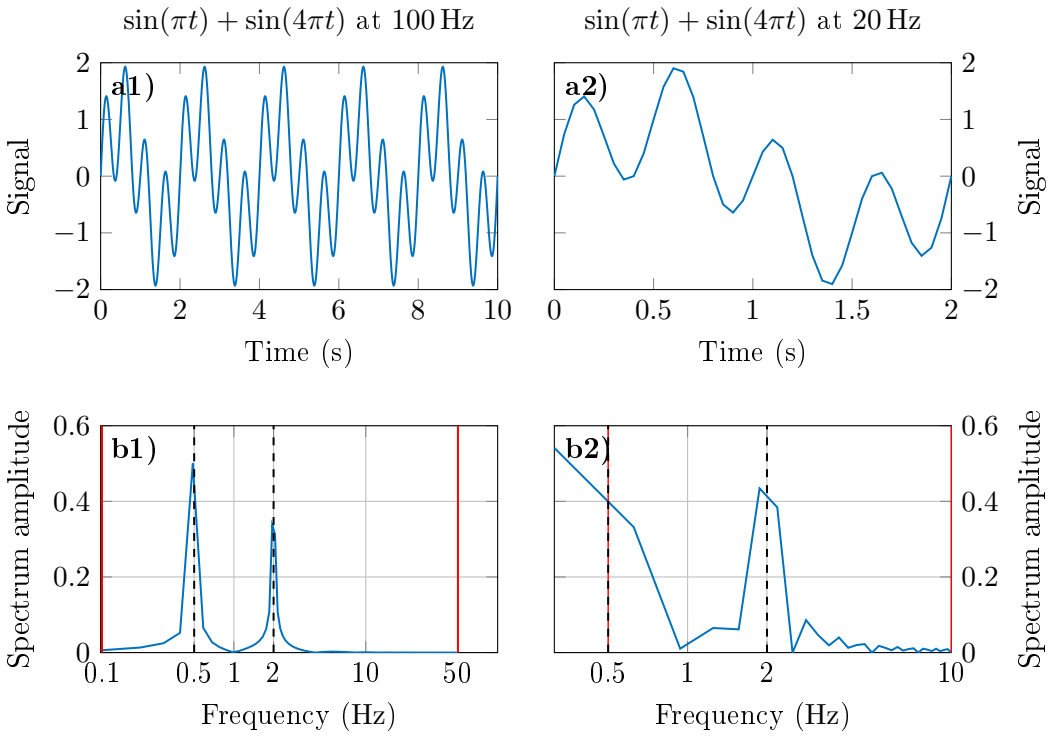

Figure 3.2 – Frequency contents of a signal s with main frequencies at 0.5 Hz and 2 Hz. a1) Signal of 10 s sampled at 100 Hz and b1) its spectrum amplitude. The frequency contents is clear between 0.1 Hz and 50 Hz (red vertical lines). a2) Signal of 2 s with a sampling frequency of 20 Hz and b2) its spectrum amplitude. The solo frequency that can be seen is that at 2 Hz, the 0.5 Hz being erased by the insufficient duration of the analysed signal.

The quality of the discrete Fourier transform depends on the duration of the signal and on the sampling frequency which limit the lower and upper frequencies of the spectrum ($f_{\min} = 1/t_{\max}$ and $f_{\max} = \mathcal{N}_f = f_s/2$ the Nyquiest frequency). The number of points of the discrete Fourier transform (often called nfft) determines the resolution of the frequency ($df = (f_{\max} - f_{\min})/\mathsf{nfft} = 1/\mathbf{lg}_s$ if $\mathsf{nfft} = N_s$, N_s being the number of samples of the signal s.), provinding that the number of points are all that of the signal itself and are note increased by a series of zeros as often done to smooth the results.

As written above, the convolution of two signals is the product of their Fourier transform. So considering the continuous signal $s(t)$, its conjugate $s^*(t)$ and its Fourier transform $S(f)$, we can demonstrate the Parseval theorem which states that the signal energy $E_s(s(t))$ is equal to the energy spectral density $E_{sd}(S(f))$

$$E_s(s(t)) = E_{sd}(S(f)) \Leftrightarrow \int_{-\infty}^{+\infty} |s(t)|^2 \,\mathrm{d}t = \int_{-\infty}^{+\infty} |S(f)|^2 \,\mathrm{d}f \tag{3.6}$$

for a discrete signal, is equal to the energy spectral density of that signal

$$E_s(s) = \int_{-\infty}^{+\infty} |s(t)|^2 \,\mathrm{d}t = \int_{-\infty}^{+\infty} |S(f)|^2 \,\mathrm{d}f. \tag{3.7}$$

This theorem is powerful since the energy can be directly analysed within a specific frequency band without any need to filter the signal.

Example 3.1.1. Two sinusoidal signals s_1 and s_2 have been added (Figure 3.3):

$$s_1(t) = 2\sin\left(\frac{2\pi t}{2}\right) \qquad s_2(t) = 4\sin\left(\frac{2\pi t}{6} + \frac{\pi}{3}\right)$$

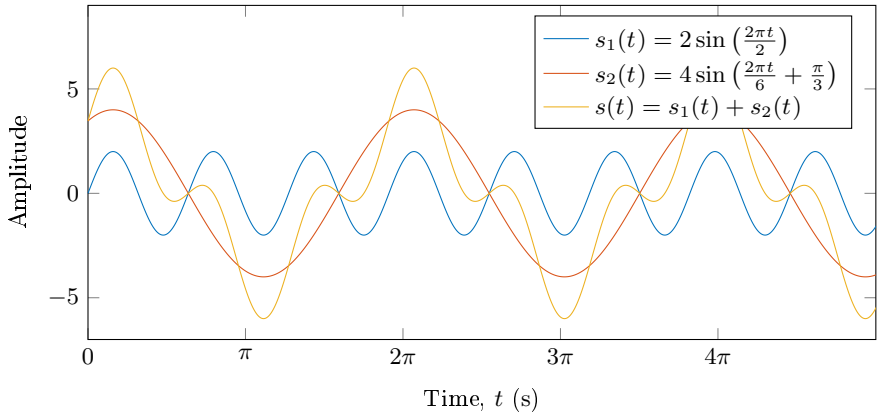

Figure 3.3 – Sinusoidal signals to illustrate the Parseval theorem.

Signal energy is $31.74\,\mathrm{Pa}^2$.s and $130.75\,\mathrm{Pa}^2$.s for s_1 ans s_2, respectively. Signal energy of s, corresponding to s_2 (i.e. $\int_{-1/3}^{1/3} S(f)\mathrm{d}f$) is equal to $110.48\,\mathrm{Pa}^2$.s, and signal energy of s, corresponding to s_1 is equal to $34.52\,\mathrm{Pa}^2$.s. Considering the fact we have discrete and finite signals, the results from s are consistent with the direct calculation of the signal energy of s_1 and s_2.

3.1.3 Hilbert transform and the envelope of the signal

Signal such as infrasonic or seismic signals are oscillating around a value leading to a complex signal analysis. A way to keep information about amplitude and get rid off the oscillations is to calculate the signal envelope from the Hilbert transform.

The Hilbert transform $\mathcal{H}$ of a real signal is defined as the convolution of a signal $s(t)$ with the Cauchy-Kernel function $1/\pi t$:

$$\mathcal{H}(s(t)) = \frac{1}{\pi t} * s(t) = \frac{1}{\pi}\int_{-\infty}^{+\infty} \frac{s(\tau)}{t-\tau}\mathrm{d}\tau. \tag{3.8}$$

Then we can calculate the analytic signal s_a as

$$s_a = s(t) + i\mathcal{H}(t), \tag{3.9}$$

where i is the complex number. The analytic signal is an extension of the signal within the complex domain and is used to calculate the signal envelope of the signal:

$$\mathrm{Env}(s(t)) = \sqrt{s^2(t) + |s_a^2(t)|}. \tag{3.10}$$

The signal envelope is used here mostly to determine the limits of events because it gives the amplitude independently from the oscillatory part (i.e. the frequency of the signal).

3.1.4 Short presentation of the wavelet decomposition

The wavelet transform is useful to study non-stationary signals, especially to process seismic records (Grossmann and Morlet, 1984). We use wavelet transform to study the

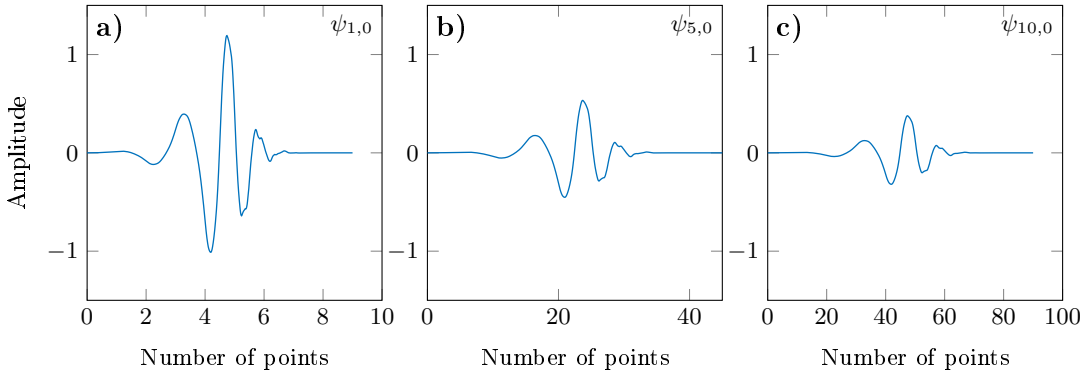

Figure 3.4 – Daubechies wavelet with 5 null-moments (db5). a) Mother wavelet $\psi_{1,0}$. Dilatation of the mother wavelet by a scale b) $\mathfrak{s} = 5$ and c) $\mathfrak{s} = 10$. Note that the x-scales are different.

temporal evolution of the frequency contents of a signal. This should be done using a windowed Fourier transform, however it requires to find a good compromise between the length of the window and the frequencies we want to look at (Figure 3.2).

The advantage of the wavelet transform is to decompose the signal with windows of different lengths depending on frequency bands, called scales of decomposition. Hence the time-frequency domain, for the windowed Fourier transform becomes the time-scale domain for the wavelet transform.

Instead of describing the signal by complex function (Fourier transform), the wavelet transform decomposes the signal with wavelet functions. Then a function, called the mother wavelet, and its translations and dilatations are used instead of the sines of the Fourier transform. The mother wavelet, $\psi_{1,0}$ is a finite oscillating wave with an average of 0. The wavelet transform of the continuous function $s(t)$, defined in $\mathbb{R}^2$ (real domain) is (Mallat, 1989)

$$\Psi_s^{\psi}(\mathfrak{s},\mathfrak{t}) = \int_{-\infty}^{+\infty} s(t)\psi_{\mathfrak{s},\mathfrak{t}}^*(t)\mathrm{d}t \qquad \psi_{\mathfrak{s},\mathfrak{t}} = \frac{1}{\sqrt{\mathfrak{s}}}\psi_{1,0}\left(\frac{t-\mathfrak{t}}{\mathfrak{s}}\right), \tag{3.11}$$

where $\psi_{\mathfrak{s},\mathfrak{t}}$ is the mother wavelet translated by $\mathfrak{t}$ and dilated by $\mathfrak{s}$ ($\mathfrak{s} > 0$), $1/\sqrt{\mathfrak{s}}$ is a factor of normalisation and $\psi_{\mathfrak{s},\mathfrak{t}}^*$ is the conjugate of $\psi_{\mathfrak{s},\mathfrak{t}}$.

As the product of two functions is equal to the scalar product of these functions, the wavelet transform $\Psi_s^{\psi}(\mathfrak{s},\mathfrak{t})$ is the correlation between $s(t)$ and $\psi_{\mathfrak{s},\mathfrak{t}}$ and thus is a measurement of the similitude between both functions. Then the higher the correlation is, the higher will be $\Psi_s^{\psi}(\mathfrak{s},\mathfrak{t})$.

Small scales allow us to analyse high frequencies, while large scales are used to study lower frequencies. Each scale of the wavelet transform can be seen as a filtered signal of the original signal. The frequency band of the scale $\mathfrak{s}$ depends on the sampling frequency of the signal and the scale. Like the Fourier transform, the wavelet transform is reversible.

In this study, we use the Daubechies wavelet with 5 null-moments as the mother wavelet (db5, figure 3.4). This wavelet is of finite dimension and is built by iterations, i.e. we can not defined it using an analytic function. The Daubechies wavelet with 5 null-moments is orthogonal with all polynomials of order lower than $m = 5$. This wavelet is a good impulsive filter, with little phase shift (Daubechies, 1988).

The Daubechies wavelet with 5 null-moments is well adapted to use the wavelet decomposition.

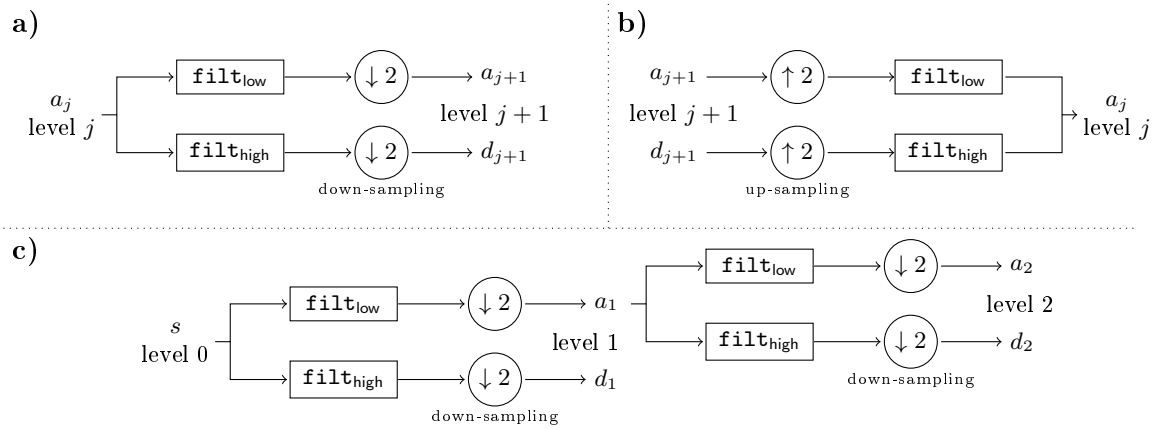

Figure 3.5 – Sketches of the wavelet decomposition. a) Analysis. b) Synthesis. c) Decomposition of the signal s using the algorithm of the discrete wavelet decomposition.

The wavelet decomposition is the equivalent of the wavelet transform for discrete signals of sampling frequency f_s instead of continuous signals.

The wavelet decomposition is based on a multi-resolution analysis (Mallat, 1989). The discrete signal s is decomposed (analysed) into coefficients of approximations a_j and coefficients of detail d_j, j being the level of decomposition (Figure 3.5a). The coefficients of approximation are decomposed a second time to give the wavelet coefficients.

The level j of the wavelet decomposition is the index of the resolution (2^j) of the decomposition and depends on the sampling frequency f_s of the signal, such as the level j is sensitive of signals with a high frequency content between $f_s/2^{j+1}$ and $f_s/2^j$ (Table A.1 in appendix A). For example, the level 4 for a signal sample at 100 Hz enhanced signals which are between 2.125 Hz and 6.250 Hz.

The fast algorithm, proposed by Mallat (1989), uses the filters $\texttt{filt}_{\text{low}}$ and $\texttt{filt}_{\text{high}}$ with impulsive response, which are low-pass and high-pass, respectively (Figure 3.5c). The coefficients of approximation a_{j+1} and details d_{j+1} of the level of decomposition $j+1$ are calculated from the coefficients of approximation a_j of the level j, such as

$$a_{j+1}(t_i) = \sum_{i=-\infty}^{+\infty} \texttt{filt}_{\text{low}}(t_i - 2m) a_j(t_i), \tag{3.12}$$

$$d_{j+1}(t_i) = \sum_{i=-\infty}^{+\infty} \texttt{filt}_{\text{high}}(t_i - 2m) a_j(t_i) \tag{3.13}$$

where i and m are integers. The reconstruction (synthesis) of the coefficients of approximation of the level j is done by up-sampling and filtering the coefficients of approximation and detail of the level $j+1$, such as (Figure 3.5b)

$$a_j(m) = \sum_{t_i=-\infty}^{+\infty} \texttt{filt}_{\text{low}}(m - 2t_i) a_{j+1}(t_i) + \sum_{t_i=-\infty}^{+\infty} \texttt{filt}_{\text{high}}(m - 2t_i) d_{j+1}(t_i). \tag{3.14}$$

The signal to noise ratio is enhanced using the wavelet decomposition. The coefficients of details highlights the signals which have a frequency content similar to the frequency content of the wavelet function.

3.1.5 Calculation of errors

The estimates we do from the measurements are more or less accurate because of the sensitivity of the instruments.

Each estimate is given with a central value Y and an interval of confidence Y' in a way the estimate ranges within the interval $Y \pm Y'$.

The interval of confidence (uncertainty) of the estimate Y can be defined by the absolute error $\mathrm{d}Y$, the relative error $\mathrm{d}Y/Y$ or the standard deviation σ_Y. In the later case, the interval $Y \pm Y'$ gives the 68.2 % interval of confidence.

In this study the uncertainty is given by the standard deviation and we suppose the absolute error $\mathrm{d}Y$ is tree times the standard deviation σ_Y because $3\sigma_Y$ gives 99.6 % of a normal distribution.

The standard deviation of Y can be calculate doing a Monte Carlo analysis.

The Monte Carlo analysis is the N calculations of the value Y for the N random draws of the M independent values X. Each values X_i is defined by its mean μ_i and standard deviation σ_i. During the k^{th} random draw the value $X_{i,k}$ is randomly taken from the distribution of X_i and $Y_k = f\left(X_{1,k}, X_{2,k}, ..., X_{M,k}\right)$ (Figure 3.6). The results of the Monte Carlo analysis is the distribution of the Y values from which the mean and standard deviation are deduced.

If the standard deviations of the independent random values $(\sigma_{X_1}, ..., \sigma_{X_M})$ are small enough, the uncertainty σ_Y can be directly deduced from the variance formula as:

$$\sigma_Y = \sqrt{\sum_{i=1}^{M} \left(\frac{\partial f}{\partial X_i}\right)^2 \sigma_{X_i}^2}. \tag{3.15}$$

Remark 1. For a normal distribution, the mean and the median are equal.

Example 3.1.2. The velocity U of an ejecta along the distance δh during the time t is

$$\mathrm{U} = f(t, \delta h) = \frac{\delta h}{t}$$

The distance δh is 10 m and we consider $\sigma_{\delta h} = 0.5\,\mathrm{m}$. The time t is 1 s with $\sigma_t = 0.01\,\mathrm{s}$. Thus the velocity U is $f(1, 10) = 10\,\mathrm{m.s^{-1}}$. Because t and δh are independent and $\sigma_{\delta h}$ and σ_t are small enough, the uncertainty is given by the variance formula as

$$\begin{aligned}\sigma_{\mathrm{U}} = \sigma_f =& \sqrt{\left(\frac{1}{t}\right)^2 \sigma_{\delta h}^2 + \left(-\frac{\delta h}{t^2}\right)^2 \sigma_t^2} \\ =& \sqrt{0.5^2 + 10^2 * 0.01^2} \\ =& \sqrt{0.26} \simeq 0.5099\,\mathrm{m.s^{-1}}\end{aligned}$$

We calculate U for $N = 1 \times 10^4$ samples taken in the normal distributions of t and δh (Figure 3.7). These calculations give an estimate of the velocity U at $\mu_{\mathrm{U}} = 10.0\,\mathrm{m.s^{-1}}$ with $\sigma_{\mathrm{U}} = 0.0598\,\mathrm{m.s^{-1}}$. This standard deviation is consistent with the standard deviation given by the variance formula.

Now increasing the standard deviation of the travel time t to $\sigma_t = 0.25\,\mathrm{s}$, the distribution of the velocity is asymmetric and the mean and standard deviation are not consistent with the values obtained from the direct calculation (figure 3.8).

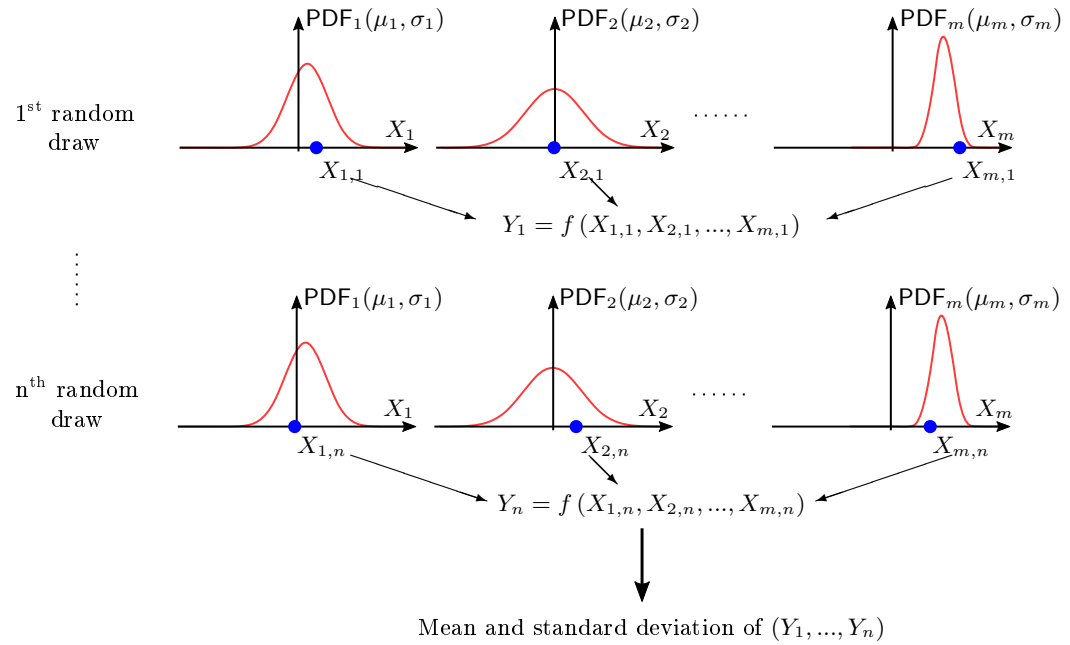

Figure 3.6 – Principle of the Monte Carlo analysis for the random values of a normal distribution.

3.2 Chain of acquisition

The source generates a physical signal without any filtering (Figure 3.9). The signal first passes through the sensor which is more or less sensible in a specific domain called the pass-band. This is the first filter. The sensor records the signal as an electric signal (in V) and send it to the digitizer. The digitizer transforms the electric signal into a digital signal in bit at the sampling frequency f_s. The digitizer applied its own filters, especially a anti-aliasing filter which follows the requirements of the Nyquist frequency of the signal $\mathcal{N}_f = f_s/2$.

The experimental set-up for the acquisition of data, is given with accurate details on the sensor such as the model of the sensor, its sensitivity, the pass-band this sensitivity

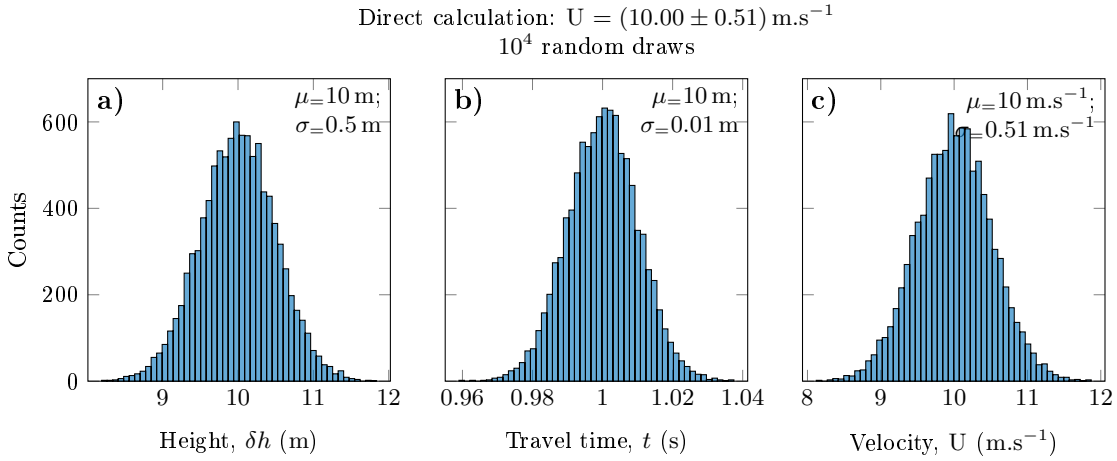

Figure 3.7 – Calculation of the velocity of an ejecta and its uncertainty using the Monte Carlo method. $U = \delta h/t$: $t = 1\,s$ with $\sigma_t = 0.01\,s$, $\delta h = 10\,m$ with $\sigma_{\delta h} = 0.5\,m$.

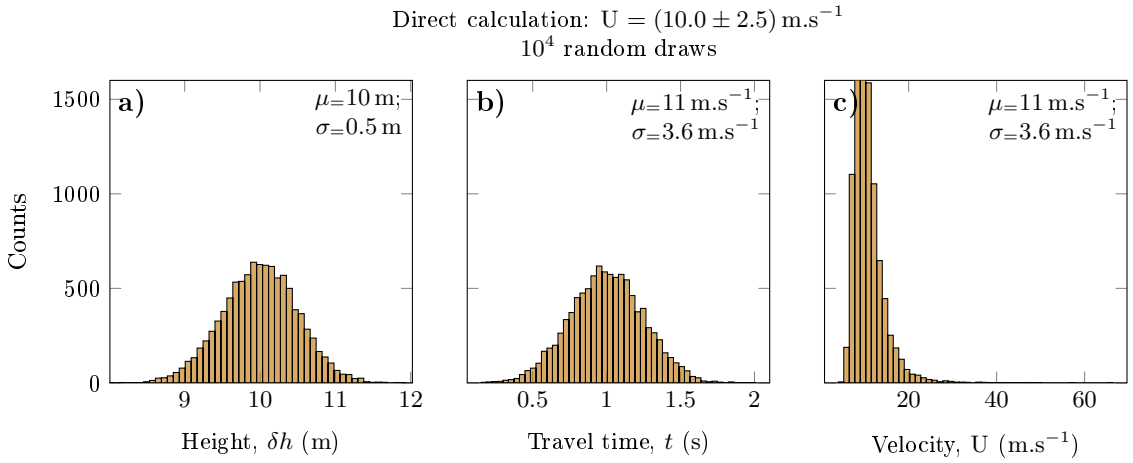

Figure 3.8 – Calculation of the velocity of an ejecta and its uncertainty using the Monte Carlo method. $U = \delta h/t$: $t = 1\,s$ with $\sigma_t = 0.25\,s$, $\delta h = 10\,m$ with $\sigma_{\delta h} = 0.5\,m$.

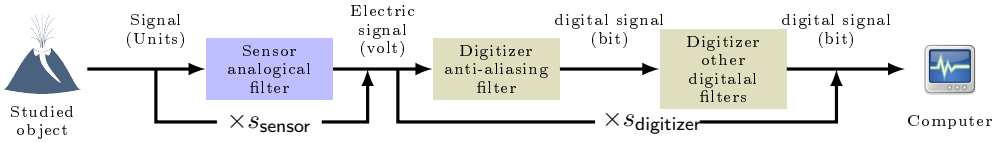

Figure 3.9 – Chain of data acquisition.

is available in and its response time if necessary. Similarly, information is given on the digitizer and the sampling frequency of the records. This information is of great importance to assess the quality of the acquisition.

We can describe each filter of the chain of acquisition by its transfer function TF

$$\mathrm{TF}(s) = \frac{\mathrm{num_{TF}}(\omega)}{\mathrm{den_{TF}}(\omega)} = \frac{n_0 + n_1\omega + n_2\omega^2 + \cdots + n_{n_\mathrm{Z}}\omega^{n_\mathrm{Z}}}{d_0 + d_1\omega + d_2\omega^2 + \cdots + d_{n_\mathrm{P}}\omega^{n_\mathrm{P}}} \tag{3.16}$$

where $\mathrm{num_{TF}}$ and $\mathrm{den_{TF}}$ are polynomes of order n_Z and n_P, respectively and where $\omega = 2\pi f$ is the angular frequency.

These transfer functions can be designed in the spectral domain using n_P poles P and n_Z zeros Z. The poles and the zeros are defined as the roots of the denominator and numerator, respectively. So we can write the numerator and denominator as

$$\mathrm{num_{TF}}(\omega) = \prod_{i=0}^{n_\mathrm{Z}} (i\omega - \mathrm{Z}_i) \tag{3.17}$$

$$\mathrm{den_{TF}}(\omega) = \prod_{i=0}^{n_\mathrm{P}} (i\omega - \mathrm{P}_i) \tag{3.18}$$

$$\tag{3.19}$$

For example, the poles and zeros of the transfer function of the LE-3Dlite MkII seismometer, given in table 3.1, are used to calculate the transfer function in figure 3.10. The transfer functions of several other sensors and digitizers are available in table A.2.

The signal indergoes several transformations from the measurements to the records that can be corrected knowing the instrumental response of each component of the chain of

Table 3.1 – Poles and zeros of the transfer function of the LE-3Dlite MkII seismometer (Lennartz electronic).

LE-3Dlite MkII *Lennartz electronic*		
Poles	$-4.440 \pm$	$4.440 \; i$
	$-1.083 \pm$	$0.0 \; i$
Zeros	$0.0 \pm$	$0.0 \; i$
	$0.0 \pm$	$0.0 \; i$
	$0.0 \pm$	$0.0 \; i$
Sensitivity	400 V/(m/s) at 1 Hz	

https://www.osop.com.pa/wp-content/uploads/2013/11/Manual_LENNARTZ_SISMOMETROS.pdf

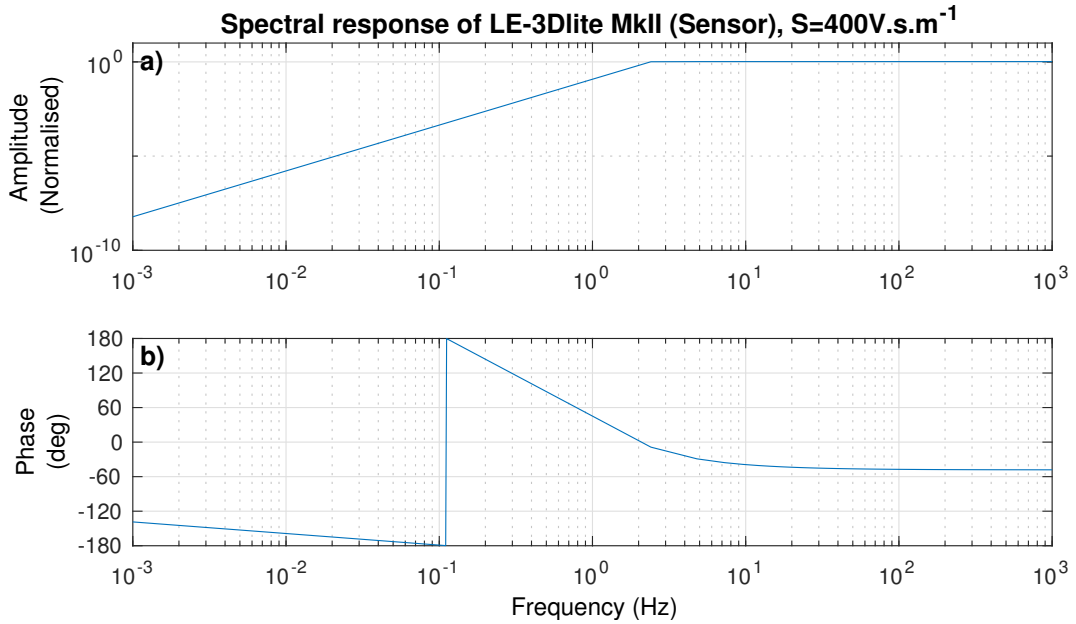

Figure 3.10 – Transfer function of the LE-3Dlite MkII seismometer (Lennartz electronic).

acquisition. The correction consists in dividing the Fourier transform of the signal with the transfer function of the sensor and then with the transfer function of the digitizer. We can do the operation in a particular frequency band if necessarry. Then we perform an inverse Fourier transform to get the corrected signal.

The infrasonic and thermal sensors used here are appropriate for what we want to study, i.e. the frequency bands we look for remain on the flat part of the spectrum amplitude of the transfer function. However, the short-period LE-3Dlite MkII seismometer does not allow us to look below 1 Hz (Figure 3.10). The signal is corrected using the transfer function of the LE-3Dlite MkII. We also need to correct the signal to look at frequencies below 1 Hz because of a small mistake on the configuration of the Quanterra Q330 digitizer rather than the broad-band Trillium 40 seismometer.

3.3 Data conversion to *mat-files*

A processing toolbox was built using MatLab with series of automatic programs in order to process a large quantity of data.

The whole toolbox was constructed to use only mat-files. Data were transformed into mat-files. The Quanterra digitizer save the records in miniseed files while the RefTek and the Geostar save the data with their own format. Data recorded by the Geostar digitizer were already converted in mat-files. Two programs are built to convert data: `ref2mat` and `ms2mat` for the data from the RefTek and miniseed files, respectively. They both read data-files in a loop and save them into mat-files (`MatSig`) with the following variables:

`tinit_*`	initial time, in day of the data in the mat-file.
`t_*`	time of the signal in second from 0. To get the time in day, we just need to add `t_*`/3600/26 to `tinit_*`
`x_*`	signal in counts

where `*` should be remplaced by the volcano nickname (YAS, PIF,...) followed by the initial time with the format yymmdd_HHMM (yy: year with the two last number; mm: the month number; dd the day of the month and HH and MM the time of the day). The corresponding mat-file is also named following this format.

The data are then transformed from counts to its units of measurements (i.e. Pa for acoustic pressure). The signal correction is done using the sensitivity of the digitizer and the sensor with the programme called `counts2geophyUnits` or is corrected from instrumental response using `pg_InstrumentalCorrection`.

The programme `pg_InstrumentalCorrection` uses pre-set transfer functions of the sensor and the digitizer. For each mat-files `MatSig`, the program calculates the Fourier transform of the signal and divides it to the normalized transfer function of the sensor and then the digitizer. It then corrects the signal from the combined sensitivity of the sensor and digitizer.

Transfer functions are built using `pg_buildTransfer` from the poles and zeros given by the contructor or resaling company or from the graph of the transfer function (still on test phase). These new transfer functions can be saved directly in the directory of the data. Pre-set transfer functions are available in the toolbox (▶ infrasonic sensor; ▶ seismic sensor; ▶ digitizer):

- ▶ LE-3Dlite-MkII (Lennartz electric)
- ▶ MB3a (developed by the CEA-DASE, sold by Seismowaves)
- ▶ MB2000 (developed by the CEA-DASE, sold by TekElec)
- ▶ MB2005 (developed by the CEA-DASE, sold by MARTEC)
- ▶ Quanterra Q330 (Kinemetrics)
- ▶ Trillium 40 (Nanometrics)

Microbarometers presented here were all developped by the CEA-DASE.

Remark 2. The miniseed files might be too big to convert them directly. The executable file *msmod* is avalaible on Linux, Mac-OS and Windows systems (`https://seiscode.iris.washington.edu/projects/msmod/files`) and is used to divide a miniseed files per day and chanels in the system terminal (msmod −CDAY data_coupee C∗.xx)

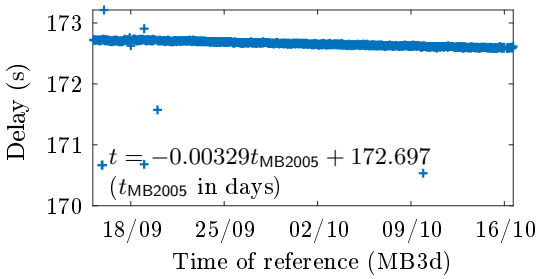

Figure 3.11 – Time lag between the time of the RefTek (t_{MB2005}) clock and the time of reference from the numerical microbarometer (t_{MB3d}).

3.4 Time correction

The GPS of the RefTek digitizer did not work during the 2016-field-campaign at Yasur. The time of the recorded data has then a time lag.

A numerical microbarometer (MB3d) was set up close to the analogical microbarometer (MB2005) which was connected to the RefTek. The distance between both sensors is about 1 m. The delay between both sensors for an acoustic wave at $340\,\mathrm{m.s^{-1}}$ is then less than 0.0029 s and can not be detected when recording at 100 Hz. We can then consider there is no delay between both sensors.

The time lag of the RefTek digitizer is measured by cross-correlation of the acoustic pressure, filtered between 0.1 Hz and 10 Hz, for each mat-file of one hour. The time lag is about 172.70 s (2 min 50 s) and is coherent with the time lag observed during the measurements (Figure 3.11). The time drift of the clock of the RefTek is often given by the cross-correlation per mat-file and is about $-0.003\,29\,\mathrm{s.d^{-1}}$.

The time of the data recorded by the RefTek is carefuly corrected. We take into account the time lag and the time drift of the clock of the RefTek to correct the time. The continuity between two mat-files of the signal is done adding are removing data points by a spline interpolation.

3.5 Filtering the data

The data often need to be filtered to remove noise.

The program `pgsig_filter_v1` filters data using Butterworth filters considering several options. The Butterworth filter can be low-pass, high-pass, passband or bandstop with cut-off frequencies chosen by the user. The user chooses also the order of the filter (`FiltOrder`) and the number of back-and-forth passes (`nbARpass` back-and-forth pass = 2 `nbARpass` passes). The filter is designed by the function `butter`. The figure 3.12 shows the transfer function of the 4th order and passband Butterworth filter with cut-off frequencies at 0.5 Hz and 5 Hz. We use that filter on infrasonic data at Erta'Ale.

Due to memory limitations, the program can not filter a whole period as a continuous signal. The data are filtered mat-file per mat-file and we need to prevent to boundary effects at the beginning and the end of the signal of each mat-file. The user can choose to

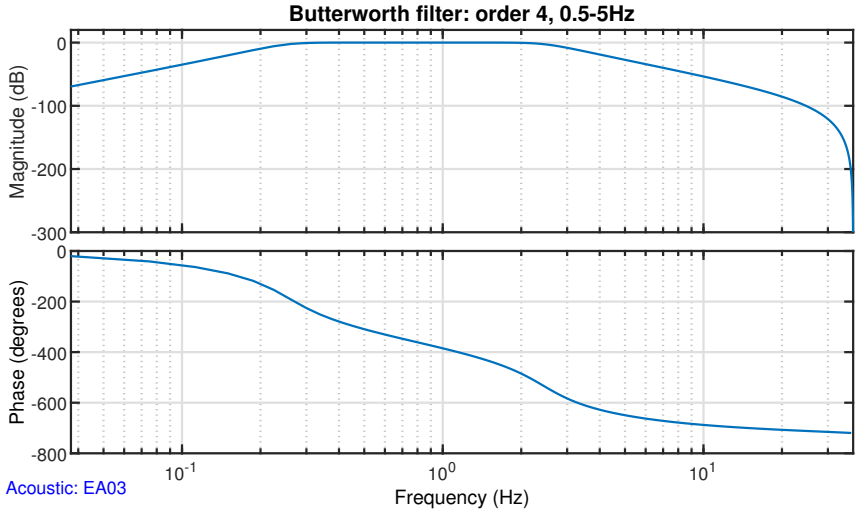

Figure 3.12 – Transfer function of a 4th order Butterworth filter of passband frequencies 0.5 Hz to 5.0 Hz.

- add mat-files $n-1$ and $n+1$, if they exist, while processing mat-file n;
- mirror the signal at the beginning and the end of the signal;
- add zeros at the beginning and the end of the signal;
- keep as it is.

The user can then decide, or not, to remove the mean and/or the linear trend of the signal.

Then the filter can be applied on the *lengthened* signal with `nbARpass` back-and-forth passes. It is essential to perform at least back-and-forth passes to maintain a zero-phase filtering (i.e. no dephasing between the original signal and filtered signal). The filtered signal of the current mat-file is extracted from the *lengthened* signal once the filter is applied. The filtered signal and the characteristics of the filter are saved a new mat-file, ending by *_fbd*. The *_fbd* suffixe is used by the programme to stop whenever it runs on data that are already filtered.

The cut-off frequencies, the filter order and the number of back-and-forth passes depends on the type of data (i.e. infrasonic, seismic and thermal) and the volcano. We have chosen to resample all records at 75 Hz, the lowest frequency of all the records and long time used at Yasur, in order to do a homogeneous data processing. Furthermore it has the advantage of saving time while processing.

Infrasonic data are filtered successively twice. First we perform a 2nd order Butterworth filter with 1 back-and-forth pass between 0.01 Hz and 20 Hz to remove obvious sources of noise while keeping a large frequency band for detecting the largest possible range of physical processes associated to the eruptive activity of the volcano. This first step enhances the frequency contents of the signal and the frequency bands of the Strombolian explosions. The frequency band used depends on the volcano and ranges such as 0.5 Hz to 5 Hz, 2 Hz to 6.5 Hz and 0.1 Hz to 10 Hz are suitable at Erta'Ale, Piton de la Fournaise and Yasur, respectively. The variability of the activity at Yasur and the low signal to noise ratio of the infrasonic records allow us to keep a large frequency band to process data. In contrast, the noisier infrasonic data at Erta'Ale and Piton de la Fournaise make us restrain the width of the frequency band. The narrowest filter is a 4th order Butterworth filter with 2 back-and-forth passes (equivalent to a 8th order filter).

Thermal data are filtered only once to remove the effects of the efficient response time of the radiometers at 0.19 Hz. We apply a low-pass filter designed by a 2nd order Butterworth filter with one back-and-forth pass. Seismic data are also filtered once to get the volcano explosion quakes (VEQ) in the frequency band 1 Hz to 6 Hz. We use a 2nd order Butterworth filter with one back-and-forth pass. Seismic data are also corrected from instrumental response between 0.1 Hz and 1 Hz and then filtered above 1 Hz to the lowest frequencies of the signal (VLP, Sections 3.2 and 3.3).

3.6 Detection of events

Each Strombolian explosion is a discrete events in time. Hence we obtain different results when estimating the strength of the Strombolian activity by considering a continuous signal or a series of discrete signals each per explosion. We call active degassing the degassing related to the sole explosions and passive degassing the degassing related to the signal existing between explosions (inter-explosion). The sum of active and passive degassing corresponds to the total degassing.

the principle of the detection of an event, here a Strombolian explosion, is quite simple and is based on the measurement of the signal to noise ratio. This signal to noise function is called a detector. A detection is triggered when the value of the detector passes over a chosen threshold.

We use different methods to detect events depending on the data type, the strength of the Strombolian activity and the noise:

- the *peaking method*,
- the STA/LTA detector on the absolute value of the signal or on the absolute value of the coefficients of the wavelet decomposition in a chosen level,
- the cross-correlation with a typical signal.

3.6.1 Peaking method

The peaking method considers all increases, here of the temperature, as a potential explosion independently from the shape of the signal or its frequency. Increases are found looking for extrema using `findpeaks` function (`imin = findpeaks(-x)` and `imax = findpeaks(x)`). All maxima (there should be only 1) before the first minimum and all minima (there should be only one too) after the last maximum are removed. We obtain as many maxima as minima, each couple representing the potential detection of an event.

Then we can calculate the value of the signal increase `dx = x(imin)-x(imax)` and select increases above a minimum value `dx_thr` as detections. All other increases are considered as noise.

3.6.2 STA/LTA detector

The STA/LTA detector is a measurement of the signal to noise ratio using a characteristic function, where STA stands for a short time average and LTA for the long time average.

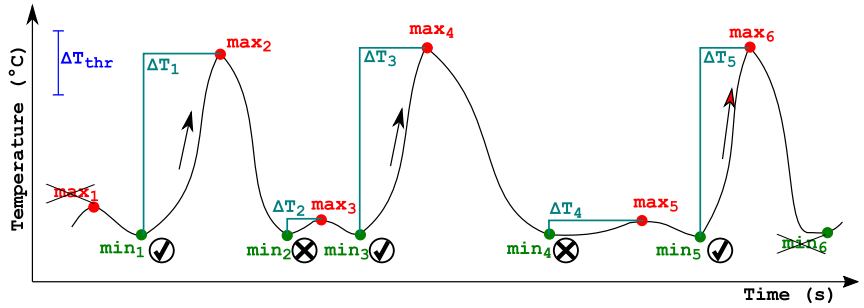

Figure 3.13 – Summary of the peaking method. Step-1: look for minima. Step-2: look for maxima. Step-3: remove extra extrema. Step-4: calculate ΔT. Step-5: compare with ΔT_{thr} ($\surd$: kept; $\otimes$: deleted).

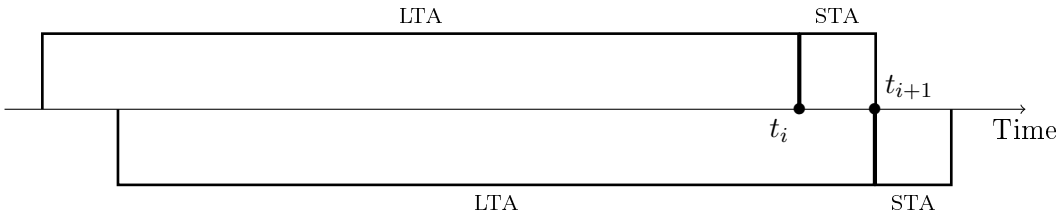

Figure 3.14 – Disposition of the sliding windows for the calculation of the STA/LTA detector.

Most of the time, the characteristic function is taken as the absolute value of the signal.

The STA and the LTA are calculated on sliding windows of length $\mathbf{lg}_{\text{STA}}$ and $\mathbf{lg}_{\text{LTA}}$, respectively. They move on the characteristic functions by a length equal to the length of the STA, the STA preceding the LTA(Figure 3.14).

The STA/LTA detector, tends to one for pure noise. The STA increases more than the LTA when an event is recorded and the STA/LTA also increases.

In practice, an event is selected if the STA/LTA is larger than a chosen threshold $[\text{STA/LTA}]_{\text{thr}}$ and if the STA/LTA was under the threshold right before. A detection is recorded by the indexes of its maximum and minimum amplitude in the LTA window that triggers the detection.

The length of the STA and the LTA are crucial for a good detection. The length of the STA must take into account the frequency, the duration and the return-time of the events under study and the LTA must be sufficiently long to measure the characteristic noise. Optionally, a time lag timeLag between two events can be set.

In the toolbox, the STA/LTA detector can be used either the absolute value of the signal (`pg_sltadetc`) or on the absolute value of the coefficients of the wavelet decomposition at one or several chosen levels (`pg_wltdetc`).

The STA/LTA detector on the absolute value of the signal considers only the amplitude of that signal while the STA/LTA detector using the wavelet decomposition depends on the frequency of the signal and so the length of the STA. Additionnaly, criteria on the shape of the waveform can be applied (Zielinski, 2012).

The user can choose to use a fixed or variable LTA. A variable value of the LTA (i.e. LTA per sliding window) matches the noise level over the time and suits well for long times series

with a variable level of noise. A fixed LTA value characterise the noise level during a chosen period and at a site of measurements and can be used to keep a same level of detectability during that period. The value of the fixed LTA is calculated as the mean value of the characteristic function over the chosen period (`pg_sltalta` and `pg_wltlta` programmes).

3.6.3 Cross-correlation

Cross-correlation can also be used to detect events. The method looks for a typical signal within the noise. The lower is the coefficient of the cross-correlation, the noiser is the signal.

That method is independent from amplitude and look for the frequency content of the signal →looks for similar signals. All signals are normalised and the amplitude and phase of each frequency is compared to that of the typical signal. The cross-correlation measures the similitude between a typical signal `xtyp` and the recorded signal `x`. The duration of the typical signal and the chosen threshold for the correlation coefficient are key parameters to choose for the detections.

Firstly, we calculate the cross-correlation profile `xcorrProfile` using the MATLAB function `xcorr`. As the length of the signal `x` is longer than the signal `xtyp`, we can not normalise the profile to correlation coefficients and each maximum is a potential event. So, for each maximum of the cross-correlation profile, we calculate the correlation coefficient `corrCoef` between the typical signal and the part of the signal, of same length, around the maximum. If the coefficient `corrCoef` exceed the chosen value `thrCorr`, we validate the detection.

3.6.4 Summary of the methods of detections

The detections are recorded in mat-files, 1 mat-file of all detections per mat-file of signal with at least 1 detection. Each mat-file contains at least:

- the number of detected events (`nbdetc`),
- the indexes of the maximum and minimum of amplitude for each detection (`ind_[`*`mat-file`*`](:,1:2)`),
- the values of the detector for each,
- the parameters for the detection.

and is named after the mat-file of signal with the nickname of the method (`debnom`) of detection as a pre-fix (Table 3.2) andthe number of events as a suffix . The mat-files of detections are written in a specific folder (`DosDet`) within the folder of the mat-files of signals (`DosSig`). The folder of detection is named depending on the method of detection and some parameters of this method (Table 3.2).

The choice of the method of detection is crucial because each method of detection has its own specificities, focussing on amplitude or on the frequency content (Table 3.2).

Table 3.2 – Characteristic of each method of detection.

Method	Peaking	STA/LTA on $\lvert s \rvert$	STA/LTA on $\lvert \Psi(s) \rvert$	Cross-correlation
Amplitude	yes	yes	yes	no
Frequency	no	no	yes	yes
Phase	no	no	no	yes
Waveform	no	optional	optional	no
Threshold	ΔT_{thr}	$\text{STA/LTA}_{\text{thr}}$	$\text{STA/LTA}_{\text{thr}}$	$\text{corrCoeff}_{\text{thr}}$
Required		$\mathbf{lg}_{\text{STA}}$, $\mathbf{lg}_{\text{LTA}}$ timeLag	$\mathfrak{s}$	s_{ref}
Optional		LTA	LTA	
Program	*none*[†]	`pg_sltadetc`	`pg_wltdetc`	`pg_ccordetc_v2`
`DosDet`	*Detc_man**[‡]	*Dets**	*Detc**	*CCor**
`debnom`	*detm*[‡]	*dets*	*detc*	*ccor*

[†]Can not be done automatically yet
[‡]Temporary

3.6.5 Selection of detections

Some detection can be wrong despite all parametric constraints on the methods of detections, either because we are focusing on specific events or because of a strong noisy signal.

A series of additional programmes exist to keep automatically detections with various parameters of selections (`pg_seldetc_*`). Among them the selection based on the maximum amplitude is available for all types of data (`pg_seldetc_pap`).

The user can choose to select the events with the maximum amplitude:

1. lower than a threshold,
2. upper than a threshold,
3. within an interval,
4. outside an interval.

The maximum amplitude of each detected events from `DosDet` is loaded from the mat-files of signals and detections (i.e. `maxamp=x_[mat-file](ind_[mat-file)](:,1)`).

All the indexes and the detector value of the detections which does not verify the criteria of selection are deleted from the workspace and a new mat-file of detections is saved in a new folder `DosDet_new`. The name of this new folder is similar to the name of `DosDet` with the suffix *_selamp_[selCriteria]* where `selCriteria` indicates the criteria of selection.

Other selections can be done based on:

- the value of the detector: `pg_seldetc_slta` for the STA/LTAdetector (on the coefficient of the wavelet decomposition or on the absolute value of the signal); `pg_seldetc_ccor` for the cross-correlation detector;
- the peak-to-peak ratio, especially for infrasonic detections `pg_seldetc_pop` ($p^+/|p^-|$)
- the peak-to-peak delay, especially for infrasonic detections `pg_seldetc_tpp` ($t_- - t_+$)
- the gas volume and maximum amplitude per event, only for infrasonic detections, gas volume from the infrasonic power and from the 2 successive integrations of the acoustic pressure: `pg_seldetc_vol` (Vol_{gas}).

The selection of detections based on the value of the detector after the detection itself is time saving because we do not need to do a new detection.

The selection of the detection based on the gas volume and the maximum amplitude is more difficult because the gas volume are not saved by mat-files of signals like the detection but with one mat-file for the whole studied period. Note that the selection based on the gas volume from the bubble volume mode has not been implemented, yet.

The gas volume and maximum acoustic pressure are directly loaded from a single mat-file of volumes (*allpwvelvol_ ** or *voljohn_ *.mat*). The user can choose to select detections manually to remove or keep them or he can choose to

- select the detections for which the gas volume is below or above a threshold
- select the detections for which the gas volume is above or below the curve $\mathrm{Vol}_{\mathsf{gas}} = a + bp^{+}$, where p^{+} is the maximum acoustic pressure of the detection.
- select the detections which for which the gas volume is within or outside gas volume limits and the maximum amplitude is within or outside the maximum amplitude limits.

The indices of detections are then loaded from each mat-files of detections and corrected considering the current selection. The new mat-files of detections are saved in the new folder `DosDet_new`. The suffix of the new folder is *_selvol_[selvolCriteria]*.

3.6.6 Detection of the Strombolian events during the field-campaigns

The infrasonic events at Yasur were detected using the STA/LTA detector on the coefficients of the wavelet decomposition of level 4 and 5 (1.172 Hz to 4.688 Hz at 75 Hz). For each level, I have fixed the LTA value to the mean of the absolute coefficient of the wavelet decomposition (Table 3.3). The STA/LTA threshold is taken at 2.5 in each case. We have chosen to use this method at Yasur, because there are several conduits that can have different geometries and thus generate various waveforms. Furthermore vents could have opened and/or closed during the records. Hence the STA/LTA detector on the coefficients of the wavelet decomposition allows us to detect various waveforms in the frequency band of the explosions.

At Erta'Ale and Piton de la Fournaise, detections on infrasonic records were done by cross-correlation using typical waveforms for each volcano. The typical waveforms are found viewing the infrasonic records and selecting events that looks like explosions. A detection using the STA/LTA method can be do to help of the selection of the signals of explosions. At Erta'Ale, we found 2827 events which are correlated at 85% to the explosion presented in Bouche et al. (2010) (23/03/2003 14:24:38, figure 3.15a). At Piton de la Fournaise, an event must be correlated at 90% to one of the typical explosions shown in figure figure 3.15b-c to be taken (10/12/2006 21:38:47 and 21:39:31). We thus detect 9387 Strombolian explosions on infrasonic data (8018 events with a maximum amplitude higher than 1 Pa). Note that there is only one conduit in the case of Erta'Ale and Piton de la Fournaise, then it is consistent to look for similar waveforms within the infrasonic records.

The STA/LTA detector on the absolute values of the signal is used to find thermal events at Yasur. The signal remains quite simple, without oscillations. It is similar to applied the STA/LTA on the signal itself because the thermal signal remains positive. I use a LTA of 30 s for the data from the lower radiometer and I have chosen the length of the STA equal

Table 3.3 – Parameters for the detection of Strombolian events at Yasur volcano. a) Detection with a STA/LTA detector on the coefficient of the wavelet decomposition of the infrasonic records (0.1 Hz to 10 Hz). Detection with a STA/LTA detector on the absolute values of the thermal signal of b) the lower radiometer and c) the upper radiometer (<4 Hz).

a) Acoustic		***YAS09****	***YAS09**†*	***YAS16***
LTA values	*level 4*	1.2271	1.3436	1.63
	level 5	1.0818	1.0469	2.38
STA/LTA threshold		2.5	2.5	2.5
Number of events		48 569	15 432	206 301
Number of events (>1 Pa)		48 189	15 405	206 082

b) Thermal: lower		***YAS09**†*	***YAS16***
Length (s)	STA	2	2
	LTA	30	30
STA/LTA threshold		1.2	1.5
Number of events		1325	5110

c) Thermal: upper		***YAS09**†*	***YAS16***
Length (s)	STA	1	2
	LTA	60	30
STA/LTA threshold		1.1	1.5
Number of events		841	3790

*Whole period
†From 28/06/2009 to 01/07/2009

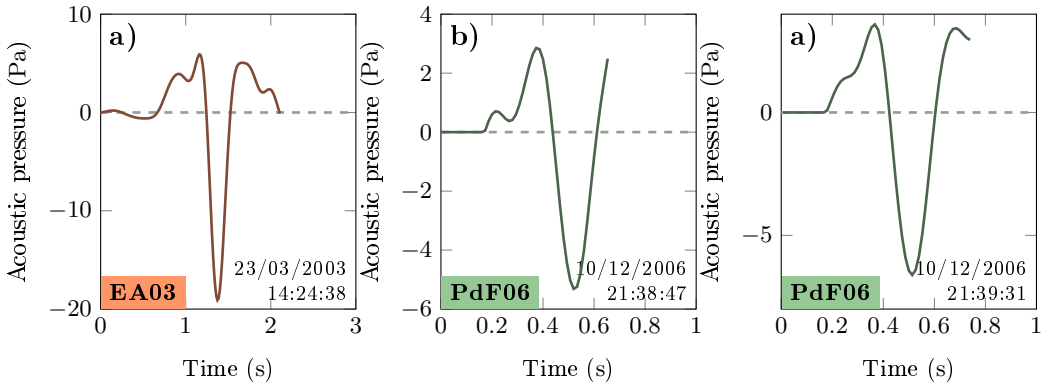

Figure 3.15 – Typical infrasonic waveforms of the weak explosions of gas pockets at a) Erta Ale and b–c) Piton de la Fournaise. These waveforms were used to detect automatically explosions by cross-correlation.

to 2 s considering the ascent duration of the signal we have observed. The best detections are obtained for STA/LTA thresholds of 1.20 and 1.50 for the lower radiometers in 2009 and 2016, respectively.

The STA/LTA detector is not sufficient on thermal records at Piton de la Fournaise because of the large number of events. The *peaking method* is used with threshold values ΔT_{thr} at 120 °C and 50 °C for the lower and upper radiometers, respectively. Finally we keep only explosions seen on both radiometers. We detect 9004 explosions on thermal data at Piton de la Fournaise. The probability that an explosion is seen on the lower radiometer but not the upper one is low because of the small height variation between both radiometers (8 m against 19 m and 24 m at Yasur). Note that the number of events detected on infrasonic records and thermal records are very similar (96 %). This validate our choice to use the method of cross-correlation to detect Strombolian explosions on infrasonic records at Piton de la Fournaise.

At Erta'Ale we had to look for thermal events manually because of the noisy records we got. We detect 111 events we can process.

Strombolian explosions, at Yasur, on seismic records filtered between 1 Hz and 6 Hz, are detected using the STA/LTA detector on the absolute values of the signal. The length of the STA and the LTA are 1 s and 60 s, respectively, and we set the minimum `timeLag` to 8 s (Battaglia et al., 2016). 8817 and 63 671 seismic events were detected with a STA/LTA threshold at 2.5 in 2009 and 2016, respectively.

3.6.7 Link between detections seen by different sensors

The same explosion recorded on two different records s_1 and s_2 is regognized by keeping the closest event from s_2, either before or after, for each event of s_1.

The detections of events should first be done for each record s_1 and s_2. We obtain the times t_1 and t_2 of these explosions with N_1 end N_2 events respectively ($N_1 < N_2$, Figure 3.16a). We look for the closest event on s_2 for each event on s_1. A maximum delay is chosen at `dtthr`. We calculate the delays `dt`, and keep only those that are (Figure 3.16b):

- below the threshold `dtthr` if we want the events of s_1 to be before the events of s_2 $t_1 < t_2$: $t_2 - t_1 <$ `dtthr`;
- above the threshold `dtthr` if we want the events of s_1 to be after the events of s_2: $t_1 < t_2$: $t_2 - t_1 >$ `dtthr`;
- between `-dtthr` and `dtthr` if we want the events of s_1 to be either before or after the events of s_2: $|t_1 < t_2|$: $t_2 - t_1 <$ `dtthr`.

The function `LinkData` looks for the shortest delay with the events of s_2 for each event $e_{1,i}$ of s_1 (Figure 3.16b–c). During that first loop, some events from s_2 can be chosen twice or more, $e_{2,j}$ is linked to $e_{1,i-1}$ and $e_{1,i}$ (Figure 3.16c). The function processes a second loop to keep only the closest event to $e_{2,j}$ (Figure 3.16d). This method can link a maximum of N_1 events but some events might not be linked depending on the chosen `dtthr`.

We perform the method twice ($t_2 < t_1$ and $t_2 > t_1$) when looking for coupled detections which can have different delays before and after the signal or reference ($\texttt{dtthr}_{\text{Before}} < t_2 - t_1 < \texttt{dtthr}_{\text{After}}$). We only keep the links with the shortest delay (function `findLinks`).

The function `LinkData` also allows us to link explosions looking for the maximum amplitudes per sliding window. However we do not know how the different types of data are coupled. So far we have used the first method (closest detections).

3.7 Classification of events

The classification of events allows us to look for characteristic waveforms. It is done by comparing the signal of pairs of events using a correlation calculation.

The programme `pg_classEvent` builds a maximum of `nClassMax` classes with at least `nEvMin_perClass` event per class with a minimum correlation coefficient `ThrCorr`. The details for the choice of these parameters is explained later.

Step 1 (Loading and selection of the signals of explosions)**.** For each detection, the signal is loaded within a window beginning `dtBefore` seconds before the maximum amplitude (i.e. p^+ for infrasonic signals) and finishing `dtAfter` seconds after the maximum amplitude.

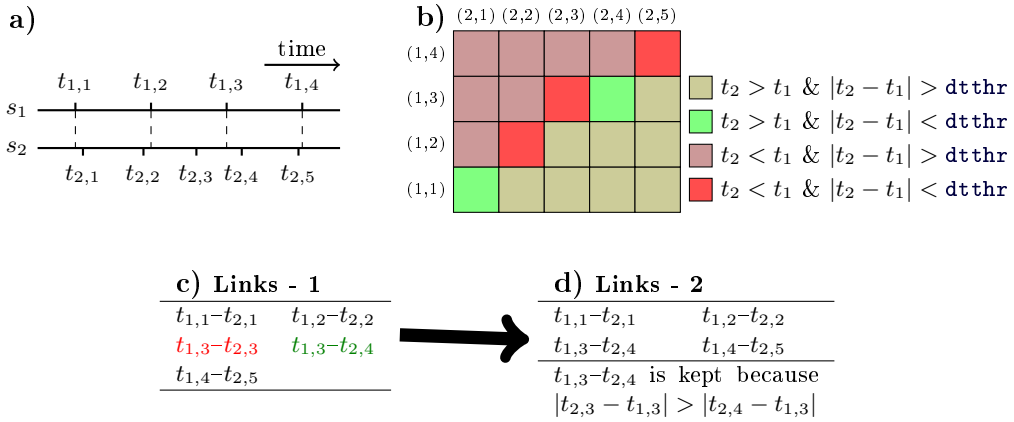

Figure 3.16 – Sketch for the links of the explosions recorded on several records.

It is important to have the same length for all the detections. We need to limit the maximum number of events to analyse at `NbDetcMax` because the calculation of the matrix of correlation need an enormous amount of memory. The programme loads all detected events and then select the `NbDetcMax` events

- either by keeping the `NbDetcMax` strongest events (maximum amplitude),
- or by keeping the `NbDetcMax` smallest events (minimum amplitude),
- or by taking randomly `NbDetcMax` events using the function `randperm`.

The results is a matrix `SigEvents` with `ceil((dtBefore+dtAfter)*Fs+1)` rows and `NbDetcMax` columns, `Fs` being the sampling frequency of the signals.

Step 2 (Calculation of the coefficients of correlation)**.** The calculation of the correlation coefficient of each pair of events is done directly on the matrix `SigEvents` using the function `corr` and gives the matrix of correlation `Correlation` of size `NbDetcMax` × `NbDetcMax`. The programme "removes" all correlation unnecessary coefficients, such as the correlation coefficients of a signal with itself (`Correlation(i,i)=1`) or the correlation coefficients below `ThrCorr` by replacing them by NaNs (Not a Number).

Step 3 (Construction of the classes: *while loop*)**.** The programme can then construct classes of events while correlation coefficients higher than `ThrCorr` remain in `Correlation` (i.e. while there is a couple of events to build a new class). For each loop `icl` a new class is defined by looking for the pair of explosions `(ix,iy)` with the maximum correlation coefficient. For each event `ie` which is correlated with events `ix` and `iy` (i.e. `Correlation(ix,ie)>=ThrCorr & Correlation(iy,ie)>=ThrCorr`) the program checks if its correlation with `ix` or `iy` is higher than other correlations. If yes, `ie` is added to the class of `icl` and all correlations with `ie` are removed, otherwise `ie` is not added. A stack is built with the signals of all events `ix`, `iy` and `ie`, all correlations with `ix` or `iy` removed and the number of events of the class `nEvent`, the time, amplitude and the correlation of each event of the class are recorded.

Step 4 (Selection of the classes)**.** At this step more than `nClassMax` classes can have been defined. The `nClassMax` classes with the maximum number of events are kept and classes with less than `nEvMin_perClass` events are also deleted. Events from the deleted classes do not belong to any class. It is possible that among the explosions in the deleted classes, some could have a sufficiently good correlation with another class to be added to that class.

Step 5 (Unclassified events)**.** The correlation of each unclassified event `ieu` with the stack of each class is calculated. The event `ieu` is part of the class for which the correlation is

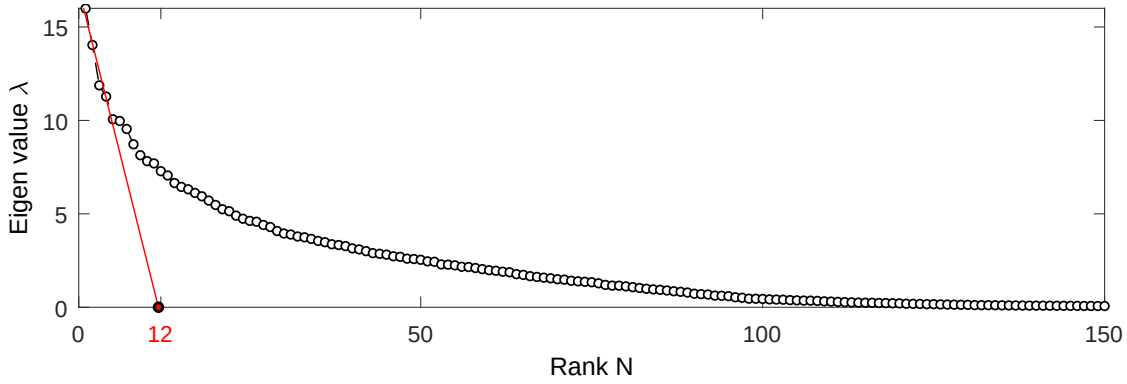

Figure 3.17 – Eigen values as a function of the rank N. We can find the maximum number of classes `nClassMax` at the intersection of the tangent in red with the x-axis.

the highest if the coefficient is higher than `ThrCorr`, otherwise it remains unclassified. The stack of each class is built again, the number of events per class and the time, maximum amplitude and correlation of each events of the class are once more recorded.

Step 2 to 5 are done using the function `doClasses`. This allows us to easily classify events per sliding window of length `dtt` (in hour) and look at time evolution of the characteristic waveforms.

The choice of the threshold `ThrCorr` for the coefficients of correlation is very empirical and depends on the tests made by the user. However, we can use a method to choose the maximum number of classes `nClassMax`. The method consists in the calculation of the number of independent vectors and the eigen values of the matrix of correlation `Correlation`. By plotting the decreasing eigen values `eigenValues` as a function of their rank `N`, we get curve similar as the one shown in figure 3.17. We can deduce the maximum number of classes `nClassMax` at the intersection of the tangent in red with the x-axis. The choice of the linear trend in figure 3.17 is also empirical but the extent of the error is clearer.

We can detect more events from a class using the detection by cross-correlation (Section 3.6.3) when we are satisfied by our definition of the classes.

Remark 1. `NbDetcMax` depends on the computer, `dtBefore`, `dtAfter` and the sampling frequency f_s of the signal.

Remark 2. An event is part of the class for which its correlation is the highest. An event can be part of one class only.

Remark 3. Some events can remained unclassified.

3.8 Gestion of the gaps of data for the estimations per sliding window

We might underestimate energy, power, or volume per sliding window because of missing data while estimating them. The programmes for these calculations propose a correction of the estimates. They also propose to process series of zeros (i.e. part of a signa that has been corrected) as a gaps (`GapGestion_Oseries`).

We estimate the energy, or the power per sliding window of length `dtt`. The window `it`

contains data during the length `dti`, then `p = dti/dtt` of data are available and `1-p` data are missing in the window `it`.

The programmes propose to correct missing data, using the function `GapGestion_correction`, by

1. using the mean value of the period
2. using the value of the window `it`
3. removing the value if `p` is lower than a threshold (replacement per `NaN`)
4. doing nothing

We explain below how the energy, power and RMS are corrected using (1) the mean value of the period or (2) the value of the window.

The correction we use should take into accounts the variability of the activity. Then using the mean value of the period (1) might be the best when there are little variations (i.e. Yasur, June-2009). However we might prefer using the value of the window (2) when there are strong variations (i.e. Yasur, Sept-Nov-2016).

3.8.1 Energy

`Eit_tot`, `Eit_calc` and `Eit_miss` are the total, calculated and missing energy in the window `it`, respectively. The mean energy for the period is `E_mean` and is calculated by $\sum_i \texttt{Eit_calc} / \sum_i dti$.

The total energy in the window `it` is

$$\texttt{Eit_tot} = \texttt{Eit_calc} + \texttt{Eit_miss}. \tag{3.20}$$

(1) When correcting using the mean value `E_mean`,

$$\begin{aligned} \texttt{Eit_miss} &= \texttt{E_mean} \frac{\texttt{dtt} - \texttt{dti}}{\texttt{dtt}} \\ &= \texttt{E_mean}\,(1 - \texttt{p})\,, \end{aligned} \tag{3.21}$$

then we get

$$\texttt{Eit_tot} = \texttt{Eit_calc} + (1 - \texttt{p})\,\texttt{E_mean}. \tag{3.22}$$

(2) When correcting using the value of the window `Eit_calc`,

$$\begin{aligned} \texttt{Eit_miss} &= \texttt{Eit_calc} \frac{\texttt{dtt} - \texttt{dti}}{\texttt{dti}} \\ &= \texttt{Eit_calc} \left(\frac{1}{\texttt{p}} - 1 \right), \end{aligned} \tag{3.23}$$

then we get

$$\texttt{Eit_tot} = \left(\frac{1}{\texttt{p}} \right) \texttt{Eit_calc}. \tag{3.24}$$

3.8.2 Power

`Pit_tot`, `Pit_calc` and `Pit_miss` are the total, calculated and missing power in the window `it`, respectively. We estimate `Pit_tot` as `Eit_tot`/`dtt`, `Pit_calc` as `Eit_calc`/`dti` and thus `Pit_miss` as `Eit_miss`/(`dtt` − `dti`). Then we have

$$\begin{aligned}\texttt{Pit_tot} &= \frac{\texttt{Eit_calc} + \texttt{Eit_miss}}{\texttt{dtt}} \\ &= \frac{\texttt{Pit_calc dti} + \texttt{Pit_miss}\,(\texttt{dtt} - \texttt{dti})}{\texttt{dtt}} \\ &= \texttt{Pit_calc p} + \texttt{Pit_miss}\,(1 - \texttt{p}) \end{aligned} \tag{3.25}$$

The mean power for the period is `P_mean` = `E_mean`/`dtt`.

(1) When correcting using the mean power of the period, we get

$$\texttt{Pit_tot} = \texttt{Pit_calc p} + \texttt{Pit_mean}\,(1 - \texttt{p}) \tag{3.26}$$

(2) When correcting using the calculated power of the window, we get

$$\begin{aligned}\texttt{Pit_tot} &= \texttt{Pit_calc p} + \texttt{Pit_calc}\,(1 - \texttt{p}) \\ &= \texttt{Pit_calc}. \end{aligned} \tag{3.27}$$

3.8.3 Root-Mean-Square:

`RMSi_tot`, `RMSi_calc` and `RMSi_miss` are the total, calculated and missing RMS in the window `it`, respectively. The mean power for the period is `RMSi_mean`. N and n are the number of points in windows of length `dtt` and `dti`, respectively and x_k is the value of the point k in the window.

$$\begin{aligned}\texttt{RMSi_tot} &= \sqrt{\frac{1}{N}\sum_{k=1}^{N} x_k^2} \\ &= \sqrt{\frac{1}{n + (N-n)}\left(\sum_{k=1}^{n} x_k^2 + \sum_{k=n+1}^{N} x_k^2\right)} \\ &= \sqrt{\frac{1}{N}\left(n\ \texttt{RMSi_calc}^2 + (N-n)\ \texttt{RMSi_miss}^2\right)} \\ &= \sqrt{\texttt{p}\ \texttt{RMSi_calc}^2 + (1 - \texttt{p})\,\texttt{RMSi_miss}^2} \end{aligned} \tag{3.28}$$

(1) When correcting using the mean RMS of the period, we get

$$\texttt{RMSi_tot} = \sqrt{\texttt{p}\ \texttt{RMSi_calc}^2 + (1 - \texttt{p})\,\texttt{RMS_mean}^2}. \tag{3.29}$$

(2) When correcting using the calculated RMS of the window, we get

$$\begin{aligned}\texttt{RMSi_tot} &= \sqrt{\texttt{p}\ \texttt{RMSi_calc}^2 + (1 - \texttt{p})\,\texttt{RMSi_calc}^2} \\ &= \texttt{RMSi_calc}. \end{aligned} \tag{3.30}$$

Chapter 4

Processing of the data

Contents

4.1 Infrasonic processing **68**
4.1.1 Characteristic points on infrasonic waveforms 68
4.1.1a Definition of the characteristic points 68
4.1.1b Determination of the limits O, D and E 70
4.1.2 Infrasonic energy and gas velocity 72
4.1.2a Type of acoustic sources 72
4.1.2b Infrasonic energy 72
4.1.2c From infrasonic energy to gas velocity 73
4.1.3 Gas volume from infrasonic records 74
4.1.3a Gas volume from infrasonic power 74
4.1.3b Gas volume from two successive integrations of the acoustic pressure 74
4.1.3c Gas volume from the bubble volume mode prior to bursting 76
4.1.4 Atmosphere density and pressure 80
4.2 Thermal processing **81**
4.2.1 Characteristic points on thermal waveforms 83
4.2.1a Definition of the characteristic points 83
4.2.1b Determination of the limits O, E and E' 84
4.2.2 Field of view of the radiometers 86
4.2.3 Thermal energy 88
4.2.3a Error on thermal energy 88
4.2.4 Ejecta velocity 88
4.3 Image processing **91**
4.3.1 Particle Imagery Velocimetry 92
4.3.2 Gas volume fraction from the analysis of video frames 93
4.4 Seismic processing **95**
4.4.1 Very Long Period events and correction of the signal 98
4.4.2 Characteristic points on seismic waveforms 101
4.4.2a Definition of the seismic characteristic points 101
4.4.2b Determination of the limits O and E 101
4.4.3 Estimation of seismic energy 102
4.4.3a Seismic energy from signal energy 103
4.4.3b Seismic energy from signal envelope 104
4.4.3c Choice of the energy formula 105
4.4.4 Polarisation analysis 106
4.4.5 Monitoring volcano: introduction to RSAM and SSAM methods 108
4.5 Combination of different type of data **109**
4.5.1 Particle size 110
4.5.2 Depth of the top of the magma column 110
4.5.3 Estimation of the gas volume fraction from the gas volume and scoria cone volume 114

When occurs a Strombolian explosion a great amount of energy is released by different mechanismes and partitionned between the atmosphere and the ground. Acoustic waves propagate into the atmosphere because of the sudden decompression of the Taylor bubble (i.e. the Strombolian explosion). Seismic waves also propagate into the ground because of the sudden decompression of the bubble. The great energy also triggers the ejection of hot gas and hot ejecta. All these processes can be measured and analysed (Figure 4.1).

Sounds, and especially infrasounds (<20 Hz) produced by Strombolian activity are mostly due to the explosion of the Taylor bubble and contain great information about the gas volume and overpressure of the bubble (Figure 4.1a).

The cloud of the explosion of the Taylor bubble contains hot gas and ejecta (ash, scoria, bombs). Infra-red radiometers and videos we use allow us to study the ejecta dynamics of the volcanic cloud but not the gas. Infra-red radiometers also allow us to measure the temperature of the ejecta (and sometimes gas) and thus to deduce a thermal energy (Figure 4.1b).

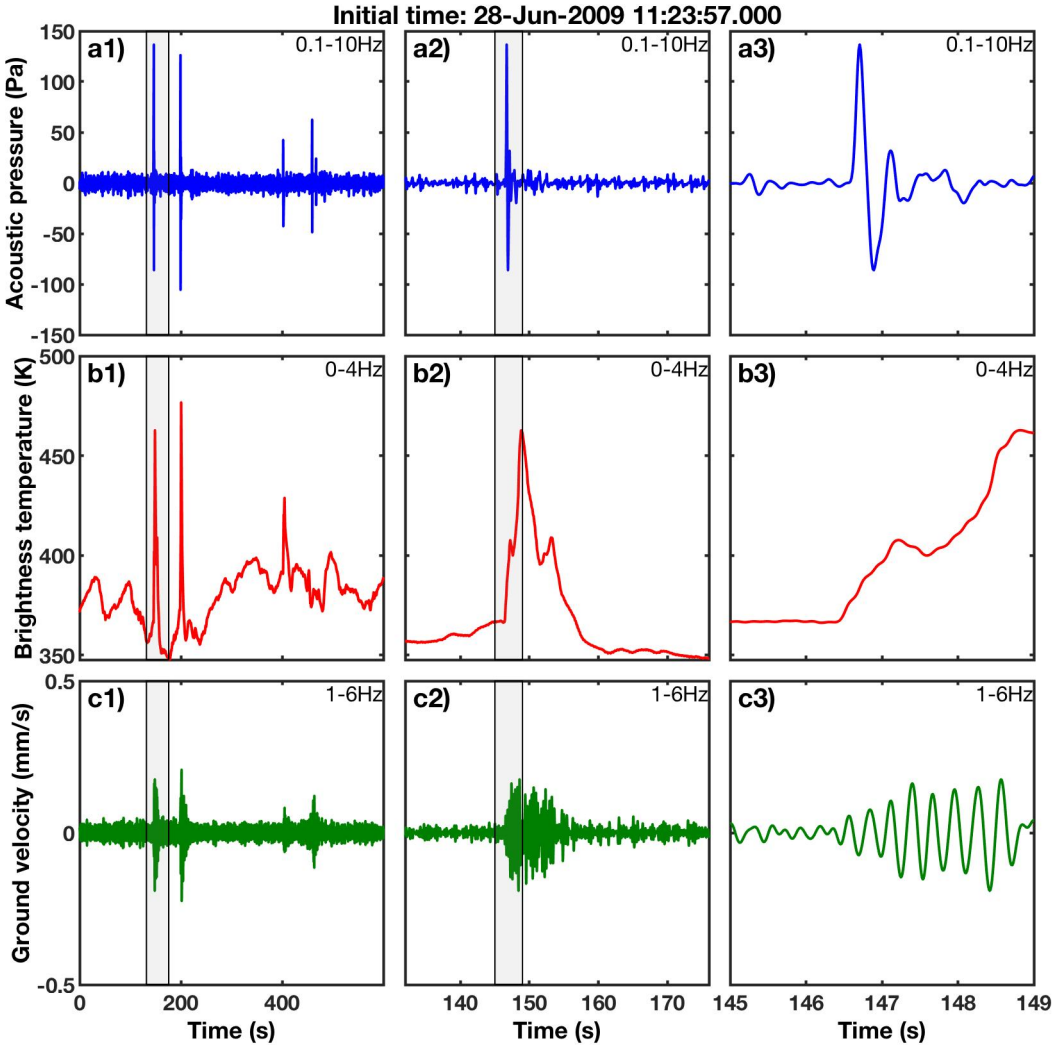

Figure 4.1 – Example of a) infrasonic, b) thermal and c) seismic records at Yasur in June 2009. 1) Large view of 10 min, 2) zoom on an explosion and 3) zoom of the beginning of the explosion. The shadowed areas in 1) and 2) show the limits of the zoom in 2) and 3), respectively.

Seismic waves mimic the ground motion due to the explosion of the Taylor bubble (EQ: 1 Hz to 6 Hz, Figure 4.1c). The formation and the rise of the Taylor bubble can also trigger seismic waves (LP and VLP).

The different duration and frequency of the waveforms of the Strombolian explosion, simultaneously recorded by the various sensors, highlight that each sensor records different mechanisms (Figure 4.1a2,b2,c2). Note also that the beginning of the explosion seen by the different sensors is shift (Figure 4.1a3,b3,c3). This is due to i) the speed of the various waves (light, seismic or infrasonic) and ii) the distance from the source to the sensor.

In the present chapter, I explain how to get useful estimates from the 1) infrasonic, 2) thermal measurements, from 3) videos and from 4) seismic measurements. At the end of the chapter, I also propose estimations from combined methods.

4.1 Infrasonic processing

One interest of infrasonic studies close to volcanoes is to be able tp give an estimate of the gas volume. Monitoring volcanic activity is also possible in a way similar to seismic monitoring, i.e. looking for anomalies on the recorded signal.

Anomalies on infrasounds can be recorded for a period or by detecting specific events. Once detected, each event should have a start, an end and perhaps some characteristic points in between.

4.1.1 Characteristic points on infrasonic waveforms

Strombolian explosions seen on infrasonic records are impulsive due to the sudden decompression of the gas pocket in the atmosphere. This impulsive event can be preceded by a precursor, possibly due to the motion of the top of the magma column as the gas bubble approaches the surface or from other processes. The sensor can also measures, right after the main peak, the variation of pressure of the following Taylor bubble in the conduit due to the propagation of the rarefaction wave following the decompression of the newly broken bubble. Hence several characteristic points have been defined to give insights into the mechanisms at work.

4.1.1a Definition of the characteristic points

Characteristic points on infrasonic waveforms (of explosions) are shown on figure 4.2 and defined as follows:

- O: the beginning of the event, is set as the beginning of the decompression of the gas pocket, and should be at 0 Pa without noise,
- Max, p^+: the maximum amplitude of the event gives the strength/intensity of each event,
- A: the first zero between the maximum (Max) and minimum amplitude, (B) marks the end of the compressive phase and the beginning of the rarefaction phase,
- B, p^-: the minimum amplitude of the event, recorded by the detection (first negative peak or minimum negative peak),

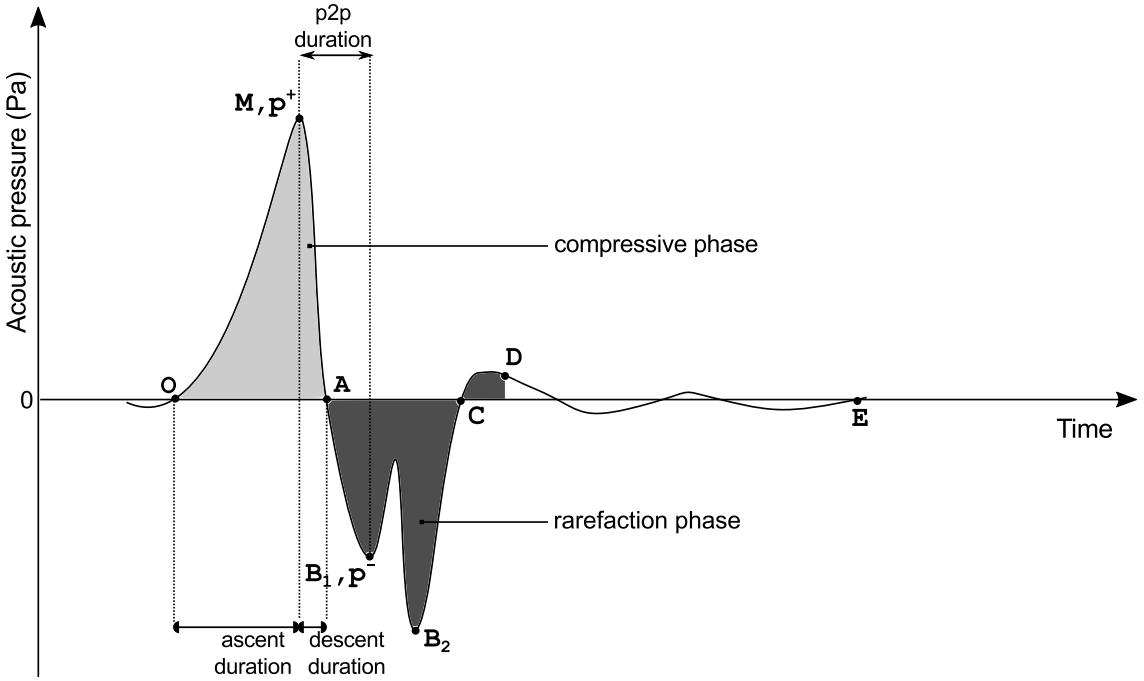

Figure 4.2 – Sketch of a typical infrasonic waveform at Yasur.

Min the minimum negative peak of the event, it thus can be the same than B,

C the first 0 after the minimum amplitude (B), indicates the end of the rarefaction phase and the end of the explosion in the simple case of the signal being a perfect sine,

D the end of the event (impulsive part, monopolar part), C might be undefined because of noise,

E the end of the event considering the tail (coda, dipolar part, renonance).

The maximum amplitude p^+ gives a direct information on the strength of the explosion. The higher p^+ is, the stronger is the explosion. Note that a natural signal is never a perfect sine.

From these characteristic points we can define 28 durations as:

O–Max Ascent duration

Max–A Descent duration

Max–B Peak to peak duration (`pnpp`)

O–A Duration of the compressive phase

A–C Duration of the rarefaction phase

A–D Duration of the rarefaction* phase: this case was added because C is often hard to find

O–D Duration of the explosion: impulsive part, monopolar part

D–E Duration of the tail of the explosion: often dipolar part

O–E Duration of the explosion: monopolar+dipolar parts

— Other combinaisons of the different points

The comparison of these different durations from an explosion to another can shed lights different waveforms and the existence of several sources. Then the temporal evolution of these durations might indicates changes in the conduit geometry, depth of explosion, gas overpressure, etc.

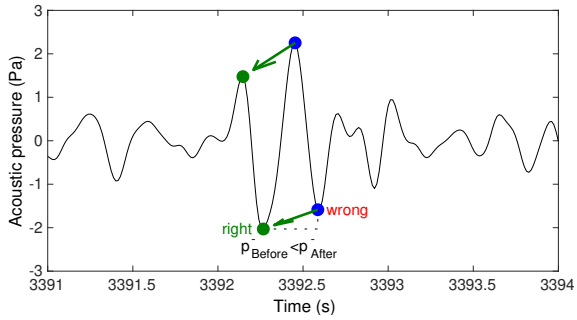

Figure 4.3 – Correction of the maximum amplitude for infrasonic waveforms with $p^+ < |p^-|$.

The characteristic points p^+ and p^- are directly given during the detection of the events. However some waveforms of explosions at Erta'Ale and Piton de la Fournaise have p^+ and p^- located at the wrong extrema (Figure 4.3). The extrema are moved foward if the minimum which is before the recorded maximum is lower than the recorded minimum.

4.1.1b Determination of the limits O, D and E

It is often difficult to always find the characteristic points on the waveform because explosion waveforms are not sine waves and because of noise. The low frequency noise can be due to oceanic waves high frequencies due to wind may also be added on the signal of explosion. We propose here several methods to find automatically the limits of the explosions:

a) application of the thresholds `hbthr` on the envelope of the signal from the Hilbert transform (Zielinski, 2012),
b) maximum on the first derivative of the kurtosis on a sliding window,
c) extrema around p^+ and p^-.

The application of the chosen method used to find the characteristic points is done on a part of the signal of time `tpart` and amplitude `xpart`. This part of the signal is set proportional to the delay (`pnpp`) between the positive and negative peaks (p^+ and p^-). Default values make the program looks in a window starting 4 times `pnpp` before p^+ and finishing 8 times `pnpp` after p^+; when assuming a sine, these values correspond to 2 and 4 times the period of the sine, respectively.

Limits from the envelope of the signal

This method look for thresholds on the normalized envelope of the signal `xpart` (Section 3.1.3). The value of the normalized envelope tends to 0 around the explosion (i.e. inter-explosion signal, Figure 4.4a)

The beginning of the explosion O is taken at the time, before p^+, where the envelope of the signal exceeds the first threshold `hbthr[1]`. The end of the explosion D is taken after p^- when the signal envelope decreases under the second threshold `hbthr[2]`. The end of the tail E is taken after D when the signal envelope decreases under the last threshold `hbthr[3]`. Default values of the thresholds `hbthr` are [0.2,0.2,0.08] for the beginning O, the end D and the end of the tail E, respectively. The choice of the thresholds are very

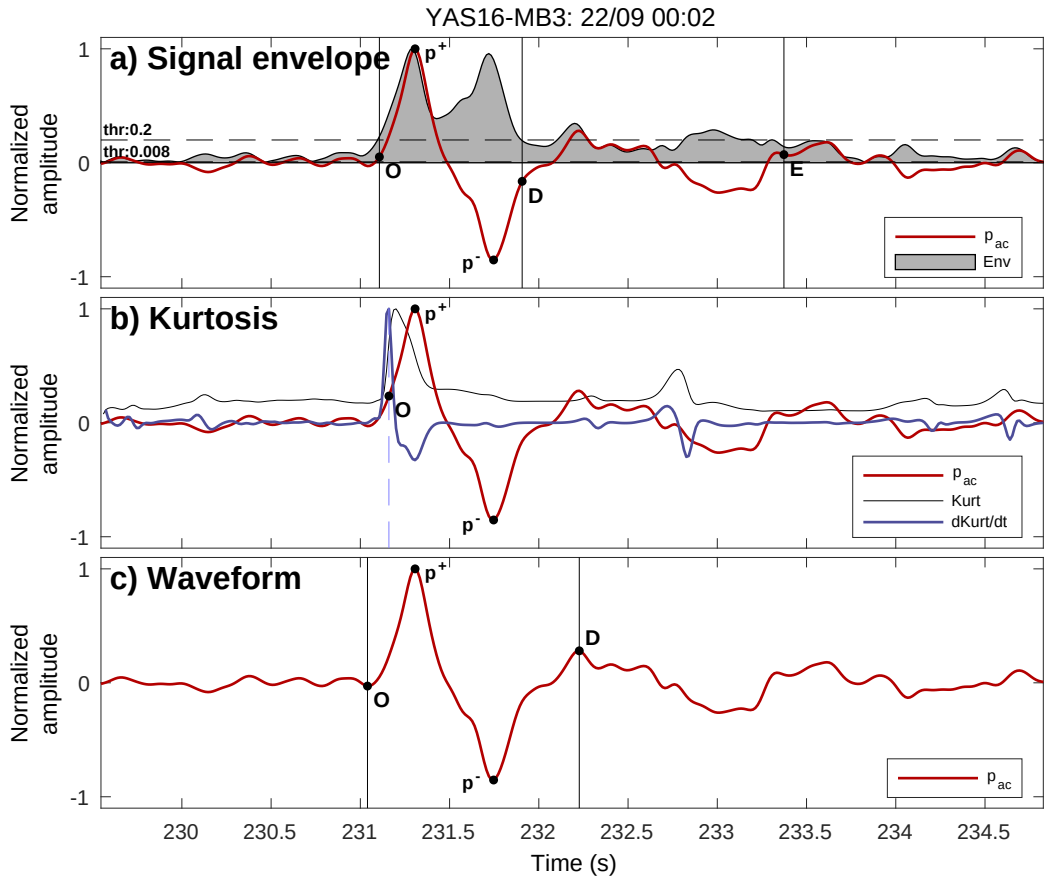

Figure 4.4 – Limits (O and D) of the explosions with three different methods. a) Signal envelope (gray) of the infrasonic signal (red) of a Strombolian explosion. b) Kurtosis per 1 s-sliding window (black) and its derivative (blue). c) Limits from the waveform of the signal (black, vertical lines): last minimum before p^+ and first maximum after p^-. Yasur-MB3, 22/09/2016–00:02, explosion at 00:05:51.

dependant on the user, but the default values are well adapted for infrasonic records from Yasur (Zielinski, 2012).

Limits from the Kurtosis

Baillard et al. (2014) had developed a method based on the kurtosis to detect and find the wave arrivals on seismic records (P and S-waves). The method consists in the calculation of the kurtosis of the signal on sliding windows of length `dtt`. Then anomalies can be detected within the ambient noise (i.e. explosions, Figure 4.4b).

The maximum on the first derivative of the kurtosis indicates the onset O of the explosion. The difficulty using this method is the choice of the length of the sliding window `dtt` which changes significantly the distribution of amplitude calculated by the kurtosis and thus the position of the beginning of the explosion. Furthermore another method is necessary to find the end of the explosion. Here we use of the previous method to find D and E (signal envelope) rather than the kurtosis.

Limits from the nearby extrema of the signal

This last method is the most restrictive as it considers only the waveform of the signal

(Figure 4.4c) and is efficient in case of low signal to noise ratio. The beginning O is taken as the last minimum before the maximum p^+ and the end D as the first maximum after the minimum p^-. We do not choose to take the zeros before and after the main peaks because of the potential offset of the signal.

The end of the tail of the signal is not found by this method. Furthermore, this method is well adapted for short and no-resonant events such as those found at Erta'Ale and Piton de la Fournaise, but this method is not adapted for the explosions at Yasur as they often present a long tail (Figure 4.4c).

4.1.2 Infrasonic energy and gas velocity

4.1.2a Type of acoustic sources

We can classify acoustic sources into 3 categories:

Monopole sources Monopoles are due to a variation of the mass flux without any external force on the flow. Monopole sources in a homogeneous medium generate acoustic waves which propagate in phase as a spherical front; i.e. the excess of pressure $(p_{\mathsf{ac}}(t) - p_{\mathsf{air}}(t))$ is the same for all points at the same distance r_{vent} from the source. The acoustic amplitude of monopole sources decreases with an attenuation of $1/r_{\mathsf{vent}}$ due to the spherical spreading. The source is a point source when the size of the source is smaller than the wavelength of the generated wave ($\lambda = 340\,\mathrm{m}$ at $1\,\mathrm{Hz}$). Then we can consider Strombolian explosions as point and monopole sources.

Dipole sources Dipoles are generated when an external force is applied on the system. The interaction of a jet with the surrounding conduit or particles within the jet can generate this type of source. The acoustic amplitude of dipole sources decreases with an attenuation of $1/r_{\mathsf{vent}}^2$ in near field (i.e. $r_{\mathsf{vent}} \ll \lambda$), and with an attenuation of $1/r_{\mathsf{vent}}$ in far field ($r_{\mathsf{vent}} \gg \lambda$). Fumaroles are good examples of dipole sources.

Quadrupole sources Quadrupoles are generated by the variations of constraints and without any external force such as product by a jet at constant flux. Gas jet with high velocity can generates this type of source due to the turbulence induced at the boundary between the jet and the surrounding.

In this study, we consider all Strombolian explosions as short, impulsive and monopole sources of acoustic waves.

4.1.2b Estimation of infrasonic energy

The excess pressure $(p_{\mathsf{ac}}(t) - p_{\mathsf{air}}(t))$, in a homogeneous atmosphere, is related to the infrasonic power $\mathcal{P}_{\mathsf{infrasonic}}(t)$ by

$$\mathcal{P}_{\mathsf{infrasonic}}(t) = \frac{2\pi r_{\mathsf{vent}}^2}{\rho_{\mathsf{atm}} c_{\mathsf{atm}}} \left(p_{\mathsf{ac}}(t) - p_{\mathsf{air}}(t)\right)^2 \tag{4.1}$$

where r_{vent} is the distance from the source to the sensor (m), ρ_{atm} is the density of the atmosphere at the elevation of the volcano ($\mathrm{kg.m^{-3}}$) and c_{atm} the sound speed. The factor 2 instead of 4 is due to the infrasonic waves being radiated in half a sphere. Other effects than this linear decay are neglected here (e.g. viscosity of the medium, heat

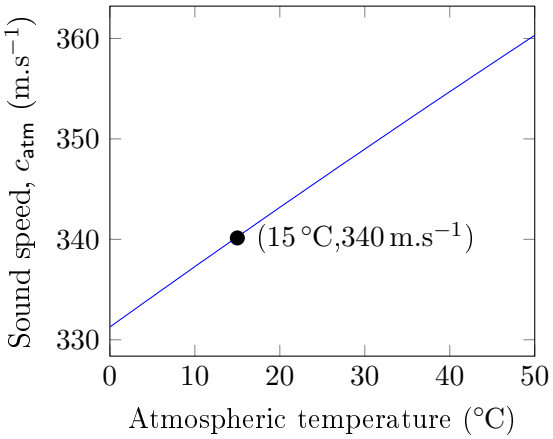

Figure 4.5 – Sound speed into the atmosphere as a function of the temperature of the atmosphere.

transfer,...). Variations of pressure due to the weather, the elevation or the topography are also neglected.

The sound speed in the atmosphere is equal to $\sqrt{\gamma R_{\text{ig}} T_{\text{atm}}} = 340\,\text{m.s}^{-1}$, with the adiabatic constant, γ in the atmosphere equal to $C_{\mathcal{P}}/C_{\mathcal{V}} = 1.4$, $R_{\text{ig}} = 287\,\text{J.kg}^{-1}\text{.K}^{-1}$ and $T_{\text{atm}} = 15\,°\text{C}$ (Lighthill (1978),figure 4.5).

We can integrate eq. (4.1) over the time to estimate the infrasonic energy as

$$\text{E}_{\text{infrasonic}} = \frac{2\pi r_{\text{vent}}^2}{\rho_{\text{atm}} c_{\text{atm}}} \int_0^{\tau} \left(p_{\text{ac}}(t) - p_{\text{air}}(t)\right)^2 \text{d}t \tag{4.2}$$

where τ is the duration of the explosion or of the sliding window on the infrasonic trace. Note that because $(p_{\text{ac}}(t) - p_{\text{air}}(t))$ is real, we can use the Parseval theorem to estimate the energy within a specific frequency band without additional filtering. The infrasonic power $\text{Pw}_{\text{infrasonic}}$ is obtained by dividing the infrasonic energy $\text{E}_{\text{infrasonic}}$ by the duration τ.

Infrasonic energy and power can be calculated either on sliding window (`pgac_pwvelvol`) or solely during each explosion (`pgac_volpw`).

4.1.2c From infrasonic energy to gas velocity

Woulff and McGetchin (1976) established the relation between the gas velocity U_{gas} and the infrasonic power $\text{Pw}_{\text{infrasonic}}$ from a dimensionless analysis of the Navier-Stokes equations and assuming a monopole source; giving

$$\text{Pw}_{\text{infrasonic}} = k \frac{\rho_{\text{atm}} 2\pi R_b^2}{c_{\text{atm}}} \text{U}_{\text{gas}}^4 \tag{4.3}$$

$$\Rightarrow \text{U}_{\text{gas}} = \left(\frac{\text{Pw}_{\text{infrasonic}} c_{\text{atm}}}{k \rho_{\text{atm}} 2\pi R_b^2} \right)^{1/4}, \tag{4.4}$$

where k is an experimental constant equal to 1 and R_b is the radius of source, assumed to be that of the bubble (m) (Vergniolle et al., 2004). The radius of the conduit R_{conduit} gives a good estimate of the bubble radius R_b for Strombolian explosions because bubbles are almost as large as the conduit. The greatest uncertainties on the gas velocity are associated to the estimates on the bubble radius R_b because $\text{U}_{\text{gas}} \propto R_b^{-1/2}$.

4.1.3 Gas volume from infrasonic records

Several models exist in the literature to estimate gas volumes (Section 1.2.1a). We use one or several among the 3 of them depending on the records and the goal of the study:

a) the gas volume from infrasonic power,
b) the gas volume from two integrations of the acoustic pressure,
c) the gas volume from the volume mode oscillation.

4.1.3a Gas volume from infrasonic power

The gas volume from infrasonic power (a) directly results from the gas velocity (Equation (4.4)) and the duration of the explosion. We consider that the gas passes through a disk of radius R_b at the velocity $\mathrm{U}_{\mathsf{gas}}$ during the duration τ to obtain the gas volume $\mathrm{Vol}_{\mathsf{gas},a}$ (Vergniolle et al., 2004):

$$\mathrm{Vol}_{\mathsf{gas},a} = \pi R_b^2 \mathrm{U}_{\mathsf{gas}} \tau. \tag{4.5}$$

This gas volume is greatly dependant on the unknown bubble radius as $\mathrm{Vol}_{\mathsf{gas}} \propto R_b^{3/2}$. For example, we have a relative error of $1 - 2^{-3/2} = 64.6\,\%$ if the real bubble radius is twice the estimated radius.

This model can be used to estimate gas volume per explosion (`pgac_volpw`) or gas volume per sliding windows (`pgac_pwvelvol`). The two combined techniques give the lower and upper limits of the gas volume released into the atmosphere. We can also obtain the gas volume per sliding window within specific frequency bands using the Parseval theorem (Figure 4.6 and section 3.1.2). The temporal evolution of gas volume in narrow frequency bands is sometimes revealing rapidly the changes in the frequency contents of the Strombolian activity. These changes in the frequency contents can be induced by

- a variation of geometry of the conduit
- the opening or closing of a vent
- a change of eruptive style due to variations of source (i.e. gas flux variations, size of the source).

4.1.3b Gas volume from two successive integrations of the acoustic pressure

The excess of pressure $(p_{\mathsf{ac}}(t) - p_{\mathsf{air}}(t))$ is a function of the variation of the mass flux for a monopole and semi-hemispherical source (Lighthill, 1978, chapitre 1, p19):

$$(p_{\mathsf{ac}}(t) - p_{\mathsf{air}}(t)) = \frac{1}{2\pi r_{\mathsf{vent}}} \frac{\mathrm{d}q(t - r_{\mathsf{vent}}/c_{\mathsf{atm}})}{\mathrm{d}t}, \tag{4.6}$$

where q is the mass flux ($\mathrm{kg.s^{-1}}$) and $p_{\mathsf{air}} = P_{\mathsf{atm}}$ the pressure of the atmosphere (Pa) which depends on the elevation of the volcanic source. We obtain the total mass flux Q (Equation (4.7a)) and then the total mass of gas M by integrating twice the mass flux q over the time (Equation (4.7b)). We finally divided the mass M by the atmosphere density

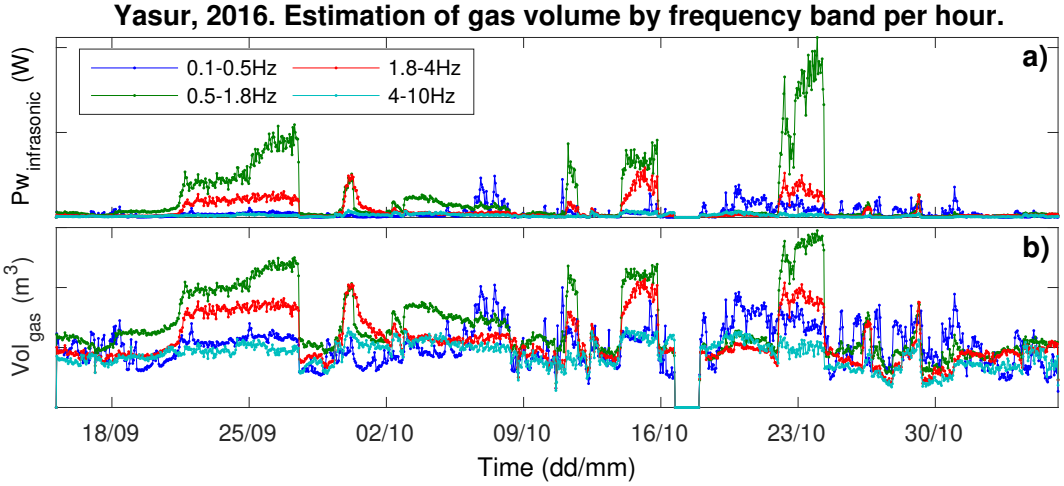

Figure 4.6 – From a) infrasonic power to b) gas volume by frequency bands and per sliding window of 1 hour at Yasur volcano in September–November 2016. Parameter: $\rho_{\mathsf{atm}} = 1.18\,\mathrm{kg.m^{-3}}$, $R_b = R_{\mathsf{conduit}} = 2.5\,\mathrm{m}$ and $r_{\mathsf{vent}} = 340\,\mathrm{m}$.

ρ_{atm} to get the gas volume (Equation (4.7c)):

$$Q = 2\pi r_{\mathsf{vent}} \int_0^t (p_{\mathsf{ac}}(t) - p_{\mathsf{air}}(t))\,\mathrm{d}t \tag{4.7a}$$

$$\Rightarrow M = \int_0^\tau \left(2\pi r_{\mathsf{vent}} \int_0^t (p_{\mathsf{ac}}(t) - p_{\mathsf{air}}(t))\,\mathrm{d}t\right)\mathrm{d}t \tag{4.7b}$$

$$\Rightarrow \mathrm{Vol}_{\mathsf{gas},b} = \frac{1}{\rho_{\mathsf{atm}}} \int_0^\tau \left(2\pi r_{\mathsf{vent}} \int_0^t (p_{\mathsf{ac}}(t) - p_{\mathsf{air}}(t))\,\mathrm{d}t\right)\mathrm{d}t. \tag{4.7c}$$

This model is valid under the following hypotheses (Johnson, 2003):

1. the instrumental response, effects of propagation, noise and variations of atmospheric pressure can be neglected;
2. the source can be compared to a point source at the vent;
3. acoustic pressure variations are sufficiently small to ensure a linear propagation of the sound waves.

For the mass flux (Lighthill, 1978)

$$q(t) = \begin{cases} \frac{A_1}{t^2+\tau_1^2}, & \text{if } t \leq 0, \\ \frac{A_2}{t^2+\tau_2^2}, & \text{if } t > 0, \end{cases} \tag{4.8}$$

with

$$\frac{A_1}{\tau_1^2} = \frac{A_2}{\tau_2^2} \tag{4.9}$$

(Figure 4.7), the acoustic pressure, calculated by eq. (4.7a), has a waveform similar to those observed at Yasur (Figure 4.7c1-c2). The third example, whose infrasonic waveform has $p^+ < |p^-|$, is not adapted because we consider here that the sudden output finishes faster than it begins and this is not compatible with the sudden decompression due to the Strombolian explosion, followed by a longer rarefaction. The resultant waveform is neither observed at Yasur, nor at Erta'Ale nor at Piton de la Fournaise.

We apply this model solely on each explosion (`pgac_voljohn`, figure 4.8). Thus we need to introduce a last model.

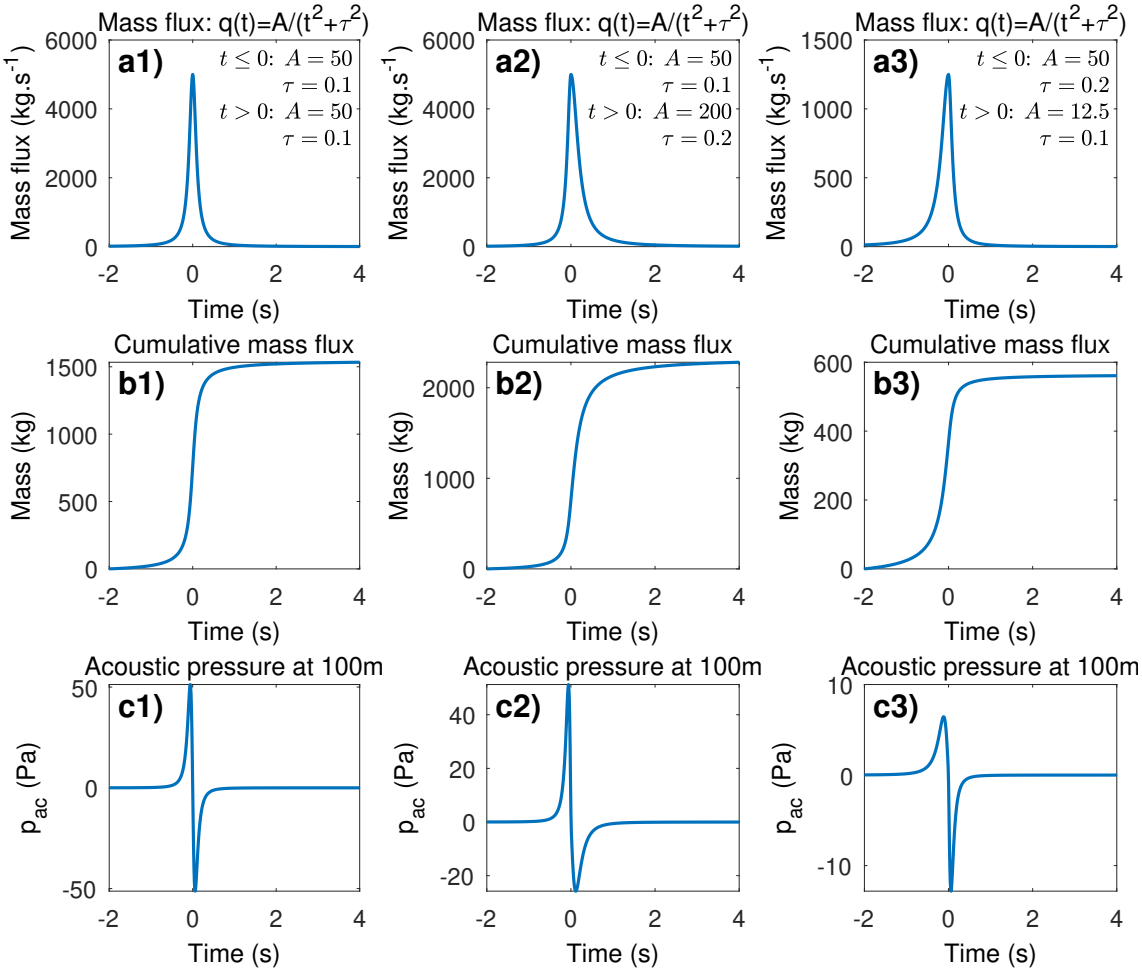

Figure 4.7 – Generation of infrasonic waveforms considering the mass flux as the function of the time such as $q(t) = A/(t^2 + \tau^2)$. a) Mass flux, b) cumulative mass flux and c) acoustic pressure for 1) $A_1 = 50$, $\tau_1 = 0.1$, $A_2 = 50$, $\tau_2 = 0.1$, 2) $A_1 = 50$, $\tau_1 = 0.1$, $A_2 = 200$, $\tau_2 = 0.2$ and 3) $A_1 = 50$, $\tau_1 = 0.2$, $A_2 = 12.5$, $\tau_2 = 0.1$.

4.1.3c Gas volume from the bubble volume mode prior to bursting (bubble vibration model)

The bubble volume mode, often referred to as the bubble vibration model, considers the infrasonic signal is due to the oscillations of the bubble at the surface of the magma column prior to explode (Vergniolle and Brandeis, 1996). In contrast, the previous models consider that the infrasonic signal is generated by the sudden input of gas into the atmosphere.

The equilibrium radius $R_{b,\mathrm{eq}}$ is calculated using the adiabatic low and depends on the initial conditions of the Taylor bubble

$$R_{b,\mathrm{eq}} = \frac{3}{2}^{1/3} \left[\left(\frac{2R_{b,0}^3}{3} + R_{b,0}^2 L_b \right) \left(1 + \frac{\Delta P_b}{P_{\mathrm{atm}}} \right)^{1/\gamma} - R_{b,0}^2 L_b \right]^{1/3}, \tag{4.10}$$

where γ is the adiabatic constant (1.1 for hot gases, Lighthill, 1978), $R_{b,0}$ the initial radius of the bubble (m) L_b the bubble length (m) and ΔP_b the initial gas overpressure (Pa).

The gas pocket is suddenly over-pressurised with an overpressure ΔP_b (Pa). This generates oscillatory variations of the gas volume which can be written as a perturbation ϵ_b on the

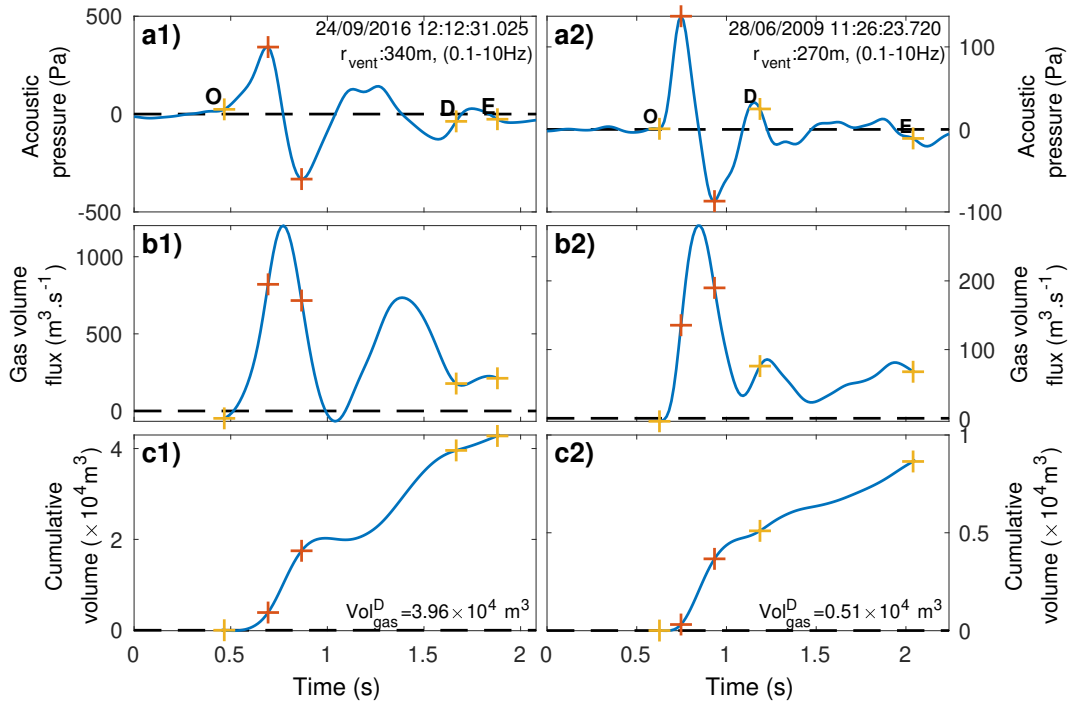

Figure 4.8 – Example of the gas volume calculation from two successive integrations of the acoustic pressure. a) Acoustic pressure, b) gas flux and c) cumulative gas flux for two explosions chosen at Yasur in 2016.

radius ($R_b = R_{b,\text{eq}} + \epsilon_b$). The oscillations are due to the transfert of kinetic energy and potential energy described by

$$\ddot{\epsilon_b} + \frac{12\mu_{\text{magma}}}{\rho_{\text{magma}} R_{b,\text{eq}}^2}\dot{\epsilon_b} + \frac{P_{\text{atm}}}{\rho_{\text{magma}} R_{b,\text{eq}} h_{b,\text{eq}}}\left[1 - \left(\frac{\text{Vol}_{\text{eq}}}{\text{Vol}_b}\right)^{\gamma}\right](1+\epsilon_b)^2 = 0, \tag{4.11}$$

where ρ_{magma} is the magma density (kg.m^{-3}), μ_{magma} the viscosity of the magma (10 Pa.s and 40 Pa.s at Erta'Ale and Piton de la Fournaise, respectively), $h_{b,\text{eq}}$ the thickness of the magma overlying the gas pocket (m) and Vol_b (m^3) the gas volume function of ϵ_b and L_b.

We can solve the differential eq. (4.11) using the Runge-Kutta method of order 3 with the

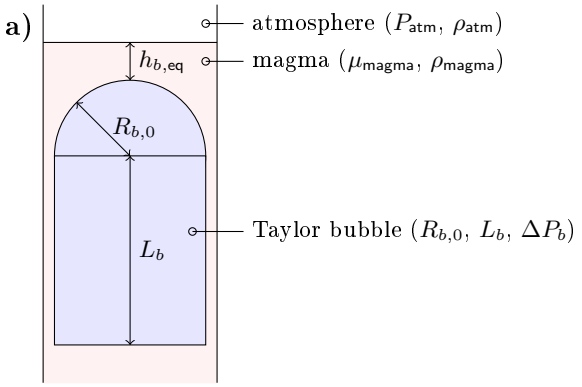

Figure 4.9 – Parameters for the bubble volume mode model.

following initial conditions:

$$\ddot{\epsilon_{b,0}} = \frac{\Delta P_b R_{b,0}^2}{\rho_{\text{magma}} R_{b,\text{eq}}^3 h_{b,\text{eq}}}, \tag{4.12}$$

$$\epsilon_{b,0} = \frac{R_{b,0}}{R_{b,\text{eq}} - 1}. \tag{4.13}$$

We can also determine the normalised amplitude A_b of the oscillation ϵ_b as

$$A_b = \frac{\Delta P_b R_{b,0}^2}{3\gamma P_{\text{atm}} R_{b,\text{eq}}^2} \left(1 + \frac{3L_b}{2R_{b,\text{eq}}}\right). \tag{4.14}$$

This parameter A_b, also called the linearity parameter, characterises the strength of the oscillations and the linearity of the model. The smaller A_b is, the more ϵ_b is linear and looks like a sinusoidal wave.

The acoustic pressure generated by the Taylor bubble can be written as a function of the variation ϵ_b and the equilibrium radius $R_{b,\text{eq}}$ (Lighthill, 1978)

$$(p_{\text{ac}}(t) - p_{\text{air}}(t)) = \frac{\mathrm{d}^2}{\mathrm{d}t^2}\left[\frac{4\pi R_b^3(t - r_{\text{vent}}/c_{\text{atm}})}{6}\right]\frac{\rho_{\text{atm}}}{2\pi r_{\text{vent}}}, \tag{4.15}$$

$$\Leftrightarrow \quad (p_{\text{ac}}(t) - p_{\text{air}}(t)) = \frac{R_{b,\text{eq}}^3 \rho_{\text{atm}}}{3r_{\text{vent}}}\frac{\mathrm{d}^2(1+\epsilon_b)^3}{\mathrm{d}t^2} \tag{4.16}$$

$$\Leftrightarrow \quad (p_{\text{ac}}(t) - p_{\text{air}}(t)) = \frac{R_{b,\text{eq}}^3 \rho_{\text{atm}}}{3r_{\text{vent}}}\left(2\dot{\epsilon_b}^2(1+\epsilon_b) + \ddot{\epsilon_b}(1+\epsilon_b)^2\right), \tag{4.17}$$

for a monopole source.

No analytical solution exists between the initial conditions of the Taylor bubble ($R_{b,0}$, L_b, ΔP_b) and the radiated acoustic pressure. A series of synthetic waveforms are calculated as a function of a choice of ($R_{b,0}$, L_b, ΔP_b, $h_{b,\text{eq}}$, μ_{magma}, ρ_{magma} and r_{vent}) to cover the full range of expected values. The best fit (cross-correlation + RMS) gives estimates on the bubble characteristics during the explosion.

The synthetic waveforms are very similar to the recorded waveforms observed at Erta'Ale and Piton de la Fournaise.

The gas volume released in the atmosphere is calculated using the ideal gas law as

$$\text{Vol}_{\text{gas},c} = \left(1 + \frac{\Delta P_b}{P_{\text{atm}}}\right)\text{Vol}_b, \qquad \text{with} \text{Vol}_b = \frac{2}{3}\pi R_{b,0}^3 + \pi R_{b,0}^2 L_b. \tag{4.18}$$

We assume $h_{b,\text{eq}}$ is approximatively equal to the size of the larger ejecta (bombs) than an explosion can produce and we fix it to 22 cm and 10 cm at Erta'Ale and Piton de la Fournaise, respectively (Bouche et al., 2010; Gurioli et al., 2018).

All the detected explosions have to be searched for the best synthetic waveform with variable $R_{b,0}$, L_b, ΔP_b (`pgac_volbubvib`).

We first create a set of synthetic waveforms with several combinations ($R_{b,0}, L_b, \Delta P_b$) and retrieve p^+, p^-, the widths (durations) `w1` = O–p^+ and `w2` = p^+–A, the linearity parameter A_b and the waveforms for each combination (`bubvib_waves`).

A first selection is done by the user on the linearity parameter A_b and the aspect ratio $2R_{b,0}/L_b$ to remove synthetic waveforms very different from the real one.

A second selection is performed, for each explosion, on the maximum and minimum amplitde (p^+ and p^-) and the widths `w1` and `w2` to speed up the computational time. The decrease of the number of synthetic waveforms is organised as follows:

$$(b_+ - a_+)p^+_{\text{data}} \leq p^+_{\text{model}} \leq (b_+ + a_+)p^+_{\text{data}}, \tag{4.19a}$$
$$(1 - a_-)p^-_{\text{data}} \leq p^-_{\text{model}} \leq (1 + a_-)p^-_{\text{data}}, \tag{4.19b}$$
$$(1 - a_1)\texttt{w1}_{\text{data}} \leq \texttt{w1}_{\text{model}} \leq (1 + a_1)\texttt{w1}_{\text{data}}, \tag{4.19c}$$
$$(1 - a_2)\texttt{w2}_{\text{data}} \leq \texttt{w2}_{\text{model}} \leq (1 + a_2)\texttt{w2}_{\text{data}}. \tag{4.19d}$$

The subscript $+$ and $-$ are associated to p^+ and p^-, respectively and the subscript 1 and 2 to the widths `w1` and `w2`. The coefficients a and b are useful to correct any bias in the recorded infrasonic waveforms.

The third selection is based on the correlation coefficient which can be constant on the entire infrasonic waveform or weighted in 3 parts defined by (Figure 4.10)

1. from O to the offset of the signal,
2. from offset to p^+ and
3. from p^+ to C.

where the offset of the signal can be defined by the point where $p = p_{\text{O}} + (p^+ - p_{\text{O}})/6$ are by the last maximum of the seconde derivative of $p(t)$ before p^+ depending on the choice of the user. The weighted correlation coefficient is

$$\text{corrCoeff} = w_{c,1}\text{corrCoeff}_1 + w_{c,2}\text{corrCoeff}_2 + w_{c,3}\text{corrCoeff}_3 \tag{4.20}$$

where the weights $w_{c,i}$ are chosen by the user ($i = \{1, 2, 3\}$). We only keep the synthetic waveforms with the correlation coefficient above the threshold `CorrCoefThr`.

The last selection consists in the choice of the best fit. This can be manually or by finding the synthetic waveform for which the residue `RES = (1-CorrCoef)*RMS` is the smallest ($\text{RMS} = \sqrt{\sum_{i=1}^{N} \left(p_{\text{ac}}(t) - p_{\text{air}}(t)\right)_{\text{model},i} - \left(p_{\text{ac}}(t) - p_{\text{air}}(t)\right)_i}$, N being the length of the signal).

Example 4.1.1. I wish to estimate the gas volume from the Strombolian explosion at Piton de la Fournaise the 10/12/2006 at 20:03:17 (Figure 4.11). This explosion has a maximum acoustic pressure of 2.68 Pa and a minimum acoustic pressure of −5.43 Pa and ascent duration O–p^+ (`w1`) and descent duration p^+–A (`w2`) of 0.133 s and 0.0533 s, respectively. I estimate the atmospheric pressure and density at the elevation of the vent (2632 m) at 7.37×10^4 Pa and 0.95 kg.m^{-3}, respectively. I use $h_{b,\text{eq}} = 10$ cm by analogy to the largest ejecta (Gurioli et al., 2018) and the magma viscosity and density are 40 Pa.s and 2.7×10^3 kg.m^{-3}, respectively (Hibert et al., 2015). The distance from the vent to the sensor is 115 m.

I have calculated 166 253 synthetic waveforms with $R_{b,0}$ ranging from 0.05 to 5 m, L_b from 0.3 to 30 m, ΔP_b from 3000 to 1×10^5 Pa and p^+ from 0.95 to 23 Pa (Figure 4.12). The recorded infrasonic waveforms and the dependence of the synthetic waveforms to A_b suggest to fix $0.15 \leq A_b \leq 0.30$, condition for which the linearity is reasonable and the synthetic waveforms similar to that at Piton de la Fournaise. 67 808 synthetic waveforms remained

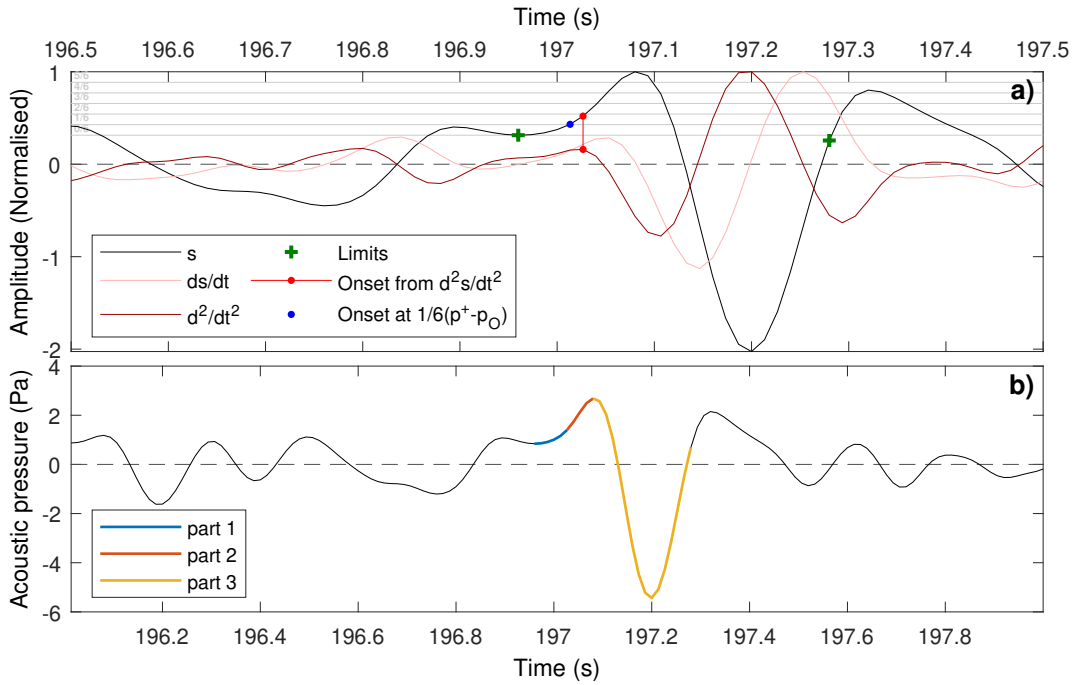

Figure 4.10 – Parts of the infrasonic waveform to calculate the weighted coefficient of correlation. Note the different time scales.

(40.79 %). Only 171 (0.10 %) synthetic waveforms are kept after applying the following constraints $b_+ = 1$, $a_+ = 0.05$, $a_- = 0.5$, $a_1 = 0.2$ and $a_2 = 1$.

The best fit is found for $R_{b,0} = 1.3\,\text{m}$, $L_b = 5.7\,\text{m}$ and $\Delta P_b = 36\,500\,\text{Pa}$ with a unweighted correlation coefficient of 0.9955 and a RMS equals 2.52 Pa giving a residue `RES` equal to 0.112 14 Pa, (Figure 4.11)

4.1.4 Atmosphere density and pressure

I use the models from U.S. Government Printing Office (1976) to estimate the atmospheric pressure and density at the elevation of the field experiments (Figure 4.14).

The atmospheric pressure P_{atm} at the elevation z in the troposphere is estimated by

$$P_{\text{atm}} = P_{\text{atm,std}} \left(\frac{T_{\text{atm,std}}}{T_{\text{atm,std}} + L_{\text{atm,std}}(z - z_{\text{std}})} \right)^{\frac{g M_{\text{mol}}}{R_{\text{ig,mol}} L_{\text{atm,std}}}} \tag{4.21}$$

where $P_{\text{atm,std}} = 101\,325\,\text{Pa}$ is the standard atmospheric pressure at the sea level, $T_{\text{atm,std}} = 288.15\,\text{K}$ is the standard temperature, $L_{\text{atm,std}} = -0.0065\,\text{K.m}^{-1}$ the standard temperature lapse rate in the troposphere. z is the height above sea level and $z_{\text{std}} = 0\,\text{m}$ the sea level elevation. $g = 9.807\,\text{m.s}^{-2}$ is the gravitational acceleration, $M_{\text{mol}} = 0.028\,96\,\text{kg.mol}^{-1}$ is the molar mass of the atmosphere and $R_{\text{ig,mol}} = 8.314\,\text{J.mol}^{-1}.\text{K}^{-1}$ is the universal gas constant.

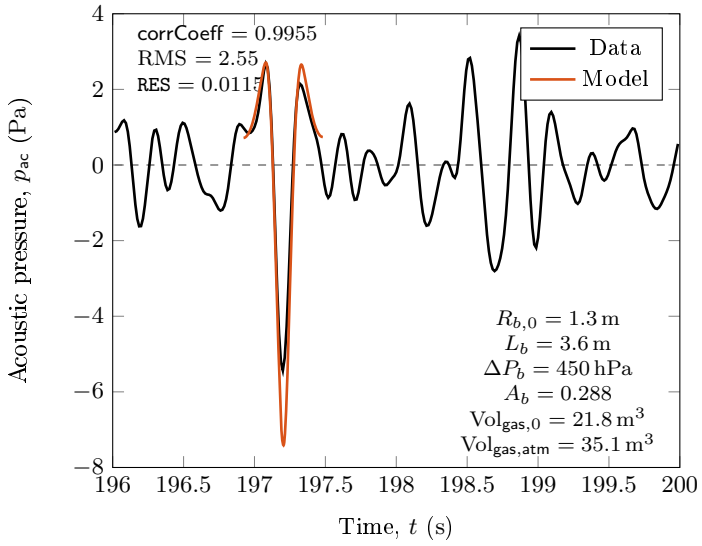

Figure 4.11 – Fit of an explosion at Piton de la Fournaise (10/12/2006, at 20:03:17) with the synthetic waveform, from the bubble volume model and selected by the automatic programme. The coefficient of the correlation is 0.9955 and the RMS equals 2.52 giving a residue of 0.112 14.

Table 4.1 – Atmospheric pressure and density at the elevation of the measurements considering the standard values at the sea level and the standard temperature of 288.15 K (15 °C).

	z (m)	P_{atm} (Pa)	z_p (m)	ρ_{atm} (kg.m^{-3})
Sea level (std)	0	101 325	0	1.2250
Erta'Ale	613	94 175	612.9	1.1545
Piton de la Fournaise	2632	73 453	2630.9	0.9442
Yasur	361	97 063	361.0	1.1831

The atmosphere density ρ_{atm} at the geopotential elevation h_p is

$$\rho_{\mathrm{atm}} = \rho_{\mathrm{atm,std}} \left(\frac{T_{\mathrm{atm,std}}}{T_{\mathrm{atm,std}} + L_{\mathrm{atm,std}}(z_p - z_{p,\mathrm{std}})} \right)^{\left(1 + \frac{gM_{\mathrm{mol}}}{R_{\mathrm{ig,mol}} L_{\mathrm{atm,std}}}\right)} \tag{4.22}$$

where $\rho_{\mathrm{atm,std}} = 1.2250\,\mathrm{kg.m}^{-3}$ is the standard atmosphere density. z_{std} is given in geopotential metres. We define the geopotential elevation as $z_p = R_{\mathrm{earth}} z/(R_{\mathrm{earth}} + z)$, where $R_{\mathrm{earth}} = 6356.8\,\mathrm{km}$ is the Earth radius.

For example, at the elevation of 1000 m the atmospheric pressure is 89 875 Pa and the atmosphere density is $1.1117\,\mathrm{kg.m}^{-3}$.

At the elevation of the field measurements we get the atmospheric pressure and density shown in the table 4.1.

4.2 Thermal processing

The intensity measured by the radiometers depends on the hot area presented by the ejecta (and gas), hence potentially contains information on temperature and the amount/size ejecta. The thermal waveform is characterised by short duration for the ascent of the temperature, followed by one or several maxima (Figure 4.15). After the peak(s) the

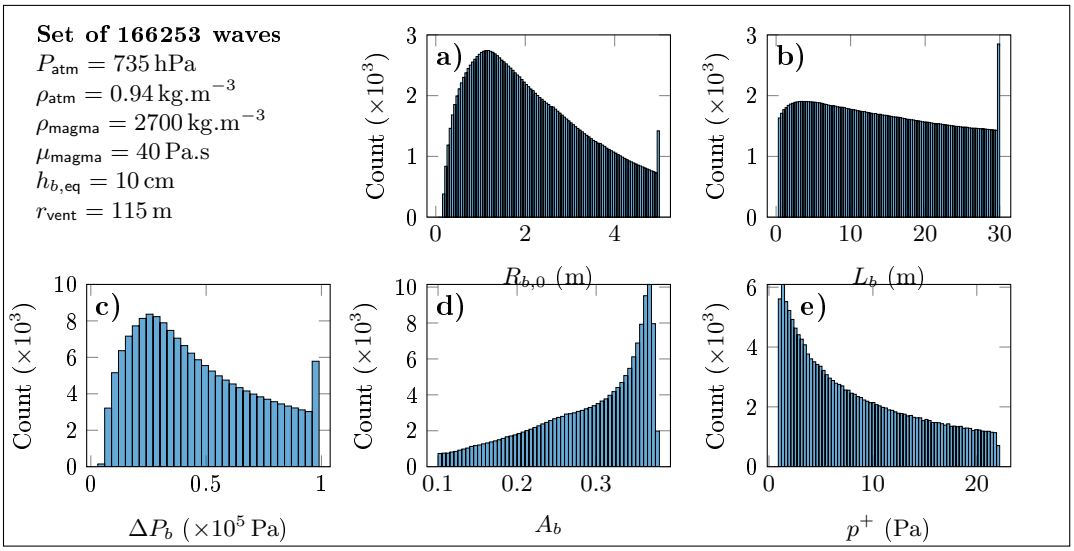

(a) All 166 253 synthetic waveforms

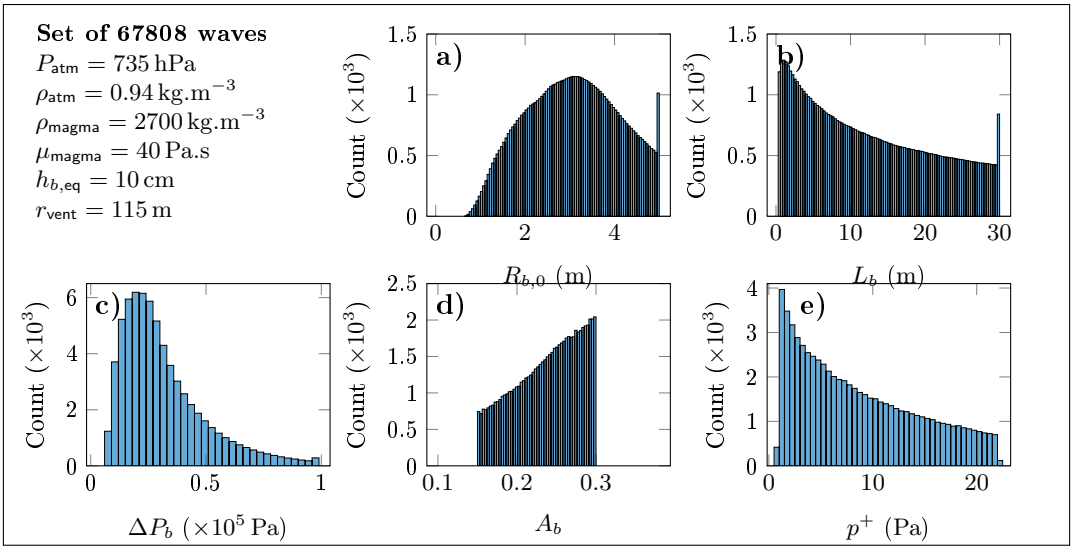

(b) 67 808 synthetic waveforms after selection on A_b and R_b/L_b

Figure 4.12 – Distribution of $R_{b,0}$, L_b, ΔP_b, A_b and p^+ of the waveform set *syntwaves_pif_d115_mu40_in1e5Pa_num166253.mat*. a) All synthetic waveforms. b) Synthetic waveforms after the selection on A_b. More details are given in the example 4.1.1. To be continued.

temperature decreases slowly to reach the initial temperature prior to the explosion or sometimes decreases below the pre-explosion temperature due to gas opacification.

The gas opacification is the ability of gases to absorb the light, here the infra-red, in a specific wavelength. The gas opacification depends on the species present in the gas mixture and on the temperature of the gas mixture. Particularly, the content of water plays an important role as the atmospheric humidity can vary a lot (Gaudin, 2012). The opacification is probably triggered by the compressive wavefront (Marchetti et al., 2013).

It is tempting to link the different part of the waveform to the different steps of the explosion. The simplest case is presented by a unique gas thrust followed by the effects of buoyancy and the fall down of the ejecta. We expect a simplified waveform with only 1 maximum (figure 4.15a). The separation between thrust and buoyancy is difficult to find because buoyancy starts before the end of the thrust and a period exists for which the

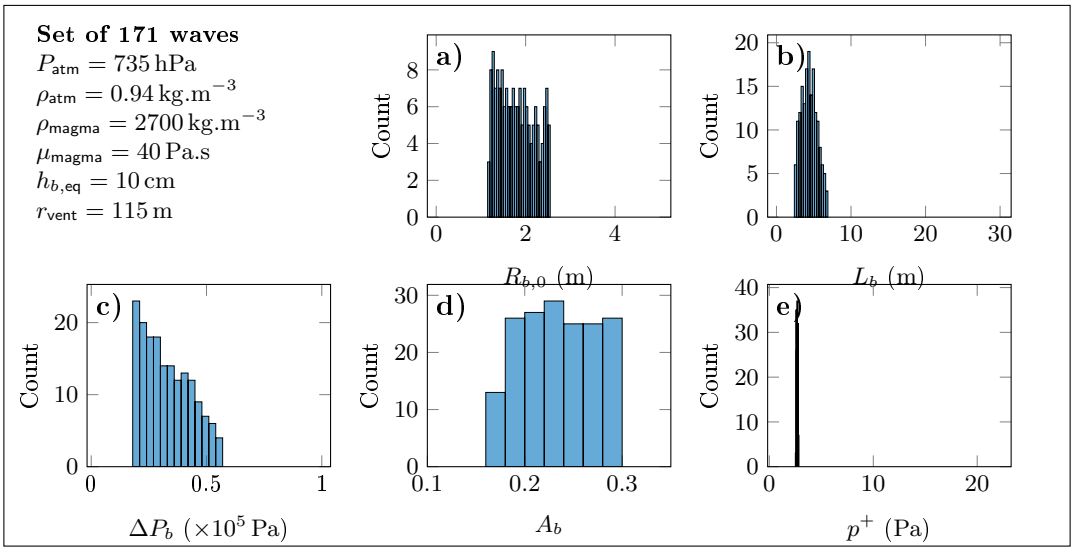

(c) 171 synthetic waveforms after selection on p^+, p^-, `w1` and `w2`

Figure 4.12 – Distribution of $R_{b,0}$, L_b, ΔP_b, A_b and p^+ of the waveform set *syntwaves_pif_d115_mu40_in1e5Pa_num166253.mat* (continued). c) Synthetic waveforms after the selection on p^+, p^-, `w1` and `w2`. More details are given in the example 4.1.1.

effects of the thrust and the effects of the buoyancy have the same order of magnitude. We can assume that the part before the maximum is mostly due to the thrust and that the part after the maximum is mostly due to buoyancy.

The brightness temperature measured by radiometers is a measurement of the infra-red radiations in the 8 µm–13 µm pass-band and is obtained by the spectral analysis of the recorded radiations. The analysis of each spectrum takes times and the temperature is given by the output of the radiometer, each 0.19 s. This *large* efficient response time leads to great errors on the thermal estimates when a temporal information is needed, compared to the sampling rate of infrasound and seismic sensors.

4.2.1 Characteristic points on thermal waveforms

4.2.1a Definition of the characteristic points

Several mechanisms can be responsible for the thermal waveform. The mechanisms can be difficult to identified on the thermal waveform. So we define the characteristic points as follows (Figure 4.16):

- O begining of the explosion (signal envelope), characterised by the offset of the thermal signal, it also corresponds to the background temperature T_{Back},
- M* highest maxima of the explosion, one maximum per thrust (`NumberOfPeaks`),
- B* minima between 2 maxima (`NumberOfPeaks`-1),
- E end of the explosion for which the temperature T_E equal the background temperature T_{Back},
- E' end of the explosion, the temperature at E' is often lower than then temperature of the background (signal envelope), then E' is reached after the period during which the temperature is below the pre-explosion temperature

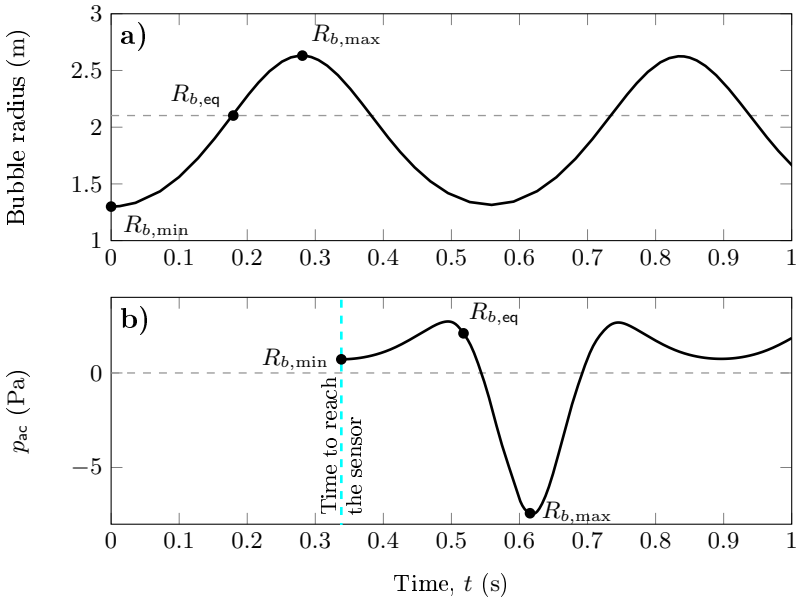

Figure 4.13 – Example of a synthetic waveform from the bubble volume model for a gas volume of $\text{Vol}_{gas} = 49.7\,\text{m}^3$: $R_{b,0} = 1.3\,\text{m}$, $L_b = 5.7\,\text{m}$, $\Delta P_b = 36\,500\,\text{Pa}$, $h_{b,\text{eq}} = 10\,\text{cm}$ and $\mu_{\text{magma}} = 10\,\text{Pa.s}$ give $A_b = 0.291$. The acoustic pressure is calculated for $r_{\text{vent}} = 115\,\text{m}$, in an atmosphere at $P_{\text{atm}} = 7.37 \times 10^4\,\text{Pa}$ and $\rho_{\text{atm}} = 0.95\,\text{kg.m}^{-3}$.

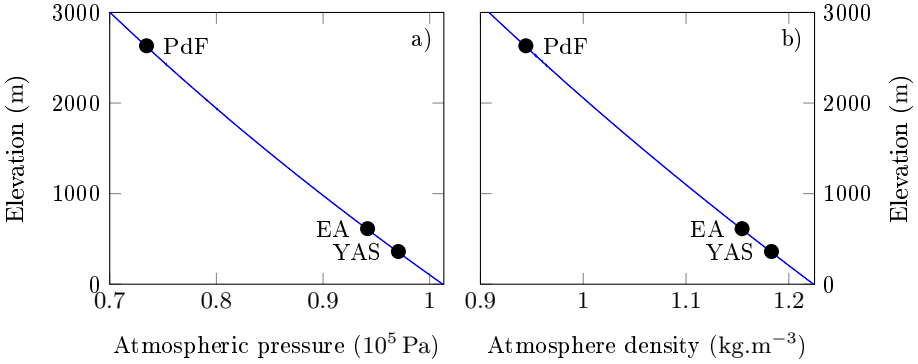

Figure 4.14 – a) Atmospheric pressure as a function of the elevation. b) Atmosphere density as a function of the elevation.

4.2.1b Determination of the limits O, E and E'

To my knowledge there is no classical technique to find specific points within the thermal waveform of a Strombolian explosion. I proposed here three methods (Figure 4.17). Two of them consider the envelope from the Hilbert transform (Section 3.1.3). The envelope is done on an gradient of the temperature, such as $\text{d}T^4/\text{d}t$ or $\text{d}^2T/\text{d}t^2$. A naive view of that parameter is that it corresponds to the velocity ($\text{d}T^4/\text{d}t$) or acceleration ($\text{d}^2T/\text{d}t^2$) of entry of the ejecta in the field of view.

Thresholds on the envelope of $\text{d}T^4/\text{d}t$

The idea comes from the black body law which says that the radiant thermal energy is proportional to $T(t)^4 - T_{\text{Back}}^4$ where $T(t)$ is the temperature at the time t and T_{Back} is the temperature of reference.

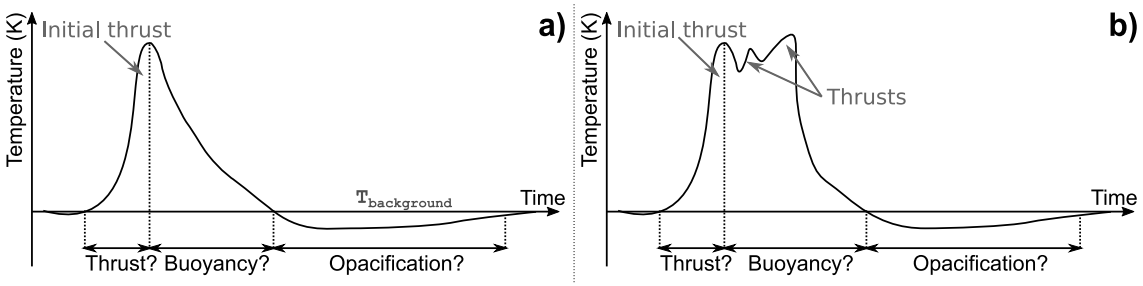

Figure 4.15 – Sketch of a) a simple and b) a complexe waveform of an explosion recorded by an IR-radiometer.

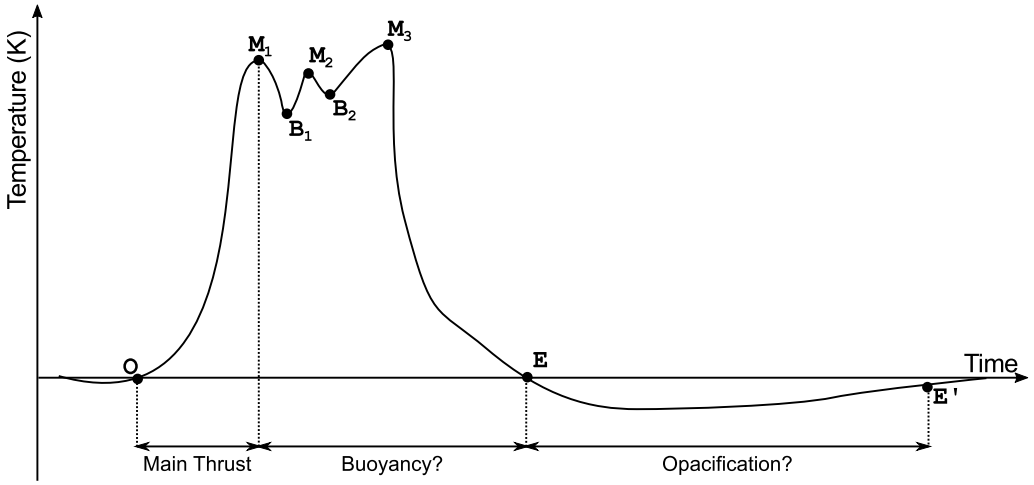

Figure 4.16 – Definition of the thermal characteristic points.

Taking the derivative of the temperature to the power of 4 allows the signal to oscillates around 0 (Figure 4.17b). Thus, we can calculate the envelope of the derivative using the Hilbert transform (section 3.1.3). We then normalized this envelope.

We define the beginning O of the event looking for the first point of the normalized envelope over the starting threshold (triggering threshold). The temperature at the beginning O is the background temperature T_{Back}. The end E is defined such as its temperature T_{E} is equal to T_{Back} with all T between O and E larger than T_{Back}. The "far" end E' is defined by the last point over the ending threshold.

Default values of the threshold were found for thermal records of the 2016 field campaign at Yasur: 0.10 and 0.05, for the triggering and ending thresholds, respectively.

Thresholds on the envelope of $\mathrm{d}^2T/\mathrm{d}t^2$

The idea is to look for the sudden changes in the slope, hence the second derivative. However, there are many variations which can blur the changes in the slope. So we used the envelope of this second derivative to enhance the detection of the limits (Figure 4.17a).

We then find out the O, E and E' the same way we do using the first method with default threshold at 0.05 and 0.01.

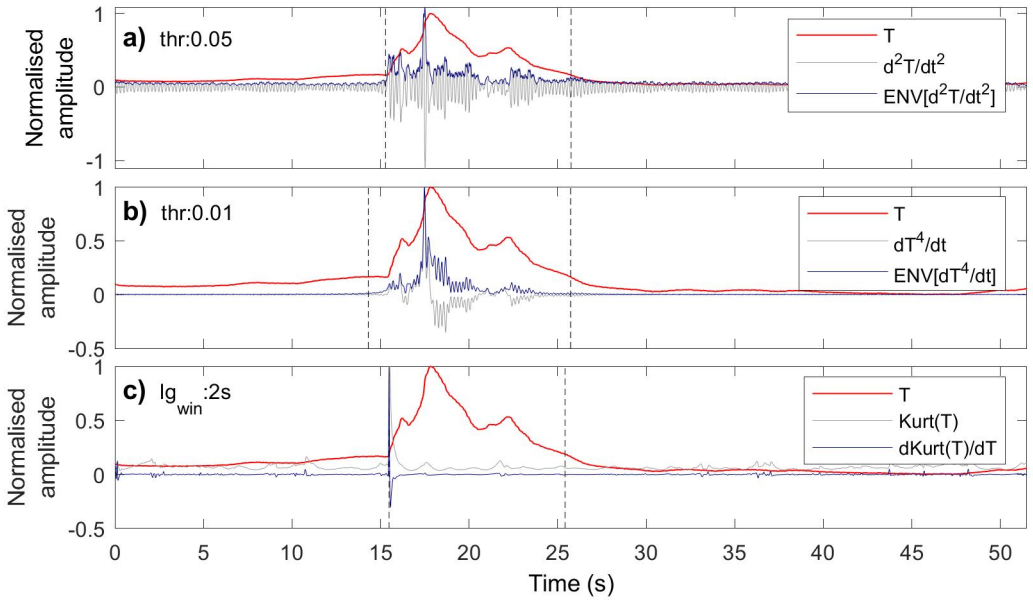

Figure 4.17 – Determination of the limits of the thermal waveform of the explosions using a) the envelope of the second derivative of the temperature (threshold at 0.05), b) the envelope of the derivative of the temperature to the power 4 (threshold at 0.01), c) the derivative of the kurtosis curve (length of the sliding window of 2 s.

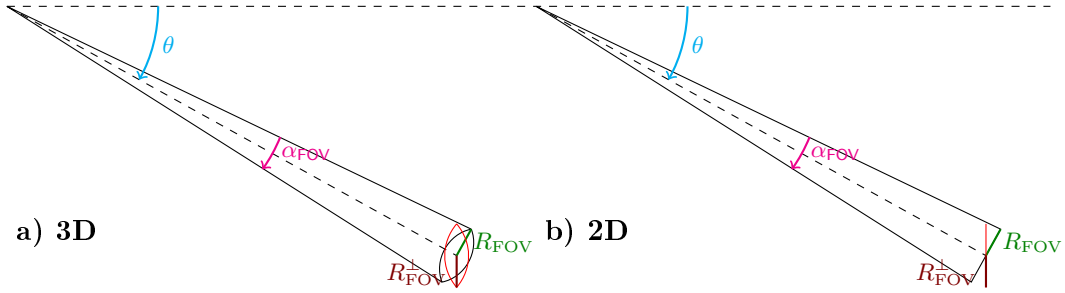

Figure 4.18 – Calculation of the field of view of the radiometer. a) 3D view and b) 2D view.

Maximum on the derivative of the kurtosis

This last method is adapted from seismic processing as the kurtosis is very efficient to detect seismic events and also the timing of the arrival of P- and S-waves (Baillard et al., 2014).

Taking the derivative of the kurtosis curve has the advantages to switch the profile of the kurtosis such as the maximum of the profile is simultaneous of a major change in the kurtosis curve. This major change indicates the beginning of the event (Figure 4.17c).

With this method, we can not determine the "far" end E' because the decay of the temperature is often too long compare to the increase of the temperature.

4.2.2 Field of view of the radiometers

The vertical field of view $\mathcal{A}^{\perp}_{\mathsf{FOV}}$ of a radiometer, with an inclination θ, at the distance r_{vent} is an ellipse and can be calculated as (figure 4.18)

$$\mathcal{A}^{\perp}_{\mathsf{FOV}} = \pi R^{\perp}_{\mathrm{FOV}} R_{\mathrm{FOV}}, \tag{4.23}$$

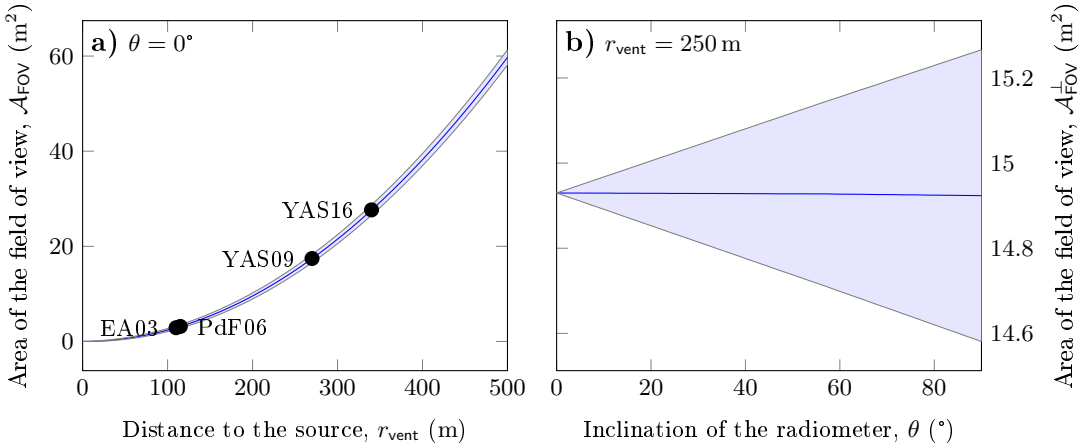

Figure 4.19 – Field of view of the Cyclops 300AF radiometers as a function of a) the distance of the source and b) the inclination of the radiometer. The angle of the field of view is $\alpha_{\text{FOV}} = 1°$ and has no error. We assume an absolute error on the distance r_{vent} of 20 m, giving a standard deviation of 6.67 m ($\mathrm{d}X = 3\sigma_X$). The error $\sigma_{\mathcal{A}_{\text{FOV}}}$ on the area is calculated using the variance formula and is shaded in blue. Note that the y-scales are different.

Table 4.2 – Field of view of the Cyclops 300AF radiometers as a function of the distance r_{vent} and the inclination θ. The angle of the field of view is $\alpha_{\text{FOV}} = 1°$ and has no error. We assume an absolute error on the distance r_{vent} of 20 m, giving a standard deviation of 6.67 m ($\mathrm{d}X = 3\sigma_X$). The area $\mathcal{A}^{\perp}_{\text{FOV}}$ of the field of view is calculated using equation 4.26 and the area $\mathcal{A}^{\theta=0}_{\text{FOV}}$ is calculated for $\theta = 0°$. The error on the area is calculated using the variance formula (Equation (3.15)).

	r_{vent} (± 6.67 m)	dz (± 3.33 m)	θ_{lower} (°)	$\mathcal{A}^{\theta=0}_{\text{FOV}}$ (m^2)	$\mathcal{A}^{\perp}_{\text{FOV}}$ (m^2)	$\mathcal{A}^{\perp}_{\text{FOV}}/\mathcal{A}^{\theta=0}_{\text{FOV}}$	$\lvert\mathcal{A}^{\perp}_{\text{FOV}} - \mathcal{A}^{\theta=0}_{\text{FOV}}\rvert / \mathcal{A}^{\perp}_{\text{FOV}}$ (%)
EA03	110	95	59.73 ± 0.16	2.90 ± 0.18	1.46 ± 0.18	0.50	98.38
PdF06	115	0	0.00 ± 0.30	3.16 ± 0.37	3.16 ± 0.37	1.00	0.00
YAS09	270	90	19.47 ± 0.02	17.44 ± 0.81	16.44 ± 0.81	0.94	6.07
YAS16	340	165	29.03 ± 0.02	27.66 ± 0.95	24.18 ± 0.95	0.87	14.37

where

$$R_{\text{FOV}} = r_{\text{vent}} \tan\left(\frac{\alpha_{\text{FOV}}}{2}\right) \tag{4.24}$$

and

$$\begin{aligned} R^{\perp}_{\text{FOV}} &= R_{\text{FOV}} \cos(\theta) \\ &= r_{\text{vent}} \tan\left(\frac{\alpha_{\text{FOV}}}{2}\right) \cos(\theta)\,. \end{aligned} \tag{4.25}$$

The vertical field of view area is then given by

$$\mathcal{A}^{\perp}_{\text{FOV}} = \pi r^2_{\text{vent}} \tan^2\left(\frac{\alpha_{\text{FOV}}}{2}\right) \cos(\theta)\,. \tag{4.26}$$

Note that the field of view area for a horizontal line of sight (i.e. $\theta = 0°$) is a disk of surface $\mathcal{A}^{\theta=0}_{\text{FOV}} = \pi R^2_{\text{FOV}}$. The vertical field of view areas $\mathcal{A}^{\perp}_{\text{FOV}}$ during the four campaigns range from 1.46 m^2 to 24.18 m^2 (Figure 4.19 and table 4.2) and the error on our estimates varies between 3.92 % and 12.14 %.

4.2.3 Estimation of thermal energy

The thermal radiant flux I_{thermal} (W.m^{-2}) of the ejecta is calculated from the brightness, temperature using the Stefan-Boltzmann law as

$$I_{\text{thermal}}(t) = \epsilon_{\text{thermal}}\sigma_{\text{thermal}}\left(T(t)^4 - T_{\text{Back}}^4\right), \tag{4.27}$$

where, $\epsilon_{\text{thermal}}$ is the emissivity of the surface of the ejecta ($\sim$0.95 for a basalt at 1000 °C, see tables 2.3 and 8.1 in Harris, 2013, for a review), σ_{thermal} the Stefan-Boltzmann constant ($5.67 \times 10^{-8}\,\text{W.m}^{-2}\text{.K}^{-4}$), T the brightness temperature (K) and T_{Back} the background temperature (K) taken at the onset of the explosion O. The total thermal energy $\text{E}_{\text{thermal}}$ (J) is then estimated by

$$\text{E}_{\text{thermal}} = \mathcal{A}_{\text{FOV}} \int_0^{\tau} I_{\text{thermal}}(t)\text{d}t, \tag{4.28}$$

where $\mathcal{A}_{\text{FOV}}$ is the area of the field of view of the radiometer (m^2) and τ the duration of the explosion (s). Thermal energy is then very dependant on the background temperature T_{Back} and the field of view area $\mathcal{A}_{\text{FOV}}$.

4.2.3a Error on thermal energy

The thermal energy is the sum of the thermal energy per unit of time

$$\text{E}_{\text{thermal}} = \sum_{i=1}^{N} \text{E}_{\text{thermal}}^i = \mathcal{A}_{\text{FOV}}\epsilon_{\text{thermal}}\sigma_{\text{thermal}}\left(T_i^4 - T_{\text{Back}}^4\right)dt. \tag{4.29}$$

The squared error on the thermal energy per unit of time is (variance formula)

$$\begin{aligned}\sigma^2_{\text{E}^i_{\text{thermal}}} = \left(T_i^4 - T_{\text{Back}}^4\right)\Big(&\left(\epsilon_{\text{thermal}}\sigma_{\text{thermal}}dt\right)^2\sigma^2_{\mathcal{A}_{\text{FOV}}} + \left(\mathcal{A}_{\text{FOV}}\sigma_{\text{thermal}}dt\right)^2\sigma^2_{\epsilon_{\text{thermal}}} + \left(\mathcal{A}_{\text{FOV}}\epsilon_{\text{thermal}}\sigma_{\text{thermal}}\right)^2\sigma^2_{dt}\Big) \cdots \\ &+ 9\left(\mathcal{A}_{\text{FOV}}\epsilon_{\text{thermal}}\sigma_{\text{thermal}}dt\right)^2\left(T_i^6 + T_{\text{Back}}^6\right)\sigma_T^2,\end{aligned} \tag{4.30}$$

when considering no error on the Stefan-Boltzmann constant σ_{thermal} and leads to an error on the total thermal energy of

$$\sigma_{\text{E}_{\text{thermal}}} = \sqrt{\sum_{i=1}^{N}\sigma^2_{\text{E}^i_{\text{thermal}}}}. \tag{4.31}$$

Example 4.2.1. This example illustrates the influence of the background temperature T_{Back}. The area of the field of view is $(2.39 \pm 0.32)\,\text{m}^2$ for a distance to the vent of 100 m. The maximum temperature at i is 995 K, and three background temperatures, 500 K, 520 K and 700 K, are used. All temperatures have an absolute error of 1 K. The sampling rate Δt is 0.01 s and we do not consider the error due to the efficient response time of the radiometer. The emissivity has no error providing that the calibration of the Zn−Se windows had been correctly made. The estimates of the total thermal energy is greatly influenced by the background temperature (Table 4.3).

4.2.4 Ejecta velocity

The estimation of the ejecta velocity is often done using thermal video. However it is harder to estimate ejecta velocity using a single temperature point such as for radiometers. Several methods are discussed in Chevalier and Donnadieu (2015).

Table 4.3 – Calculation of the thermal radiant flux depending on the background temperature.

T_{Back} (K)	E^i_{th} (J)	$\sigma_{E^i_{th}}$ (J)	$\sigma_{E^i_{th}}/E^i_{th}$ (%)
500	1120.30	149.40	13.34
520	1107.40	147.70	13.34
700	903.50	120.60	13.34

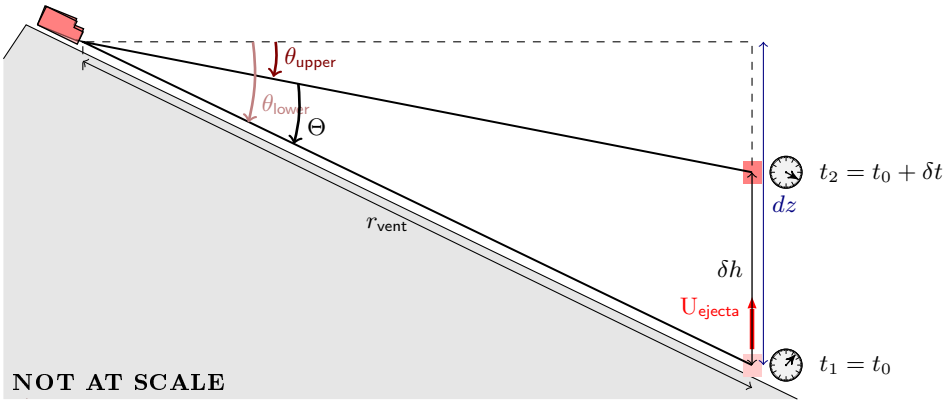

Figure 4.20 – Sketck for the estimation of ejecta velocity from simultaneous records from two radiometers.

Estimations using only 1 sensor should be easy, in theory:

1. the first ejecta enters the field of view
2. the first ejecta reaches the top of the field of view, but there is not enough ejecta to cover the whole field of view: first increase of the waveform to an inflexion point?
3. ejecta cover the whole field of view: second increase of the waveform to a maximum?
4. falling and cooling of the ejecta: decrease of the waveform, depends on the fall rate, the cooling rate and the potential re-injection or not of hot material.

However, the methods that are proposed are not adapted for chopped signals.

In our case, it is more apropriate to estimate the ejecta velocity by using the delay of an explosion recorded simultaneously on two radiometers measuring at different heights (Sahetapy-Engel et al., 2008). At the time t_{lower}, the first ejecta enter the field of view of the lower radiometer; then at the time t_{upper}, the ejecta enter the field of view of the upper radiometer (Figure 4.20). We can then estimate the velocity of the front of the volcanic cloud, assuming the ejecta are thrown verticaly from the vent, i.e. the conduit is not inclined below the vent and the wind is not significant.

The angle θ_{lower} between the horizontal line passing by the sensor location and the inclined line passing by the sensor location and the vent location is given by (Figure 4.20)

$$\theta_{\text{lower}} = \sin^{-1}\left(\frac{dz}{r_{\text{vent}}}\right), \tag{4.32}$$

where dz is the difference of elevation between the sensor and the vent.

The boxes, which protect the radiometers, are fixed with an angle $\Theta = 4°$ between the

Table 4.4 – Estimation of the angle θ_{lower} of the radiometers with the horizontal plan and estimation of the height δh at the distance of the vent. The errors are given by the variance formula. $\sigma_{r_{\text{vent}}} = 6.67\,\text{m}$, $\sigma_{dz} = 3.33\,\text{m}$ and $\sigma_\Theta = 0.08°$ ($\text{d}\Theta = 0.25°$). The maximum velocity $\text{U}_{\text{ejecta,max}}$ we can estimate is given by $\delta h/0.25$ (Low-pass filter at 4 Hz: 0.25 s).

	r_{vent} ($\pm 6.7\,\text{m}$)	dz ($\pm 3.3\,\text{m}$)	θ_{lower} (°)	θ_{upper} (°)	δh (m)	$\text{U}_{\text{ejecta,max}}$ (m/s)
EA03	110	95	59.7 ± 0.16	-	-	-
PdF06	115	0	0.0 ± 0.03	-4.0 ± 0.09	8.0 ± 0.5	32
YAS09	270	90	19.5 ± 0.02	15.5 ± 0.09	18.0 ± 0.7	72
YAS16	340	165	29.0 ± 0.02	25.0 ± 0.09	21.2 ± 0.8	85

vertical inclination of the two radiometers. The angle θ_{upper} is

$$\theta_{\text{upper}} = \theta_{\text{lower}} - \Theta. \tag{4.33}$$

The distance δh between the bottom of the field of view of each radiometer, for a distance r_{vent} from the vent is (Figure 4.20)

$$\delta h = r_{\text{vent}} \left(\sin\left(\theta_{\text{lower}}\right) - \sin\left(\theta_{\text{upper}}\right) \right). \tag{4.34}$$

The distance δh between the bottom field of view of each radiometer is independent from the measurements and ranges from 8 m to 21 m (Table 4.4).

The error on these parameters are given using the variance formula by

$$\sigma_{\theta_{\text{lower}}} = \sqrt{\left(\frac{1}{r_{\text{vent}}} \frac{1}{\sqrt{1 - \frac{dz}{r_{\text{vent}}}}} \right)^2 \sigma_{dz}^2 + \left(\frac{-dz}{r_{\text{vent}}^2} \frac{1}{\sqrt{1 - \frac{dz}{r_{\text{vent}}}}} \right)^2 \sigma_{r_{\text{vent}}}^2}, \tag{4.35}$$

$$\sigma_{\theta_{\text{upper}}} = \sqrt{\sigma_{\theta_{\text{lower}}}^2 + \sigma_\Theta^2}, \tag{4.36}$$

$$\sigma_{\delta h} = \sqrt{\frac{\delta h}{r_{\text{vent}}^2} \sigma_{r_{\text{vent}}}^2 + r_{\text{vent}}^2 \left(\cos^2\left(\theta_{\text{lower}}\right) \sigma_{\theta_{\text{lower}}}^2 + \cos^2\left(\theta_{\text{upper}}\right) \sigma_{\theta_{\text{upper}}}^2 \right)}, \tag{4.37}$$

for θ_{lower}, θ_{upper} and δh, respectively. We estimate the error on the distance and on the difference of elevation are $\sigma_{r_{\text{vent}}} = 6.67\,\text{m}$ and $\sigma_{dz} = 6.67\,\text{m}$, respectively ($\text{d}r_{\text{vent}} = 20\,\text{m}$ and $\text{d}dz = 20\,\text{m}$).

The ejecta velocity is estimated by

$$\text{U}_{\text{ejecta}} = \frac{\delta h}{\delta t}, \tag{4.38}$$

where $\delta t = t_{\text{upper}} - t_{\text{lower}}$ is the delay observed between the records on both radiometers. The estimates of the velocity is an averaged velocity on the distance δh.

The error of the ejecta velocity is estimated using the variance formula by

$$\sigma_{\text{U}_{\text{ejecta}}} = \sqrt{\left(\frac{1}{\delta t} \right)^2 \sigma_{\delta h}^2 + \left(-\frac{\delta h}{\delta t^2} \right)^2 \sigma_{\delta t}^2}, \tag{4.39}$$

where $\sigma_{\delta t} = \sigma_{t_{\text{th}}} \sqrt{2} = 0.12\,\text{s}$ ($\text{d}t_{\text{th}} = \text{respTime} = 0.25\,\text{s}$). The uncertainties on the ejecta velocity are mostly due to the long response time of the radiometer (Figure 4.21). This

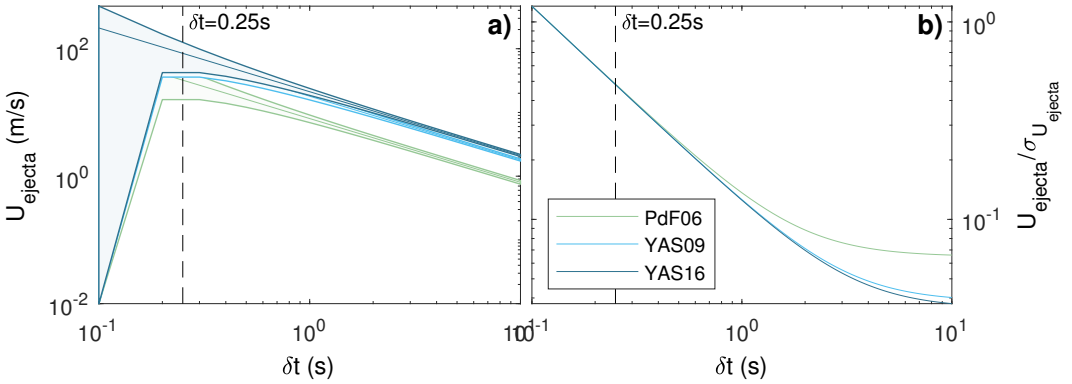

Figure 4.21 – Estimation of the error on the ejecta velocity at Piton de la Fournaise, Yasur-2009 and Yasur-2016. a) Velocity as a function of the delay between both radiometers. b) Relative error as a function of the delay between both radiometers.

response time gives the highest velocity that can be measured by the flying time between both radiometers (Table 4.4).

$$\mathrm{U}_{\mathsf{ejecta,max}} = \delta h / \mathsf{respTime}. \tag{4.40}$$

The ejecta velocity can be calculated by the programme `pgth_calcVelocity`. The user can choose to calculate the delay of an explosion from the two records by i) looking for the beginning O of the event, ii) looking for the first maximum M_1 of the event or iii) by cross-correlation between both signals.

Looking for the delay between the beginnings is the most accurate method because the beginning of the event on thermal waveforms indicates when the first ejecta enter the field of view of the radiometer. This delay gives then the velocity of the front of the volcanic cloud entering the lower radiometer and the the upper radiometer. Looking for the first maximum is a good alternative when we have difficulties to determine the beginning of the event on the thermal waveform. However the estimation of the initial velocity of the ejecta might be underestimated because of the deceleration of the ejecta. The cross-correlation gives a mean delay between the record of the same explosion seen by the two radiometers. This delay is very sensitive to the thermal waveforms and can be wrong because all the ejecta seen by the lower radiometer can not reach the upper radiometer and because all the fragments do not cool down at the same speed. The error is bigger when the height between both radiometers is greater (i.e. the distance to the vent is larger in our case)

Our estimates of the velocity from the simultaneous records of explosions by the radiometers is the velocity seen by the radiometers just above the vent. The top of the magma column, where the gas pocket explodes, can be lower than the surface of the vent, i.e. lower than bottom of the field of view of the lower radiometer (Figure 1.3). In that case we do not have access to the initial velocity of the ejecta.

4.3 Image processing

Analysis of a series of images is very useful to study the dynamics of the volcanic cloud, especially to estimate the upward velocity of the ejecta (front of the plume or particle per particle).

I use the Particle Imagery Velocimetry (PIV) method, on videos recorded at Yasur in 2009, to get estimates of the upward velocity of the volcanic clouds providing that the scale of the video is known.

The videos taken during the 2009 field campaign at Yasur were recorded by a Sony camera (DSR-PD170P) with a resolution of 640 px × 480 px and 25 frames per second (fps). The videos were synchronised with the GPS by filming the time on the GPS display.

4.3.1 Particle Imagery Velocimetry

The PIV methods consists in the comparison between two successive binary (i.e. black and white) images, using spatial cross-correlation, to get the displacement of an object.

The cross-correlation is done on sub-images as we want to retrieve a field of velocities rather than an averaged velocity over the whole image. The size of the sub-images is crucial as an object can be tracked only if it remains in the same sub-image. To measure velocities up to 100 m.s^{-1}, we should be able measure a displacement of 100 m, i.e. 330 px at a distance of 270 m (Yasur 2009). Moreover the size of the pixel on the video determines the size of the smallest objectscal that can be seen by the method. At Yasur, in June 2009, the size of the smallest object, here ejecta, is 30 cm.

I use *DaVis-7.2* software (Lavision softwares) to process a multi-pass PIV. First, the analysis is done with two passes on sub-images of 128 px to 128 px and an overlap of 50 % (∼39 m × 36 m at 270 m), and then with two passes on sub-images of 64 px to 64 px and an overlap of 50 % (∼19.50 m × 18.00 m at 270 m). This constraints the maximum velocity to 38 m.s^{-1}. The results is given as matrices of vertical and horizontal displacements. I save the results as ASCII files to analyse them with MatLab.

The analysis was done only for video-07 of the 2009-field campaign at Yasur. No zoom was used during that video, then the scale of the pixel is perfectly well known. I retreive the maximum upward velocity (Figure 4.22d and 4.23), in the sub-images that can accounts for the field of view of both radiometers, from each ASCII files to build the upward velocity of the ejecta around the field of view of the two radiometers (Figure 4.24).

The figures 4.22 and 4.23 shows the details of the PIV analysis of an explosion at Yasur in 2009. The temporal evolution on the images is represented from left to right with 1 extracted frame each 10 frames, hence giving a delay between images of 0.40 s. The maximum velocity in the field of view of the radiometers is displayed in figure 4.22d and 4.23d. The maximum velocity of ejecta, deduced from the PIV in the field of view of the radiometers, is 13.30 m.s^{-1}. This value is slightly under-estimated compared to the ejecta velocity deduced from the flying time between the two radiometers at (16.4 ± 1.9) m.s^{-1}. This can be explained because the video can also records ejecta going downward which minimises the maximum velocity in the window. In the other hand, the radiometer is not sensible to the motion but records the temperature of the objects in its field of view whose the surface temperature srtongly depends on their size. Furthermore, the choice of the size of the sub-images is such that the width of the sub-images is larger than the diameter of the field of view of the radiometers (Sub-image (64 px × 64 px): 19.50 m; $d_{\mathsf{FOV}} = 4.71$ m). We can not choose smaller sub-images, because it would limit the maximum velocity at 19 m.s^{-1}.

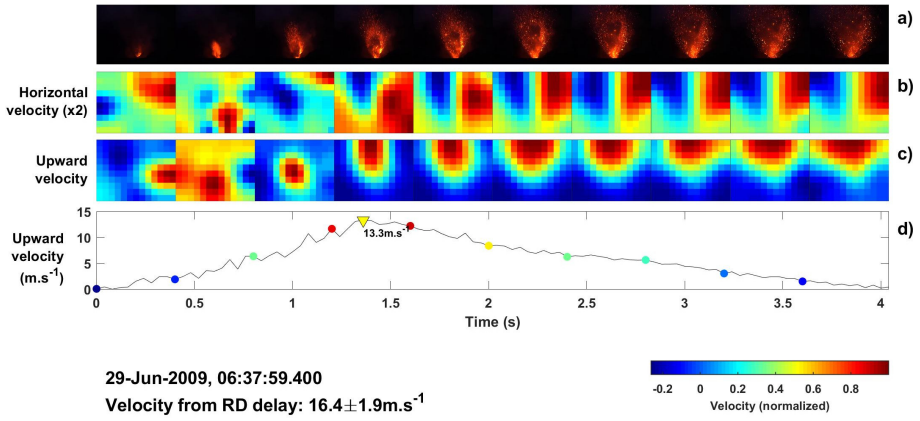

Figure 4.22 – Calculation of ejecta velocity using PIV method. a) One image each 10 frames recorded on video 6 at Yasur, in June 2009 (1 image every 0.40 s). Maps of the b) horizontal and c) upward velocities. Horizontal velocities are positive from left to right. d) Maximum of the upward velocity in the field of view of the radiometers (Figure 4.24). The accurate times of the images is marked on d) as dots whose color corresponds to the velocity.

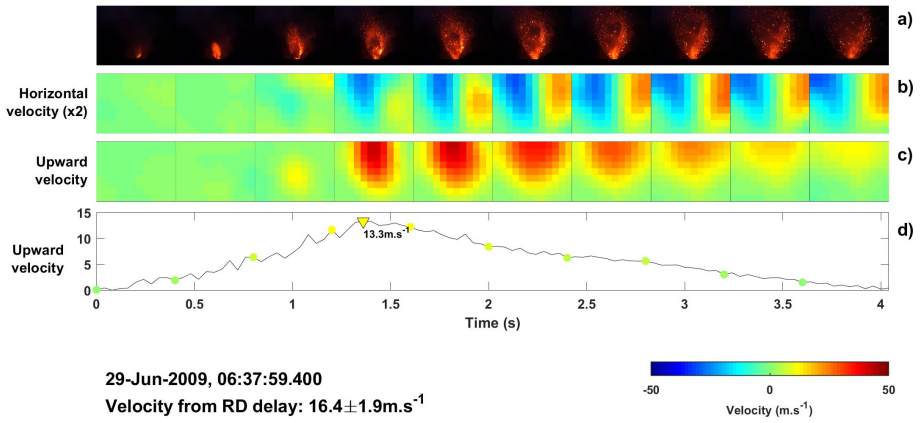

Figure 4.23 – Calculation of ejecta velocity using PIV method. a) One image each 10 frames recorded on video 6 at Yasur, in June 2009 (1 image every 0.40 s). Maps of the b) horizontal and c) upward velocities. Horizontal velocities are positive from left to right. d) Maximum of the upward velocity in the field of view of the radiometers (Figure 4.24). The accurate times of the images is marked on d) as dots whose color corresponds to the velocity.

4.3.2 Gas volume fraction from the analysis of video frames

An RGB-image is recorded as a 3D-matrix whose 1st and 2nd dimension give the location of a pixel and 3rd dimension gives a trio of values between 0 and 255 (between 0 and 1 when using the rgb-scale) that decomposes the colour of the pixel in red, green and blue (Figure 4.27).

We can decompose each frame of the video (Figure 4.27a) in reds, greens and blues (Figure 4.27b).

This decomposition allows us to convert each frame gray scales. Three gray scale exist:

1. the average scale (Figure 4.27c1):
   $\mathrm{GRAY}_{\mathrm{ave}} = (\mathrm{RED} + \mathrm{GREEN} + \mathrm{BLUE})/3$;
2. the lightness scale (Figure 4.27c2):
   $\mathrm{GRAY}_{\mathrm{lig}} = (\min(\mathrm{RED}, \mathrm{GREEN}, \mathrm{BLUE}) + \max(\mathrm{RED}, \mathrm{GREEN}, \mathrm{BLUE}))/2$, it is an average

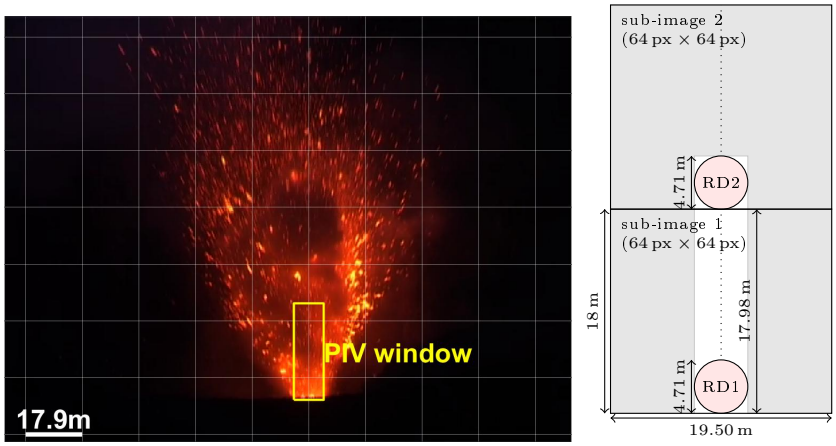

(a) (b) Sketch

Figure 4.24 – Approximation of the combined fields of view of the radiometers at Yasur, in June 2009.

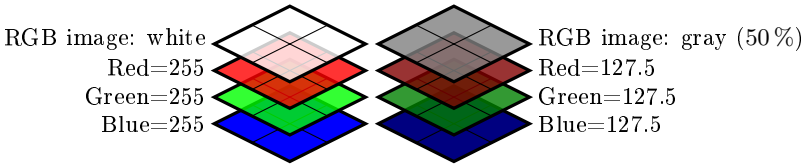

Figure 4.25 – Sketch of the RGB decomposition of the colours.

of the most and less prominent colours;

3. the luminosity scale (Figure 4.27c3):
   $\mathsf{GRAY}_{\mathsf{lum}} = 0.21\mathsf{RED} + 0.72\mathsf{GREEN} + 0.07\mathsf{BLUE}$, it is a weighted average for human perception.

The gray scales allow us to correct the red scale such as the pixels that really appear red on the RGB-image keep a high red-index `Idx` (Figure 4.27d):

$$\mathtt{Idx}_{\mathsf{red-gray}} = \frac{\mathsf{RED} - \mathsf{GRAY} + 255}{255 \times 2} \tag{4.41}$$

These red-indexes highlight two surfaces depending on which gray scale the red scale is corrected from (Figure 4.27d). The surface in yellows is cooler because hot ejecta are less numerous. It highlights the contour of the volcanic cloud. The surface in reds is richer in ejecta. We can count the pixels of each surface by defining two thresholds. The lowest threshold, $N_{\mathsf{thr,low}}$ must be chosen to count the number of pixels of the surface $\mathcal{S}_{\mathsf{total}}$ of the volcanic cloud. The highest threshold, $N_{\mathsf{thr,high}}$ must be chosen to get the high density hot surface $\mathcal{S}_{\mathsf{ejecta}}$ of the ejecta.

We assume that the total volume and the ejecta volume are proportional to the total surface and ejecta surface to the power 3/2 based on dimension analysis, respectively (Figure 4.26), the exact coefficient in front of this relationships being found from the shape of the volume. However, knowing this coefficient is unnecessary when calculating the gas volume fraction. It can be expressed as

$$\alpha_{\mathsf{gas}} = 1 - \frac{\mathrm{Vol}_{\mathsf{ejecta}}}{\mathrm{Vol}_{\mathsf{total}}} = 1 - \left(\frac{\mathcal{S}_{\mathsf{ejecta}}}{\mathcal{S}_{\mathsf{total}}}\right)^{3/2} = 1 - \left(\frac{N_{\mathsf{thr,high}}}{N_{\mathsf{thr,low}}}\right)^{3/2}. \tag{4.42}$$

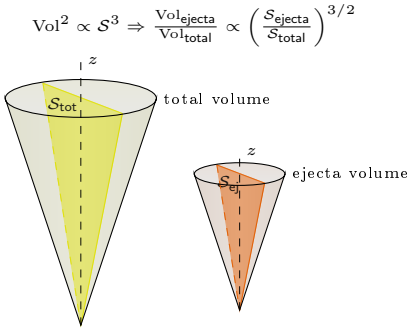

Figure 4.26 – Sketch of the estimation of the total and ejecta volume of the volcanic cloud. We have approximated the surfaces as triangles.

A preliminary test can be done on red, green, blue and gray scales (Figure 4.28). We assume that the threshold $N_{\mathsf{thr,low}} = 0.25$ gives the total surface $\mathcal{S}_{\mathsf{total}}$ (Figure 4.28b), and that the threshold $N_{\mathsf{thr,high}} = 0.50$ gives the surface of the ejecta $\mathcal{S}_{\mathsf{ejecta}}$ (Figure 4.28a).

Total surfaces between $2 \times 10^3\,\mathrm{m}^2$ and $5.70 \times 10^3\,\mathrm{m}^2$ are found using the red scale RED on the video of an explosion at Yasur on June, 29th 2016 (06:37:59), while the total surface on green, blue and gray scales does not exceed $3\,\mathrm{m}^2$. The ejecta surface on the red scale is up to $2 \times 10^3\,\mathrm{m}^2$. The gas volume fraction varies from 0.81 to 0.99 at the time of the maximum total surface (2.28 s).

We observe that the gas volume fraction varies with time during the explosion (Figure 4.29b and Figure 4.30). It decreases to low gas volume fractions, when looking at the red scale, before increasing again to high values of gas volume fraction (Figure 4.29b). We suspect that this short decrease (∼0.30 s) is due to the sudden decompression of the gas bubble that expelled hotter ejecta at the beginning that at the end of the explosion.

The red-indexes (corrected red scales) visually give well marked limits for both surfaces (Figure 4.27). We choose visually the thresholds at 0.60 and 0.75 for the total surface and ejecta surface, respectively.

Our best estimates are given when we correct the red scale by the luminosity scale (best view of the envelope in figure 4.27d3) which gives a mean and median values at 0.96 and 0.97, respectively (Figure 4.30 and table 4.5). However the thresholds used to find the envelopes can be adjusted to get better estimations.

We clearly see on figure figure 4.27a) and d3) that the hotter pixels, i.e. the yellow pixels are not counted as ejecta. This bias is induced by our choice to use the red scale as a reference. A more accurate estimation of the gas volume fraction could be done using a combination of the red and green scales to obtain the reds and yellow pixel.

We propose another method to estimate the gas volume fraction, based on the gas flux and the volume of the cone of ejecta (Section 4.5.3).

4.4 Seismic processing

Several volcanic processes can be responsible for the seismic events. The magma ascension through rocks from depth causes fracturing and vibrations which propagate to the sensors.

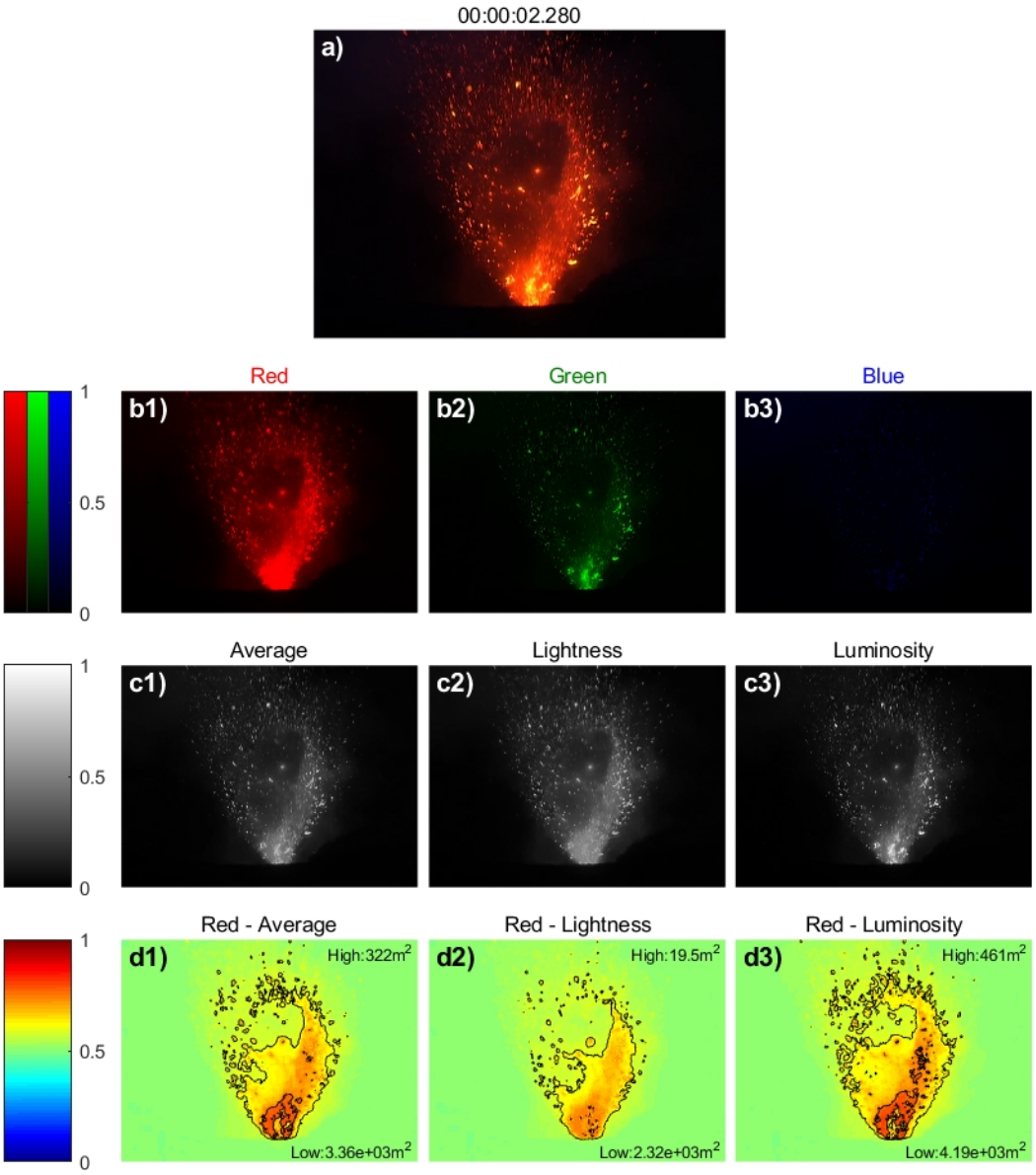

Figure 4.27 – Analysis of a video frame to get the number of pixel with hot liquids or solids. a) Video frame (29-June-2009, 06:37:59.4) in RGB scale. b) Decomposition of the RGB-frame in 1) red , 2) green and 3) blue. c) Conversion in gray scale: 1) average, 2) lightness and 3) Luminosity. d) Red component corrected from the gray scale.

The formation and rise of large bubble of gas (Taylor bubble) also generate seismic waves (Very Long Period: VLP, Nabyl et al., 1997; Aster, 2003). The explosion of a gas pocket at the surface of the magma column may generate the magma motion around and under the gas pocket and produce seismic waves which can propagate in the surrounding rocks to the sensors. The emplacement of lava flows may also generates seismic waves (Hibert et al., 2015).

These processes can generate compressive waves (P-waves), shear-waves (S-waves) and surface waves (Love and Rayleigh) depending on their mechanism and depth. These different types of waves have different properties such as their velocities and propagation plane. For example, P-waves are faster than S-waves with velocities around $2.50\,\mathrm{km.s^{-1}}$ and $1.40\,\mathrm{km.s^{-1}}$ in magmatic rocks, respectively (ratio of 1.8 Scarpa et al., 2002).

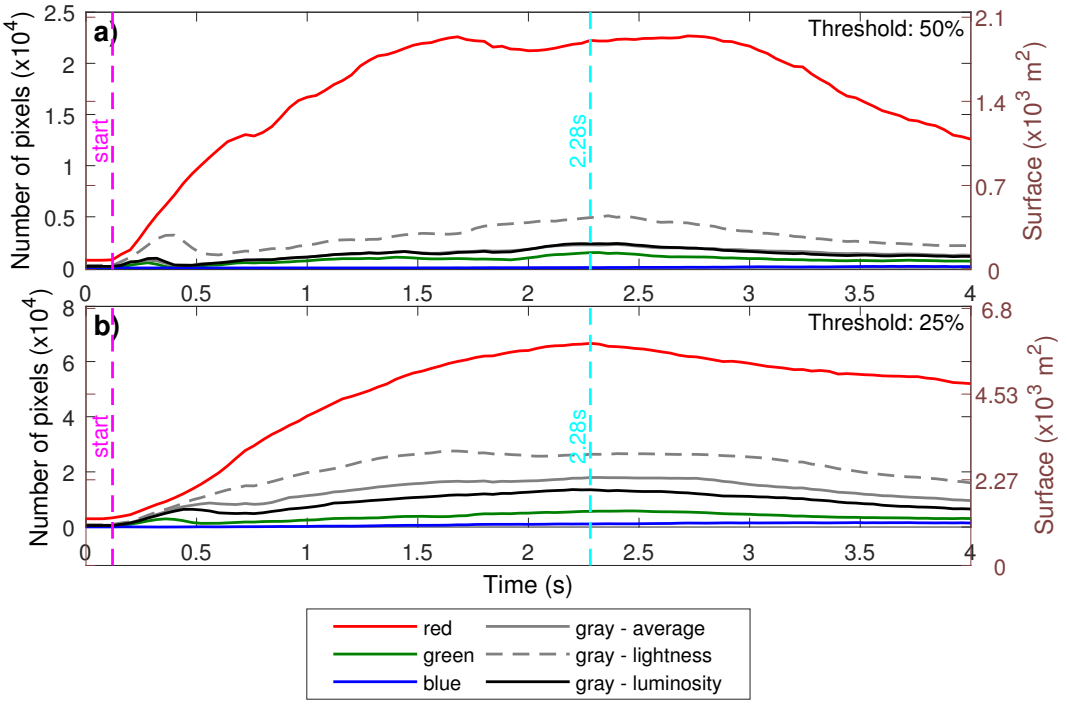

Figure 4.28 – Count of the number of pixel having its red, green, blue or gray component higher than a) 0.5 and b) 0.25. The equivalent surface is given for a distance of 270 m

The analysis of seismic records is complex because of the different types of waves (P, S, surface) and the different processes.

Seismic sensors measure ground motions either in term of displacement, velocity or acceleration. We need to measure the motion in 3 directions to obtain the full motion of the ground and a record of the process or event. Three directions are often chosen as North-South (N), East-West (E) and vertical (Z). They are also often transformed into radial and tangential directions when the location of the seismic source is known or assumed to be below the conduit.

Seismic records can be analysed component per component or all components simultaneously.

Table 4.5 – Results of the estimations of the gas volume fraction of a Strombolian explosion, based on the count of pixels (29/06/2009 06:37:59.4).

Scale	Min	q_1	Mean	Median	STD	q_3	Max	at 2.28 s
Red	0.433	0.747	0.763	0.784	0.101	0.812	0.883	0.807
Green	0.840	0.870	0.894	0.896	0.0318	0.910	0.997	0.865
Blue	0.969	0.984	0.992	0.995	0.0100	1.000	1.00	0.993
Average	0.761	0.957	0.958	0.963	0.0299	0.969	0.993	0.956
Lightness	0.593	0.926	0.921	0.951	0.0797	0.956	0.968	0.920
Luminosity	0.758	0.933	0.936	0.941	0.0315	0.950	0.992	0.927
Red - Average	0.693	0.969	0.966	0.981	0.0543	0.988	0.995	0.970
Red - Lightness	1.00	1.00	1.00	1.00	0	1.00	1.00	1.00
Red - Luminosity	0.639	0.963	0.955	0.970	0.0611	0.980	0.992	0.964

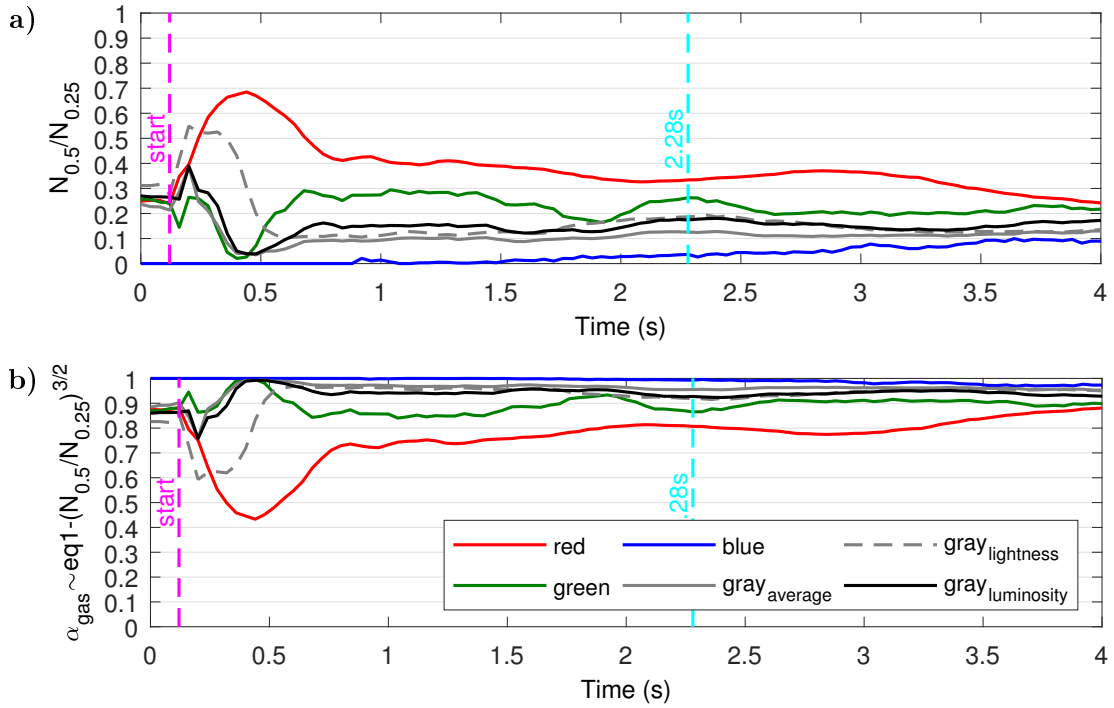

Figure 4.29 – Estimation of the gas volume fraction as a function of time for red, green, blue and gray scales of the video frames. a) Proportion of the number of pixels having a scaled value above 0.25 and 0.50. b) Gas volume fraction deduced from the proportion of the number of pixel.

4.4.1 Very Long Period events and correction of the signal

Strombolian explosions generate high frequency seismic waves (>1 Hz) as well as frequency below 1 Hz (Nabyl et al., 1997; Aster, 2003). They also discuss the generation of the VLP (0.50 Hz) such as the coalescence of the gas and the vibration of the gas pocket. VLP signals are produced quasi-simultaneously with explosion quakes, suggesting that they are intimately related to explosions. As explained before, the recorded signal is filtered below 1 Hz by the process of acquisition of the data (Section 3.2). A correction on both signals from seismic stations is needed to enlarge the frequency response of the seismic measurements.

The signal of YASH station is corrected using the corresponding transfer functions in the frequency band 0.10 Hz–1 Hz (Transfer function for YASH station, VMGD Figure 4.31). We choose to not correct below 0.10 Hz to keep a good signal to noise ratio and to avoid bias induced by the sudden phase shift at 0.10 Hz (Figure 4.31b).

The intrumental correction is not done yet for the seismic records from Melkem station. It should be done soon as proposed below.

The quanterra Q330 digitizer of the Melkem station was not correctly configured. This lead to the record of the ground velocity as a short period whereas the seismometer, a Trillium 40s, is broadband. Fortunately another seismic station, operated by Jean Battaglia and Jean-Philippe Métaxian, was collocated to our station for at least one whole day on the 7th of February 2009 (Y32, e.g. Battaglia and Brenguier, 2016).

This station is composed of a Guralp CMG-40T broadband seismometer and a Kephren digitizer (Agecodagis SARL). Both seismometers are close (<10 m) compared to the wavelength

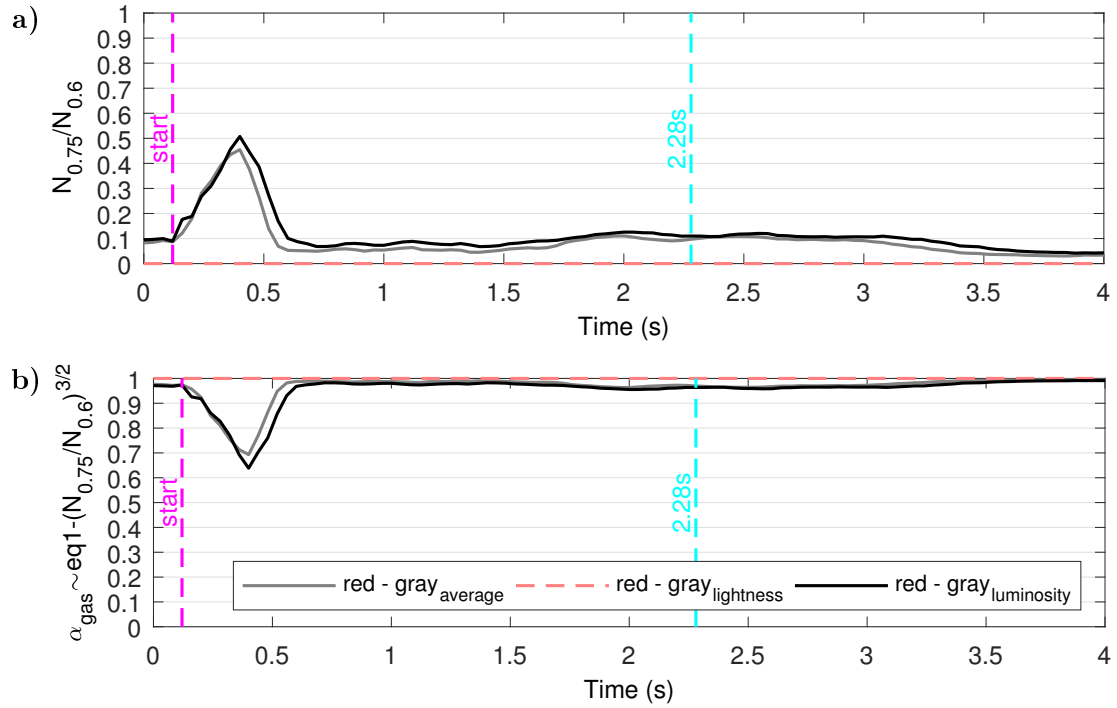

Figure 4.30 – Estimation of the gas volume fraction as a function of time for the red scale corrected from the gray scales of the video frames. a) Proportion of the number of pixels having a scaled value above 0.6 and 0.75. b) Gas volume fraction deduced from the proportion of the number of pixel.

of the seismic waves (∼250 m at 0.10 Hz and ∼7500 m at 3 Hz). The signal s_{Y32} from Y32 is corrected from the instrumental response of the seismometer (Figure 4.32).

The recorded signal s_{M} from our Melkem station is filtered by the chain of acquisition (Trillium 40 + Q330 badly configured, section 3.2). The convolution of the signal $s = s_{\mathsf{Y32}}$ with the filter from the chain of acquisition, in the time domain, gives the signal s_{M}. In the spectral domain, this is equivalent to

$$S_{\mathsf{M}} = S_{\mathsf{Y32}} \times \mathrm{TF}, \tag{4.43}$$

where S_{M} and S_{Y32} are the Fourier transform (`fft`) of s_{M} and s_{Y32}, respectively.

In theory, we can correct the short period signal s_{M} using the transfer function TF directly designed by

$$\mathrm{TF} = \frac{S_{\mathsf{M}}}{S_{\mathsf{Y32}}}. \tag{4.44}$$

However, we need to smooth the spectra S_{M} and S_{Y32} to get a consistent transfer function (figure 4.34).

The spectra S^s_{M} and S^s_{Y32} are smoothed spectra of S_{M} and S_{Y32}, respectively, such as (figure 4.35)

$$S^s_{\mathsf{n}} = \mathtt{smooth}\left(|S_{\mathsf{n}}|\right) \times \exp\left(i \times \mathtt{smooth}(\varphi_{\mathsf{n}})\right), \tag{4.45}$$

where $n = \{\mathsf{M}, \mathsf{Y32}\}$, $|S_{\mathsf{n}}|$ is the amplitude of S_{n} and φ_{n} the phase. The phase does not vary for frequencies above 0.10 Hz (figure 4.35a1 and b1). This can be a bias due to the

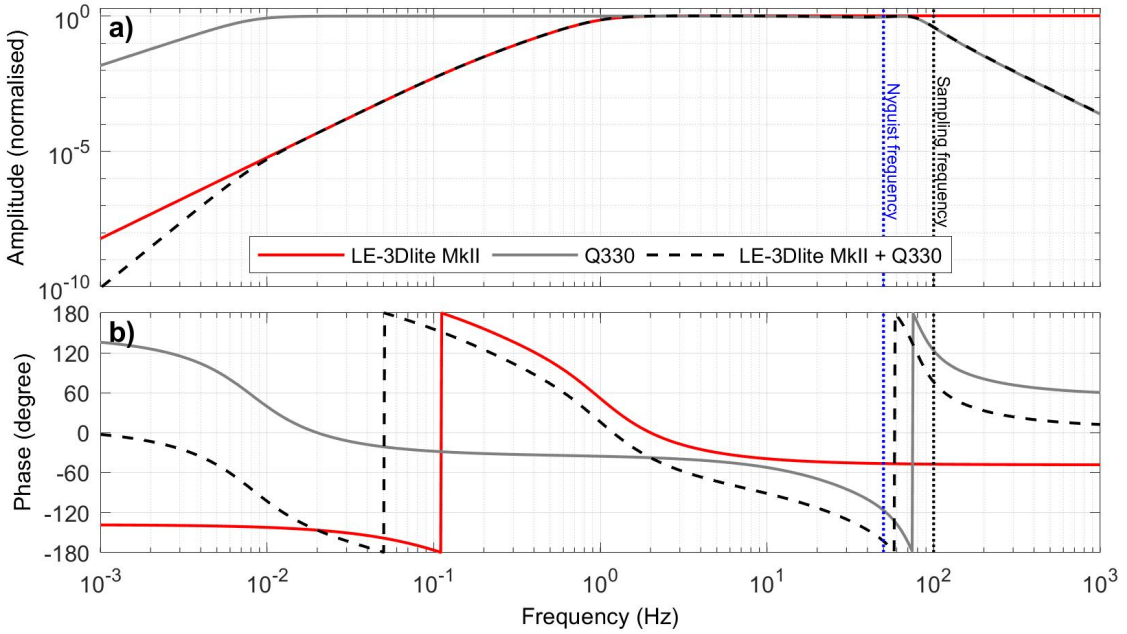

Figure 4.31 – Combined transfer functions of the quanterra digitizer and LE-3Dlite MkII seismometer which are used by the Vanuatu Meteorology and Geohazards Departement to record the ground velocity at YASH station. a) Normalised amplitude and b) phase.

smoothing of the spectra. Another way to smooth the spectra is to calculate a spectrum each 100 s of the signal and to stack all spectra. However the phase of the signal is not clearer (Figure 4.36). We then need to better constrain the phase of the signal.

The transfer function is then calculated by (figure 4.37)

$$\mathrm{TF} = \frac{S^s_{\mathrm{M}}}{S^s_{\mathrm{Y32}}}, \tag{4.46}$$

assuming that the phase of each signal is correct and saved the same way the transfer functions obtained from poles and zeros.

The amplitude of the function transfer, is obtained from the simultaneous records at two close stations. This is highly consistent to the transfer function from the poles and zeros, kindly given by Nanometric, of the Trillium 40T as a short-period (Correspondence with Peter Devanney, table 4.6). However we see an un-consistency between the phases of the two transfer functions. Note also that the transfer function given by the poles and zeros (table 4.6) gives only the correction for the low frequencies (figures 4.37 and 4.38). We are curently exchanging with seismologists in order to validate our method of calculation of the transfer function and to resolve the issue we have with the phase of the signals.

The earthquakes that can potentially be recorded by seismometers are collected from the USGS database (Table A.4). The records are manually corrected from these earthquakes if needed.

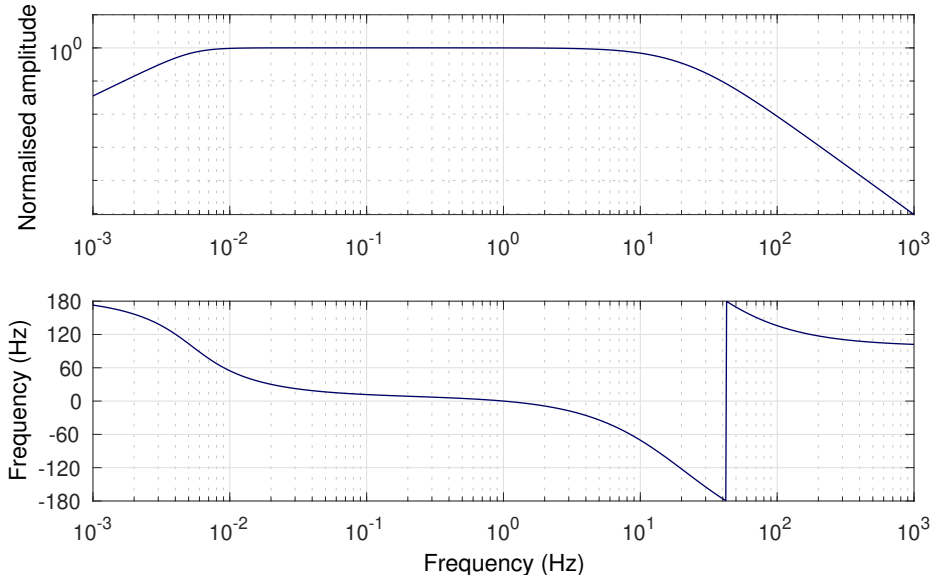

Figure 4.32 – Instrumental response of the Guralp CMG-40T seismometer.

4.4.2 Characteristic points on seismic waveforms

4.4.2a Definition of the seismic characteristic points

The characteristic points on seismic waveforms (of explosions) are shown on figure 4.39 and defined as follows:

O the beginning of the event,
$u_{\max}$ the maximum amplitude of the event gives the strength/intensity of each event,
$u_{\min}$ the minimum amplitude that directly follows the maximum amplitude,
E the end of the event.

These characteristic points can be define for volcanic explosion quakes (VEQ), long period events (LP) and very long period events (VLP).

The only characteristic duration we define is the the whole duration O–E of the event on the seismic records.

4.4.2b Determination of the limits O and E

The limits of an event are found in a part `xpart` of the signal. The part of the signal begins `dtBefore` before the maximum and ends `dtAfter` the maximum.

Either the envelope of the signal `[ENV]` or the squared smoothed-envelope of the displacement `[ENVds2]` is used to determine the limits of a seismic event (Equations (4.47) and (4.48)). The former is well adapted for VLP and LP events which have lower frequencies than the VEQ.

The limits on VEQ are the hardest to find due to the high frequency contents of the signals (Figure 4.40a-b). The displacement presents less oscillations than the ground velocity but

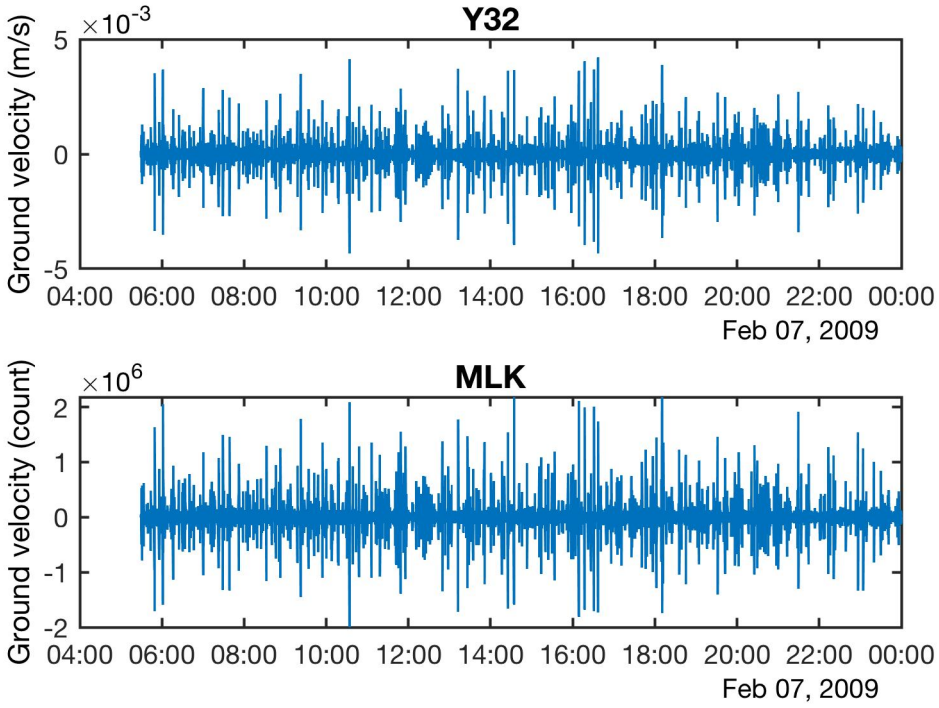

Figure 4.33 – Vertical component of seismic records at Yasur, from Mount Melkem. a) Signal of reference from Y32 station (Guralp CMG-40T + Kephren, Battaglia and Brenguier (2016)). b) Signal from our seismic station with a short-period set-up on the digitizer (Trillium 40T + Q330) that is to correct.

is still too oscillating to use directly the envelope of the displacement (Figure 4.40c). The envelope is smoothed with a sliding window of length `envSmooth_lg` to enhance the envelope (removing high frequencies). The length of the window for the smoothing function is proportional to the frequency of the events `EventFrequency`. The smoothed envelope is squared to dilate the amplitude and have a better resolution (Figure 4.40d).

$$\texttt{[ENV]} : \mathrm{Env}(u) \quad \text{signal envelope of the ground velocity.} \tag{4.47}$$

$$\begin{aligned} \texttt{[ENVd]} &: \mathrm{Env}(d) && \text{signal envelope of the displacement,} \\ \texttt{[ENVds]} &: \texttt{smooth}(\mathrm{Env}(d), \texttt{envSmooth_lg}) && \text{removed from high frequency,} \\ \texttt{[ENVds2]} &: \texttt{smooth}(\mathrm{Env}(d), \texttt{envSmooth_lg})^2 && \text{and dilated} \end{aligned} \tag{4.48}$$

Remark 4. We could also have chosen a root-mean-square threshold instead of dilating the envelope.

4.4.3 Estimation of seismic energy

The seismic energy can be calculated depending on the type of wave with the two following methods:

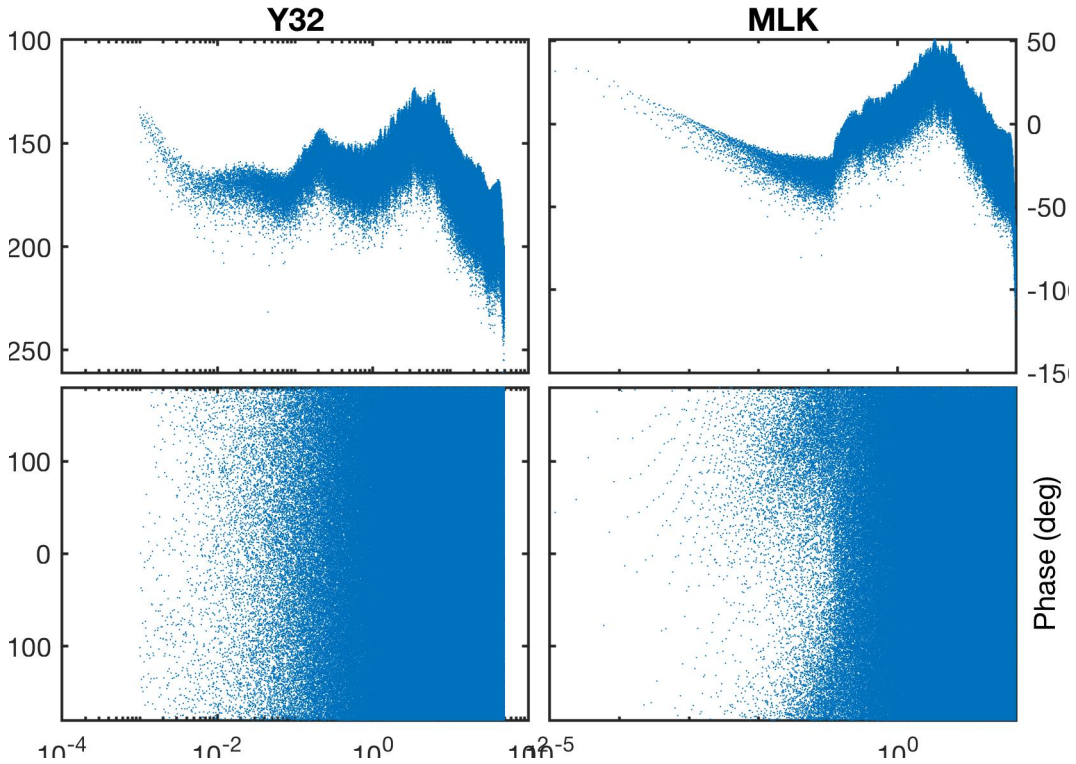

Figure 4.34 – Fourier transform (`fft`) of the signal from both seismic stations on November, 7th 2009 (Figure 4.33). a) Y32 station and b) Melkem station (MLK).

1. the seismic energy from the signal energy considers body waves (Johnson and Aster, 2005),
2. the seismic energy from signal envelope considers surface waves (Hibert et al., 2015).

The key assumption is that on the type of seismic waves (P, S, surface).

4.4.3a Seismic energy from signal energy

That first method makes an estimates of the seismic energy using the signal energy (section 3.1.2). This seismic energy from signal energy is based on the hypotheses that 1) the ground velocity is the response to the seismic kinetic energy at a location of the volcano, 2) the induced ground velocity is due to pure body waves, 3) the propagation of seismic waves is radial and isotropic and 4) we can neglect attenuation (Johnson and Aster, 2005).

The potential energy is equal to kinetic energy because of energy conservation giving the seismic energy $\mathrm{E}_{\mathsf{seismic}}$ as a function of the ground velocity $u(t)$:

$$\mathrm{E}_{\mathsf{seismic}} = 2\pi r_{\mathsf{vent}} \rho_{\mathsf{rock}} c_{\mathsf{rock}} \int_0^{\tau} \mathsf{S}^2_{\mathsf{seismic}} u^2(t) \mathrm{d}t, \tag{4.49}$$

where $\rho_{\mathsf{rock}} = 2000\,\mathrm{kg.m^{-3}}$ and $c_{\mathsf{rock}} = 2500\,\mathrm{m.s^{-1}}$ are the rock density and seismic P-wave velocity into the rock and $\mathsf{S}_{\mathsf{seismic}}$ accounts for the site effects. The duration τ is can either be the duration of a seismic event or the duration of a sliding window.

Uncertainties mostly come from the site effects $\mathsf{S}_{\mathsf{seismic}}$ and the choice of a fixed velocity for P-wave propagation. Site effects are very important close to volcanoes because of important

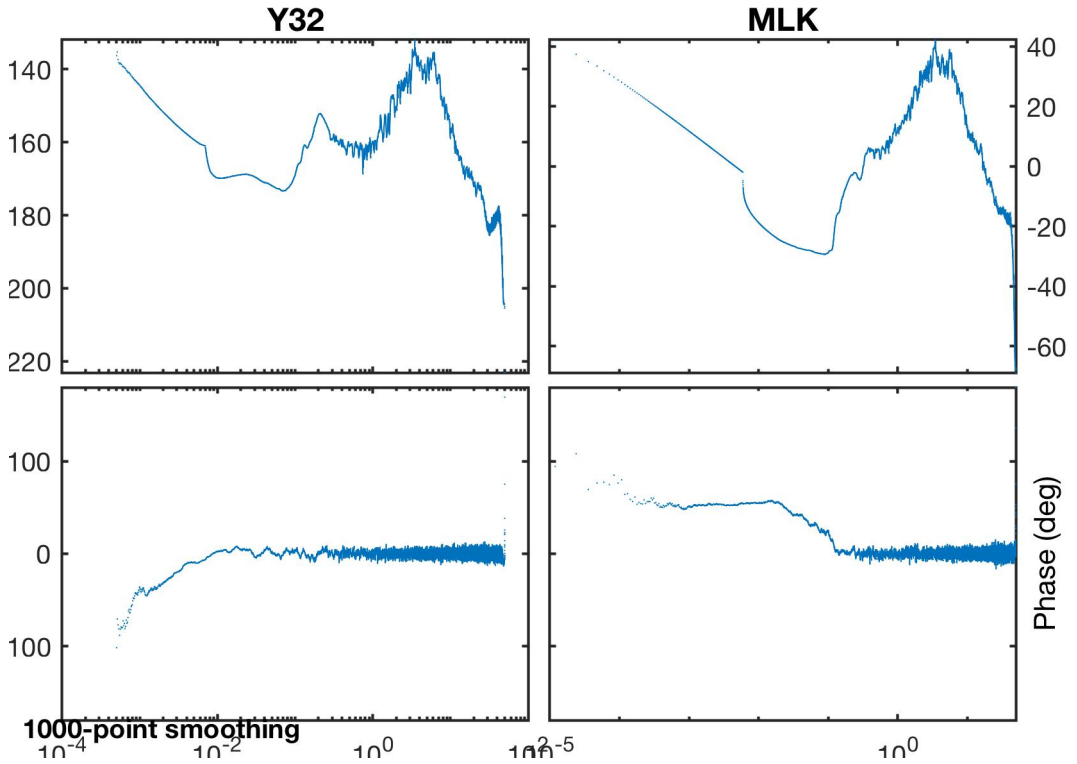

Figure 4.35 – Smoothed Fourier transform (5000-point smoothing) of the signal from both station on November, 7th 2009. a) Y32 station and b) Melkem station (MLK).

impedance contrasts between the magma and the deep layers. Moreover seismic energy is overestimated if the surface waves are significant. We consider that the attenuation can be negligible at near field (<2 km). In the other case, we need to correct the seismic energy from the attenuation $\mathsf{A}_{\mathsf{seismic}}$ such as

$$\mathrm{E}_{\mathsf{seismic}} = \frac{2\pi r_{\mathsf{vent}} \rho_{\mathsf{rock}} c_{\mathsf{rock}}}{\mathsf{A}_{\mathsf{seismic}}} \int_0^{\tau} \mathsf{S}^2_{\mathsf{seismic}} u^2(t) \mathrm{d}t, \quad \mathsf{A}_{\mathsf{seismic}}(r_{\mathsf{vent}}) = \exp\left(-\frac{\pi f_{\mathsf{event}} r_{\mathsf{vent}}}{c_{\mathsf{rock}} \mathsf{Q}_{\mathsf{seismic}}}\right), \tag{4.50}$$

where f_{event} is the frequency of the seismic events, and $\mathsf{Q}_{\mathsf{seismic}}$ the empirical quality-factor. $\mathsf{Q}_{\mathsf{seismic}}$ is dependent on the event frequency f_{event}.

We can use Parseval's theorem to get seismic energy in a specific frequency band because the ground velocity $u(t)$ is real, as for infrasonic energy. The calculation of seismic and infrasonic energies are very similar if $\mathsf{S}_{\mathsf{seismic}} = 1$:

$$\mathrm{E}_{\mathsf{infrasonic}} \propto \int_0^{\tau} \left(p_{\mathsf{ac}}(t) - p_{\mathsf{air}}(t)\right)^2 \mathrm{d}t \qquad \mathrm{E}_{\mathsf{seismic}} \propto \int_0^{\tau} u(t)^2 \mathrm{d}t.$$

4.4.3b Seismic energy from signal envelope

Seismic energy from the signal envelope considers that most of energy is dissipated by surface waves (Love and Rayleigh waves). The seismic energy can be approximated in an isotropic and homogeneous medium of propagation by (Hibert et al., 2015)

$$\mathrm{E}_{\mathsf{seismic}} = \int_0^{\tau} 2\pi r_{\mathsf{vent}} \rho_{\mathsf{layer}} h_{\mathsf{layer}} c_{\mathsf{layer}} \mathrm{Env}^2(u(t)) e^{-\beta r_{\mathsf{vent}}} \mathrm{d}t, \tag{4.51}$$

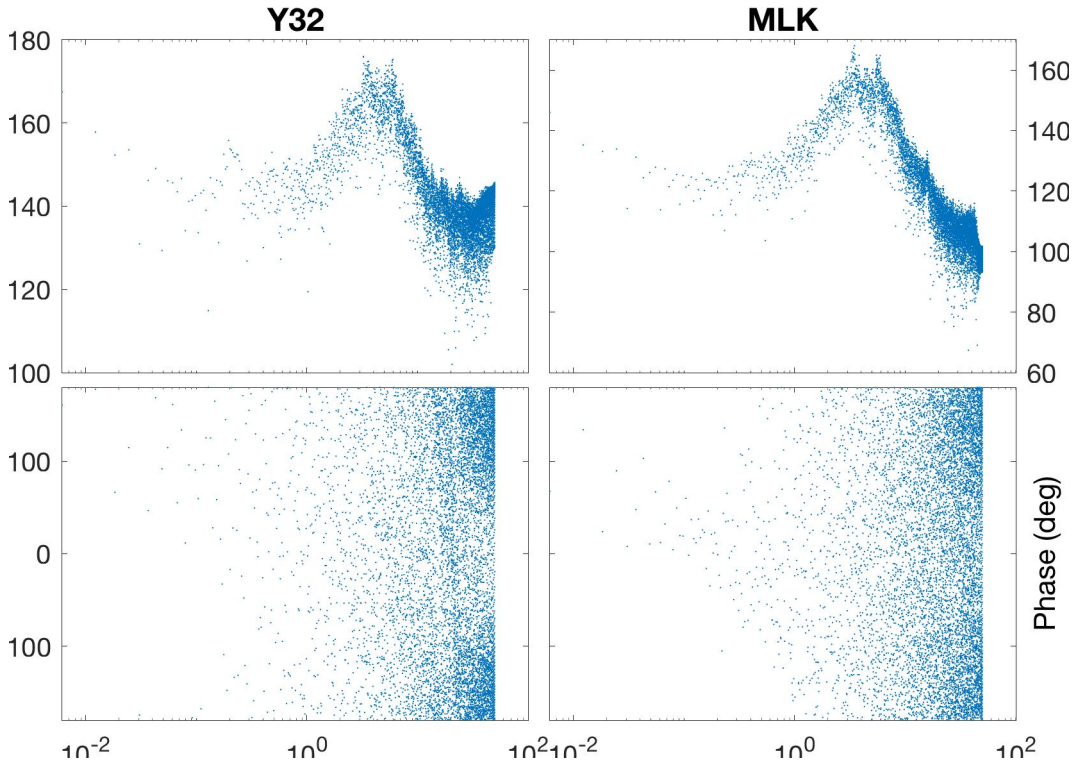

Figure 4.36 – Stacked Fourier transform (`fft`) of the signal part of 100 s from both seismic stations on November, 7th 2009 (Figure 4.33). a) Y32 station and b) Melkem station (MLK).

where $\rho_{\text{layer}} = 2000\,\text{kg.m}^{-3}$ is the density of the shallow layer of thickness $h_{\text{layer}} = c_{\text{layer}}/f_{\text{event}}$ and $c_{\text{layer}} = 800\,\text{m.s}^{-1}$ is the velocity of surface waves in that layer. $\text{Env}(u(t))$ is the signal envelope of the ground velocity u and β is a damping factor. The damping factor β accounts for amplitude attenuation and is dependant on the frequency of the event, f_{event}, as

$$\beta = \frac{\pi f_{\text{event}}}{\text{Q}_{\text{seismic}} c_{\text{layer}}}, \tag{4.52}$$

with $\text{Q}_{\text{seismic}}$ the quality factor.

Note that $e^{\beta r_{\text{vent}}}$, for this model, is equal to $1/\text{A}_{\text{seismic}}$ in the previous model for body waves (Equation (4.50)) leading to

$$\text{E}_{\text{seismic}} = \frac{1}{\text{A}_{\text{seismic}}} \int_0^\tau 2\pi r_{\text{vent}} \rho_{\text{layer}} h_{\text{layer}} c_{\text{layer}} \text{Env}^2(u(t)) \text{d}t.$$

These energies estimates are very similar.

4.4.3c Choice of the energy formula

I choose to estimate the seismic energy considering body waves (Section 4.4.3a) because

(i) I am looking for compression-dilatation processes (bubble formation, rise and explosion),
(ii) the numerous and successive processes supply continuous body waves,
(iii) the surface waves have little time to expand because the seismic sensors are near-field (500 m and 1500 m in 2009 and 2016, respectively)

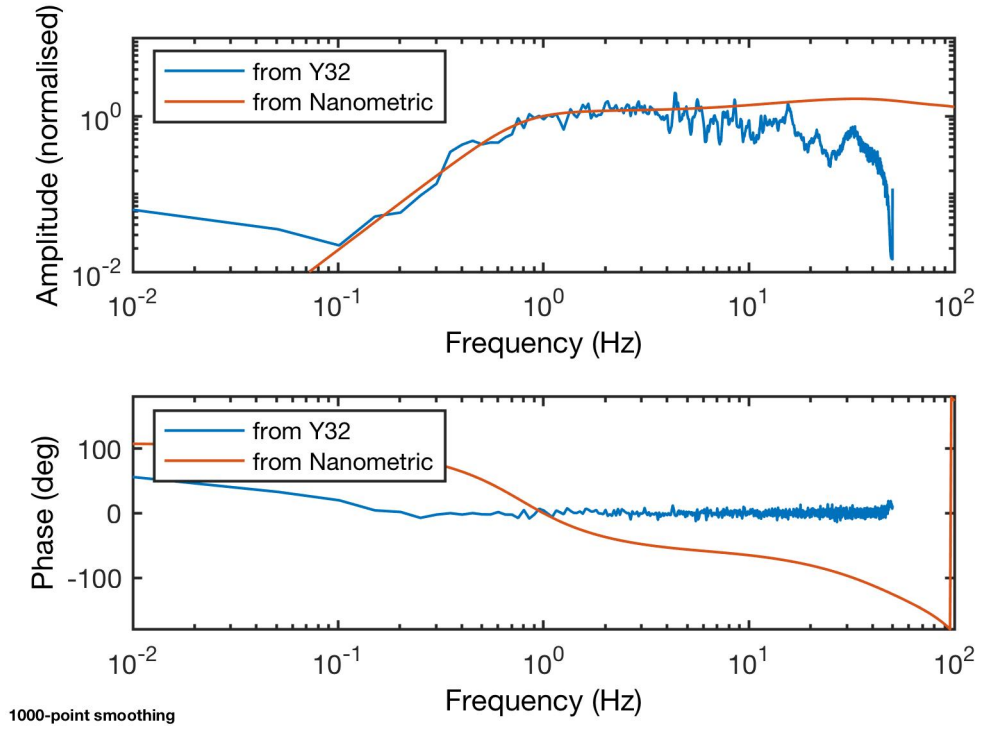

Figure 4.37 – Transfer function (blue) of the seismic station composed by a Trillium 40 and a Quanterra 330 configured in short period. a) Amplitude and b) phase. The red line show the transfer function from the poles and zeros kindly given by Nanometric (Correspondance with Peter Devanney) and the amplitude is very consistent with the transfer function obtained by the simultaneous records at two close stations. The peaks on the transfer function obtained by the simultaneous records at two close stations account mostly for the volcanic signals.

(iv) it gives an analogy to infrasonic energy and the processing is easier and thus faster (no need to calculate the signal envelope and there are fewer parameters).

4.4.4 Polarisation analysis

The polarisation analysis of the seismic waves, recorded by a three components seismometer, gives the displacement of the particles induced by the seismic wave propagation. It allows the identification and the interpretation of the different seismic phases (P-, S-waves, surface waves), when the distance to the source is sufficient.

However the seismic stations at Yasur are very close to the source, (500 m and 1500 m, for Melkem and YASH, respectively), and the identification of the different phases is difficult (Table 4.7). We use the polarisation analysis, here, to estimate the azimuth of the source and the incidence of the seismic wave at the station.

The diagram of polarisation (hodogram) of the North and East components gives the azimuth α of the seismic source (Figures 4.41a, 4.42 and 4.43a1).

We can transform the North and East components to radial and tangential components

Table 4.6 – Poles and zeros of the transfer function of the LE-3Dlite MkII seismometer (Lennartz electronic).

Trillium 40T short-period *Nanometrics*			
Poles	−3.480	± 3.48	i
	−86.300	± 0.00	i
	−241.000	± 178.00	i
	−535.000	± 719.00	i
Zeros	0.000	± 0.00	i
	0.000	± 0.00	i
	−60.000	± 0.00	i
	−323.000	± 0.00	i
	−2530.000	± 0.00	i
Sensitivity	400 V/(m/s) at 1 Hz		

So I edited the Trillium 40 RESP file from the IRIS DMC to change the low corner frequency for short period mode, **Nanometrics engineers, correspondent: Peter Devanney**

Table 4.7 – Time delay between the P and S-waves assuming $c^P_{\mathsf{rock}} = 2500\,\mathrm{m.s^{-1}}$ and $c^S_{\mathsf{rock}} = 1400\,\mathrm{m.s^{-1}}$

Station	**Melkem**	**YASH**
Distance to the source (m)	500	1500
Arrival time delay (s)	0.15	0.47
Number of points at 100 Hz	15	47
Number of points after filtering under 25 Hz	3.75	11.75

25 Hz is the upper limit of the filters we use for seismic data.

by a rotation of the North-East components with an angle $\alpha = \beta - \pi$ (Figure 4.41a)

$$\begin{bmatrix} R \\ T \end{bmatrix} = M_{2D} \begin{bmatrix} N \\ E \end{bmatrix}, \tag{4.53}$$

where

$$M_{2D} = \begin{bmatrix} \cos\alpha & \sin\alpha \\ -\sin\alpha & \cos\alpha \end{bmatrix}. \tag{4.54}$$

The diagram of polarisation of the radial and vertical components (Figure 4.43b2) gives the angle of incidence inc of the seismic waves at the station (Figure 4.41b).

We can assume a homogeneous medium from the source to the near-field sensor, for simplicity. The path from the source to the sensor can then be approximated by a straight line and the angle of incidence can be used to estimate the depth $\mathsf{Z}_{\mathsf{inc}}$ of the source as

$$\mathsf{Z}_{\mathsf{inc}} = r_{\mathsf{vent}} \tan(\mathsf{inc}). \tag{4.55}$$

However, the minimum depth that can be estimated is constrained by the topography (Figures 4.44 and 4.45), with a minimum depth, below the vents, of ∼400 m and ∼25 m observed at YASH and Melkem stations, respectively. These depths correspond to angles of incidence of 11.3° and 9.1° at YASH and Melkem stations, respectively. Note that only the vertical component was working at Melkem station during the 2009-field campaign.

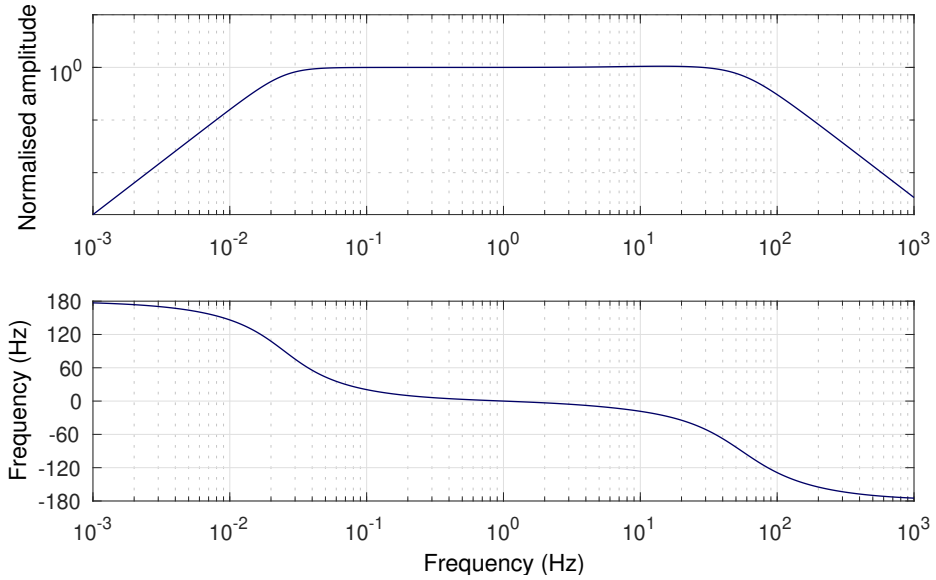

Figure 4.38 – Instrumental response of the Trillium 40 seismometer.

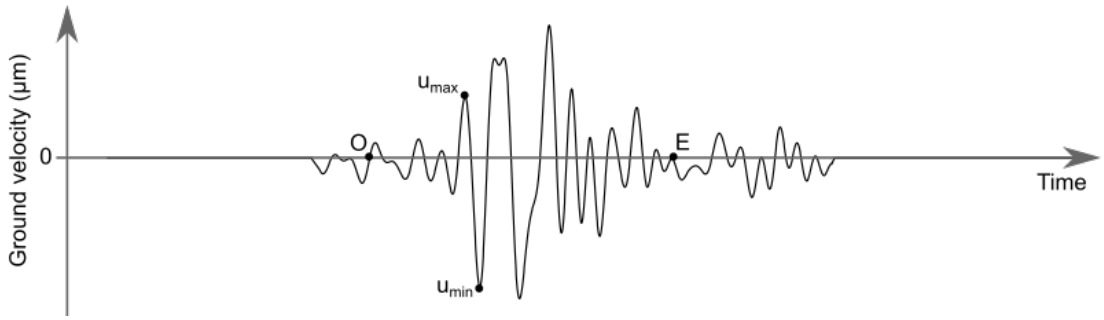

Figure 4.39 – Synthetic seismic waveform on the model of Yasur typical waveforms of explosion.

The seismic waves from shallower sources have more complex pathes. They probably travel downward, following a path of high wave speed, before traveling upward to the station. In that case they can have similar angle of incidence than deep source (i.e. below the minimum depth given by the topography). Furthermore, the medium from the source to the sensor is not homogeneous (Perrier et al., 2012).

This shows the difficulties to estimate the depth of a seismic event using only one sensor. We could simulate the propagation of the seismic waves of a synthetic source at various depth below the vents and obtain the diagram of polarisation of each simulation (Métaxian et al., 2009). We could then compare the synthetic diagrams of polarisation with the diagram obtained from YASH station to estimate the depth of the seismic source. Note that VLPs are large sources triggered by the motion of a large volume of magma and that the angle of incidence gives only the position of the center of this large volume of magma.

4.4.5 Monitoring volcano: introduction to RSAM and SSAM methods

Real-Time Seismic Amplitude Measurements (RSAM) and Seismic Spectral Amplitude Measurements (SSAM) are often used to monitor volcanoes in near real-time (Figure 4.46).

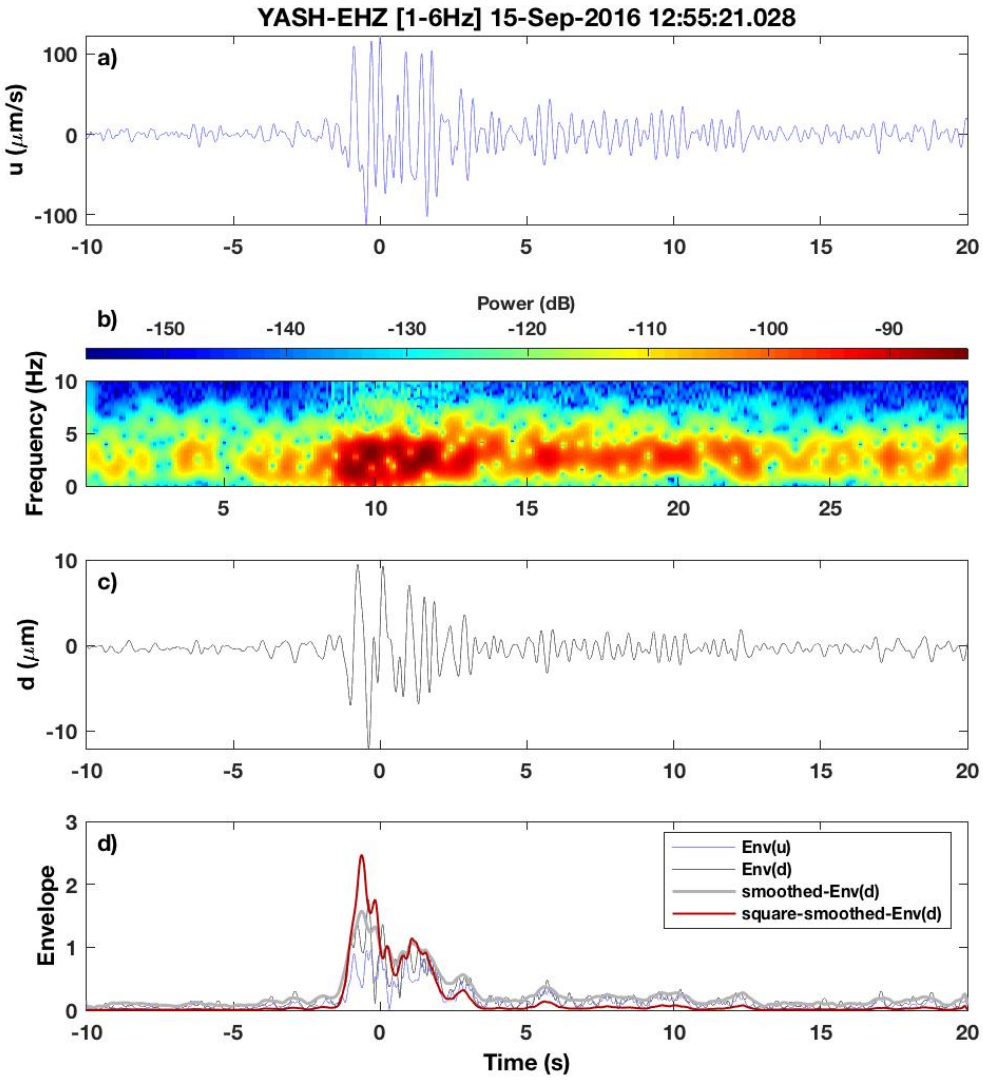

Figure 4.40 – Example of the signal envelopes of an explosion on seismic records [YASH-EHZ, 1 Hz to 6 Hz]. a) Ground velocity. b) Spectrogram of the ground velocity (`WINDOW` = 100, `NOVERLAP` = 90, `NFFT` = 1024, `Fs` = 100). c) Displacement (temporal integration of the ground velocity). d) Normalised signal-envelopes. The limits of the event on the squared and smoothed envelope of the displacement (thick red) are easy to distinct.

The RSAM averages the absolute value of the signal in a sliding window (as an example) for each channel (e.g. Endo and Murray, 1991) and is quite similar to a RMS (Root-Mean-Square) calculation (Figure 4.46a). The length of the sliding window is set to have a good compromise between the time calculation and the accuracy of the RSAM.

The SSAM is sligthly more complicated as it performs a fast Fourier transform each 5 s and then averages the spectrum amplitude over 60 s intervals in several frequency bands. (e.g. Rogers and Stephens, 1995, Figure 4.46b-c). A pseudo-spectrogram is obtianed in quasi-real time and any changes of frequency contents, which may indicate a changes in the Strombolian activity, will be clear.

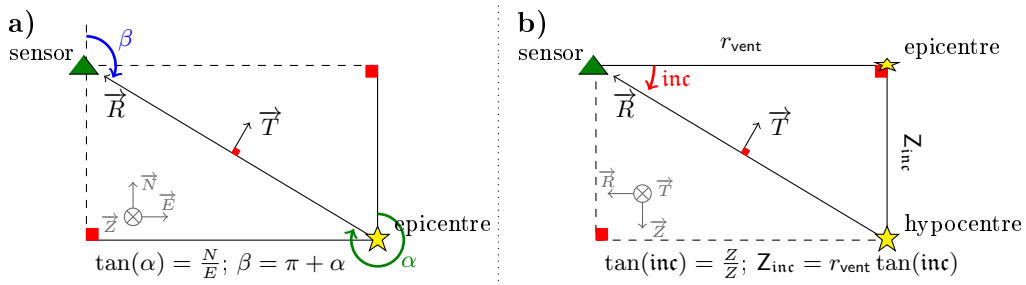

Figure 4.41 – Sketch for the polarisation analysis. a) Calculation of the azimuth α to convert the seismic components from North and East to radial and tangential components. b) Calculation of the angle of incidence **inc**.

4.5 Combination of different type of data

One of the interest of the multi-disciplinary studies is to perform budget of energy. The Volcanic Acoustic-Seismic Ratio of energy (VASR) is the most used of the parameters able to quantify the budget of energy (e.g. Johnson and Aster, 2005). Here we calculate also the Volcano Acoustic-Thermal Ratio (VATR) to assess the relative role of infrasonic and thermal energies.

We use these multi-displinary studies to estimate the depth of the magma column from the thermo acoustic delay and the mean ejecta size per explosion from the gas and ejecta velocities.

The link of an event recorded by several sensor is done using the function `LinkData` (Section 3.6.7).

4.5.1 Particle size

The comparison of ejecta and gas velocity is another way to discuss about the energy partitioning. The kinetic energy of the gas and ejecta can be compared and can be used to understand the two-phase dynamic.

The particle size can be estimated from the gas and ejecta velocities by a dimensionless analysis of the equation of motion for a turbulent system (Steinberg and Babenko, 1978). We assume that the particle of diameter D_P and density ρ_{ejecta} is carried with a velocity $\mathrm{U}_{\text{ejecta}}$ by the gas flow of velocity U_{gas} and density ρ_{gas}. The dimensionless equation of the motion is solved for fragments having terminal velocities, i.e. the dimensionless weight of the particle is equal to the dimensionless dynamic pressure of the gas. The particle size is then given by (Steinberg and Babenko, 1978)

$$D_P = \frac{3 C_D \rho_{\text{gas}}}{4 g \rho_{\text{ejecta}}} \left(\mathrm{U}_{\text{gas}} - \mathrm{U}_{\text{ejecta}}\right)^2 , \tag{4.56}$$

where $C_D = 0.50$ is the drag coefficient, $\rho_{\text{gas}} = 0.80\,\text{kg.m}^{-3}$ the gas density, $g = 9.81\,\text{m.s}^{-2}$ the constant of gravity and $\rho_{\text{ejecta}} = 850\,\text{kg.m}^{-3}$ the density of ejecta.

This estimate of the ejecta size is very important as it is a key parameter for models of plume dynamics. However, it is difficult to estimate some parameters in eq. (4.56), such as the gas and ejecta densities and the ejecta velocity. We assume that the gas and ejecta

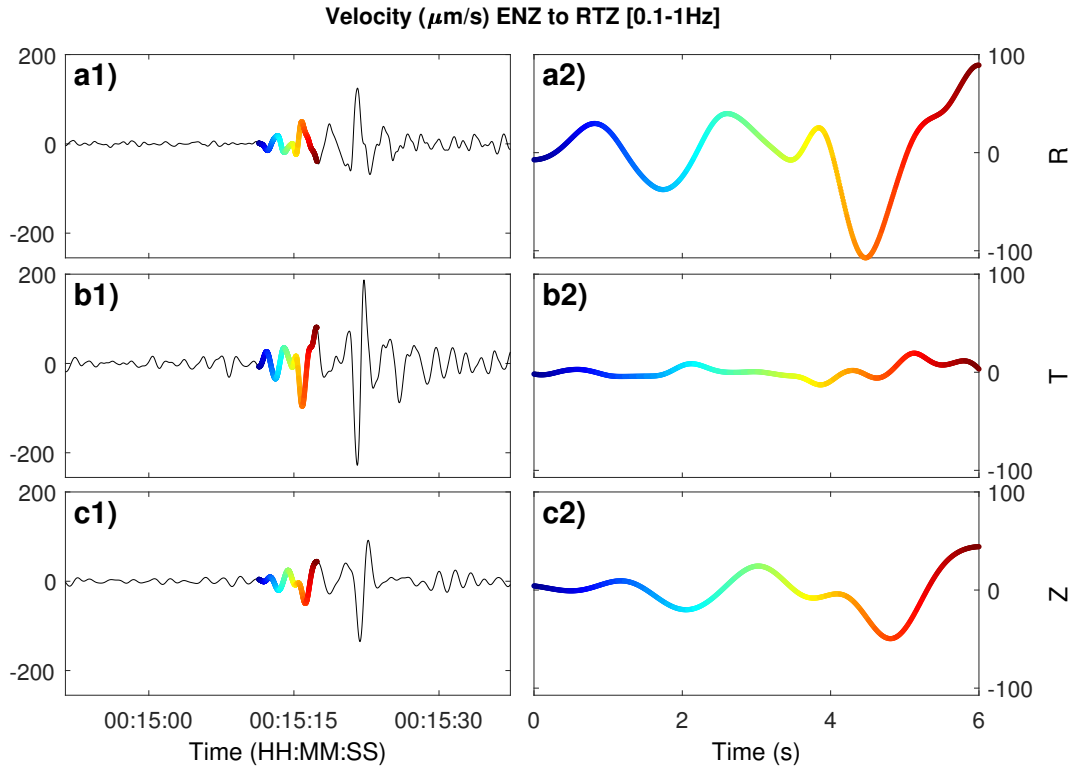

Figure 4.42 – Transformation of a VLP signal at Yasur (20-Sep-2016 00:15:12) from its (N,E,Z) components to its (R,T,Z) components. 1) Recorded signal (N,E,Z): a1) North component, b1) East component and c1) vertical component. 2) Transformation to (R,T,Z): a2) radial component, b2) tangential component and c2) unchanged vertical component. Signals in the radial, tangent and vertical plans are calculated using equations 4.53 and 4.54.

densities are constant in this study because our aim is to give a rough approximation of the mean particle size per explosion. A more accurate study could have been done using a range of values for the ejecta and gas densities (such as in, Harris et al., 2012) and a Monte Carlo analysis.

4.5.2 Depth of the top of the magma column

The depth of the magma column ΔH, i.e. the height of the top of the magma column into the conduit, is estimated from the thermo-infrasonic delay $\Delta t = t_{\text{thermal}} - t_{\text{infrasonic}}$. A simple sketch (Figure 4.47) is used to estimate the delays as

$$t_{\text{infrasonic}} = t_0 + \frac{\Delta H}{c_{\text{conduit}}} + \frac{r_{\text{vent}}}{c_{\text{atm}}} \tag{4.57a}$$

$$t_{\text{thermal}} = t_0 + \frac{\Delta H}{\text{U}_{\text{ejecta}}} + \underbrace{\frac{r_{\text{vent}}}{c_{\text{light}}}}_{\simeq 0} \tag{4.57b}$$

where c_{conduit} is the sound speed into the conduit and $c_{\text{light}} = \sim 3 \times 10^8\,\text{m.s}^{-1}$ is the light velocity. Equations (4.38), (4.57a) and (4.57b) give that the depth of the magma column

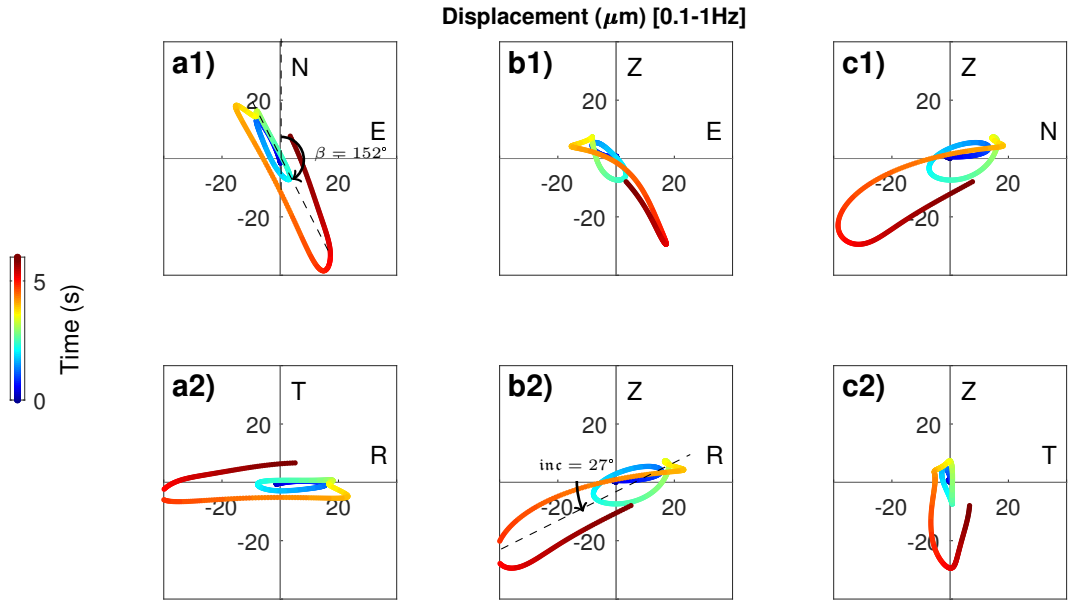

Figure 4.43 – Diagrams of polarisation of a VLP at Yasur (20-Sep-2016 00:15:12). Particle displacement in 1) the NEZ plans and 2) the RTZ plans. The colour scale gives the time (figure 4.42). The diagram a1) gives the azimuth α of the source ($\sim$152°). Signals in the radial and tangent plans are calculated using equations 4.53 and 4.54. The diagram b2) gives the angle of incidence $\mathbf{inc}$ ($\sim$27°, giving a source at $\sim$900 m below the vent when assuming a straight line from the source to the sensor.).

ΔH is

$$\Delta H = \left(t_{\text{thermal}} - t_{\text{infrasonic}} + \frac{r_{\text{vent}}}{c_{\text{atm}}}\right) \frac{c_{\text{conduit}} \mathrm{U}_{\text{ejecta}}}{c_{\text{conduit}} - \mathrm{U}_{\text{ejecta}}} \tag{4.58a}$$

$$= \left(\Delta t + \frac{r_{\text{vent}}}{c_{\text{atm}}}\right) \frac{c_{\text{conduit}} \delta h}{\delta t c_{\text{conduit}} - \delta h} \tag{4.58b}$$

Sound speed in the conduit The speed of sound in a homogeneous medium of compressibility $\beta_{S,}$ and density ρ is

$$c = \frac{1}{(\rho \beta_{S,})^{1/2}} \tag{4.59}$$

The sound speed in the conduit considering a homogeneous two-phase flow between gas and ejecta is estimated by (Wood, 1955)

$$c_{\text{conduit}} = \frac{1}{(\rho_{\text{conduit}} \beta_{S,\text{conduit}})^{1/2}}, \tag{4.60}$$

where ρ_{conduit} and $\beta_{S,\text{conduit}}$ are the density and the compressibility of the gas-ejecta mixture calculated for a gas volume fraction α_{gas} by

$$\rho_{\text{conduit}} = \alpha_{\text{gas}} \rho_{\text{gas}} + (1 - \alpha_{\text{gas}}) \rho_{\text{ejecta}} \tag{4.61a}$$

$$\beta_{S,\text{conduit}} = \alpha_{\text{gas}} \beta_{S,\text{gas}} + (1 - \alpha_{\text{gas}}) \beta_{S,\text{ejecta}}$$

$$= \frac{\alpha_{\text{gas}}}{\rho_{\text{gas}} c_{\text{gas}}^2} + \frac{1 - \alpha_{\text{gas}}}{\rho_{\text{ejecta}} c_{\text{ejecta}}^2}. \tag{4.61b}$$

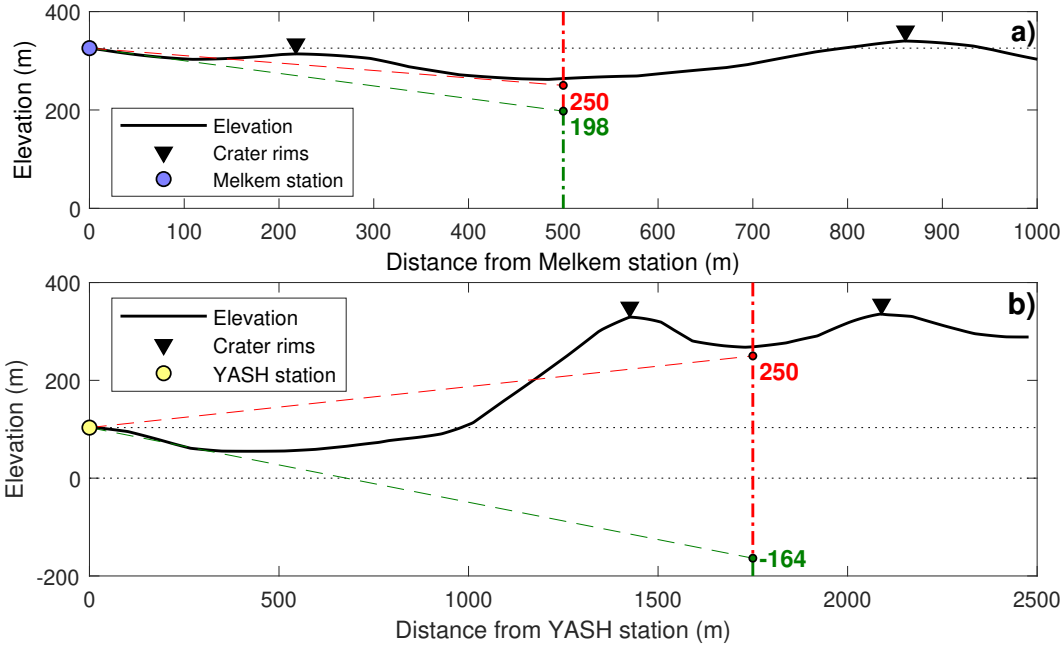

Figure 4.44 – Topographic profils at Yasur volcano. a) From Melkem and b) from YASH (Figure 4.45). The red and dashed vertical lines show the elevation for which the path to the sensor can not be a straight line. The green and dashed vertical lines show the elevation for which the path to the sensor can be a straight line. The profils are retreived from Google Earth, using Geocontext (Geocontext, 2018).

Equations (4.60) and (4.61) give the sound speed in the conduit as

$$c_{\text{conduit}} = \frac{1}{\sqrt{(\alpha_{\text{gas}}\rho_{\text{gas}} + (1-\alpha_{\text{gas}})\rho_{\text{ejecta}})\left(\frac{\alpha_{\text{gas}}}{\rho_{\text{gas}}c_{\text{gas}}^2} + \frac{1-\alpha_{\text{gas}}}{\rho_{\text{ejecta}}c_{\text{ejecta}}^2}\right)}}. \tag{4.62}$$

The proportion of gas and ejecta in the conduit impacts a lot on the sound speed (Figure 4.48). For example, an ejecta volume fraction of 1.50 ‰ is sufficient to decrease the sound speed in the conduit from $700\,\text{m.s}^{-1}$ to $350\,\text{m.s}^{-1}$.

Error estimations on the depth of the magma column Uncertainties on the depth of the magma column come from the sound speed in the conduit c_{conduit}, the velocity of the ejecta U_{ejecta} and the thermo-infrasonic delay Δt because of (i) inaccuracies in the detection of the limits of the explosions and (ii) the relatively long efficient response time of the radiometer.

The error on that depth is estimated using the variance formula by

$$\begin{aligned}\sigma_{\Delta H}^2 = &\left(\frac{\partial \Delta H}{\partial t_{\text{thermal}}}\right)^2 \sigma_{t_{\text{thermal}}}^2 + \left(\frac{\partial \Delta H}{\partial t_{\text{infrasonic}}}\right)^2 \sigma_{t_{\text{infrasonic}}}^2 + \left(\frac{\partial \Delta H}{\partial r_{\text{vent}}}\right)^2 \sigma_{r_{\text{vent}}}^2 + \left(\frac{\partial \Delta H}{\partial c_{\text{atm}}}\right)^2 \sigma_{c_{\text{atm}}}^2 \cdots \\ &+ \left(\frac{\partial \Delta H}{\partial c_{\text{conduit}}}\right)^2 \sigma_{c_{\text{conduit}}}^2 + \left(\frac{\partial \Delta H}{\partial \text{U}_{\text{ejecta}}}\right)^2 \sigma_{\text{U}_{\text{ejecta}}}^2\end{aligned} \tag{4.63}$$

We set

$$\Delta t_{\Delta H=0} = t_{\text{thermal}} - t_{\text{infrasonic}} + \frac{r_{\text{vent}}}{c_{\text{atm}}}, \qquad \Delta U = \frac{c_{\text{conduit}}\,\text{U}_{\text{ejecta}}}{c_{\text{conduit}} - \text{U}_{\text{ejecta}}}.$$

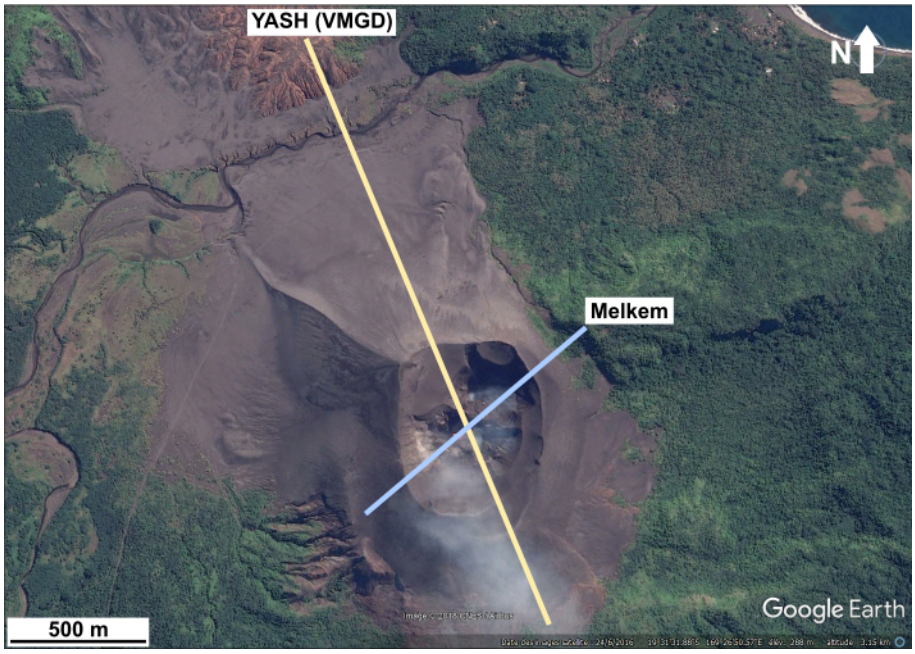

Figure 4.45 – Trace of the profils of figure 4.44.

Then we can write $\sigma^2_{\Delta H}$ as

$$\begin{aligned}\sigma^2_{\Delta H} =& \Delta U^2 \left[\sigma^2_{t_{\text{thermal}}} + \sigma^2_{t_{\text{infrasonic}}} + \frac{1}{c^2_{\text{atm}}}\sigma^2_{r_{\text{vent}}} + \frac{r^2_{\text{vent}}}{c^4_{\text{atm}}}\sigma^2_{c_{\text{atm}}}\right] \cdots \\ &+ \Delta U^2 \Delta t^2_{z=0} \left[\left(\frac{1}{\text{U}_{\text{ejecta}}} + \frac{1}{c_{\text{conduit}} - \text{U}_{\text{ejecta}}}\right)^2 \sigma^2_{\text{U}_{\text{ejecta}}} + \left(\frac{1}{c_{\text{conduit}}} - \frac{1}{c_{\text{conduit}} - \text{U}_{\text{ejecta}}}\right)^2 \sigma^2_{c_{\text{conduit}}}\right]\end{aligned} \tag{4.64}$$

Example 4.5.1. At Yasur in 2016, the distance from the source to the vent is $r_{\text{vent}} = 340 \pm 6.7\,\text{m}$, the sound speed in the atmosphere is $(340.00 \pm 6.66)\,\text{m.s}^{-1}$. We assume an ejecta velocity of $\text{U}_{\text{ejecta}} = (20.00 \pm 1.75)\,\text{m.s}^{-1}$ (Figure 4.21). The sound speed in the conduit is estimated at $(91.02 \pm 14.29)\,\text{m.s}^{-1}$ for a gas-rich explosion ($\alpha_{\text{gas}} = 0.970 \pm 0.009$). The thermo-infrasonic delay is $\Delta t = 1.48\,\text{s}$ (median value of Δt) with an error $\sigma_{\Delta t} = 0.08\,\text{s}$ We then estimate the depth of the magma column at $(64.13 \pm 7.97)\,\text{m}$ (12.4 %).

4.5.3 Estimation of the gas volume fraction from the gas volume and scoria cone volume

We can estimate the flux of ejecta φ_{ejecta} from the volume of the scoria cone Vol_{cone} and the duration of the eruption τ_{eruption} using the data from Maurice and Bernard (1977) (Table 4.8) by

$$\varphi_{\text{ejecta}} = \frac{\text{Vol}_{\text{cone}}}{\tau_{\text{eruption}}}, \tag{4.65}$$

giving the mean and median values of $124\,\text{m}^3.\text{h}^{-1}$ and $25\,\text{m}^3.\text{h}^{-1}$, respectively. We assume these values are also representative for the eruption initiated the 30th of August, 2006 because of the strong similarity of the eruptions we can observe.

The gas flux φ_{gas} is estimated from the return time between two successive explosions and the gas volume per explosions at Piton de la Fournaise ($780\,\text{m}^3.\text{h}^{-1}$, $275\,\text{m}^3.\text{h}^{-1}$ and $943\,\text{m}^3.\text{h}^{-1}$ for the mean, median and standard deviation values, respectively).

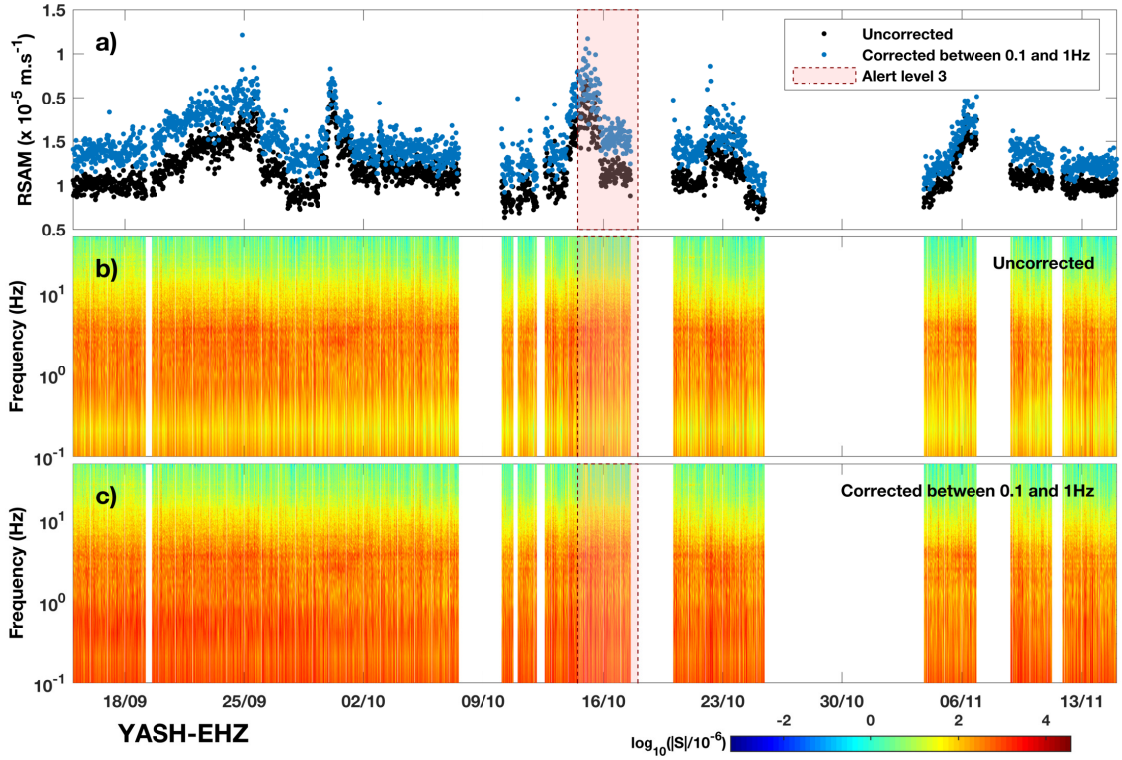

Figure 4.46 – RSAM and SSAM calculation during the 2016-field campaign at Yasur for the EHZ component. a) RSAM per 30 min sliding window and SSAM (spectrogram) per 30 min sliding window for b) the raw data and c) corrected data (between 0.10 Hz and 1 Hz) of the EHZ components of YASH station (VMGD, 1500 m from the summit of Yasur.)

The gas volume fraction α_{gas} is estimated by

$$\alpha_{\text{gas}} = \frac{\varphi_{\text{gas}}}{\varphi_{\text{gas}} + \varphi_{\text{ejecta}}}, \tag{4.66}$$

and has values of 86 % and 70 % when using mean and median values, respectively.

We perform a Monte Carlo analysis in order to get better estimates of the gas volume fraction (See section 3.1.5). The input of the Monte Carlo analysis are the duration of the eruptions $\tau_{\text{eruption}} = (15.8 \pm 13.4)$ d, the volumes of the cones $\text{Vol}_{\text{cone}} = (43.9 \pm 98.3)\,\text{m}^3$ and the gas flux $\varphi_{\text{gas}} = (780 \pm 943)\,\text{m}^3.\text{h}^{-1}$. We have chosen to use normal distributions for these parameters. The results give an estimate of the gas volume fraction of (72.9 ± 24.3) % (median: 81.00 %, figure 4.49).

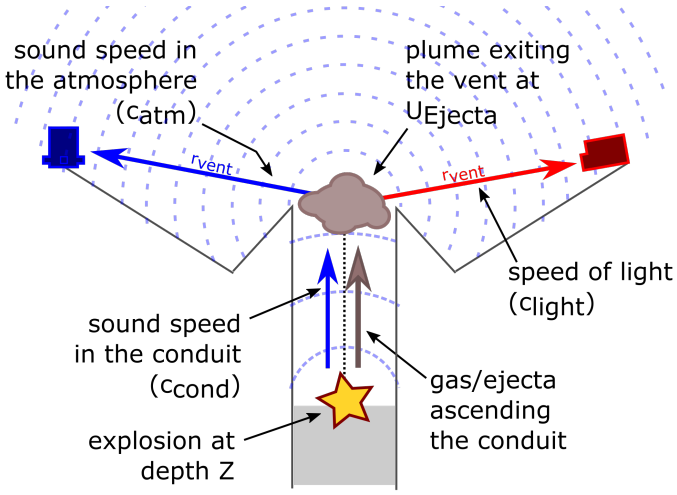

Figure 4.47 – Infrasonic and thermal (IR) wave propagation from the source to the sensor (Not at scale).

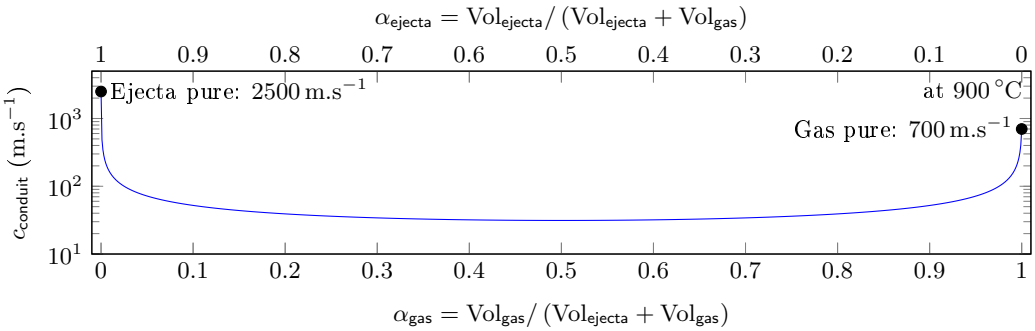

Figure 4.48 – Speed of sound in the conduit as a function of gas volume fraction and ejecta volume fraction. For a pure gas, we consider the gas density at 1 kg.m^{-3} and a sound speed of 700 m.s^{-1} at 900 °C. We consider a sound speed of 2500 m.s^{-1} in a magma at 2000 kg.m^{-3}.

Table 4.8 – Duration and cone volume of eruptions at Piton de la Fournaise (Maurice and Bernard, 1977) and estimation of the gas volume fraction assuming a gas flux of 780 m^3.h^{-1}.

Starting date	$\tau_{eruption}$ (day)	Vol_{cone} (10^3 m^3)	φ_{ejecta} (m^3.h^{-1})	α_{gas} (%)
09/06/1972	3	15	208	80
25/07/1972	18	12	27.80	100
07/09/1972	7	2	11.90	100
09/09/1972	14	7	20.80	100
10/10/1972	5	1	8.33	100
27/10/1972	3	1.6	22.20	100
01/01/2001	8	20	104	90
01/11/1972	26	400	641	50
02/11/1972	15	7	19.40	100
07/11/1972	37	3	3.38	100
09/11/1972	14	3	8.93	100
15/11/1972	13	50	160	80
10/05/1973	28	100	149	80
04/11/1975	10	40	167	80
18/12/1975	50	20	16.70	100
19/12/1975	2	20	417	70
Mean	15.80	44	124	90
Standard deviation	13.40	98	177	10
Median	13.50	14	25	100
Total	253	700	116	90

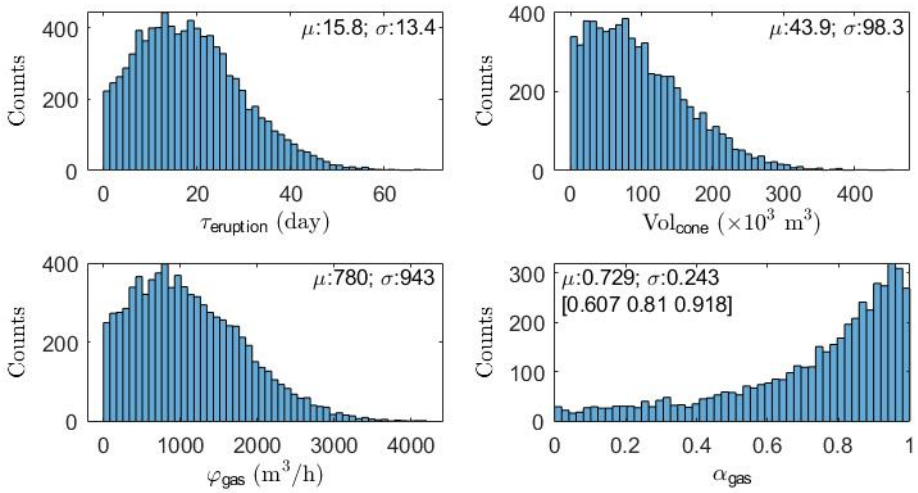

Figure 4.49 – Monte Carlo analysis: estimation of the gas volume fraction, at Piton de la Fournaise from the ejecta flux, based on the volume of the scoria cone, and the active volume flux based on infrasonic records (explosions, bubble vibration model).

Chapter 5

A global inventory of Strombolian activity calibrated at Erta'Ale, Piton de la Fournaise and Yasur

À Jean et Rolande, parce qu'ils ont éveillé ma passion au travers des films de Katia et Maurice Krafft.

Katia and Maurice Krafft (United States Geological Survey)

Abstract

Strombolian activity, widely spread across the world, is often persistent and have been extensively studied. However, there is still lack of knowledge on thermal and infrasonic energies and meaningful statistical analysis sometimes are difficult to obtain. Here we discuss simultaneous records of infrasonic and thermal signals (radiometers with 1° viewing angle) for understanding and quantifying Strombolian activity for the largest range of strength of the activity. The aim of this work is three-fold. Firstly we give the range of values of many physical parameters for the two end-members of Strombolian activity, such as Erta'Ale (Ethiopia) and Piton de la Fournaise (Reunion island) on one side and Yasur (Vanuatu) on the other side for the weak and strong Strombolian activity, respectively. Thermal and infrasonic energies range from 2 J to 4×10^6 J and from 18 J to 3.70×10^8 J, respectively. Ejecta velocity ($0.10\,\mathrm{m.s^{-1}}$ to $100\,\mathrm{m.s^{-1}}$), estimated from 2 vertically spaced radiometers, is found to be in agreement with that estimated by Particle Image Velocimetry on the images, despite the different window of measuring. Gas flux, emitted by the Strombolian activity, range from $4 \times 10^5\,\mathrm{m^3.h^{-1}}$ to $1 \times 10^7\,\mathrm{m^3.h^{-1}}$, among which $50\,\mathrm{m^3.h^{-1}}$–$1 \times 10^6\,\mathrm{m^3.h^{-1}}$ accounts only for the Strombolian explosions. Secondly, we show that infrasonic measurements can be used to estimate the total gas flux as an alternative of geochemical measurements (SO_2 flux + gas composition ratio). The infrasonic measurements are also a good alternative to estimate the gas flux of each species, including the very reactive ones, when knowing the proportion of each species. Thirdly we show that despite the large range of strengths of Strombolian activity the mechanism of magma fragmentation remains the same. The interest of using continuous geophysical measurements, such as infrasonic records, is to provide very accurate estimates of gas volume at high sample rate and continuously for very long periods. This study has wide implications for quantifying the impact of Strombolian activity on the local atmosphere dynamics and on local biochemical cycles, in the ocean (through nutrient deposition).

Contents

5.1 Introduction **125**
5.2 Strombolian activity **127**
5.3 Targeted volcanoes **127**
5.4 Measurements **128**
5.5 Methodology **130**
5.5.1 Qualitative analysis of the waveforms 130
5.5.2 Pre-processing 131
5.5.3 Infrasonic processing 133
5.5.4 Thermal processing 134
5.5.5 Thermo-infrasonic processing 135
5.5.6 Gas flux from SO_2 and gas ratio measurements 136
5.5.7 Basic considerations: analysing a boxplot 137
5.6 Results **137**
5.6.1 Distribution of the key parameters 137
5.6.2 Distribution of energy, velocity and volume 139
5.6.3 Considerations on the depth of the magma column 141
5.6.4 Budget of energy 143
5.6.5 Inputs into the atmosphere 147
5.6.5a Size of the ejecta 147
5.6.5b Hourly gas flux 149
5.7 Extrapolation to other volcanoes **150**
5.8 Conclusion **154**

This chapter introduces a statistical study on the Strombolian activity that is recorded worldwide. This chapter is written with the aim to be published soon. Certain parts would be to moved in the appendices for the publication.

Yves Gaudemer (IPGP) has helped me to understand the Monte Carlo analysis for the estimates of the uncertainties on the ejecta velocity from the thermal records and I have extended the method to the estimation of the depth of the top of the magma column.

Pascale Besson (IPGP) has helped me to enlarge the calculation range of the gas volume from gas measurements by including more data (section 5.7).

5.1 Introduction

The impact of volcanic eruptions on the climate is now known (e.g. Pollack et al., 1976; Sigurdsson, 1990). Volcanoes release gases whose chemistry can interact with the atmosphere, while being transformed into aerosols during transport. These gases also change atmospheric radiative transfer and dynamics pattern and have an impact on bio-chemical cycles through nutrient deposition in the ocean (Kent et al., 1999). For example sulphate aerosols are responsible for acid rains, often reported on Tanna (Vanuatu) and cause several health problems and crop damage (e.g. Cronin and Sharp, 2002).

Among gases that are playing a crucial role on our environement, some are released in significant amounts such as the SO_2, the HCl, etc., whereas others are present in minor quantities such as halogens (F, Br, e.g. Mather et al., 2012; Zelenski et al., 2013; Jourdain et al., 2016).

The SO_2 is produced at a few kilometre depth below the vent in minor quantities, compared to CO_2 or H_2O but is now extremely measured close to volcanoes. Measurements occur either during field campaign at many volcanoes (Bani and Lardy, 2007; Galle et al., 2003; Barrancos et al., 2008, e.g.) or now in continuous at several volcanological observatories such as Kilauea (United States), Stromboli, Vulcano and Etna (Italy) (Burton et al., 2014; Vita et al., 2012), Piton de la Fournaise (Île de la Réunion, France).

The interest of measuring the SO_2 flux is that this gas species does not exist in the normal atmosphere outside of human pollution. Elsewhere the SO_2 flux must have a volcanic origin.

Another important piece of information is obtained using multi-gas and FTIR (Fourier Transform Infra-Red spectrometer) devices. These two methods estimate the ratio of diatomic gases such as CO_2/SO_2, H_2O/SO_2 and HCl/SO_2 (e.g. Oppenheimer et al., 2006; Métrich et al., 2011; La Spina et al., 2015). The oldest method, still the most frequent, is that of multi-gas which is only done at a site of measurements. Therefore the estimates are obtained after significant dilution. In contrast the FTIR method measure directly the volcanic source at the vent providing a clear view.

The SO_2 flux which is often only known at the order of magnitude due to uncertainties such as the wind speed and with a *strong* averaging due to the few tens of minutes of the recording, can be combined with the gas composition obtained from multi-gas or FTIR measurements to obtain the released gas flux of each gas species which plays a crucial role in the atmosphere dynamics.

Alternatively, the gas volume produced by any volcanic activity can be estimated from infrasonic measurements (Woulff and McGetchin, 1976; Vergniolle et al., 2004; Vergniolle and Brandeis, 1996; Johnson, 2003). The amount of active degassing, that is due to over-pressurised gas, and that of passive degassing, only sightly over-pressurised gas, can be assessed. Knowing both gas volume is important as their gas composition is very different due to a different depth of formation. These estimations of gas volumes include all gas species released by volcanic activity.

The other factor that plays a significant role on the climate is the amount of ashes. Volcanologists often estimate sizes in a range much higher than that inhaled to understand the atmosphere dynamics (e.g. Gurioli et al., 2018; Gaudin et al., 2014b; Horwell and Baxter, 2006). However this technical limitation is partially overcome by assuming that the amount of tiny particles is proportional to the amount of the smallest detectable fragments.

So far, the role of volcanic eruptions on the climate has only been studied for large Plinian columns whose injection in the stratosphere level (Mather, 2015; Koyaguchi et al., 2009, from 6 km to 16 km to 50 km, e.g.). However the role of more minor eruptions, whose eruptive columns remains in the troposphere (<6 km to 16 km) have been mostly ignored (e.g. Jourdain et al., 2016; Sellitto et al., 2017). But the persistent activity displayed by some Strombolian volcanoes, may account for a significant yearly volume of reactive gas released in the troposphere, so far often unknown.

Strombolian activity, whose various magma composition (e.g. Métrich et al., 2011; Lemma, 2017; Albarède et al., 1997; Francalanci et al., 2004) lead to a wide range of magma viscosity (e.g. Gaudin et al., 2014b; Schmincke, 2004; Hibert et al., 2015) and thus wide range of activity, has been widely studied by numerous methods during short or long periods at many volcanoes. The ejecta and sometimes the gas velocity have been deduced from images (visible, thermal), radar, infrasounds, etc. Among the most studied volcano, Stromboli stands out. If these parameters are well known at Stromboli, there is still lack of knowledge on thermal and infrasonic energies.

The wide range of strength between the weak and strong Strombolian activity, here given by Erta'Ale and Piton de la Fournaise on one side and Yasur on the other side, ranges by several orders of magnitude on the explosivity, i.e. the distance reached by ejecta, the maximum height, the gas volume and the amount of ashes produced by each explosion, poses the question whether the mechanism of the Strombolian explosions is the same for weak and strong explosions.

In this study we estimate the gas volumes from infrasonic measurements at three typical volcanoes presenting Strombolian activity such as Erta'Ale and Yasur, both in persistent Strombolian activity and Piton de la Fournaise whose semi-persistent activity in 2006 lasted for half of the year. Our choice of volcanoes has been based on covering most of the tectonic contexts and also the full range of strength of Strombolian activity.

The aim of this quantitative and statistical study is three-fold. Firstly we give the range of values of many physical parameters, including gas volumes, thermal and infrasonic energies for the two end-members of Strombolian activity, such as Erta'Ale and Piton de la Fournaise on one side and Yasur on the other side for the weak and strong Strombolian activity, respectively. Secondly, we show that infrasonic measurements can be used to estimate the total gas flux as an alternative of geo-chemical measurements (SO_2 flux + gas composition ratio). Thirdly we show that despite the large range of strengths of

Strombolian activity the mechanism of magma fragmentation remains the same.

5.2 Characteristics of Strombolian activity at Stromboli

The Strombolian activity, named after Stromboli volcano in Italy, is characterized by series of mild Strombolian explosions. A Strombolian explosion is due to a large and over-pressurised gas pocket rising the volcanic conduit and exploding at the surface of the magma (Section 1.2.2).

Stromboli, 750 m high, is in persistent Strombolian activity for at least 14 centuries and is now very well studied (Rosi et al., 2000). Its 3 craters can have from 5 to 15 active vents at the same time. The mild Strombolian activity at Stromboli can be interrupted by much stronger explosions, as during paroxysmal activity (Métrich et al., 2005; Andronico and Pistolesi, 2010; Calvari et al., 2006, 2012; La Felice and Landi, 2011; Aiuppa et al., 2009; Andronico et al., 2013, e.g. 05/04/2003, 15/12/2006, 15/03/2007, 07/09/2008, 08/11/2009, 24/11/2009) or lava flows (e.g. Frebruary–March 2007 Ripepe et al., 2009; Aiuppa et al., 2009).

The typical recurrence time of Strombolian explosions is 270 s at Stromboli (13 ev.h^{-1}, Delle Donne et al., 2006). Two types of Strombolian explosions are observed, indicating that Strombolian activity can vary between the ash-rich and long lasting eruptions (10 s to 20 s), that are driven by buoyancy (type 2 eruptions) on one side, and the short bombs and scoria-rich eruptions (5 s to 10 s) that are driven by momentum on the other side (Patrick et al., 2007). Furthermore a puffing activity was observed with low infrasonic amplitudes and short return times (Colò et al., 2010; Ripepe et al., 2008). Ripepe et al. (2008) also find that there is a common feeding system up to 550 m above see level, for all 3 craters of Stromboli.

Ejecta upward velocity ranges from to 10 m.s^{-1} to 150 m.s^{-1} and their size can range from 0.30 cm to 100 cm (Gaudin et al., 2014b; Hort et al., 2003). Infrasonic amplitude of explosions is up to 80 Pa at 350 m (280 Pa at 100 m). The gas output from Stromboli is estimated at 6.10 kt.d^{-1}–12.30 kt.d^{-1} (6.20×10^6 m^3.h^{-1}, Allard et al., 1994). Infrasonic energy is estimated between 2.50×10^4 J.ev^{-1} and 8×10^6 J.ev^{-1} with an average of 1.60×10^6 J.ev^{-1} and a standard deviation of 1.80×10^6 J.ev^{-1} (Marchetti et al., 2009).

In practice, the Strombolian activity is widespread worldwide with a range of strength. Thus, we study the Strombolian activity at three volcanoes. Erta'Ale, Piton de la Fournaise are analog for weak Strombolian activity and Yasur is analog for mild and strong Strombolian activity.

5.3 Targeted Strombolian volcanoes

Infrasonic and thermal measurements were simultaneously recorded during 4 field campaigns at Erta'Ale in March 2003 (EA03), Piton de la Fournaise in November–December 2006 (PdF06), Yasur in June 2009 (mild and steady activity, YAS09) and in September–November 2016 (mild to strong vigorous and unsteady activity, YAS16).

The lava lake of Erta'Ale are located north eastern of Ethiopia, in the Danakil depression,

northern Afar (Tazieff, 1994). The emitted magma is a low-differentiated and low-viscous basalt (transitional basalt, 10 Pa.s, Lemma, 2017; Bouche et al., 2010). In March 2003, the active lava lake in the southern crater had a low level of magma and a daily sinking of the crust was observed (Bouche et al., 2010). Large bubbles were observed either at the edges of the lava lake or at a specific location over the conduit. These bubbles produced Strombolian explosions. We focus on the bubbles coming directly from the conduit as they represent the direct input from the reservoir. Acoustic pressure and brightness temperature were measured at 110 m from the centre of the lava lake for 5 days from March, 22 to March 27 (Figure 5.1a).

Piton de la Fournaise is a shield volcano on Réunion Island, France, in the Indian Ocean. This hot spot volcano produces low-differentiated and low-viscous magma (basalts, 40 Pa.s Albarède et al., 1997; Di Muro et al., 2014; Hibert et al., 2015). Most of the eruptions occur in the Enclos Fouqué caldera since its formation 4745 years ago (Gillot and Nativel, 1989) and can generate either lava flows, lava fountains or weak Strombolian explosions. The eruption initiated on August, 30 2006 was recorded, for the last part of the eruption, using thermal and infrasonic sensors at 115 m from November, 18 to December, 31 (Figure 5.1b). We focus on the 4-day Strombolian phase of the 10–14 of December 2006, during which the signal to noise ratio was the best and the sensors working. Strombolian explosions were located at the only active vent at that time.

Yasur volcano is a pyroclastic cone on Tanna Island, Vanuatu, in the Pacific Ocean. Yasur persistent Strombolian activity is due to the subduction of the New Hebrides (Firth et al., 2014). Stronger Strombolian explosions occur due to a more viscous and differentiated magma (basaltic trachy-andesite, 10^4 Pa.s, Métrich et al., 2011; Gaudin et al., 2014b). A first period of typical activity was recorded from June, 18 to July, 1 2009 using thermal and acoustic sensors at 270 and 280 m, respectively (Figure 5.1c). We focus on the last few days (from June, 28) where the quality of thermal records is optimum. The second period was recorded at 340 m for almost two months from September, 15 to November, 10 2016. Strombolian activity was there much more vigorous with alternation of quiet and strong phases. We only get thermal measurements until October, 10 because of ashes, produced during vigrous phases, covering the solar pannels and thermal sensor not abble to restart automatically when the ashes were displaced by wind or rain. We then focus on the first weeks of the data. During each acquisition several vents were active. We have chosen to keep separately both acquisitions in order to illustrate the variability of Strombolian activity at a same volcano.

5.4 Measurements

Measurements were recorded on a Geostar (Erta'Ale) and a RefTek 130 (Piton de la Fournaise and Yasur) digitizers with sampling frequency of 75 Hz, 1000 Hz, 1000 Hz and 100 Hz at Erta'Ale, Piton de la Fournaise and Yasur 2009 and 2016, respectively. The sensitivities of the digitizers for a gain of 1 is 0.15 mV.bit^{-1} and 1.59×10^{-3} mV.bit^{-1} for the Geostar and the RefTek 130, respectively.

The acoustic pressure was measured by MB2000 (Erta'Ale) and MB2005 (Piton de la Fournaise and Yasur) microbarometers (developed by the CEA-DASE). The sensitivity of the MB2000 microbarometer is 5 mV.Pa^{-1} in the low frequency band [10^{-3} Hz–80 Hz], while the sensitivity of the MB2005 microbarometer is 1 mV.Pa^{-1} in the band pass 10^{-3} Hz–40 Hz. Pipes, ∼30 cm length, were connected to air-entries and covered by scoria as a

(a) Erta Ale: 13/03/2013 (Google Earth)

(b) Piton de la Fournaise: 21/11/2006 (from Dupont (2010))

(c) Yasur: 26/06/2016 (Google Earth)

Figure 5.1 – Location of sensors at (a) Erta'Ale and (c) Yasur. Note that scales are different. (b) Disposition of the sensors at Piton de la Fournaise, the radiometers in a home-made box on the left and the microbarometer MB2005 on the right. The radius of the bubble, in (b), is around 2 m.

natural filter.

The microbarometers measure acoustic pressure or infrasonic waves from every directions and thus from all active vents. The propagation of these infrasonic waves can be disturbed by the wind or the topography.

The brightness temperature was measured using Cyclops 300AF thermometers (Minolta-Land). These thermometers record infra-reds radiations (8 µm–13 µm) in a 1° field of view with a sensitivity of $1\,°C.mV^{-1}$ and an efficient response time of 0.19 s (5.27 Hz). The diameter of the field of view d_{FOV} ranges from 1.92 m to 5.93 m and the area $\mathcal{A}_{FOV}$ from $1.46\,m^2$ to $24.18\,m^2$ due to the different vent-sensor distances and different inclinations of the sensors (Section 4.2.2).

At Piton de la Fournaise and Yasur, two radiometers were used simultaneously to record the brightness temperature at two different heights above the vent. The angle between both radiometers is fixed at 4°, leading to height differences ΔH from 8.02 to 21.15 m (Table 4.4). One should note that the gas and ejecta cloud of an explosion might not reach the upper radiometer depending on the strength of the explosion.

Radiometers are sensible to the existence of hot liquids and solids and their temperature. However, they do not record the gas, due to its very low radiation compared to that of the liquids and solids. The gases can blind the radiometers because they do not let pass the infra-reds (gas opacification). Moreover, due to their small field of view, the Cyclops 300AF record the ejecta from only one vent even if there are several active vents (i.e. Yasur). This small field of view above the vent can also lead to uncertainties when the wind blows the gas and ejecta mixture out of the field of view or when the explosion is inclined.

The radiometers were put into boxes of protection with Zn–Se windows. These windows work as filter and are invisible to infra-red radiations. In theory, these Zn–Se windows let pass 85 % of the infra-red radiations because they are polished on one face, and are handled anti-reflections one the other face (face that is inside the boxes of protection, only 70 % would have remain if the two faces would have been anti-reflection). These windows oxidise due to acid gas and ash, leading to a decrease of the amount of infra-red radiations passing through the windows and hitting the sensor. As the windows were new and because of the weak activity at Erta'Ale and Piton de la Fournaise, we infer the oxidation of the windows can be neglected during field campaigns in 2003 and 2006.

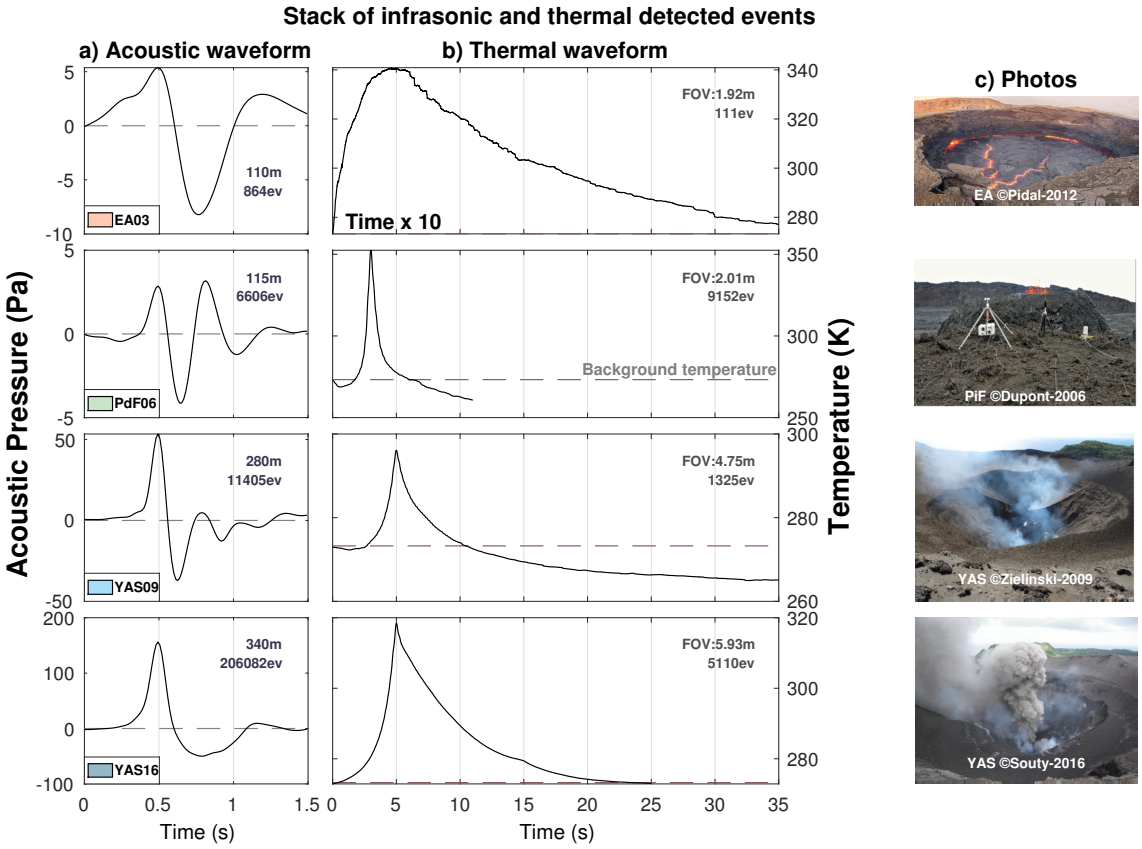

Figure 5.2 – Stacked (a) infrasonic and (b) thermal waveforms of explosions at 1) Erta'Ale, 2) Piton de la Fournaise and 3–4) Yasur volcanoes in June 2009 and Sept-Nov 2016, respectively. Note that the time of Erta Ale thermal waveform which is 10 times longer than other thermal waveforms.

However, the calibrations before and after the field campaign of 2016 make us increase the brightness temperature by a factor 2 for thermal records in 2016. We assume these calibrations are also acceptable for measurements in 2009 because of the short time of the experiments with available thermal data (3 days, here) and the relatively quiet activity at that moment.

5.5 Methodology

5.5.1 Qualitative analysis of the waveforms

It is important to remember that microbarometers measure the acoustic pressure ($\sim$ gas motion) from every direction, while radiometers can only record the temperature of ash and ejecta in the small zone within their field of view. Then radiometers record explosions only at one single vent while microbarometers record explosions from all vents.

Explosions seen on infrasonic records are impulsive due to the sudden decompression of the gas pocket (figure 5.2a). The maximum acoustic pressure p^+, i.e. the maximum amplitude of the compressive phase, is lower than the minimum acoustic pressure $|p^-|$ (minium amplitude of the rarefaction phase) at Erta'Ale and Piton de la Fournaise ($p^+ < |p^-|$, Figure 5.2a1–2). However at Yasur the compressible phase reaches a lower acoustic pressure than the rarefaction phase ($p^+ > |p^-|$, Figure 5.2a3–4). The infrasonic waveforms

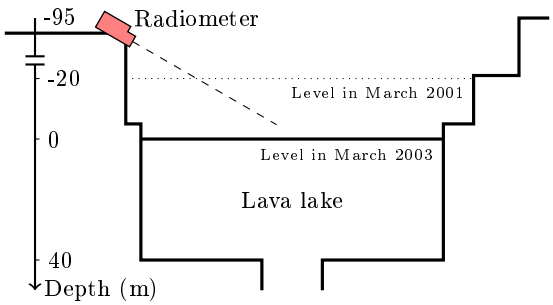

Figure 5.3 – Sketch of the topography of the South lava lake at Erta'Ale. (Adapted from Bouche et al. (2010).)

at Erta'Ale are ∼1 s long and are longer than infrasonic waveforms at Piton de la Fournaise (∼0.75 s) and Yasur (∼0.50 s). The infrasonic waves have typical frequencies of 1 Hz, 3 Hz and 2 Hz at Erta'Ale, Piton de la Fournaise and Yasur, respectively. The long rarefaction phase observed on infrasonic waveform at Yasur in Sept-Nov 2016 can be due to the response of any underlying bubble to the decompression associated to the explosion and/or to the oscillations of the former cylindrical tail of the bursted bubble ((Figures 1.3 and 4.2 Kremers et al., 2013)).

The thermal waveforms at Erta'Ale are very long and are not only representative of the Strombolian activity because even with a restricted filed of view, it reocrds the temperature at the surface of the lava lake around the bursting bubble (Figure 5.2b1 and 5.3). The cold and quasi-solid crust of the lava lake breaks when the gas bubble reaches the surface of the magma column and before the bubble explodes. The hot surface of the lava lake is measured by the radiometer. After the explosion, it takes times for the crust to cool down.

The radiometers record the initial thrust (or spray as it is called in Harris et al. (2012)), one or several closely spaced thrusts close in time, the mixture of the pyroclasts with the atmosphere due to buoyancy effects and the fall and cooling of the pyroclasts. The thermal waveform is then characterised by a short duration ascent of the temperature, followed by one or several maxima. Then the temperature decreases slowly to reach the initial temperature, or even sometimes lower temperatures due to gas opacification. Thermal records at Piton de la Fournaise and Yasur are very similar with an increase of the temperature faster than the decrease (Figure 5.2a2–4). The differences are due to the duration of the emission (duration of the jet) and the duration of the buoyancy (hot ashes in suspension).

5.5.2 Pre-processing

All records were re-sampled at 75 Hz, the lowest sampling frequency of the Geostar digitizer.

The infrasonic data were first pre-filtered between 0.01 Hz and 20 Hz to find the prevalent frequency band of the Strombolian activity at the different volcanoes. We then apply a second filter depending on the strength of the activity, the Strombolian activity frequencies and the noise (0.50 Hz–5 Hz at Erta'Ale, 2 Hz–6.50 Hz at Piton de la Fournaise and 0.10 Hz–10 Hz at Yasur). Thermal data were filtered above 4 Hz because of the efficient response time of the Cyclops 300AF radiometer at 0.19 s.

The detection of Strombolian explosions was performed using several methods depending

Table 5.1 – Parameters of automatic detections. Numbers between braces indicates the order of the Butterworth filter and the number of back-and-forth passes. Note that all data were resampled at 75 Hz.

	EA03	***PdF06***	***YAS09***	***YAS16***
Acoustic				
Pre-Filter [2,1]	0.01–20 Hz	0.01–20 Hz	0.01–20 Hz	0.01–20 Hz
Filter [4,2]	0.50–5 Hz	2–6.50 Hz	0.10–10 Hz	0.10–10 Hz
Detection	x-corr	x-corr	wlt:4–6	wlt:4–5
Threshold	0.80	0.90	2.5	2.5
Details	23/03/03 14:24:38†	10/12/06 21:38:47, 21:39:31	LTA:1.34,1.05	LTA:1.63,2.38
Number of events	1 371	9 387	15 432	206 301
Number of events (>1 Pa)*	864	8 018	15 405	206 082
Thermal				
Calibration	None	None	T(°C) × 2	T(°C) × 2
Low-pass filter [2,1]	4 Hz	4 Hz	4 Hz	4 Hz
Detection	manual	peaking	STA/LTA	STA/LTA
Threshold			1.2	1.5
Details	-	ΔT_1 =120 °C ΔT_2 =70 °C	STA: 2 s LTA: 30 s	STA: 2 s LTA: 30 s
Number of events (RD1)	111	9 263	10 399	15 254
Coupled detections				
Number of events	17	2333	579	3591

* We set this minimum amplitude for detection to keep to avoid noisy signals.
† Bouche et al. (2010)

on the waveform (Figure 5.2), the data quality, the strength of the activity and the noise (Table 5.1).

At Yasur, we use a STA/LTA detector on the coefficient of the wavelet decomposition of level 4–5 (1.17 Hz–4.69 Hz at 75 Hz) to detect the Strombolian events on the infrasonic records at Yasur (11 401 and 106 079 events in 2009 and 2016, respectively). We detect 1323 explosions in 2009 and 5079 in 2016 on thermal records using the STA/LTA detector directly on the signal (STA: 1 s; STA: 60 s). The signal of the lower and upper radiometers were processed independently as the explosive mixture might never reaches the field of view of the upper radiometer (δh = 18 m–21 m in 2009 and 2016, respectively). The low ratio between the number of explosions detected on infrasonic or thermal records is due to the multi-vent activity of Yasur the reduced amount of ejecta in gas-rich explosion or the sometimes high background temperature (residual bombs around vents).

At Erta'Ale and Piton de la Fournaise, detections on infrasonic records were done by cross-correlation using typical waveforms for each volcano. The typical waveforms were selected by looking manually for signals on the infrasonic records. At Erta'Ale, we found 2827 events which fit at 85% the explosion discussed in Bouche et al. (2010) (23/03/2003 14:24:38, figure 5.4a). At Piton de la Fournaise, an event must be correlated at 90% to one of the typical explosions shown in figure 5.4b–c to be taken into account (10/12/2006 21:38:47 and 21:39:31). We thus detect 9387 Strombolian explosions on infrasonic data.

At Erta'Ale we had to look for thermal events manually because of the noisy records we got. We detect 111 events we can process. We could not use the STA/LTA detector efficiently at Piton de la Fournaise because of the numerous events on thermal records. Instead, we consider all increases of the temperature as a potential explosion independently for both records from the lower and upper radiometers. A first selection is done applying a minimum

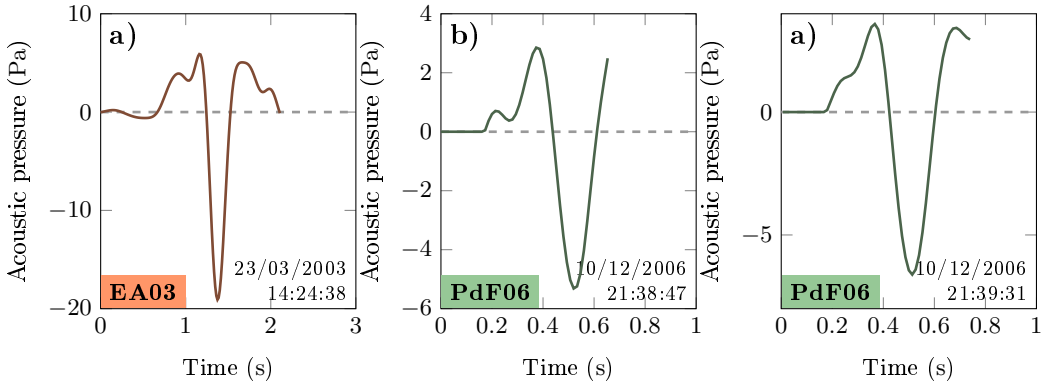

Figure 5.4 – Typical infrasonic waveforms of the explosions of gas pockets at a) Erta Ale and b–c) Piton de la Fournaise. These waveforms were used to detect automatically explosions by cross-correlation.

amplitude variation between the onset and the maximum of the explosion (lower: 120 °C, upper: 50 °C). Finally we only keep 9004 explosions seen on both radiometers. The probability that an explosion is seen on the lower radiometer but not the upper one is low because of the small distance between both radiometers (8 m against 18 m and 21 m at Yasur) and because explosions are not inclined. We consider detections on infrasonic records with maximum amplitudes under 1 Pa are too weak to be kept because of the general noise.

Links between explosions seen by the lower and the upper radiometers are defined by looking for the closest detected event measured by the upper radiometer to an event measured by the lower radiometer. The maximum allowed delay between both events is given by the minimum ejecta velocity ($0.10\,\mathrm{m.s^{-1}}$) and the distance to the vent.

Coupling infrasonic and thermal detections is done by looking for the closest infrasonic detection to a thermal detection. We impose the range of thermo-infrasonic delays $t_{\mathrm{th}} - t_{\mathrm{ac}}$ to be between −10 s and 30 s. The difficulty here is the very short time between explosions at Piton de la Fournaise and Yasur volcanoes (Return times of 45 s and 20 s in average on infrasonic at Piton de la Fournaise and Yasur, respectively).

The detection quantify the number of explosions and their amplitude (acoustic pressure or brightness temperature). The duration of the explosions on infrasonic and thermal records are determined using the envelope of the signal (Sections 4.1.1b and 4.2.1b). The duration and amplitude of the explosions are key parameters to estimate the infrasonic and thermal energies.

5.5.3 Infrasonic processing

We assume the Strombolian explosions are monopole sources and generate infrasonic waves that propagate in all direction at the same speed and attenuate with a factor $1/r_{\mathsf{vent}}$, r_{vent} being the vent-sensor distance.

The infrasonic energy, in an homogeneous atmosphere is

$$\mathrm{E}_{\mathsf{infrasonic}} = \frac{2\pi r_{\mathsf{vent}}^2}{\rho_{\mathsf{atm}} c_{\mathsf{atm}}} \int_0^{\tau} \left(p_{\mathsf{ac}}(t) - p_{\mathsf{air}}(t)\right)^2 \mathrm{d}t \tag{5.1}$$

where r_{vent} is the distance from the source to the sensor (m), ρ_{atm} is the density of the atmosphere at the elevation of the volcano (kg.m^{-3}), $c_{\text{atm}} = \sqrt{\gamma R_{\text{ig}} T_{\text{atm}}} = 340\,\text{m.s}^{-1}$ the sound speed and $(p_{\text{ac}}(t) - p_{\text{air}}(t))$ is the excess of pressure (Lighthill, 1978). Other effects than the linear decay are neglected (e.g. viscosity of the medium, heat transfer,...). Variations of pressure due to the weather, the elevation or the topography are also neglected. The infrasonic power $\text{Pw}_{\text{infrasonic}}$ is obtained by dividing the infrasonic energy $\text{E}_{\text{infrasonic}}$ by the duration τ.

Woulff and McGetchin (1976) established the relation between the gas velocity U_{gas} and the infrasonic power $\text{Pw}_{\text{infrasonic}}$ from a dimensionless analysis of the Navier-Stokes equations and assuming a monopole source; giving

$$\text{U}_{\text{gas}} = \left(\frac{\text{Pw}_{\text{infrasonic}} c_{\text{atm}}}{k \rho_{\text{atm}} 2\pi R_b^2} \right)^{1/4}, \tag{5.2}$$

where k is an experimental constant equal to 1 and R_b is the radius of source, assumed to be that of the bubble (m) (Vergniolle et al., 2004). The radius of the conduit R_{conduit} gives a good estimate of the bubble radius R_b for Strombolian explosions because bubbles are almost as large as the conduit. The greatest uncertainties on the gas velocity are associated to the estimates on the bubble radius R_b because $\text{U}_{\text{gas}} \propto R_b^{-1/2}$.

The origin of the sound and estimates of the gas volume depends on the magma viscosity. A gas pocket within a low viscous magma, such at Erta'Ale and Piton de la Fournaise, oscillates when driving by an inner gas over-pressure, i.e. has small variations of volumes, to restore equilibrium prior to breaking (Kobayashi et al., 2010; Vergniolle and Gaudemer, 2015). The oscillations generate the infrasonic waves when the gas remains trapped (vocal cords, guitar strings). The pre-bursting parameters of the bubble $(R_{b,0}, L_b, \Delta P_b)$ can be estimated using the model based on volume mode oscillations prior to breaking, called for short the bubble vibration model, for the low-viscous magma at Erta'Ale and Piton de la Fournaise (see Section 4.1.3c and Vergniolle and Brandeis, 1996). We assume a magma viscosity of 10 Pa.s and 40 Pa.s (Lemma, 2017; Hibert et al., 2015) and a thickness of the film of magma of 22 cm and 10 cm from visual observations (Bouche et al., 2010; Di Muro et al., 2014) at Erta'Ale and Piton de la Fournaise, respectively.

In contrast, a high viscous magma, such at Yasur, confines the inner gas over-pressure close to the surface, to an extent that bubble volume oscillations are suppressed for the bubble to directly explodes at the surface. The explosion, i.e. the sudden decompression of the bubble, generates the infrasonic waves. The bursting volume of the bubble can be estimated by the two successive integrations of the acoustic pressure for the viscous magma at Yasur (see Section 4.1.3b and Johnson, 2003) by

$$\text{Vol}_{\text{gas},b} = \frac{1}{\rho_{\text{atm}}} \int_0^{\tau} \left(2\pi r_{\text{vent}} \int_0^{t} (p_{\text{ac}}(t) - p_{\text{air}}(t))\,\text{d}t \right) \text{d}t \tag{5.3}$$

where P_{atm} and ρ_{atm} are the pressure and the density of the atmosphere that depends on the elevation of the volcanic source. We call that model for short he gas flux model.

The gas volume per sliding window can be estimated from the gas velocity, assuming that the gas pass through a disk of radius R_{conduit} during the duration of the event as $\text{Vol}_{\text{gas},a} = \pi R_b^2 \text{U}_{\text{gas}} \tau$ (see Section 4.1.3c and Vergniolle et al., 2004). This gas volume per sliding window accounts for the active (explosions) and passive (inter-explosion) degassing.

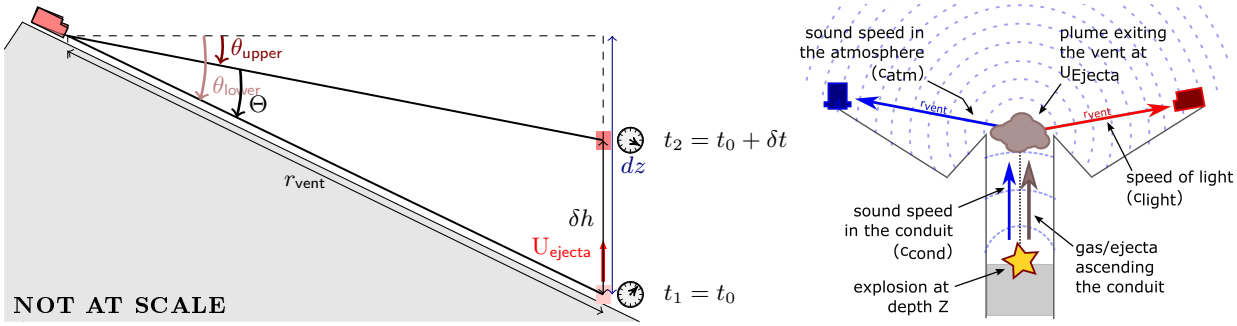

(a) Velocity of the ejecta (b) Depth of the magma column

Figure 5.5 – a) Sketch for the estimation of ejecta velocity from simultaneous records from two radiometers. b) Infrasonic and thermal (IR) wave propagation from the source to the sensor. (Not at scale)

5.5.4 Thermal processing

The thermal energy is estimated from the brightness temperature and using the Stefan-Boltzmann law by (e.g. Marchetti et al., 2009)

$$\mathrm{E}_{\mathsf{thermal}} = \epsilon_{\mathsf{thermal}} \sigma_{\mathsf{thermal}} \mathcal{A}_{\mathsf{FOV}} \int_0^{\tau} \left(T(t)^4 - T_{\mathsf{Back}}^4 \right) \mathrm{d}t, \tag{5.4}$$

where, $\epsilon_{\mathsf{thermal}}$ is the emissivity of the surface of the ejecta (~0.95 for a basalt at 1000 °C, see tables 2.3 and 8.1 in Harris, 2013, for a review), $\sigma_{\mathsf{thermal}}$ the Stefan-Boltzmann constant ($5.67 \times 10^{-8}\,\mathrm{W.m^{-2}.K^{-4}}$), T the brightness temperature (K), T_{Back} the background temperature (K) taken as the temperature just before the explosion and $\mathcal{A}_{\mathsf{FOV}}$ the area of the field of view (m^2) of the radiometer. Thermal energy is then very dependent on the background temperature T_{Back} and the field of view area $\mathcal{A}_{\mathsf{FOV}}$.

The offset of the thermal signal on each detection corresponds to the entry of the first ejecta into the field of view of the radiometer. The delay of the onset on the simultaneous records from two radiometers at different elevation is equal to the flying time of the ejecta between the lower to the upper radiometer. The ejecta velocity $\mathrm{U}_{\mathsf{ejecta}}$ ($\mathrm{m.s^{-1}}$) at Piton de la Fournaise and Yasur can be estimated by (Figure 5.5)

$$\mathrm{U}_{\mathsf{ejecta}} = \frac{r_{\mathsf{vent}} \left(\sin\theta_1 - \sin\theta_2 \right)}{t_{0,\mathsf{upper}} - t_{0,\mathsf{lower}}}. \tag{5.5}$$

Uncertainties are mostly due to the long efficient response time of the radiometers (Section 4.2.4).

We also perform a Particle Imagery Velocimetry (PIV, DaVis 7.2, Lavision Softwares) calculation to compare the ejecta velocity from the flying time of the ejecta between both radiometers and the ejecta velocity recorded on videos at Yasur in June 2009. We perform the PIV using 2 passes on sub-images of 128 px × 128 px and 2 passes on sub-images of 64 px × 64 px with 50 % of overlaps of the sub-images. The video-camera was measuring the same vent that the radiometers were and has a resolution of $3.33\,\mathrm{px.m^{-1}}$ at the distance from the vent giving a maximum velocity of $38\,\mathrm{m.s^{-1}}$.

5.5.5 Thermo-infrasonic processing

The particle size, i.e. the equivalent diameter of the ejecta, can be estimated from the gas and ejecta velocities by a dimensionless analysis of the equation of motion for a turbulent system and for ejecta having terminal velocities (Steinberg and Babenko, 1978). We assume that the particle of diameter D_P and density ρ_{ejecta} is carried with a velocity U_{ejecta} by the gas flow of velocity U_{gas} and density ρ_{gas}. The dimensionless analysis of the equation of motion gives (i.e. the dimensionless weight of the particle is equal to the dimensionless dynamic pressure of the gas; Steinberg and Babenko, 1978)

$$D_P = \frac{3C_D\rho_{\text{gas}}}{4g\rho_{\text{ejecta}}}\left(\text{U}_{\text{gas}} - \text{U}_{\text{ejecta}}\right)^2, \tag{5.6}$$

where $C_D = 0.50$ is the drag coefficient $\rho_{\text{Gas}} = 0.80\,\text{kg.m}^{-3}$ the gas density, $g = 9.81\,\text{m.s}^{-2}$ the constant of gravity and $\rho_{\text{Ejecta}} = 850\,\text{kg.m}^{-3}$ the density of ejecta. The main limitations of the estimations of the particle size using eq. (5.6) lies mostly in the unknown dusty gas density supporting the weight of the ejecta. The uncertainties on the gas and ejecta densities and the ejecta velocities is such that we estimate a rough approximation of the particle size. However these estimates of the ejecta size is very important as it is a key parameter for models of plume dynamics.

The depth of the top of the magma column ΔH, i.e. the elevation of the top of the magma column into the conduit, is estimated from the thermo-acoustic delay $\Delta t = t_{\text{thermal}} - t_{\text{infrasonic}}$ by (Figure 5.5b, e.g. Ripepe et al., 2002)

$$\Delta H = \left(t_{\text{thermal}} - t_{\text{infrasonic}} + \frac{r_{\text{vent}}}{c_{\text{atm}}}\right)\frac{c_{\text{conduit}}\text{U}_{\text{ejecta}}}{c_{\text{conduit}} - \text{U}_{\text{ejecta}}} \tag{5.7}$$

where c_{conduit} is the sound speed into the conduit.

The sound speed in the conduit, considering a homogeneous two-phase flow between gas and ejecta and a dilute suspension, is estimated by (Wood, 1955)

$$c_{\text{conduit}} = \frac{1}{\sqrt{\left(\alpha_{\text{gas}}\rho_{\text{gas}} + (1-\alpha_{\text{gas}})\rho_{\text{ejecta}}\right)\left(\frac{\alpha_{\text{gas}}}{\rho_{\text{gas}}c_{\text{gas}}^2} + \frac{1-\alpha_{\text{gas}}}{\rho_{\text{ejecta}}c_{\text{ejecta}}^2}\right)}}. \tag{5.8}$$

The proportion of gas and ejecta in the conduit impacts a lot on the sound speed.

5.5.6 Gas flux from SO_2 and gas ratio measurements

We can estimate the gas volume flux from the SO_2 flux (COSPEC, DOAS, U.V. camera) and gas ratio (FTIR, multigas) measurements. We consider only the most voluminous species of gas: CO_2, H_2O, SO_2 and HCl.

The mass flux q_{X} (kg.s^{-1}) of each species X is calculated, from the mass flux q_{SO_2} of the SO_2, given in kg.s^{-1}, and the molar ratio [X] / [SO_2], by

$$q_{\text{X}} = \frac{[\text{X}]}{[SO_2]}q_{SO_2}\frac{M_{\text{X}}}{M_{SO_2}}, \tag{5.9}$$

where M_{X} and M_{SO_2} are the molar mass, in g.mol^{-1}, of the species X and SO_2, respectively.

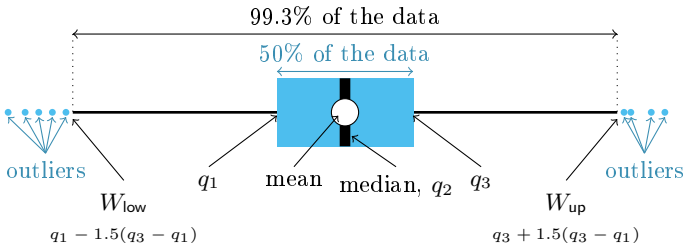

Figure 5.6 – Identification of the different patterns of a boxplot. The colored boxes are limited by the 25^{th} and 75^{th} percentiles (q_1 and q_3) of the data and thus contains 50% of the data. Vertical thick lines show the median (50^{th} percentile) and the white circle the mean of the data. Horizontal thin lines correspond to the whiskers, such as the lowest bound is $q_1 - 1.5(q_3 - q_1)$ and the uppest bound is $q_3 + 1.5(q_3 - q_1)$. For a normal distribution, 99.3% of the data are within these whiskers. Light dots around the whiskers show the outliers. You can refer to the MatLab documentation of the boxplot function.

The gas volume flux of X ($\text{m}^3.\text{s}^{-1}$) is

$$\text{Vol}_{\text{X}} = \frac{q_{\text{X}}}{\rho_{\text{X}}}; \tag{5.10}$$

where ρ_{X} is the density of the species X, at the pressure P_{atm} and temperature T_{magma}, calculated using the ideal gas law, by

$$\rho_{\text{X}} = \frac{P_{\text{atm}} M_{\text{X}} \times 10^{-3}}{R_{\text{ig,mol}} T_{\text{magma}}}, \tag{5.11}$$

with the universal molar gas constant $R_{\text{ig,mol}} = 8.31\,\text{J.mol}^{-1}.\text{K}^{-1}$.

The total gas volume flux is obtained by summing the gas volume flux of each species

$$\varphi_{\text{gas}} = \sum_i \text{Vol}_{\text{X}_i}, \qquad \text{X}_i = \{\text{CO}_2; \text{H}_2\text{O}; \text{SO}_2; \text{HCl}\}. \tag{5.12}$$

An example can be found in appendix B.1.

5.5.7 Basic considerations: analysing a boxplot

We chose to present the results in boxplots instead of histograms (Figure 5.6). Firstly, it gives more quantitative values such as the mean, the median, the 25^{th} and 75^{th} percentiles. Secondly, due to the numerous cases and parameters, histograms would have taken many pages and thus would have been less readable. Thirdly, it gives a good idea of the symmetry of the distribution and of the values that are sightly abnormal.

A boxplot consists in a plain box which represents 50% of the data. The lower and upper limits are the 25^{th} and 75^{th} percentiles, q_1 and $q3$ respectively. The median (q_2) is displayed by the vertical thick line inside the box and is more or less aligned with the centre of the box. The mean is shown by the white circle and can also be offset from the centre of the box. When the mean and the median are aligned in the center of the box, the distribution is symmetric. The whiskers defined by $W_{\text{low}} = q_1 - 1.5(q_3 - q_1)$ and $W_{\text{up}} = q_3 + 1.5(q_3 - q_1)$ contains 99.3% of the data for a normal distribution and are at the edges of the horizontal and thin lines on both sides of the box. The outliers spread out of the whiskers as dots and show the *abnormal* values.

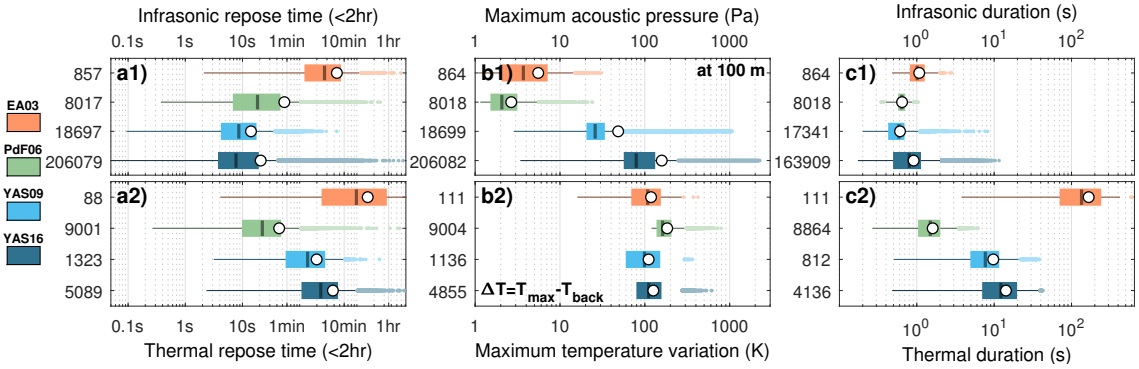

Figure 5.7 – Distribution of a) time interval between two successive explosions, b) maximum variation of amplitude per explosions and c) duration of explosions detected on 1) infrasonic records and 2) thermal records. The maximum acoustic pressure per event is scaled at 100 m Numbers in y-axis indicates the number of events taken into account for the distribution.

5.6 Results

5.6.1 Distribution of the key parameters: amplitude, duration and repose time

The amplitude and the duration of Strombolian explosions and the repose time between two successive Strombolian explosions are key parameters because they characterise the Strombolian activity at a low level of data processing (figure 5.7). These key parameters are the least error-prone results. The quality of the determination of theses key parameters determines the quality of the calculations of the energies, the velocities and the volumes per explosion.

The infrasonic repose times dt_{explo} range from 0.05 s to 6449 s (if $dt_{explo} < 2$ h, or 0.05 s to 3248 s if $dt_{explo} < 1$ h) (figure 5.7a1). The Strombolian explosions at Yasur are more frequent than at Piton de la Fournaise or Erta'Ale. The mean and median repose times are [21.3,10.7] and [17.1,10.1] at Yasur in 2009 and 2016 while the mean and median repose times are [454,272] and [53.9,18.3], at Erta'Ale and Piton de la Fournaise, respectively. The median values are similar for the infrasonic repose times at Yasur in 2009 and 2016. The mean value in 2009, however is higher than the mean value in 2016 possibly because of the duration of the quiet phases exceeds the duration of the vigorous phases (see figure 6.9).

The thermal repose times range from 0.27 s to 7197 s (if $dt_{explo} < 2$ h, or 0.27 s to 3543 s if $dt_{explo} < 1$ h). (figure 5.7a2). The thermal repose times at Yasur are longer than the infrasonic repose times because the infrasonic sensor records explosions from all vents while the thermal sensor records explosions at two vents in 2009 (one almost behind the other one) and 1 vent in 2016. The mean and median values in 2009 are almost twice the mean and median values in 2016 (1 vents in 2016 against 2 vents in 2009; 2009: [198,138]; 2016: [368,232]).

The maximum acoustic presssure per Strombolian explosion is up to 2268 Pa at 100 m (figure 5.7b1). The maximum acoustic pressure is higher at Yasur ([57,28] and [158,79]) than at Erta'Ale ([5.5,3.7])) or Piton de la Fournaise ([2.7,2.0]). The Strombolian explosions at Yasur are stronger than at Erta'Ale or Piton de la Fournaise, as expected. This wide range of the maximum acoustic pressures shows the variability of the Strombolian activity. The Strombolian explosions at Yasur are stronger in 2016 than in 2009. These different distributions at Yasur volcano, at different times, show the temporal variability of the

Strombolian activity at a same volcano and highlight the need of giving lower and upper bounds to the parameters that characterise the Strombolian activity.

The maximum acoustic pressure per explosion at Yasur is a good example to understand the differences between the mean and median values. The mean value of the maximum acoustic pressure at Yasur in 2016 is 158 Pa at 100 m. This mean value exceeds the 3rd percentile (133 Pa) of the distribution of maximum acoustic pressure. The mean value of the maximum acoustic pressure is increased by the less frequent but very strong explosions. The mean value of a distribution is not revealing of its distribution when given alone. For a normal distribution, the mean and the standard deviation values are self sufficient. For assymetric distributions, the mean value must be given with additional values such as the quartiles (q_1, q_2, q_3) to represent the distribution.

The maximum temperature variation per Strombolian explosion is up to 795 K. The maximum temperature variation is larger at Piton de la Fournaise than at Yasur because i) the magma is less differentiated, and then hotter at Piton de la Fournaise than at Yasur and ii) because the background temperature measured between two successive explosions is lower at Piton de la Fournaise than at Yasur. The radiometer is horizontal at Piton de la Fournaise and then sees the sky behind the explosion while at Yasur, the radiometer is inclined to the vent and sees the hot surface of the volcano. While we would have expected Erta'Ale and Piton de la Fournaise to have similar distributions of the maximum variation of temperature due to the initial temperature of the magma, we observe that Erta'Ale lies below Piton de la Fournaise. One interpretation could be related to the bias of the thermal measurements at the surface of the lava lake, whose background temperature is always higher than the temperature of the Strombolian cone at Piton de la Fournaise.

The infrasonic durations reflect the frequency of explosions. The shorter the infrasonic waveform is, the higher is the frequency of the explosion and so its energy. The typical infrasonic duration is around 1 s at Erta'Ale (figure 5.7c1). Explosions on infrasonic records are shorter at Yasur and Piton de la Fournaise than at Erta'Ale. The explosions at Piton de la Fournaise and at Yasur generates higher frequencies than at Erta'Ale and thus are more energetic. The distribution of infrasonic durations is wider at Yasur than at Piton de la Fournaise. The range of activity is then wider at Yasur than at Piton de la Fournaise.

The thermal durations of the Strombolian explosions are harder to interpret as thermal signals are more complex than infrasonic signals due to the interaction of several mechanisms (input of the ejecta into the atmosphere, buoyancy, falling down and cooling of the ejecta, etc.). The thermal durations of the Strombolian explosions are very long at Erta'Ale because of the recording of the lava lake temperature. The thermal durations of Strombolian explosions at Piton de la Fournaise are shorter than at Yasur because i) the Taylor bubbles are less voluminous at Piton de la Fournaise than at Yasur and/or ii) Strombolian explosions are richer in ashes at Yasur than at Piton de la Fournaise and these ashes remain longer in suspension than the scoria and iii) strong explosions can excite additionnal sources of resonances and trigger an oscillating motion of the magma column that can be recorded by the radiometer.

5.6.2 Distribution of energy, velocity and volume

The infrasonic and thermal energies are also good indicators of the strength of an explosion (Figure 5.8a). Infrasonic energies range from 18 J to 3.7×10^8 J while thermal energies

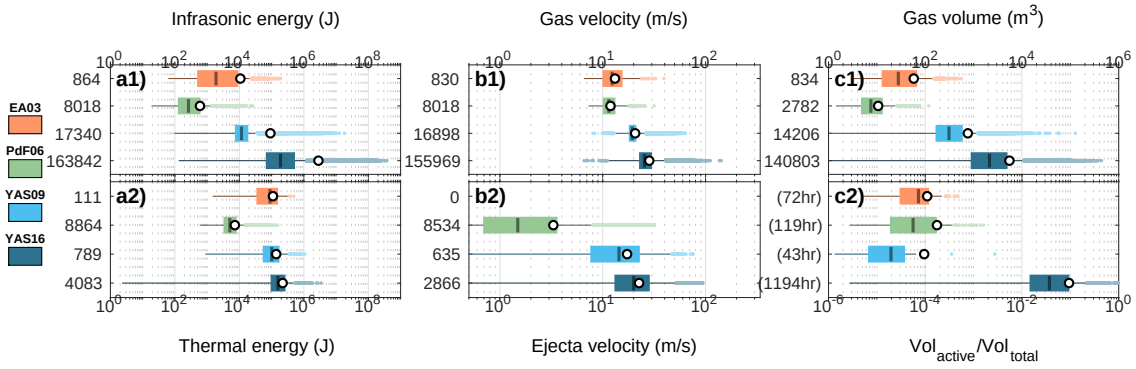

Figure 5.8 – Distribution of a) energy, b) velocity and c) volumes for 1) events detected on infrasonic records and 2) events detected on thermal records. The ejecta velocity is estimated using their time flight between the two radiometers, based on the onset of the explosion. The method to calculate gas volume per explosion was chosen depending on the volcano and its typical waveforms: we use the bubble vibration mode model to estimate gas volume at Erta'Ale and Piton de la Fournaise, and the volume from two successive integrations of the acoustic pressure at Yasur. Numbers in y-axis indicates the number of events taken into account for the distribution.

range only from 2 J to 3.6×10^6 J. Infrasonic range is then much more dynamic (wide). As expected, Strombolian explosions at Yasur have higher infrasonic energies than at Erta'Ale and Piton de la Fournaise. Infrasonic energy is higher at Erta'Ale than at Piton de la Fournaise. Thermal energy is higher at Erta'Ale due to the record of the lava lake surface. However while temperature variations are larger at Piton de la Fournaise, we observe that thermal energy is smaller. This is due to the fact that thermal duration are much longer at Yasur (longer/bigger gas pockets and/or more ashes).

The gas and ejecta velocities reflect more the dynamic of the explosions than energies which inform on the strength of the explosions. The difference between gas and ejecta velocities reflects the two-phase flow behaviour of explosions with larger gas velocities than ejecta velocities (Figure 5.8b). Indeed ejecta are set into motion by the gas decompression and only the smallest fragments are abble to move at the gas velocity. Strombolian explosions at Yasur have higher velocities than at Erta'Ale and Piton de la Fournaise, as expected.

However the long response time of the radiometers leads to large errors on the ejecta velocity (Figure 4.21). The comparison of the ejecta velocity from the thermal records with the ejecta velocity from the PIV analysis shows some difference but we observe the same order of magnitude for both methods (Figure 5.9), despite some divergences that are probably due to the larger window when using the PIV method than the diameter of the field of view of the radiometers (Figure 4.24b). Moreover, the location of the video and the radiometers is such that two vents were recorded during the field campaign in June 2009 (Figure 5.10). We assume that vents are separated by a distance exceeding twice the conduit diameter for the vents to be maintained separated (>10 m). The record of the two vents can increase the uncertainty on the vent-sensor distance (r_{vent}) and thus on the estimates of ejecta velocity.

I was careful during the 2016-field campaign to target only one vent, but this is surely available only when I stayed on Tanna (before the 20th of September). Vents could have closed up or opened in the field of view of the radiometers after that date. At Piton de la Fournaise, only one vent was active during the studied period.

As written above (§5.5.3), the method to calculate the gas volume depends essentially on the magma viscosity. A gas pocket within a low viscous magma, such at Erta'Ale and

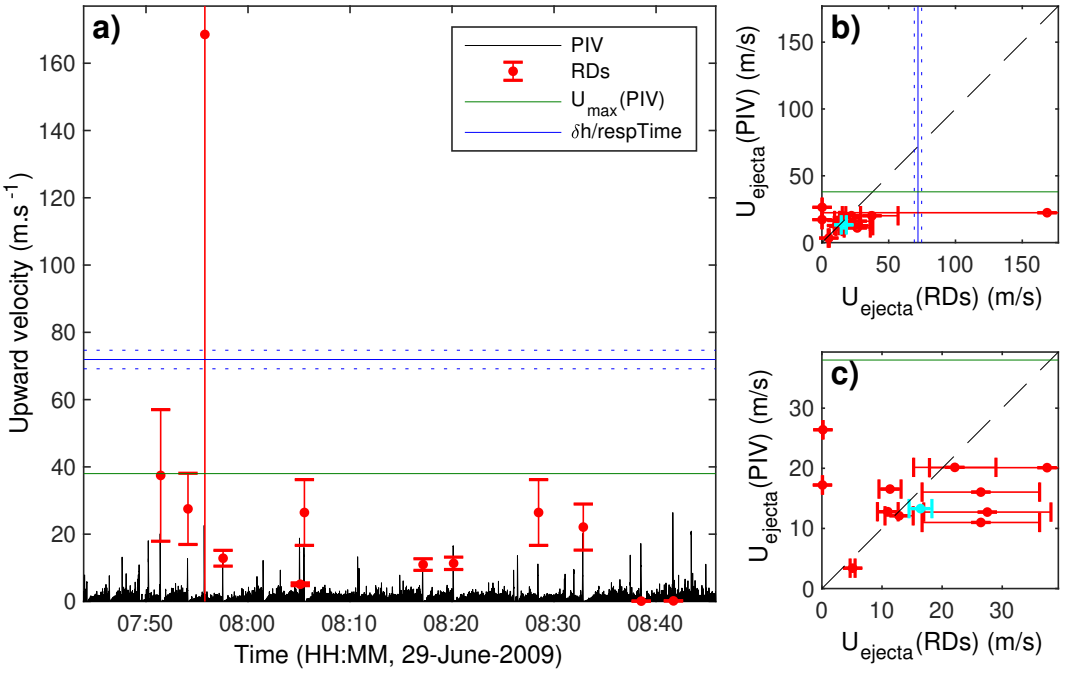

Figure 5.9 – Comparison of the two methods to estimate the ejecta velocity. a) Velocity profile from the PIV (black, video7-YAS09) the value of the velocities from the thermal records (red). b) Comparison of the velocity from both methods. c) Comparison from of the velocity from both methods (ZOOM). The cyan point is the example from video6-YAS09 (figures 4.22 and 4.22)

Piton de la Fournaise, oscillates to restore equilibrium and generates the infrasonic waves when the gas remains trapped (bubble vibration model). In contrast, a gas pocket in a high viscous magma, such at Yasur can not oscillates and generates the infrasonic waves when exploding (gas flux model).

The gas volumes range from $1.3 \times 10^2\,\mathrm{m}^3$ to $2.3 \times 10^4\,\mathrm{m}^3$ (Figure 5.8c). We observe the stronger explosions of Yasur is due to longer gas pockets (more voluminous pockets but the radius of the bubble is constrained by the radius of the conduit).

The comparison between the gas volume from the gas flux model and the gas volume from bubble vibration model at Erta'Ale and Piton de la Fournaise gives a ratio between both volumes of 0.13 and 0.25 at Erta'Ale and Piton de la Fournaise, respectively (Figure 5.11). This shows how important is the choice of the appripriate model for the source of sound, whose volume can only be correctly estimated by one method and not the two simultaneously.

The ratio of active gas volume (explosions) to total gas volume (explosions and inter-explosion) gives a qualitative information on the efficiency of the passive degassing (inter-explosion) and the strength of the explosions (Figure 5.8c2). The strong difference of that ratio observed at Yasur can be easily explained by a higher rate of explosions and the occurence of stronger explosions in Sept-Nov 2016 (Figure 5.7a1,b1), while the passive degassing remains quite similar (Figure 5.18).

5.6.3 Considerations on the depth of the top of the magma column

We can calculate the depth of the explosions (i.e. the depth of the top of the magma column), from the thermo-infrasonic delay. We assume, from the viewing of the videos,

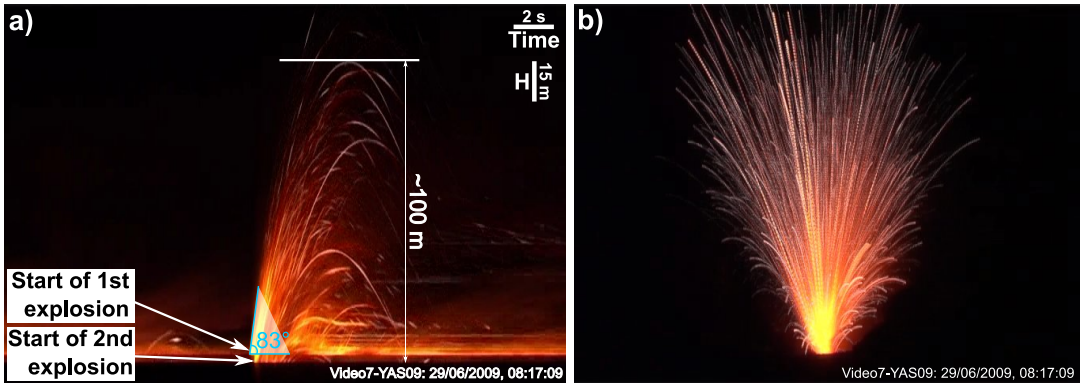

Figure 5.10 – a) Horizontal stack of a column of pixels, from the video frames, centered on the center of the vent (video7-YAS09). b) Stack of the video frames of an explosion at Yasur using *ImageJ* (*Image/Staks/Zproject with maximum intensity*). Explosion taken on video7-YAS09 (29/06/2009 - 08:17:09). The angle designed in cyan gives a initial velocity of the explosion at ∼66 m.s^{-1} and we measure a maximum height of ∼100 m.

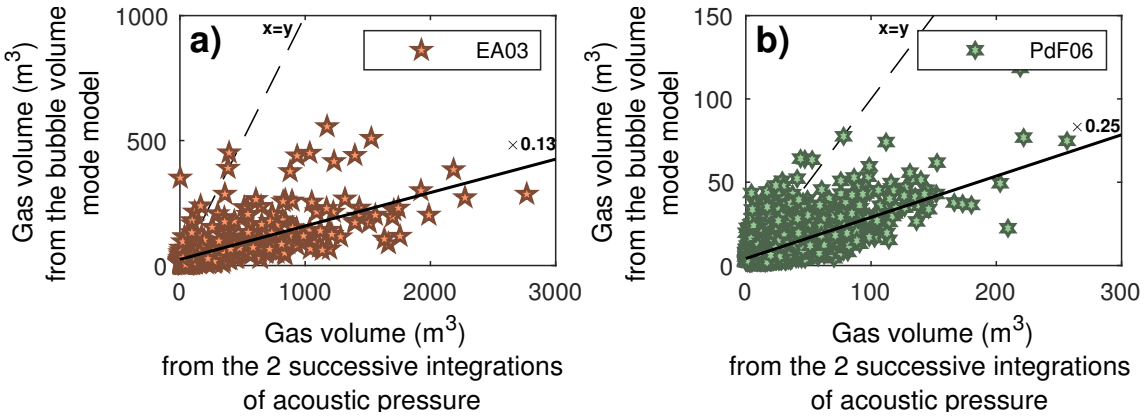

Figure 5.11 – Comparison between the gas volume from the gas flux model and the gas volume from the bubble vibration model at a) Erta'Ale b) and Piton de la Fournaise.

that the mean gas volume fraction is 0.95 at Piton de la Fournaise and 0.50 and 0.97 at Yasur for ash-rich and gas-rich respectively.

We assume the gas and ejecta densities are 0.8 kg.m^{-3} and 850 kg.m^{-3}, respectively (Harris et al., 2012). The sound speed into the conduit, in case of an ejecta pure medium, is assumed to be 2500 m.s^{-1} (Kress and Carmichael, 1991). The sound speed into the conduit, in case of a gas pure medium, is 742 m.s^{-1} and 768 m.s^{-1} for magma temperature of 1100 °C and 1200 °C at Yasur and Piton de la Fournaise, respectively (Métrich et al., 2011; Di Muro et al., 2014). The sound speed into the gas-ejecta mixture within the conduit is then estimated between 45.5 m.s^{-1} and 131.5 m.s^{-1} (Table 5.2).

The estimates of the depth are widely spread because of the numerous uncertainties (Figure 5.12b–c). The greatest uncertainty is due to the chopped signal of the radiometers that accounts for the ejecta velocity and the thermo-acoustic delay (Figure 5.12a, figure 5.8b1 and figure B.2). The mean values seems to be over-estimated because of these uncertainties while the median values are more consistent with the distribution of depths (Figure 5.12b4–c4, table 5.3a).

We can not estimate the depth of the top of the magma column at the initiation of each explosion, because of these large uncertainties. However we can perform a Monte Carlo

Table 5.2 – Parameters for the calculation of the sound speed into the conduit at Piton de la Fournaise and Yasur.

	T_{magma} (°C)	$c_{conduit}^{gas\ pure}$ (m/s)	$c_{conduit}^{ejecta\ pure}$ (m/s)	ρ_{gas} (kg/m^3)	ρ_{ejecta} (kg/m^3)	α_{gas} ( )	$c_{conduit}^{mixture}$ (m/s)
PdF	1200	768	2500	0.80	850	0.95	107.20
YAS: gas-rich	1100	742	2500	0.80	850	0.97	131.50
YAS: ash-rich	1100	742	2500	0.80	850	0.50	45.50

Table 5.3 – Estimates of the depth of the magma columns. a) Direct calculation (95 % of the data). b) Monte Carlo analysis (95 % of the data).

a) Direct calculation (m)	q_1	median	mean	std	q_3
PdF06	−2.9	1.6	8.9	26.2	11.2
YAS09: gas-rich	−5.1	0.4	9.5	58.8	11.0
YAS09: ash-rich	−9.0	0.3	9.7	85.3	13.6
YAS16: gas-rich	0.6	33.7	63.1	114.3	89.9
YAS16: ash-rich	0.2	33.6	74.4	243.2	113.9

b) Monte Carlo analysis (m)	q_1	median	mean	std	q_3
PdF06	−1.2	2.1	4.6	11.2	6.9
YAS09	−31.8	0.7	6.3	94.9	40.7
YAS09: gas-rich	−29.0	0.9	6.2	70	37.4
YAS09: ash-rich	−35.5	0.8	8.5	146.0	45.1
YAS16	−22.3	51.4	76.2	210	141.7
YAS16: gas-rich	55.2	59.3	59.8	6.1	63.9
YAS16: ash-rich	−30.7	54.8	74	350	162.2

analysis to take into accounts the uncertainties and give a range of value for the level of magma (See section 3.1.5). Input parameters are normaly distributed with a mean μ and a standard deviation σ (See sub-figures a1) to b2) in figure 5.13 as an example. Other example are given in appendix B.4). The results are given in table 5.3b. The median depth estimated, for gas-rich explosions, directly from the data is 0.40 m at Yasur in June 2009, while the median from the Monte Carlo analysis is 0.90 m (Table 5.3). The error is then not large. However, the error on the mean depth, for gas-rich explosions at Yasur in June 2009, is bigger with an estimate of 9.50 m from the direct calculation and 6.20 m from the Monte Carlo analysis. Note that, when the level of magma is very shallow as in June 2009, obtaining negative depth of the top of the magma column is part of the uncertainty. The similar number of negative (30 302) and positive (31 353) values suggets that the top of the magma column is very close to the surface (Figure 5.13).

The differences between the spreading of the results using the direct calculation or the Monte Carlo analysis are large (Figure 5.14b–c). However error from the direct calculation or the Monte Carlo analysis remains small for the median and mean values (Figure 5.14a). Then, the estimation of the depth of the top of the magma column can be done using only one of the proposed method.

The depth of the magma column is very shallow during the field campaigns (<100 m). The top of the magma column can be assumed, from the field observations and the estimates of the depth, to be at the same level than the surface during the field campaigns at Piton de la Fournaise and at Yasur in 2009. However, the top of the magma column, at Yasur in 2016 is sightly deeper (∼50 m) than in 2009 (∼0 m). The difference of depth will be

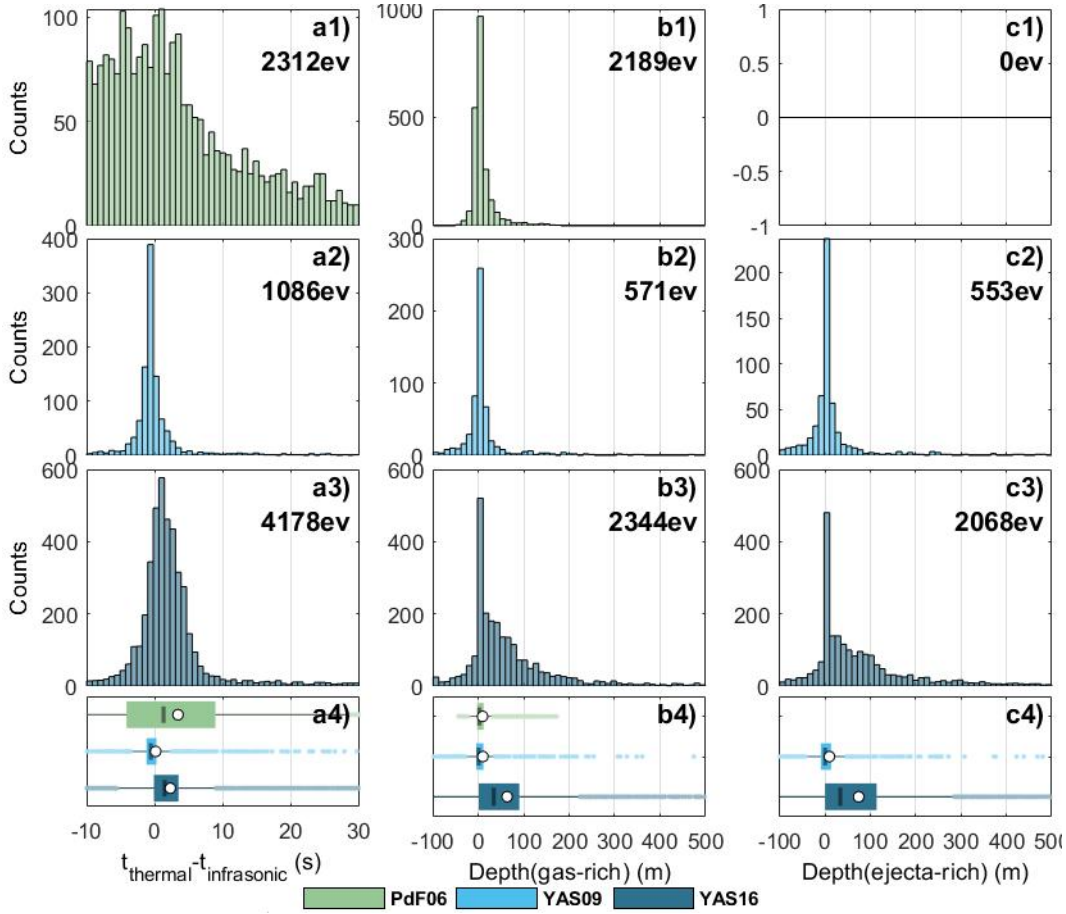

Figure 5.12 – Estimation of the depth of the magma column, considering fixed value of the gas volume fraction for the calculation of the sound speed into the conduit. a) Thermo-infrasonic delay. b) Depth of the explosions considering gas-rich explosions ($\alpha_{gas} = 0.95$ and 0.97 at Piton de la Fournaise and Yasur, respectively). c) Depth of the explosions considering ash-rich explosions ($\alpha_{gas} = 0.50$ at Yasur).

discussed in the next chapter (Chapter 6).

The depths were estimated here considering that the conduit, below the targeted vent, is not inclined. This hypothis seems valid at Yasur, in June 2009, as no prefered trajectories were observed (figure 5.10, the stack is obtained using *ImageJ* and the command *Image/Staks/Zproject with maximum intensity* and can be compared to a long time exposure photo). I did not see any inclination of the gas and magma mixture released during explosions at the targeted vent in 2016 (observed from different point of view).

5.6.4 Budget of energy

It is interesting to look at the partionning between thermal and infrasonic energies, especially because of the different spreading of these energies (Figure 5.8a and B.2). No trend appears by comparing the thermal energy to the infrasonic energy (Figure 5.15a). However a clear cut exists between the infrasonic energy of the weak Strombolian explosions at Piton de la Fournaise and the infrasonic energy of the strong Strombolian explosions at Yasur. The few points of comparable energies at Erta'Ale are probably due to strong bias because of the difficulties, related to the weak signal to noise ratio, we had to link the few thermal

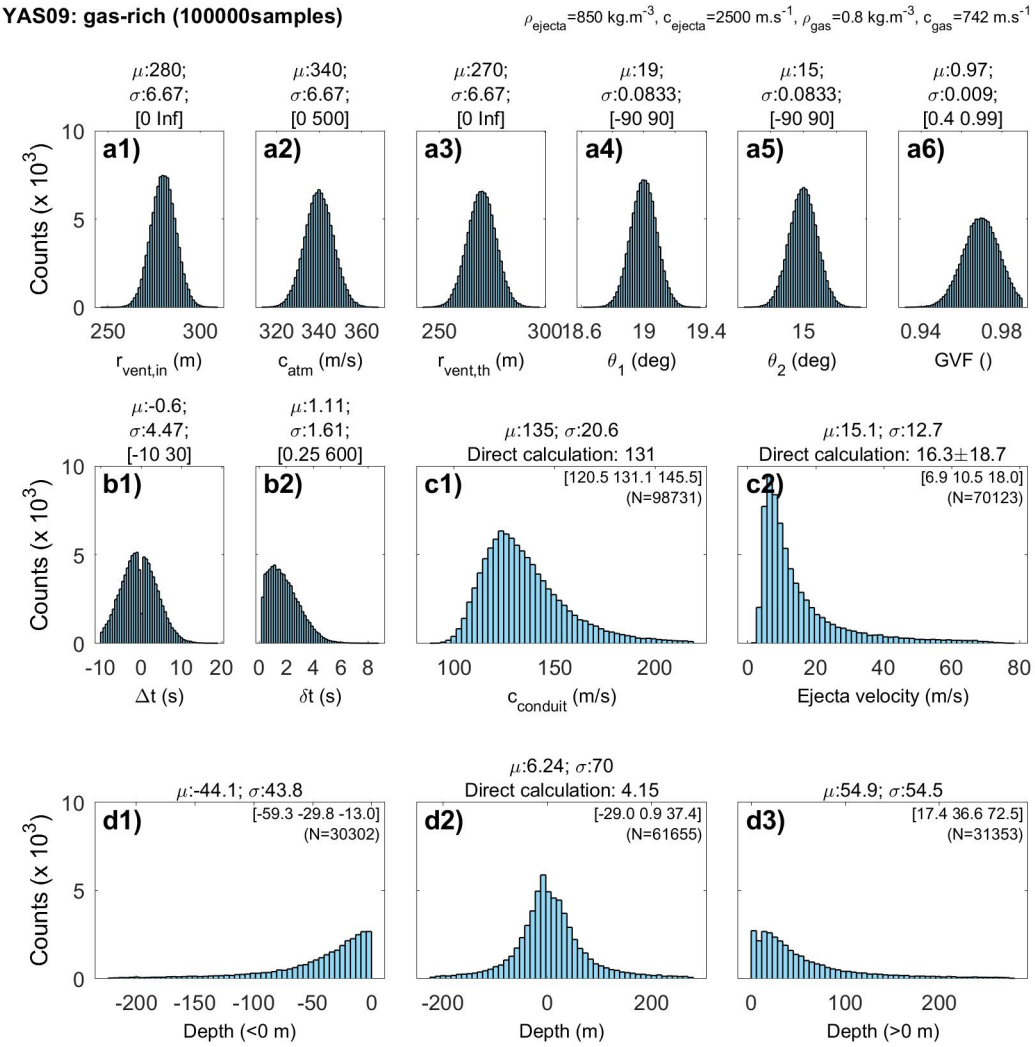

Figure 5.13 – Monte Carlo analysis to estimate the depth of the magma column for gas-rich explosions at Yasur in June 2009. a) Parameters: 1) $r_{\text{vent}}^{\text{infrasonic}} = (280.00 \pm 6.67)\,\text{m}$; 2) $c_{\text{atm}} = (340.00 \pm 6.67)\,\text{m.s}^{-1}$; 3) $r_{\text{vent}}^{\text{thermal}} = (270.00 \pm 6.67)\,\text{m}$; 4) $\theta_1 = (19.0 \pm 0.8)°$; 5) $\theta_2 = (15.0 \pm 0.8)°$; 6) $\alpha_{\text{gas}} = 0.970 \pm 0.009$. b) Measurements on the records: 1) thermo-infrasonic delay and 2) delay of the radiometers. c) Intermediate estimates: 1) sound speed in the conduit and 2) ejecta velocity. d) Results: 1) depth below 0 m, 2) all depth and 3) depth above 0 m.

events to the infrasonic events. However the infrasonic energy at Erta'Ale fills the gap between the infrasonic energy of the weak explosions at Piton de la Fournaise and the infrasonic energy of the strong explosions at Yasur (Figure 5.8a1 and B.2a). The thermal energy at Erta'Ale is bias from the appearance of the hot former bubble bottom, after the explosion, which is not observed at Piton de la Fournaise nor at Yasur.

Marchetti et al. (2009) use the infrasonic and thermal energies to approximate the buoyant energy $\text{E}_{\text{buoyant}}$ and gas-thrust energy $\text{E}_{\text{gas-thrust}}$, such as

$$\begin{cases} \text{E}_{\text{gas-thrust}} &= \text{E}_{\text{infrasonic}}, \\ \text{E}_{\text{buoyant}} &= \text{E}_{\text{thermal}} - \text{E}_{\text{gas-thrust}}. \end{cases} \tag{5.13}$$

They made the implicite approximations that i) the infrasonic energy is only due to the gas-thrust (i.e. there is no other processes responsible for the infrasonic energy), ii) the gas-thrust energy is similar to the ejecta-thrust energy and iii) the buoyancy exists mostly for ejecta (the radiometers are little sensible to the gas considering that they see the

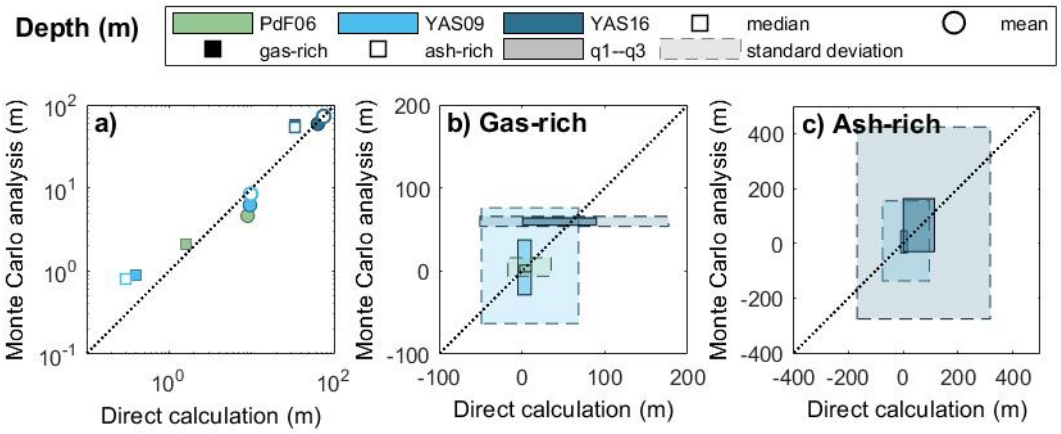

Figure 5.14 – Comparison of the depth estimates obtained from the direct calculation and obtained from the Monte Carlo analysis. a) Comparison of the mean (◯) and median (□). Comparison of the spreading for b) gas rich explosions and c) ash rich explosions. The dotted lines show $x = y$. Data are taken from table 5.3.

whole eruptive column). The gas-thrust and buoyancy energy partitionning highlights two different trends for the Vulcanian activity (Santiaguito and Fuego shadowed in blue) and the Strombolian activity (Villarrica and Stromboli sahdowed in pink) when plotting the buoyant energy as a function of the gas-thrust energy (Figure 5.15b).

Our estimates of *buoyant* energies are smaller than the *buoyant* energy of Strombolian explosions at Villarrica and Stromboli (data from Marchetti et al. (2009)). This is related to the difference in the fields of view. Thermal measurements at Villarrica and Stromboli were done using infra-red radiometers with a large field of view that contains the whole eruptive column (15°: from 29 m to 652 m) while the field of view of the radiometers we have used at Erta'Ale Piton de la Fournaise and Yasur are small (1°: from 1.92 m to 5.93 m). Our measurements reflects only what is directly out going from the vent and falling back into the vent, and is thus less dependant on the state of the atmosphere (wind, temperature, pressure, meteorologic conditions, etc.). In contrast, Marchetti et al. (2009) have a record of additionnal mechanisms such as the falling and cooling down of the ejecta farther from the vent and the whole buoyancy of the volcanic cloud averaged on a larger height (Figure 5.15c). Hence the name *buoyant* given for $E_{thermal} - E_{gas\text{-}thrust}$ is not accurate in our case and we can not directly compare their results with our results.

However, the relationship between $E_{thermal} - E_{gas\text{-}thrust}$ and the infrasonic energy gives the evidence that Strombolian explosions have a similar mechanism of fragmentation despite the large range of intensity at Yasur and Piton de la Fournaisewhich give the two end members of the Strombolian activity in term of intensity. By extension, this result suggests that Stromboli and Villarrica, that clearly produce explosions different from those produced by Vulcanian activity (Fuego and Santiaguito, Marchetti et al., 2009) will be behaving similarly to Piton de la Fournaise and Yasur providing a 1° field of view radiometer measuring just above the vent. Hence it is likely that Strombolian explosions behave similarly worldwide. Note also that our observation at Yasur in June 2009 and Sept-Nov 2016 are very similar despite the fact that the explosions were deeper in 2016 than in 2009.

The ratio of gas and ejecta velocities is another way to study the budget of energy and characterise the two-phase flow dynamics of the Strombolian explosions. There are some

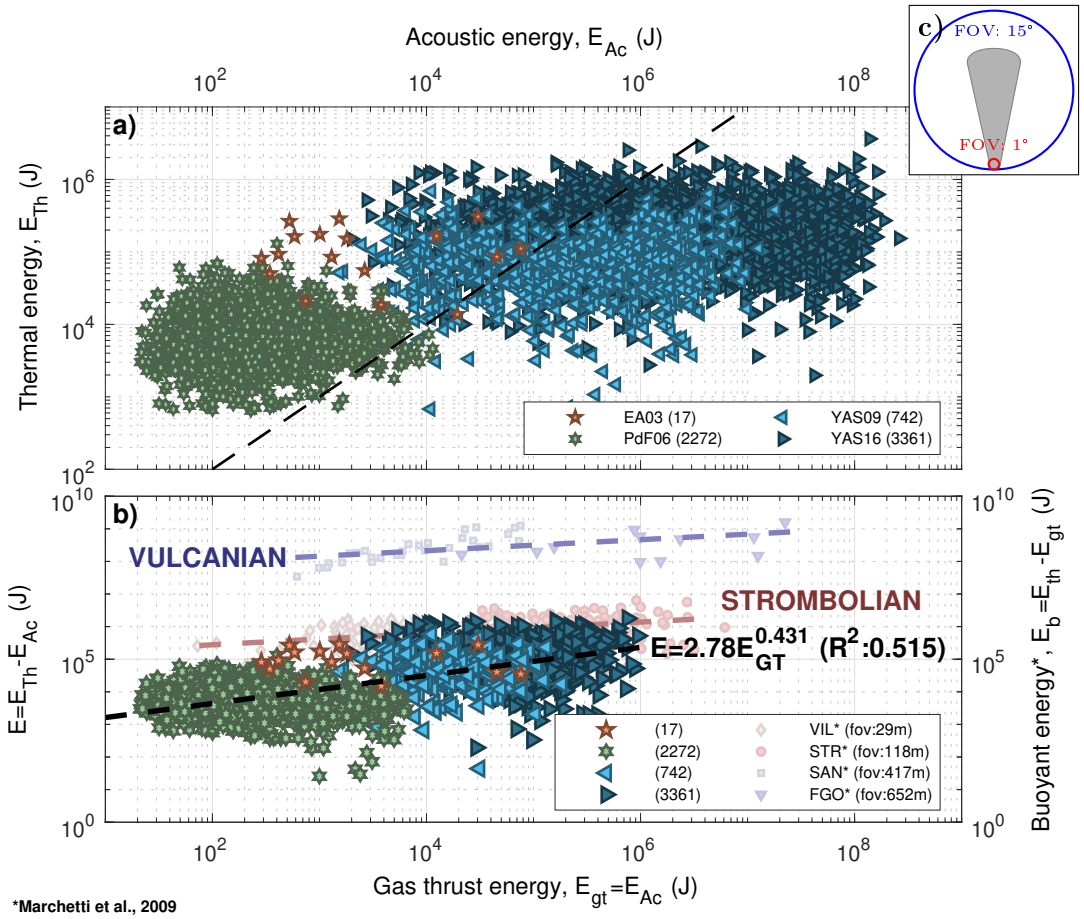

Figure 5.15 – Budget of energy at Erta'Ale, Piton de la Fournaise and Yasur. a) Thermal energy as a function of infrasonic energy. b) Buoyant energy as a function of the gas thrust energy with the data from Marchetti et al. (2009) as the underlayer. The numbers within the parentheses indicate the number of explosions displayed on the figure. c) Sketch of the difference of the field of view area for two radiometers, at the same distance to a hot source, with their angle of field of view equal to 1° and 15°.

events for which $U_{ejecta} > U_{gas}$. We do not expect to have events for which $U_{ejecta} > U_{gas}$ because we suppose it is the initial gas-thrust (i.e. the sudden decompression of the Taylor bubble) which gives a part of its energy to the ejecta and thus the initial velocity to these ejecta. These events with $U_{ejecta} > U_{gas}$ have either i) their ejecta velocity which is over-estimated, or ii) their gas velocity which is under-estimated either iii) wrong links between the thermal and the infrasonic detections (we are missing a thermal or an infrasonic event during the detection) or iv) are only buoyancy driven by a hot source and not by a too small gas decompression.

The distribution of the velocity ratios at Piton de la Fournaise is unimodal while it is bimodal at Yasur (Figure 5.16a1–a3). We suppose then there is only one mechanism at Piton de la Fournaise while there are probably two mechanisms at Yasur. This bimodality was not seen previously. Perhaps the sole parameters we were looking at, maximum amplitudes, durations, energies, are not self-sufficient to highlight this bimodality. Furthermore the maximum amplitudes and the energies give the strength/intensity and not the motion, and thus not the mechanisms.

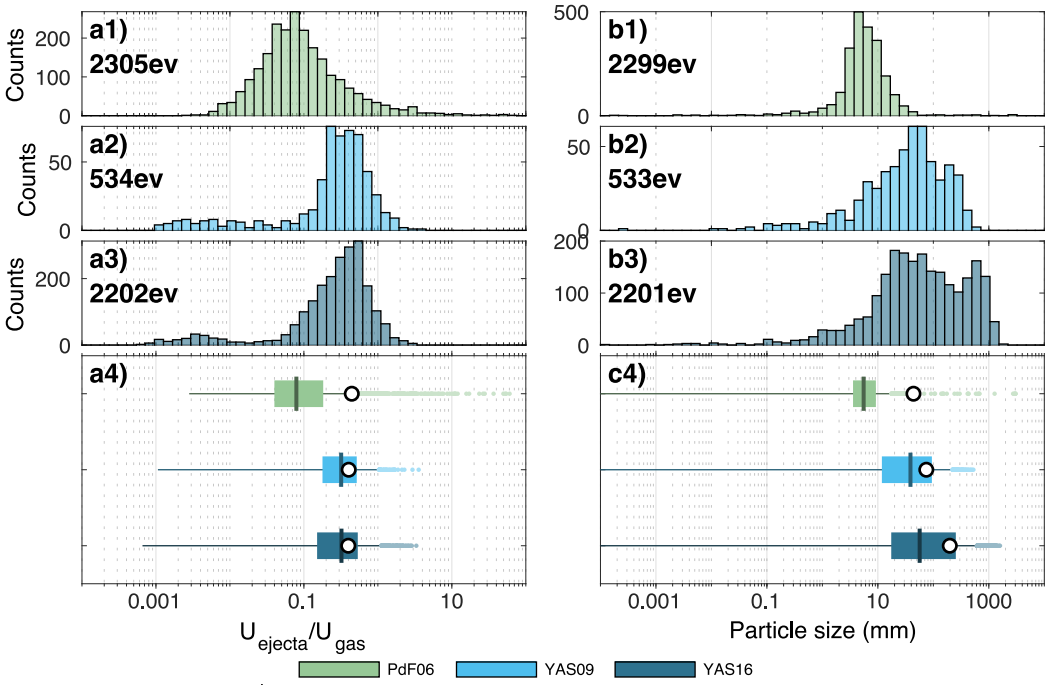

Figure 5.16 – Distribution of a) the velocity ratio , b) and the particle size at 1) Piton de la Fournaise and 2–3) Yasur with 4) the corresponding boxplots.

5.6.5 Inputs into the atmosphere

5.6.5a Size of the ejecta

Marchetti et al. (2009) suggest that the difference between Vulcanian and Strombolian energy partitioning is due to the fragmentation mechanism and thus lead to different particle sizes.Particle sizes are thinner for Vulcanian eruptions than Strombolian eruptions because the fragmentation is more efficient (Marchetti et al., 2009). However, among the same type of eruption, a large energy lead to large fragments (ejecta) because too low energies can not throw big ejecta (Figure 5.16).

Yasur can eject bombs up to a fiew metres in diameter (Figure 5.16c2–c4) and can also eject very thin particles (ash, <1 mm; table 5.4). These ashes are very light and can travel far from the volcano and damage crops, pollute water or triggers ash-respiratory and cardiovascular hazard, etc. (Hansell et al., 2006). The ashes at Yasur volcano can have a significant impact on the inhabitants of Tanna Island i) because this volcano is in persistent activity and ii) because the inhabitants are very dependent on their local ressources (water, crops, etc). The mean size of ejecta can reach 5 cm–10 cm at Piton de la Fournaise (Figure 5.16c1,c4)). These mean sizes of ejecta, calculated from eq. (5.6), are consistent with the field observations (see Figure 5.17 and Gurioli et al., 2018).

The mean particle size per explosion increases with the ratio of infrasonic energy to thermal energy (Figure 5.18a). Note that the energies are only based on amplitude and duration, while the mean ejecta diameter depends on the gas velocity, also derived from the infrasonic waveforms, and on the ejecta velocity. We can then estimate a range for the mean size of the ejecta knowing the thermo-infrasonic partitioning of energy. This is of great interest because the danger from ejecta depends on their size. The smallest ejecta (ash) can be inhaled and the biggest one (bombs) can injure people. We also see a clear departure

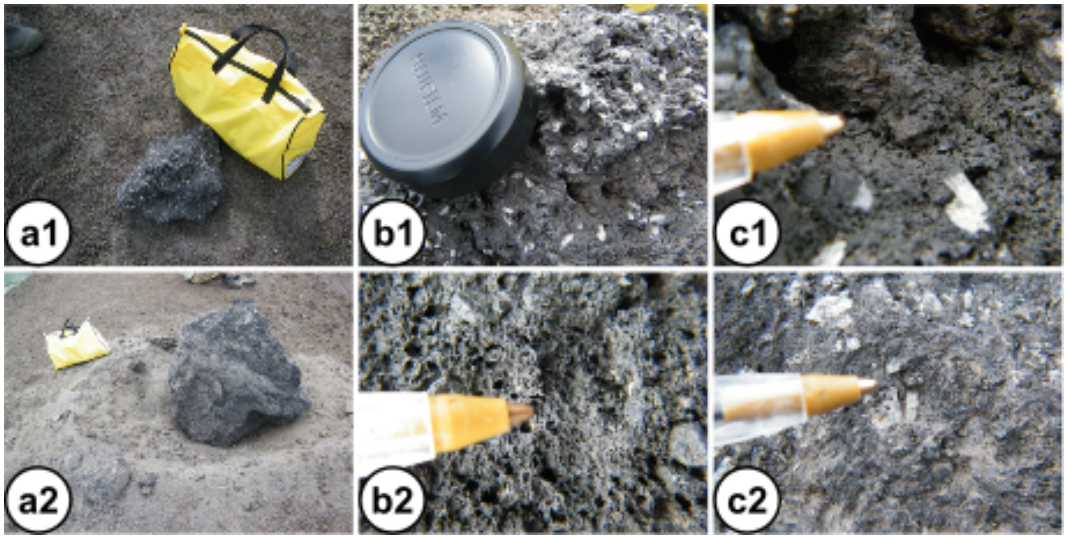

Figure 5.17 – Bombs that have fall down on the crater rim of Yasur during the 2016-field campaign. 1) Between 11:30pm, 15/09/2016 and 00:30am, 16/09/2016, UTC (10:03am and 11:30am, 16/09/2016, local), low wind. 2) The 15/09/2016 before 11:30pm (during the night between the 15/09/2016 and the 16/09/2016, local). a2) We can see the *crater* that was done by the bombs. b1–c2) we can see the different texture of the bombs.

Table 5.4 – Nomenclature of the size of ejecta.

Name	Size range	φ scale[1]
Fine ash	<0.06 mm	>4
Coarse ash	0.06 mm–2 mm	−1 to 4
Lapilli	2 mm–64 mm	−6 to −1
Blocks and bombs	>64 mm	< -6

[1] $\varphi = -\log_2 D_P/D_0$, $D_0 = 1$ mm

from the trend for very large fragments (1 m) which are of the same order of magnitude than the vent. The ratio of infrasonic and thermal energies also highlights the difference between ash-rich (bottom left corner) and gas-rich (top right corner) explosions at Yasur (Figure 5.18a). Figure 5.18a also shows that the smallest explosions at Yasur bear similarity of that of the Piton de la Fournaise, despite having very different range of thermal and infrasonic energies (Figure 5.8a).

5.6.5b Hourly gas flux

One of the aim of this study is to characterise the impact of the Strombolian activity, worldwide, especially the gas volume input into the atmophere (Figure 5.18b). The gas volume flux from infrasonic records can be separated into active degassing (explosions) and total degassing (explosions and inter-explosions). The hourly gas flux of explosions ranges from $5.30\,\mathrm{m^3.h^{-1}}$ to $9.20 \times 10^6\,\mathrm{m^3.h^{-1}}$ while total hourly gas flux ranges from $1.50 \times 10^4\,\mathrm{m^3.h^{-1}}$ to $2.10 \times 10^7\,\mathrm{m^3.h^{-1}}$ (Figure 5.18b). There is at least one order of magnitude between the hourly gas flux from explosions and the total hourly gas flux. The passive degassing (total - active) expulses more voluminous quantities of gas than the active degassing (2–4 order of magnitude of difference).

The total degassing flux at Yasur is of the same order of magnitude in June-2009 and

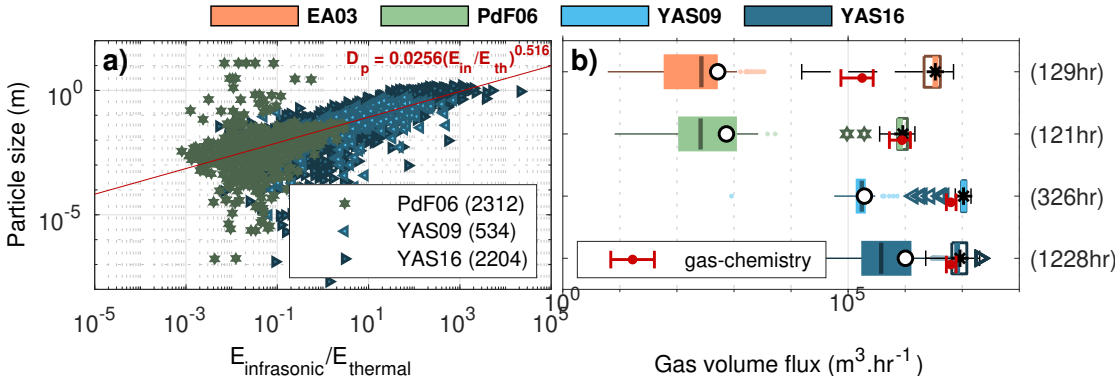

Figure 5.18 – Input into the atmosphere. a) Infrasonic to thermal energy ratio as a function of particle size. b) Distribution of the active gas flux (explosions, plain boxes) and total gas flux (explosions+inter-explosion, empty boxes). The estimates of the gas flux from geo-chemical measurements is shown in red, with the errorbars that give the minimum and maximum values and the circles that gives the mean values (Erta'Ale: Sawyer et al. (2008b); Piton de la Fournaise: Tulet et al. (2017); Yasur: Bani and Lardy (2007); Métrich et al. (2011)).

Sept-Nov-2016 (Figure 5.18b). However the active degassing is much more important in 2016 when the Strombolian activity was vigorous. We suggest that the activity in Sept-Nov-2016 was stronger than in June 2009 because the passive degassing was less efficient than in June-2009 (i.e. some thing pluges the conduit(s), the magma is more viscous).

We can also observe that, except for Erta'Ale activity, where the records are very noisy, the gas volume flux from gas chemistry is of the same order of magnitude than the total gas volume flux from infrasonic records (Figure 5.18b). This high level of noise show the limits on the validity of the estimates of the total gas flux from infrasonic records.

5.7 Extrapolation to other volcanoes

The aim of this section is to characterise the Strombolian activity of various volcanoes as weak, mild or strong from their known parameters (Table 5.5 and figure 5.19). We also wish to provide a quantitative comparison on the total gas volume obtained from combining gas chemistry (FTIR, multigas) with SO_2 flux and from infrasound. The goal is also to classify volcanoes as a function of their total degassing but also for each specific gas phase such as major volatiles (H_2O, CO_2, SO_2 and minor species which may be very toxic or playing a major role on climate or the oceans such as the hallogens mainly transformed into HCl, BrO, HF, etc.

The maximum acoustic pressure is our reference to describe the intensity of the Strombolian activity at a volcano because it is the most widely measured parameter (Figure 5.20a) and it represents the strength of a Strombolian explosion. The classificication, discuted here, is based on the references up to now.

Erta'Ale, Piton de la Fournaise and Villarrica clearly have a weak Strombolian activity compared to other volcanoes (Figure 5.20a). We set the uppest limit of the weak activity at 20 Pa (at 100 m) such as it corresponds to the largest explosions measured at Piton de la Fournaise (Erta'Ale being very uncertain due to the high level of noise.).

We set the limit between mild and strong activity at 400 Pa, the uppest value of the

Table 5.5 – Tectonic context and main rock type of various volcanoes known to have Strombolian activity. Volcanoes in bold letters are the volcanoes studied here. Each information presented in this table were found on the *Global Volcanism Program* web-site of the Smithsonian Institution (Smithsonian Institution (2013)). The location of these volcanoes is shown on the map, figure 5.19.

	Location	Tectonic context[1]	Main rock type	Inhabitants <30 km	
Arenal	Costa Rica	CM	Andesite / Basaltic Andesite	96 512	[ARE]
Benbow & Marum	Vanuatu	IA	Basalt / Picro-Basalt	10 826	[AMB]
Erebus	Antarctica	HS	Phonolyte	0	[ERE]
Erta'Ale	Ethiopia	CR	Transitional basalt	8857	[EA]
Etna	Italy	3P	Trachy-basalt	1 016 540	[ETN]
Heimaey	Iceland	OR	Basalt / Picro-Basalt	2188	[HEI]
Karymsky	Russia	CM	Basaltic andesite	291	[KAR]
Klyuchevskoy	Russia	CM	Basalt / Picro-Basalt	292	[KLY]
Massaya	Nicaragua	CM	Basalt / Picro-Basalt	1 914 707	[MAS]
Nyiragongo	Congo	CR	Foidite	1 006 436	[NYU]
Pacaya	Guatemala	CM	Basalt / Picro-Basalt	2 454 482	[PAC]
Piton de la Fournaise	France	HS	Basalt / Picro-Basalt	246 792	[PdF]
Sangay	Ecuador	CM	Andesite / Basaltic Andesite	15 130	[SAN]
Shishaldin	United States	CM	Basalt / Picro-Basalt	10	[SHI]
Stromboli	Italy	IA	Basalt	3894	[STR]
Tungurahua	Ecuador	CM	Andesite / Basaltic Andesite	183 640	[TUN]
Tolbachik	Russia	CM	Basalt / Picro-Basalt	225	[TOL]
Villarica	Chile	CM	Basaltic andesite	35 118	[VIL]
Yasur	Vanuatu	IA	Basaltic trachy-andesite	24 748	[YAS]

[1] **Tectonic contexts.** Extension: [CR] continental rift and [OR] oceanic ridge; Compression: [CM] continental margin and [IA] island arc; Intra-plate: [HS] hot-spot; [3P] triple point.

maximum acoustic pressure at Stromboli (Figure 5.20a). Shishaldin and Stromboli both have a mild Strombolian activity. Whereas Nyiragongo and Pacaya have a weak Strombolian activity. The other volcanoes are difficult to classify due to a lack of measurements.

We could find estimates of the infrasonic energy only for a few number of volcanoes (Figure 5.20b). The infrasonic energy at Stromboli was estimated during a *typical* activity (Marchetti et al., 2009) and can be taken as a reference for the mild Strombolian activity. The number of estimates allows us to classify Erebus and Karymsky as mild to strong Strombolian volcanoes (Johnson and Aster, 2005) and Villarrica as a weak Strombolian volcano (Marchetti et al., 2009).

The maximum temperature variation, which is poorly documented (Figure 5.20d), and the infrasonic duration (Figure 5.20c) do not reveal any clear trend.

The thermal energy is also poorly documented because the limits of the explosions (start and stop) are often difficult to find (Figure 5.20e). Sufficient data were found only for Stromboli and Villarrica (Marchetti et al., 2009) even if the direct comparison with our estimates is biased because of the size of the field of view is very different (Section 5.6.4 and figure 5.15).

The thermal duration of Strombolian explosions depends mostly on the duration of the explosion (i.e. the length of the Taylor bubble and the secondary effects due to the main pulse in acoustic pressure), the duration of the buoyancy effects and the falling down of the ejecta into the vent. This duration is lengthened at Yasur because we have longer gas pockets than at Piton de la Fournaise (Figure 5.20f) and because of the quantity of ashes is more voluminous than at Piton de la Fournaise.

The repose time between two explosions is strongly related to the accuracy we have on the detection of the events. It is then not a good parameter to define the Strombolian activity

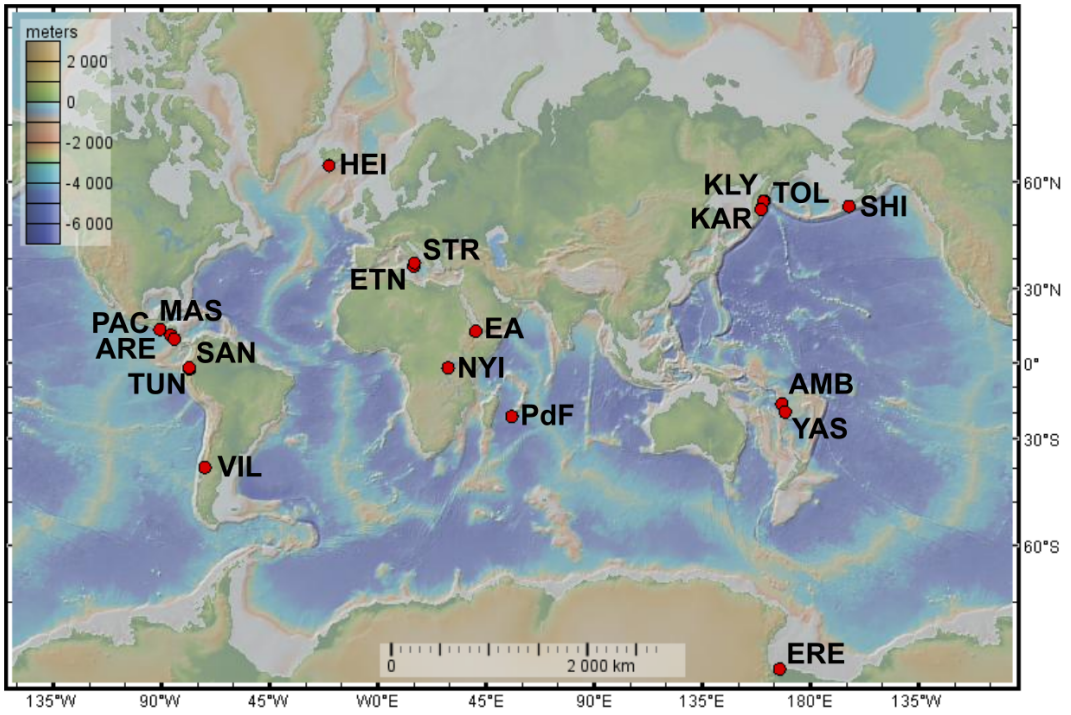

Figure 5.19 – Location of the selected volcanoes (See table 5.5).

as weak, mild or strong unless the signal to noise ratio is large (Figure 5.20g).

The gas and ejecta velocity are poorly documented as two separated phases and relie on different types of techniques (Figures 5.20j and 5.20k). The ejecta velocity is high at Stromboli compared to the ejecta velocity as Yasur. Most of the estimates of the ejecta velocity use different methods, such as Doppler radar or image analysis, than the time flight of the ejecta between two radiometers (square data). The long efficient time of the radiometer limits the highest ejecta velocity that we can measure.

This difference of the methods used to estimate the ejecta velocity might lead to errors on the particle size (Figure 5.20l). However orders of magnitude rather than accurate estimates are sufficient here as the goal is to provide bounds for the weakes and strongest Strombolian activity worldwide, despite the differences in the methods used.

It is also difficult to find estimates of the gas flux (Figures 5.20m to 5.20o), often only estimated as a SO_2 flux (Figure 5.20i). The gas flux, which can be deduced from the gas chemistry (FTIR or multigas) combined to the SO_2 flux is very rarely estimated, a notable exception being that of Yasur (Métrich et al., 2011). Here we have estimated the gas flux from chemistry at various volcanoes based on data found in the litterature (Figure 5.20i). The total gas flux from infrasound records at Piton de la Fournaise and Yasur are consistent with the total gas flux from gas-chemistry measurements (Figure 5.18b). The good bulk agreement on the total gas flux obtained from infrasound and chemistry (FTIR or multigas combined to SO_2 flux) suggests that continuous infrasound measurements could be easily used to estimate total gas flux instead of SO_2 flux, difficult to measure in continuous and the gas composition, never measured in continuous.

The yearly amount of gas emitted by the worldwide Strombolian activity is voluminous despite the low gas flux, because the Strombolian activity is often persistent (Ambrym, Yasur, Stromboli, Erta'Ale, etc.). We estimate SO_2 gas flux at Yasur volcano (Vanuatu) to

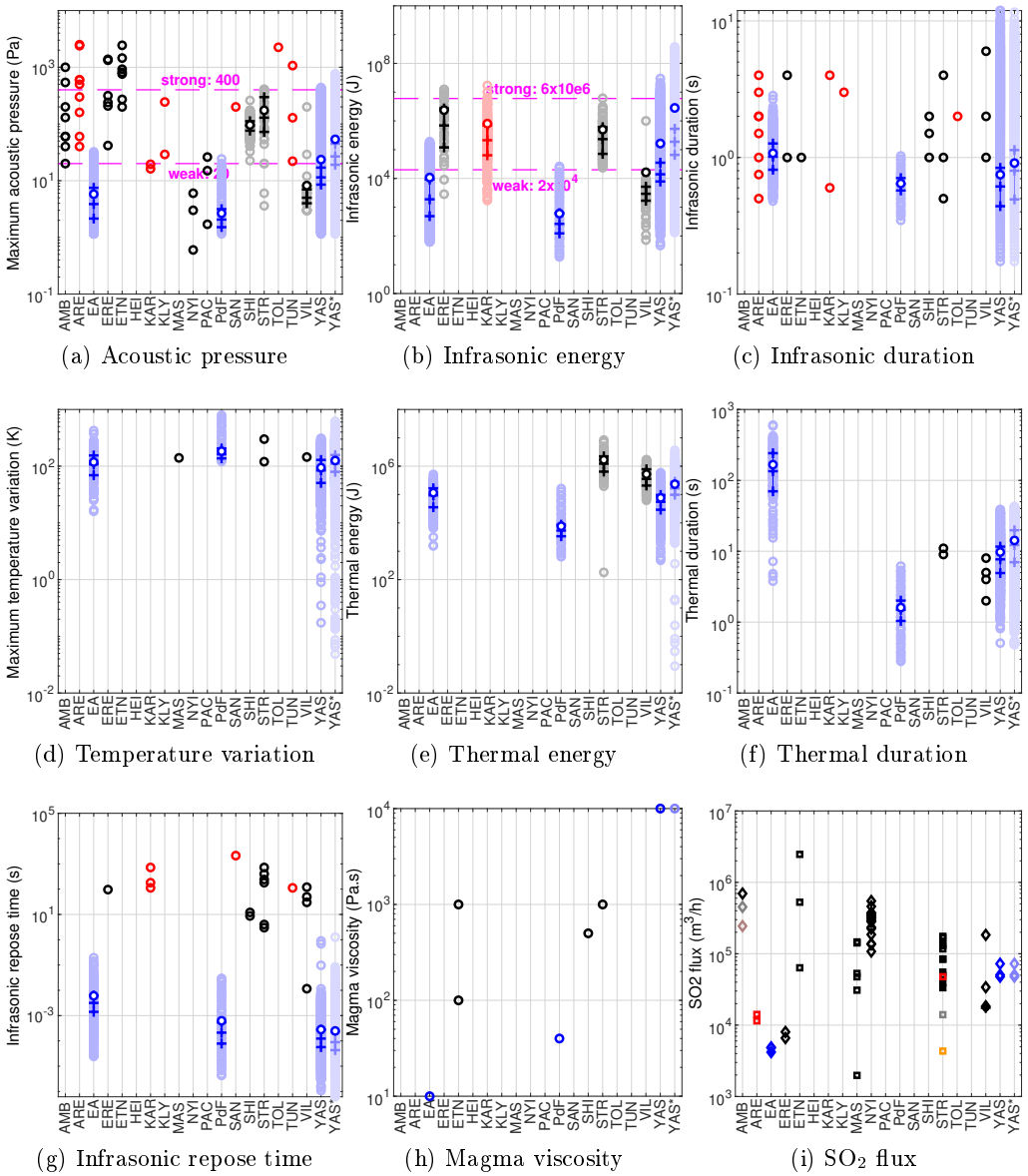

(a) Acoustic pressure (b) Infrasonic energy (c) Infrasonic duration

(d) Temperature variation (e) Thermal energy (f) Thermal duration

(g) Infrasonic repose time (h) Magma viscosity (i) SO_2 flux

Figure 5.20 – Characterisation of the Strombolian activity at several volcanoes. Each black or red empty circle represent a value found in the literature. Red circles show data for volcanoes that rather do Vulcanian explosions. Blue empty circles represent the values from this paper. When there are more than 10 values we add the quartiles (q_1, q_2 = med and q_3 as crosses) and the mean (white-plain circle). More details are given for the SO_2 flux and the total gas flux from chemistry measurements. The list of references for the data is given in §5.7. To be continued.

be around 683 t.d^{-1} (Bani and Lardy, 2007). The total volume of SO_2 emitted by Yasur in 100 years is arround 25 Mt. Ambrym accounts for 13 % of the volcanic SO_2 worldwide with SO_2 gas flux that can reach 5 kt.d^{-1} in average (i.e. 1.83 Mt.year^{-1} or 183 Mt/100year) and is comparable to the gas flux at Etna (Bani et al., 2012; Allard et al., 1991). At Stromboli between 400 and 800 t of SO_2 are measured per day (i.e. 146 kt.year^{-1}–292 kt.year^{-1} or 14.60 Mt/100year–29.20 Mt/100year, Allard et al., 1994).

Twenty mega-tonne of SO_2 were emitted during the 1991 eruption of Pinatubo (e.g. McCormick, 1992; Hanuš and Vaněk, 1983), while 1982 El Chichon Plinian eruption has released 3.30 Mt of SO_2 (Krueger, 1983) and 1981 Plinian Mt-St Helens eruption around 2 Mt (Gerlach and McGee, 1994). However these explosive eruptions have large typical

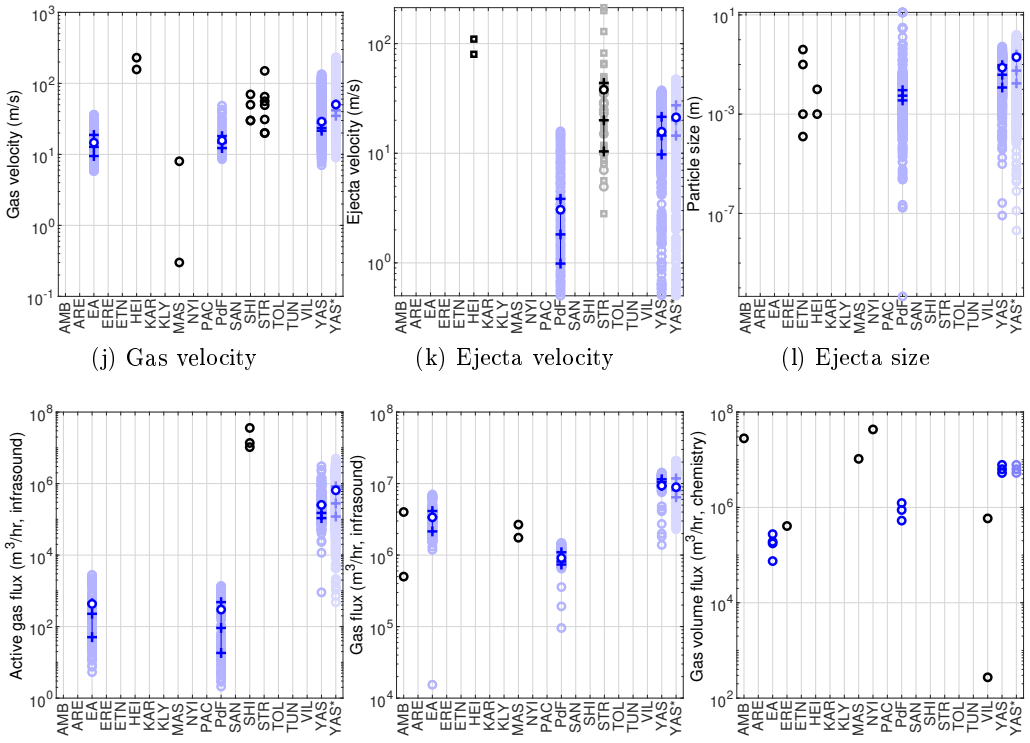

(j) Gas velocity (k) Ejecta velocity (l) Ejecta size

(m) Active gas flux (infrasound) (n) Total gas flux (infrasound) (o) Total gas flux (chemistry)

Figure 5.20 – Characterisation of the Strombolian activity at several volcanoes (continued).

return times (≥100 year), reducing drastically the SO_2 volume released in the atmosphere, when averaged over several centuries.

References for the values of the Strombolian activity

- Ambrym [AMB]: Zielinski (2012); Allard et al. (2016b,a); Bani et al. (2012)
- Arenal [ARE]: Garcés et al. (1998); Hagerty et al. (2000); Johnson (2003)
- Erebus [ERE]: Johnson and Aster (2005); Rowe et al. (2000); Johnson et al. (2008a); Gerst et al. (2013); Johnson (2003); Johnson et al. (2004); Oppenheimer and Kyle (2008)
- Etna [ETN]: Vergniolle and Ripepe (2008); Spina et al. (2015)
- Heimaey [HEI]: Blackburn et al. (1976)
- Karymsky [KAR]: Johnson and Aster (2005); Johnson and Lees (2000); Johnson (2003)
- Klyuchevskoy [KLY]: Johnson (2003)
- Massaya [MAS]: Branan et al. (2008); Burton et al. (2000)
- Nyiragongo [NYI]: Barrière et al. (2018); Sawyer et al. (2008a)
- Pacaya [PAC]: Dalton et al. (2010)
- Sangay [SAN]: Johnson and Lees (2000)
- Shishaldin [SHI]: Vergniolle et al. (2004); Vergniolle and Caplan-Auerbach (2004); Petersen and McNutt (2007)
- Stromboli [STR]: Marchetti et al. (2009); Johnson (2003); Marchetti and Harris (2008); Vergniolle et al. (1996); Vergniolle and Brandeis (1996); Patrick et al. (2007); Colò et al. (2010); Ripepe et al. (2002); Delle Donne and Ripepe (2012); Blackburn et al. (1976); Harris et al. (2012); Harris (2013); Gaudin et al. (2014b); Chevalier and

Donnadieu (2015)
- Tungurahua [TUN]: Fee et al. (2010)
- Tolbachik [TOL]: Johnson (2003)
- Villarica [VIL]: Marchetti et al. (2009); Johnson et al. (2004, 2011); Gurioli et al. (2008); Moussallam et al. (2016); Richardson et al. (2014); Sawyer et al. (2011)

5.8 Conclusion

The aim of this study is to provide bounds on many physical parameters to characterise the Strombolian activity and give an idea of the impact of the Strombolian activity worldwide. Indeed, our statistical study can only provide an order of magnitude but many of the parameters were previously baddly known, such as the infrasonic and thermal durations, hence energies, gas and ejecta velocities, etc.

We have deduced various parameters, for the Strombolian activity, from the thermal (radiometers) and infrasonic records, such as the strength of the Strombolian explosions (maximum acoustic pressure, infrasonic and thermal energies), their dynamics (gas and ejecta velocities, durations) and their impacts on the environnement (gas volume, particle size).

We have shown that the Strombolian explosions occur at shallow depth below the vent ($<$100 m), despite the large error due to the long response time of the radiometers and the uncertainties on the ejecta velocity.

The budget of energy, as defined by Marchetti et al. (2009) (buoyant energy as a function of the gas thrust energy) highlights that the same mechanism of fragmentation is responsible for all Strombolian explosions. However, this budget highlights the bias induced by the size of the field of view of a radiometer, that leads to the records of different objects and mechanisms. This budget of energy is then not sufficient to identified Strombolian explosions.

The gas flux during Strombolian activity is lower than the gas flux during stronger eruptions, such as Vulcanian or Plinian eruptions. However, the persistence of the Strombolian activity, compared to the long return times of the explosive eruptions, leads to a gas volume released during the Strombolian activity and explosive eruptions of the same order of magnitude, when averaged on typical return time.

Our comparison of the various parameters for various volcanoes in Strombolian activity has highlighted the difficulty to find available data, despite the numerous geo-physical studies at Strombolian volcanoes. The parameters that are the most measured are the maximum acoustic pressure and the infrasonic energy. These parameters give clear cut-off between the weak, mild and strong Strombolian activity and can be summarised in the future by the sole maximum acoustic pressure per event. The other parameters might highlight some patterns, now unseen due to the lack of estimates.

A collaborative work or data base would enhance the catalogue we have started here, and improve that quantitative study to characterise the Strombolian activity.

Chapter 6

The temporal variations of the Strombolian activity at Yasur volcano

À Serge et Yvette, parce que je les aime tout autant.

Mount Etna (05/05/2015) ©V. Souty

Abstract

We use infrasonic, seismic and thermal records from two field campaigns at Yasur to study the variability of the Strombolian activity. Strombolian activity during June 2009 field campaign was calm and steady while the activity during September-November 2016 was vigorous with an alternation of quiet and strong phases. While thermal analysis seems to remain poor to understand the variability of Strombolian activity, the seismo-infrasonic study highlights two couplings. In the first regime, called typical, the infrasonic amplitudes and energies are small ($<$340 Pa at 100 m; $<5 \times 10^7$ J), while in the second regime, corresponding to the vigourous phases, both these parameters become much larger, with a clear cut-off between the two regimes. This suggests the existence of two different regimes associated to the behaviour of the foam layer trapped at the top of the magma reservoir. In the typical regime, the gas flux from explosions remains below 1.50×10^6 m^3.h^{-1} and the foam is probably stable (without massive coalescence events) and spreads towards the conduit while releasing each of its small bubbles (13 µm–14 µm). In this case, the large slugs observed at the surface probably results from progressive coalescence into the conduit, likely to be initiated in the bottommost part of the volcanic conduit. In the vigorous regime, the slugs are likely to be produced by a massive foam coalescence, whose extent is limited by the magma viscosity. These deep slugs, whose infrasonic signature is very similar among themselves and larger than those generated during typical activity, leads to high seismic and infrasonic amplitudes due to their relatively deep formation.

Contents

6.1 Introduction **163**
6.2 Context **164**
6.3 Data acquisition **166**
6.4 Processing of the data **168**
6.4.1 Pre-processing 168
6.4.2 Infrasonic records 169
6.4.3 Thermal records 170
6.4.4 Seismic records 171
6.4.5 Combined methods 171
6.5 Results **172**
6.5.1 Temporal variability 172
6.5.2 Infrasonic analysis 173
6.5.3 Thermal analysis 176
6.5.4 Seismic analysis 177
6.5.5 Thermo-infrasonic analysis 178
6.5.6 Seismo-infrasonic analysis 179
6.5.7 Analysis of the simultaneous infrasonic, seismic and thermal records 180
6.5.8 Phases of intensity 182
6.6 Discussion **188**
6.6.1 Coexistence of two mechanisms for the formation the large gas pockets 188
6.6.2 Bubble diameter in the reservoir 192
6.6.3 Depth of the magma column 195
6.7 Conclusion **197**

6.1 Introduction

One of the objective of the scientists is to understand the variability of the volcanic activity and also to use that knowledge to develop efficient techniques to monitor volcanoes and assess hazards. The variability of the volcanic activity can either result from changes in the main parameters describing the eruptive activity or as a change in eruptive style (i.e. lava flow, Strombolian, Vulcanian, Plinian, etc.). The variability of the eruptive style is now well documented (e.g. Walker, 1973; Newhall and Self, 1982) despite some subtitle transitions from one style to another (ex: Strombolian to Vulcanian, Strombolian to Hawaiian; e.g. Jaupart and Vergniolle, 1988; Vergniolle and Ripepe, 2008). However the temporal variability of the volcanic activity is more difficult to study either because few eruptions occurs at a volcano during human life (e.g. Marzocchi and Zaccarelli, 2006) or because long acquisitions of data are difficult to perform .

Nowadays more and more remote-sensing techniques allow the scientists to monitor volcanoes that are difficult to access (difficult terrain, geopolitic conflicts), such as far-field infrasounds, seismic or SO_2 measurements from satellite (e.g. Carn et al., 2017; Coppola et al., 2016; Matoza et al., 2017; Endo and Murray, 1991; Rogers and Stephens, 1995). These techniques have the advantages to be performed whatever the volcanic hazards and can be deployed for long periods of time. However the analysis of the data can be difficult because many other processes can be recorded and because of the distortion of the signal due to the path of propagation may occur (Example of the atmospheric effects, Tailpied et al., 2017).

Near-field remote-sensing measurements remain the most accurate techniques to monitor the Strombolian activity especially because Strombolian activity consists in series of small and short explosions at open-vent volcanoes (see Harris and Ripepe, 2007a) that are more difficult to detect at long distance than stronger eruptions such as Vulcanian or Plinian eruptions. However near-field techniques are more difficult to maintain for long times because of issues such as the power supply, accessibility and the premature aging of the instruments (oxidation, etc.). Nevertheless, the Strombolian activity is often persistent such at Stromboli, Erebus or Yasur volcanoes (Rosi et al., 2000; Kyle, 1994; Firth et al., 2014). Hence the necessity to understand the temporal variability of the Strombolian activity to warn the major changes toward a more dangerous activity. For example, Yasur has reached Vulcanian activity in 1994, 2004 and 2013 (Vanuatu Meteorology and Geohazard Departement, 2018) and Stromboli also had *paroxysmal* eruptions such as in September 2008 and November 2009 (Calvari et al., 2012; Andronico and Pistolesi, 2010).

It is commonly admitted that a Strombolian explosions are generated by a large Taylor bubble (i.e. a cylindrical bubble, filling most of the conduit, trapped up with a more rounded noise) rising the conduit by buoyancy and exploding at the surface because the pressure inside and outside the Taylor bubble is not at equilibrium. Two main models for the formation of the large gas pockets and their rising dynamic are often discussed and may coexist: (i) the rise speed dependant model and (ii) the collapsing foam model.

(i) The rise speed dependant model suggests that the formation of the large pockets is due to the progressive coalescence of gas when it rises to the surface and consider a homogeneous two-phase flow (Parfitt and Wilson, 1994; Parfitt, 2004).
(ii) The collapsing model proposes that large gas pockets are produced by the partial collapse of a foam layer at the top of the reservoir, whose stability depends on the magma viscosity, and then these pockets rise the conduit as a separated two-phase flow with the viscous magma (Jaupart and Vergniolle, 1988, 1989).

Both models agree that surface activity can change depending on gas contents.

We have shown in the previous chapter (chapter 5) that all Strombolian eruptions have the same mechanism of fragmentation (see also Marchetti et al., 2009). Short-time and cyclic processes of the Strombolian activity were also highlighted at Erta'Ale, Stromboli and Etna indicating a similar mechanism for the Strombolian activity (e.g. Harris et al., 2005a; Ripepe et al., 2002; Lautze et al., 2004). There has been several studies prompted by the paroxysmal activity of Stromboli in December 2002–April 2003 (e.g. Métrich et al., 2005; Calvari et al., 2006) and by its effusive activity on Frebruary 2007 (Ripepe et al., 2009; Aiuppa et al., 2009). However, to my knowledge, there is a small number of studies focusing on larger temporal variations of the Strombolian activity (VLP, SO_2 measurements, e.g. Giudicepietro et al., 2009; Coppola et al., 2016), and none on multidisciplinary geophysical studies, except for the study of Meier et al. (2016), which characterised only the surface activity at Yasur (Doppler radar, infra-red videos and infrasound for 15 days).

We propose here to study the temporal evolution of the Strombolian activity at Yasur to assess surface and deep mechanisms. Simultaneous and near-field infrasonic, seismic and thermal data that were recorded during two field campaigns in June 2009 and Sept-Nov 2016. The Strombolian activity was typical and steady during the ∼15 days of the field campaign in June 2009. However the Strombolian activity was unsteady during the ∼50 days of the field campaign in Sept-November 2016, with an alternation of strong and quiet phases of activity.

We first present Yasur volcanoes and the data acquisition during the two field campaigns (Sections 6.2 and 6.3). We then explain the methods we use to study the temporal evolution of the Strombolian activity at Yasur (Section 6.4). In section 6.5, we present the results of our study, first by sole methods and then by combining the techniques. We explain the temporal variation of the Strombolian activity observed here in section 6.6. Finally, after a brief summary of this study we suggest future studies to better understand the temporal variability of the Strombolian activity (Section 6.7).

6.2 Context

The New Hebrides subduction, part of the ring of fire, is very active with the Australian plate diving under the Pacific plate with velocities up to 17 cm.year^{-1} (Figure 6.1, e.g. Calmant et al., 2003; Bergeot et al., 2009; Baillard et al., 2015). The Vanuatu archipelago, which results from that subduction, is composed by 83 (volcanic) islands which can be threatened by earthquakes or by volcanic eruptions. The Vanuatu Meteorology and Geohazard Departement (VMGD) monitors 6 active volcanoes and quantifies their activity using alert levels from 0 to 5 on the base of the seismic activity.

We focus on Yasur volcano located on Tanna Island in the south of the archipelago (32 000 inhabitants, World Health Organization Western Pacific Region, 2017), where the subduction has a velocity around 12 cm.year^{-1} (e.g. Calmant et al., 2003; Bergeot et al., 2009; Baillard et al., 2015). Yasur is an open-vent volcano lying in Siwi caldera and is in persistent Strombolian activity for 630–850 years, producing a basaltic trachy-andesite magma (Firth et al., 2014; Métrich et al., 2011). This persistent activity was preceded by a period during which the activity was stronger (Vulcanian, sub-Plinian) but the eruptions less frequent (Firth et al., 2014). Old an buried lava flows also exist (Brothelande et al., 2016a). Hence the necessity to understand the variation of the Strombolian activity.

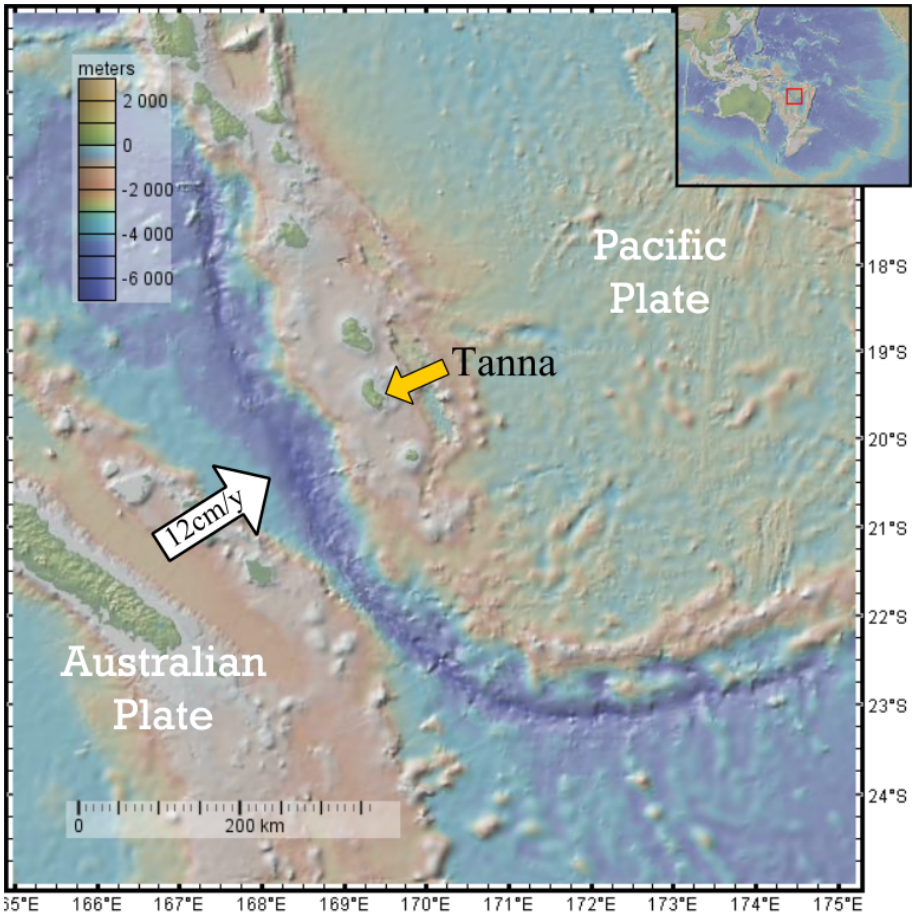

Figure 6.1 – Topography of the New Hebrides subduction zone.

Yasur produces high quantities of gas, 1.50 %–2.50 % of the volcanic SO_2 of the troposphere, but only half of the degassed magma has erupted since the past 1000 years (Bani and Lardy, 2007; Métrich et al., 2011). The magma that has not erupted is stored below Siwi caldera and is probably responsible for the Yenkahe block resurgence (Métrich et al., 2011).

Minor events, that consist in weakly over-pressurized bursts occur continuously while major events, less frequent, characterise the Strombolian activity at Yasur. These two types of explosions are not clearly correlated and thus indicate the existence of two sources of degassing (Spina et al., 2015).

An multi-disciplinary study have shown smooth variations of the surface activity at Yasur during a 15-day field campaign in Aug-Sept 2008 (Kremers et al., 2013; Meier et al., 2016). Ash-free explosions (figure 6.2a,b and d) occur when the infrasonic amplitudes are high, spectral contents rich in high frequencies, whereas ash-rich explosions (figure 6.2c) occur when the infrasonic amplitudes are low and spectral contents poorer in high frequency. Meier et al. (2016) also observed different infrasonic waveforms between both types of explosions that are probably due to different explosion dynamics. Kremers et al. (2013) have shown, from the inversion of the moment tensor of seismic records, that there is a sole mechanism for the different craters. They also estimated slug length between 68 m and 177 m, giving slug volume between 1.30×10^3 m^3 and 3.50×10^3 m^3 if we assume that the radius of the slug is 2.50 m (radius of the conduit).

Previous thermal studies on the Strombolian explosions and the gas ratio also demonstrate

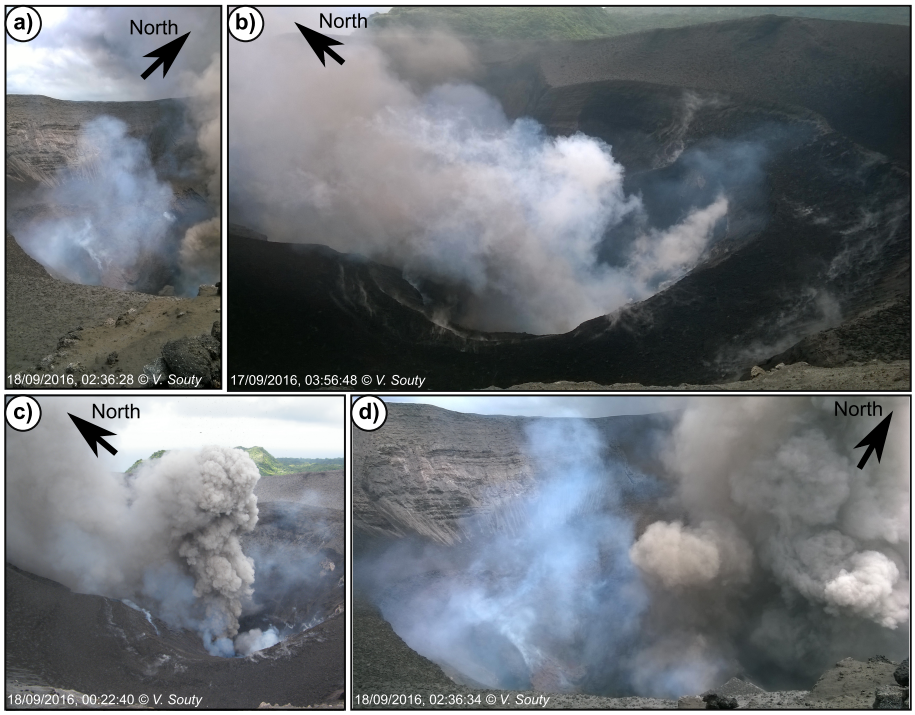

Figure 6.2 – Strombolian explosions at Yasur during the 2016 field campaign. a) and b) Gas-rich explosion. c) Ash-rich explosion. d) Almost simultaneous gas-rich explosion (left) and ash-rich explosion (right).

the existence of two sources of degassing at Yasur (Bani et al., 2013; Oppenheimer et al., 2006). The deepest source is rich in CO_2 and SO_2 while the uppest source is rich in HCl (Oppenheimer et al., 2006). Bani et al. (2013) proposed that the former source produces Taylor's bubble by massive foam coalescence and the latter source by progressive coalescence in the conduit.

6.3 Data acquisition

Infrasonic and thermal measurements were recorded on a RefTek 130 digitizer with sampling frequency of 1000 Hz and 100 Hz in 2009 and 2016, respectively (Figure 6.3). The sensitivity of the RefTek 130 for a gain of 1 is 1.59×10^{-3} mV.bit^{-1}.

The acoustic pressure was measured by MB2005 microbarometers (developed by the CEA-DASE and sold by MARTEC). The sensitivity of the MB2005 microbarometer is 1 mV.Pa^{-1} in the band pass 10^{-3} Hz–40 Hz. Pipes, ~30 cm long, were connected to air-entries and covered by scoria as a natural filter.

Additionaly we present infrasonic data from the permanent station on Mount Melkem obtained for the long time series from 2003 to the end 2014 (Figure 6.3). The measurements were done using a MB2000 (developed by the CEA-DASE and sold by TekElec) with a sensitivity of 5 mV.Pa^{-1} in the band-pass 10^{-3} Hz–80 Hz and recorded by a Geostar digitizer with a sampling frequency of 75 Hz, before 2008 and by a Quanterra 330 digitizer (Q330) with a sampling frequency of 100 Hz after 2008. The sensitivity of the Geostar and the Quanterra is 0.15 mV.bit^{-1} and 2.38×10^{-3} mV.bit^{-1}, respectively.

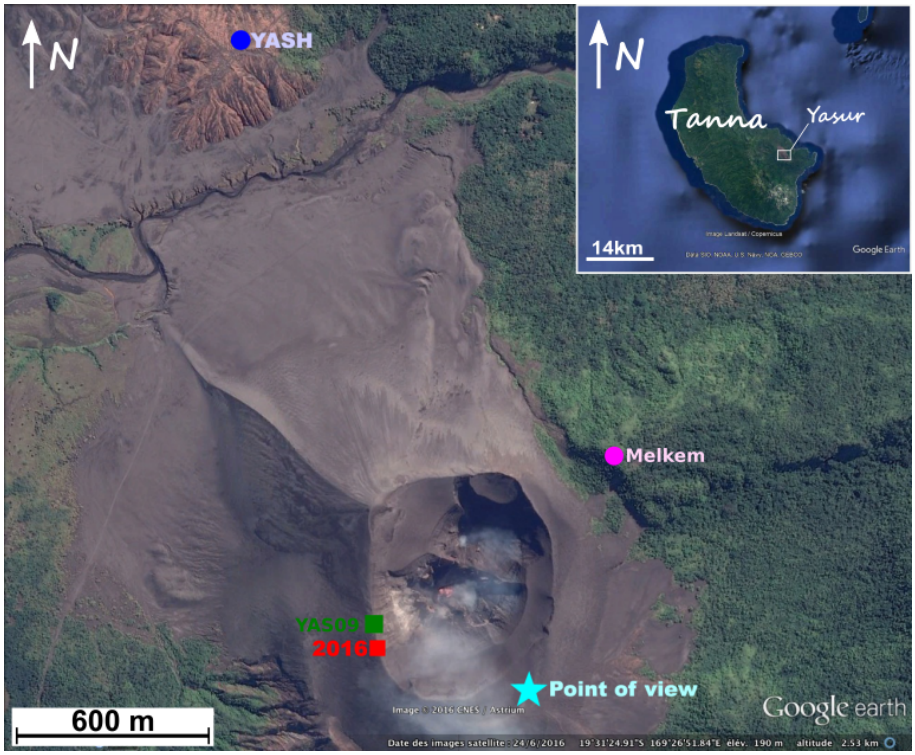

Figure 6.3 – Location of Yasur on Tanna Island (insert) and location of the site of measurements at Yasur.

The brightness temperature was measured using two Cyclops 300AF radiometers (Minolta-Land). These thermometers record infra-red radiations (8 µm–13 µm) in a 1° field of view with a sensitivity of 1 °C.mV^{-1} and an efficient response time of 0.19 s (5.27 Hz). The two radiometers were used simultaneously to record the brightness temperature at two different heights above the vent and the angle between the radiometers was 4°. The radiometers were put into boxes for protection with Zn-Se windows, that are transparent to infra-red radiations providing that they are in perfect clean. Unfortunately these windows oxidise due to acid gas and ash, letting less and less infra-red radiations pass through and hit the sensor. The calibrations we did before and after the field campaign of 2016 make us increase the brightness temperature by a factor 2 for thermal records in 2016. We assume these calibrations are also acceptable for measurements in 2009 because of the short time during which the thermal data are available (3 days, here) and because of the relatively quiet activity at that time.

The time from the RefTek station is corrected for the 2016-field campaign because the GPS of the RefTek station was broken. The time lag is calculated by cross-correlation of the infrasonic signal from the MB2005 with the infrasonic signal of a MB3d microbarometer (developed by the CEA-DASE and sold by SeismoWaves), that was installed close to the MB2005 (<2 m). The numerical MB3d microbarometer has an in-build GPS.

In June 2009, the ground velocity was recorded by a Q330 digitizer using a broad band Trillium 40 (Nanometrics, lend by the CEA) from Melkem, at a distance of about 500 m from the center of the crater (Figure 6.3). The sensitivity of the Trillium 40 is 1553 V/(m/s) in the band-pass 40.20 s–85.50 Hz. However we do not get the full dynamics of the measurements because of a small mistake when configuring the Q330 digitizer that makes the records to be filtered as short-period. The instrumental correction will be done soon from the comparison of the measurements of the ground velocity done simultaneously by

a colocated broad band seismometer in Frebruary 2009, to add the relevant low frequency band. Additionnaly, we should have the poles and zeros of the short period filter applied by the quanterra.

In Sept-Nov 2016, the ground velocity was measured from YASH permanent station, belonging to the Vanuatu Meteorology and Geohazards Departement, at ∼1500 m from the summit of Yasur (Figure 6.3), by a short period LE-3Dlite MkII seismoter (Lenartz electronic) with a sensitivity of 400 V/(m/s) in the band-pass 1 Hz–80 Hz. The measurements are also recorded by a Q330 digitizer. The records are corrected from the instrumental response between 0.10 Hz and 1 Hz using the transfer function of the digitizer and the seismometer.

6.4 Processing of the data

6.4.1 Pre-processing

All records were re-sampled at 75 Hz, the lowest sampling frequency of the Geostar digitizer in order to make the analysis also valid for the long time series from 2003 to 2014.

The infrasonic data are first pre-filtered between 0.01 Hz and 20 Hz (2nd order Butterwoth filter) to find the prevalent frequency band of the Strombolian activity. We then apply a second filter (0.10 Hz–10 Hz, 4th order Butterwoth filter), which is adapted to the strength of the activity, the frequencies of the activity and the noise at Yasur. Thermal data are filtered above 4 Hz because of the efficient response time of the Cyclops 300AF radiometer at 0.19 s. Seismic data are filtered between 1 Hz and 6 Hz to look for the volcanic explosion quakes (Battaglia et al., 2016).

Strombolian explosions, on infrasonic records, are detected using a STA/LTA detector on the coefficients of the wavelet decomposition of levels 4–5 (1.17 Hz–4.69 Hz at 75 Hz) with fixed LTA at 1.23 and 1.63 for the level 4 and 1.08 and 2.38 for the level 5 in 2009 and 2016, respectively. We detect explosions on thermal records using the STA/LTA detector directly on the absolute signal (STA: 1 s; STA: 60 s). The signal of the lower and upper radiometers were processed independently as a volcanic mixture (ash+gas) might never reaches the field of view of the upper radiometer.

The links between explosions seen by the lower and the upper radiometers are performed by looking for the closest detected event measured by the upper radiometer to an event measured by the lower radiometer. The maximum allowed delay between both events is given by the minimum ejecta velocity (0.10 $m.s^{-1}$) we thought exists and the distance to the vent.

Coupling infrasonic and thermal detections is done by looking for the closest infrasonic detection to a thermal detection. We impose the range of thermo-infrasonic delays $t_{\text{thermal}} - t_{\text{infrasonic}}$ to be between −10 s and 30 s. Seismo-infrasonic detections are coupled assuming a range of delays between −1 s and 10 s. The difficulty here is the closely spaced occurence of the explosions in time.

The detection gives the number of the explosions and their amplitude (acoustic pressure, brightness temperature or ground velocity). The duration of the explosions on the records

are determined using the envelope of the signal. The duration and amplitude of the explosions are key parameters to estimate energies.

In order to have an easy comparison of amplitudes, we have scaled all acoustic pressure and ground velocities for a distance of 100 m, considering that seismic and acoustic attenuation are both in $1/r_{\mathsf{vent}}$ in near field.

6.4.2 Infrasonic records

We assume the Strombolian explosions are monopole sources and generate infrasonic waves that propagate in all direction at the same speed and attenuate with a factor $1/r_{\mathsf{vent}}$, r_{vent} being the vent-sensor distance.

The infrasonic energy in an homogeneous atmosphere is

$$\mathrm{E}_{\mathsf{infrasonic}} = \frac{2\pi r_{\mathsf{vent}}^2}{\rho_{\mathsf{atm}} c_{\mathsf{atm}}} \int_0^{\tau} \left(p_{\mathsf{ac}}(t) - p_{\mathsf{air}}(t)\right)^2 \mathrm{d}t \tag{6.1}$$

where r_{vent} is the distance from the source to the sensor (m), $\rho_{\mathsf{atm}} = 1.18\,\mathrm{kg.m^{-3}}$ is the density of the atmosphere at the elevation of the volcano and $c_{\mathsf{atm}} = \sqrt{\gamma R_{\mathsf{ig}} T_{\mathsf{atm}}} = 340\,\mathrm{m.s^{-1}}$ the sound speed (Lighthill, 1978). Other effects than the linear decay are neglected (e.g. viscosity of the medium, heat transfer,...). Variations of pressure due to the weather conditions, the elevation or the topography are also neglected. The infrasonic power $\mathrm{Pw}_{\mathsf{infrasonic}}$ is obtained by dividing the infrasonic energy $\mathrm{E}_{\mathsf{infrasonic}}$ by the duration τ.

Woulff and McGetchin (1976) established the relation between the gas velocity $\mathrm{U}_{\mathsf{gas}}$ and the infrasonic power $\mathrm{Pw}_{\mathsf{infrasonic}}$ from a dimensionless analysis of the Navier-Stokes equations for dipole and quadrupole radiations and with an empirical coefficient. A similar analysis was later done for monopole sources, estimating theoretically the coefficient for an hemisphere and a flat surface (Vergniolle and Caplan-Auerbach, 2004). We obtain

$$\mathrm{U}_{\mathsf{gas}} = \left(\frac{\mathrm{Pw}_{\mathsf{infrasonic}} c_{\mathsf{atm}}}{k \rho_{\mathsf{atm}} 2\pi R_b^2}\right)^{1/4}, \tag{6.2}$$

where k is an experimental constant equal to 1 and R_b is the radius of source, assumed to be that of the bubble (m) (Vergniolle et al., 2004). The radius of the conduit $R_{\mathsf{conduit}} = 2.50\,\mathrm{m}$ gives a good estimate of the bubble radius R_b for Strombolian explosions because bubbles are almost as large as the conduit and do not expand sideways when rising (Figure 1.3).

The explosion, i.e. the sudden decompression of the bubble, generates the infrasonic waves. The bursting volume of the bubble can be estimated by the two successive integrations of the acoustic pressure for the viscous magma at Yasur by (see Section 4.1.3b and Johnson, 2003)

$$\mathrm{Vol}_{\mathsf{gas},b} = \frac{1}{\rho_{\mathsf{atm}}} \int_0^{\tau} \left(2\pi r_{\mathsf{vent}} \int_0^{t} \left(p_{\mathsf{ac}}(t) - p_{\mathsf{air}}(t)\right) \mathrm{d}t\right) \mathrm{d}t \tag{6.3}$$

where $P_{\mathsf{atm}} = 97\,063\,\mathrm{Pa}$ is the pressure of the atmosphere that depend on the elevation of the volcanic source (361 m at Yasur).

The gas volume per sliding window can be estimated from the infrasonic power, assuming that the gas pass through a disk of radius R_{conduit} during the duration of the event as

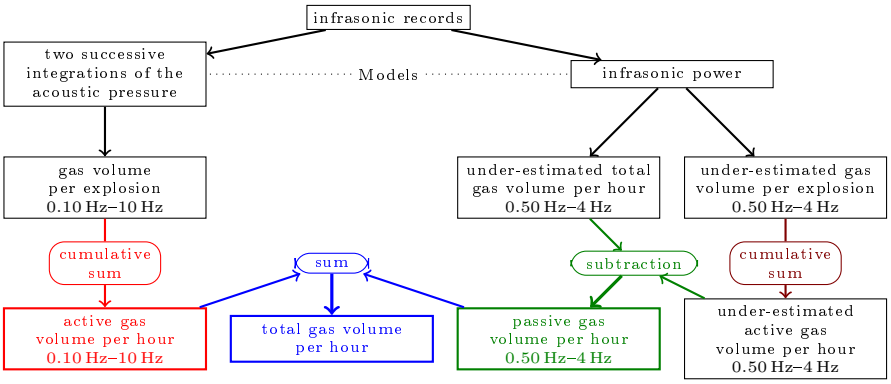

Figure 6.4 – Estimation of the active, passive and total gas flux. The gas volume from the infrasonic power is under-estimated because of the use of a fixed bubble radius equal to that of the conduit for simplicity. Note that we have used, here in the calculation, the active gas volume from acoustic power, despite its underestimation of the real actif gas volume because the total gas volume from acoustic power per hour is calculated using the conduit radius.

$\mathrm{Vol}_{\mathsf{gas},a} = \pi R_b^2 \mathrm{U}_{\mathsf{gas}} \tau$ (see Section 4.1.3a and Vergniolle et al., 2004). This gas volume per sliding window accounts for the active (explosions) and passive (inter-explosion) degassing.

Although it is easy to calculate the cumulative gas volume per given time, the limits of the explosions (start and end) are difficult to find when the explosions do not radiate a sufficient acoustic pressure. The gas volume per hour from active degassing (i.e. explosions) is then estimated from the mean volume of gas per event and multiplying by the number of events (Figure 6.4):

$$\mathrm{Vol}_{\mathsf{active}} = \mathrm{mean}(\mathrm{Vol}_{\mathsf{gas,ev}}) N_{\mathsf{ev}}. \tag{6.4}$$

The gas volume per hour from passive degassing (i.e. inter-explosion) is estimated by substracting the cumulative gas volume of explosions per hour (from infrasonic power in the frequency band 0.50 Hz–4 Hz) to the gas volume per hour from infrasonic power in the frequency band 0.50 Hz–4 Hz; small explosions, whose gas volumes could not be estimated due to uncertain limits are ignored (Figure 6.4). Note that we have used, here in the calculation, the active gas volume from acoustic power, despite its underestimation of the real actif gas volume because the total gas volume from acoustic power per hour is calculated using the conduit radius. The total gas volume per hour is estimated by summing the cumulative active and passive gas flux per hour.

6.4.3 Thermal records

The thermal energy is estimated from the brightness temperature and using the Stefan-Boltzmann law by (e.g. Marchetti et al., 2009)

$$\mathrm{E}_{\mathsf{thermal}} = \epsilon_{\mathsf{thermal}} \sigma_{\mathsf{thermal}} \mathcal{A}_{\mathsf{FOV}} \int_0^\tau \left(T(t)^4 - T_{\mathsf{Back}}^4 \right) \mathrm{d}t, \tag{6.5}$$

where, $\epsilon_{\mathsf{thermal}}$ is the emissivity of the surface of the ejecta (~0.95 for a basalt at 1000 °C, see tables 2.3 and 8.1 in Harris, 2013, for a review), $\sigma_{\mathsf{thermal}}$ the Stefan-Boltzmann constant (5.67×10^{-8} W.m^{-2}.K^{-4}), T the brightness temperature (K), T_{Back} the background temperature (K) taken as the temperature just before the explosion and $\mathcal{A}_{\mathsf{FOV}}$ the area of the field of view (m^2) of the radiometer. Thermal energy is then very dependant on the background

temperature T_{Back}, the field of view area $\mathcal{A}_{\mathsf{FOV}}$ and on the choice for the limits of the explosions.

The offset of the thermal signal on each detection corresponds to the entry of the first ejecta into the field of view of the radiometer. The delay of the onset on the simultaneous records from two radiometers with their field of view at different elevation is equal to the flying time of the ejecta to rise from the lower to the upper radiometer. The ejecta velocity $\mathrm{U}_{\mathsf{ejecta}}$ ($\mathrm{m.s}^{-1}$) can be estimated by

$$\mathrm{U}_{\mathsf{ejecta}} = \frac{r_{\mathsf{vent}} \left(\sin\theta_1 - \sin\theta_2\right)}{t_{0,\mathsf{upper}} - t_{0,\mathsf{lower}}}. \tag{6.6}$$

Uncertainties are mostly due to the long efficient response time of the radiometers (Section 4.2.4, e.g. Chevalier and Donnadieu, 2015; Harris, 2013).

6.4.4 Seismic records

We can estimate the seismic energy, assuming that the ground velocity is due to pure body waves, by (Johnson and Aster, 2005)

$$\mathrm{E}_{\mathsf{seismic}} = \frac{2\pi r_{\mathsf{vent}} \rho_{\mathsf{rock}} c_{\mathsf{rock}}}{\mathsf{A}_{\mathsf{seismic}}} \int_0^\tau \mathsf{S}^2_{\mathsf{seismic}} u^2(t) \mathrm{d}t, \quad \mathsf{A}_{\mathsf{seismic}}(r_{\mathsf{vent}}) = \exp\left(-\frac{\pi f_{\mathsf{event}} r_{\mathsf{vent}}}{c_{\mathsf{rock}} \mathsf{Q}_{\mathsf{seismic}}}\right), \tag{6.7}$$

where $\rho_{\mathsf{rock}} = 2000\,\mathrm{kg.m}^{-3}$ and $c_{\mathsf{rock}} = 2500\,\mathrm{m.s}^{-1}$ are the rock density and seismic P-wave velocity into the rock, $\mathsf{A}_{\mathsf{seismic}}$ is the attenuation and $\mathsf{S}_{\mathsf{seismic}}$ accounts for the site effects and are neglected here; $\mathsf{Q}_{\mathsf{seismic}}$ is the quality factor.

The main seismic frequency of explosions is estimated by looking for the maximum amplitude of the signal spectrum of the explosion.

6.4.5 Combined methods

The particle size, i.e. the equivalent diameter of the ejecta, can be estimated from the gas and ejecta velocities by a dimensionless analysis of the equation of motion for a turbulent system and for ejecta having terminal velocities (Steinberg and Babenko, 1978). We assume that the particle of diameter D_P and density ρ_{ejecta} is carried with a velocity $\mathrm{U}_{\mathsf{ejecta}}$ by the gas flow of velocity $\mathrm{U}_{\mathsf{gas}}$ and density ρ_{gas}. The dimensionless analysis of the equation of motion for a tubulent flow gives (Steinberg and Babenko, 1978)

$$D_P = \frac{3 C_D \rho_{\mathsf{gas}}}{4 g \rho_{\mathsf{ejecta}}} \left(\mathrm{U}_{\mathsf{gas}} - \mathrm{U}_{\mathsf{ejecta}}\right)^2, \tag{6.8}$$

where $C_D = 0.50$ is the drag coefficient, $\rho_{\mathsf{gas}} = 0.80\,\mathrm{kg.m}^{-3}$ the dusty gas density, $g = 9.81\,\mathrm{m.s}^{-2}$ the constant of gravity and $\rho_{\mathsf{ejecta}} = 850\,\mathrm{kg.m}^{-3}$ the density of ejecta. The uncertainties on the gas and ejecta densities and the ejecta velocities is such that we estimate a rough approximation of the particle size. However these estimates of the ejecta size is very important as it is a key parameter for models of plume dynamics.

The depth of the top of the magma column ΔH, i.e. the elevation of the top of the magma column into the conduit, is estimated from the thermo-acoustic delay $\Delta t = t_{\mathsf{thermal}} -$

$t_{\text{infrasonic}}$ by (Figure 4.47, e.g. Ripepe et al., 2002)

$$\Delta H = \left(t_{\text{thermal}} - t_{\text{infrasonic}} + \frac{r_{\text{vent}}}{c_{\text{atm}}} \right) \frac{c_{\text{conduit}} \mathrm{U}_{\text{ejecta}}}{c_{\text{conduit}} - \mathrm{U}_{\text{ejecta}}} \tag{6.9}$$

where c_{conduit} is the sound speed into the conduit.

The sound speed in the conduit is estimated assuming a homogeneous two-phase flow between gas and ejecta by (Wood, 1955)

$$c_{\text{conduit}} = \frac{1}{\sqrt{(\alpha_{\text{gas}}\rho_{\text{gas}} + (1-\alpha_{\text{gas}})\rho_{\text{ejecta}}) \left(\frac{\alpha_{\text{gas}}}{\rho_{\text{gas}} c_{\text{gas}}^2} + \frac{1-\alpha_{\text{gas}}}{\rho_{\text{ejecta}} c_{\text{ejecta}}^2} \right)}}, \tag{6.10}$$

where α_{gas} is the gas volume fraction and visualy range between 0.50 % and 0.97 % on videos. The proportion of gas and ejecta in the conduit has significant effects on the sound speed (Figure 4.48).

The thermo-infrasonic delay Δt, measured at the distance r_{vent}, is corrected for value it will have if the infrasonic and thermal sensors were located at 100 m:

$$\begin{aligned} \Delta H &= \left(\Delta t + \frac{r_{\text{vent}}}{c_{\text{atm}}} \right) \left(\frac{\mathrm{U}_{\text{ejecta}} c_{\text{conduit}}}{c_{\text{conduit}} - \mathrm{U}_{\text{ejecta}}} \right) \\ &= \left(\Delta t_s + \frac{r_s}{c_{\text{atm}}} \right) \left(\frac{\mathrm{U}_{\text{ejecta}} c_{\text{conduit}}}{c_{\text{conduit}} - \mathrm{U}_{\text{ejecta}}} \right) \\ \Rightarrow \Delta t_s &= \Delta t + \frac{r_s - r_{\text{vent}}}{c_{\text{atm}}}, \end{aligned} \tag{6.11}$$

where Δt_s is the thermo-infrasonic delay scaled at the distance of reference $r_s = 100$ m. The difference between the scaled and measured delays is -0.53 s and -0.71 s in June 2009 and Sept-Nov 2016, respectively.

We define the volcanic acoustic-seismic ratio (VASR) and volcanic acoustic-thermal ratio (VATR) per sliding window by

$$\text{VASR} = \frac{\text{RMS}_{\text{infrasonic}}}{\text{RMS}_{\text{seismic}}}, \tag{6.12}$$

$$\text{VATR} = \frac{\text{RMS}_{\text{infrasonic}}}{\text{RMS}_{\text{thermal}}}, \tag{6.13}$$

respectively. The VASR and VATR per sliding window acount for the passive and active activity (i.e. explosions and inter-explosions).

We define the volcanic acoustic-seismic ratio ($\text{VASR}_{\text{event}}$) and volcanic acoustic-thermal ratio ($\text{VATR}_{\text{event}}$) per explosion by

$$\text{VASR}_{\text{event}} = \frac{\text{E}_{\text{infrasonic}}}{\text{E}_{\text{seismic}}}, \tag{6.14}$$

$$\text{VATR}_{\text{event}} = \frac{\text{E}_{\text{infrasonic}}}{\text{E}_{\text{thermal}}}, \tag{6.15}$$

respectively.

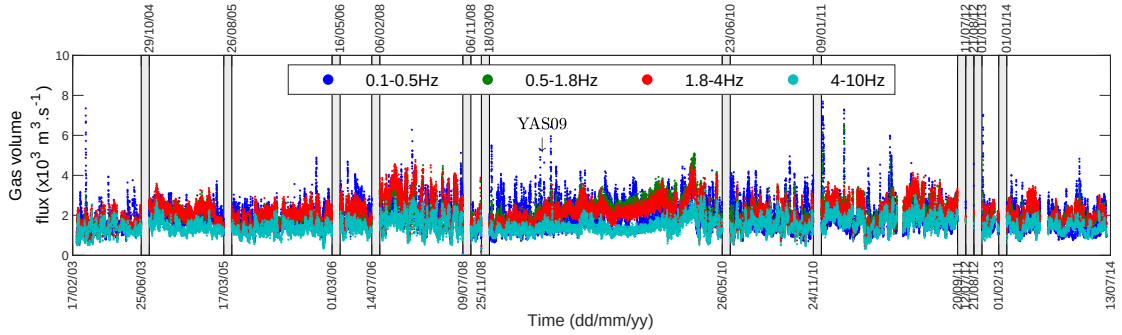

Figure 6.5 – Gas volume flux by frequency bands from infrasonic records at Yasur from 2003 to 2014, including active and passive degassing . Gaps in the records appear as gray rectangles with the dates of start and stop of the gap at the bottom and at the top, respectively.

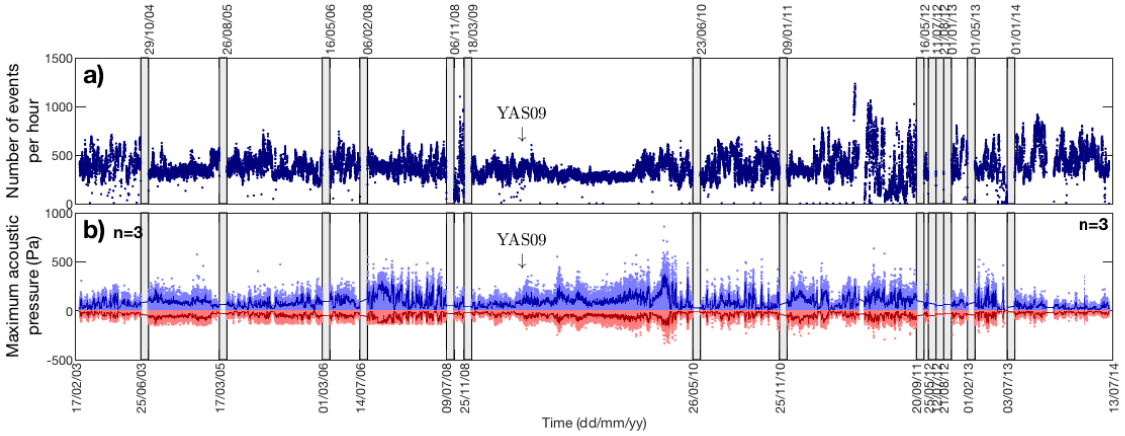

Figure 6.6 – Summary of the detection on infrasonic records at Yasur from 2003 to 2016: a) Number of event per hour. b) Maximum (blue dots) and minimum (red dots) acoustic pressure per event; the curves show the mean of the maximum and minimum acoustic pressure of the 3 strongest explosions. The infrasonic sensor is located ∼500 m north-east from the centre of the crater. Gaps in the records appear as gray rectangles with the dates of start and stop of the gap at the bottom and at the top, respectively.

6.5 Results

6.5.1 Temporal variability

We have shown in the previous chapter (Chapter 5) that the Strombolian activity can vary between volcanoes. We also have shown that the Strombolian activity can vary in time at the same volcano with the data from the two field campaigns at Yasur (see figures 5.7, 5.8, 5.12 and 5.16 from previous chapter). In the present chapter, we focus on the temporal variability of the Strombolian activity at Yasur.

The acoustic pressure is measured quasi-continuously by a permanent station on from Mount Melkem, since 2003, at a distance of 500 m from the centre of the crater. The station is partially broken since the cyclone Pam, in March 2015 and has not been repared yet. The gas volume flux obtained from these almost 12 years of records, equivallent to 4.5 years in continuous, also shows the temporal variability of the Strombolian activity, at Yasur, in terms of total degassing (passive + active, figure 6.5). The number of events per hour and

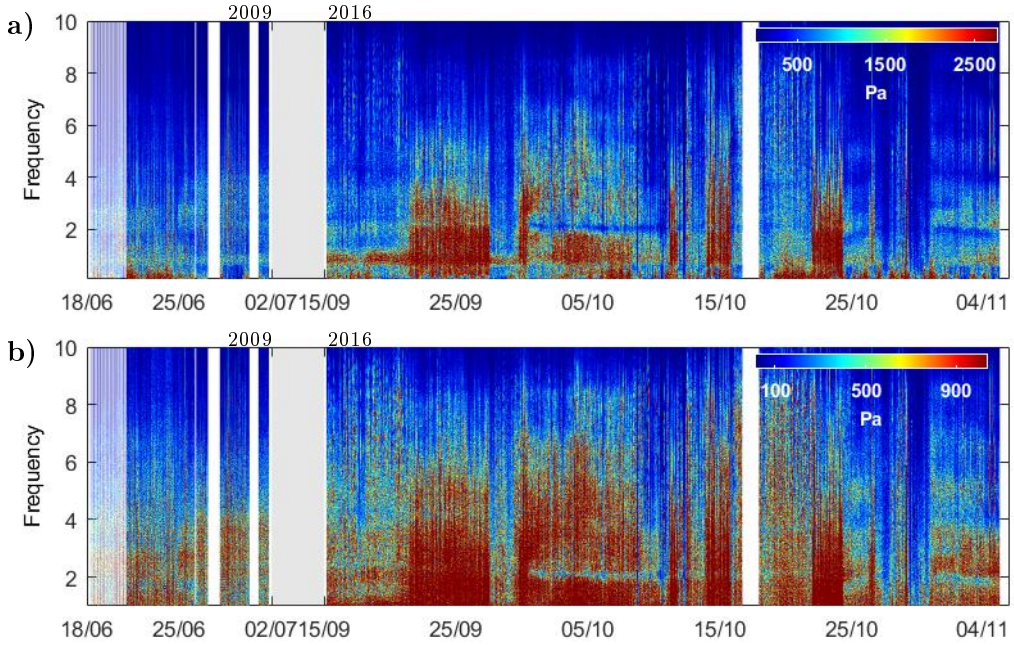

Figure 6.7 – Frequency contents of the infrasonic records during the two field campaigns at Yasur between a) 0.10 Hz and 10 Hz and b) 1 Hz and 10 Hz. Each vertical line corresponds to a spectra per hour, and the number of vertical lines corresponds to the number of hours during the two field campaigns. Note the different scale of the amplitude.

the maximum acoustic pressure per event show the temporal activity of the Strombolian activity at Yasur in terms of active degassing (i.e. emitted by the Strombolian explosions, figure 6.6). We observe that the transition from a quiet activity to a strong activity can vary in duration and that the strong phases of activity can also vary in duration. We are interested in finding precursors to these increases of the intensity of the Strombolian activity.

We focus on the two field campaings at Yasur for which we have simultaneous infrasonic, thermal and seismic records. We have chosen to present each data type before combining them.

6.5.2 Infrasonic analysis

The results from the infrasonic processing during both field campaigns are shown on figures 6.7 to 6.13.

The frequency contents of the infrasonic records present variations with time (Figure 6.7). We observe phases of activity with dominant frequencies that are higher (2 Hz–4 Hz) than during other phases. These phases dominated by high frequencies are associated to ash-poor and strong Strombolian explosions (Meier et al., 2016). The infrasonic energy per sliding window and by frequency bands also reveals that the frequency contents vary in time (Figure 6.8). We also observe, sometimes, a high level of low frequencies ($<$25/06/2009).

The frequency bands of detection (0.50 Hz–1.80 Hz and 1.80 Hz–4 Hz) are often dominant over the two other frequency bands (0.10 Hz–0.50 Hz and 4 Hz–10 Hz) indicating that there is a quite high signal to noise ratio on our records (Figure 6.8c). The high frequencies (4 Hz–10 Hz) are very weak. However the low frequencies (0.10 Hz–0.50 Hz) can be dominant, such

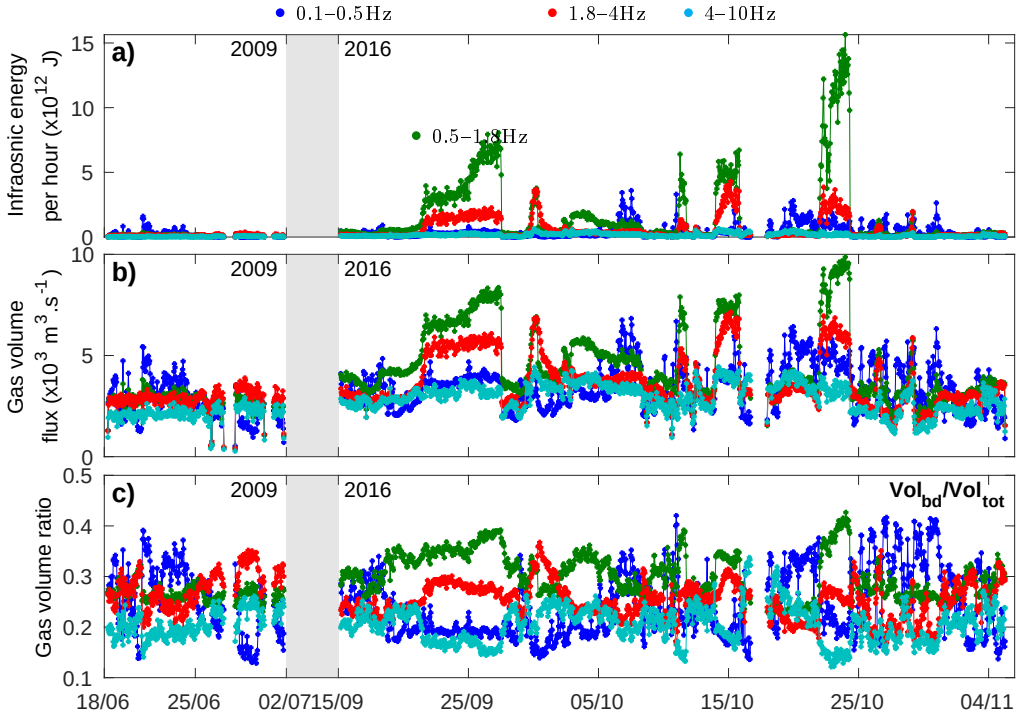

Figure 6.8 – a) Infrasonic energy per hour by frequency bands, b) gas volume flux by frequency bands and c) proportion of the gas volume flux by frequency bands at Yasur during the two field campaigns. No correction is applied on the gas volume flux. The significant level of the 0.10 Hz–0.50 Hz frequency band early in June 2009 is associated to bad weather conditions and oceanic noise.

as before the 25th of June 2009. These low frequencies are probably due to the bad weather and/or oceanic waves and decreases the signal to noise ratio. The quality of our data in that case is deteriorated (Figure 6.9c and 6.10c).

We detect 172 ev.h^{-1} in average and the maximum acoustic pressure can reach 2270 Pa at 100 m (Figure 6.9a–b). The rate of explosions and the maximum acoustic pressure is very variable in time and is correlated to the gas volume flux per sliding window in the frequency bands of the explosions (0.50 Hz–4 Hz). The activity is almost steady during the 15 days in June 2009. However we observe an alternation of quiet and strong phases of activity in Sept-Nov 2016. We then wonder why or how the activity in June 2009 can remain steady and why the activity in Sept-Nov 2016 is unsteady.

The infrasonic duration of the Strombolian variations also varies (0.20 s–10 s) but is not as clear as the variability of the rate of explosions nor the maximum acoustic pressure (Figure 6.9c). Moreover the infrasonic duration is over-estimated when there are energetic low frequencies (0.10 Hz–0.50 Hz). This bias makes us to reduce the maximum duration to 5 s.

The infrasonic energy and the gas velocity per explosion are well corraleted (Figure 6.10a–b) because the gas velocity is proportional to the infrasonic energy to the power 1/4 and because the Parseval theorem is used to estimate the infrasonic energy only between 0.50 Hz and 4 Hz. This narrower frequency band corrects the bias induced by the low frequencies. There is also a strong visual correlation between the maximum acoustic pressure and the infrasonic energy and the gas velocity.

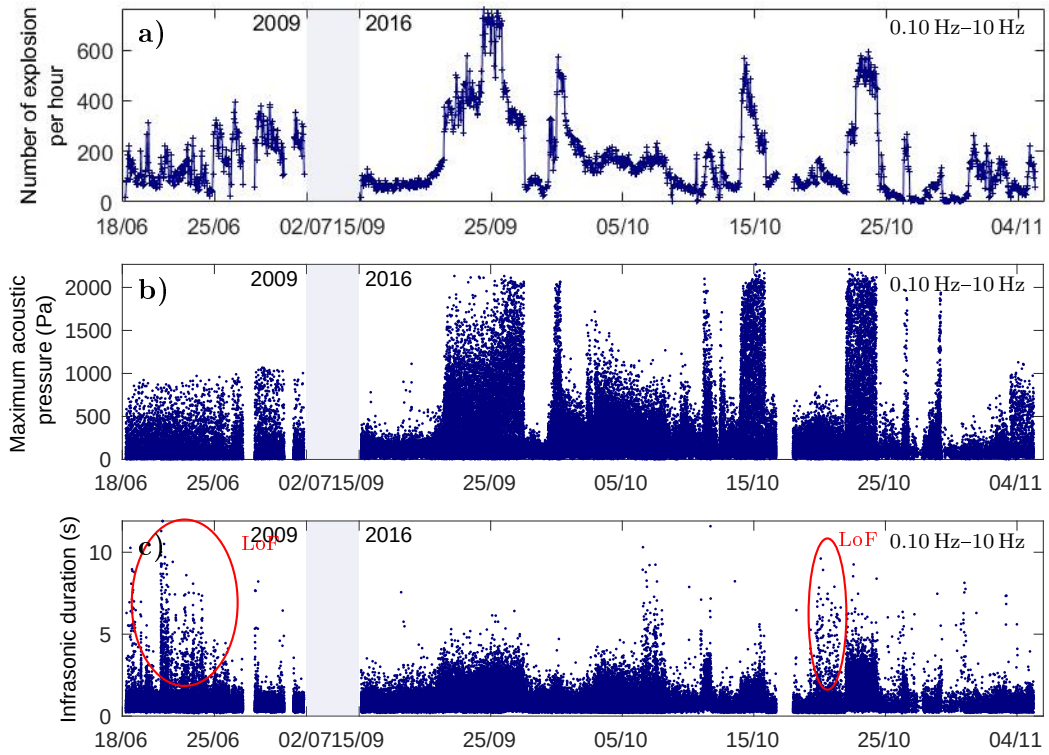

Figure 6.9 – Key parameters of Strombolian explosions on infrasonic records as a function of time, during the two field campaign at Yasur. a) Number of events per hour. b) Maximum acoustic pressure per event, scaled at 100 m. c) Duration of the explosions seen by the infrasonic sensor. The red ellipses highlight periods during which the estimates are of bad quality due to the existence of residual strong low frequency, 0.10 Hz–0.50 Hz despite the filtering.

However the gas volume per Strombolian explosion, calculated on the signal filtered between 0.10 Hz and 10 Hz, is often abnormously increased for the small explosions when there are too much low frequencies because the two succesive integrations increase the offset due to the low frequencies (Figure 6.10c and figure 6.11). We have chosen to keep the wide frequency band, despite this bias, because the low frequencies have a small effect on the strong explosions and because the strong explosions have information within the low frequencies (tail of the infrasonic waveform). The over-estimated values of the gas volume of the small explosions can be removed using the programme for the selection of the explosions (see section 3.6.5).

One of the most important information is the gas flux that can be estimated either for the active degassing (explosions), for the passive degassing (inter-explosion) or for the total degassing (explosions + inter-explosion, figure 6.12). The gas flux from passive degassing is 2–50 times the gas flux from active degassing. The active and passive degassing are roughly correlated when comparing strong and quiet phases. However strong phases do not always have the same increase for the active and passive degassing (see the thick crosses in figure 6.12a–b)

The critical value of the gas flux above which the activity switches from quiet to strong is $4.0 \times 10^3\,\mathrm{m^3.s^{-1}}$ (passive: $3.6\,\mathrm{m^3.s^{-1}}$; active: $420\,\mathrm{m^3.s^{-1}}$, figure 6.12). The exact value of the transition quiet–strong is extremely clear on the 21st of September 2016 where the increase in gas flux starts progressively before its sudden increase. Using this value for the critical gas flux also matches all transitions quiet to strong and strong to quiet. There is a slight crossing of the transition on the 28th of June 2009 on the passive degassing,

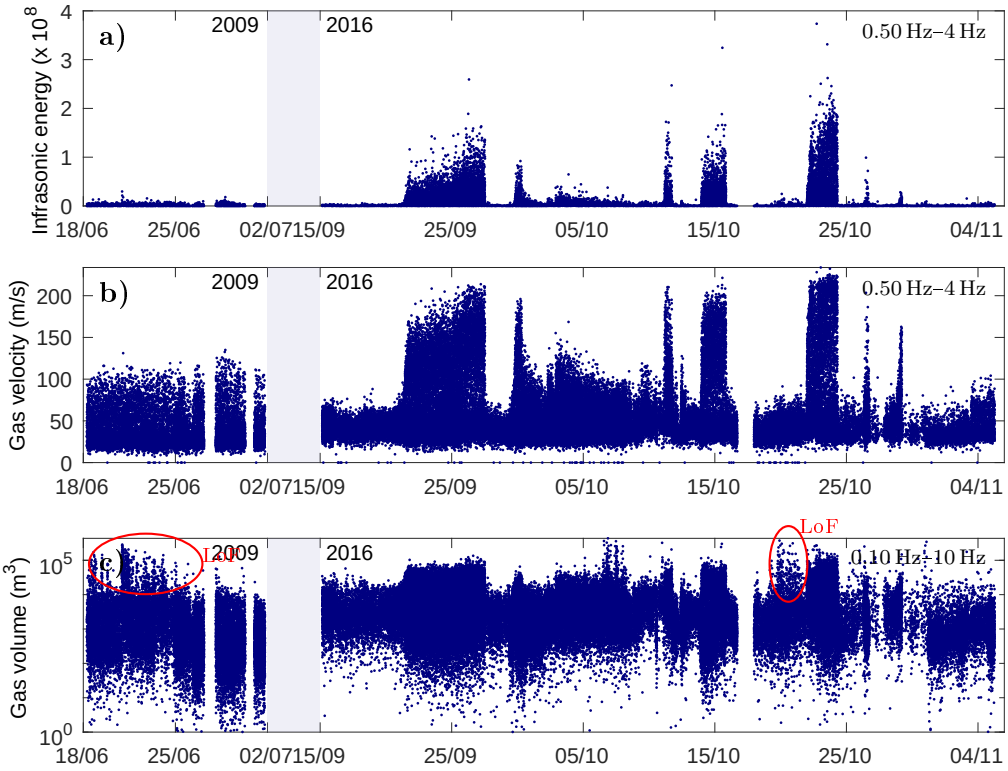

Figure 6.10 – Estimation of a) infrasonic energy, b) gas velocity and c) gas volume per event during the two field campaigns at Yasur. The red ellipses highlight periods during which the estimates are of bad quality due to the existence of residual strong low frequency, 0.10 Hz–0.50 Hz despite the filtering.

suggesting that other small sources of degassing might exist.

The comparison of the degassing in the 0.50 Hz–1.80 Hz and 0.50 Hz–1.80 Hz frequency bands highlights variations of the main frequency of the Strombolian activity with sometimes higher amplitude in the 0.50 Hz–1.80 Hz band than in the 0.50 Hz–1.80 Hz (around the 25/09/2016) and vise-versa (around the 01/10/2016, Figure 6.13)

6.5.3 Thermal analysis

The results from the thermal processing are presented in figures 6.14 and 6.15.

The variation of the brightness temperature is up to 600 K during Strombolian explosions (Figure 6.14a). However the maximum variation of the brightness temperature per explosion does not have a clear temporal variations (Figure 6.14a) in contrast to the maximum acoustic pressure (Figure 6.9b). The thermal duration per Strombolian explosion have also little variations (Figure 6.14b). However we can observe an increase of the thermal duration before the 20th of September that is followed by the shortening of the signal between the 20th and 30th of September 2016 (Orange dashed lines in figure 6.14b). The decrease in the duration of the thermal signals seems to be correlated to the strong activity seen on infrasonic records during at that time (Figures 6.9 and 6.10). The shortening of the duration can be explained by the existence of gas-rich Strombolian explosions that have a too low quantity of ashes to stay above the threshold of detection of the radiometers for a long time. This is consistent with the high frequency contents on infrasonic records during

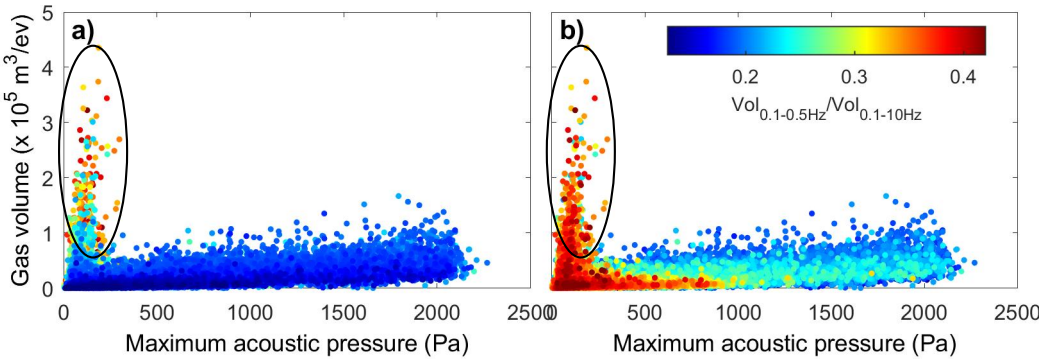

Figure 6.11 – Gas volume per event as a function of the maximum acoustic pressure and the proportion of low frequencies (0.10 Hz–0.50 Hz). a) Descent order and b) ascent order of the proportion of the low frequencies . Ellipses show the periods associated to energetic low frequencies and the wrongly estimated gas volumes.

that period (Figure 6.7).

It is difficult to get information from the thermal energy per event and from the ejecta velocity because the key parameters from the thermal records (maximum temperature variation and thermal duration) give little information themselves (Figure 6.15), because the measurements recorded by the radiometers are very sensitive to the number of ejecta, their size and surface temperature within the field of view and because the gas opacification can blind the radiometers (see section 4.2 and Gaudin, 2012). Moreover, the estimates of thermal energy and ejecta velocity are easy biased because of the long efficient response time of the radiometers (Sections 2.3 and 4.2.3a).

6.5.4 Seismic analysis

The results from the seismic processing is presented in figures 6.16 and 6.17.

The maximum ground velocity ranges from a few micrometres per second to a few millimetres per second s(Figure 6.16a–b). We observe noticeable variations in time on the ground velocity, although not very large, and some of them are at the same time than the variations we have observed on infrasonic records. The seismic duration of the Strombolian explosions ranges from a few seconds to a few tens of seconds and does not have clear variations (Figure 6.16c). We observe a bimodality on the distribution of the seismic duration with a cut off around 10 s (Figure 6.16d).

The seismic energy varies in time similarly to the variations of the infrasonic energy. However, the coupling between infrasonic and seismic parameters does not seem to be the same all time; for example higher seismic energy around the 15th of October than the 25th of September (Figure 6.17a), whereas infrasonic energy reaches the same order of magnitude the 15th of October and the 25th of September (Figure 6.10a).

We observe on the temporal evolution of the main seismic frequency of the Strombolian explosions that the seismic records from June 2009 have not been corrected from the instrumental response, yet (Figure 6.17c). Two dominant frequencies appears at 1.75 Hz and 2.50 Hz (Figure 6.17d). However there is no clear temporal variations of the main frequency of the events.

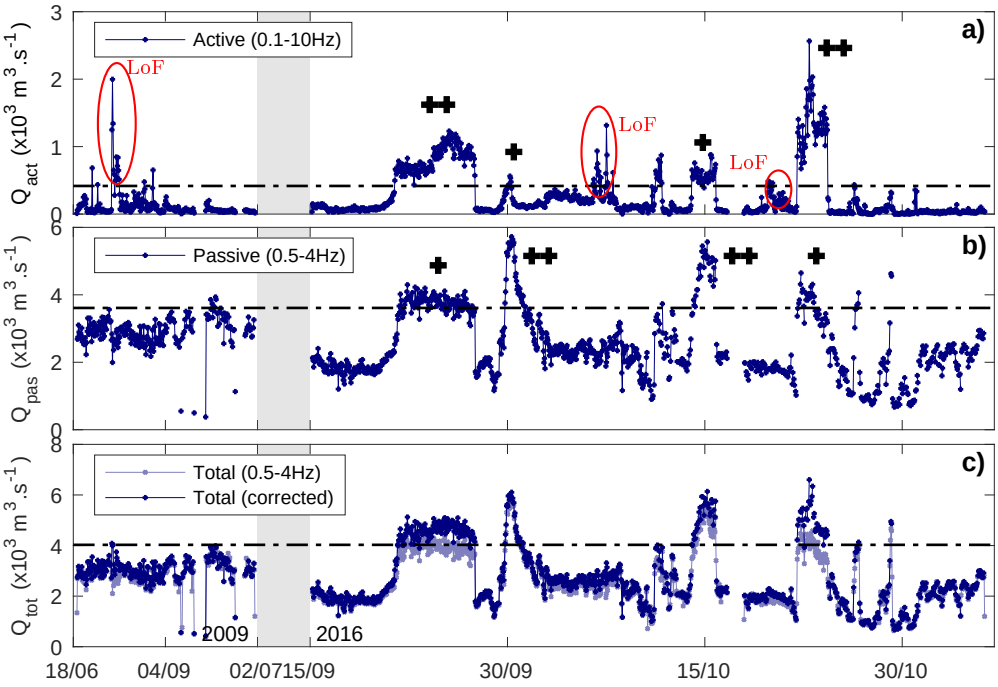

Figure 6.12 – Proportion of active and passive degasing as a function of time. Gas flux from a) active (small and strong explosions) and b) passive degasing. c) Total gas flux. The thick crosses show the relative increases between the passive and active gas fluxes. The red ellipses highlight periods during which the estimates are of bad quality due to the existence of residual strong low frequency, 0.10 Hz–0.50 Hz despite the filtering.

6.5.5 Thermo-infrasonic analysis

The thermo-infrasonic ratio of energy mostly depends on the infrasonic energy (Figure 6.18a) because of the strong variations existing on infrasonic records (Figure 6.10a) and because the thermal energy has little temporal changes (Figure 6.15a). A high ratio of infrasonic to thermal energy indicates gas-rich explosions because the infrasonic measurements record gas motion while the thermal measurements are measuring the amount and temperature of hot solids or liquids above the vent and are less sensitive to the gas. The time of high ratios of energy, i.e. of gas-rich explosions, is consistent with the previous observation on the thermal duration and the infrasonic spectrogram (Figures 6.7 and 6.14b). Note that the transitions from quiet to strong are very sudden and well marked.

The ratio of the ejecta velocity to gas velocity mirrors the ratio of infrasonic energy to thermal energy (Figure 6.18b). During periods dominated by gas-rich explosions such as the one around the 25th September of 2016, the gas velocity increases more than the ejecta velocity, possibly because larger fragments are ejected (Figure 6.18c). The mean size of the ejecta per event varies with both the ratio of energies and the maximum acoustic pressure (Figure 6.18c). The stronger is the activity, the bigger the average size of ejecta can be, with sizes up to 1.50 m in equivalent diameter.

The thermo-infrasonic delay is shorter during the 2009-field campaign than during the 2016-field campaign (scaled at 100 m, Figure 6.19a) indicating that the top of the magma column is deeper in 2016 than in 2009. The calculation of the depth of the magma column (Equation (6.9)) is biased by the efficient response time of the radiometers that enlarge errors on the thermo-infrasonic delay and on the ejecta velocity. It is then difficult to

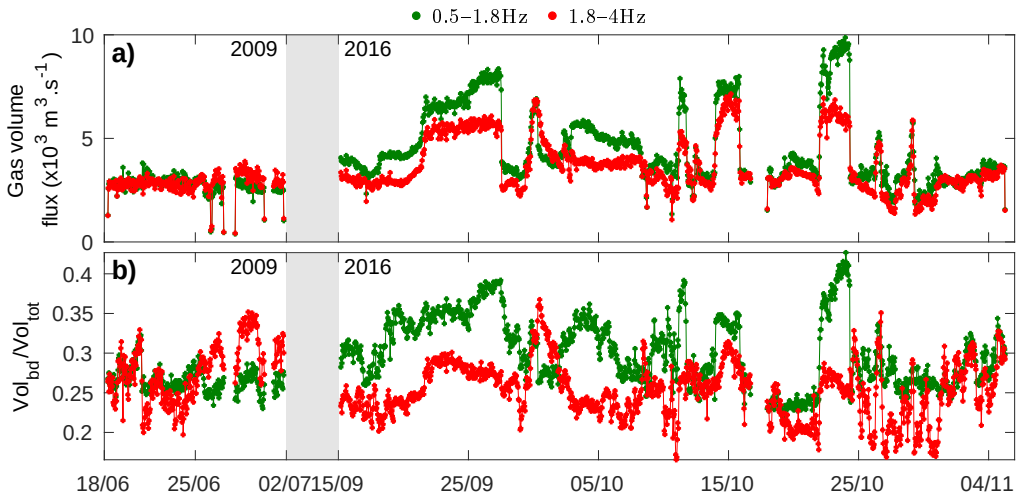

Figure 6.13 – a) Gas volume flux at Yasur during the two field campaigns and b) proportion of the hourly volume of gas by frequency band, 0.50 Hz–1.80 Hz and 1.80 Hz–4 Hz exclusivelly. No correction is applied on the gas volume flux.

give an estimation of the depth from the estimates per event (Figure 6.19b). However the estimates obtained from Monte Carlo analyses (Section 5.6.3) show that the depth of the magma column remains shallow (2009: 0 m–5 m, 2016: 60 m–90 m, figures 5.13 and B.4 to B.8)

6.5.6 Seismo-infrasonic analysis

The ratio of infrasonic to seismic energy ($\text{VASR}_{\text{event}}$) is correlated with the evolution of the infrasonic energy (Figure 6.20). The variations of the VASR can be due to several sources conditions (Johnson and Aster, 2005):

- a high density plume (i.e. ash-rich, ejecta-rich) produces a low VASR, while a low density plume (gas-rich) produces high VASR;
- a high impedance contrast between the magma and the surrounding rock generates lower VASR than a low impedance contrast;
- a long and narrow conduit (i.e. a deep source) produces a lower VASR than a short and wide conduit;
- a large source region produces lower VASR than a small source region.

We assume that the source region remains small for all Strombolian explosions. The impedance between the magma and the surrounding rocks is assumed to be constant (little variations of the magma composition, temperature and gas volume fraction during the period of observation). The variation of the VASR can be either be due to variations of the plume density or to variations of the depth of the explosions. There are no visual correlation between the depth of the magma column and the VASR (Figures 6.19 and 6.20b). We then deduce that the variations of the VASR are mostly due to the variation of the plume density. The phases with the highest ratio of infrasonic to seismic energy, i.e. the phases with low density plume occur at the same time than our previous observations for the temporal evolution of the gas-rich and ash-rich explosions (Figures 6.7 and 6.15a).

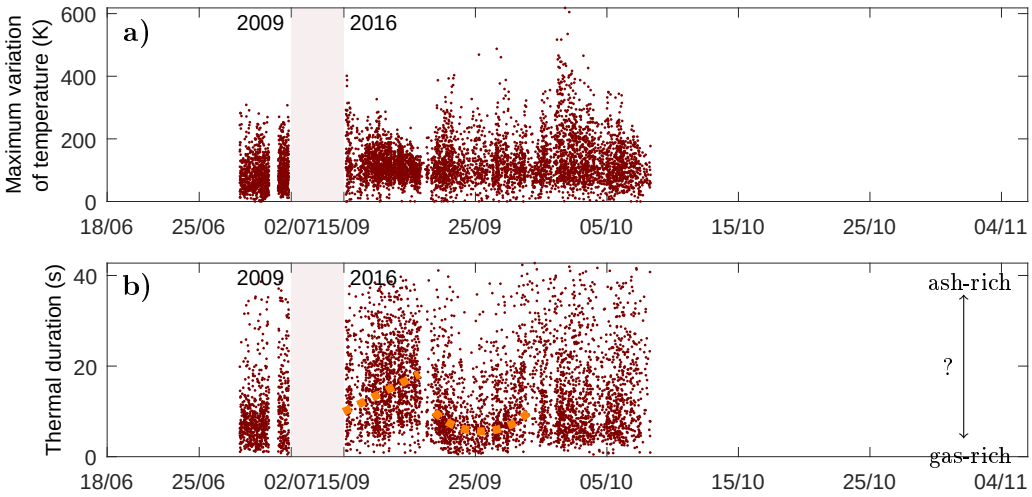

Figure 6.14 – Key parameters of Strombolian explosions on thermal records from the lower radiometer as a function of time, during the two field campaigns at Yasur. a) Maximum variation of temperature per event. b) Duration of the explosions seen by the thermal sensor. The orange dashed lines in b) show the trends that seems to exist.

6.5.7 Analysis of the simultaneous infrasonic, seismic and thermal records

The calculation of the RMS per sliding window of 30 min gives the temporal evolution of the total degassing (active and passive degassing). (Figure 6.21). The infrasonic RMS is correlated to the other infrasonic parameters such as infrasonic energy per sliding window, maximum acoustic pressure, gas velocity and volume, etc. (Figure 6.21a. The thermal RMS has a large and regular decrease in 2009 (Figure 6.21b). This decrease might be either due to the oxydation of the Zn−Se window or due to the variation of the magma level that was observed to be high at that moment. The thermal RMS does not have strong variations in 2016 (Figure 6.21b). The little and cyclic variations (light red) are probably due to the day-night cycle. The seismic RMS seems to be correlated to the infrasonic RMS, however the variations are smoother (Figure 6.21c). The abnormaly large values of the seismic RMS are probably not due to Strombolian explosions but due to an incomplete correction of the earthquakes.

The ratio of energy based on the calculation of the RMS per sliding window (i.e. explosion and inter-explosion), is quite similar to the ratio of energy based on the detections (i.e. explosion, Figures 6.18, 6.20 and 6.22).

The figures 6.23 and 6.24 show the distributions of the key parameters from the different techniques for all events detected on each record independently and for all events detected quasi-simultaneously on the three records, respectively. The events that are detected quasi-simultaneously on the three records were linked looking for the closest event from one record to another (See the method in section 3.6.7). The distributions of the other infrasonic and thermal parameters can be found in the previous chapter (Chapter 5). The distributions of the other seismic parameters can be found in section 6.5.4.

We observe small variations of the distribution of the maximum acoustic pressure, the infrasonic energy and the seismic durations when we compare all explosions (unlinked, Figure 6.23) to explosions that are found on the infrasonic, thermal and seismic records (linked, Figure 6.24). The link between the different techniques highlights a bimodality on the maximum acoustic pressure and the infrasonic energy distribution. However the

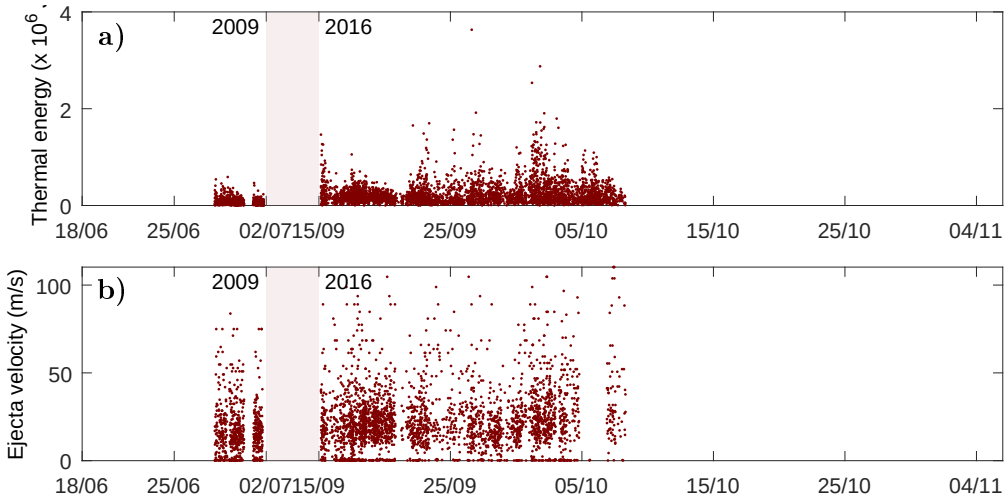

Figure 6.15 – Estimation of a) thermal energy, and b) ejecta velocity per event during the two field campaigns at Yasur.

link between the different techniques erases the bimodality observed on the distribution of the seismic durations. In summary, the typical repose time of explosions is best estimated when using infrasonic, thermal and seismic records independently to one another (unlinked, Figure 6.23). However when the three records are combined, the typical repose time, although only for one specific vent, might suffer from the lack of detectins on one record, due to noise. Furthermore, linking explosions on the three records unsure the best quality of the detections. This reduces the number of small explosions, in practice much more numerous than large explosions, thereby it enhances the two different modes on certain histograms (Figure 6.24).

The high number of parameters makes the analysis of the results difficult. We then focus on unlinked infrasonic data. Indeed, the temporal variations are clear and the variation of the distribution, when considering all or only linked detections, is due to the fact that the infrasonic and seismic sensors record the activity from all vents and the thermal sensor only from one vent.

6.5.8 Phases of intensity

We have determined 34 phases of activity based on the number of detected events and the maximum acoustic pressure per event. We can classify these phases as strong, intermediate and quiet (Figure 6.25 and table 6.1). The strong phases can be long or short, lasting from 9 h–65 h and they can have a precursor (P05, P10). The strong phases can end suddenly (P07, P21, P26) or progressively (P10, P16). Is the length of the strong phases, their precursor and their end is an indicator for different mechanisms? We also observe that the intermediate phases P33 and P34 are similar to the activity in June 2009 (P01) and thus wonder if these phases P33-34 mark the beginning of a new steady period of activity such as in June 2009.

A premilinary study on phases P02 to P08, that have very clear transitions between the strong activity and the quiet activity, highlights two trends when comparing the maximum acoustic pressure per explosion and the maximum ground velocity (Figure 6.26a–b). Strombolian explosions with low maximum acoustic pressure have a wider range of

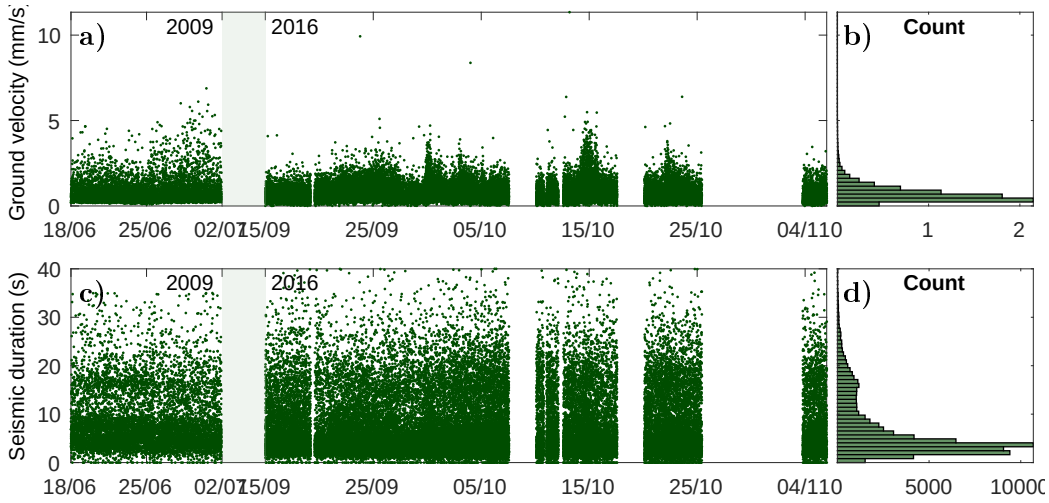

Figure 6.16 – Key parameters of Strombolian explosions on seismic records as a function of time, during the two field campaign at Yasur. Maximum ground velocity per event a) as a function of time and b) the associated histogram. Duration of the explosions seen by the seismic sensor c) as a function of time and d) the associated histogram.

maximum ground velocity than the Strombolian explosions with a high maximum acoustic pressure. The limits between weak and strong explosions can be set at 340 Pa for a distance from the source of 100 m. This limits at 340 Pa is also valide when looking the maximum acoustic pressure as a function of the maximum ground velocity for the whole field campaigns (Figure 6.26c–d).

The trend with low maximum acoustic pressure (<340 Pa at 100 m) exists for all phases indicating that there is a persistent mechanism that leads to the small Strombolian explosions. The trend with the high maximum acoustic pressure is then due to a additional mechanism that is superimposed to the persistent mechanism. This superimposed mechanism is associated to stronger Strombolian explosions than for the persistent mechanism. These observations are consistent with the observation of Spina et al. (2015).

We now focus on the distributions of the infrasonic delays, the infrasonic energy and the gas volume for the strong explosions (>340 Pa) to characterise the strong phases of activity (Figures 6.27 to 6.29 and figures C.5, C.8 and C.9 for an sole view of the strong explosions).

The distributions of the infrasonic return time of the phases P05 to P07 is very similar for the strong explosions with the mode around 100 s (Figure 6.27). The small explosions are more frequent with a mode around 5 s during phases P05 to P07. The distribution of the infrasonic energy during these three phases is also very similar with a mode around 10^5 J for small explosions and around 5×10^7 J for strong explosions (Figure 6.28). The distribution of the gas volume for the strong explosions has a mode at 2×10^4 m^3 per event and at 2×10^3 m^3 for the small explosions and is also similar for phases P05 to P07 (Figure 6.35). The strong phase P05–P07 has been separated in three parts because of the different number of events per 30 minutes and of the increase of the maximum acoustic pressure from P05 to P07 (Figure 6.25b-c). However the distribution of the gas volume per event and the distribution of the return time, for the strong explosions, are key parameters because they characterise the gas flux responsible for these strong explosions. Phases P05–P07 can be part of the same category called S1 for the strong explosions.

We can also associate phases P20–P21 and P25–P26 with a similar reasoning. The distributions

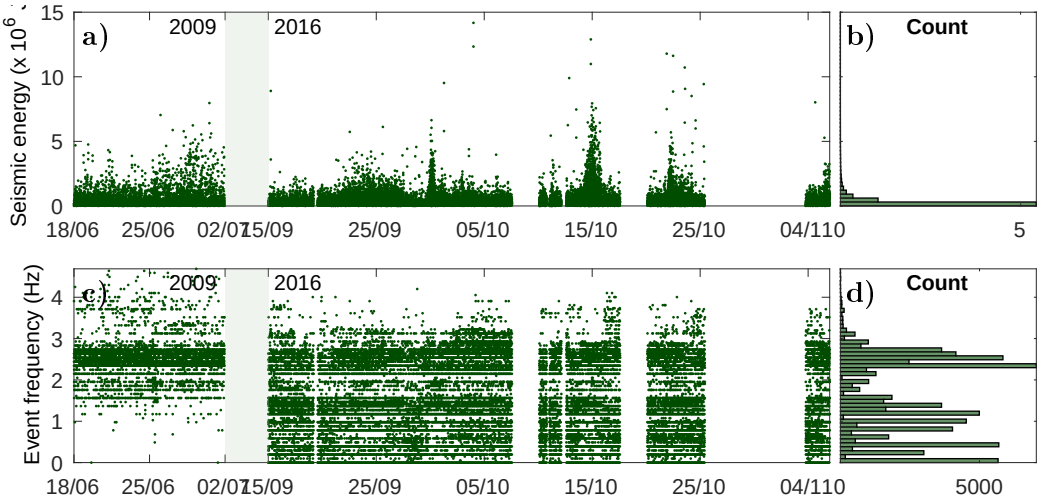

Figure 6.17 – Seismic energy and main seismic frequency per event during the tow field campaign at Yasur. Seismic energy a) as a function of time and b) the associated histogram. Main frequency per event c) as a function of time and d) the associated histogram.

of the infrasonic return time, infrasonic energy and gas volume of P16, P20–P21 and P25–P26 are also similar to the distributions of the infrasonic return time, infrasonic energy and gas volume of P05–P07. Phases P16, P20–P21 and P25–P26 can then be part of the category S1.

The distributions of the infrasonic return time, infrasonic energy and gas volume for the strong explosions of the phases P10, P28 and P31 seems too different for these strong phases to be part of the category S1. Both phases P10 and P31 have a precursor charaterised by an intermediate phase that have an increasing activity (P09 and P30). These phases P10 and P31 have similar distributions and then can be part of the same category S2 for the strong phases. The strong phase P28 does not seem to belong to S1 nor S2 when looking at the distribution of the infrasonic return time of the strong explosions. However the modes of the infrasonic energy and gas volume are similar to the values of P31. We then decide to put P28 into S2.

The distribution of return time of the strong explosions during phases P01 and P33–34 are similar despite the diffence of duration of these three phases (Table 6.1). The modes of the distribution of the gas volume for the small explosions are similar for the three phases. However the distribution of the gas volume during P01 has a bump with larger volumes because of the bias induced by low frequencies (0.10 Hz–0.50 Hz) on the infrasonic records (Figures 6.8 and 6.10c). The gas volume distribution is then not a good parameter to characterise the small Strombolian explosions when there are too much bias associated to low frequencies. The distributions of the infrasonic energy for the strong explosions during phases P33 and P34 are similar but they have a lower mode than the infrasonic energy during P01. We choose to put P01 and P33–34 in the same category I1, despite their small differences (distributions), because they have explosions with maximum acoustic pressure of the same order of magnitude and an infrasonic RMS similar (Figure 6.25a and c).

We choose to put P03–04 and P09 in the same category I2 because they occur at the transition between a quiet phase and a strong phase with a progressive increase of the activity and because the distribution of the infrasonic return and infrasonic energy for the small explosions are similar during these three phases (Figures 6.25, 6.27 and 6.28). The distributions for the strong explosions are slightly different because the transition have not

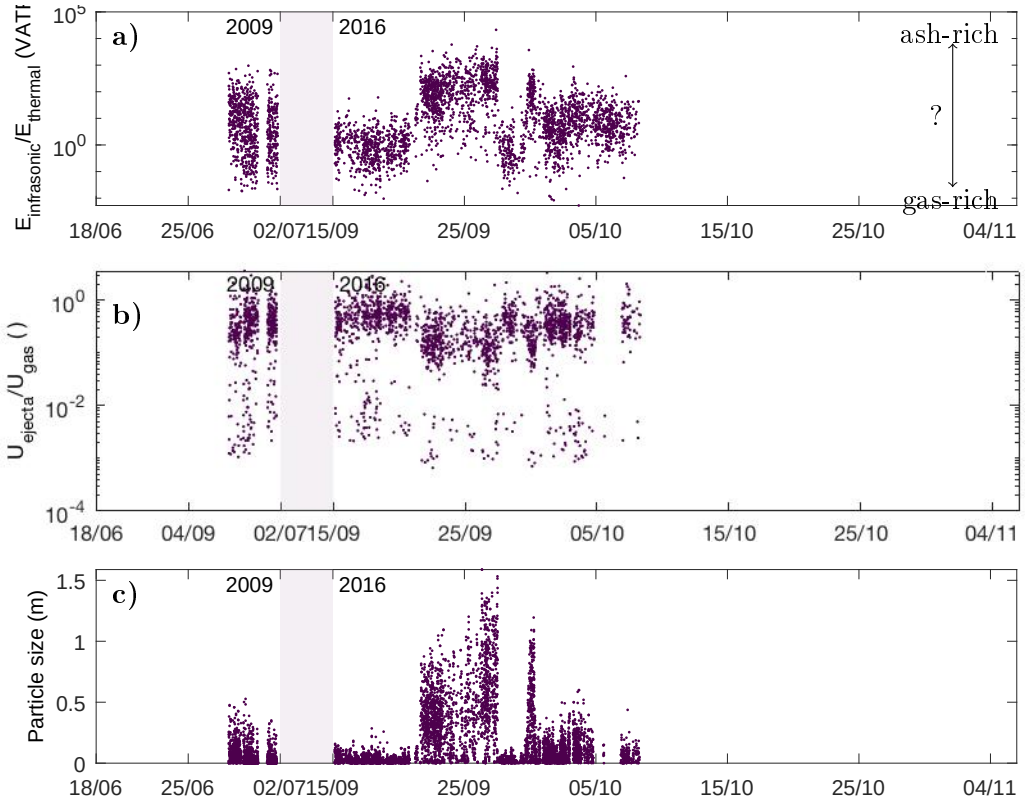

Figure 6.18 – Ratio of energy from simultaneous thermo-infrasonic records during the two field campaigns at Yasur. a) Ratio of infrasonic energy to thermal energy (VATR). b) Ratio of ejecta velocity to gas velocity. c) Mean particle size per event.

the same duration.

The phases P12 and P18 have maximum acoustic pressure per event of the same order of magnitude, higher than the maximum acoustic pressure of the other intermediate phases. However, we can not put them with the strong phases because they both have a low infrasonic RMS and they do not reach the critical gas flux neither for the active degassing nor for the passive degassing (the peak corresponds to P16, Figures 6.12 and 6.25). The distributions of the infrasonic return time, the infrasonic energy and the gas volume for the strong explosions during phases P12 and P18 are very similar. Furthermore, we observe a smoother decrease of the activity during phases P12 and P18 than during strong phasesof categories S1 and S2. The phases P12 and P18 can then be part of the same category I3.

It is more difficult to built categories with the phases of quiet activity because we must focus on the small explosions instead of the strong explosions. The small explosions are more difficult to detect than the strong explosions. Then we have less accurate distributions for the small explosions than for the strong explosions. However the phases P02, P08, P13, P19 and P30 can be part of the same category Q1. The phase P15 can also be part of Q1 because the distribution of the infrasonic return time, the infrasonic energy and the gas volume during the phases P13 and P15 are very similar for the strong explosions. The phases P22 and P24 are put together in category Q2.

The figure 6.30 summarises the main phases built based on the infrasonic parameters. The detailed comparison of the distribution for the main phase is also available in tables C.1 to C.8. The detailed comparison of the distribution for the main phase is also available in

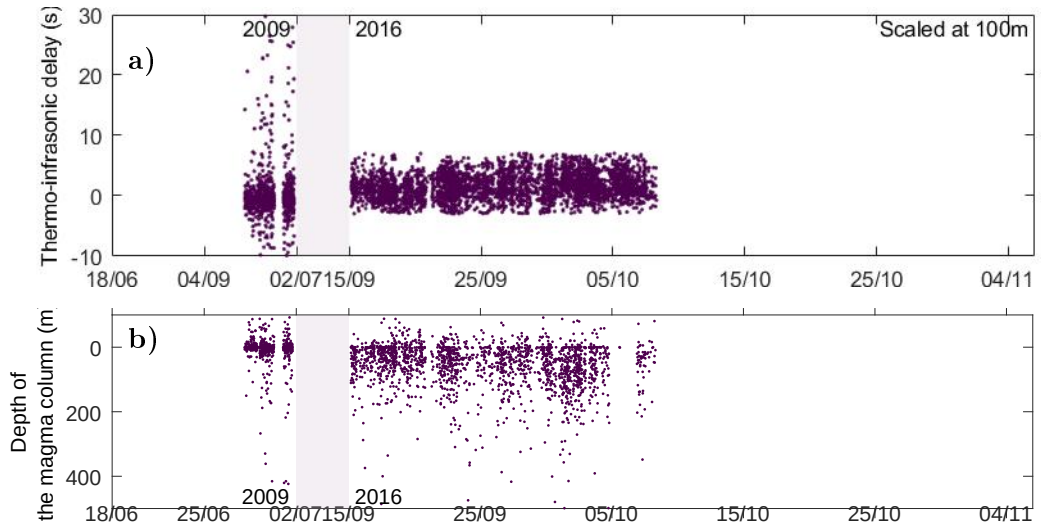

Figure 6.19 – Estimation of the depth of the top of the magma column during the two field campaigns at Yasur. a) Thermo-infrasonic delay scaled at 100 m. b) Depth of the top of the magma column.

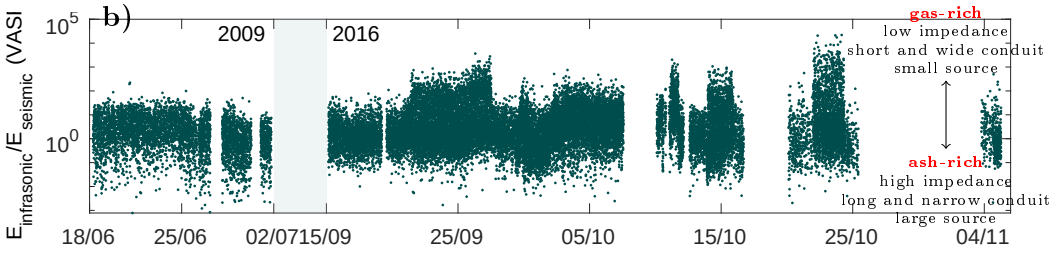

Figure 6.20 – Ratio of infrasonic energy to seismic energy (VASR) during the two field campaigns at Yasur.

tables C.1 to C.8.

It is also interesting to compare the infrasonic and seismic RMS per phases (Figure 6.31). We can focus on the phases P02 to P08. The quiet phase P02 has low infrasonic and seismic RMS. The infrasonic and seismic RMS then increase during the intermediate phases P03–P04 to the strong phase P05. The infrasonic and seismic RMS continue to increase to the strong phase P06. However, the seismic RMS decreases during the strong phase P07 while the infrasonic RMS continue to increase. Finally the infrasonic RMS decrease suddenly to the quiet phase P08 without any transition. The infrasonic and seismic RMS of the phases P02 and P08 are of the same order of magnitude.

The construction of the figure of the infrasonic RMS as a function of the seismic RMS highlights two trends (Figure 6.31). The trend for small infrasonic and seismic RMS remains stable with time while the trend for the high infrasonic and seismic RMS vary. This observation is compatible with the hypothesis of the existence of a mechanism during the strong phases that is superimposed to a persitent mechanism.

We now look to the distributions of the most determinant parameters for explosions that are recorded by the infrasonic and seismic sensors (Figures 6.33 to 6.35, 6.37, 6.38 and C.2). The advantage of looking for linked infrasonic and seismic detections is that we are sure they are really due to Strombolian explosions. Using linked explosions is most

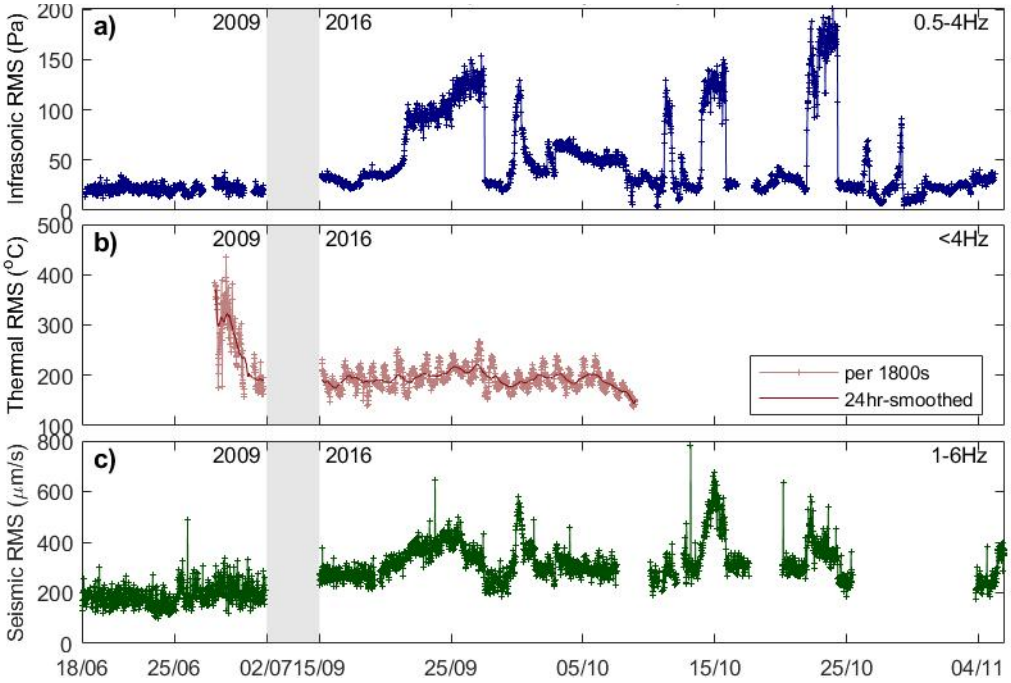

Figure 6.21 – RMS per 30 minutes during both field campaigns at Yasur: a) infrasonic, b) thermal and c) seismic. The seismic RMS is done on the seismic records corrected from earthquakes found in the UGSS database.

appropriate because the detections on seismic records are not as easily done as for infrasonic records, due to the slow start of the waveforms and a relatively long duration (Figures 6.23 and 6.24). However using solely linked detections is not the best way to estimate the typical return time, best detected on unliked explosions on infrasonic records where the detections are reliable. Furthermore the gaps on seismic records are more frequent than on infrasonic records. This leads to inaccuracy in the histograms. The other advantage in using explosions linked in seismic and infrasonic records is to provide the whole temporal sequence, despite several gaps, in contrast to analyses done when infrasonic, thermal and seismic signals were associated. While infrasonic records were fully analysed by unsing the sole records, using explosions linked in seismic and infrasonic reduces the number of small explosions below seismic detections. This also allows a more reliable analysis of the seismic detections for its distribution and its comparison with a given explosion.

The proportion of strong explosions is, as expected, higher when combining infrasonic and seismic events than when looking for all infrasonic events(Figure 6.32). The distribution of hte infrasonic return time of the strong explosions (>340 Pa at 100 m) are very similar when looking for all infrasonic events (unlinked, Figure 6.27) and for infrasonic events linked to seismic events (Figure 6.33). However the distributions of hte return time are veery different for small explosions with the bimodality of the distributions that disappears when looking linked events.

The distribution of the infrasonic durations are (incredibly) very similar for strong explosions when looking for unlinked (Figure C.11) and linked events (Figure C.12). The distribution of the infrasonic durations look quite similar for small explosions when looking for unlinked and linked events for phases P01–P15, P17–P19, P22, P24–26 and P33–34.

The distribution of the infrasonic energy are similar for strong explosions when looking for unlinked (Figure 6.34) and linked events (Figure 6.34). We observe small differences

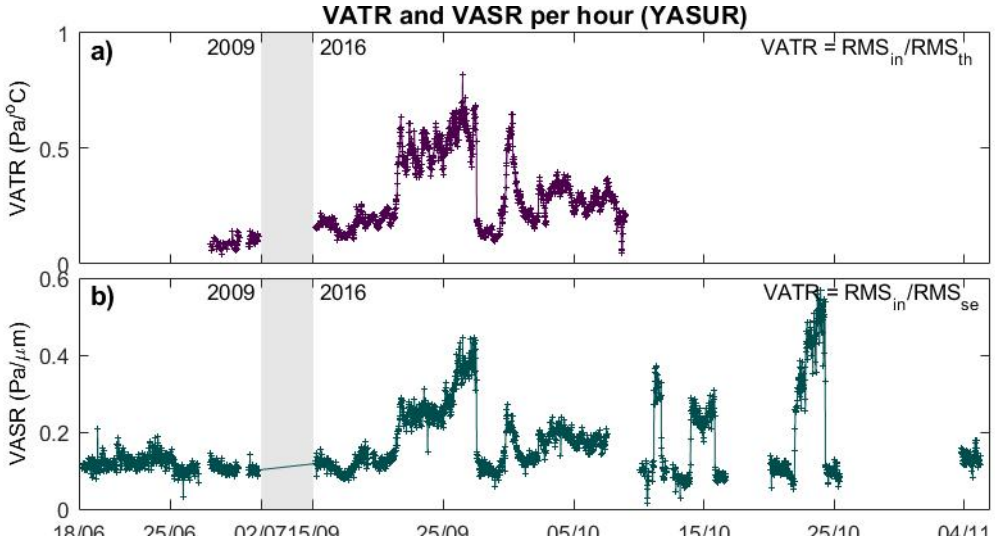

Figure 6.22 – Ratio of RMS per 30 minutes during both field campaigns at Yasur. a) Infrasonic to thermal RMS and b) infrasonic to seismic RMS.

of the distributions of the infrasonic energy of small explosions when looking for unlinked (Figure 6.34) and linked events (Figure 6.34). The phases P01 has a longer tail for its distribution of the infrasonic energy of small explosions when the events are unlinked than when the event are linked. That longer tail is due to the energetic low frequencies (0.10 Hz–0.50 Hz) during that phase (Figure 6.8). The phase P11 has also different distribution of the infrasonic energy per small explosions when looking for unlinked or linked detections, with the bump observed on the distribution of unlinked small explosions that increased until it disappear on the distribution of the linked small explosions. This can be due to the increase of the infrasonic energy in the 0.50 Hz–1.80 Hz frequency band (Figure 6.13).

The distribution of the gas volume are very similar for strong explosions when looking for unlinked (Figure 6.35) and linked events (Figure 6.35). However the distributions of the gas volume for the small explosions when looking for unlinked and linked events can be very different due to the bias induced by the energetic low frequencies that is increased because the gas volume doubly depends on the duration and the ampllitude of the signal (two successive integration of the acoustic pressure).

The analysis of the distributions of the infrasonic duration, the gas volume and velocity of the infrasonic and seismo-infrasonic detections is not unconsistent with our classification except for P28 that seems to stand aside from all categories (Tables C.1 to C.5). The analysis of the distributions of the seismic parameters per phase for seismic detections linked to infrasonic detections does not reveals great unconsistency with our classification (Tables C.6 to C.8). The small unconsistencies we have observed are often due to the lack of data due to the seismic gaps.

6.6 Discussion

The activity at Yasur, in Sept-Nov 2016 had alternations of vigorous and quiet phases with fast transitions from a state to another, whereas the activity in June 2009 was typical and stable. In Aug-Sept 2008, Meier et al. (2016) also observed various states of the surface activity at Yasur but with smoother transitions than in Sept-Nov 2016, and the level of

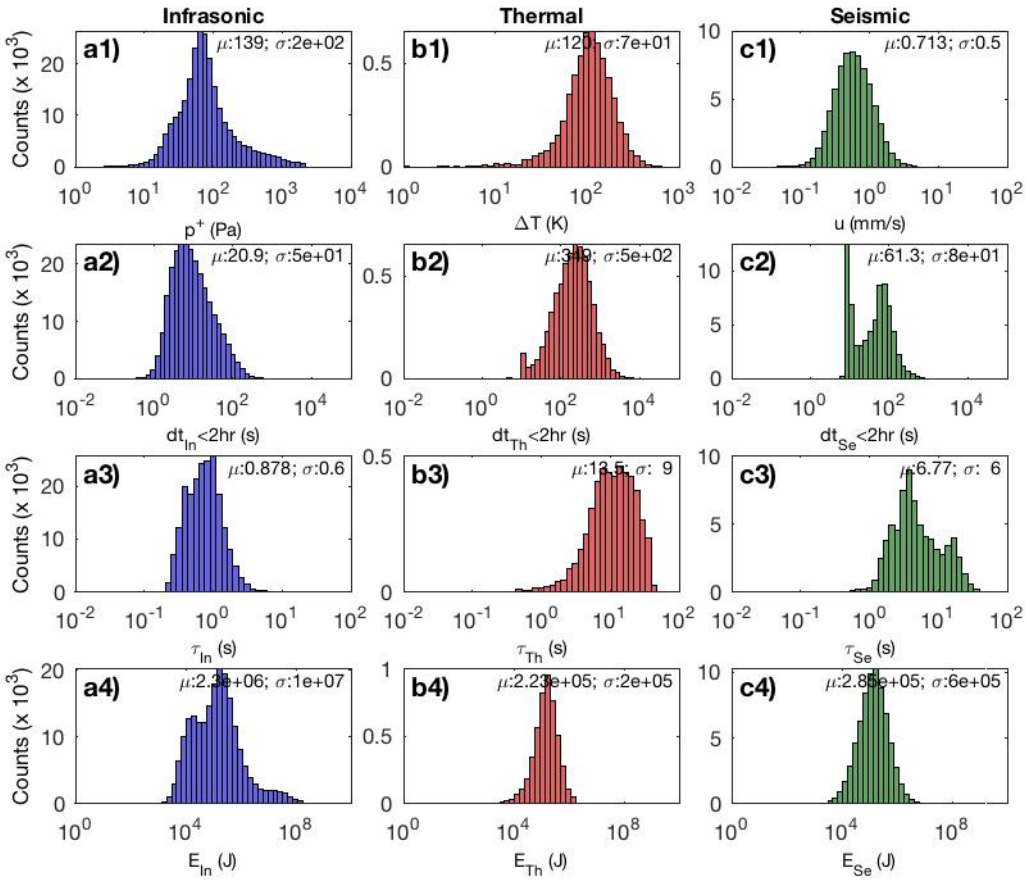

Figure 6.23 – Distribution of a) infrasonic, b) thermal and c) seismic key parameters for all Strombolian explosions during both field campaigns at Yasur, condering records as independent. 1) Amplitude, 2) delay between two successive events, 3) duration and 4) energy.

activity, based on the maximum acoustic pressure, does not exceed the level observed in June 2009 (up to 900 Pa at 100 m).

6.6.1 Coexistence of two mechanisms for the formation the large gas pockets

Our results highlight that there are at least two sources of degassing (seismo-infrasonic distribution) and that the explosions can be ash-rich or gas-rich (frequency contents of the infrasonic records, thermal duration, VATR and VASR per event). Small explosions (<340 Pa at 100 m) are the results of a continuous mechanism of degassing while strong explosions are due to an intermittent mechanism that triggers a stronger seismo-infrasonic coupling. These strong explosions are also probably richer in gas than the small explosions (Figure 6.39, Meier et al. (2016)).

The distributions of the key parameters for the small Strombolian explosions are more widely spread that the distributions of the same key parameters for the strong explosions, especially the distributions of the infrasonic return times and the gas volume per event (Figures 6.27, 6.29, C.5 and C.9). The second key constraint is provided by looking at the emitted gas flux at the vent (Figure 6.12). For both active and passive degassing, there is a critical value of the gas flux, $420\,m^3.s^{-1}$ and $3.60 \times 10^3\,m^3.s^{-1}$, respectively, for which the eruptive pattern switch from quiet to vigourous. These critical values are also the same

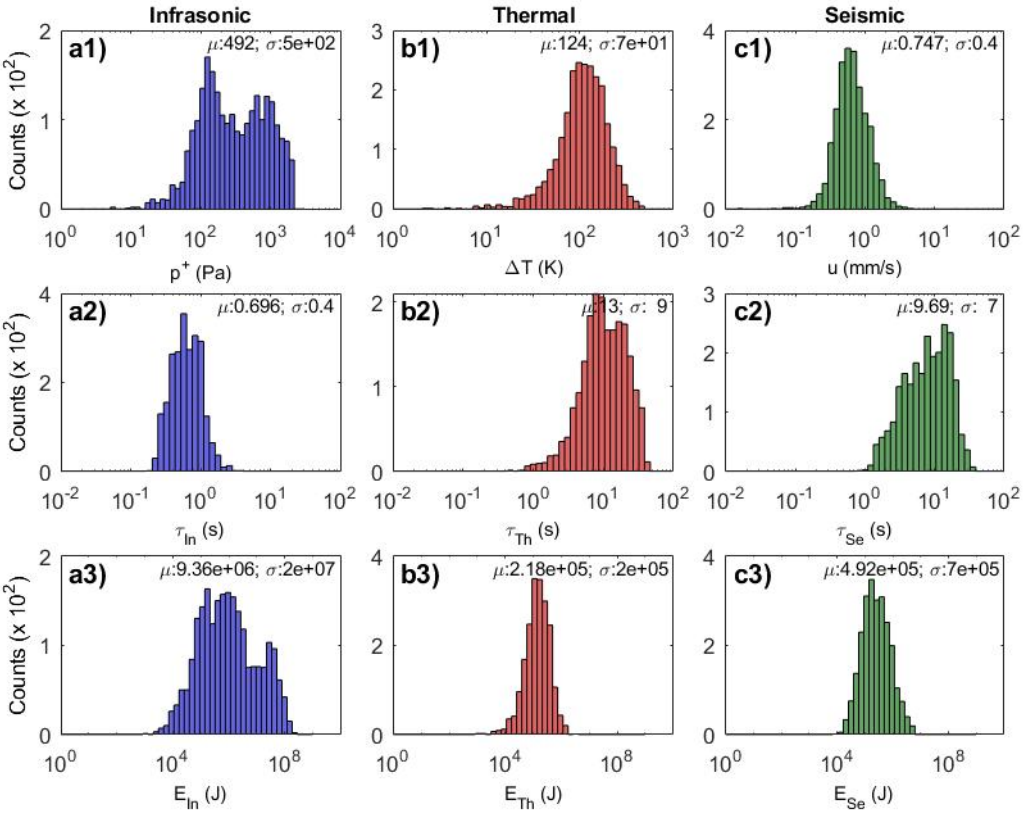

Figure 6.24 – Distribution of a) infrasonic, b) thermal and c) seismic key parameters for all linked Strombolian explosions during both field campaigns at Yasur. 1) Amplitude, 2) duration and 3) energy. Each detection on infrasonic records is associated to the closest detection on thermal and seismic records.

for the transition vigourous to quiet. The very short time scale at which the transition from quiet to vigourous, but also from vigourous to quiet suggests that the transition is triggered by the start of an instability which passes between off and on.

The extremely well constrained value of the critical gas flux, above which the regime is vigourous, suggests that the key parameter for the instability is the gas flux. This strongly points out to the instability of the foam layer at the top of the reservoir, which also has the underlying gas flux as one of the key controlling parameters. We can therefore explain the difference of regimes by the state of equilibrium of the foam layer, stable or unstable, that is trapped at the top of the magma reservoir (Figure 6.40).

The foam is probably stable during the quiet and intermediate regime, i.e. there is no massive coalescence event. The foam spreads toward the conduit progressively by releasing small bubbles in the conduit. These small bubbles coalesce progressively into the conduit while rising by buoyancy and can be impacted by several effects such as the rarefaction wave propagating downward the conduit after an explosion at the surface of the top of the magma column (Figure 6.40a).

During vigorous regimes, the foam layer a the top of the reservoir is probably unstable because the critical thickness has been exceeded by the arrival of an additional gas flux from below (Figure 6.40b). The most likely cause of the transition is an increase of the underlying gas flux that was estimated at the surface at $\sim$420 $m^3.s^{-1}$ for the small and strong explosions. The strong resemblance of the infrasonic waveforms of the Strombolian

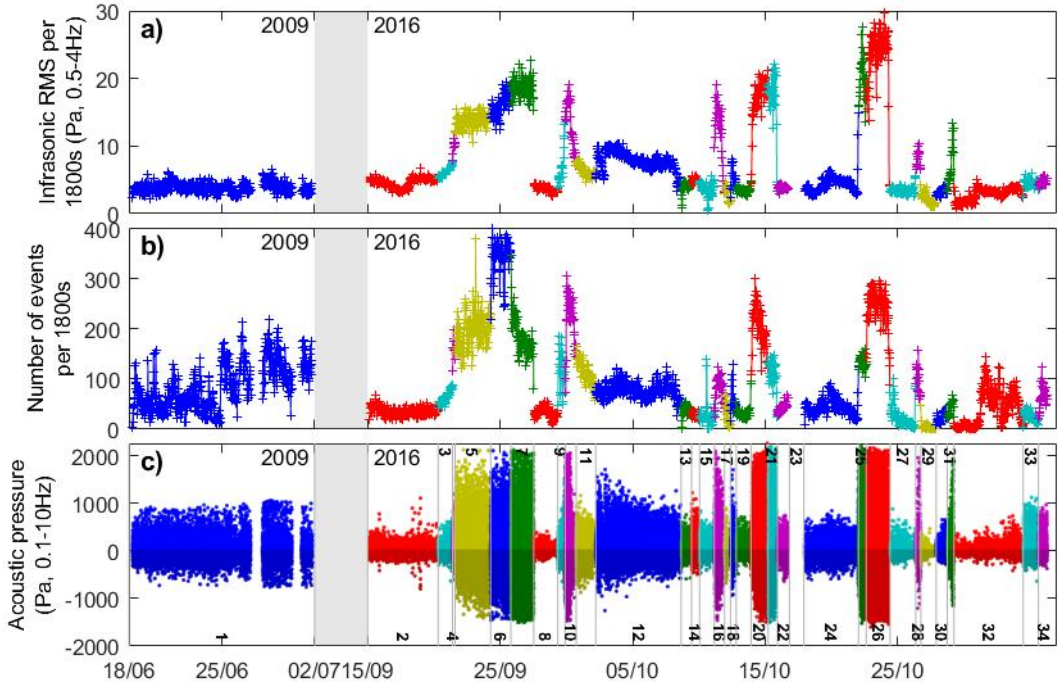

Figure 6.25 – Determination on the phases of activity based on the infrasonic data during both field campaigns at Yasur. a) Infrasonic RMS per 30 minutes. b) Number of explosions per 30 minutes. c) Maximum acoustic pressure per event (compressive phase: >0 Pa; dilatation phase: <0 Pa).

explosions (correlation coefficient ∼80 %, figure C.18) and the very peaked histograms on their gas volume and typical return times suggest that our interpretation has catched for the first time, several viscous massive coalescence events which are correctly quantified.

The existence of transitions from quiet to strong and vice-versa suggest that the underlying gas flux is probably composed by a permanent background gas flux, that can vary on long periods compared to our study, on which pulses of gas flux are superimposed. The gas flux has also been shown to have periods of being turned on and off at Erta'Ale (Vergniolle and Bouche, 2016) and at Etna (Vergniolle and Gaudemer, 2012).

The increase of the underlying gas flux, during strong phases, increases the rate of the explosions, decreasing the delay between two successive explosions, such that the surface of the magma column has no time to cool and form a thick crust and remain liquid. In contrast, during quiet phases, the delay between two successive explosions is longer, and a crust at the top of the magma column might potentially form. Hence, we observe more ash-rich explosions during quiet phases than during strong phases (Figures 6.18 and 6.20, Meier et al. (2016)).

The cumulative gas volume of the strong explosions during each strong phase (additional gas volume) and the duration of the quiet phase preceding each strong phase (repose time) are very well correlated (0.98, figure 6.41d). These volumes are surely accumulated during quiet phases and released during the strong phases, when the foam layer at the top of the reservoir is unstable. The proportionality of $1.45 \times 10^6\,\mathrm{m^3.h^{-1}}$ ($\sim 400\,\mathrm{m^3.s^{-1}}$), between the repose time and the additional gas volume gives an estimate of the additional gas flux, that is responsible for the massive coalescence. This value is consistent with the critical value of the active gas flux we have determined previously for the triggering of the strong phases (Figure 6.12).

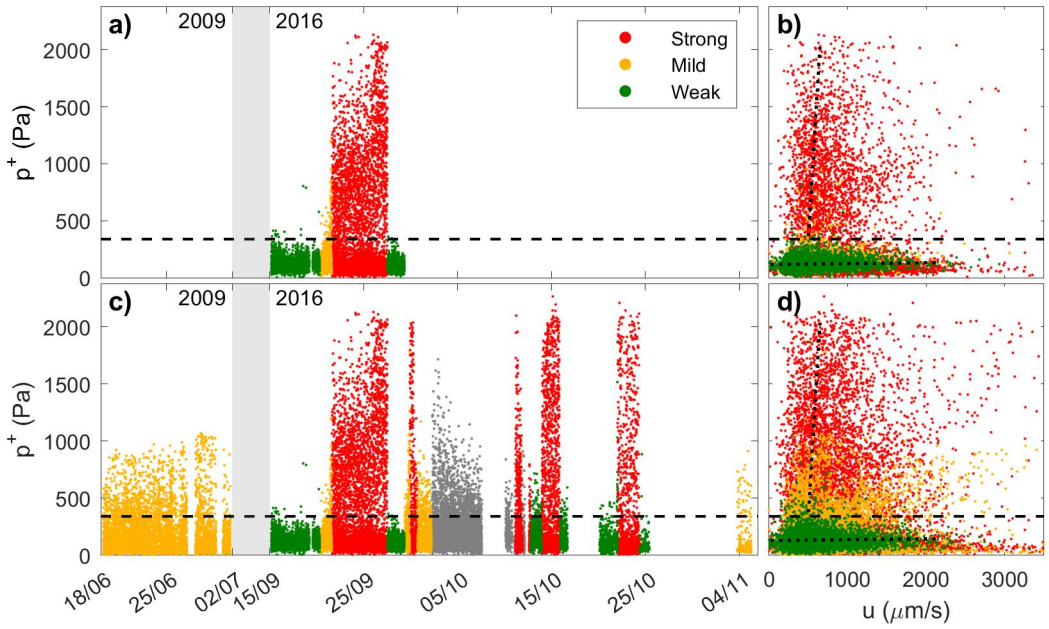

Figure 6.26 – Determination of the critical value of the maximum acoustic pressure, based on the seismo-infrasonic comparison, for an explosion to be small or strong. a) Maximum acoustic pressure as a function of time for a) phases 2 to 8 and c) all phases. b) Maximum acoustic pressure as a function of the maximum ground velocity for b) phases 2 to 8 and d) all phases. Intermediate gray data are not classify as mild because of a different origin.

The correlation between the cumulative volume and the repose time, when using the small explosions to calculate the cumulative volume, is less good (0.76, figure 6.41c) because small explosions are not generated by the massive coalescence at the top of the reservoir, but are only led by the larger volumes of the strong explosions. Some phases of activity were not take into account for this analysis due to their different patterns. For example, we do not take into account phase P12 which is a phase of relaxation that is not well characterised yet. However we assume that the system is stable again since the phase P13. We also combine phases P17–19, including P18 because we suspect that P18 is similar to P12, and because its short duration has little impact on the on the repose time P17–P19.

The coexistence of the two mechanisms of bubble formation discussed here is also consistent with the previous study of Oppenheimer et al. (2006), which found out a deep source and a shallow source of degassing from FTIR measurements and validates the proposition of Bani et al. (2013) which said that the deep source produces Taylor's bubble by massive foam coalescence and the shallow source by progressive coalescence in the conduit.

The coexistence of the two mechanisms of bubble formation discussed here is also consistent with the previous study of Oppenheimer et al. (2006), which found out a deep source and a shallow source of degassing from FTIR measurements and validates the proposition of Bani et al. (2013) which said that the deep source produces Taylor's bubble by massive foam coalescence and the shallow source by progressive coalescence in the conduit. Multigas measurements at Stromboli over a 3-months period of typical Strombolian activity also hilight a deep source of degassing (>4 km, rich in CO_2 and a shallow source of degassing (<1 km Aiuppa et al., 2010). These two sources of degassing suggest the coexistence of both mechanisms of bubble formation at Stromboli. However they both seemed to be persistent during the whole period of measurements (Aiuppa et al., 2010). Further study is therefore needed to validate the coexistence of the two mechanisms at Stromboli and

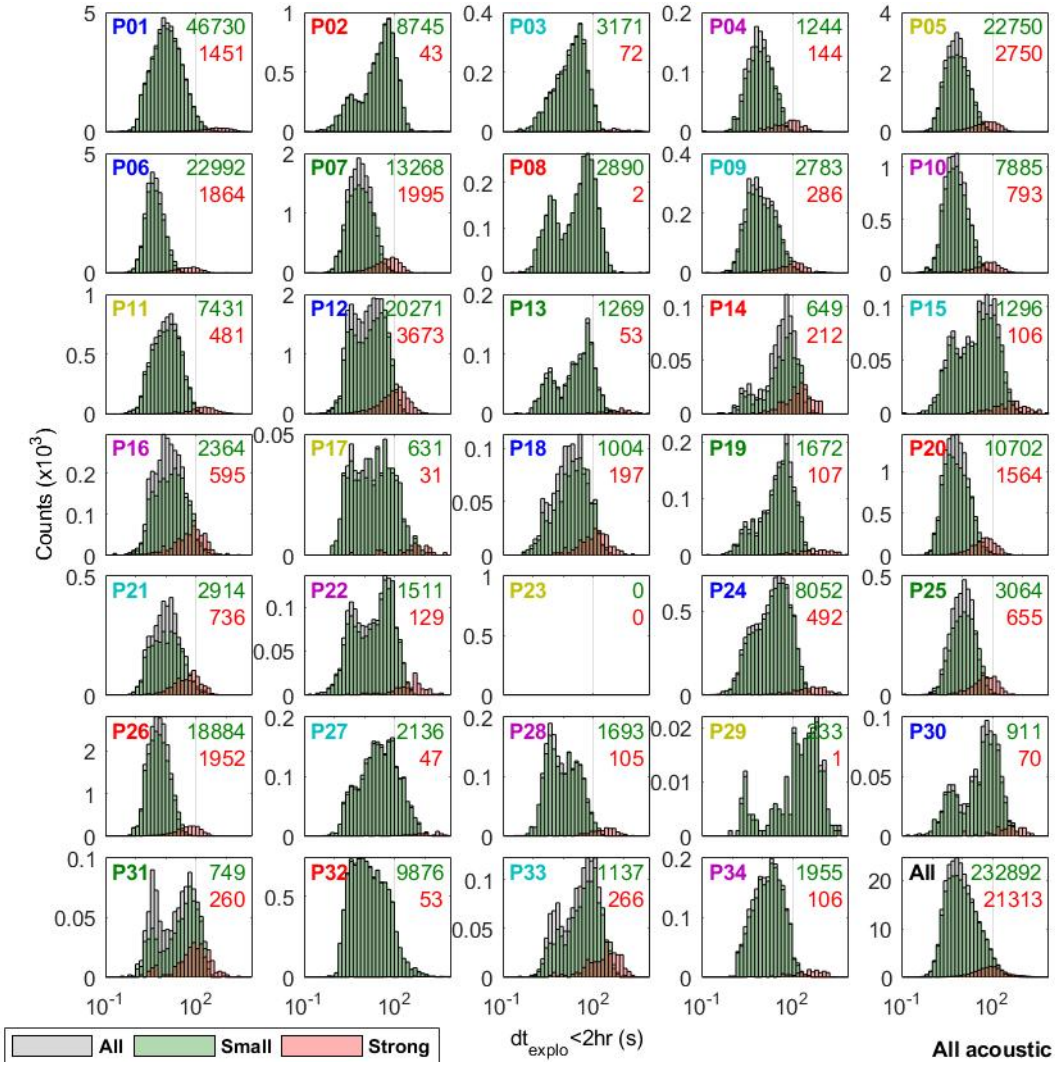

Figure 6.27 – Distribution of the return time between two successive events per phase for all infrasonic events. The phase number is indicated north-west of each subplot. The number of small (<340 Pa) and strong (>340 Pa) explosions is indicated, north-east of each subplot, in green and red, respectively.

can be similar as the one we presented here for Yasur.

6.6.2 Bubble diameter in the reservoir

The initiation of the massive coalescence of the foam depends on the dimensionless height $\bar{h}_{\text{foam}}$, in the reservoir which is given by (Figure 6.40, Jaupart and Vergniolle, 1989)

$$\bar{h}_{\text{foam}} = \left(\frac{3 Q_{\text{gas,res}} \mu_{\text{foam}}}{\pi \alpha_{\text{gas,foam}}^2 \rho_{\text{magma}} g} \right)^{1/4} \Bigg/ \left(\frac{4 \sigma_{b,\text{tension}}}{\alpha_{\text{gas,foam}} \rho_{\text{magma}} g d_{b,\text{res}}} \right), \tag{6.16}$$

where $Q_{\text{gas,res}}$, $\alpha_{\text{gas,foam}}$ and $d_{b,\text{res}}$ are the gas flux, the gas volume fraction (60 %) and the diameter of the gas bubble into the reservoir. ρ_{magma} is the magma density (2700 kg.m^{-3}), g the constant of gravity (9.81 m.s^{-2}) and $\sigma_{b,\text{tension}}$ the surface tension of the bubble (0.10 kg.s^{-2} for a wet basalt, Mangan and Sisson, 2005). The foam viscosity μ_{foam} is proportional to the magma viscosity such as μ_{magma} (Jaupart and Vergniolle, 1989;

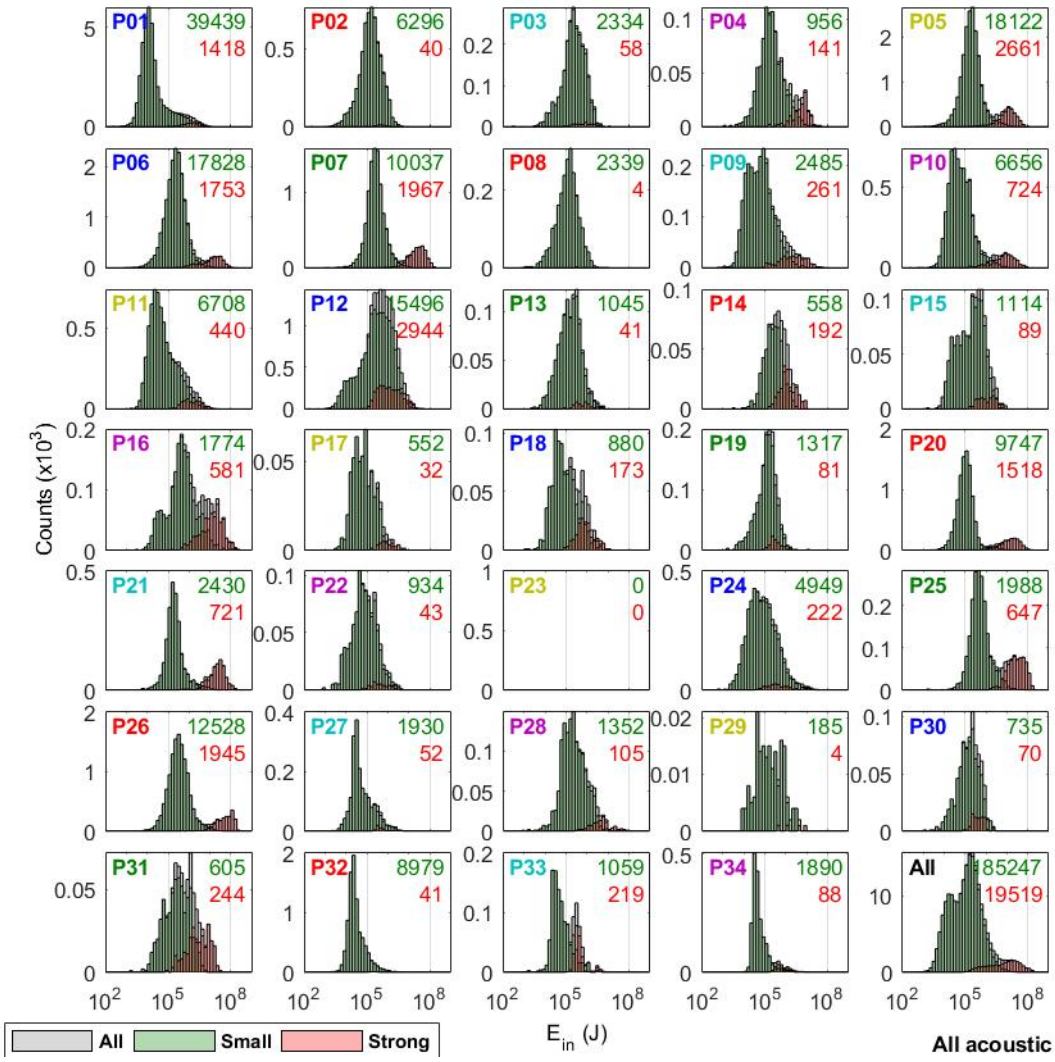

Figure 6.28 – Distribution of the infrasonic energy per phase for all infrasonic events. The phase number is indicated north-west of each subplot. The number of small (<340 Pa) and strong (>340 Pa) explosions is indicated, north-east of each subplot, in green and red, respectively.

Vergniolle et al., 2004).

$$\mu_{\text{foam}} = \frac{\mu_{\text{magma}}}{(1 - \alpha_{\text{gas,foam}})^{5/2}}. \tag{6.17}$$

The magma viscosity is calculated using the model of Shaw (1972), the 7 compositions of Yasur products, magma temperature (1107 °C) and dissolved water content (1 %) given in Métrich et al. (2011). The magma viscosity ranges from 488 Pa.s to 1263 Pa.s with the mean and median values at 930 Pa.s and 962 Pa.s, respectively and a standard deviation of 309 Pa.s. We use a rounded magma viscosity at 10^3 Pa.s, giving the foam viscosity $\mu_{\text{foam}} = 9.88 \times 10^3$ Pa.s.

The critical gas flux, in the reservoir, at which a given stable foam becomes unstable, is obtained when the dimensionless foam height exceeds the threshold,

$$\bar{h}_{\text{foam}} = \frac{1}{C_{\text{geom}}}, \tag{6.18}$$

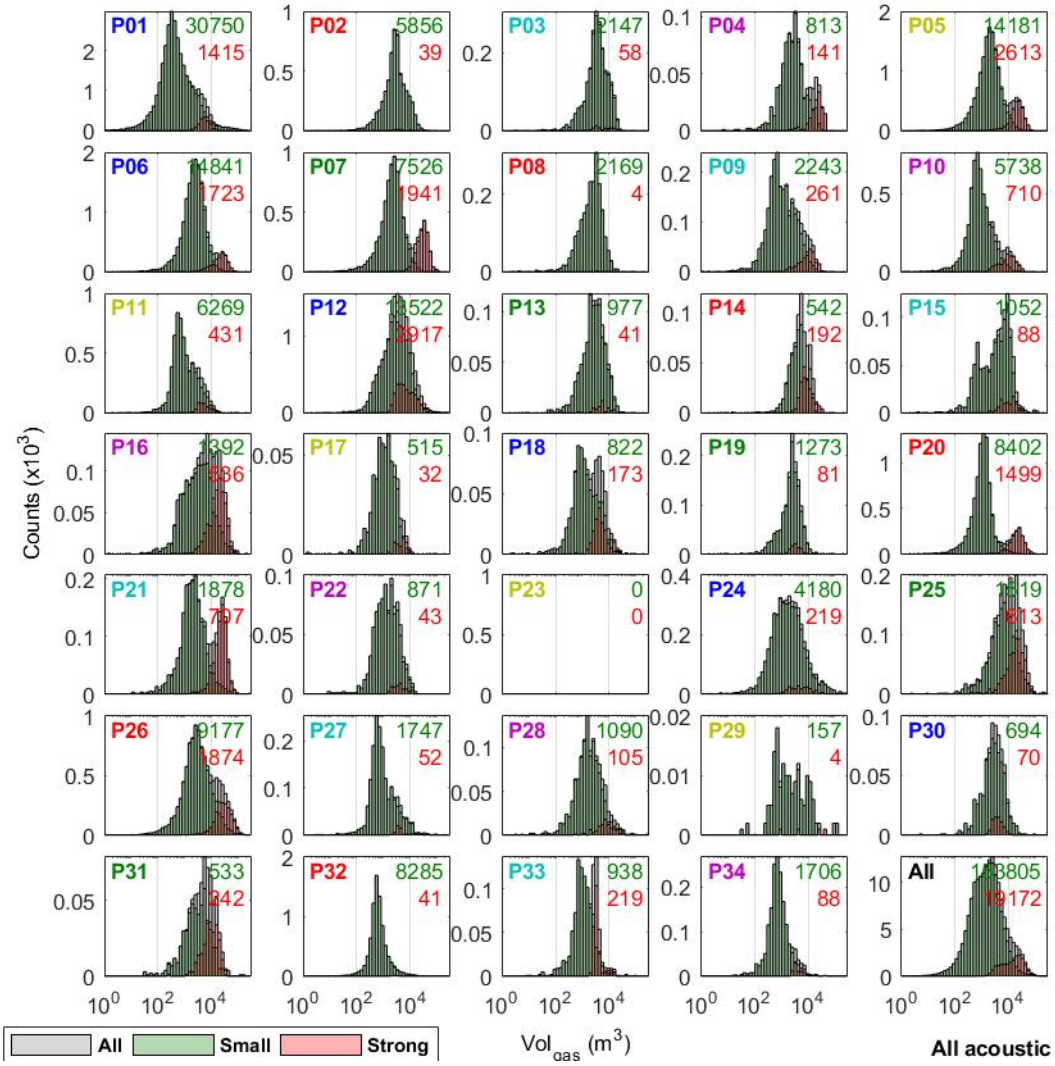

Figure 6.29 – Distribution of the gas volume per phase for all infrasonic events. The phase number is indicated north-west of each subplot. The number of small (<340 Pa) and strong (>340 Pa) explosions is indicated, north-east of each subplot, in green and red, respectively.

with C_{geom} the geometrical factor given by (Jaupart and Vergniolle, 1989):

$$C_{\text{geom}} = \left(-\log\left(\frac{S_{\text{vent}}}{S_{\text{res}}}\right) + \frac{S_{\text{vent}}}{S_{\text{res}}} - 1 \right)^{1/4}, \tag{6.19}$$

where $S_{\text{vent}} = \pi R^2_{\text{conduit}} = 19.6\,\text{m}^2$ is the surface of the vent and S_{res} is the surface of the reservoir. The surface of the reservoir, which is unknown at Yasur, ranges probably from that at Erta'Ale ($7.55 \times 10^4\,\text{m}^2$, Bouche et al. (2010)) to that at Kilauea ($10^6\,\text{m}^2$, Yang et al. (1992)) with an intermediate value equivalent to that at Etna ($2 \times 10^5\,\text{m}^2$, Vergniolle (2008)). The dimensionless foam height ranges then from 0.56 to 0.61 (Table C.9).

The critical gas flux deduced from the infrasonic records can be calculated at the depth of the reservoir (~1 km when considering the magma depth of the Yenkahe resurgent domes, Brothelande and Merle, 2015; Brothelande et al., 2016b) using the ideal gas law for a rock density of $2700\,\text{kg.m}^{-3}$, giving critical values at $1.5\,\text{m}^3.\text{s}^{-1}$, $13.2\,\text{m}^3.\text{s}^{-1}$ and $14.8\,\text{m}^3.\text{s}^{-1}$ for the active, passive and total degassing, respectively. We thus estimate the upper and lower limits of the bubble diameter in the reservoir by combining eqs. (6.16), (6.18) and (6.19) for the active and total gas flux, respectively. Values of the bubble diameter range range

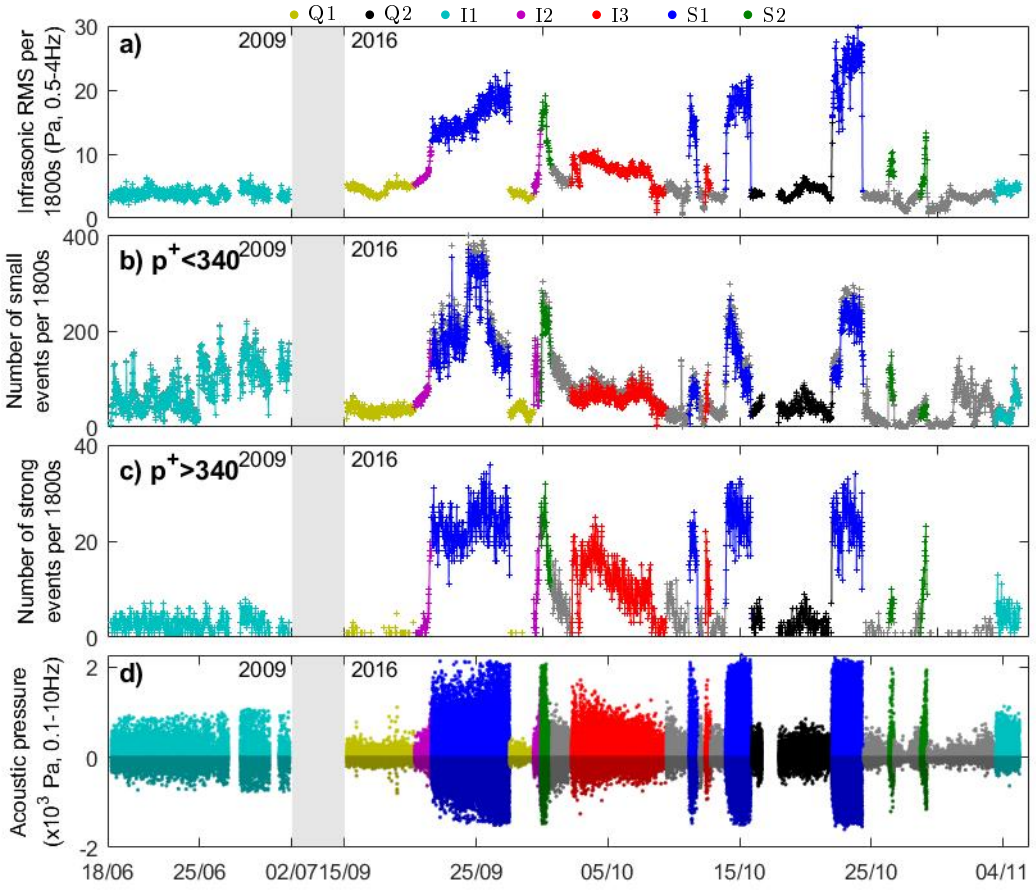

Figure 6.30 – Category of the phases of activity based on the distribution of key parameters. a) Infrasonic RMS per 30 minutes. Number of b) small and c) strong explosions per 30 minutes. d) Maximum acoustic pressure per event (compressive phase: >0 Pa; dilatation phase: <0 Pa).

from 13 µm to 14 µm and from 7 µm to 8 µm when assuming the active and total gas flux, respectively (Table 6.2).The tables C.9 and C.10 and figure C.20 show the effect of the variation of the magma viscosity, the surface tension and the surface of the reservoir.

In order to best compare our determination of bubble diameter at Yasur to that found at other basaltic volcanoes, we have to return to eq. (6.16). This equation shows that the main parameters controlling the transition between a stable and an unstable foam is the ratio $\sigma_{\text{gas}}/d_{b,\text{res}}$ due to the weak dependence on the gas flux and magma viscosity. We choose now to use an overestimated value of the surface tension identical to that of the dry basalts (0.36 kg.s^{-2}, Proussevitch et al. (1993)). In this condition, the bubble diameter, estimated between 47 µm and 50 µm (Tables C.9 and C.10), is significantly smaller than that of other basaltic volcanoes (Vergniolle, 2008; Vergniolle and Bouche, 2016), due to the large viscosity and large gas flux present at Yasur (Table 6.2). Note also that the gas flux at Etna is probably overestimated because it is deduced from the maximum height of the lava fountains rather than from a direct estimation of gas volumes. Despite all these uncertainties, the fact remains that the bubble diameter at Yasur is closer to the critical radius at nucleation (see a review in Vergniolle and Gaudemer, 2015) than in the case of other basaltic volcanoes.

Table 6.1 – Phases of activity during the field campaigns at Yasur.

	Start	End	Duration (hr)	Strength	Category
P01	18/06, 00hr	02/07/09, 00hr	336	I	I1
P02	15/09, 00hr	20/09/16, 07hr	128	Q	Q1
P03	20/09, 07hr	21/09/16, 09hr	26	I	I2
P04	21/09, 09hr	21/09/16, 14hr	5	I	I2
P05	21/09, 14hr	24/09/16, 06hr	65	S	S1
P06	24/09, 06hr	25/09/16, 19hr	36	S	S1
P07	25/09, 19hr	27/09/16, 12hr	42	S	S1
P08	27/09, 12hr	29/09/16, 08hr	44	Q	Q1
P09	29/09, 08hr	29/09/16, 21hr	13	I	I2
P10	29/09, 21hr	30/09/16, 17hr	20	S	S2
P11	30/09, 17hr	02/10/16, 05hr	36		
P12	02/10, 05hr	08/10/16, 15hr	154	I	I3
P13	08/10, 15hr	09/10/16, 10hr	19	Q	Q1
P14	09/10, 10hr	10/10/16, 01hr	15	I	
P15	10/10, 01hr	11/10/16, 03hr	27	Q	Q1
P16	11/10, 03hr	11/10/16, 22hr	19	S	S1
P17	11/10, 22hr	12/10/16, 09hr	11	I	
P18	12/10, 09hr	12/10/16, 19hr	10	I	I3
P19	12/10, 19hr	13/10/16, 22hr	27	Q	Q1
P20	13/10, 22hr	15/10/16, 05hr	31	S	S1
P21	15/10, 05hr	15/10/16, 22hr	17	S	S1
P22	15/10, 22hr	16/10/16, 19hr	22	Q	Q2
P23	16/10, 19hr	17/10/16, 22hr	26	?	?
P24	17/10, 22hr	22/10/16, 00hr	99	Q	Q2
P25	22/10, 00hr	22/10/16, 14hr	14	S	S1
P26	22/10, 14hr	24/10/16, 10hr	43	S	S1
P27	24/10, 10hr	26/10/16, 08hr	46	Q	
P28	26/10, 08hr	26/10/16, 17hr	9	S	S2?
P29	26/10, 17hr	27/10/16, 21hr	28	Q	
P30	27/10, 21hr	28/10/16, 17hr	20	Q	Q1
P31	28/10, 17hr	29/10/16, 05hr	12	S	S2
P32	29/10, 05hr	03/11/16, 10hr	125	Q	
P33	03/11, 10hr	04/11/16, 14hr	28	I	I1
P34	04/11, 14hr	05/11/16, 09hr	19	I	I1

6.6.3 Depth of the magma column

We expected a higher level of magma when the underlying gas flux is enough to produce massive coalescence (Figure 6.40).

However, in June 2009, the level of magma is very close to the surface of the vent (i.e. the bottom of the field of view of the lower radiometer, figures 5.12, 5.13, 6.19, B.4 and B.5 and field observations), whereas the critical value of the gas volume flux, for which the massive coalescence can exist, is not exceeded. The thickness of the foam layer, in that case can be maintained just below the critical thickness, so that the foam remains stable.

In Sept-Nov 2016, the level of magma is deeper below the surface of the vent (Figures 6.19 and B.6 to B.8). The vigorous activity, at Yasur, before our measurements in Sept-Nov 2016 (see the correspondance with Esline Garaebiti, appendix D.1), has probably already emptied a part of the magma within the conduit, hence a lower level of the magma column.

Furthermore, a deeper magma level, below the surface of the vent, in 2016 than in 2009 does not only mean that the height of the magma column above the reservoir is lower in 2016 than in 2009. Indeed the progressive construction of the volcanic cone, due to the

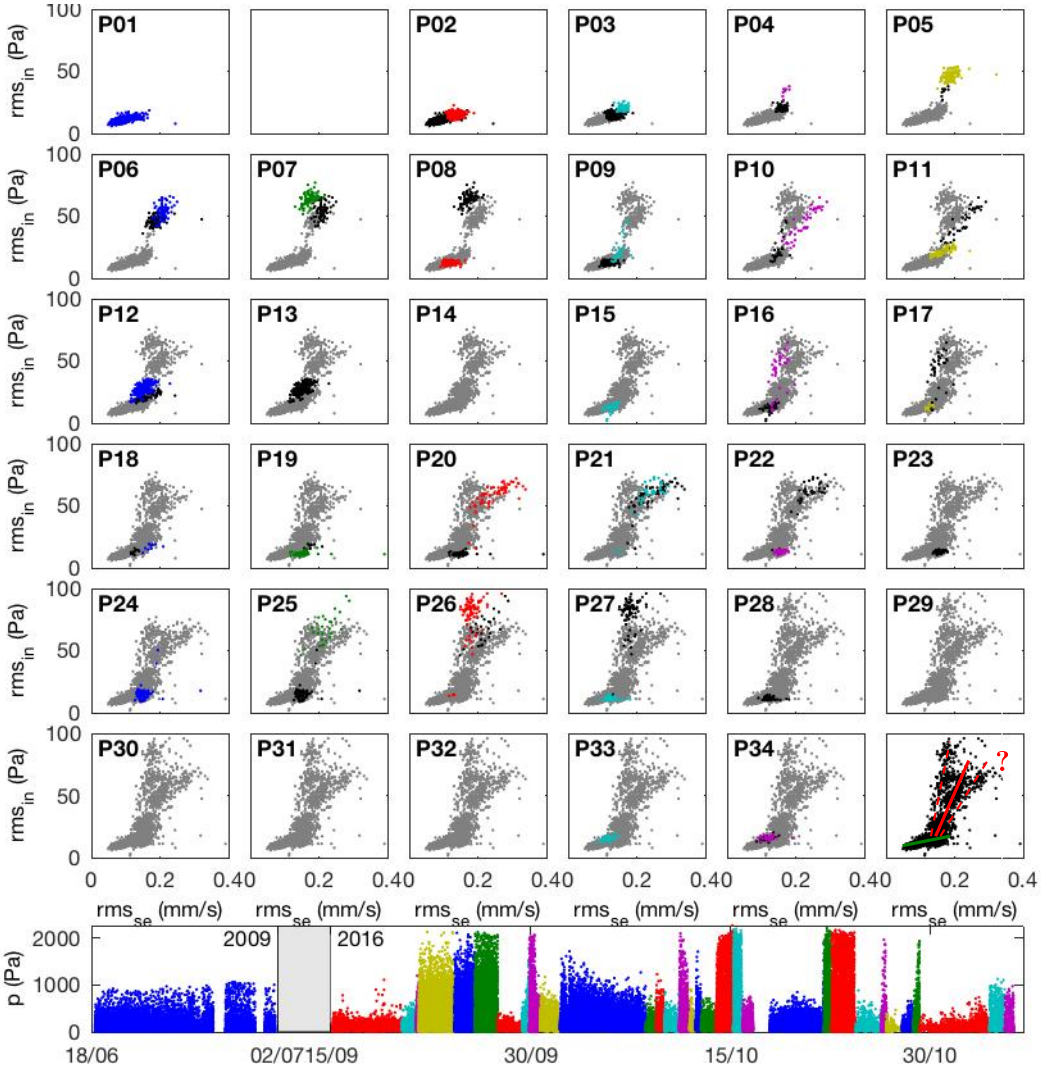

Figure 6.31 – Infrasonic RMS per 30 min as a function of the seismic RMS per 30 minutes. Gray dots show the RMS during the phase $p-2$ and previous, black dots show the RMS during the phase $p-1$ and the coloured dots show the RMS of the current phase p.

accumulation of ejecta at the surface, can be responsible for the apparent deepening of the source (Figure 6.42). Note also that the resolution of our method to estimate de depth of the magma column is not sufficiantly accurate to see the temporal changes (Figure 6.19).

6.7 Conclusion

We have processed $\sim$ 70 days of infrasonic, thermal and seismic data in order to understand the temporal variability of the Strombolian activity at Yasur.

We have shown that two mechanisms co-exist for the formation of the Taylor bubbles that are responsible of the Strombolian explosions at Yasur:

(i) the progressive coalescence of tiny bubbles rising the conduit is persistent and probably due to a constant and persistent gas flux,
(ii) the massive coalescence of the foam, accumulated at the top of the reservoir, is

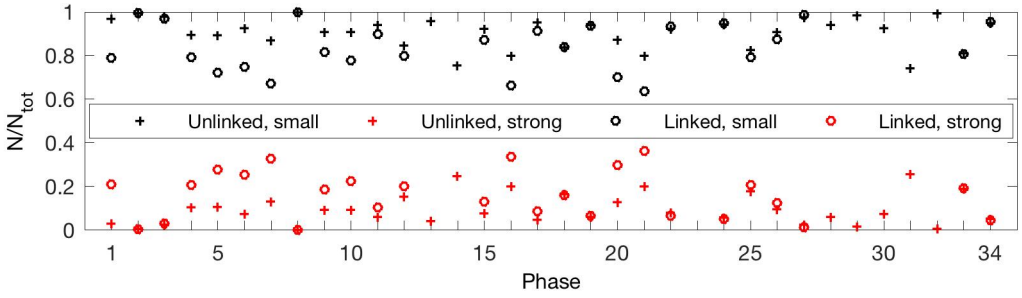

Figure 6.32 – Proportion of small and strong explosions per phase.

Table 6.2 – Bubble diameter in the reservoir at several basaltic volcanoes.

	$Q_{gas,res}$ ($m^3.s^{-1}$)	Method*	μ_{magma} (Pa.s)	σ_{gas} ($kg.s^{-2}$)	$d_{b,res}$ (µm)	Ref.†
Active degassing						
Erta'Ale	2.3×10^{-6}–5.9×10^{-6}	IN	10	0.36	400–600	1
Etna	5.2×10^{-2}–8.3×10^{-2}	IN	10	0.36	500–590	2
Yasur	1.5	IN	1000	0.10	13–14	3
Total degassing						
Etna	1.9×10^{-2}–4.0×10^{-2}	LF	10	0.36	400–440	2
Kilauea Iki	2.0–2.9	LF	10	0.36	180–200	2
Mauna Ulu	2.7–3.9	LF	10	0.36	170–180	2
Pu'u 'O'o	0.5–0.5	LF	10	0.36	290–260	2
Yasur	14.8	IN	1000	0.10	7–8	3

*IN: gas flux from infrasonic records; LF: gas flux from the height of the lava fountain.
†1: Vergniolle and Bouche (2016); 2: Vergniolle (2008); 3: this study.

intermittent and might be due to a temporarily and superimposed gas flux.

These two mechanisms lead, at the surface, to small explosions (<340 Pa at 100 m) from the former mechanism and strong (>340 Pa at 100 m) and regular explosions from the latter mechanism, which have a different seismo-infrasonic relationships. Furthermore, the strong explosions seems to be poorer in ash than the small explosions (VATR, VASR per explosion, figure 6.39). This can be later explored by estimating the ejecta volume fraction per event, using videos, based of the number/area of pixels representing ejecta in a referece area.

The intermittent increase of the gas flux at depth can be observed on infrasonic records, when the gas flux exceeds, in the reservoir (∼1 km), the critical values at 1.5 $m^3.s^{-1}$, 13.2 $m^3.s^{-1}$ and 14.8 $m^3.s^{-1}$ for the active, passive and total degassing, respectively. The critial value of the active gas flux gives estimates of the bubble diameter in the reservoir between 13 mm–14 mm. These estimates are consistent with the bubble diameters at other basaltic volcanoes (Etna, Kilauea, Erta'Ale) and the size of bubbles at nucleation. We also have shown that the additional gas flux can be estimated at 72.90 $m^3.s^{-1}$, from the cumulative gas volume during strong phases and the repose time between two strong phases.

Note also that the persistent gas flux, maintaining the progressive coalescence into the conduit, must be sufficient strong to avoid the conduit to be blocked by magma cooling and thus the accumulation of gas at depth.

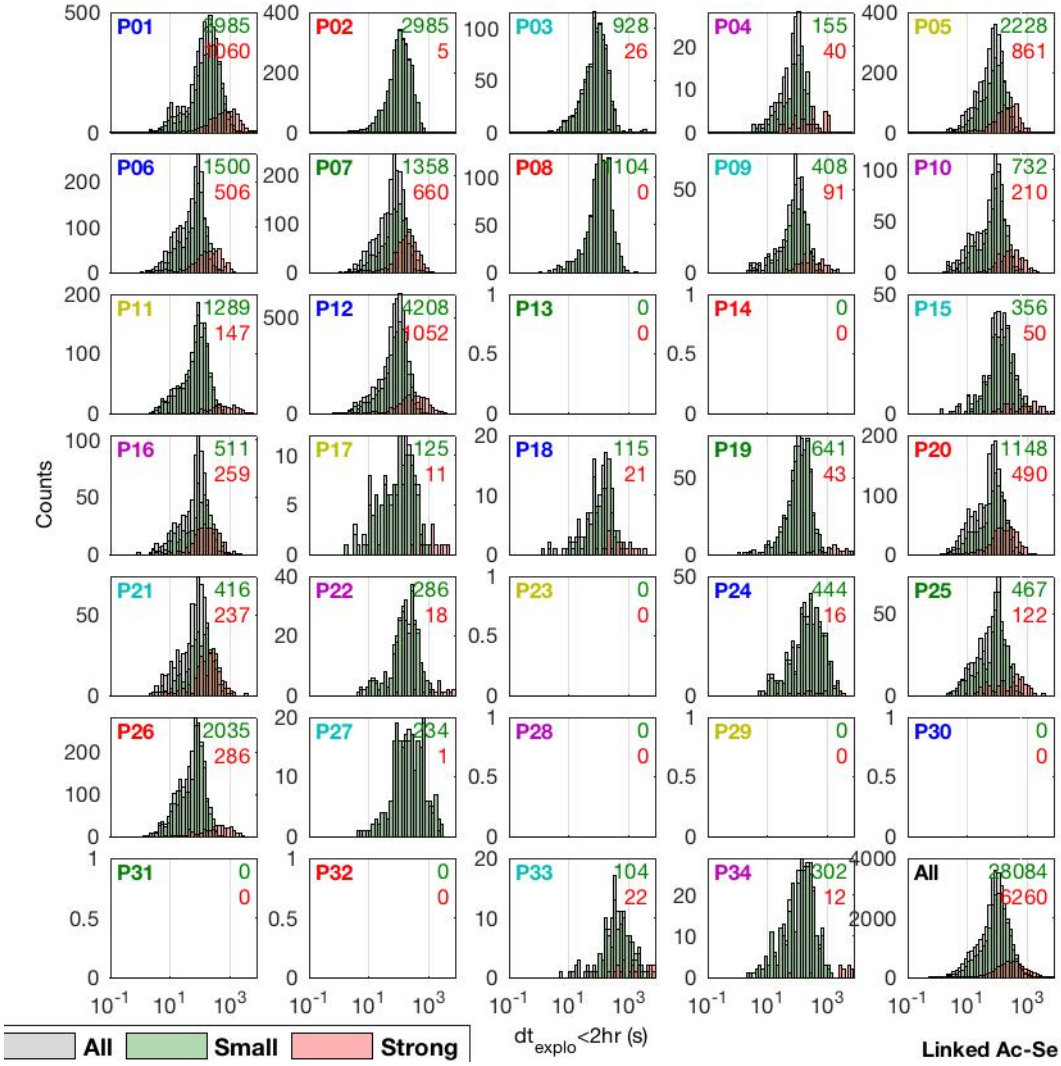

Figure 6.33 – Distribution of the return time between two successive events per phase for all seismo-infrasonic events. The phase number is indicated north-west of each subplot. The number of small (<340 Pa) and strong (>340 Pa) explosions is indicated, north-east of each subplot, in green and red, respectively.

It would be interesting to perform similar studies at Stromboli and Erebus volcanoes, both in persistent Strombolian activity, in order to

1. validate the coexistence of the progressive coalescence in the conduit and the massive coalescence at the top of the reservoir,
2. find the critical values of the gas flux (passive, active) for foam layer to become unstable,
3. find the critical value of the maximum acoustic pressure for the explosions to be generated by the massive coalsence.

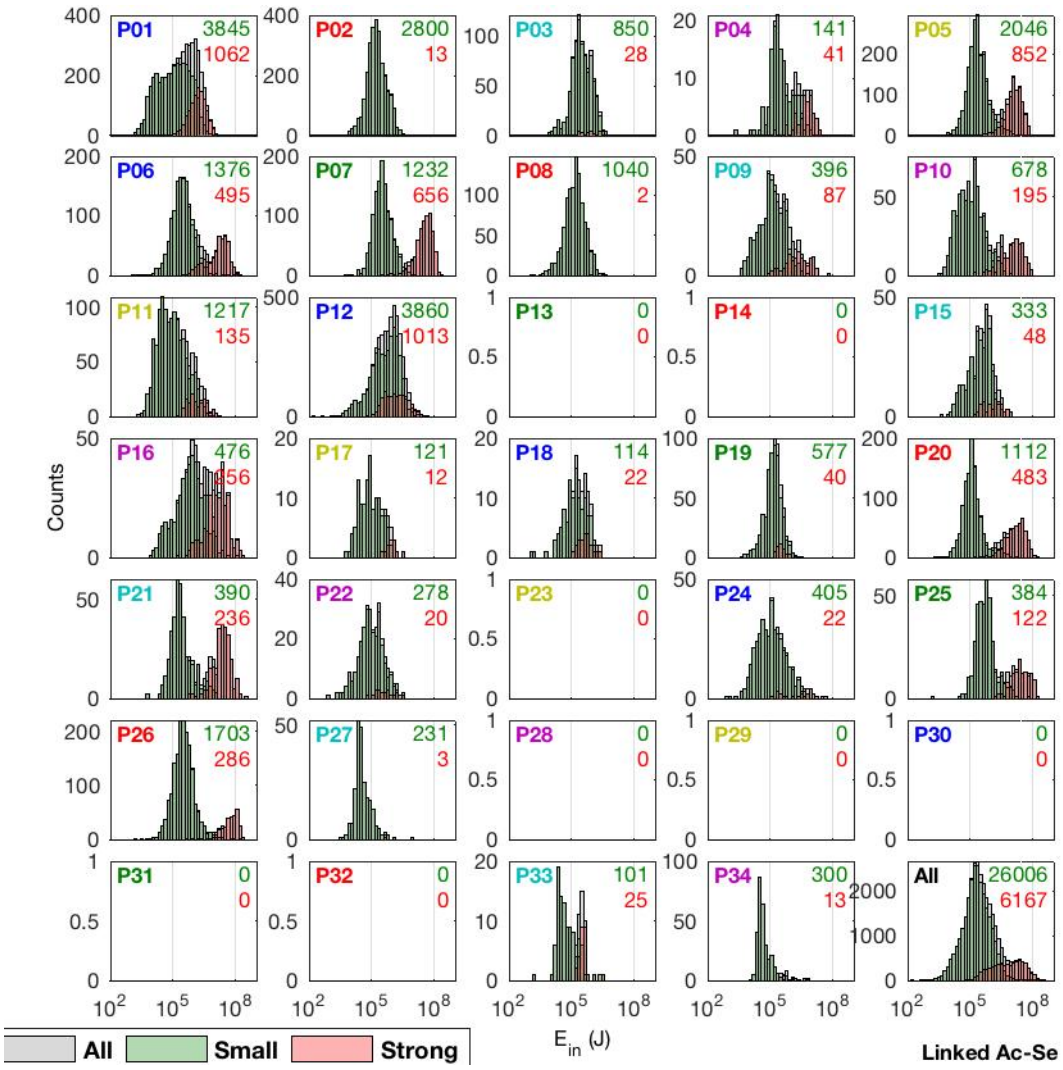

Figure 6.34 – Distribution of the infrasonic energy per phase for all seismo-infrasonic events. The phase number is indicated north-west of each subplot. The number of small (<340 Pa) and strong (>340 Pa) explosions is indicated, north-east of each subplot, in green and red, respectively.

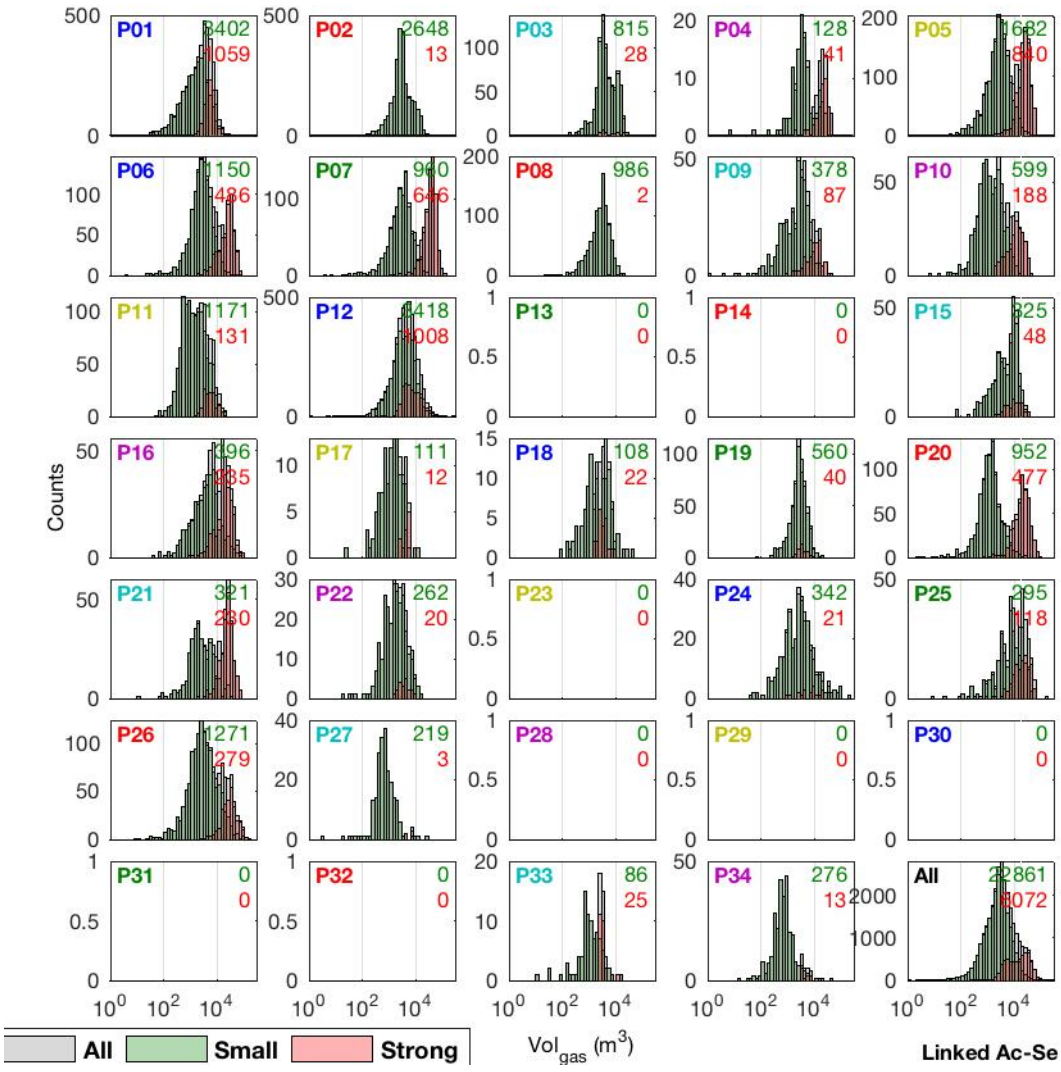

Figure 6.35 – Distribution of the gas volume per phase for all seismo-infrasonic events. The phase number is indicated north-west of each subplot. The number of small (<340 Pa) and strong (>340 Pa) explosions is indicated, north-east of each subplot, in green and red, respectively.

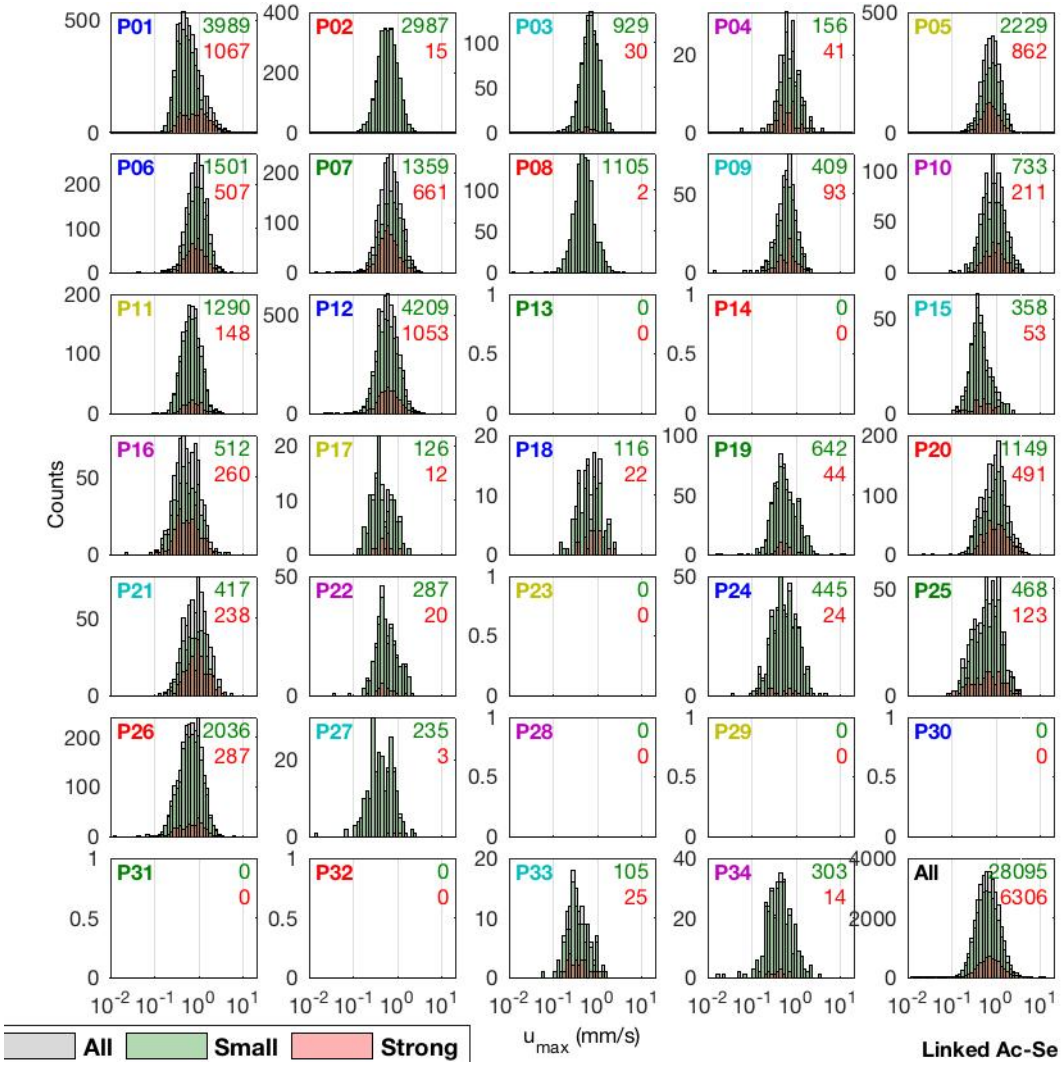

Figure 6.36 – Distribution of the ground velocity per phase for all seismo-infrasonic events. The phase number is indicated north-west of each subplot. The number of small (<340 Pa) and strong (>340 Pa) explosions is indicated, north-east of each subplot, in green and red, respectively.

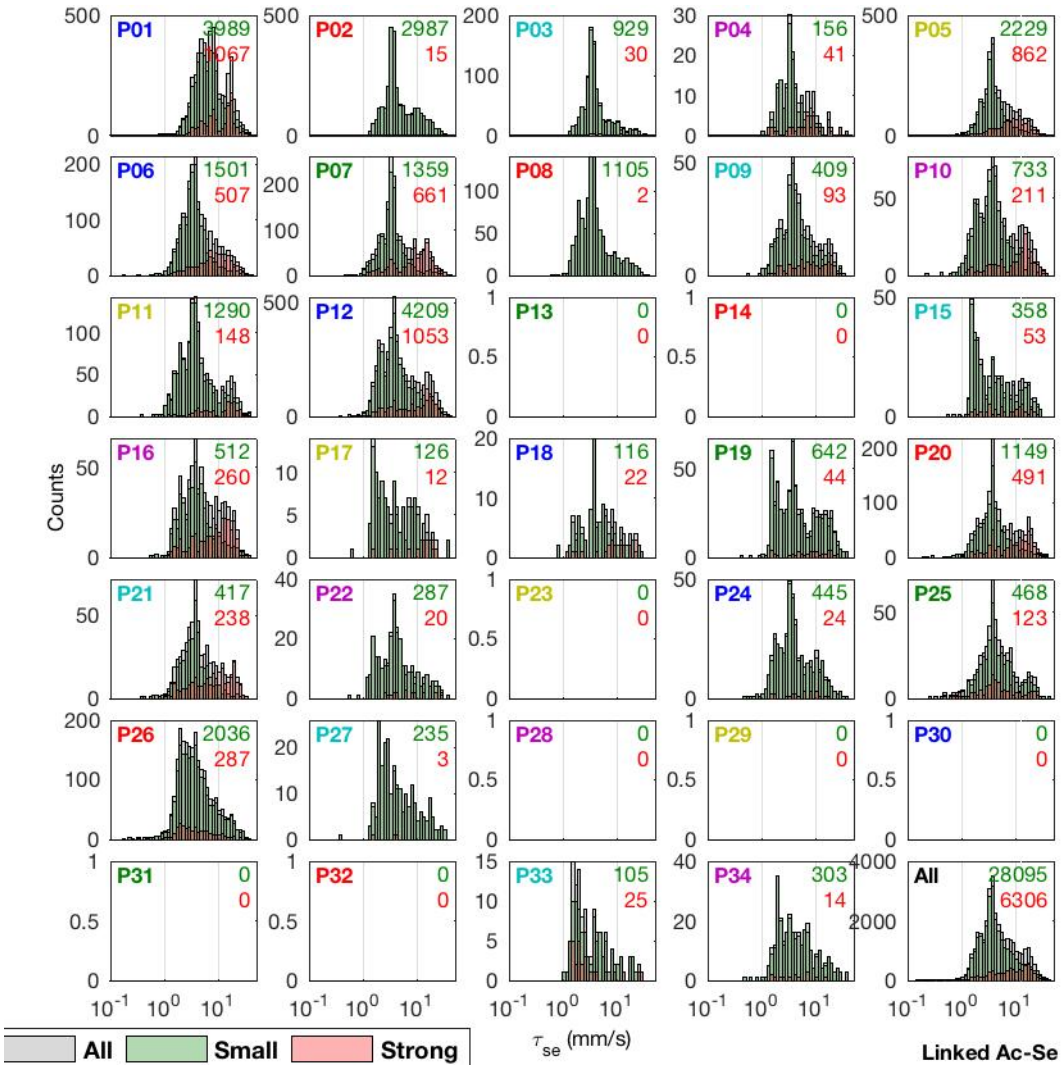

Figure 6.37 – Distribution of the seismic duration per phase for all seismo-infrasonic events. The phase number is indicated north-west of each subplot. The number of small (<340 Pa) and strong (>340 Pa) explosions is indicated, north-east of each subplot, in green and red, respectively.

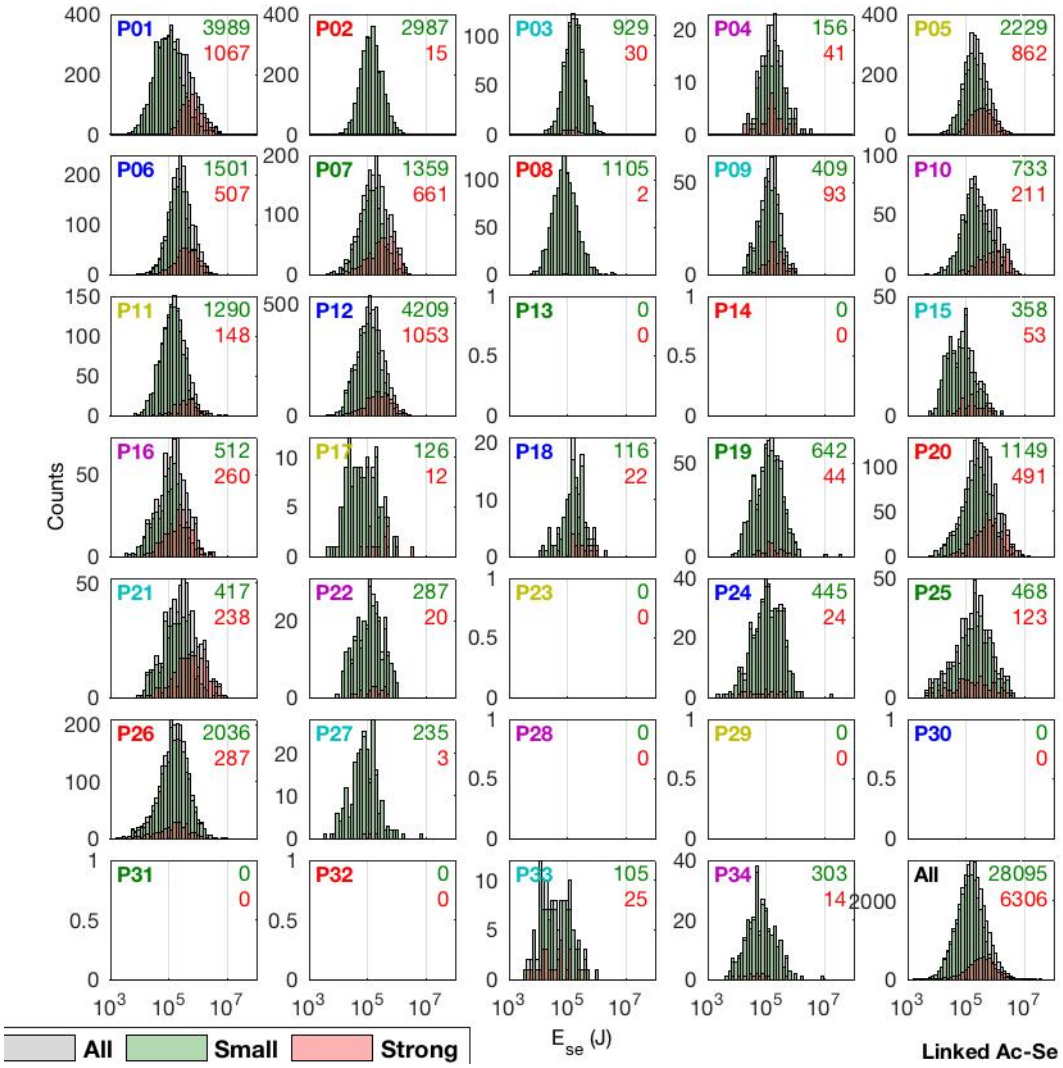

Figure 6.38 – Distribution of the seismic energy per phase for all seismo-infrasonic events. The phase number is indicated north-west of each subplot. The number of small (<340 Pa) and strong (>340 Pa) explosions is indicated, north-east of each subplot, in green and red, respectively.

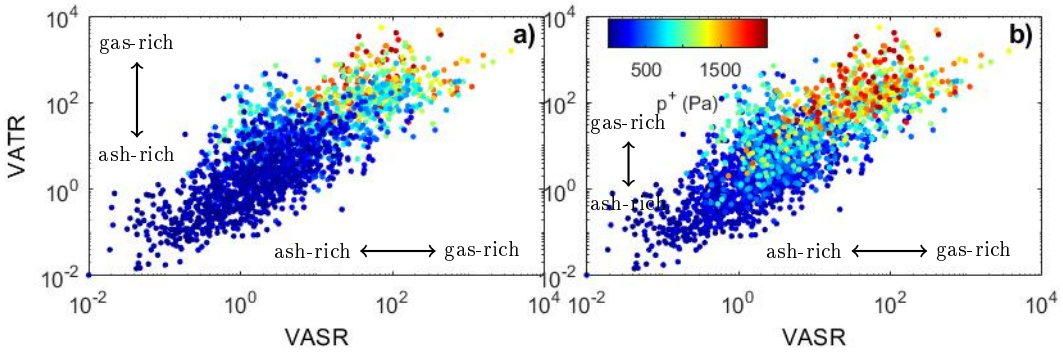

Figure 6.39 – VATR per event as a function of the VASR per event.

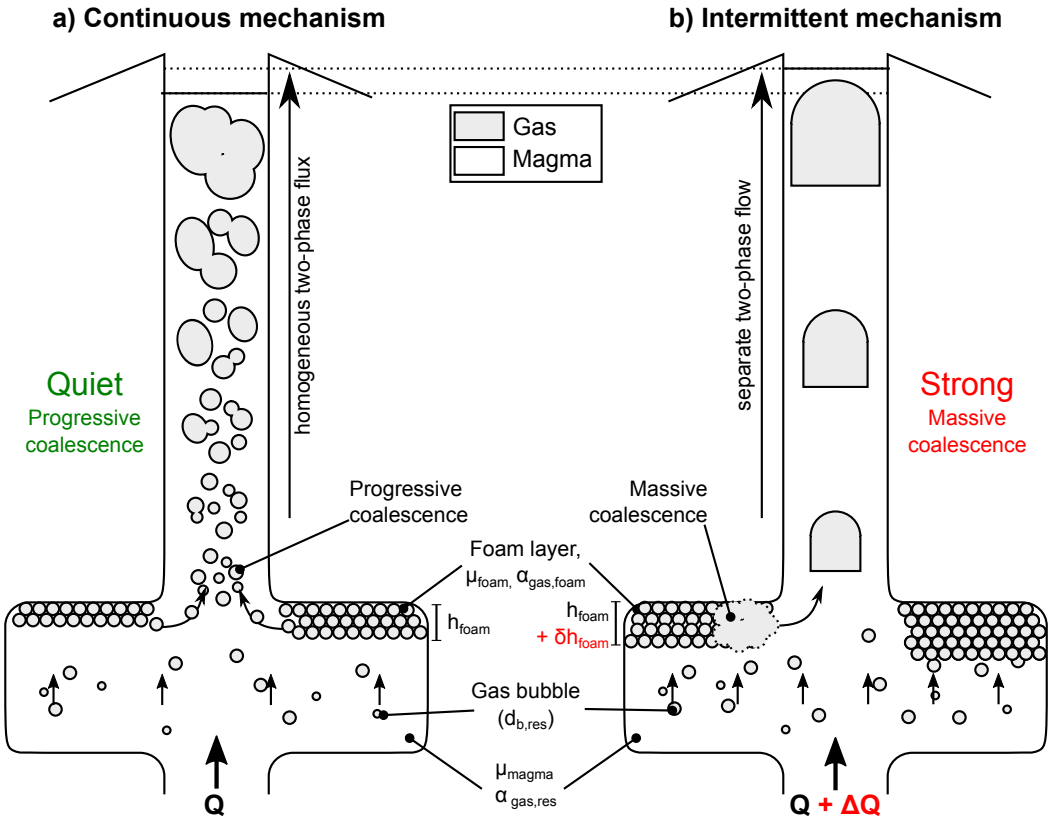

Figure 6.40 – Skeches for the a) persistent and b) intermittent mechanisms of degassing at Yasur.

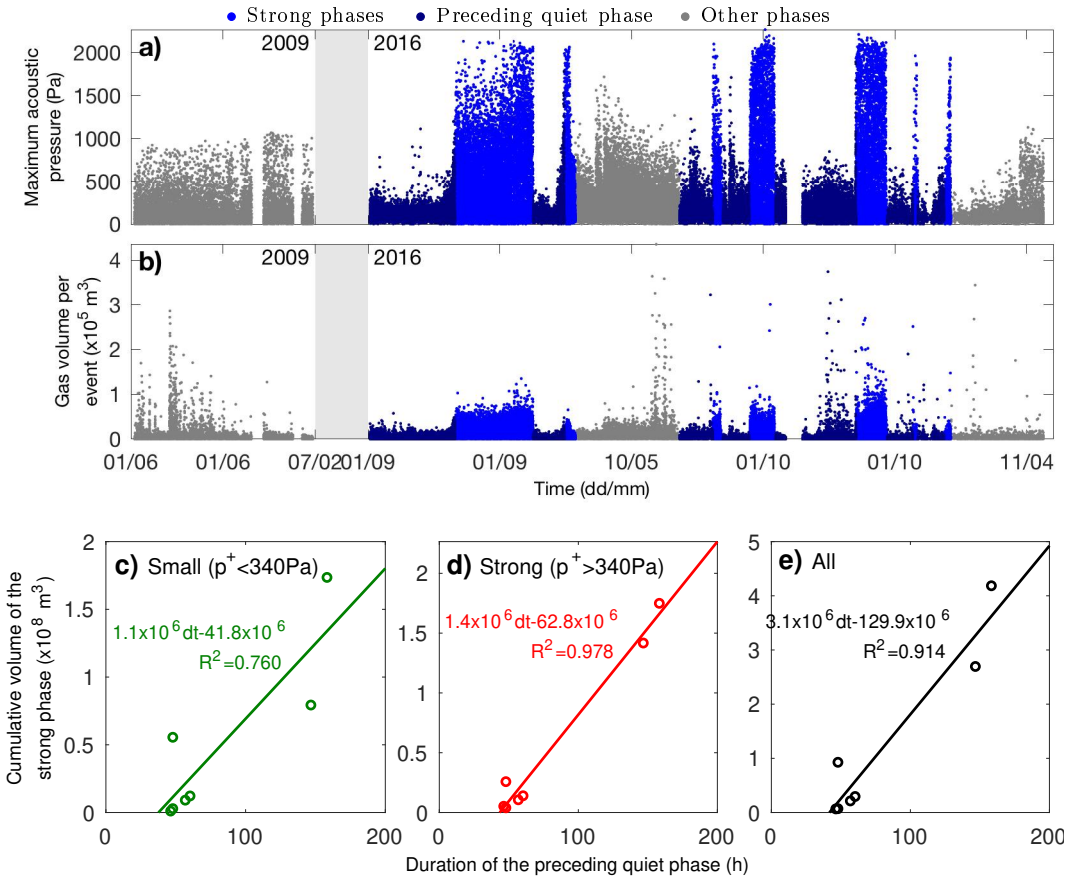

Figure 6.41 – Cumulative volume of each strong phase as a function of the duration of the quiet phase that precedes the strong phase. a) Maximum acoustic pressure and b) gas volume per explosion as a function of time. Cumulative volume of a) the small explosions, b) the strong explosions and c) all explosions of the strong phase as a function of the duration of the quiet phase preceding the strong phase.

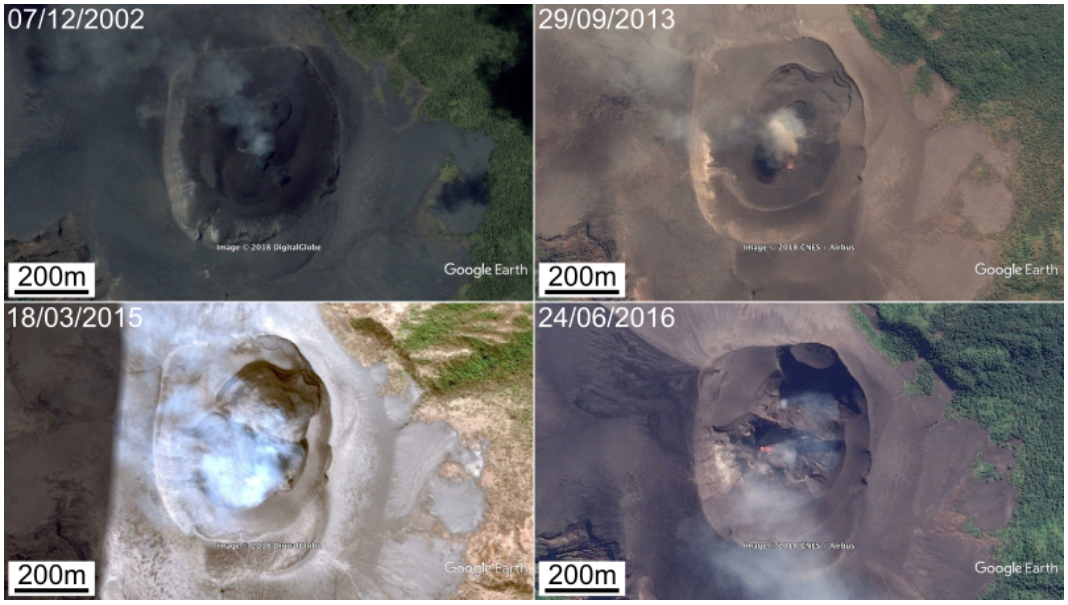

Figure 6.42 – Satellite view of Mount Yasur in December 2002, September 2013, March 2015 and June 2016 (Google Earth).

Chapter 7

Conclusions et perspectives

Contents

7.1 Conclusions **211**
7.1.1 Variabilité mondiale de l'activité Strombolienne 211
7.1.2 Variabilité temporelle de l'activité Strombolienne, l'exemple du Yasur 212
7.2 Perspectives **212**
7.2.1 Fraction volumique du gaz 212
7.2.2 Signaux sismiques 213
7.2.3 Classification des formes d'ondes 213
7.2.4 Renforcer la définition de l'activité Strombolienne 213
7.2.5 Surveillance 213

7.1 Conclusions

Le traitement de données infrasoniques et thermiques à l'Erta'Ale et au Piton de la Fournaise et de données infrasoniques, thermiques et sismiques et l'analyse de vidéos au Yasur ont permis d'étudier la variabilité de l'activité strombolienne selon deux axes.

7.1.1 Variabilité mondiale de l'activité Strombolienne

L'étude en parallèle de l'Erta'Ale, du Piton de la Fournaise et du Yasur a permiS de mettre en avant la variabilité de l'activité Strombolienne à l'échelle mondiale avec une classification en terme d'activité faible, intermédiaire ou forte. Le paramètre essentiel pour cette classification, nous paraît être l'amplitude infrasonique liée aux explosions stromboliennes. En effet, il est le paramètre pour lequel nous avons pu trouver le plus de données et aussi parce qu'il est le paramètre le moins entaché d'erreurs ou de biais par rapport à des paramètres tels que la variation de température qui dépend beaucoup de la fenêtre de mesure et de la sensibilité effective du capteur (radiomètre ou caméra thermique) ou encore les énergies qui sont très dépendantes de la détermination de la limites des explosions enregistrées par les capteurs. La surprise vient de la difficulté à interpréter quantitativement les signaux thermiques, qui pourtant doivent contenir de l'information sur la vitesse et la quantité des éjecta dans le champ de vue des radiomètres.

Nous avons ainsi pu déterminer que les volcans en faible activité strombolienne, tels que l'Erta'Ale, le Piton de la Fournaise ou encore le Villarrica, produisent des explosions stromboliennes dont l'amplitude infrasonique ne dépasse pas 20 Pa à une distance de 100 m de la source. Les volcans en forte activité strombolienne, tels que le Yasur, Ambrym ou l'Arenal, peuvent en revanche produire des explosions stromboliennes dont l'amplitude infrasonique excède 400 Pa.

Cette étude a également permis de valider l'existence d'un mécanisme unique de fragmentation pour toutes les explosions stromboliennes, de faibles à fortes, à partir d'un bilan d'énergies définies en terme d'énergie de flottabilité et d'énergie du jet initial. Ce bilan d'énergie reste, cependant, insuffisant pour caractériser l'activité strombolienne, notamment parce que nous manquons 25 % des explosions au Yasur, par rapport au bilan entre les énergies infrasoniques et thermiques, et à cause du biais induit par la taille de la fenêtre des mesures thermiques (Figure 5.15).

Les estimations des flux de gaz émis au Yasur et au Piton de la Fournaise à partir des données infrasoniques et celles à partir des données géo-chimiques permettent de donner pour chaque catégorie d'activité, faible, intermédiaire ou forte, un ordre de grandeur du volume total de gaz émis par heure et de quantifier l'impact de chacun des volcans, en activité strombolienne, sur l'environnement. En effet, le flux de gaz de chacune des espèces chimiques, dont les espèces toxiques ou à effets de serre pour l'atmosph7re, peut être quantifié connaissant leur proportion d'émission (FTIR, multigas). Un volcan ayant une faible activité strombolienne émet ainsi environ $10^6\,\mathrm{m^3.h^{-1}}$, tandis qu'un volcan ayant une forte activité strombolienne émet de $10^7\,\mathrm{m^3.h^{-1}}$ au Yasur à $3\times10^7\,\mathrm{m^3.h^{-1}}$ à Ambrym. Pour des volcans en activité persistante sur plusieurs siècles, comme le Yasur ou le Stromboli, ces volumes de gaz, émis dans l'atmosphère, sont non négligeables.

7.1.2 Variabilité temporelle de l'activité Strombolienne, l'exemple du Yasur

L'étude de l'activité strombolienne du Yasur, à partir de données infrasoniques, sismiques et thermiques et sur ∼70 jours, nous a permis de confirmer l'existence de deux mécanismes à l'œuvre pour la formation des grandes poches de gaz responsables des explosions stromboliennes (comparaison sismo-infrasonique). La coalescence progressive dans le conduit est probablement le mécanisme persistant au Yasur et produit des explosions stromboliennes de faible amplitude infrasonique ($\leq$340 Pa à 100 m). La coalescence massive de la mousse au toit du réservoir est probablement le mécanisme intermittent, qui s'ajoute à la coalescence progressive dans le conduit et qui produit des explosions stromboliennes plus fortes (>340 Pa à 100 m). Il serait intéressant dans le futur de voir si un mécanisme similaire est à l'œuvre sur d'autres volcans en activité persistante strombolienne, comme le Stromboli ou l'Erebus.

Nous avons estimé que seul le régime persistant existe tant que le flux de gaz en profondeur reste faible, sous une valeur critique que nous avons estimé à 1.5 $m^3.s^{-1}$, à partir des données infrasoniques. Ce flux de gaz critique nous à permis d'estimer la tailles des bulles de gaz dans le réservoir à 13 µm–14 µm, valeurs qui sont cohérentes avec les tailles estimées dans les réservoirs d'autres volcans basaltiques (Erta'Ale, Etna et Kilauea) et la taille des bulles à la nucléation.

Nous avons également montré au Yasur que l'activité strombolienne peut produire des explosions plus ou moins riches en cendres (spectrogrammes infrasoniques, comparaisons thermo-infrasonique et sismo-infrasonique) et que les explosions les plus riches en gaz, c'est-à-dire les plus pauvres en cendres, sont essentiellement produites pendant les phases où la coalescence massive est possible. Une analyse de polarisation, sur les données sismiques de 2016, pourrait permettre de quantifier autrement les deux mécanismes mis en évidence au Yasur dans cette étude, en estimant la profondeur des VLP par exemple, et ainsi permettre d'identifier les phases d'activité faibles et fortes par un simple traitement sismique.

De nombreux points restent encore à éclaircir malgré la quantité importante de données qui a été traitée pendant cette thèse.

7.2 Perspectives

7.2.1 Fraction volumique du gaz

Le type d'explosion, riche en gaz ou en cendre reste un point important à déterminer. La fraction volumique de gaz par explosion nous permettrait de caractériser proprement ces deux types d'explosions. La vitesse du son dans le conduit, qui est très dépendante de la fraction volumique de gaz, serait donc plus adaptée pour calculer la profondeur de la colonne de magma sous la bouche éruptive (Section 4.5.2).

Plusieurs pistes sont à suivre pour l'estimation de la fraction volumique de gaz. L'analyse de vidéo permet de compter le nombre de pixels où il y a du liquide magmatique chaud (Section 4.3.2). Nous savons qu'en 2009, un pixel de la vidéo fait environ 30.50 cm × 28.10 cm (∼0.09 m^2) au niveau de la bouche éruptive. La vidéo nous permet d'estimer la surface chaude que l'on peut extrapoler en un volume en considérant que les fragments sont sphériques. Nous pouvons également estimer le flux volumique d'éjecta, à partir du volume du cône strombolien et la durée de l'éruption, comme au Piton de la Fournaise, pour le

comparer au flux volumique de gaz (Section 4.5.3).

7.2.2 Signaux sismiques

L'étude, plus compliquée, des enregistrements sismiques peut être poursuivie en cherchant les signaux longues périodes (LP) et très long périodes (VLP). Associés aux signaux sismiques et/ou infrasoniques des explosions, ces LP et VLP peuvent permettre une meilleure compréhension de l'histoire d'une poche de gaz, depuis sa formation jusqu'à son explosion. L'analyse de polarisation des VLP, peut par exemple permettre d'estimer leur profondeur et donc la profondeur de formation de la poche de gaz. Associée au délai explosion-VLP, la profondeur du VLP permet d'estimer la vitesse d'ascension de la poche de gaz.

7.2.3 Classification des formes d'ondes

La recherche, sur une partie de la longue série temporelle (2003–2008), de formes d'onde infrasoniques caractéristiques pour les explosions riches en cendres a été commencée durant cette thèse sans grand succès. Une recherche plus ciblée par rapport aux résultats, récents, de l'étude de l'activité du Yasur peut être envisagée. Notamment, la classification des formes d'ondes sismiques, infrasoniques et thermiques ainsi que leur couplage peut permettre de mieux contraindre les types d'explosions (riche en gaz, ou en cendre). Il faut, pour cela, faire plusieurs séries de classes, par phase d'activité et par explosions faibles (<340 Pa) ou fortes (>340 Pa).

7.2.4 Renforcer la définition de l'activité Strombolienne

Il serait nécessaire de faire une étude multi-disciplinaire, similaire, sur une longue période continue au Stromboli et à l'Erebus. Nous pourrions alors vérifier la coexistence de la coalescence progressive dans le conduit et massive dans le réservoir. Les flux de gaz critiques nécessaires pour rendre la mousse au toit du réservoir instable pourrons alors être estimer si nécessaire. Cela permettrait de renforcer, encore, notre intuition que les mécanismes liés à l'activité strombolienne sont communs à tous les volcans pouvant produire une activité strombolienne et donc de renforcer la définition qualitative de l'activité strombolienne.

7.2.5 Surveillance

Cette étude ne nous a pas permis de mettre en évidence des précurseurs aux phases fortes de l'activité du Yasur. Une étude plus précise des transitions de phases est donc nécessaire. Par exemple l'estimation des flux de gaz par 10 min plutôt qu'une heure, pourrait déjà permettre de confirmer ou non la simultanéité des changements de flux de gaz actifs et passifs.

La compréhension des biais des différentes techniques est aussi à explorer. Elle est en outre indispensable pour développer les techniques les plus fiables possible pour la surveillance des volcans en activité strombolienne.

Une perspective également très intéressante et utile est la construction d'un catalogue

collaboratif de données géophysiques et géochimiques de l'activité strombolienne. Ceci permettrait de mieux quantifier les limites de l'activité strombolienne. L'objectif principal de cette quantification est d'anticiper d'éventuels changements majeurs de l'activité volcanique tels que l'occurence de phases paroxysmales (éruptions vulcaniennes), la formation de coulées de lave, ou encore l'arrêt, en surface, de l'activité.

Bibliography

Infrared measurements on volcanic gas and fume: Kilauea eruption, 1968, author=Naughton, John J and Derby, James V and Glover, Richard B, journal=Journal of Geophysical Research, volume=74, number=12, pages=3273–3277, year=1969, publisher=Wiley Online Library.

A. Aiuppa, C. Federico, G. Giudice, G. Giuffrida, R. Guida, S. Gurrieri, M. Liuzzo, R. Moretti, and P. Papale. The 2007 eruption of Stromboli volcano: Insights from real-time measurement of the volcanic gas plume CO2/SO2ratio. *Journal of Volcanology and Geothermal Research*, 182(3-4):221–230, 2009. ISSN 03770273. doi: 10.1016/j.jvolgeores.2008.09.013.

A. Aiuppa, A. Bertagnini, N. Métrich, R. Moretti, A. Di Muro, M. Liuzzo, and G. Tamburello. A model of degassing for stromboli volcano. *Earth and Planetary Science Letters*, 295(1-2):195–204, 2010.

F. Albarède, B. Luais, G. Fitton, M. Semet, E. Kaminski, B. G. J. Upton, P. Bachélery, and J.-L. Cheminée. The geochemical regimes of Piton de la Fournaise Volcano (Réunion) during the last 530 000 years. *Journal of Petrology*, 38(2):171–201, 1997. ISSN 14602415. doi: 10.1093/petroj/38.2.171. URL http://petrology.oxfordjournals.org/content/38/2/171.abstract.

P. Allard, J. Carbonnelle, D. Dajlevic, J. L. Bronec, P. Morel, M. C. Robe, J. M. Maurenas, R. Faivre-Pierret, D. Martin, J. C. Sabroux, and P. Zettwoog. Eruptive and diffuse emissions of CO2 from Mount Etna. *Nature*, 351(6325):387–391, 5 1991. ISSN 00280836. doi: 10.1038/351387a0. URL http://www.nature.com/doifinder/10.1038/351387a0.

P. Allard, J. Carbonnelle, N. Métrich, H. Loyer, and P. Zettwoog. Sulphur output and magma degassing budget of Stromboli volcano. *Nature*, 368(6469):326–330, 3 1994. ISSN 0028-0836. doi: 10.1038/368326a0. URL http://www.nature.com/doifinder/10.1038/368326a0.

P. Allard, M. Burton, and F. Muré. Spectroscopic evidence for a lava fountain driven by previously accumulated magmatic gas. *Nature*, 433(7024):407–410, 2005. ISSN 00280836. doi: 10.1038/nature03246.

P. Allard, A. Aiuppa, P. Bani, N. Métrich, A. Bertagnini, P. J. Gauthier, H. Shinohara, G. M. Sawyer, F. Parello, E. Bagnato, B. Pelletier, and E. Garaebiti. Prodigious emission rates and magma degassing budget of major, trace and radioactive volatile species from Ambrym basaltic volcano, Vanuatu island Arc. *Journal of Volcanology and Geothermal Research*, 322:119–143, 2016a. ISSN 03770273. doi: 10.1016/j.jvolgeores.2015.10.004. URL http://dx.doi.org/10.1016/j.jvolgeores.2015.10.004.

P. Allard, M. Burton, G. M. Sawyer, and P. Bani. Degassing dynamics of basaltic lava lake at a top-ranking volatile emitter: Ambrym volcano, Vanuatu arc. *Earth and Planetary Science Letters*, 448:69–80, 2016b. ISSN 0012821X. doi: 10.1016/j.epsl.2016.05.014.

M. Alletti, A. Burgisser, B. Scaillet, and C. Oppenheimer. Chloride partitioning and solubility in hydrous phonolites from erebus volcano: A contribution towards a multi-component degassing model. *GeoResJ*, 3:27–45, 2014.

D. Andronico and M. Pistolesi. The November 2009 paroxysmal explosions at Stromboli. *Journal of Volcanology and Geothermal Research*, 196(1-2):120–125, 2010. ISSN 03770273. doi: 10.1016/j.jvolgeores.2010.06.005. URL http://dx.doi.org/10.1016/j.jvolgeores.2010.06.005.

D. Andronico, J. Taddeucci, A. Cristaldi, L. Miraglia, P. Scarlato, and M. Gaeta. The 15 March 2007 paroxysm of Stromboli: Video-image analysis, and textural and compositional features of the erupted deposit. *Bulletin of Volcanology*, 75(7):1–19, 2013. ISSN 02588900. doi: 10.1007/s00445-013-0733-2.

R. Aster. Very long period oscillations of Mount Erebus Volcano. *Journal of Geophysical Research*, 108(B11):2522, 2003. ISSN 0148-0227. doi: 10.1029/2002JB002101. URL http://doi.wiley.com/10.1029/2002JB002101.

R. Aster, D. Zandomeneghi, S. Mah, S. McNamara, D. B. Henderson, H. Knox, and K. Jones. Moment tensor inversion of very long period seismic signals from Strombolian eruptions of Erebus Volcano. *Journal of Volcanology and Geothermal Research*, 177 (3):635–647, 2008. ISSN 03770273. doi: 10.1016/j.jvolgeores.2008.08.013. URL http://dx.doi.org/10.1016/j.jvolgeores.2008.08.013.

C. Baillard, W. C. Crawford, V. Ballu, C. Hibert, and A. Mangeney. An automatic kurtosis-based P-and S-phase picker designed for local seismic networks. *Bulletin of the Seismological Society of America*, 104(1):394–409, 2014. ISSN 00371106. doi: 10.1785/0120120347.

C. Baillard, W. C. Crawford, V. Ballu, M. Régnier, B. Pelletier, and E. Garaebiti. Seismicity and shallow slab geometry in the central Vanuatu subduction zone. *Journal of Geophysical Research: Solid Earth*, 120(8):5606–5623, 2015. ISSN 21699356. doi: 10.1002/2014JB011853.

P. Bani and M. Lardy. Sulphur dioxide emission rates from Yasur volcano, Vanuatu archipelago. *Geophysical Research Letters*, 34(20), 2007. ISSN 00948276. doi: 10.1029/2007GL030411.

P. Bani, C. Oppenheimer, P. Allard, H. Shinohara, V. Tsanev, S. A. Carn, M. Lardy, and E. Garaebiti. First estimate of volcanic SO2 budget for Vanuatu island arc. *Journal of Volcanology and Geothermal Research*, 211-212:36–46, 2012. ISSN 03770273. doi: 10.1016/j.jvolgeores.2011.10.005. URL http://linkinghub.elsevier.com/retrieve/pii/S0377027311002745http://dx.doi.org/10.1016/j.jvolgeores.2011.10.005.

P. Bani, A. J. Harris, H. Shinohara, and F. Donnadieu. Magma dynamics feeding Yasur's explosive activity observed using thermal infrared remote sensing. *Geophysical Research Letters*, 40(15):3830–3835, 2013. ISSN 00948276. doi: 10.1002/grl.50722.

J. Barrancos, J. I. Roselló, D. Calvo, E. Padrón, G. Melián, P. A. Hernández, N. M. Pérez, M. M. Millán, and B. Galle. SO2 emission from active volcanoes measured simultaneously by COSPEC and mini-DOAS. *Pure and Applied*

Geophysics, 165(1):115–133, 2008. ISSN 00334553. doi: 10.1007/s00024-007-0290-8. URL http://content.ebscohost.com.insu.bib.cnrs.fr/ContentServer.asp?EbscoContent=dGJyMMTo50Sep7A4zdnyOLCmr1Cep7NSsKe4SrCWxWXS&ContentCustomer=dGJyMOzpsE2xp7dJuePfgeyx9Yvf5ucA&T=P&P=AN&S=R&D=asn&K=31226934.

J. Barrière, N. d'Oreye, A. Oth, H. Geirsson, N. Mashagiro, J. B. Johnson, B. Smets, S. Samsonov, and F. Kervyn. Single-Station Seismo-Acoustic Monitoring of Nyiragongo's Lava Lake Activity (D.R. Congo). *Frontiers in Earth Science*, 6(June):82, 2018. ISSN 2296-6463. doi: 10.3389/feart.2018.00082. URL https://www.frontiersin.org/article/10.3389/feart.2018.00082.

M. L. BAS, R. L. Maitre, A. Streckeisen, B. Zanettin, and I. S. on the Systematics of Igneous Rocks. A chemical classification of volcanic rocks based on the total alkali-silica diagram. *Journal of petrology*, 27(3):745–750, 1986.

J. Battaglia and F. Brenguier. Active Volcanoes of the Southwest Indian Ocean. pages 223–250, 2016. doi: 10.1007/978-3-642-31395-0. URL http://link.springer.com/10.1007/978-3-642-31395-0.

J. Battaglia, J. P. Métaxian, and E. Garaebiti. Earthquake-volcano interaction imaged by coda wave interferometry. *Geophysical Research Letters*, 39(11), 2012. ISSN 00948276. doi: 10.1029/2012GL052003.

J. Battaglia, J.-P. Métaxian, and E. Garaebiti. Short term precursors of Strombolian explosions at Yasur volcano (Vanuatu). *Geophysical Research Letters*, 43(5):1960–1965, 2016. ISSN 19448007. doi: 10.1002/2016GL067823.

N. Bergeot, M. N. Bouin, M. Diament, B. Pelletier, M. Régnier, S. Calmant, and V. Ballu. Horizontal and vertical interseismic velocity fields in the vanuatu subduction zone from GPS measurements: Evidence for a central vanuatu locked zone. *Journal of Geophysical Research: Solid Earth*, 114(6):1–20, 2009. ISSN 21699356. doi: 10.1029/2007JB005249.

E. A. Blackburn, L. Wilson, and R. S. J. Sparks. Mechanisms and dynamics of strombolian activity. *Journal of the Geological Society*, 132(4):429–440, 8 1976. ISSN 0016-7649. doi: 10.1144/gsjgs.132.4.0429. URL http://jgs.lyellcollection.org/cgi/doi/10.1144/gsjgs.132.4.0429.

E. Bouche, S. Vergniolle, T. Staudacher, A. Nercessian, J. C. Delmont, M. Frogneux, F. Cartault, and A. Le Pichon. The role of large bubbles detected from acoustic measurements on the dynamics of Erta 'Ale lava lake (Ethiopia). *Earth and Planetary Science Letters*, 295(1-2):37–48, 2010. ISSN 0012821X. doi: 10.1016/j.epsl.2010.03.020. URL http://dx.doi.org/10.1016/j.epsl.2010.03.020.

Y. K. Branan, A. J. Harris, I. M. Watson, J. C. Phillips, K. Horton, G. Williams-Jones, and H. Garbeil. Investigation of at-vent dynamics and dilution using thermal infrared radiometers at Masaya volcano, Nicaragua. *Journal of Volcanology and Geothermal Research*, 169(1-2):34–47, 2008. ISSN 03770273. doi: 10.1016/j.jvolgeores.2007.07.021.

E. Brothelande and O. Merle. Estimation of magma depth for resurgent domes: An experimental approach. *Earth and Planetary Science Letters*, 412(Supplement C): 143–151, 2015. ISSN 0012821X. doi: 10.1016/j.epsl.2014.12.011. URL http://www.sciencedirect.com/science/article/pii/S0012821X1400764X.

E. Brothelande, J. F. Lénat, M. Chaput, L. Gailler, A. Finizola, S. Dumont, A. Peltier, P. Bachèlery, S. Barde-Cabusson, S. Byrdina, P. Menny, J. Colonge, G. A. Douillet, J. Letort, L. Letourneur, O. Merle, F. Di Gangi, D. Nakedau, and E. Garaebiti. Structure and evolution of an active resurgent dome evidenced by geophysical investigations: The Yenkahe dome-Yasur volcano system (Siwi caldera, Vanuatu). *Journal of Volcanology and Geothermal Research*, 322:241–262, 2016a. ISSN 03770273. doi: 10.1016/j.jvolgeores.2015.08.021.

E. Brothelande, A. Peltier, J. L. Got, O. Merle, M. Lardy, and E. Garaebiti. Constraints on the source of resurgent doming inferred from analogue and numerical modeling — Implications on the current feeding system of the Yenkahe dome–Yasur volcano complex (Vanuatu). *Journal of Volcanology and Geothermal Research*, 322:225–240, 2016b. ISSN 03770273. doi: 10.1016/j.jvolgeores.2015.11.023.

M. R. Burton, C. Oppenheimer, L. A. Horrocks, and P. W. Francis. Remote sensing of C02and H2O emission rates from Masaya volcano, Nicaragua. *Geology*, 28(10):915–918, 2000. ISSN 00917613. doi: 10.1130/0091-7613(2000)028<0915:RSOCAH>2.3.CO;2.

M. R. Burton, G. G. Salerno, L. D'Auria, T. Caltabiano, F. Murè, and R. Maugeri. SO2 flux monitoring at Stromboli with the new permanent INGV SO2 camera system: A comparison with the FLAME network and seismological data. *Journal of Volcanology and Geothermal Research*, 300:95–102, 2014. ISSN 03770273. doi: 10.1016/j.jvolgeores.2015.02.006. URL http://dx.doi.org/10.1016/j.jvolgeores.2015.02.006.

S. Calmant, B. Pelletier, P. Lebellegard, M. Bevis, F. W. Taylor, and D. A. Phillips. New insights on the tectonics along the New Hebrides subduction zone based on GPS results. *Journal of Geophysical Research: Solid Earth*, 108(B6):1–22, 2003. ISSN 01480227. doi: 10.1029/2001JB000644. URL http://doi.wiley.com/10.1029/2001JB000644.

S. Calvari, L. Spampinato, L. Lodato, A. J. Harris, and M. Ripepe. The 5 April 2003 vulcanian paroxysmal explosion at Stromboli volcano (Italy) from field observations and thermal data. *Journal of Volcanology and Geothermal Research*, 149(1-2):160–175, 2006. ISSN 03770273. doi: 10.1016/j.jvolgeores.2005.06.006.

S. Calvari, R. Büttner, A. Cristaldi, P. Dellino, F. Giudicepietro, M. Orazi, R. Peluso, L. Spampinato, B. Zimanowski, and E. Boschi. The 7 September 2008 Vulcanian explosion at Stromboli volcano: Multiparametric characterization of the event and quantification of the ejecta. *Journal of Geophysical Research: Solid Earth*, 117(5):1–17, 2012. ISSN 21699356. doi: 10.1029/2011JB009048.

G. Carazzo, E. Kaminski, and S. Tait. The route to self-similarity in turbulent jets and plumes. *Journal of Fluid Mechanics*, 547:137–148, 2006.

S. Carn. On the detection and monitoring of effusive eruptions using satellite so2 measurements. *Geological Society, London, Special Publications*, 426:SP426–28, 2016.

S. A. Carn, V. E. Fioletov, C. A. McLinden, C. Li, and N. A. Krotkov. A decade of global volcanic SO2 emissions measured from space. *Scientific Reports*, 7:1–12, 2017. ISSN 20452322. doi: 10.1038/srep44095.

K. V. Cashman, R. Sparks, and C. Hawkesworth. Volatile controls on magma ascent and eruption. *The State of the Planet: Frontiers and Challenges in Geophysics*, 150:109–124, 2004.

M. Chaput and E. A. Finizola. Etude du système hydrothermal du complexe Yasur-Bloc résurgent du Yenkahe (Ile de Tanna , Vanuatu). Approche multidisciplinaire Présenté par. *Master Report. Laboratoire Magmas et Volcans, Clermont-Ferrand*, 2009.

L. Chevalier and F. Donnadieu. Considerations on ejection velocity estimations from infrared radiometer data: A case study at Stromboli volcano. *Journal of Volcanology and Geothermal Research*, 302:130–140, 2015. ISSN 03770273. doi: 10.1016/j.jvolgeores.2015.06.022.

B. A. Chouet, N. Hamisevicz, and T. R. McGetchin. Photoballistics of volcanic jet activity at Stromboli, Italy. *Journal of Geophysical Research*, 79(32):4961–4976, 1974. ISSN 01480227. doi: 10.1029/JB079i032p04961. URL http://doi.wiley.com/10.1029/JB079i032p04961.

B. A. Chouet, P. Dawson, T. Ohminato, M. Martini, G. Saccorotti, F. Giudicepietro, G. De Luca, G. Milana, and R. Scarpa. Source mechanisms of explosions at Stromboli Volcano, Italy, determined from moment-tensor inversions of very-long-period data. *Journal of Geophysical Research: Solid Earth*, 108(B1):7–1, 2003. ISSN 01480227. doi: 10.1029/2002JB001919. URL http://doi.wiley.com/10.1029/2002JB001919.

B. A. Chouet, P. Dawson, and M. Martini. Shallow-conduit dynamics at Stromboli Volcano, Italy, imaged from waveform inversions. *Geological Society, London, Special Publications*, 307(1):57–84, 2008. ISSN 0305-8719. doi: 10.1144/SP307.5. URL http://sp.lyellcollection.org/lookup/doi/10.1144/SP307.5.

L. Colò, M. Ripepe, D. R. Baker, and M. Polacci. Magma vesiculation and infrasonic activity at {S}tromboli open conduit volcano. *Earth and Planetary Science Letters*, 292 (3):274–280, 2010.

D. Coppola, M. Laiolo, and C. Cigolini. Fifteen years of thermal activity at Vanuatu's volcanoes (2000–2015) revealed by MIROVA. *Journal of Volcanology and Geothermal Research*, 322:6–19, 2016.

S. J. Cronin and D. S. Sharp. Environmental impacts on health from continuous volcanic activity at Yasur (Tanna) and Ambrym, Vanuatu. *International Journal of Environmental Health Research*, 12(2):109–123, 2002. ISSN 09603123. doi: 10.1080/09603120220129274.

M. P. Dalton, G. P. Waite, I. M. Watson, and P. A. Nadeau. Multiparameter quantification of gas release during weak Strombolian eruptions at Pacaya Volcano, Guatemala. *Geophysical Research Letters*, 37(9), 2010. ISSN 00948276. doi: 10.1029/2010GL042617.

I. Daubechies. Orthonormal bases of compactly supported wavelets. *Communications on pure and applied mathematics*, 41(7):909–996, 1988.

D. Delle Donne and M. Ripepe. High-frame rate thermal imagery of strombolian explosions: Implications for explosive and infrasonic source dynamics. *Journal of Geophysical Research: Solid Earth*, 117(9):n/a–n/a, 2012. ISSN 21699356. doi: 10.1029/2011JB008987. URL http://dx.doi.org/10.1029/2011JB008987.

D. Delle Donne, G. Lacanna, E. Marchetti, M. Ripepe, and G. Ulivieri. Monitoring explosive volcanic activity using thermal images, Stromboli volcano, Italy. In *AGU Fall Meeting Abstracts*, 2006.

A. Di Muro, N. Métrich, D. Vergani, M. Rosi, P. Armienti, T. Fougeroux, E. Deloule, I. Arienzo, and L. Civetta. The shallow plumbing system of Piton de la Fournaise

Volcano (La Réunion Island, Indian Ocean) revealed by the major 2007 caldera-forming eruption. *Journal of Petrology*, 55(7):1287–1315, 2014. ISSN 14602415. doi: 10.1093/petrology/egu025.

F. Donnadieu. Volcanological applications of doppler radars: A review and examples from a transportable pulse radar in l-band. In *Doppler Radar Observations-Weather Radar, Wind Profiler, Ionospheric Radar, and Other Advanced Applications*. InTech, 2012.

F. Donnadieu, G. Dubosclard, R. Cordesses, T. Druitt, C. Hervier, J. Kornprobst, J. F. Lénat, P. Allard, and M. Coltelli. Remotely monitoring volcanic activity with ground-based Doppler radar. *Eos*, 86(21):20–22, 2005. ISSN 00963941. doi: 10.1029/2005EO210001.

P. Dubuisson, H. Herbin, F. Minvielle, M. Compiègne, F. Thieuleux, F. Parol, and J. Pelon. Remote sensing of volcanic ash plumes from thermal infrared: A case study analysis from SEVIRI, MODIS and IASI instruments. *Atmospheric Measurement Techniques*, 7 (2):359–371, 2014. ISSN 18671381. doi: 10.5194/amt-7-359-2014.

R. A. Duncan. Geochronology of basalts from the Ninetyeast Ridge and continental dispersion in the eastern Indian Ocean. *Journal of Volcanology and Geothermal Research*, 4(3-4):283–305, 1978.

R. A. Duncan. Hotspots in the southern oceans—an absolute frame of reference for motion of the Gondwana continents. *Tectonophysics*, 74(1-2):29–42, 1981.

R. A. Duncan, J. Backman, L. C. Peterson, and others. The volcanic record of the Reunion hotspot. In *Proceedings of the Ocean Drilling Program, scientific results*, volume 115, pages 3–10. Ocean Drilling Program, Texas A&M University College Station, TX, 1990.

A. Dupont. *Étude du son produit par la Soufrière de Guadeloupe et le Piton de la Fournaise : implications pour la dynamique éruptive et la surveillance volcanique*. PhD thesis, 2010. URL http://www.theses.fr/2010GLOB0005.

T. Elias, A. J. Sutton, C. Oppenheimer, K. A. Horton, H. Garbeil, V. Tsanev, A. J. McGonigle, and G. Williams-Jones. Comparison of COSPEC and two miniature ultraviolet spectrometer systems for SO2measurements using scattered sunlight. *Bulletin of Volcanology*, 68(4):313–322, 2006. ISSN 02588900. doi: 10.1007/s00445-005-0026-5.

E. T. Endo and T. L. Murray. Real-time Seismic Amplitude Measurement(RSAM): a volcano monitoring and prediction tool. *Bulletin of Volcanology*, 53(7):533–545, 1991. ISSN 0258-8900. doi: 10.1007/BF00298154.

D. Fee, M. Garces, and A. Steffke. Infrasound from Tungurahua Volcano 2006-2008: Strombolian to Plinian eruptive activity. *Journal of Volcanology and Geothermal Research*, 193(1-2):67–81, 2010. ISSN 03770273. doi: 10.1016/j.jvolgeores.2010.03.006. URL http://dx.doi.org/10.1016/j.jvolgeores.2010.03.006.

C. W. Firth, H. K. Handley, S. J. Cronin, and S. P. Turner. The eruptive history and chemical stratigraphy of a post-caldera, steady-state volcano: Yasur, Vanuatu. *Bulletin of Volcanology*, 76(7):1–23, 2014. ISSN 14320819. doi: 10.1007/s00445-014-0837-3.

L. Francalanci, S. Tommasini, and S. Conticelli. The volcanic activity of Stromboli in the 1906-1998 AD period: Mineralogical, geochemical and isotope data relevant to the understanding of the plumbing system. *Journal of Volcanology and Geothermal Research*, 131(1-2):179–211, 2004. ISSN 03770273. doi: 10.1016/S0377-0273(03)00362-7.

B. Galle, C. Oppenheimer, A. Geyer, A. J. S. McGonigle, M. Edmonds, and L. Horrocks. A miniaturised ultraviolet spectrometer for remote sensing of SO2 fluxes: A new tool for volcano surveillance. *Journal of Volcanology and Geothermal Research*, 119(1-4): 241–254, 2003. ISSN 03770273. doi: 10.1016/S0377-0273(02)00356-6.

M. A. Garcés, M. T. Hagerty, and S. Y. Schwartz. Magma acoustics and time-varying melt properties at arenal volcano, costa rica. *Geophysical research letters*, 25(13):2293–2296, 1998.

D. Gaudin. Imagerie infrarouge thermique haute résolution : potentiels et limitations pour la géologie. page 201, 2012.

D. Gaudin, M. Moroni, J. Taddeucci, P. Scarlato, and L. Shindler. Pyroclast Tracking Velocimetry: A particle tracking velocimetry-based tool for the study of Strombolian explosive eruptions. *Journal of Geophysical Research: Solid Earth*, 119(7):5369–5383, 2014a. ISSN 21699356. doi: 10.1002/2014JB011095.

D. Gaudin, J. Taddeucci, P. Scarlato, M. Moroni, C. Freda, M. Gaeta, D. M. Palladino, J. Taddeuci, P. Scarlato, M. Moroni, C. Freda, M. Gaeta, and D. M. Paladino. Pyroclast Tracking Velocimetry illuminates bomb ejection and explosion dynamics at Stromboli (Italy) and Yasur (Vanuatu) volcanoes. *Journal of Geophysical Research: Solid Earth*, 119(7):5384–5397, 2014b. ISSN 21699356. doi: 10.1002/2014JB011096.

Geocontext. Geocontext app, 2018. URL file:///E:/SEISMIC/profil_yash.mat.

T. M. Gerlach and K. A. McGee. Total sulfur dioxide emissions and pre-eruption vapor-saturated magma at Mount St. Helens, 1980–88. *Geophysical Research Letters*, 21(25): 2833–2836, 1994. ISSN 19448007. doi: 10.1029/94GL02761.

A. Gerst, M. Hort, R. C. Aster, J. B. Johnson, and P. R. Kyle. The first second of volcanic eruptions from the Erebus volcano lava lake, Antarctica. Energies, pressures, seismology, and infrasound. *Journal of Geophysical Research: Solid Earth*, 118(7):3318–3340, 2013. ISSN 21699356. doi: 10.1002/jgrb.50234.

W. F. Giggenbach, P. R. Kyle, and G. L. Lyon. Present volcanic activity on Mount Erebus, Ross Island, Antarctica. *Geology*, 1(3):135–136, 1973.

P. Gillot and P. Nativel. Eruptive history of the Piton de la Fournaise volcano, Reunion Island, Indian Ocean. *Journal of Volcanology and Geothermal Research*, 36(1-3):53–65, 1989. ISSN 03770273. doi: 10.1016/0377-0273(89)90005-X. URL http://linkinghub.elsevier.com/retrieve/pii/037702738990005X.

F. Girault, G. Carazzo, S. Tait, F. Ferrucci, and É. Kaminski. The effect of total grain-size distribution on the dynamics of turbulent volcanic plumes. *Earth and Planetary Science Letters*, 394:124–134, 2014.

F. Girault, G. Carazzo, S. Tait, and E. Kaminski. Combined effects of total grain-size distribution and crosswind on the rise of eruptive volcanic columns. *Journal of Volcanology and Geothermal Research*, 326:103–113, 2016.

F. Giudicepietro, L. D'Auria, M. Martini, T. Caputo, R. Peluso, W. De Cesare, M. Orazi, and G. Scarpato. Changes in the VLP seismic source during the 2007 Stromboli eruption. *Journal of Volcanology and Geothermal Research*, 182(3-4):162–171, 2009. ISSN 03770273. doi: 10.1016/j.jvolgeores.2008.11.008. URL http://dx.doi.org/10.1016/j.jvolgeores.2008.11.008.

P. Gleckler, T. Wigley, B. Santer, J. Gregory, K. AchutaRao, and K. Taylor. Volcanoes and climate: Krakatoa's signature persists in the ocean. *Nature*, 439(7077):675, 2006.

A. Grossmann and J. Morlet. Decomposition of Hardy Functions into Square Integrable Wavelets of Constant Shape. *SIAM Journal on Mathematical Analysis*, 15(4):723–736, 1984. ISSN 0036-1410. doi: 10.1137/0515056. URL http://epubs.siam.org/doi/10.1137/0515056.

L. Gurioli, A. J. Harris, B. F. Houghton, M. Polacci, and M. Ripepe. Textural and geophysical characterization of explosive basaltic activity at Villarrica volcano. *Journal of Geophysical Research: Solid Earth*, 113(8):1–16, 2008. ISSN 21699356. doi: 10.1029/2007JB005328.

L. Gurioli, A. D. Muro, I. Vlastélic, S. Moune, S. Thivet, M. Valer, N. Villeneuve, G. Boudoire, A. Peltier, P. Bachèlery, V. Ferrazzini, N. Métrich, M. Benbakkar, N. Cluzel, C. Constantin, J.-l. Devidal, C. Fonquernie, and J.-m. Hénot. Integrating field , textural , and geochemical monitoring to track eruption triggers and dynamics : a case study from Piton de la Fournaise. *Solid Earth*, pages 431–455, 2018. ISSN 18699529. doi: 10.5194/se-9-431-2018.

M. T. Hagerty, S. Y. Schwartz, M. A. Garcés, and M. Protti. Analysis of seismic and acoustic observations at Arenal Volcano, Costa Rica, 1995-1997. *Journal of Volcanology and Geothermal Research*, 101(1-2):27–65, 2000. ISSN 03770273. doi: 10.1016/S0377-0273(00)00162-1.

A. L. Hansell, C. J. Horwell, and C. Oppenheimer. The health hazards of volcanoes and geothermal areas. *Occupational and Environmental Medicine*, 63(2):149–156, 2006. ISSN 13510711. doi: 10.1136/oem.2005.022459.

V. Hanuš and J. Vaněk. Deep structure of the vanuatu (new hebrides) island arc: intermediate depth collision of subducted lithospheric plates. *New Zealand Journal of Geology and Geophysics*, 26(2):133–154, 1983. ISSN 11758791. doi: 10.1080/00288306.1983.10422513.

A. J. Harris. *Thermal Remote Sensing of Active Volcanoes*. Cambridge University Press, 2013. ISBN 9781139029346. doi: 10.1017/CBO9781139029346. URL http://ebooks.cambridge.org/ref/id/CBO9781139029346.

A. J. Harris and M. Ripepe. Synergy of multiple geophysical approaches to unravel explosive eruption conduit and source dynamics–A case study from Stromboli. *Chemie der Erde-Geochemistry*, 67(1):1–35, 2007a. ISSN 00092819. doi: 10.1016/j.chemer.2007.01.003.

A. J. Harris and M. Ripepe. Temperature and dynamics of degassing at Stromboli. *Journal of Geophysical Research: Solid Earth*, 112(3), 2007b. ISSN 21699356. doi: 10.1029/2006JB004393.

A. J. Harris, R. Carniel, and J. Jones. Identification of variable convective regimes at erta ale lava lake. *Journal of Volcanology and Geothermal Research*, 142(3-4):207–223, 2005a.

A. J. Harris, J. Dehn, M. Patrick, S. Calvari, M. Ripepe, and L. Lodato. Lava effusion rates from hand-held thermal infrared imagery: An example from the June 2003 effusive activity at Stromboli. *Bulletin of Volcanology*, 68(2):107–117, 2005b. ISSN 02588900. doi: 10.1007/s00445-005-0425-7.

A. J. Harris, M. Ripepe, and E. A. Hughes. Detailed analysis of particle launch velocities, size distributions and gas densities during normal explosions at Stromboli. *Journal of Volcanology and Geothermal Research*, 231:109–131, 2012.

C. Hibert, A. Mangeney, M. Polacci, A. D. Muro, S. Vergniolle, V. Ferrazzini, A. Peltier, B. Taisne, M. Burton, T. Dewez, G. Grandjean, A. Dupont, T. Staudacher, F. Brenguier, P. Kowalski, P. Boissier, P. Catherine, and F. Lauret. Toward continuous quantification of lava extrusion rate: Results from the multidisciplinary analysis of the 2 January 2010 eruption of Piton de la Fournaise volcano, la Réunion. *Journal of Geophysical Research: Solid Earth*, 120(5):3026–3047, 2015. ISSN 21699356. doi: 10.1002/2014JB011769.

J. P. Holman. *Heat Transfer*. London: McGraw Hill, 2nd edn edition, 1992.

M. Hort, R. Seyfried, and M. Vöge. Radar Doppler velocimetry of volcanic eruptions: Theoretical considerations and quantitative documentation of changes in eruptive behaviour at Stromboli volcano, Italy. *Geophysical Journal International*, 154(2):515–532, 2003. ISSN 0956540X. doi: 10.1046/j.1365-246X.2003.01982.x.

C. J. Horwell and P. J. Baxter. The respiratory health hazards of volcanic ash: A review for volcanic risk mitigation. *Bulletin of Volcanology*, 69(1):1–24, 2006. ISSN 02588900. doi: 10.1007/s00445-006-0052-y.

H. C. Hottel. Radiant heat transmission. In e. W. H. McAdams., editor, *Heat Transmission*, pages 55—-125. New York: McGraw-Hill, 1954.

K. Iacovino. Linking subsurface to surface degassing at active volcanoes: A thermodynamic model with applications to Erebus volcano. *Earth and Planetary Science Letters*, 431: 59–74, 2015. ISSN 0012821X. doi: 10.1016/j.epsl.2015.09.016. URL http://dx.doi.org/10.1016/j.epsl.2015.09.016.

T. Ilanko, C. Oppenheimer, A. Burgisser, and P. Kyle. Cyclic degassing of Erebus volcano, Antarctica. *Bulletin of Volcanology*, 77(6), 2015. ISSN 14320819. doi: 10.1007/s00445-015-0941-z.

M. R. James, S. J. Lane, B. A. Chouet, and J. S. Gilbert. Pressure changes associated with the ascent and bursting of gas slugs in liquid-filled vertical and inclined conduits. *Journal of Volcanology and Geothermal Research*, 129(1-3):61–82, 2004. ISSN 03770273. doi: 10.1016/S0377-0273(03)00232-4.

M. R. James, S. J. Lane, and B. A. Chouet. Gas slug ascent through changes in conduit diameter: Laboratory insights into a volcano-seismic source process in low-viscosity magmas. *Journal of Geophysical Research: Solid Earth*, 111(5):1–25, 2006. ISSN 21699356. doi: 10.1029/2005JB003718.

C. Jaupart and S. Vergniolle. Laboratory models of Hawaiian and Strombolian eruptions. *Nature*, 331(6151):58–60, 1988.

C. Jaupart and S. Vergniolle. The Generation and Collapse of a foam Layer at the Roof of a Basaltic Magma Chamber. *Journal of Fluid Mechanics*, 203(347):347–380, 1989. ISSN 14697645. doi: 10.1017/S0022112089001497.

E. R. Johnson, P. J. Wallace, K. V. Cashman, H. D. Granados, and A. J. Kent. Magmatic volatile contents and degassing-induced crystallization at Volcán Jorullo, Mexico: Implications for melt evolution and the plumbing systems of monogenetic volcanoes. *Earth and Planetary Science Letters*, 269(3-4):477–486, 2008a. ISSN 0012821X. doi: 10.1016/j.epsl.2008.03.004.

J. B. Johnson. Generation and propagation of infrasonic airwaves from volcanic explosions. *Journal of Volcanology and Geothermal Research*, 121(1-2):1–14, 2003. ISSN 03770273. doi: 10.1016/S0377-0273(02)00408-0.

J. B. Johnson and R. C. Aster. Relative partitioning of acoustic and seismic energy during Strombolian eruptions. *Journal of Volcanology and Geothermal Research*, 148(3-4):334–354, 2005. ISSN 03770273. doi: 10.1016/j.jvolgeores.2005.05.002.

J. B. Johnson and J. M. Lees. Plugs and chugs - seismic and acoustic observations of degassing explosions at Karymsky, Russia and Sangay, Ecuador. *Journal of Volcanology and Geothermal Research*, 101(1-2):67–82, 2000. ISSN 03770273. doi: 10.1016/S0377-0273(00)00164-5.

J. B. Johnson, R. C. Aster, and P. R. Kyle. Volcanic eruptions observed with infrasound. *Geophysical Research Letters*, 31(14), 2004. ISSN 00948276. doi: 10.1029/2004GL020020.

J. B. Johnson, R. Aster, K. R. Jones, P. Kyle, and B. McIntosh. Acoustic source characterization of impulsive Strombolian eruptions from the Mount Erebus lava lake. *Journal of Volcanology and Geothermal Research*, 177(3):673–686, 2008b. ISSN 03770273. doi: 10.1016/j.jvolgeores.2008.06.028.

J. B. Johnson, J. Lees, and N. Varley. Characterizing complex eruptive activity at Santiaguito, Guatemala using infrasound semblance in networked arrays. *Journal of Volcanology and Geothermal Research*, 199(1-2):1–14, 2011. ISSN 03770273. doi: 10.1016/j.jvolgeores.2010.08.005. URL http://dx.doi.org/10.1016/j.jvolgeores.2010.08.006http://dx.doi.org/10.1016/j.jvolgeores.2010.08.005.

L. K. Jones, P. R. Kyle, C. Oppenheimer, J. D. Frechette, and M. H. Okal. Terrestrial laser scanning observations of geomorphic changes and varying lava lake levels at Erebus volcano, Antarctica. *Journal of Volcanology and Geothermal Research*, 295:43–54, 2015. ISSN 03770273. doi: 10.1016/j.jvolgeores.2015.02.011. URL http://dx.doi.org/10.1016/j.jvolgeores.2015.02.011.

L. Jourdain, T. J. Roberts, M. Pirre, and B. Josse. Modeling the reactive halogen plume from Ambrym and its impact on the troposphere with the CCATT-BRAMS mesoscale model. *Atmospheric Chemistry and Physics*, 16(18):12099–12125, 2016. ISSN 16807324. doi: 10.5194/acp-16-12099-2016. URL www.atmos-chem-phys.net/16/12099/2016/.

E. Kaminski, S. Tait, and G. Carazzo. Turbulent entrainment in jets with arbitrary buoyancy. *Journal of Fluid Mechanics*, 526:361–376, 2005.

A. J. Kent, M. D. Norman, I. D. Hutcheon, and E. M. Stolper. Assimilation of seawater-derived components in an oceanic volcano: Evidence from matrix glasses and glass inclusions from Loihi seamount, Hawaii. *Chemical Geology*, 156(1-4):299–319, 1999. ISSN 00092541. doi: 10.1016/S0009-2541(98)00188-0.

T. Kobayashi, A. Namiki, and I. Sumita. Excitation of airwaves caused by bubble bursting in a cylindrical conduit: Experiments and a model. *Journal of Geophysical Research: Solid Earth*, 115(10), 2010. ISSN 21699356. doi: 10.1029/2009JB006828.

T. Koyaguchi, K. Ochiai, and Y. J. Suzuki. The effect of intensity of turbulence in umbrella cloud on tephra dispersion during explosive volcanic eruptions: Experimental and numerical approaches. *Journal of Volcanology and Geothermal Research*, 186(1-2):68–78, 2009. ISSN 03770273. doi: 10.1016/j.jvolgeores.2009.01.014. URL http://dx.doi.org/10.1016/j.jvolgeores.2009.01.014.

S. Kremers, J. Wassermann, K. Meier, C. Pelties, M. van Driel, J. Vasseur, and M. Hort. Inverting the source mechanism of Strombolian explosions at Mt. Yasur, Vanuatu, using a multi-parameter dataset. *Journal of Volcanology and Geothermal Research*, 262:104–122, 2013. ISSN 03770273. doi: 10.1016/j.jvolgeores.2013.06.007. URL http://dx.doi.org/10.1016/j.jvolgeores.2013.06.007.

V. C. Kress and I. S. E. Carmichael. The compressibility of silicate liquids containing Fe203 and the effect of composition, temperature, oxygen fugacity and pressure on their redox states. Technical report, 1991. URL https://api-istex-fr.insu.bib.cnrs.fr/document/1B5C64E052B8F1575030DE57822DE77AB05C75FA/fulltext/pdf?auth=ip,fede&sid=ebsco,istex-view.

A. J. Krueger. Sighting of el chichon sulfur dioxide clouds with the nimbus 7 total ozone mapping spectrometer. *Science (New York, N.Y.)*, 220(4604):1377–9, 1983. ISSN 0036-8075. doi: 10.1126/science.220.4604.1377. URL http://www.sciencemag.org/content/220/4604/1377.short.

P. Kyle, J. Moore, and M. Thirlwall. Petrologic evolution of anorthoclase phonolite lavas at Mount Erebus, Ross Island, Antarctica. *Journal of Petrology*, 33(4):849–875, 1992.

P. R. Kyle. *Volcanological and environmental studies of Mount Erebus, Antarctica*. Amer Geophysical Union, 1994.

S. La Felice and P. Landi. The 2009 paroxysmal explosions at Stromboli (Italy): Magma mixing and eruption dynamics. *Bulletin of Volcanology*, 73(9):1147–1154, 2011. ISSN 02588900. doi: 10.1007/s00445-011-0502-z.

A. La Spina, M. Burton, P. Allard, S. Alparone, and F. Murï¿½. Open-path FTIR spectroscopy of magma degassing processes during eight lava fountains on Mount Etna. *Earth and Planetary Science Letters*, 413:123–134, 2015. ISSN 0012821X. doi: 10.1016/j.epsl.2014.12.038. URL http://dx.doi.org/10.1016/j.epsl.2014.12.038.

M. Landès, L. Ceranna, A. Le Pichon, and R. S. Matoza. Localization of microbarom sources using the IMS infrasound network. *Journal of Geophysical Research: Atmospheres*, 117(D6), 2012.

N. C. Lautze, A. J. Harris, J. E. Bailey, M. Ripepe, S. Calvari, J. Dehn, S. K. Rowland, and K. Evans-Jones. Pulsed lava effusion at Mount Etna during 2001. *Journal of Volcanology and Geothermal Research*, 137(1-3 SPEC. ISS.):231–246, 2004. ISSN 03770273. doi: 10.1016/j.jvolgeores.2004.05.018.

C. Le Losq, D. R. Neuville, R. Moretti, P. R. Kyle, and C. Oppenheimer. Rheology of phonolitic magmas - the case of the Erebus lava lake. *Earth and Planetary Science Letters*, 411:53–61, 2015. ISSN 0012821X. doi: 10.1016/j.epsl.2014.11.042. URL http://dx.doi.org/10.1016/j.epsl.2014.11.042.

J. Lefèvre, C. Menkes, P. Bani, P. Marchesiello, G. Curci, G. A. Grell, and R. Frouin. Distribution of sulfur aerosol precursors in the SPCZ released by continuous volcanic degassing at Ambrym, Vanuatu. *Journal of Volcanology and Geothermal Research*, 322:76–104, 2016. ISSN 03770273. doi: 10.1016/j.jvolgeores.2015.07.018. URL http://dx.doi.org/10.1016/j.jvolgeores.2015.07.018.

E. Lemma. Compositional variation of Erta Ale basaltic eruption with time. (June), 2017.

J. Lighthill. *Waves in Fluids*. Cambridge University Press, 1978. ISBN 0521216896.

P. F. Linden, G. K. Batchelor, H. K. Moffatt, and M. G. Worster. Convection in the environment. *Perspectives in fluid dynamics: A collective introduction to current research*, pages 289–345, 2000.

Z. Lu, C. J. Wicks, J. Power, D. Dzurisin, W. Thatcher, and T. Masterlark. Interferometric synthetic aperture radar studies of Alaska volcanoes. *IEEE International Geoscience and Remote Sensing Symposium, 2002 (IGARSS'02)*, 1(March 1996):191–194, 2002. doi: 10.1109/IGARSS.2002.1024984.

S. Mallat. A theory for multi resolution signal decomposition: the wavelet representation. *Penn Libraries*, 11(7):674–693, 1989. ISSN 0162-8828. doi: 10.1109/34.192463.

M. Manga. A model for discharge in spring-dominated streams and implications for the transmissivity and recharge of quaternary volcanics in the Oregon Cascades. *Water Resources Research*, 33(8):1813–1822, 1997.

M. Mangan and T. Sisson. Evolution of melt-vapor surface tension in silicic volcanic systems: Experiments with hydrous melts. *Journal of Geophysical Research: Solid Earth*, 110(B1), 2005.

E. Marchetti and A. J. Harris. Trends in activity at Puu Oo during 2001-2003; insights from the continuous thermal record. *Geological Society of London Special Publication 307*, 307(1):85–101, 2008. ISSN 0305-8719. doi: 10.1144/SP307.6.

E. Marchetti, M. Ripepe, A. J. Harris, and D. Delle Donne. Tracing the differences between Vulcanian and Strombolian explosions using infrasonic and thermal radiation energy. *Earth and Planetary Science Letters*, 279(3-4):273–281, 2009. ISSN 0012821X. doi: 10.1016/j.epsl.2009.01.004. URL //www.sciencedirect.com/science/article/pii/S0012821X09000156.

E. Marchetti, M. Ripepe, D. Delle Donne, R. Genco, A. Finizola, and E. Garaebiti. Blast waves from violent explosive activity at Yasur Volcano, Vanuatu. *Geophysical Research Letters*, 40(22):5838–5843, 2013. ISSN 00948276. doi: 10.1002/2013GL057900.

W. Marzocchi and L. Zaccarelli. A quantitative model for the time-size distribution of eruptions. *Journal of Geophysical Research: Solid Earth*, 111(4):1–13, 2006. ISSN 21699356. doi: 10.1029/2005JB003709.

T. A. Mather. Volcanoes and the environment: Lessons for understanding Earth's past and future from studies of present-day volcanic emissions. *Journal of Volcanology and Geothermal Research*, 304:160–179, 2015. ISSN 03770273. doi: 10.1016/j.jvolgeores.2015.08.016. URL http://dx.doi.org/10.1016/j.jvolgeores.2015.08.016.

T. A. Mather, M. L. Witt, D. M. Pyle, B. M. Quayle, A. Aiuppa, E. Bagnato, R. S. Martin, K. W. Sims, M. Edmonds, A. J. Sutton, and E. Ilyinskaya. Halogens and trace metal emissions from the ongoing 2008 summit eruption of Kīlauea volcano, Hawai'i. *Geochimica et Cosmochimica Acta*, 83:292–323, 2012. ISSN 00167037. doi: 10.1016/j.gca.2011.11.029. URL http://dx.doi.org/10.1016/j.gca.2011.11.029.

R. S. Matoza, D. N. Green, A. Le Pichon, P. M. Shearer, D. Fee, P. Mialle, and L. Ceranna. Automated detection and cataloging of global explosive volcanism using the International Monitoring System infrasound network. *Journal of Geophysical Research: Solid Earth*, 122(4):2946–2971, 2017. ISSN 21699356. doi: 10.1002/2016JB013356.

K. Maurice and R. Bernard. *La Fournaise, Volcan actif de l'Ile de la Réunion*. 1977.

M. P. McCormick. Initial assessment of the stratospheric and climatic impact of the 1991 Mount Pinatubo eruption: Prologue. *Geophysical Research Letters*, 19(2):149–149, 1992. ISSN 19448007. doi: 10.1029/91GL00075.

K. Meier, M. Hort, J. Wassermann, and E. Garaebiti. Strombolian surface activity regimes at Yasur volcano, Vanuatu, as observed by Doppler radar, infrared camera and infrasound. *Journal of Volcanology and Geothermal Research*, 322:184–195, 2016. ISSN 03770273. doi: 10.1016/j.jvolgeores.2015.07.038.

J.-P. Métaxian, G. S. O'Brien, C. J. Bean, B. Valette, and M. Mora. Locating volcano-seismic signals in the presence of rough topography: wave simulations on arenal volcano, costa rica. *Geophysical Journal International*, 179(3):1547–1557, 2009.

N. Métrich, A. Bertagnini, P. Landi, M. Rosi, O. Belhadj, L. Giacomelli, and E. I. Volcanoes. Triggering mechanism at the origin of paroxysms at Stromboli (Aeolian Archipelago , Italy): The 5 April 2003 eruption. *Geophysical Research Letters*, 32 (April 2003):3–6, 2005. ISSN 00948276. doi: 10.1029/2004GL022257. URL http://doi.wiley.com/10.1029/2004GL022257.

N. Métrich, P. Allard, A. Aiuppa, P. Bani, A. Bertagnini, H. Shinohara, F. Parello, A. Di Muro, E. Garaebiti, O. Belhadj, D. Massare, others, D. Massare, and others. Magma and volatile supply to post-collapse volcanism and block resurgence in Siwi caldera (Tanna Island, Vanuatu arc). *Journal of Petrology*, 52(6):1077–1105, 2011. ISSN 00223530. doi: 10.1093/petrology/egr019.

A. Michaud-Dubuy, G. Carazzo, E. Kaminski, and F. Girault. A revisit of the role of gas entrapment on the stability conditions of explosive volcanic columns. *Journal of Volcanology and Geothermal Research*, 357:349–361, 2018.

I. Molina, A. Burgisser, and C. Oppenheimer. A model of the geochemical and physical fluctuations of the lava lake at Erebus volcano, Antarctica. *Journal of Volcanology and Geothermal Research*, 308:142–157, 2015. ISSN 03770273. doi: 10.1016/j.jvolgeores.2015.10.027. URL http://dx.doi.org/10.1016/j.jvolgeores.2015.10.027.

Y. Moussallam, P. Bani, A. Curtis, T. Barnie, M. Moussallam, N. Peters, C. I. Schipper, A. Aiuppa, G. Giudice, A. Amigo, G. Velasquez, and C. Cardona. Sustaining persistent lava lakes: Observations from high-resolution gas measurements at Villarrica volcano, Chile. *Earth and Planetary Science Letters*, 454:237–247, 2016. ISSN 0012821X. doi: 10.1016/j.epsl.2016.09.012.

A. Nabyl, J. Dorel, and M. Lardy. A comparative study of low-frequency seismic signals recorded at Stromboli volcano, Italy, and at Yasur volcano, Vanuatu. *New Zealand Journal of Geology and Geophysics*, 40(4):549–558, 1997. ISSN 11758791. doi: 10.1080/00288306.1997.9514783.

C. G. Newhall and S. Self. The volcanic explosivity index (VEI) an estimate of explosive magnitude for historical volcanism. *Journal of Geophysical Research*, 87(C2):1231, 1982. ISSN 0148-0227. doi: 10.1029/JC087iC02p01231.

K. Notsu, T. Mori, G. Igarashi, Y. Tohjima, and H. Wakita. Infrared spectral radiometer: A new tool for remote measurement of SO2 of volcanic gas. *Geochemical Journal*, 27 (4-5):361–366, 1993.

C. Oppenheimer and P. R. Kyle. Probing the magma plumbing of Erebus volcano, Antarctica, by open-path FTIR spectroscopy of gas emissions. *Journal of Volcanology*

and Geothermal Research, 177(3):743–754, 2008. ISSN 03770273. doi: 10.1016/j.jvolgeores.2007.08.022. URL http://dx.doi.org/10.1016/j.jvolgeores.2007.08.022.

C. Oppenheimer, A. J. S. McGonigle, P. Allard, M. J. Wooster, and V. Tsanev. Sulfur, heat, and magma budget of Erta 'Ale lava lake, Ethiopia. *Geology*, 32(6):509–512, 2004. ISSN 00917613. doi: 10.1130/G20281.1.

C. Oppenheimer, P. Bani, J. A. Calkins, M. R. Burton, and G. M. Sawyer. Rapid FTIR sensing of volcanic gases released by Strombolian explosions at Yasur volcano, Vanuatu. *Applied Physics B: Lasers and Optics*, 85(2-3):453–460, 2006. ISSN 09462171. doi: 10.1007/s00340-006-2353-4.

C. Oppenheimer, A. S. Lomakina, P. R. Kyle, N. G. Kingsbury, and M. Boichu. Pulsatory magma supply to a phonolite lava lake. *Earth and Planetary Science Letters*, 284(3-4):392–398, 2009. ISSN 0012821X. doi: 10.1016/j.epsl.2009.04.043. URL http://dx.doi.org/10.1016/j.epsl.2009.04.043.

E. A. Parfitt. A discussion of the mechanisms of explosive basaltic eruptions. *Journal of Volcanology and Geothermal Research*, 134(1-2):77–107, 2004. ISSN 03770273. doi: 10.1016/j.jvolgeores.2004.01.002.

E. A. Parfitt and L. Wilson. Modelling the transition between Hawaiin-style lava fountaining and Strombolian explosive volcanic activity. *Abstracts of the 25th Lunar and Planetary Science Conference*, 121(1):1049–1050, 1994. URL http://adsabs.harvard.edu/full/1994LPI....25.1049P.

E. A. Parfitt, L. Wilson, and C. A. Neal. Factors influencing the height of Hawaiian lava fountains: implications for the use of fountain height as an indicator of magma gas content. *Bulletin of Volcanology*, 57(6):440–450, 1995. ISSN 02588900. doi: 10.1007/BF00300988.

D. Patanè, C. Chiarabba, O. Cocina, P. De Gori, M. Moretti, and E. Boschi. Tomographic images and 3D earthquake locations of the seismic swarm preceding the 2001 Mt. Etna eruption: Evidence for a dyke intrusion. *Geophysical Research Letters*, 29(10):3–6, 2002. ISSN 0094-8276. doi: 10.1029/2001GL014391.

M. R. Patrick, A. J. Harris, M. Ripepe, J. Dehn, D. A. Rothery, and S. Calvari. Strombolian explosive styles and source conditions: Insights from thermal (FLIR) video. *Bulletin of Volcanology*, 69(7):769–784, 2007. ISSN 02588900. doi: 10.1007/s00445-006-0107-0.

L. Perrier, J. P. Métaxian, J. Battaglia, and E. Garaebiti. Estimation of the near-surface velocity structure of the Yasur-Yenkahe volcanic complex, Vanuatu. *Journal of Volcanology and Geothermal Research*, 227-228:50–60, 2012. ISSN 03770273. doi: 10.1016/j.jvolgeores.2011.12.006.

N. Peters, C. Oppenheimer, D. R. Killingsworth, J. Frechette, and P. Kyle. Correlation of cycles in Lava Lake motion and degassing at Erebus Volcano, Antarctica. *Geochemistry, Geophysics, Geosystems*, 15(8):3244–3257, 2014a. ISSN 15252027. doi: 10.1002/2014GC005399. URL http://dx.doi.org/10.1016/j.epsl.2014.03.032.

N. Peters, C. Oppenheimer, P. Kyle, and N. Kingsbury. Decadal persistence of cycles in lava lake motion at Erebus volcano, Antarctica. *Earth and Planetary Science Letters*, 395:1–12, 2014b.

T. Petersen and S. R. McNutt. Seismo-acoustic signals associated with degassing explosions recorded at Shishaldin Volcano, Alaska, 2003–2004. *Bulletin of volcanology*, 69(5):527–536, 2007.

J. B. Pollack, O. B. Toon, C. Sagan, A. Summers, B. Baldwin, and W. M. Camp '•. Volcanic Explosions and Climatic Change' A Theoretical Assessment. Technical Report 6, 1976. URL https://api-istex-fr.insu.bib.cnrs.fr/document/B0D270AEDE35A29A4997874C5C38F4604CCB9F44/fulltext/pdf?auth=ip,fede&sid=ebsco,istex-view.

A. J. Prata and C. Bernardo. Retrieval of volcanic so2 column abundance from atmospheric infrared sounder data. *Journal of Geophysical Research: Atmospheres*, 112(D20). doi: 10.1029/2006JD007955. URL https://agupubs.onlinelibrary.wiley.com/doi/abs/10.1029/2006JD007955.

A. A. Proussevitch, D. L. Sahagian, and V. A. Kutolin. Stability of foams in silicate melts. *Journal of Volcanology and Geothermal Research*, 59(1-2):161–178, 1993.

V. J. Realmuto, M. J. Abrams, M. F. Buongiorno, and D. C. Pieri. The use of multispectral thermal infrared image data to estimate the sulfur dioxide flux from volcanoes: a case study from Mount Etna, Sicily, July 29, 1986. *Journal of Geophysical Research: Solid Earth*, 99(B1):481–488, 1994.

J. P. Richardson, G. P. Waite, and J. L. Palma. Varying seismic-acoustic properties of the fluctuating lava lake at {V}illarrica volcano, {C}hile. *Journal of Geophysical Research: Solid Earth*, 119(7):5560–5573, 2014. doi: 10.1002/2014jb011002.

M. Ripepe, P. Poggi, T. Braun, and E. Gordeev. Infrasonic waves and volcanic tremor at Stromboli. *Geophysical research letters*, 23(2):181–184, 1996.

M. Ripepe, A. J. Harris, and R. Carniel. Thermal, seismic and infrasonic evidences of variable degassing rates at Stromboli volcano. *Journal of Volcanology and Geothermal Research*, 118(3-4):285–297, 2002. ISSN 03770273. doi: 10.1016/S0377-0273(02)00298-6.

M. Ripepe, E. Marchetti, P. Poggi, A. J. Harris, A. Fiaschi, and G. Ulivieri. Seismic, acoustic, and thermal network monitors the 2003 eruption of Stromboli Volcano. *Eos, Transactions American Geophysical Union*, 85(35):329–332, 2004.

M. Ripepe, D. D. Donne, A. J. Harris, E. Marchetti, and G. Ulivieri. Dynamics of Strombolian activity. *The Stromboli Volcano: An Integrated Study of the 2002-2003 Eruption*, pages 39–48, 2008.

M. Ripepe, D. Delle Donne, G. Lacanna, E. Marchetti, and G. Ulivieri. The onset of the 2007 Stromboli effusive eruption recorded by an integrated geophysical network. *Journal of Volcanology and Geothermal Research*, 182(3):131–136, 2009. ISSN 03770273. doi: 10.1016/j.jvolgeores.2009.02.011.

J. A. Rogers and C. D. Stephens. SSAM: Real-time seismic spectral amplitude measurement on a PC and its application to volcano monitoring. *Bulletin of the Seismological Society of America*, 85(2):632–639, 1995.

M. Rosi, A. Bertagnini, and P. Landi. Onset of the persistent activity at Stromboli Volcano (Italy). *Bulletin of Volcanology*, 62(4-5):294–300, 11 2000. ISSN 0258-8900. doi: 10.1007/s004450000098. URL http://link.springer.com/10.1007/s004450000098.

C. A. Rowe, R. C. Aster, P. R. Kyle, R. R. Dibble, and J. W. Schlue. Seismic and acoustic observations at Mount Erebus volcano, Ross island, Antarctica, 1994–1998. *Journal of Volcanology and Geothermal Research*, 101(1):105–128, 2000.

S. T. Sahetapy-Engel and A. J. Harris. Thermal-image-derived dynamics of vertical ash plumes at Santiaguito volcano, Guatemala. *Bulletin of volcanology*, 71(7):827–830, 2009.

S. T. Sahetapy-Engel, A. J. Harris, and E. Marchetti. Thermal, seismic and infrasound observations of persistent explosive activity and conduit dynamics at Santiaguito lava dome, Guatemala. *Journal of Volcanology and Geothermal Research*, 173(1):1–14, 2008.

G. M. Sawyer, S. A. Carn, V. I. Tsanev, C. Oppenheimer, and M. Burton. Investigation into magma degassing at Nyiragongo volcano, democratic Republic of the Congo. *Geochemistry, Geophysics, Geosystems*, 9(2):1–17, 2008a. ISSN 15252027. doi: 10.1029/2007GC001829.

G. M. Sawyer, C. Oppenheimer, V. I. Tsanev, and G. Yirgu. Magmatic degassing at Erta ' Ale volcano , Ethiopia. *Journal of Volcanology and Geothermal Research*, 178 (4):837–846, 2008b. ISSN 0377-0273. doi: 10.1016/j.jvolgeores.2008.09.017. URL http://dx.doi.org/10.1016/j.jvolgeores.2008.09.017.

G. M. Sawyer, G. G. Salerno, J. S. L. Blond, R. S. Martin, L. Spampinato, T. J. Roberts, T. A. Mather, M. L. I. Witt, V. I. Tsanev, and C. Oppenheimer. Gas and aerosol emissions from Villarrica volcano , Chile. *Journal of Volcanology and Geothermal Research*, 203(1-2):62–75, 2011. ISSN 0377-0273. doi: 10.1016/j.jvolgeores.2011.04.003. URL http://dx.doi.org/10.1016/j.jvolgeores.2011.04.003.

R. Scarpa, F. Tronca, F. Bianco, and E. Del Pezzo. High resolution velocity structure beneath Mount Vesuvius from seismic array data. *Geophysical research letters*, 29(21), 2002.

H.-U. Schmincke. *Volcanism*, volume 28. Springer Science & Business Media, 2004.

P. Sellitto, C. Zanetel, G. Salerno, A. Tapparo, D. Meloni, G. Pace, T. Caltabiano, P. Briole, and B. Legras. The impact of Mount Etna sulfur emissions on the atmospheric composition and aerosol properties in the central Mediterranean : A statistical analysis over the period 2000 e 2013 based on observations and Lagrangian modelling. *Atmospheric Environment*, 148:77–88, 2017. ISSN 1352-2310. doi: 10.1016/j.atmosenv.2016.10.032. URL http://dx.doi.org/10.1016/j.atmosenv.2016.10.032.

H. Shaw. Viscosities of magmatic silicate liquids; an empirical method of prediction. *American Journal of Science*, 272(9):870–893, 1972.

L. Shindler, M. Moroni, and A. Cenedese. Spatial-temporal improvements of a two-frame particle-tracking algorithm. *Measurement Science and Technology*, 21(11), 2010. ISSN 13616501. doi: 10.1088/0957-0233/21/11/115401.

H. Shinohara. A new technique to estimate volcanic gas composition: plume measurements with a portable multi-sensor system. *Journal of Volcanology and Geothermal Research*, 143(4):319–333, 2005.

H. Sigurdsson. Assessment of the atmospheric impact of volcanic eruptions. Technical report, 1990. URL https://pubs.geoscienceworld.org/books/book/388/chapter/3797353/.

H. Sigurdsson, B. F. Houghton, S. R. McNutt, H. Rymer, and J. Stix. Introduction. In H. Sigurdsson, B. F. Houghton, S. R. McNutt, H. Rymer, and J. Stix, editors, *The encyclopedia of Volcanoes, Second edition*. Elsevier, 2015.

Smithsonian Institution. Global Volcanism Program | Regional Volcanoes, 2013. URL http://volcano.si.edu/region.cfm?rn=6.

N. Spilliaert, P. Allard, N. Me, and A. V. Sobolev. Melt inclusion record of the conditions of ascent , degassing , and extrusion of volatile-rich alkali basalt during the powerful 2002 flank eruption of Mount Etna (Italy). 111, 2006. doi: 10.1029/2005JB003934.

L. Spina, J. Taddeucci, A. Cannata, S. Gresta, L. Lodato, E. Privitera, P. Scarlato, M. Gaeta, D. Gaudin, and D. M. Palladino. Explosive volcanic activity at Mt. Yasur: A characterization of the acoustic events (9–12th July 2011). *Journal of Volcanology and Geothermal Research*, 322(July 2003):175–183, 2015. ISSN 03770273. doi: 10.1016/j.jvolgeores.2015.07.027.

G. S. Steinberg and J. I. Babenko. Experimental velocity and density determination of volcanic gases during. Technical report, 1978. URL https://api-istex-fr.insu.bib.cnrs.fr/document/D067ED3A8285132D253EF36CA50F277CDAAD6C1C/fulltext/pdf?auth=ip,fede&sid=ebsco,istex-view.

P. Stelling, J. Beget, C. Nye, J. Gardner, J. D. Devine, and R. M. M. George. Geology and petrology of ejecta from the 1999 eruption of Shishaldin Volcano , Alaska. *Bull Volcanol*, pages 548–561, 2002. doi: 10.1007/s00445-002-0229-y.

J. Suckale, B. H. Hager, L. T. E. Tanton, J. C. Nave, and L. T. Elkins-tanton. It takes three to tango : 2 . Bubble dynamics in basaltic volcanoes and ramifications for modeling normal Strombolian activity. 115(1):1–17, 2010. doi: 10.1029/2009JB006917.

J. Taddeucci, P. Scarlato, A. Capponi, E. Del Bello, C. Cimarelli, D. M. Palladino, and U. Kueppers. High-speed imaging of Strombolian explosions: The ejection velocity of pyroclasts. *Geophysical Research Letters*, 39(2):0–6, 2012. ISSN 00948276. doi: 10.1029/2011GL050404.

D. Tailpied, A. Le Pichon, E. Marchetti, J. Assink, and S. Vergniolle. Assessing and optimizing the performance of infrasound networks to monitor volcanic eruptions. *Geophysical Journal International*, 208(1):437–448, 2017. ISSN 1365246X. doi: 10.1093/gji/ggw400.

H. Tazieff. Permanent lava lakes: observed facts and induced mechanisms. *Journal of Volcanology and Geothermal Research*, 63(1-2):3–11, 1994. ISSN 03770273. doi: 10.1016/0377-0273(94)90015-9.

P. Tulet, A. Di Muro, A. Colomb, C. Denjean, V. Duflot, S. Arellano, B. Foucart, J. Brioude, K. Sellegri, A. Peltier, A. Aiuppa, C. Barthe, C. Bhugwant, S. Bielli, P. Boissier, G. Boudoire, T. Bourrianne, C. Brunet, F. Burnet, J. P. Cammas, F. Gabarrot, B. Galle, G. Giudice, C. Guadagno, F. Jeamblu, P. Kowalski, J. Leclair De Bellevue, N. Marquestaut, D. Mékies, J. M. Metzger, J. Pianezze, T. Portafaix, J. Sciare, A. Tournigand, and N. Villeneuve. First results of the Piton de la Fournaise STRAP 2015 experiment: Multidisciplinary tracking of a volcanic gas and aerosol plume. *Atmospheric Chemistry and Physics*, 2017. ISSN 16807324. doi: 10.5194/acp-17-5355-2017.

U.S. Government Printing Office. U.S. Standard atmosphere. *U.S. Government Printing Office*, 1976.

L. Vanderkluysen, A. J. Harris, K. Kelfoun, C. Bonadonna, and M. Ripepe. Bombs behaving badly: Unexpected trajectories and cooling of volcanic projectiles. *Bulletin of Volcanology*, 74(8):1849–1858, 2012. ISSN 02588900. doi: 10.1007/s00445-012-0635-8.

Vanuatu Meteorology and Geohazard Departement. Yasur. URL http://www.vmgd.gov.vu/vmgd/index.php/geohazards/volcano/our-active-volcanos/tanna/yasur.

Vanuatu Meteorology and Geohazard Departement. VMGD - Yasur, 2018. URL http://www.vmgd.gov.vu/vmgd/index.php/geohazards/volcano/our-active-volcanos/tanna/yasur.

S. Vergniolle. From sound waves to bubbling within a magma reservoir: comparison between eruptions at Etna (2001, Italy) and Kilauea (Hawaii). *Geological Society, London, Special Publications*, 307(1):125–146, 2008. ISSN 0305-8719. doi: 10.1144/SP307.8.

S. Vergniolle and E. Bouche. Gas-driven lava lake fluctuations at Erta 'Ale volcano (Ethiopia) revealed by MODIS measurements. *Bulletin of Volcanology*, 2016. ISSN 14320819. doi: 10.1007/s00445-016-1047-y.

S. Vergniolle and G. Brandeis. Strombolian explosions: 1. A large bubble breaking at the surface of a lava column as a source of sound. *Journal of Geophysical Research: Solid Earthfile*, 101(B9):20433–20447, 1996. ISSN 01480227. doi: 10.1029/96JB01178.

S. Vergniolle and J. Caplan-Auerbach. Acoustic measurements of the 1999 basaltic eruption of Shishaldin volcano, Alaska: 2. Precursor to the subplinian phase. *Journal of volcanology and geothermal research*, 137(1):135–151, 2004.

S. Vergniolle and Y. Gaudemer. Decadal evolution of a degassing magma reservoir unravelled from fire fountains produced at Etna volcano (Italy) between 1989 and 2001. 74:725–742, 2012. doi: 10.1007/s00445-011-0563-z. URL https://link-springer-com.insu.bib.cnrs.fr/content/pdf/10.1007%2Fs00445-011-0563-z.pdf.

S. Vergniolle and Y. Gaudemer. From Reservoirs and Conduits to the Surface : Review of Role of Bubbles in Driving Basaltic Eruptions. pages 289–321, 2015.

S. Vergniolle and C. Jaupart. Separated two-phase flow and basaltic eruption. *Journal of Geophysical Research: Solid Earth*, 91:12842–12860, 1986.

S. Vergniolle and M. T. Mangan. Hawaiian and Strombolian eruptions. In *Encyclopedia of Volcanoes*, pages 447–461. Academic p edition, 2000.

S. Vergniolle and M. Ripepe. From Strombolian explosions to fire fountains at Etna Volcano (Italy): what do we learn from acoustic measurements? *Geological Society, London, Special Publications*, 307(1):103–124, 2008. ISSN 0305-8719. doi: 10.1144/SP307.7. URL http://sp.lyellcollection.org/.

S. Vergniolle, G. Brandeis, and J.-C. Mareschal. Strombolian explosions: 2. Eruption dynamics determined from acoustic measurements. *Journal of Geophysical Research: Solid Earth*, 101(B9):20449–20466, 1996. ISSN 01480227. doi: 10.1029/96JB01925. URL http://doi.wiley.com/10.1029/96JB01925.

S. Vergniolle, M. Boichu, and J. Caplan-Auerbach. Acoustic measurements of the 1999 basaltic eruption of Shishaldin volcano, Alaska: 1. Origin of Strombolian activity. *Journal of Volcanology and Geothermal Research*, 137(1):109–134, 2004.

S. Vergniolle, C. Zielinski, J. Battaglia, J. P. Metaxian, P. Bani, A. L. Pichon, M. Lardy, P. Millier, M. Frogneux, and F. Gallois. A Precursory Phase to a Sudden Enhanced Activity at Yasur volcano (Vanuatu): Insights from Simultaneous Infrasonic and Seismic Records. In *AGU Fall Meeting Abstracts*, 2015.

F. Vita, S. Inguaggiato, N. Bobrowski, L. Calderone, B. Galle, and F. Parello. Continuous SO2 flux measurements for Vulcano Island, Italy. *Annals of Geophysics*, 55(2):301–308, 2012. ISSN 15935213. doi: 10.4401/ag-5759.

M. Voge and M. Hort. Installation of a doppler radar monitoring system at merapi volcano, indonesia. *IEEE Transactions on Geoscience and Remote Sensing*, 47(1):251–271, 2009.

G. P. L. Walker. Explosive volcanic eruptions - a new classification scheme. *Geologische Rundschau*, 62(2):431–446, 1973. ISSN 00167835. doi: 10.1007/BF01840108.

L. Wilson and J. W. Head III. Ascent and eruption of basaltic magma on the earth and moon. *Journal of Geophysical Research: Solid Earth*, 86(B4):2971–3001, 1981.

J. B. Witter, P. Hernandez, A. J. L. Harris, and N. Pérez. Quantification of the mass flux of H2O gas (steam) at three active volcanoes using thermal infrared imagery. *Pure and applied geophysics*, 169(10):1875–1889, 2012.

A. B. Wood. *A textbook of sound: being an account of the physics of vibrations with special reference to recent theoretical and technical developments*. G. Bell, 1955.

World Health Organization Western Pacific Region. Vanuatu: Tanna Island devastated by Tropical Cyclone Pam, 2017. URL http://www.wpro.who.int/southpacific/mediacentre/releases/2015/cyclone-pam-19Mar/en/.

G. Woulff and T. R. McGetchin. Acoustic noise from volcanoes: theory and experiment. *Geophysical Journal International*, 1(4):601–616, 1976.

X. Yang, P. M. Davis, P. T. Delaney, and A. T. Okamura. ø '. 97:3305–3324, 1992.

M. E. Zelenski, T. P. Fischer, J. M. de Moor, B. Marty, L. Zimmermann, D. Ayalew, A. N. Nekrasov, and V. K. Karandashev. Trace elements in the gas emissions from the Erta Ale volcano, Afar, Ethiopia. *Chemical Geology*, 2013. ISSN 00092541. doi: 10.1016/j.chemgeo.2013.08.022.

C. Zielinski. *Écouter les volcans pour mieux les comprendre: volcans de la zone de subduction du Vanuatu*. PhD thesis, Paris 7, 2012.

Appendices

Chapter A

Methodology

A.1 Transfer functions

Table A.1 – Frequency bands of levels from 1 to 10 for the Daubechies wavelet with 5 null-moments (db5) for signal at sampling frequencies of a) 75 Hz and b) 100 Hz. Note that in both cases, the levels 4 and 5 suits well for the infrasonic Strombolian explosions seen at Yasur between 1.80 Hz and 4 Hz

a) $f_s = 75$ Hz		**b)** $f_s = 100$ Hz	
level 1	18.75 – 37.50 Hz	level 1	25 – 50 Hz
level 2	9.38 – 18.75 Hz	level 2	12.50 – 25 Hz
level 3	4.69 – 9.38 Hz	level 3	6.25 – 12.50 Hz
level 4	2.34 – 4.69 Hz	level 4	3.13 – 6.25 Hz
level 5	1.17 – 2.34 Hz	level 5	1.56 – 3.13 Hz
level 6	0.59 – 1.17 Hz	level 6	0.78 – 1.56 Hz
level 7	0.29 – 0.59 Hz	level 7	0.39 – 0.78 Hz
level 8	0.15 – 0.29 Hz	level 8	0.20 – 0.39 Hz
level 9	0.07 – 0.15 Hz	level 9	0.10 – 0.20 Hz
level 10	0.04 – 0.07 Hz	level 10	0.05 – 0.10 Hz

Table A.2 – Poles and zeros of the transfer function of a–d) microbarometers and e–f) seismometers.

a) MB2000 *CEA-DASE*			
Poles	$-206.69 \pm$	0.0	i
	$-177.70 \pm$	177.8	i
	$-4.30 \pm$	819.6	i
	$-4.00 \pm$	1116.7	i
	$-0.06 \pm$	0.0	i
Zeros	$-468\,820.00 \pm$	0.0	i
	$0.00 \pm$	0.0	i
Sensitivity	$100\,\mathrm{mV.Pa^{-1}}$ at 1 Hz		
https://prod.sandia.gov/techlib-noauth/access-control.cgi/2014/1420108.pdf			

b) MB2005 *CEA-DASE*			
Poles	$-206.69 \pm$	0.0	i
	$-177.70 \pm$	177.8	i
	$-4.30 \pm$	819.6	i
	$-4.00 \pm$	1116.7	i
	$-0.06 \pm$	0.0	i
Zeros	$-468\,820.00 \pm$	0.0	i
	$0.00 \pm$	0.0	i
Sensitivity	$97\,\mathrm{mV.Pa^{-1}}$ at 1 Hz		
https://prod.sandia.gov/techlib-noauth/access-control.cgi/2014/1420108.pdf			

c) MB3a *Seismowaves, CEA-DASE*			
Poles	$-0.06 \pm$	0.0	i
	$-156.25 \pm$	0.0	i
	$-142.22 \pm$	706.2	i
Zeros	$-1156.25 \pm$	0.0	i
	$0.00 \pm$	0.0	i
Sensitivity	$20\,\mathrm{mV.Pa^{-1}}$ at 1 Hz		
https://prod.sandia.gov/techlib-noauth/access-control.cgi/2014/1420108.pdf			

d) MB3d *Seismowaves, CEA-DASE*			
Poles	$\pm$		i
	$\pm$		i
	$\pm$		i
Zeros	$\pm$		i
	$\pm$		i
Sensitivity	$20\,\mathrm{mV.Pa^{-1}}$ at 1 Hz		
not-found			

e) LE-3Dlite MkII *Lennartz electronic*			
Poles	$-4.440 \pm$	4.44	i
	$-1.083 \pm$	0.00	i
Zeros	$0.000 \pm$	0.00	i
	$0.000 \pm$	0.00	i
	$0.000 \pm$	0.00	i
Sensitivity	400 V/(m/s) at 1 Hz		
https://www.osop.com.pa/wp-content/uploads/2013/11/Manual_LENNARTZ_SISMOMETROS.pdf			

f) Trillium 40 *Nanometrics*			
Poles	$-272 \pm$	218	i
	$56.50 \pm$	0	i
	$-0.11 \pm$	0.1	i
Zeros	$0 \pm$	0	i
	$0 \pm$	0	i
	$51.50 \pm$	0	i
Sensitivity	1500 V/(m/s) at 1 Hz		
https://www.passcal.nmt.edu/webfm_send/948			

A.2 Measurements for the calibration of the thermal system

Table A.3 – Radiometers calibration: Measurements of known temperatures before and after the field campaign of September–November 2016. In 2016, we used a cooking plate set at its maximum power (200 °C) and the temperature was controlled by a handhold infra-red thermometer. First experiments in 2017 use boiling water (100 °C). Second experiments use another cooking plate with a maximum temperature at 400 °C. In 2017, the temperature was controlled by a FLIR camera.

Temperature of calibration (°C)	***Radiometer*** (Serial number)	***Zn–Se window***	***Emissivity***†	***Distance to the source*** (m)	***Temperature measurements*** (°C)
Calibration 1: August 2016, cooking plate at 200 °C (handhold thermometer)					
200	20002764	none	0.85	0.73	165.0
200	20002764	thin	0.85	0.73	123.0
200	20002764	thick	0.85	0.73	152.0
200	20003181	none	0.85	0.44	182.0
200	20003181	thin	0.85	1.13	116.0
200	20003181	thick	0.85	1.13	143.0
Calibration 2: November 2017, boiling water at 100 °C (FLIR)					
100	20002764	none	1	0.95	88.6
100	20002764	thin	1	0.95	36.8
100	20002764	thick	1	0.95	42.2
100	20002764	none	0.85	0.95	96.1
100	20002764	thin	0.85	0.95	40.7
100	20002764	thick	0.85	0.95	44.9
100	20003181	none	1	0.95	85.6
100	20003181	thin	1	0.95	37.1
100	20003181	thick	1	0.95	41.0
100	20003181	none	0.85	0.95	91.1
100	20003181	thin	0.85	0.95	39.6
100	20003181	thick	0.85	0.95	45.7
Calibration 3: November 2017, cooking plate at 460 °C (FLIR)					
460	20002764	none	1	0.95	399
460	20002764	thin	1	0.95	101.5
460	20002764	thick	1	0.95	128.5
460	20002764	none	0.85	0.95	444
460	20002764	thin	0.85	0.95	110.5
460	20002764	thick	0.85	0.95	138.7
460	20003181	none	1	0.95	370
460	20003181	thin	1	0.95	92.0
460	20003181	thick	1	0.95	114.5
460	20003181	none	0.85	0.95	409
460	20003181	thin	0.85	0.95	105.0
460	20003181	thick	0.85	0.95	131.0

†Emissivity configuration of the radiometer ($\epsilon_{\text{thermal}}$). It corresponds to the temperature measured by the radiometer corrected by the emissivity as $T_{\text{records}} = T_{\text{measurement}}/\epsilon_{\text{thermal}}$.

A.3 List of Earthquakes (USGS)

Table A.4 – Lists of the earthquakes of magnitude 4 and above that occured at a maximum distance of 1000 km from Yasur (USGS database)

Time	Magnitude	Distance (km)	Latitude (°)	Longitude (°)	Depth (km)
19/06/09 11:24:25.100	4.3	913.9	−11.7920	166.5560	254.8
20/06/09 12:40:29.090	4.8	891.9	−12.1950	166.0610	44.1
25/06/09 00:09:24.130	4.4	50.5	−19.0990	169.6050	35.0
25/06/09 06:43:48.050	5.2	29.1	−19.3060	169.2960	35.0
25/06/09 11:45:09.490	4.8	41.2	−19.2650	169.1670	35.0
25/06/09 21:02:46.410	4.4	166.4	−20.9570	169.9150	81.5
26/06/09 07:42:14.410	4.8	571.5	−14.8110	167.3050	165.0
29/06/09 11:56:33.210	5.1	260.2	−21.5740	170.6550	176.2
15/09/16 01:14:36.800	4.2	534.8	−15.0805	167.5240	109.7
15/09/16 16:02:57.360	4.4	463.7	−15.4826	168.3791	10.0
15/09/16 17:35:57.230	4.3	681.1	−13.5580	168.0111	10.0
16/09/16 09:22:08.480	4.8	844.1	−12.5070	166.4361	61.5
16/09/16 12:47:05.960	4.5	295.0	−22.0337	170.3742	11.8
17/09/16 03:31:58.780	5.8	438.1	−16.0566	167.4862	31.0
17/09/16 14:38:11.670	4.2	646.3	−13.9865	167.6088	223.4
17/09/16 16:47:01.750	4.5	328.0	−22.3345	170.4124	10.0
20/09/16 09:33:23.930	4.3	643.0	−14.0932	167.3768	177.6
20/09/16 09:55:55.520	4.5	892.7	−11.9637	166.6444	54.3
20/09/16 13:59:43.880	4.5	872.3	−12.2353	166.4330	83.9
20/09/16 22:31:31.740	4.8	492.7	−22.8078	172.6395	10.0
22/09/16 03:50:30.030	4.4	244.7	−21.4517	170.5830	155.0
22/09/16 12:05:58.190	4.9	396.7	−16.2234	168.0297	166.3
25/09/16 15:41:18.580	4.4	812.1	−12.5831	167.0895	188.1
26/09/16 12:41:11.290	4.4	867.1	−19.5173	177.7195	10.0
26/09/16 21:15:09.910	5.2	860.4	−19.5756	177.6564	10.0
26/09/16 21:30:45.710	5.0	868.1	−19.5626	177.7301	10.0
26/09/16 21:45:20.580	4.7	840.6	−19.4821	177.4657	10.0
26/09/16 22:07:50.150	4.6	874.2	−19.6215	177.7892	10.0
28/09/16 17:16:12.160	4.8	981.1	−11.2155	166.3716	122.8
29/09/16 04:35:22.430	4.3	725.8	−13.7760	166.2217	218.6
29/09/16 12:53:04.480	4.4	199.9	−18.2892	168.0671	48.8
29/09/16 21:09:51.240	4.3	481.1	−15.8195	167.1027	138.7
01/10/16 03:33:02.380	5.1	752.9	−13.1076	167.1984	206.3
01/10/16 03:33:02.380	5.1	752.9	−13.1076	167.1984	206.3
01/10/16 10:37:59.810	4.8	837.8	−12.5309	166.5319	67.1
01/10/16 10:37:59.810	4.8	837.8	−12.5309	166.5319	67.1
01/10/16 18:42:49.580	4.5	647.2	−23.6095	173.9076	10.0
01/10/16 18:42:49.580	4.5	647.2	−23.6095	173.9076	10.0
01/10/16 18:44:29.580	4.3	822.6	−12.5154	166.9881	255.9
01/10/16 18:44:29.580	4.3	822.6	−12.5154	166.9881	255.9
01/10/16 20:06:44.590	4.5	705.7	−13.9513	166.2778	10.0
01/10/16 20:06:44.590	4.5	705.7	−13.9513	166.2778	10.0
02/10/16 12:01:40.440	4.4	507.1	−22.6114	173.0457	10.0
02/10/16 23:35:14.790	4.6	116.3	−20.5130	169.0744	40.9
03/10/16 01:45:37.830	4.2	409.7	−17.9330	172.9527	35.7
03/10/16 03:15:24.580	4.4	562.6	−14.9115	167.2744	131.7
03/10/16 22:56:21.900	4.4	496.4	−15.4758	167.4774	114.3
05/10/16 23:11:36.090	4.6	200.5	−21.2312	170.0732	110.9
06/10/16 16:09:28.490	4.3	507.6	−15.2428	167.7931	97.6
07/10/16 04:16:12.260	4.4	222.7	−17.8271	168.3263	63.3
08/10/16 00:14:29.020	4.5	1000.0	−11.1947	165.9324	35.0
08/10/16 11:02:42.910	4.4	634.4	−14.1559	167.4327	204.4
10/10/16 09:01:01.700	4.3	421.3	−22.9125	171.2702	10.0

Continued on next page

Table A.4 – *Continued from previous page*

Time	Magnitude	Distance (km)	Latitude (°)	Longitude (°)	Depth (km)
10/10/16 23:19:35.530	4.5	232.2	−21.5255	170.0922	83.4
12/10/16 04:57:35.490	4.8	984.2	−11.6862	165.1774	34.7
13/10/16 22:56:08.230	4.6	365.4	−16.6920	167.6964	35.0
14/10/16 00:13:05.690	4.9	490.1	−22.7618	172.6553	10.0
14/10/16 03:15:04.400	4.4	845.1	−12.5603	166.2820	34.1
14/10/16 09:31:20.360	4.5	52.0	−19.0851	169.6083	264.3
14/10/16 22:30:30.420	4.8	835.7	−12.4055	166.9442	186.3
15/10/16 18:47:09.030	4.6	840.0	−12.2882	167.1957	229.5
16/10/16 00:37:49.370	4.3	139.3	−18.9264	168.2804	38.1
16/10/16 11:39:24.910	4.7	594.7	−14.5512	167.3932	196.6
17/10/16 03:50:46.930	4.5	778.4	−17.1347	176.3771	10.0
17/10/16 12:10:04.610	4.4	570.6	−14.7275	167.5443	137.4
18/10/16 01:53:26.620	4.1	393.7	−16.2590	168.0122	189.9
18/10/16 19:45:31.550	4.1	436.2	−15.6414	168.8809	243.6
20/10/16 10:33:05.060	4.4	108.6	−18.6505	168.9899	219.5
21/10/16 01:27:58.910	4.3	779.5	−12.5188	169.2688	604.7
22/10/16 07:34:41.420	4.4	565.1	−23.2467	173.1644	10.0
22/10/16 18:23:48.430	4.3	96.1	−20.2187	169.9965	98.7
23/10/16 04:15:46.070	4.3	517.9	−15.1730	167.7110	109.7
23/10/16 17:24:13.750	4.5	641.4	−14.1494	167.2644	165.7
25/10/16 06:16:54.240	4.6	780.1	−12.9611	166.8699	122.8
25/10/16 17:01:00.300	5.1	749.6	−13.7314	165.8501	30.5
26/10/16 12:43:26.870	4.1	130.1	−18.5630	170.1473	253.4
26/10/16 14:08:28.960	4.3	492.0	−15.6434	167.2195	98.6
27/10/16 21:59:09.190	4.4	368.9	−16.6617	167.6863	44.7
27/10/16 22:54:00.480	4.6	741.7	−13.2396	167.1212	218.7
29/10/16 04:21:33.280	5.1	592.3	−14.7943	166.8858	31.4
30/10/16 14:08:20.790	4.5	298.3	−16.9478	168.6665	226.0
31/10/16 17:22:35.170	4.5	730.9	−12.9559	169.2604	626.7
01/11/16 21:35:34.910	5.0	707.1	−13.6619	166.8781	109.6
02/11/16 15:50:18.820	4.4	945.4	−11.4631	166.6460	119.8
04/11/16 06:45:03.520	5.0	70.2	−18.9198	169.2618	211.9

Chapter B

Global inventory of Strombolian activity

B.1 Example of the calculation of total gas flux from SO_2 and gas ratio measurements

I use the data of the 29th of October, 2007 at Yasur from Métrich et al. (2011). The SO_2 flux is 620 $t.d^{-1}$ (7.18 $kg.s^{-1}$) and the CO_2/SO_2, H_2O/SO_2 and HCl/SO_2 molar ratios of gas are 1.80, 120 and 0.53, respectively (Table B.1).

The molar mass of the gas species is 18 $g.mol^{-1}$, 36 $g.mol^{-1}$, 44 $g.mol^{-1}$ and 64 $g.mol^{-1}$ for the H_2O, HCl, CO_2 and SO_2, respectively. I calculate the gas mass flux using eq. (5.9) at 8.88 $kg.s^{-1}$, 242.19 $kg.s^{-1}$, 2.14 $kg.s^{-1}$ and 7.18 $kg.s^{-1}$ for the H_2O, HCl, CO_2 and SO_2, respectively.

The density of the gas species, at magma temperature $T_{\text{magma}} = 1373$ K and at atmospheric pressure $P_{\text{atm}} = 97\,063$ Pa, is calculated using the ideal gas law (Equation (5.11)) at 0.15 $kg.m^{-3}$, 0.31 $kg.m^{-3}$, 0.37 $kg.m^{-3}$ and 0.54 $kg.m^{-3}$ for the H_2O, HCl, CO_2 and SO_2, respectively. The gas volume flux per species is then estimated at 1583 $m^3.s^{-1}$, 7 $m^3.s^{-1}$, 24 $m^3.s^{-1}$ and 13 $m^3.s^{-1}$ for the H_2O, HCl, CO_2 and SO_2, respectively and the total volume flux is 1627 $m^3.s^{-1}$ (Table B.1).

Table B.1 – Estimate of the total gas volume flux from geochemistry measurements. Example of the 29th of October, 2007 at Yasur (Métrich et al., 2011). $T_{\text{magma}} = 1373$ K and $P_{\text{atm}} = 97\,063$ Pa. $R_{\text{ig,mol}} = 8.31$ $J.mol^{-1}.K^{-1}$.

Gas species (X)	Molar mass ($g.mol^{-1}$)	Density ($kg.m^{-3}$)	Molar ratio ($[X]/[SO_2]$)	Mass flux ($kg.s^{-1}$)	Mass flux ($t.d^{-1}$)	Volume flux ($m^3.s^{-1}$)
H_2O	18	0.15	120	242	20 909	1583
HCl	36	0.31	0.5	2	185	7
CO_2	44	0.37	1.8	9	767	24
SO_2	64	0.54	1	7	620	13
Total	-	-	-	260	22 481	1627

B.2 Histograms of the key parameters

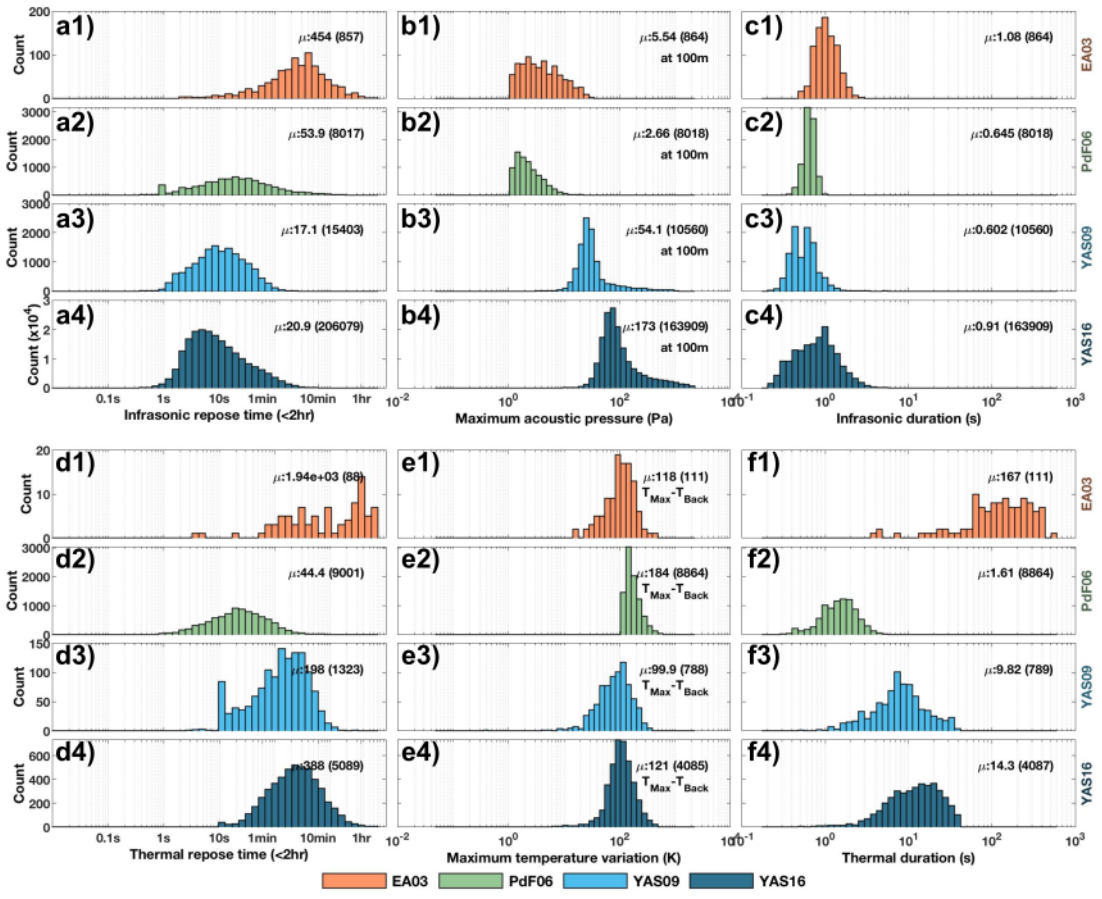

Figure B.1 – Distribution of the key parameters at the three volcanoes (histograms).

B.3 Histograms of the energy, velocity and volumes

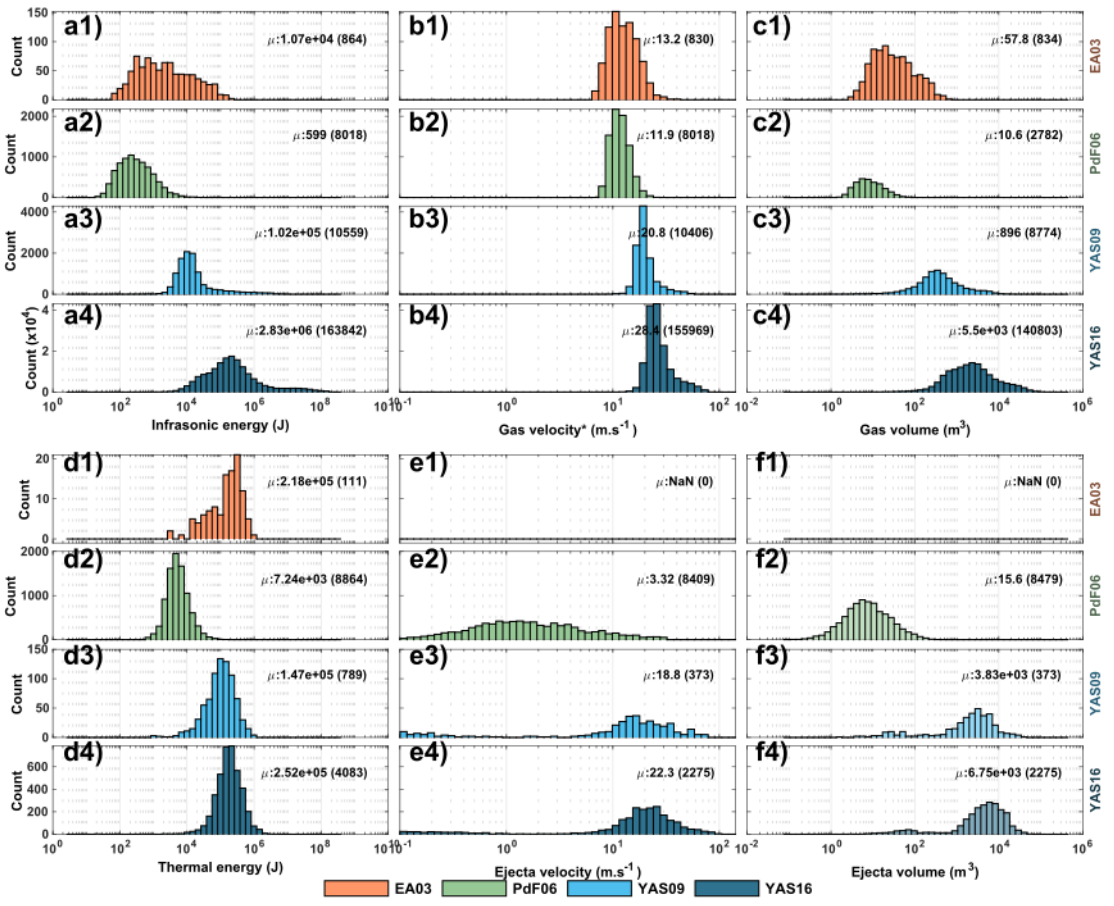

Figure B.2 – Distribution of energy, velocity and volume at the three volcanoes (histograms).

B.4 Depth estimates from the Monte Carlo analysis

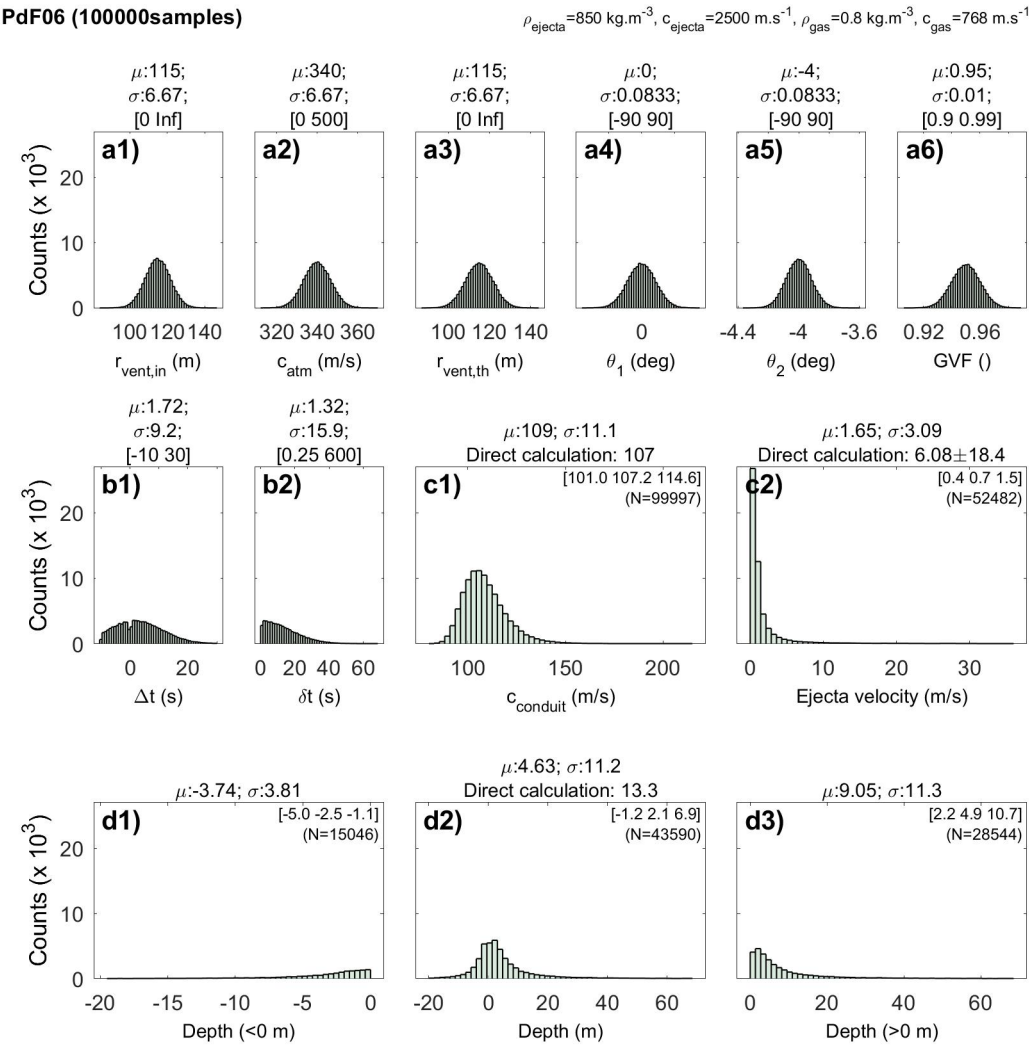

Figure B.3 – Monte Carlo analysis to estimate the depth of the magma column at Piton de la Fournaise in December, 2006. a) Parameters: 1) $r_{\text{vent}}^{\text{infrasonic}} = (115.00 \pm 6.67)\,\text{m}$; 2) $c_{\text{atm}} = (340.00 \pm 6.67)\,\text{m.s}^{-1}$; 3) $r_{\text{vent}}^{\text{thermal}} = (115.00 \pm 6.67)\,\text{m}$; 4) $\theta_1 = (0.0 \pm 0.8)°$; 5) $\theta_2 = (-4.0 \pm 0.8)°$; 6) $\alpha_{\text{gas}} = 0.95 \pm 0.01$. b) Measurements on the records: 1) thermo-infrasonic delay and 2) delay of the radiometers. c) Intermediate estimates: 1) sound speed in the conduit and 2) ejecta velocity. d) Results: 1) depth below 0 m, 2) all depth and 3) depth above 0 m.

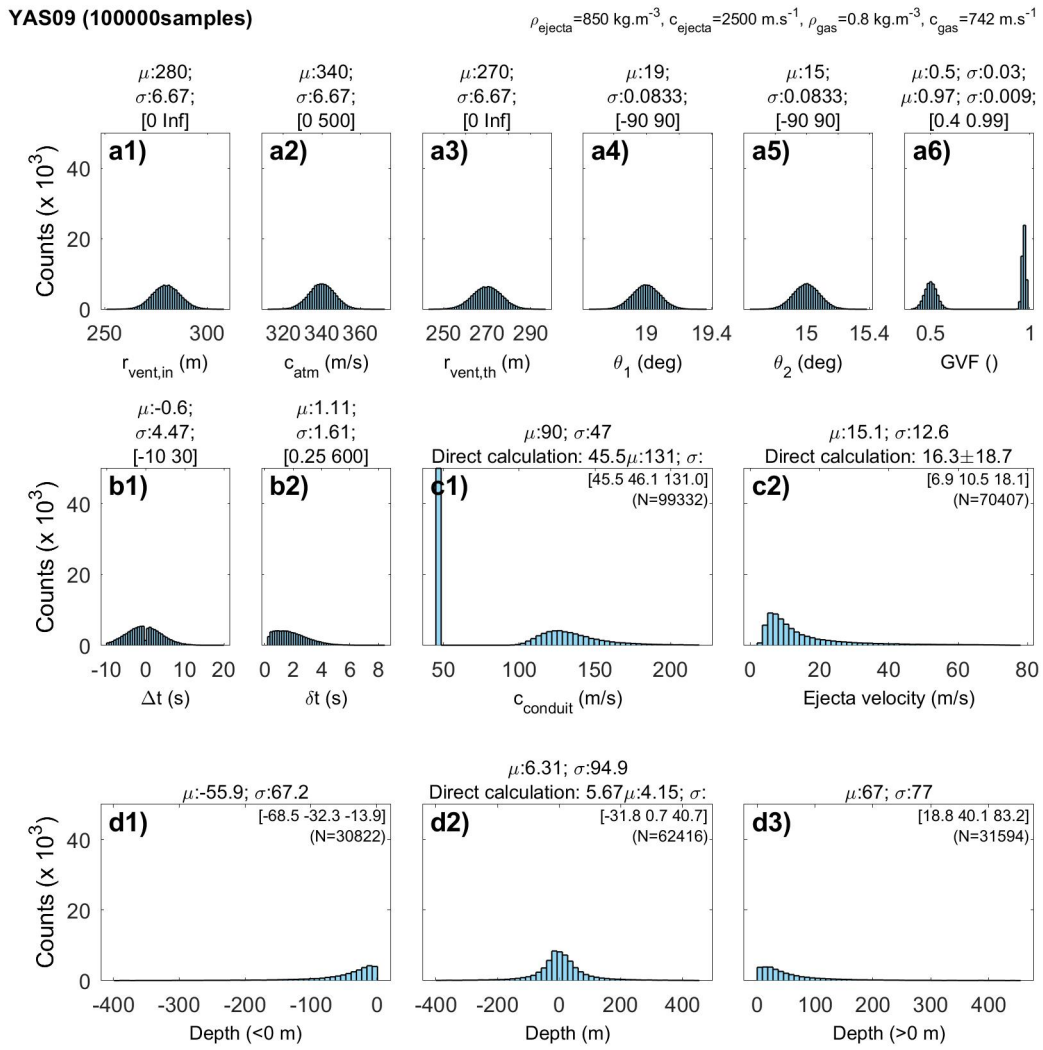

Figure B.4 – Monte Carlo analysis to estimatethe depth of the magma column at Yasur in June 2009. a) Parameters: 1) $r_{\text{vent}}^{\text{infrasonic}} = (280.00 \pm 6.67)\,\text{m}$; 2) $c_{\text{atm}} = (340.00 \pm 6.67)\,\text{m.s}^{-1}$; 3) $r_{\text{vent}}^{\text{thermal}} = (270.00 \pm 6.67)\,\text{m}$; 4) $\theta_1 = (19.0 \pm 0.8)^\circ$; 5) $\theta_2 = (15.0 \pm 0.8)^\circ$; 6) $\alpha_{\text{gas}} = 0.970 \pm 0.009$ and 0.50 ± 0.03. b) Measurements on the records: 1) thermo-infrasonic delay and 2) delay of the radiometers. c) Intermediate estimates: 1) sound speed in the conduit and 2) ejecta velocity. d) Results: 1) depth below 0 m, 2) all depth and 3) depth above 0 m.

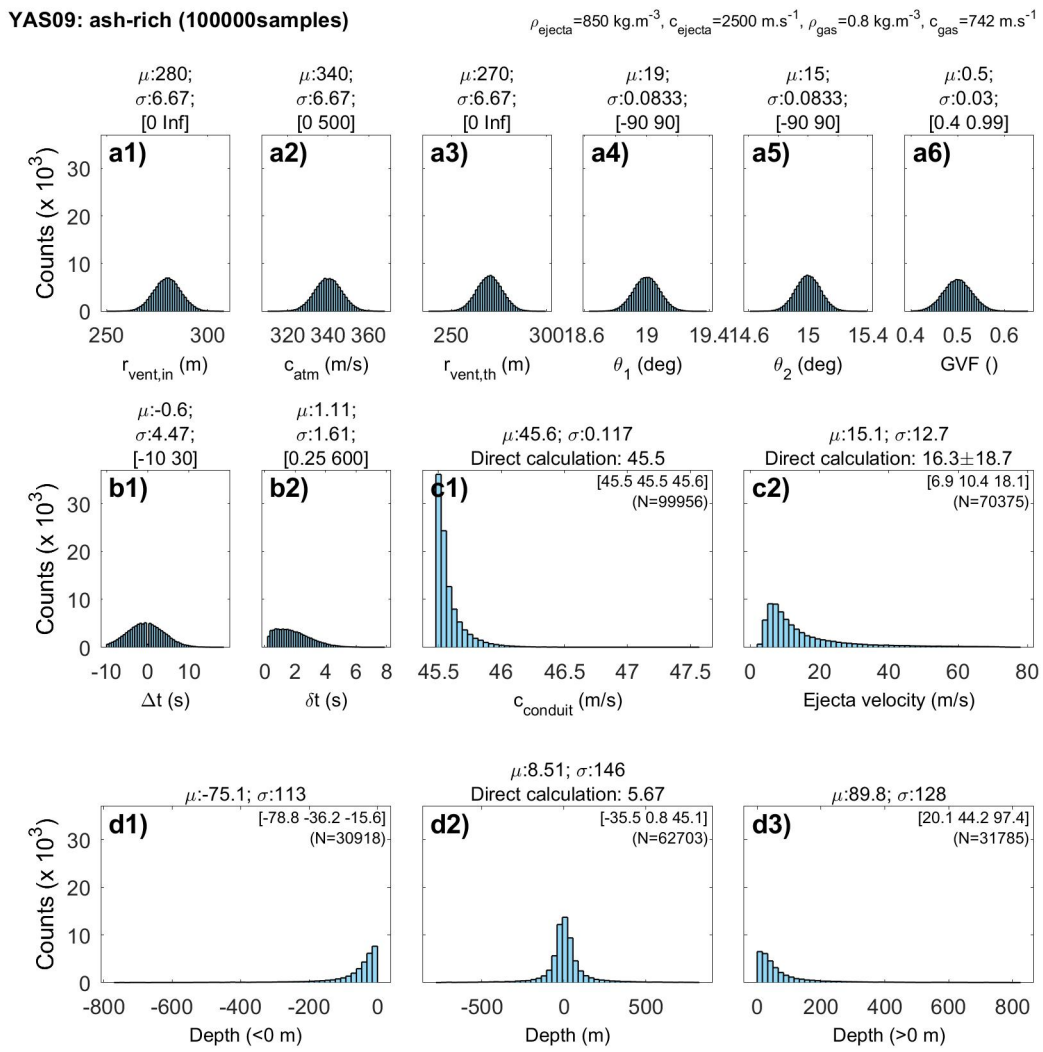

Figure B.5 – Monte Carlo analysis to estimate of the depth of the magma column for ash-rich explosions at Yasur in June 2009. a) Parameters: 1) $r_{\text{vent}}^{\text{infrasonic}} = (280.00 \pm 6.67)\,\text{m}$; 2) $c_{\text{atm}} = (340.00 \pm 6.67)\,\text{m.s}^{-1}$; 3) $r_{\text{vent}}^{\text{thermal}} = (270.00 \pm 6.67)\,\text{m}$; 4) $\theta_1 = (19.0 \pm 0.8)°$; 5) $\theta_2 = (15.0 \pm 0.8)°$; 6) $\alpha_{\text{gas}} = 0.50 \pm 0.03$. b) Measurements on the records: 1) thermo-infrasonic delay and 2) delay of the radiometers. c) Intermediate estimates: 1) sound speed in the conduit and 2) ejecta velocity. d) Results: 1) depth below 0 m, 2) all depth and 3) depth above 0 m.

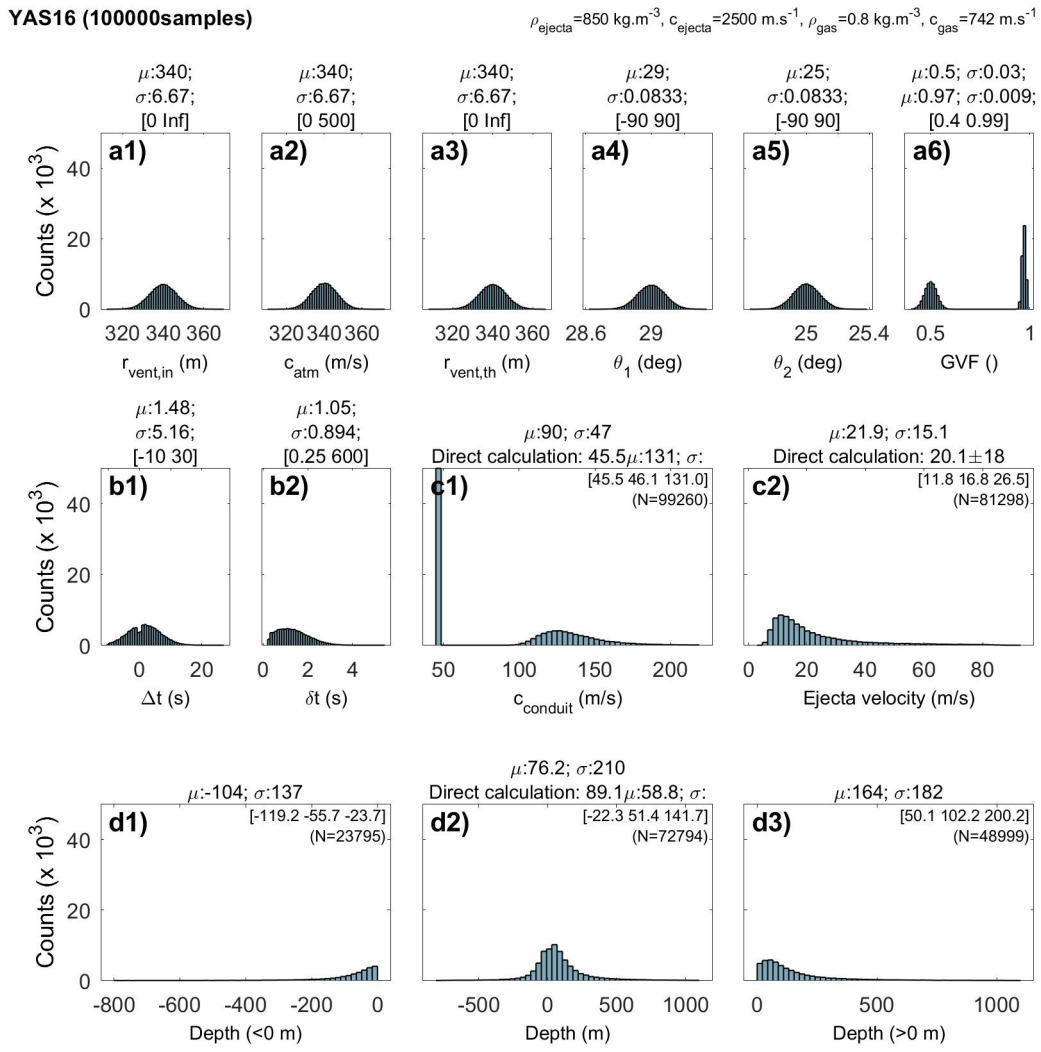

Figure B.6 – Monte Carlo analysis to estimate the depth of the magma column at Yasur in Sept-Nov 2016. a) Parameters: 1) $r_{\text{vent}}^{\text{infrasonic}} = (340.00 \pm 6.67)\,\text{m}$; 2) $c_{\text{atm}} = (340.00 \pm 6.67)\,\text{m.s}^{-1}$; 3) $r_{\text{vent}}^{\text{thermal}} = (340.00 \pm 6.67)\,\text{m}$; 4) $\theta_1 = (29.0 \pm 0.8)°$; 5) $\theta_2 = (25.0 \pm 0.8)°$; 6) $\alpha_{\text{gas}} = 0.970 \pm 0.009$ and 0.50 ± 0.03. b) Measurements on the records: 1) thermo-infrasonic delay and 2) delay of the radiometers. c) Intermediate estimates: 1) sound speed in the conduit and 2) ejecta velocity. d) Results: 1) depth below 0 m, 2) all depth and 3) depth above 0 m.

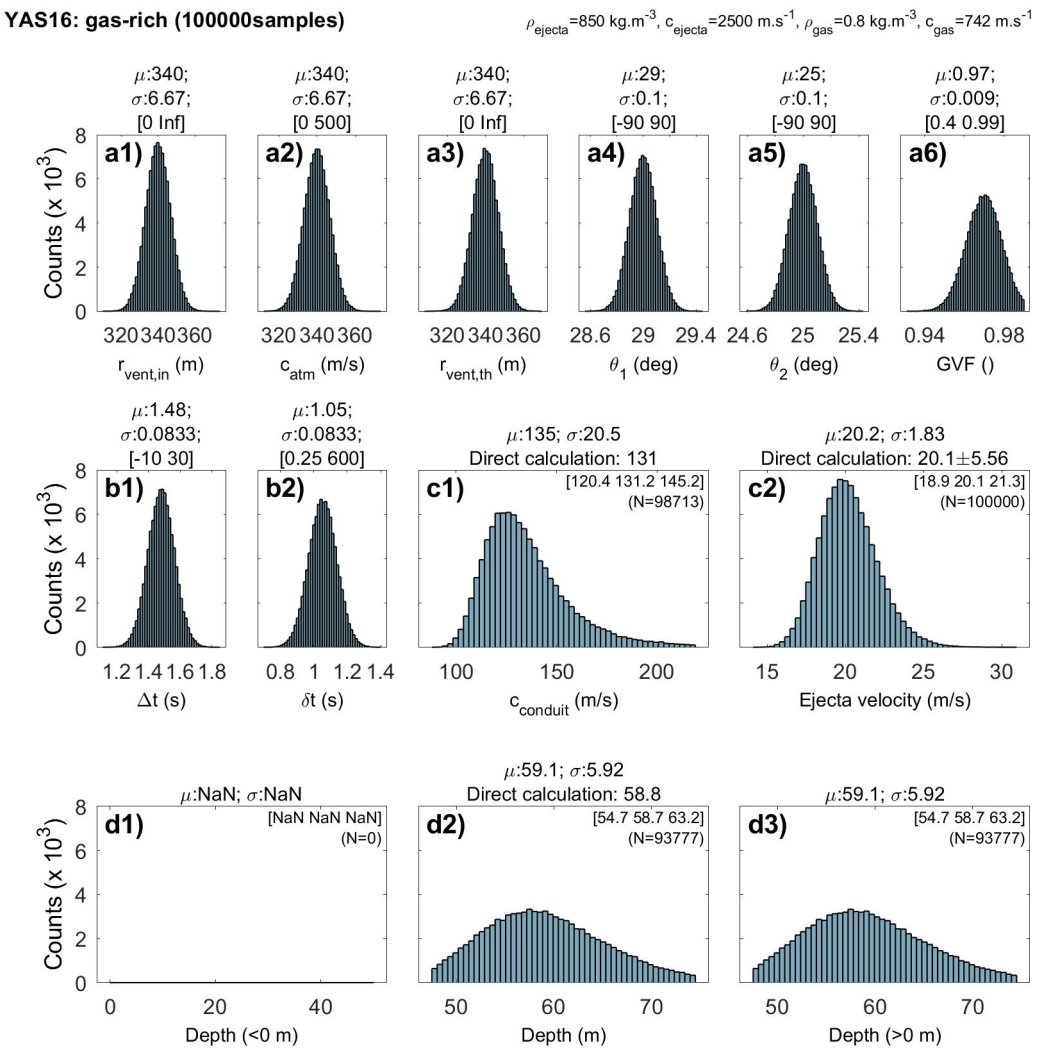

Figure B.7 – Monte Carlo analysis to estimate the depth of the magma column for gas-rich explosions at Yasur in Sept-Nov 2016. a) Parameters: 1) $r_{\text{vent}}^{\text{infrasonic}} = (340.00 \pm 6.67)$ m; 2) $c_{\text{atm}} = (340.00 \pm 6.67)\,\text{m.s}^{-1}$; 3) $r_{\text{vent}}^{\text{thermal}} = (340.00 \pm 6.67)$ m; 4) $\theta_1 = (29.0 \pm 0.8)°$; 5) $\theta_2 = (25.0 \pm 0.8)°$; 6) $\alpha_{\text{gas}} = 0.970 \pm 0.009$. b) Measurements on the records: 1) thermo-infrasonic delay and 2) delay of the radiometers. c) Intermediate estimates: 1) sound speed in the conduit and 2) ejecta velocity. d) Results: 1) depth below 0 m, 2) all depth and 3) depth above 0 m.

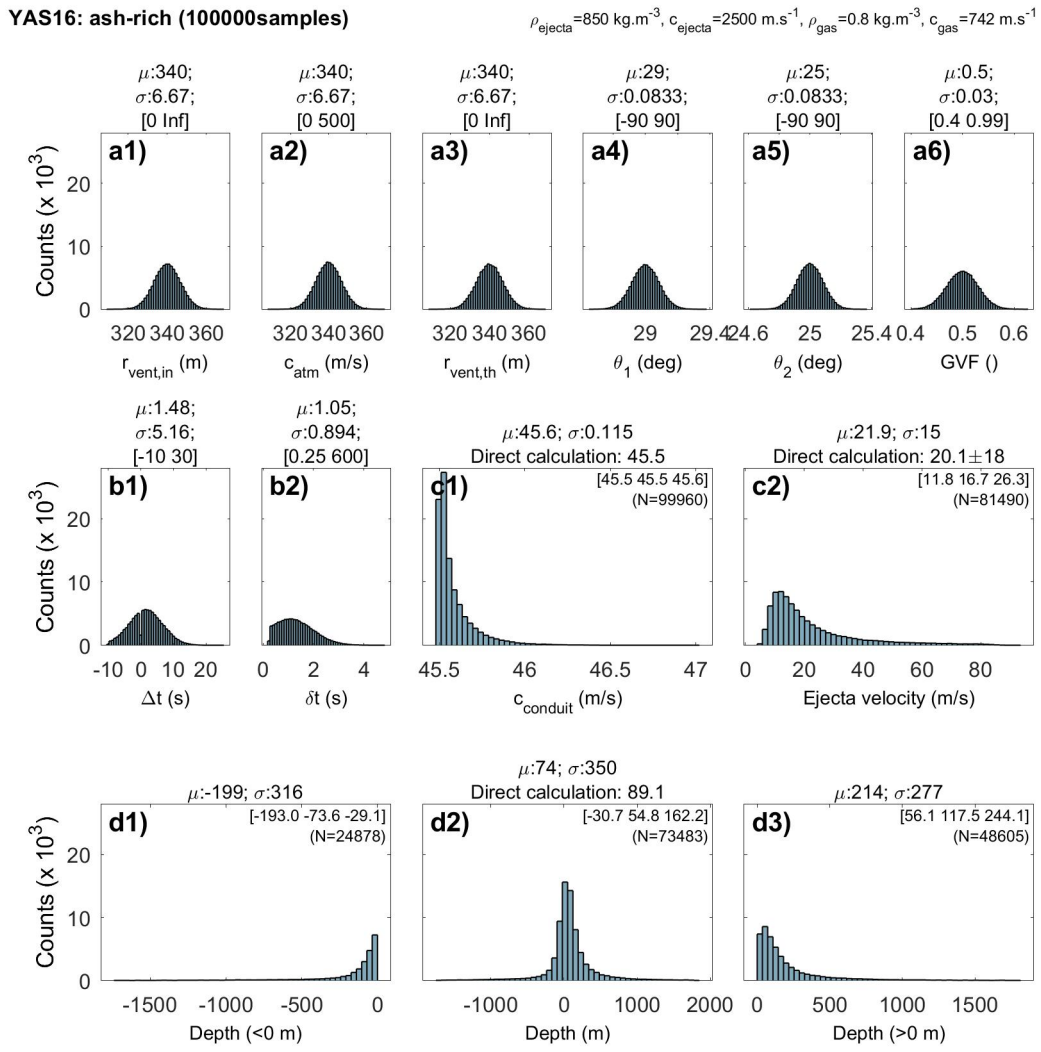

Figure B.8 – Monte Carlo analysis to estimate the depth of the magma column for ash-rich explosions at Yasur in Sept-Nov 2016. a) Parameters: 1) $r_{\text{vent}}^{\text{infrasonic}} = (340.00 \pm 6.67)\,\text{m}$; 2) $c_{\text{atm}} = (340.00 \pm 6.67)\,\text{m.s}^{-1}$; 3) $r_{\text{vent}}^{\text{thermal}} = (340.00 \pm 6.67)\,\text{m}$; 4) $\theta_1 = (29.0 \pm 0.8)°$; 5) $\theta_2 = (25.0 \pm 0.8)°$; 6) $\alpha_{\text{gas}} = 0.50 \pm 0.03$. b) Measurements on the records: 1) thermo-infrasonic delay and 2) delay of the radiometers. c) Intermediate estimates: 1) sound speed in the conduit and 2) ejecta velocity. d) Results: 1) depth below 0 m, 2) all depth and 3) depth above 0 m.

Chapter C

Temporal activity at Yasur

C.1 Histograms of the Strombolian explosions per phase

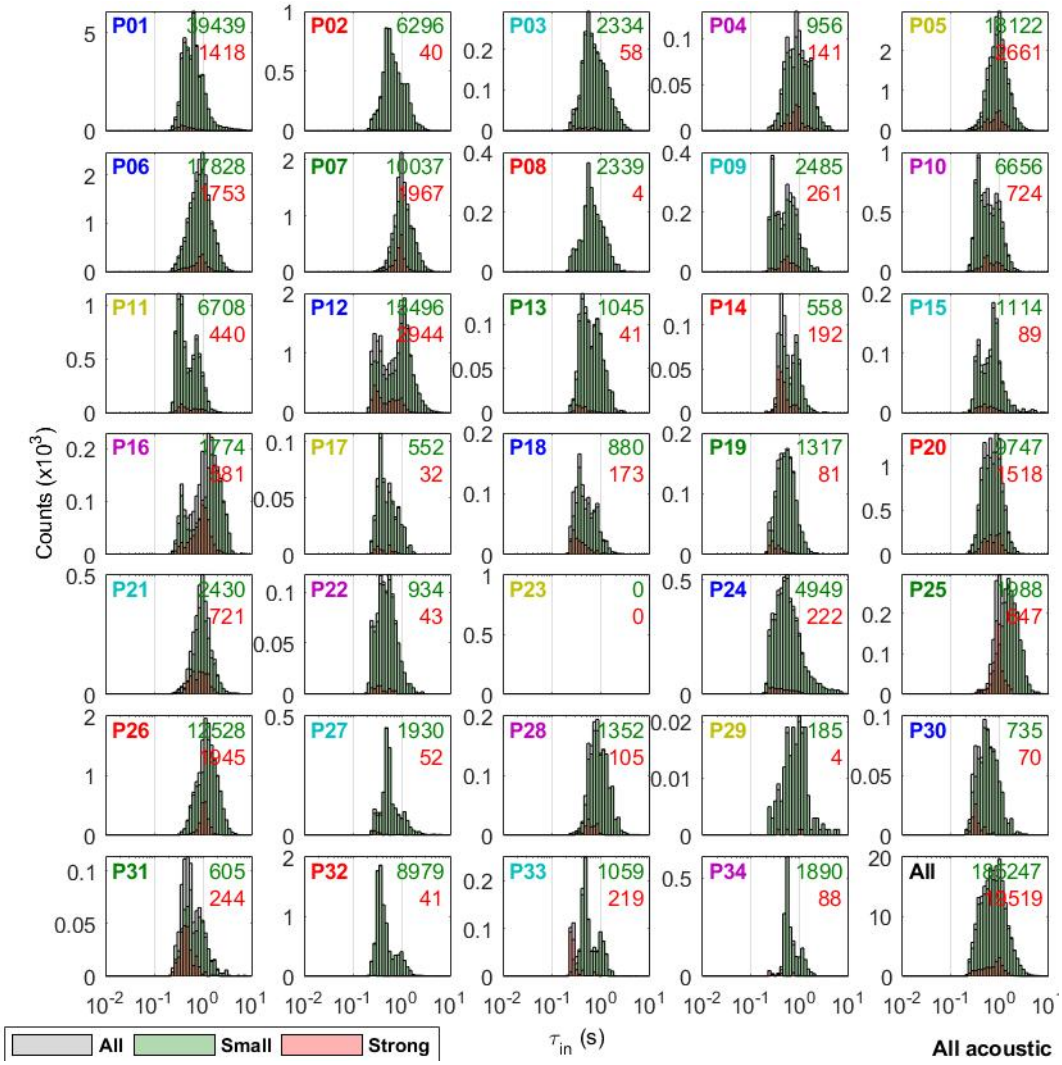

Figure C.1 – Distribution of the infrasonic duration per phase for all infrasonic events. The phase number is indicated north-west of each subplot. The number of small (<340 Pa) and strong (>340 Pa) explosions is indicated, north-east of each subplot, in green and red, respectively.

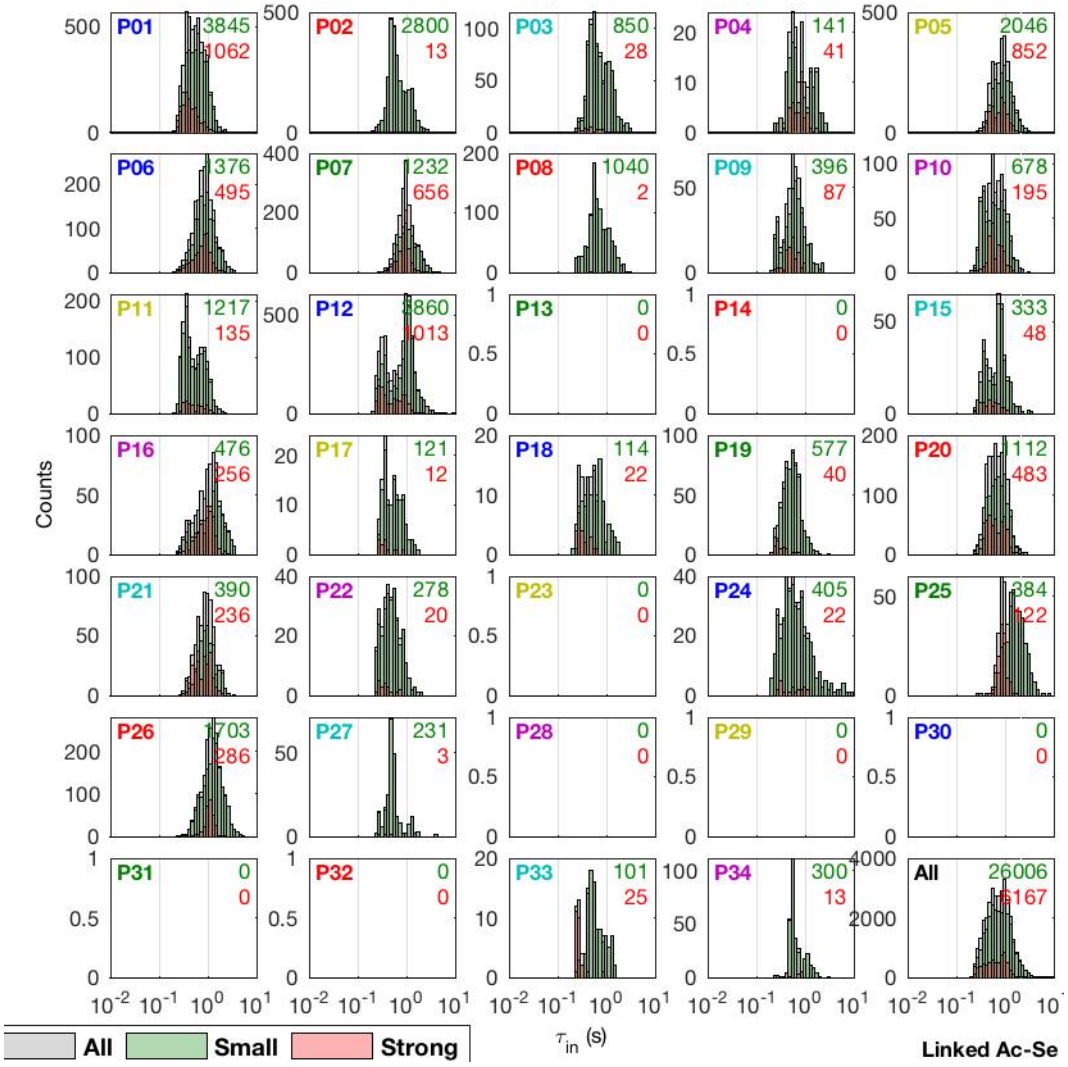

Figure C.2 – Distribution of the infrasonic duration per phase for all seismo-infrasonic events. The phase number is indicated north-west of each subplot. The number of small (<340 Pa) and strong (>340 Pa) explosions is indicated, north-east of each subplot, in green and red, respectively.

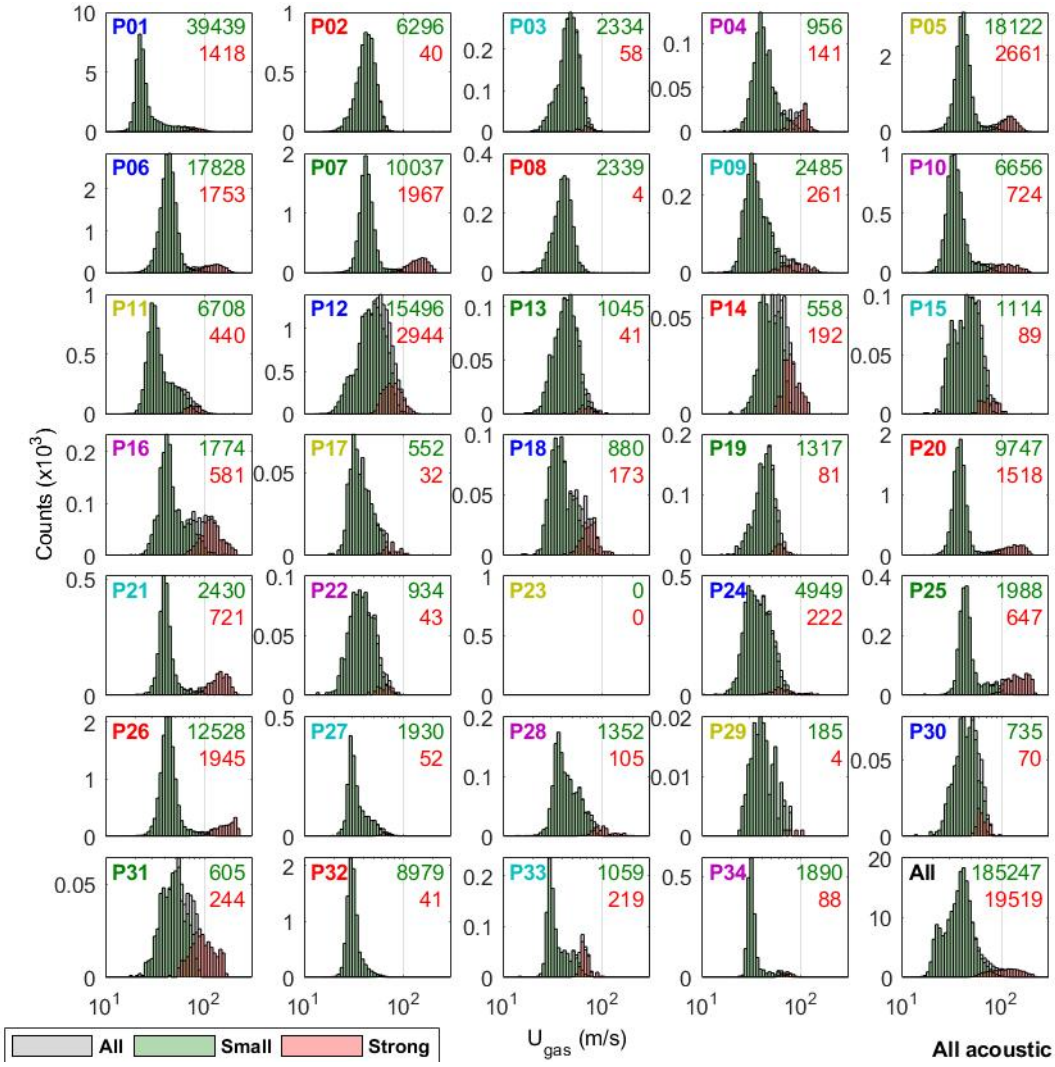

Figure C.3 – Distribution of the gas velocity per phase for all infrasonic events. The phase number is indicated north-west of each subplot. The number of small (<340 Pa) and strong (>340 Pa) explosions is indicated, north-east of each subplot, in green and red, respectively.

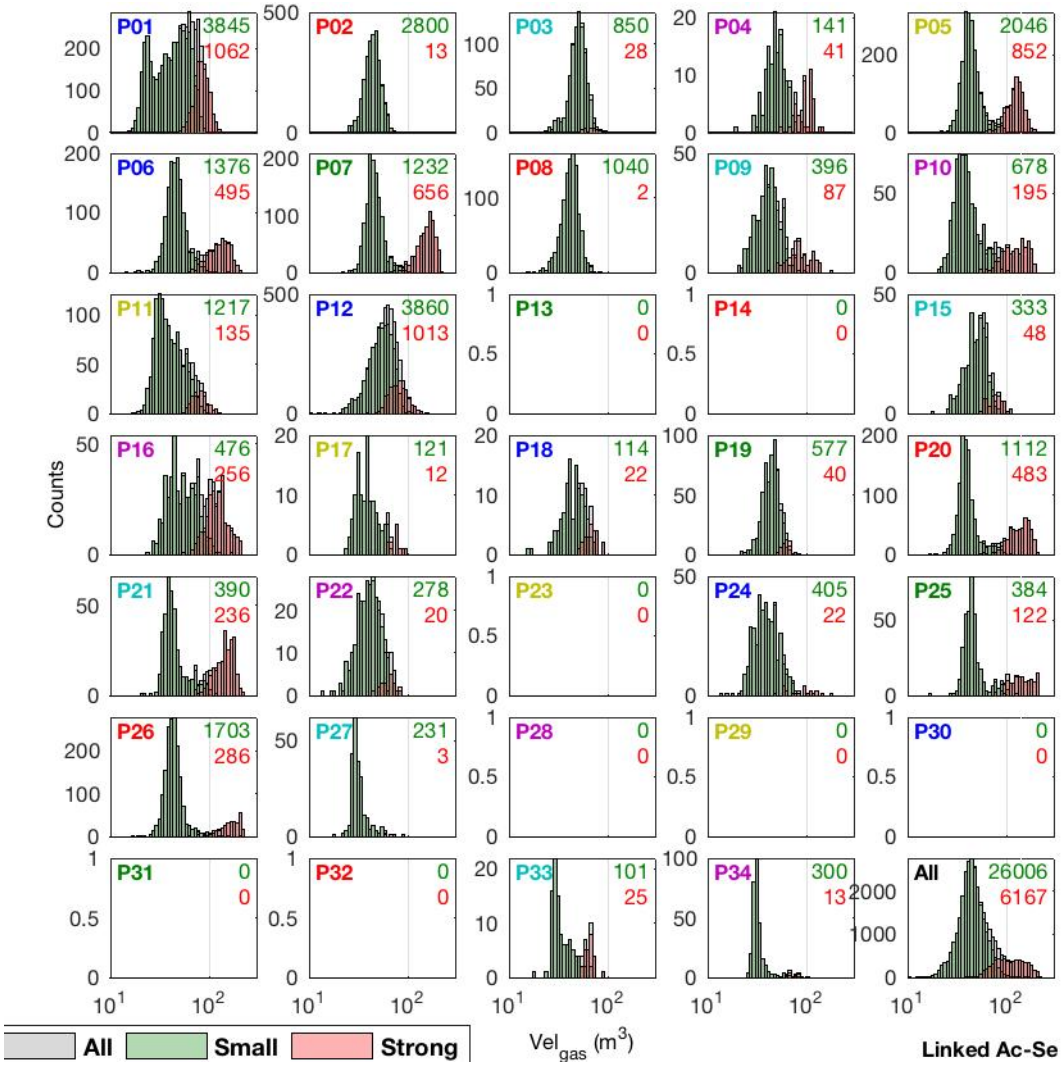

Figure C.4 – Distribution of the gas velocity per phase for all seismo-infrasonic events. The phase number is indicated north-west of each subplot. The number of small (<340 Pa) and strong (>340 Pa) explosions is indicated, north-east of each subplot, in green and red, respectively.

C.2 Histograms of the strong Strombolian explosions per phase

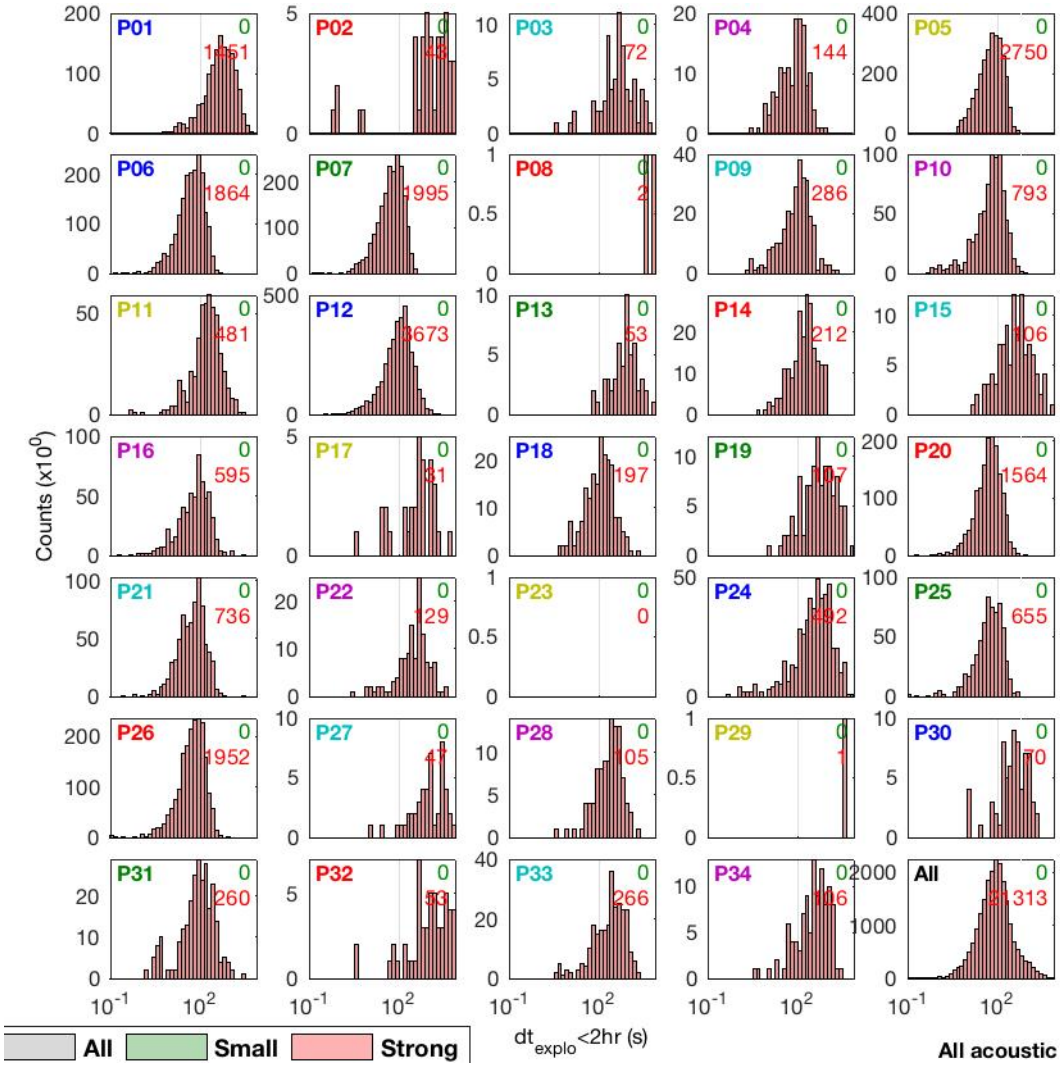

Figure C.5 – Distribution of the return time between two successive events per phase for all strong infrasonic events (>340 Pa at 100 m). The phase number is indicated north-west of each subplot. The number of strong explosions is indicated, north-east of each subplot, in red.

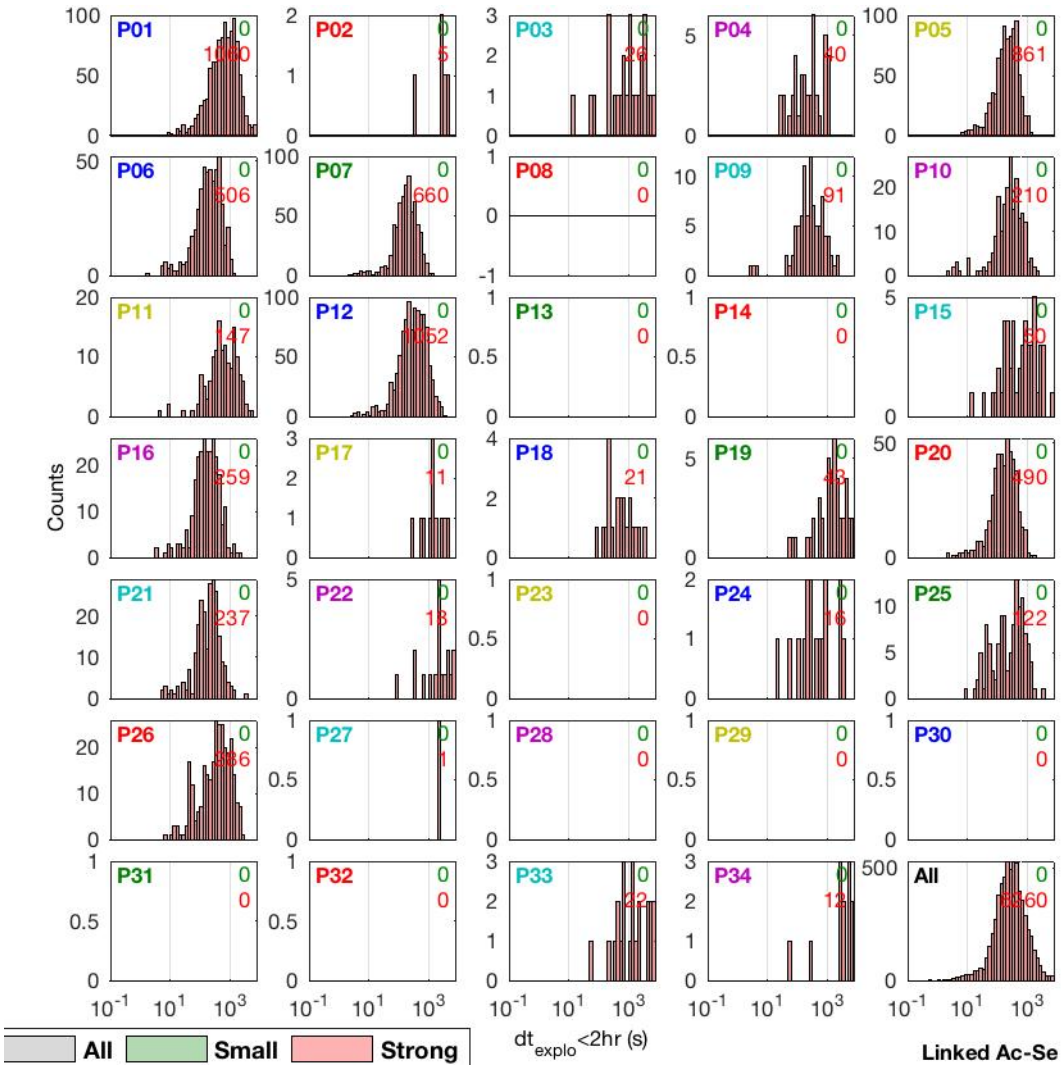

Figure C.6 – Distribution of the return time between two successive events per phase for all strong seismo-infrasonic events (>340 Pa at 100 m). The phase number is indicated north-west of each subplot. The number of strong explosions is indicated, north-east of each subplot, in red.

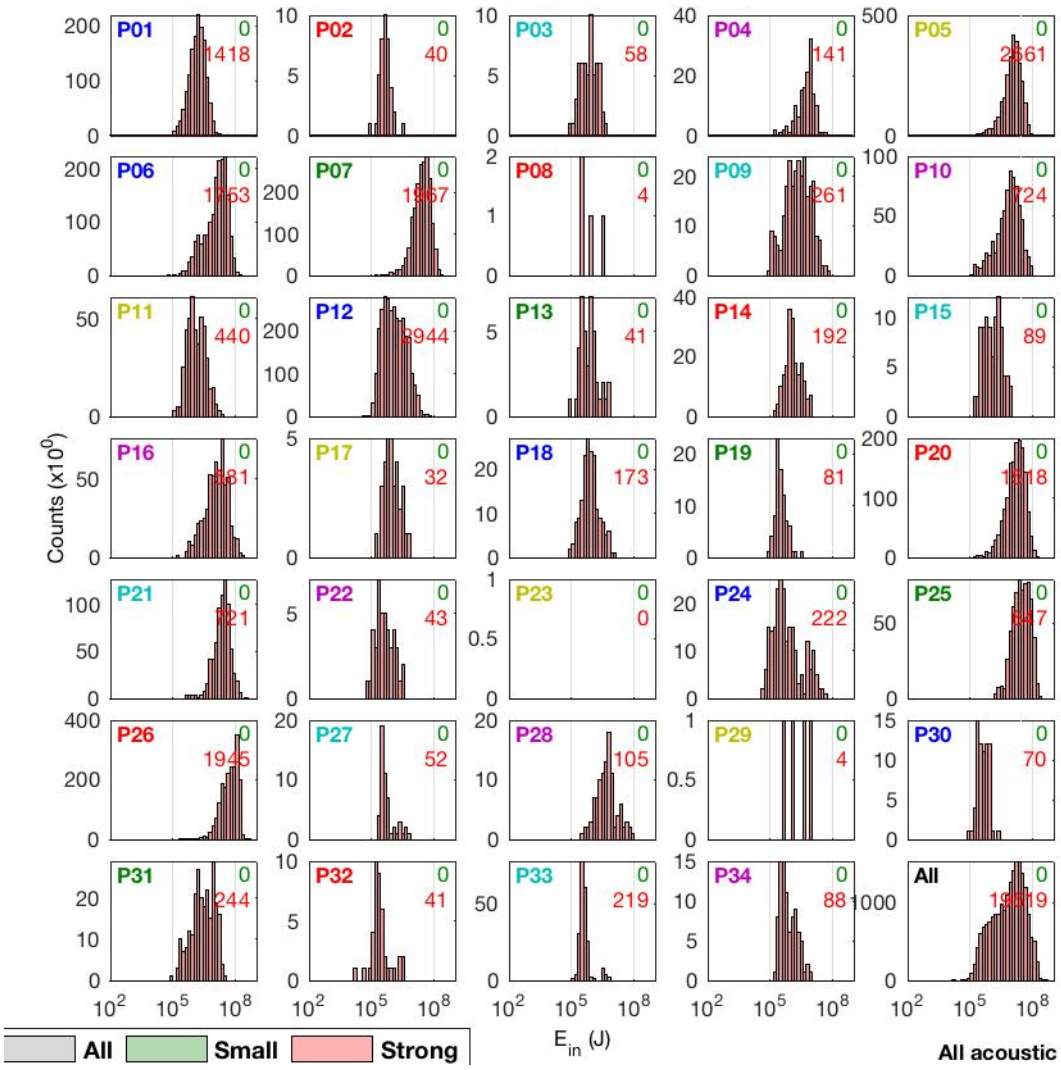

Figure C.7 – Distribution of the infrasonic energy per phase for all strong infrasonic events (>340 Pa at 100 m). The phase number is indicated north-west of each subplot. The number of strong explosions is indicated, north-east of each subplot, in red.

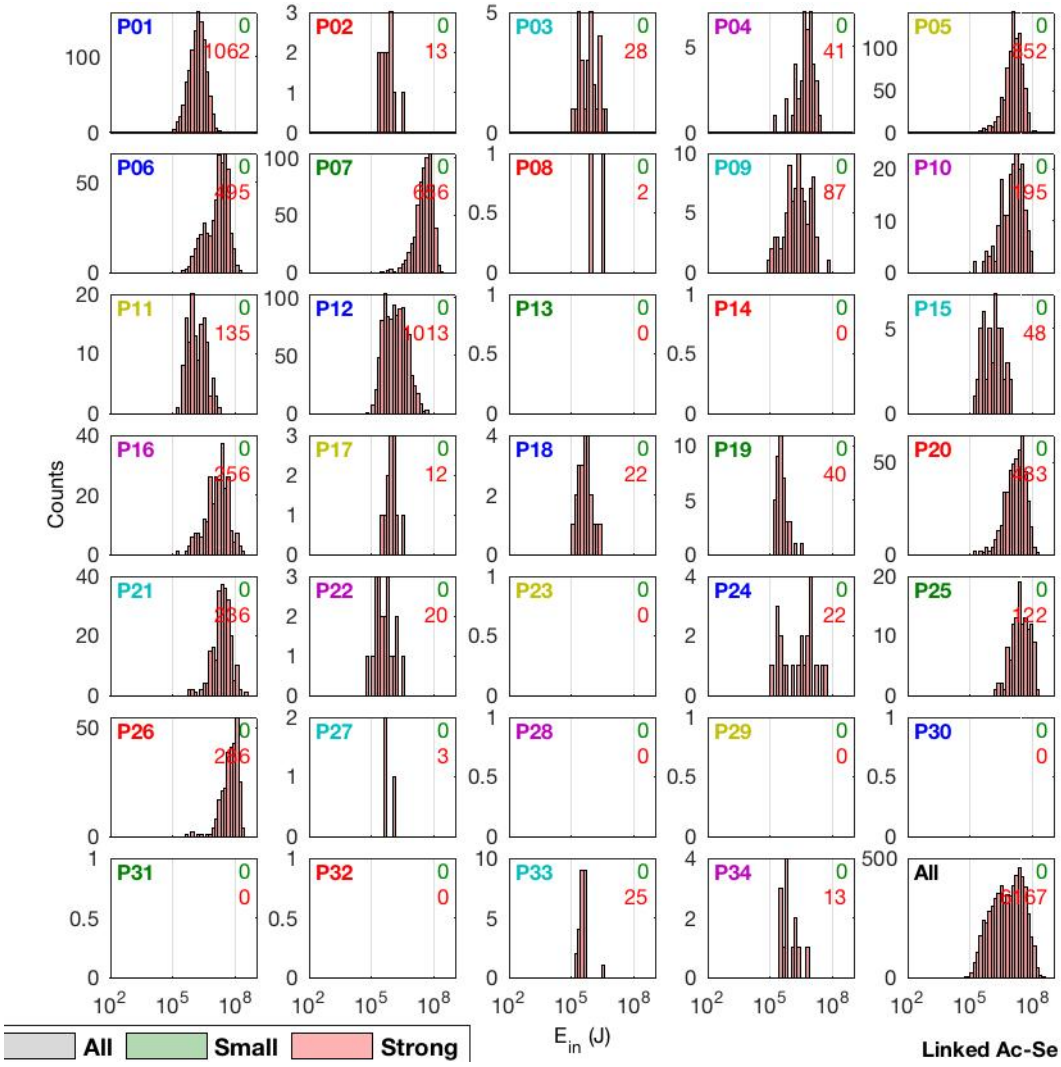

Figure C.8 – Distribution of the infrasonic energy per phase for all strong seismo-infrasonic events (>340 Pa at 100 m). The phase number is indicated north-west of each subplot. The number of strong explosions is indicated, north-east of each subplot, in red.

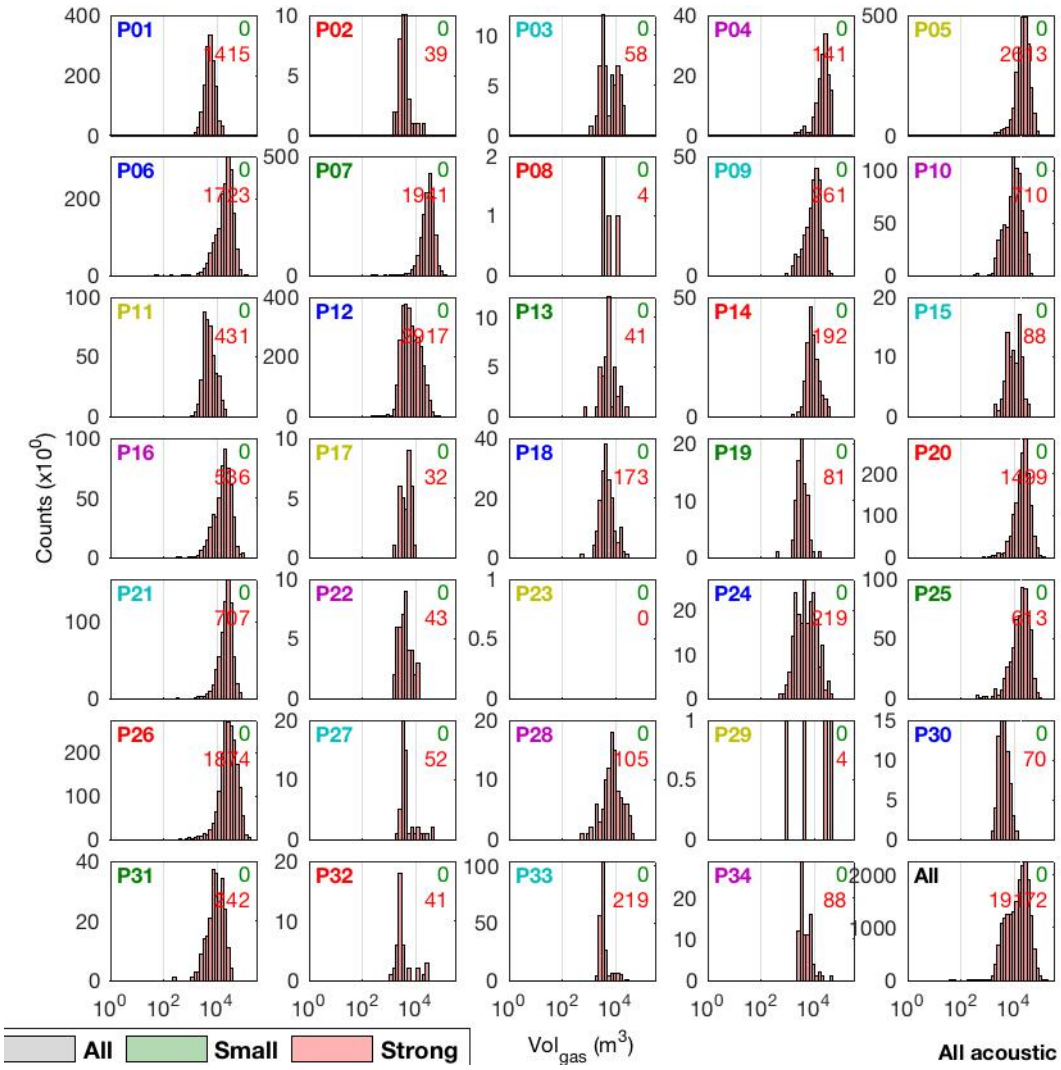

Figure C.9 – Distribution of the gas volume per phase for all strong infrasonic events (>340 Pa at 100 m). The phase number is indicated north-west of each subplot. The number of strong explosions is indicated, north-east of each subplot, in red.

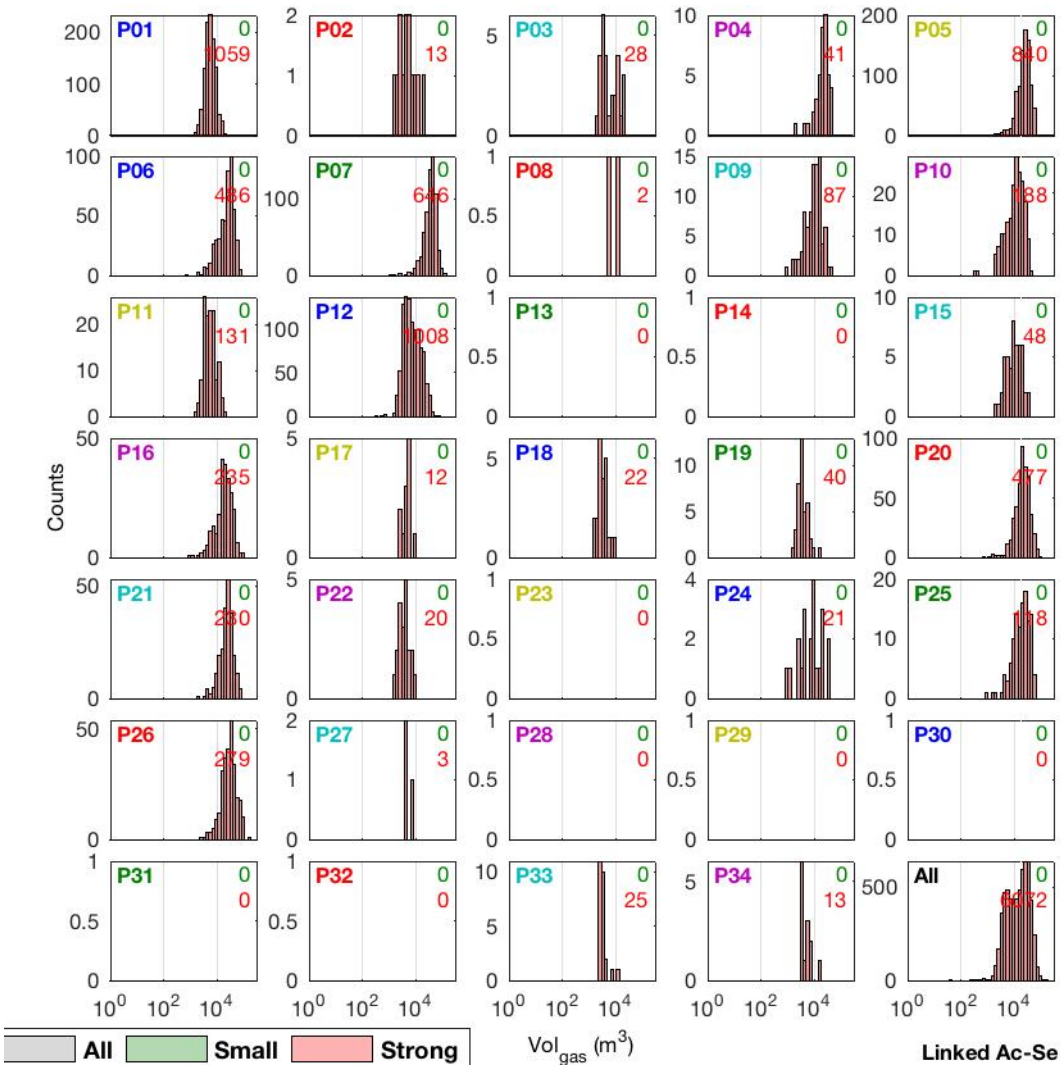

Figure C.10 – Distribution of the gas volume per phase for all strong seismo-infrasonic events (>340 Pa at 100 m). The phase number is indicated north-west of each subplot. The number of strong explosions is indicated, north-east of each subplot, in red.

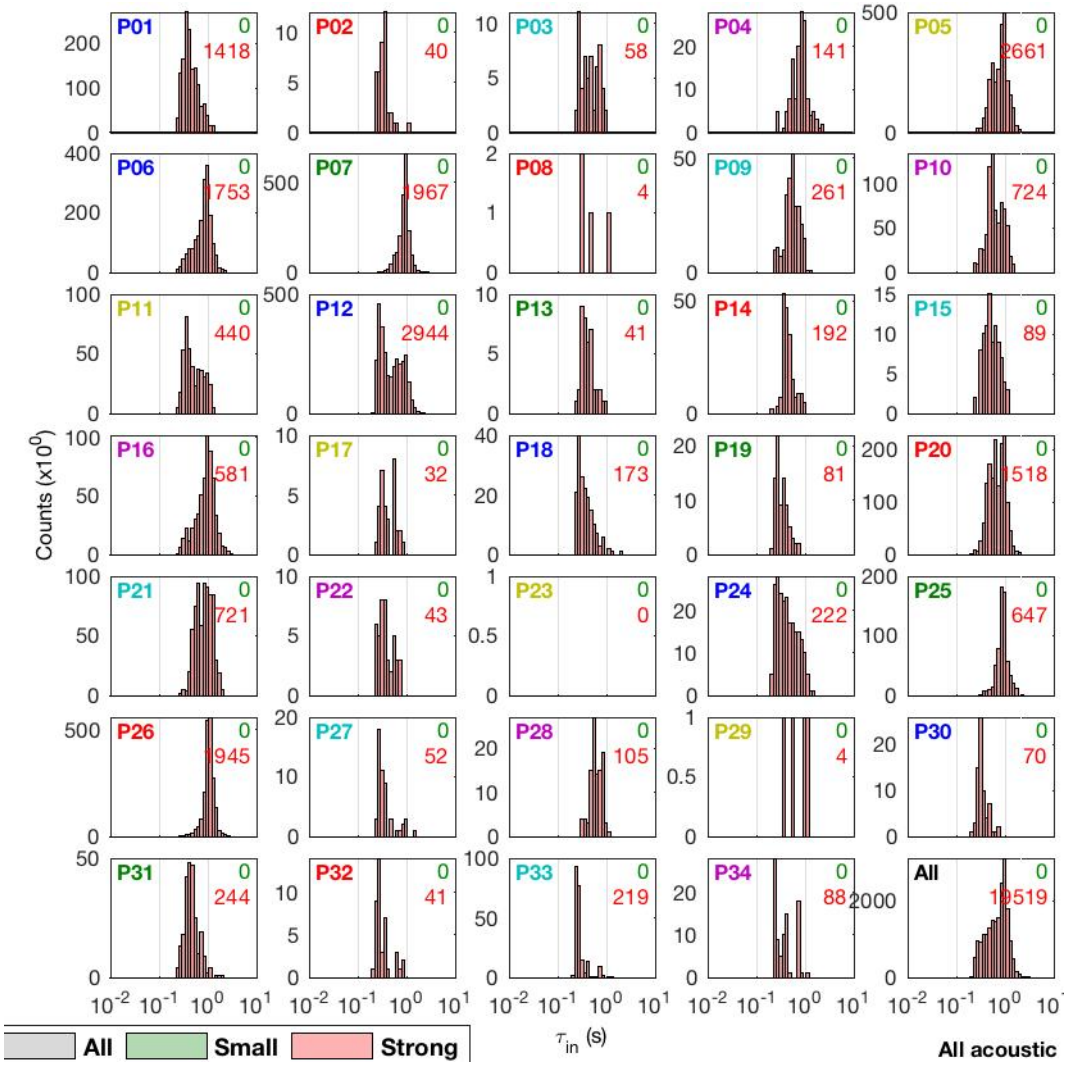

Figure C.11 – Distribution of the infrasonic duration per phase for all strong infrasonic events (>340 Pa at 100 m). The phase number is indicated north-west of each subplot. The number of strong explosions is indicated, north-east of each subplot, in red.

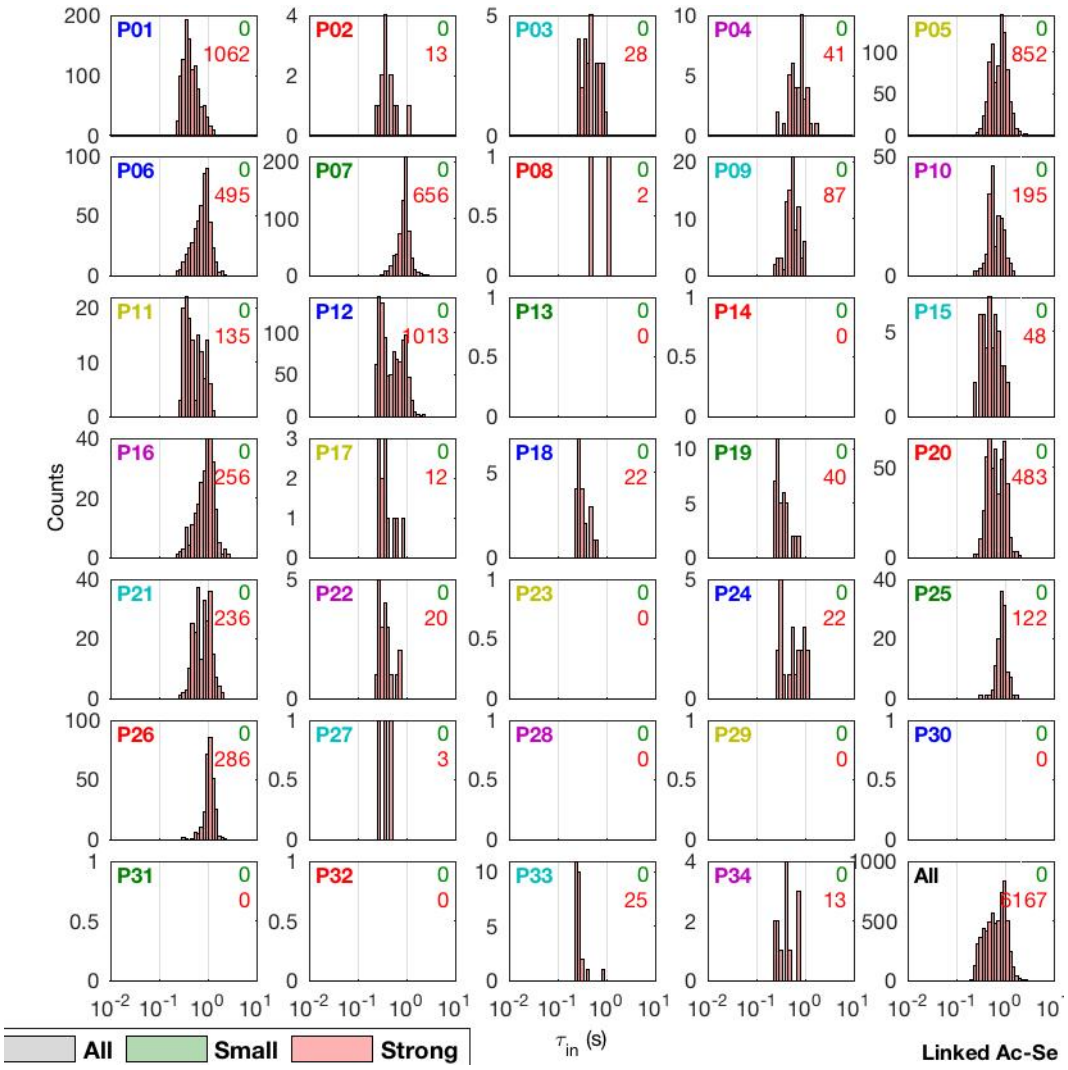

Figure C.12 – Distribution of the infrasonic duration per phase for all strong seismo-infrasonic events (>340 Pa at 100 m). The phase number is indicated north-west of each subplot. The number of strong explosions is indicated, north-east of each subplot, in red.

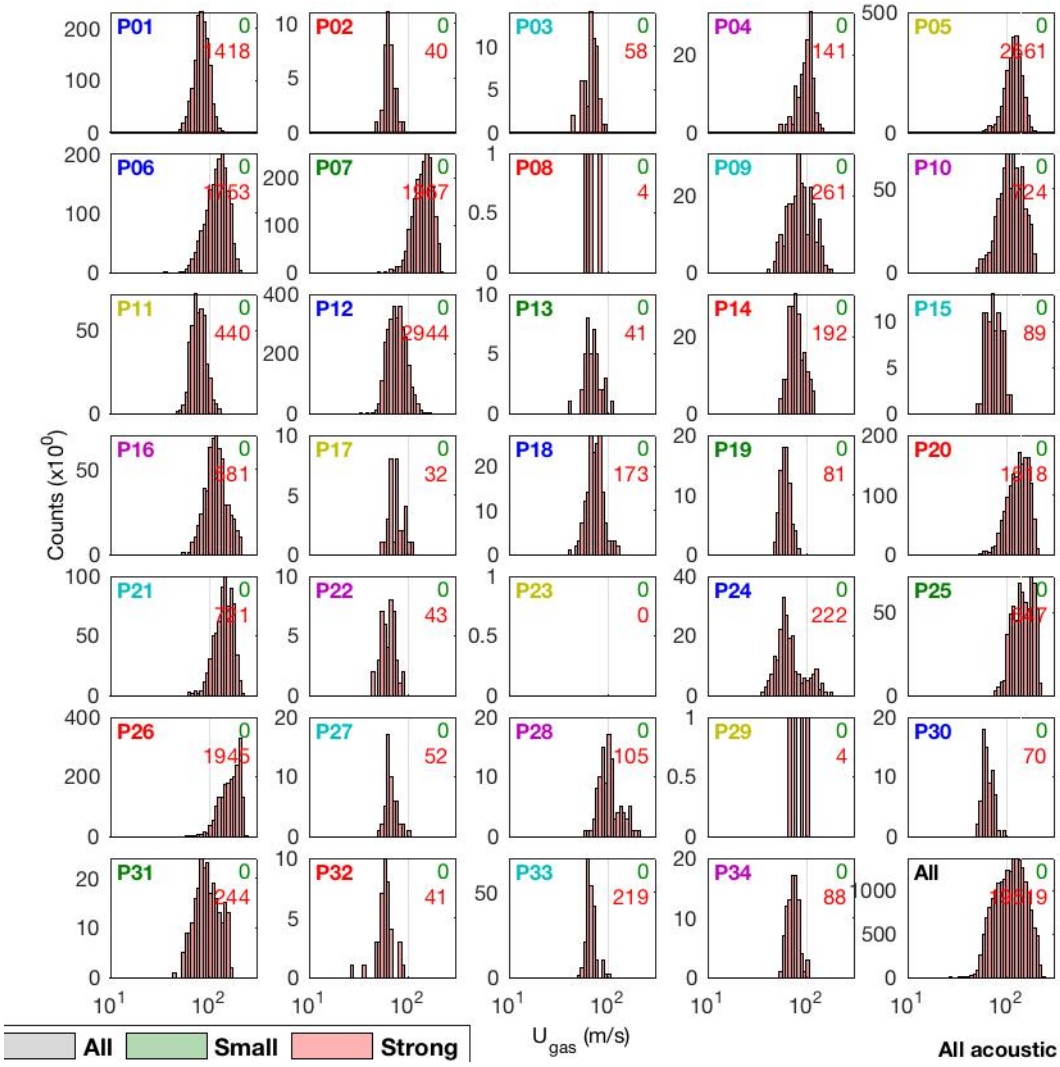

Figure C.13 – Distribution of the gas velocity per phase for all strong infrasonic events (>340 Pa at 100 m). The phase number is indicated north-west of each subplot. The number of strong explosions is indicated, north-east of each subplot, in red.

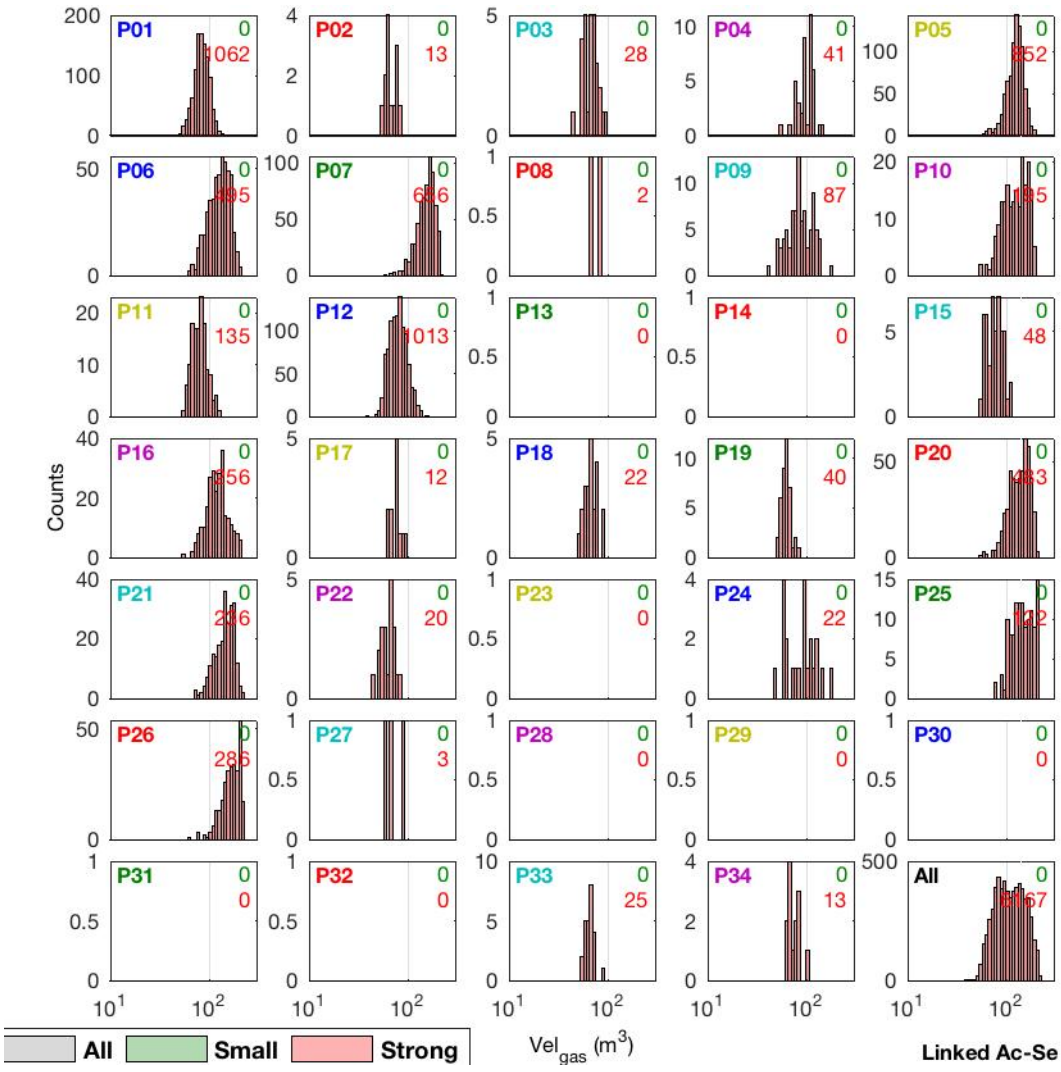

Figure C.14 – Distribution of the gas velocity per phase for all strong seismo-infrasonic events (>340 Pa at 100 m). The phase number is indicated north-west of each subplot. The number of strong explosions is indicated, north-east of each subplot, in red.

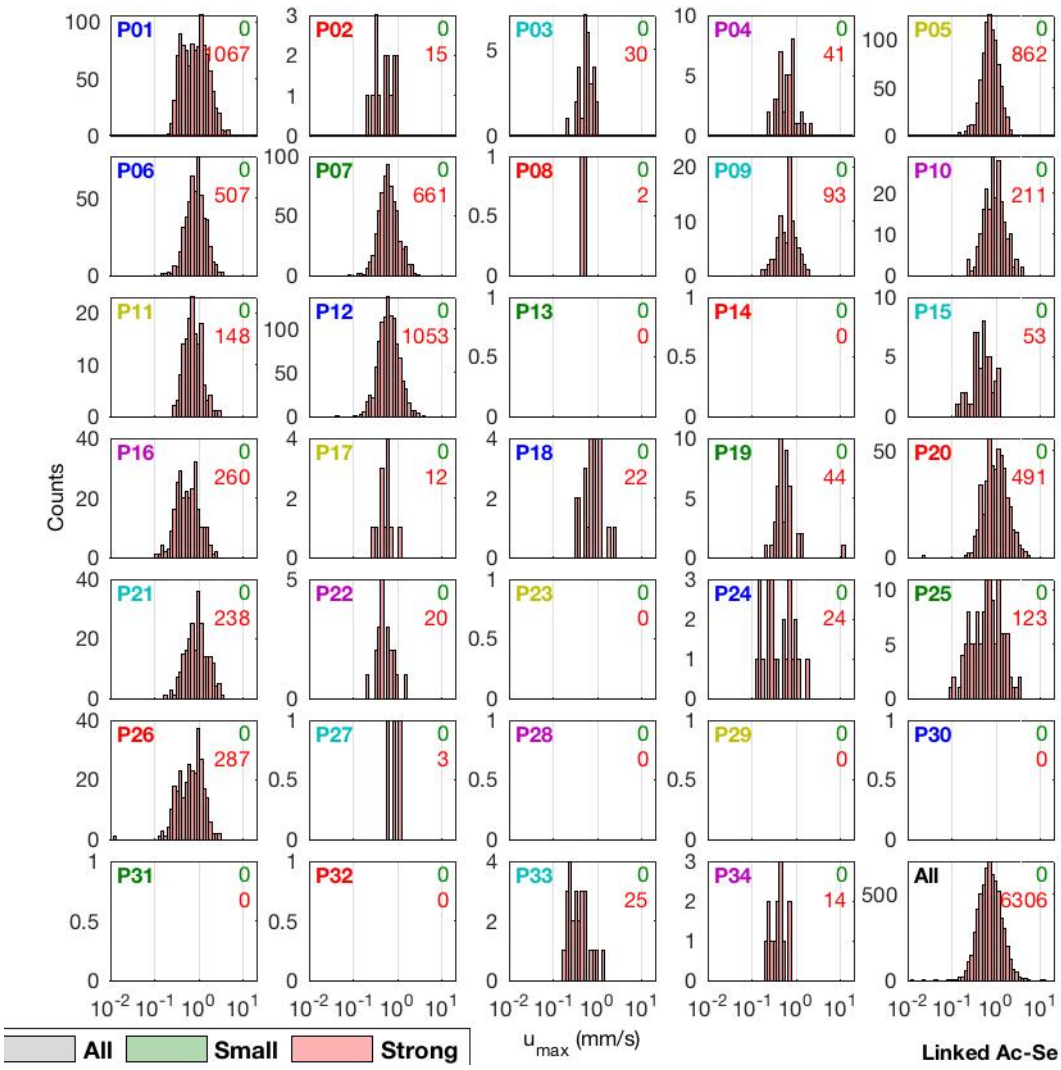

Figure C.15 – Distribution of the ground velocity per phase for all strong seismo-infrasonic events (>340 Pa at 100 m). The phase number is indicated north-west of each subplot. The number of strong explosions is indicated, north-east of each subplot, in red.

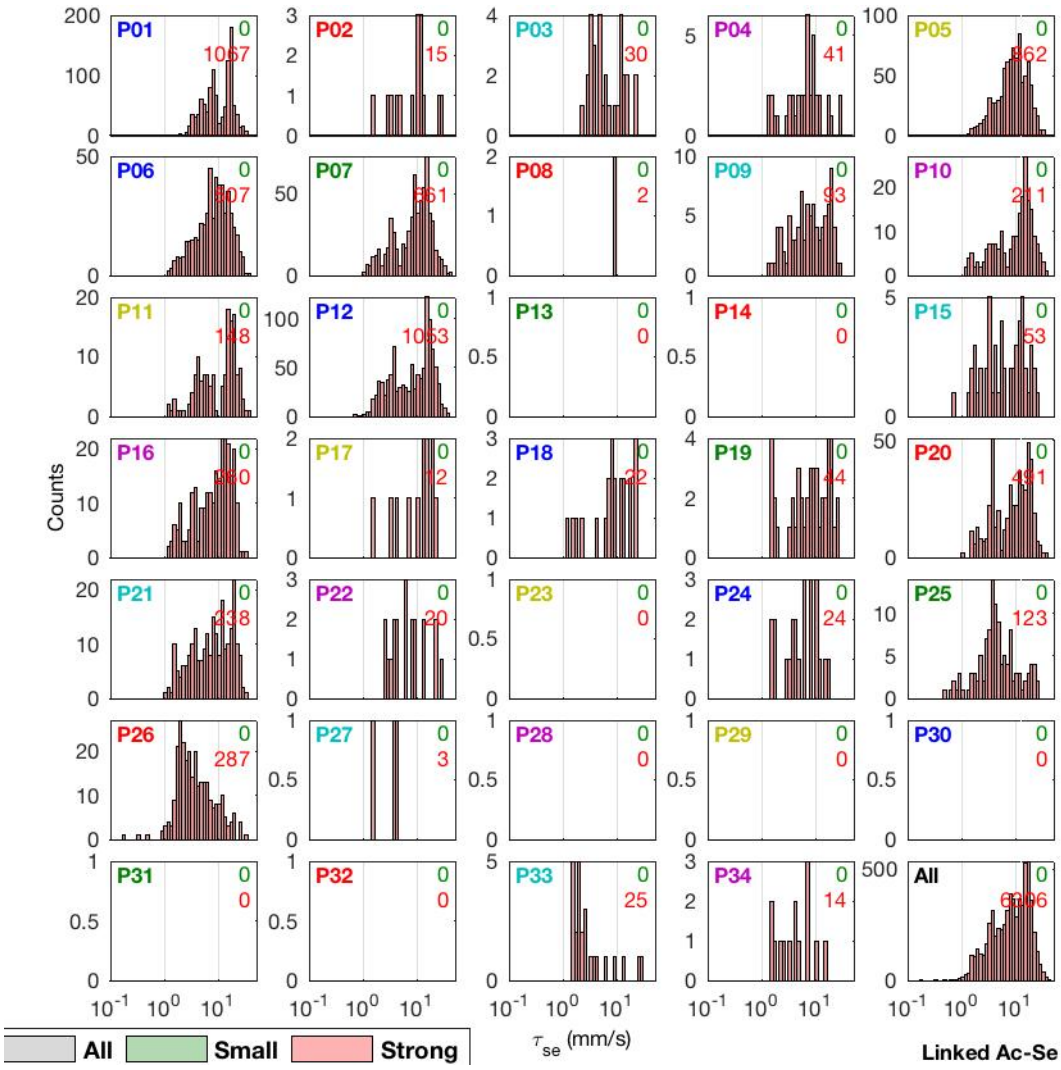

Figure C.16 – Distribution of the seismic duration per phase for all strong seismo-infrasonic events (>340 Pa at 100 m). The phase number is indicated north-west of each subplot. The number of strong explosions is indicated, north-east of each subplot, in red.

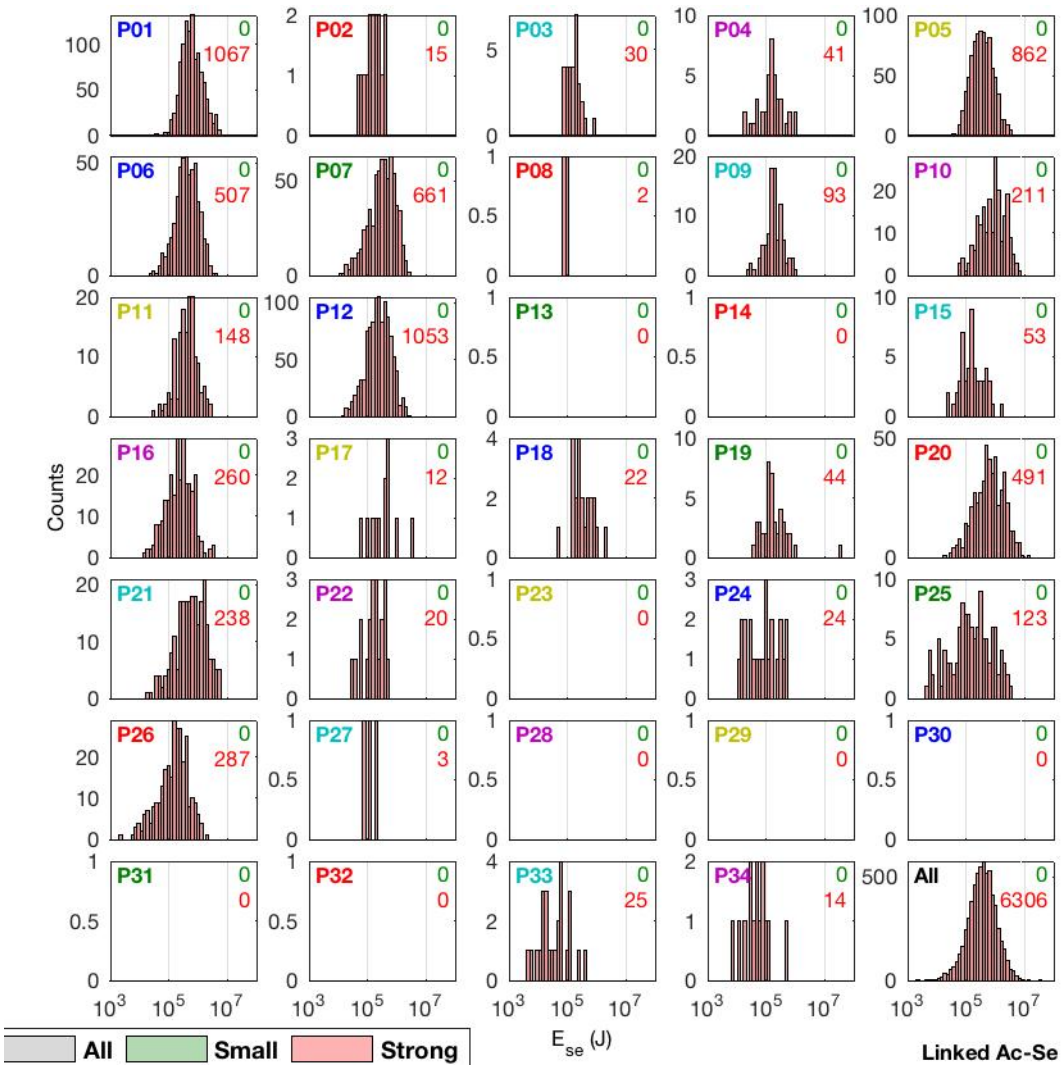

Figure C.17 – Distribution of the seismic energy per phase for all strong seismo-infrasonic events (>340 Pa at 100 m). The phase number is indicated north-west of each subplot. The number of strong explosions is indicated, north-east of each subplot, in red.

C.3 Stack of all strong infrasonic events

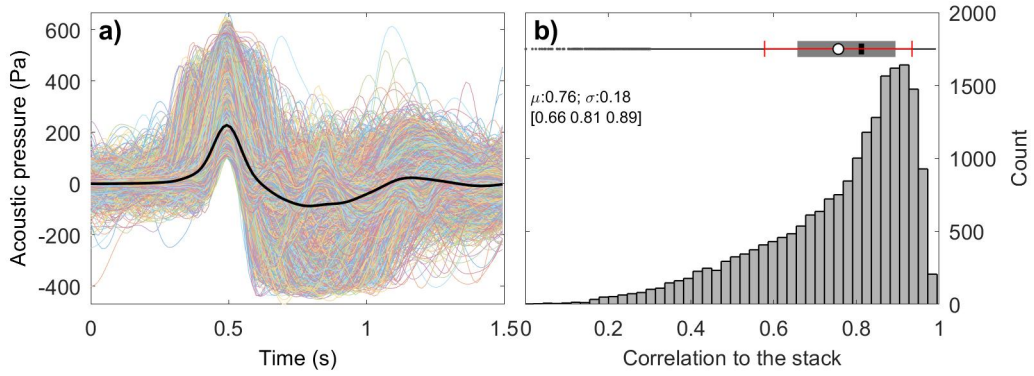

Figure C.18 – a)Stack of all strong events detected on infrasonic records at Yasur in Sept-Nov 2016. b) distribution of the correlation coefficient of each strong event to the stack, with the boxplot.

C.4 Classes of infrasonic waveform of the strong Strombolian explosions per phase

The classification is done using the programme `pg_classEvent` with a minimum coefficient of correlation at 85 %, a maximum of 10 classes per phases and a minimum of 20 events per classes (Section 3.7).

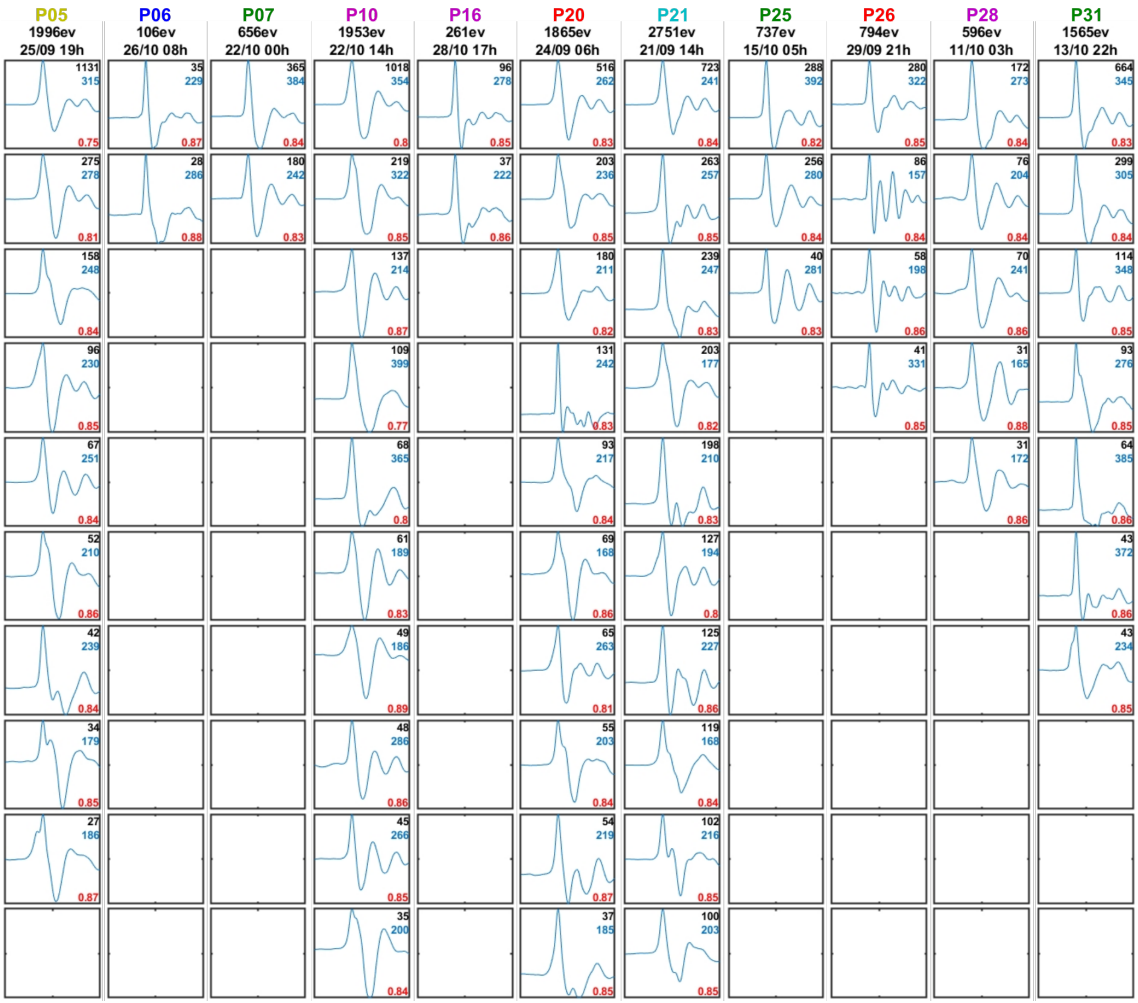

Figure C.19 – Classes, per phase, of infrasonic waveforms of the strong Strombolian explosions. The red number at the bottom right indicate the mean correlation of the classe, the black and blue numbers at the top right the number of events and the amplitude, in Pascal at 340 m (Parameters: `ThrCorr` = 85 %, `nClassMax` = 85 and `nEvMin_perClass` = 85)

C.5 Tables of comparison of the distributions

Table C.1 – Comparison of the distributions of the infrasonic duration per phase for infrasonic events.

Category	**Small explosions**	**Strong explosions**
Q1: P02; P08	OK	not enough data
Q2: P22; P24	$\sim$ OK; LoF during P24	not enough data for P22; LoF in P24
I1: P01; P33–34	$\sim$ OK	not enough data in P33–34
I2: P03–04; P09	bi-modality better marked in P09	P04$\sim$P09; P03$\neq$ or not enough data
I3: P12; P18	bi-modality better marked in P12; LoF in P12	bi-modality better marked in P12; LoF in P12
S1: P05–07; P16; P20–21; P25–26	bi-modality for P16	larger distributions for P20–21
S2: P10; P28; P31	P10 and P31 OK	OK

OK means that the distributions are similar; $\sim$ OK means that the distributions are quite similar
LoF means there are energetic low frequencies (0.10 Hz–0.50 Hz) during that phases that can induce a bias

Table C.2 – Comparison of the distributions of the infrasonic duration per phase for seismo-infrasonic events.

Category	**Small explosions**	**Strong explosions**
Q1: P02; P08	OK	not enough data
Q2: P22; P24	longer tail for P24 (LoF)	$\sim$ OK but not enough data for P24 and LoF during P24
I1: P01; P33–34	$\sim$ OK	not enough data for P33–34
I2: P03–04; P09	OK	not so bad
I3: P12; P18	bi-modality of P12 better marked	not enough data for P18
S1: P05–07; P16; P20–21; P25–26	large distribution for P16 than for P05–P07; longer duration for P25	not so bad
S2: P10; P28; P31	seismic gaps during P28 and P31	seismic gaps during P28 and P31

OK means that the distributions are similar; $\sim$ OK means that the distributions are quite similar
LoF means there are energetic low frequencies (0.10 Hz–0.50 Hz) during that phases that can induce a bias

Table C.3 – Comparison of the distributions of the gas velocity per phase for all infrasonic events.

Category	Small explosions	Strong explosions
Q1: P02; P08	OK	not enough data
Q2: P22; P24	OK	not enough data but OK
I1: P01; P33–34	OK	not enough data but not so bad
I2: P03–04; P09	OK	P04∼P09, not P03
I3: P12; P18	similar modes but bump that is not on the same side of the mode	∼ OK
S1: P05–07; P16; P20–21; P25–26	very narrow distributions; P16 and P25 have a tail towards the high values	OK
S2: P10; P28; P31	all ≠; P10∼S1; P16∼P28	P10 and P31 OK; P28 not so bad

OK means that the distributions are similar; ∼ OK means that the distributions are quite similar
LoF means there are energetic low frequencies (0.10 Hz–0.50 Hz) during that phases that can induce a bias

Table C.4 – Comparison of the distributions of the gas velocity per phase for seismo-infrasonic events.

Category	Small explosions	Strong explosions
Q1: P02; P08	OK	not enough data
Q2: P22; P24	OK	not enough data
I1: P01; P33–34	P33–34 OK; two modes for P01 (LoF?)	not enough data for P33–34
I2: P03–04; P09	P04 and P09 OK; P03 looks like P02 and P08	not so bad
I3: P12; P18	∼ OK	∼ OK seismic gap
S1: P05–07; P16; P20–21; P25–26	OK except for P16 that is very wide	P05–07 and P16 OK; P20–21 and P25–26 have higher velocities
S2: P10; P28; P31		seismic gap in P28 and P21; P10∼ P20–21,25–26

OK means that the distributions are similar; ∼ OK means that the distributions are quite similar
LoF means there are energetic low frequencies (0.10 Hz–0.50 Hz) during that phases that can induce a bias

Table C.5 – Comparison of the distributions of the gas volume per phase for seismo-infrasonic events.

Category	Small explosions	Strong explosions
Q1: P02; P08	∼ OK	not enough data
Q2: P22; P24	∼ OK; longer tail towards the high values for P24 (LoF)	not enough data
I1: P01; P33–34	not so bad; part of the small of P01 hidden by the strong but LoF during P01	∼ OK but not enough data P33-34
I2: P03–04; P09	P03–04 OK; P09 not so bad	not enough data
I3: P12; P18	OK	seismic gap in P18
S1: P05–07; P16; P20–21; P25–26	wonderful bi-modality small/strong except for P25–26; small OK except for P25	OK
S2: P10; P28; P31	P10 larger than P05–07	seismic gap in P28 and P31; P10 has a bump that does not exists on S1

OK means that the distributions are similar; ∼ OK means that the distributions are quite similar
LoF means there are energetic low frequencies (0.10 Hz–0.50 Hz) during that phases that can induce a bias

Table C.6 – Comparison of the distributions of the ground velocity per phase for seismo-infrasonic events. Be aware that P01 and P02–34 were recorded from two different sites, with different sensors and that the records of P01 are not correct from the instrumental response, yet.

Category	**Small explosions**	**Strong explosions**
Q1: P02; P08	OK	not enough data
Q2: P22; P24	$\sim$ OK	not enough data
I1: P01; P33–34	OK	$\sim$ OK but not enough data
I2: P03–04; P09	OK	$\sim$ OK but not enough data
I3: P12; P18	seismic gaps in P18	seismic gaps in P18
S1: P05–07; P16; P20–21; P25–26	OK	P05 and P07 slightly smaller than other phases of S1
S2: P10; P28; P31	seismic gaps in P28 and P31	seismic gaps in P28 and P31; P10 at the same level than P06

OK means that the distributions are similar; $\sim$ OK means that the distributions are quite similar

Table C.7 – Comparison of the distributions of the seismic duration per phase for seismo-infrasonic events. Be aware that P01 and P02–34 were recorded from two different sites, with different sensors and that the records of P01 are not correct from the instrumental response, yet.

Category	**Small explosions**	**Strong explosions**
Q1: P02; P08	OK	not enough data
Q2: P22; P24	OK	not enough data
I1: P01; P33–34	lower mode for P33–34	not enough data for P33-34; two modes in P01
I2: P03–04; P09	OK	not enough data
I3: P12; P18	$\sim$ OK but seismic gaps in P18	seismic gaps in P18
S1: P05–07; P16; P20–21; P25–26	$\sim$ OK except for P26	P05–07 OK; longer duration during P16; P20$\sim$P21; P25$\sim$P26
S2: P10; P28; P31	seismic gaps in P28 and P31; $\neq$ S1	seismic gaps in P28 and P31

OK means that the distributions are similar; $\sim$ OK means that the distributions are quite similar

Table C.8 – Comparison of the distributions of the seismic energy per phase for seismo-infrasonic events. Be aware that P01 and P02–34 were recorded from two different sites, with different sensors and that the records of P01 are not correct from the instrumental response, yet.

Category	**Small explosions**	**Strong explosions**
Q1: P02; P08	OK	not enough data
Q2: P22; P24	OK; $\neq$Q1 which has narrower distributions	not enough data
I1: P01; P33–34	$\sim$ OK	not enough data in P33–34;
I2: P03–04; P09	OK	$\sim$ OK but not enough data for P03
I3: P12; P18	$\sim$ OK but seismic gaps in P18	seismic gaps in P18
S1: P05–07; P16; P20–21; P25–26	$\sim$ OK; P06 stronger than P05 and P07; P25–26 larger	larger for P20–21; larger again for P25–26
S2: P10; P28; P31	P10$\sim$P05; P10 larger than P06–07; ;seismic gaps in P28 and P31	higher mode for P10 than S1;seismic gaps in P28 and P31

OK means that the distributions are similar; $\sim$ OK means that the distributions are quite similar

C.6 Bubble diameter in the reservoir

Table C.9 – Calculation of the bubble diameter in the reservoir for a critical gas flux at $1.5\,m^3.s^{-1}$ in the reservoir (active degassing). The influence of the magma viscosity and the surface tension is shown in figure C.20

σ_{gas} ($kg.s^{-2}$)	μ_{magma} (Pa.s)	μ_{foam} (Pa.s)	S_{res} (m^2)	C_{geom}	$\bar{h}_{foam}$	$d_{b,res}$ (µm)
0.10	10^1	9.9×10^1	7.6×10^4	1.64	0.61	44
0.10	10^1	9.9×10^1	2.0×10^5	1.69	0.59	42
0.10	10^1	9.9×10^1	1.0×10^6	1.77	0.56	41
0.10	10^2	9.9×10^2	7.6×10^4	1.64	0.61	25
0.10	10^2	9.9×10^2	2.0×10^5	1.69	0.59	24
0.10	10^2	9.9×10^2	1.0×10^6	1.77	0.56	23
0.10	10^3	9.9×10^3	7.6×10^4	1.64	0.61	14
0.10	10^3	9.9×10^3	2.0×10^5	1.69	0.59	13
0.10	10^3	9.9×10^3	1.0×10^6	1.77	0.56	13
0.10	10^4	9.9×10^4	7.6×10^4	1.64	0.61	8
0.10	10^4	9.9×10^4	2.0×10^5	1.69	0.59	8
0.10	10^4	9.9×10^4	1.0×10^6	1.77	0.56	7
0.36	10^1	9.9×10^1	7.6×10^4	1.64	0.61	158
0.36	10^1	9.9×10^1	2.0×10^5	1.69	0.59	153
0.36	10^1	9.9×10^1	1.0×10^6	1.77	0.56	146
0.36	10^2	9.9×10^2	7.6×10^4	1.64	0.61	89
0.36	10^2	9.9×10^2	2.0×10^5	1.69	0.59	86
0.36	10^2	9.9×10^2	1.0×10^6	1.77	0.56	82
0.36	10^3	9.9×10^3	7.6×10^4	1.64	0.61	50
0.36	10^3	9.9×10^3	2.0×10^5	1.69	0.59	48
0.36	10^3	9.9×10^3	1.0×10^6	1.77	0.56	46
0.36	10^4	9.9×10^4	7.6×10^4	1.64	0.61	28
0.36	10^4	9.9×10^4	2.0×10^5	1.69	0.59	27
0.36	10^4	9.9×10^4	1.0×10^6	1.77	0.56	26

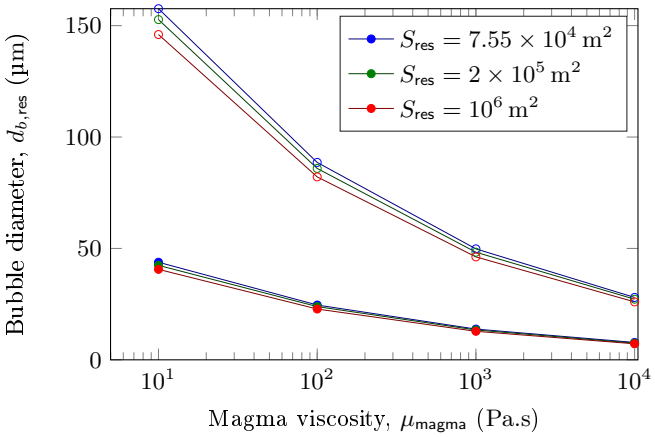

Figure C.20 – Bubble diameter $d_{b,\text{res}}$ in the reservoir as a function of the magma viscosity μ_{magma} for dry magma ($\sigma_{\text{gas}} = 0.36\,\text{kg.s}^{-2}$, open symbols) and for wet magma ($\sigma_{\text{gas}} = 0.10\,\text{kg.s}^{-2}$, plain symbols). The critical gas flux is that of the active degassing ($1.5\,\text{m}^3\text{.s}^{-1}$ in the reservoir.)

Table C.10 – Calculation of the bubble diameter in the reservoir for a critical gas flux at $14.8\,\text{m}^3\text{.s}^{-1}$ in the reservoir (total degassing).

σ_{gas} (kg.s^{-2})	μ_{magma} (Pa.s)	μ_{foam} (Pa.s)	S_{res} (m^2)	C_{geom}	$\bar{h}_{\text{foam}}$	$d_{b,\text{res}}$ (µm)
0.10	10^1	9.9×10^1	7.6×10^4	1.64	0.61	25
0.10	10^1	9.9×10^1	2.0×10^5	1.69	0.59	24
0.10	10^1	9.9×10^1	1.0×10^6	1.77	0.56	23
0.10	10^2	9.9×10^2	7.6×10^4	1.64	0.61	14
0.10	10^2	9.9×10^2	2.0×10^5	1.69	0.59	14
0.10	10^2	9.9×10^2	1.0×10^6	1.77	0.56	13
0.10	10^3	9.9×10^3	7.6×10^4	1.64	0.61	8
0.10	10^3	9.9×10^3	2.0×10^5	1.69	0.59	8
0.10	10^3	9.9×10^3	1.0×10^6	1.77	0.56	7
0.10	10^4	9.9×10^4	7.6×10^4	1.64	0.61	4
0.10	10^4	9.9×10^4	2.0×10^5	1.69	0.59	4
0.10	10^4	9.9×10^4	1.0×10^6	1.77	0.56	4
0.36	10^1	9.9×10^1	7.6×10^4	1.64	0.61	89
0.36	10^1	9.9×10^1	2.0×10^5	1.69	0.59	87
0.36	10^1	9.9×10^1	1.0×10^6	1.77	0.56	83
0.36	10^2	9.9×10^2	7.6×10^4	1.64	0.61	50
0.36	10^2	9.9×10^2	2.0×10^5	1.69	0.59	49
0.36	10^2	9.9×10^2	1.0×10^6	1.77	0.56	47
0.36	10^3	9.9×10^3	7.6×10^4	1.64	0.61	28
0.36	10^3	9.9×10^3	2.0×10^5	1.69	0.59	27
0.36	10^3	9.9×10^3	1.0×10^6	1.77	0.56	26
0.36	10^4	9.9×10^4	7.6×10^4	1.64	0.61	16
0.36	10^4	9.9×10^4	2.0×10^5	1.69	0.59	15
0.36	10^4	9.9×10^4	1.0×10^6	1.77	0.56	15

Chapter D

Vanuatu

D.1 Correspondance with Benjamin Simons (Auckland university) and Esline Garaebiti (VMGD)

Esline: (15/08/2016) *The Activity in Tanna these days is quite rough, approaching the Yasur crater is almost forbidden.*

Benjamin: (13/10/2016) *The activity has benn VERY dangerous the last three days so time in these areas. A large bomb landed only 1m from your east site yesterday and was still hot when we arrived. The west has had bombs flying at low angles over the ridge for many days. The time we can spend there is very limited.*

Benjamin: (15/10/2016) *Im really sorry to tell you that the activity is still very high. Bombs landing in all directions. I have not been able to get to you're stations. I can't even get to either of my sites (the weather post or ir site). As a result of this I think that my cameras have stopped as the solar panels will be caked and hard drives full, and the weather station will be completely chocked with ash. Im loosing a lot of data as well.*

Benjamin: (17/10/2016) *Some good and bad news. The good is that activity is now getting back to normal levels. Rain and ash are still issues but we have been able to get to the crater rim to check the eastern site. I cleared your solar panel today and noticed that your mb is still operational. We haven't been able to access the west rim yet but may have a chance tomorrow.*

Benjamin: (18/11/2016) *Yasur is still quite low in activity. I am in the process of arranging an activity log so will let you know when I finish it to give you an idea of how the activity changed over the 3 months.*

Benjamin: (30/01/2017) *Good to know you now have the MB record. That's interesting about the levels of variation in pressure. I've been looking through my observation data and noticed some real phases of higher magnitude and more frequent explosions as well as a few periods of very low power and low eruption frequency.*

D.2 Alert bulletins

Table D.1 – VANUATU VOLCANO ALERT BULLETIN - TANNA ACTIVITY (Vanuatu Meteorology and Geohazard Departement). The exclusion zones can be found in figure D.1. The Vanuatu Volcanic Alert Level System is described in table D.2.

Year	n°	Date	Level	Extract	Exclusion zone
2018	7	24/09	2	Yasur volcano is continuing in the major unrest state. [...] **Alert Level for Yasur has been at the Level 2 since 18th October 2016.**	permanent zone
2018	6	23/08	2	*idem.*	permanent zone
2018	5	11/07	2	*idem.*	permanent zone
2018	4	07/06	2	*idem.*	permanent zone
2018	3	25/04	2	*idem.*	permanent zone
2018	2	19/03	2	*idem.*	permanent zone
2018	1	30/01	2	Yasur volcano is continuing in the major unrest state. The Volcanic Alert Level remains at Level 2. [...] **Alert Level for Yasur has been at the Level 2 since 18th October 2016.**	permanent zone
2017	11	08/12	2	Yasur volcanic activity continue to remain at the level of major unrest state. [...] Latest observation and analysis of seismic data confirm that explosions remain strong and volcanic bombs may fall in and/or around the crater. Eruptive vents may emitted volcanic ash and gas cloud. Nearby villages from the volcano may affected by ash falls and volcanic gas especially those exposed to trade wind direction. **Alert Level for Yasur was at the Level 2 since 18th October 2016.**	permanent zone
2017	10	31/10	2	*idem.*	permanent zone
2017	9	29/09	2	*idem.*	permanent zone
2017	8	30/08	2	*idem.*	permanent zone
2017	7	21/07	2	*idem.*	permanent zone
2017	6	22/06	2	*idem.*	permanent zone
2017	5	22/05	2	*idem.*	permanent zone
2017	4	19/04	2	*idem.*	permanent zone
2016	10	18/10	2	The Alert Level for Tanna Volcano **is lowered to Level 2.**	permanent zone
2016	9	**15/10**	3	The Alert Level for Tanna Volcano **has increased to Level 3.** This means that volcanic explosions could become more intense, volcanic bombs may fall in and/or around the crater to the parking area and volcanic gas and ashes can also affect some villages especially areas exposed to trade winds.	permanent zone, **danger zone A**
2016	8	10/10	2	The Alert Level for Tanna Volcano remains at Level 2.	permanent zone
2016	7	09/09	2	*idem.*	permanent zone
2016	6	02/08	2	*idem.*	permanent zone
2016	5	28/06	2	*idem.*	permanent zone

Table D.2 – Vanuatu Volcanic Alert Level System. From http://www.vmgd.gov.vu/vmgd/images/geo-media/docs/VVAL_System-V2.0.png

5	very large eruption	Danger beyond caldera, on entire and surrounding islands and also a chance of flank eruption
4	moderate eruption	Danger on volcanic cone, caldera and all island, possibility of very large eruption and also chance of flank eruption
3	minor eruption	Danger on volcanic cone, within caldera and other specific area, possibility of moderate eruption and also chance of flank eruption
2	major unrest	Danger around the crater rim and specific area, notable/large unrest, considerable possibility of eruption and also chance of flank eruption
1	signs of volcanic unrest	notable signs of unrest, possible danger near eruptive vents
0	normal	No signs of change in the activity, limited danger

Figure D.1 – Yasur safety zones. From http://www.vmgd.gov.vu/vmgd/images/geo-media/docs/yasur_safety.pdf

UNIVERSITÉ SORBONNE PARIS CITÉ

The variability of the Strombolian activity

par
Viviane Souty

Résumé
L'activité strombolienne, caractérisée par des séries de petites explosions, existe dans le monde entier et dans divers contexts tectoniques. La variabilité de l'activité Strombolienne est observée à l'échelle mondiale et à l'échelle d'un édifice volcanique. Deux études multi-disciplinaires nous ont permis de caractériser la variabilité de l'activité strombolienne.
Une étude thermo-infrasonique à l'Erta'Ale (Éthiopie), au Piton de la Fournaise (Ile de la Réunion) et au Yasur (Vanuatu) a permis de caractériser l'activité faible et forte à partir de nombreux paramètres géophysiques. Le bilan énergétique thermo-infrasonique valide l'existence d'un mécanisme unique de fragmentation pour l'activité strombolienne. Nous montrons aussi que l'activité strombolienne, souvent persistente émet des gros volumes de gaz qui peuvent intéragir avec l'atmosphère. Ces volumes moyennés sur quelques siècles sont équivalents aux volumes de gaz émis par de plus grosses éruptions volcaniques, beaucoup moins fréquentes, telle que l'éruption du Pinatubo en 1991.
Des données infrasoniques, sismiques et thermiques acquises pendant deux mission de terrain au Yasur révèle la coexistence des deux mécanismes de formation des bulles que sont la coalescence progressive dans le conduit et la coalescence massive au toit du réservoir. La coalescence massive au toit du réservoir est généré pour un flux critique au delà duquel la mousse de gaz au toit du réservoir devient instable. Cette valeur critique permet d'estimer un diamètre des bulles dans le réservoir en accord avec les valeurs données pour d'autres systèmes basaltiques (Etna, Italie ; Kilauea, USA ; Erta'Ale, Éthiopie).
Mots clés : Strombolien ; infrasons ; thermique ; sismique ; Yasur ; Piton de la Fournaise.

Abstract
Strombolian activity, characterised by series of small explosions at open-vent volcanoes, exists worldwide in various tectonic contexts. The variability of the Strombolian activity can be observed on a global scale and on the scale of a volcanic system. We performed two multidisciplinary studies to characterise the variability of the Strombolian activity.
A thermo-infrasonic study at Erta'Ale (Ethiopia), Piton de la Fournaise (Réunion Island, France) and Yasur (Tanna Island, Vanuatu) allowed us to characterised the Strombolian activity as small and strong from numerous geophysical parameters. The thermo-infrasonic energy budget validated the existence of a sole mechanism of fragmentation for all Strombolian explosions. The Strombolian activity, often persistent, produces large volumes of gas that can interact with the atmosphere. These larges gas volumes are of the same order of magnitude, when averaged on a few centuries, than the gas volumes produced by larger volcanic eruptions, far less frequent, such as the Pinatubo eruption in 1991.
Infrasonic, seismic and thermal measurements during two field campaigns at Yasur highlighted the coexistence of the progressive coalescence into the conduit and the massive coalescence in the reservoir that are responsible for the bubble formation. The massive coalescence exists, when the critical gas flux, above which the foam layer at the top of the reservoir becomes unstable, is exceeded. This critical gas flux allowed us to estimate the bubble diameter in the reservoir and gave consistent values compared to values obtained at other basaltic systems (Etna, Italy; Kilauea, USA; Erta'Ale, Ethiopia).
Keywords: Strombolian; infrasounds; thermal; seismic; Yasur; Piton de la Fournaise.